

Zhong, Yanyong (2025) *Hydrogen release in composite complex hydride systems*. PhD thesis.

https://theses.gla.ac.uk/85517/

Copyright and moral rights for this work are retained by the author

A copy can be downloaded for personal non-commercial research or study, without prior permission or charge

This work cannot be reproduced or quoted extensively from without first obtaining permission from the author

The content must not be changed in any way or sold commercially in any format or medium without the formal permission of the author

When referring to this work, full bibliographic details including the author, title, awarding institution and date of the thesis must be given

Enlighten: Theses
https://theses.gla.ac.uk/
research-enlighten@glasgow.ac.uk

Hydrogen release in composite complex

hydride systems



Yanyong Zhong

Submitted in fulfilment the requirements for the

Degree of Doctor of Philosophy

School of Chemistry

College of Science and Engineering

University of Glasgow

July 2025

Abstract

Pollution and global warming can result from the rapid usage of fossil fuel resources. In the future, fossil fuels will be run out. As a result, renewable and clean energy sources such as hydrogen technologies may be a good choice to be developed. Many renewable energy sources, have drawbacks, such as high storage and transition costs. One method is to store energy chemically as a clean fuel. Hydrogen have one of the greatest possibilities due to its availability, high energy density, and ability to be produced sustainably.

Currently, the most mature hydrogen storage technologies are compressed gas tanks and liquid hydrogen storage. However, both approaches face certain limitations. For compressed gas tanks, hydrogen's low density requires a large storage volume; applying high pressure can reduce the volume, but this necessitates tank materials with exceptional compressive strength. Liquid hydrogen storage, on the other hand, requires cryogenic conditions at approximately -253 °C, which poses significant technical and economic challenges. In this context, the development of solid-state hydrogen storage emerges as a promising alternative, as it offers greater stability compared with gaseous or liquid hydrogen and enables higher volumetric storage capacity relative to weight. Nevertheless, the practical application of solid-state storage still faces critical challenges, including limited reversibility, high desorption temperatures, and insufficient hydrogen release rates. Therefore, this study investigates five representative solid-state hydrogen storage systems to elucidate their properties and characteristics, thereby providing insights for the future development of solid-state hydrogen storage technologies.

This thesis investigated the dehydrogenation kinetics and reaction mechanisms of five hydride systems: NaH-NaOH, NaAlH₄-NaOH, NaBH₄-NaOH, Ca₄Mg₃H₁₄-NaH, and NaAlH₄/MgH₂-Guanidine(CH₅N₃). The selection of these systems was based on their potential for practical hydrogen storage. Sodium-based hydrides and hydroxides are inexpensive, lightweight, and exhibit relatively high theoretical hydrogen capacities, making them promising candidates for large-scale applications. The NaH-NaOH, NaAlH₄-NaOH, and NaBH₄-NaOH systems were studied to evaluate the influence of hydroxide incorporation on the hydrogen release behaviour of simple and complex sodium hydrides. The Ca₄Mg₃H₁₄-NaH system was chosen as a mixed alkaline composite, where synergistic effects may arise from multicomponent interactions. In addition, the NaAlH₄/MgH₂-Guanidine(CH₅N₃) system was introduced as an organic-inorganic hybrid, providing a new strategy to improve dehydrogenation pathways through organic molecular. Through thermal treatment, ball milling, catalyst addition, and variations in molar ratios, the dehydrogenation behaviour of these systems was systematically optimized. Thermal

analysis, X-ray diffraction, and Raman spectroscopy were employed to monitor phase change and deduce the corresponding reaction mechanisms.

In the NaH-NaOH system, ball milling significantly improved dehydrogenation kinetics, enabling a two-step mechanism. The first step involves the formation of a solid solution, NaH_{1-x}(OH)_x, between 170 °C and 210 °C, followed by the decomposition of this intermediate to release hydrogen. Under optimal ball milling conditions (400 rpm, 2 hours) and at a NaH:NaOH molar ratio of 1.15:1, the system exhibited the lowest dehydrogenation peak temperature (346 °C) and the highest hydrogen release (3.08 wt.%). Prior to catalyst optimization, the activation energy of the ball-milled NaH-NaOH system was determined to be 75.85 kJ mol⁻¹. Subsequent addition of catalysts significantly reduced the activation energy, with 5 wt.% Ni and SiC showing the most pronounced effects, lowering the activation energy to 41.24 kJ mol⁻¹ and 46.79 kJ mol⁻¹, respectively. SiC primarily reduces the activation energy via physical mechanisms. As a milling aid, SiC decreases particle size, increases the contact area of reactants, and shortens hydrogen diffusion pathways, thereby facilitating the reaction. In terms of the Arrhenius relationship, this process enhances the pre-exponential factor (A) and increases the probability of effective molecular interactions, which is reflected in an apparent reduction of the activation energy (E_a). Ni nanoparticles may disperse uniformly across the NaOH-NaH interface, providing active sites that facilitate hydrogen atom desorption.

For the NaAlH₄-NaOH system, the mechanistic insights gained from the NaH-NaOH system were applied to enhance the kinetics of NaAlH₄ decomposition. This led to changes in the third step of NaAlH₄ decomposition, which is crucial for improving the overall kinetics. In the hand-mixed NaAlH₄-NaOH system, the following reactions were observed:

$$NaAlH_4 + 4NaOH = 1/3Na_3AlH_6 + 2/3Al + H_2 + 4NaOH$$

 $1/3Na_3AlH_6 + 4NaOH = NaH + 1/3Al + 1/2H_2 + 4NaOH$
 $NaH + Al + 4NaOH = Na_5AlO_4 + 5/2H_2$

Notably, the first step of the dehydrogenation reaction transitions from an exothermic to an endothermic process with the addition of NaOH. When even more NaOH is added (e.g., in a 1:4 NaAlH₄:NaOH ratio), the second step of the dehydrogenation reaction also shifts from exothermic to endothermic. Under ball-milling conditions, NaOH reacts with NaAlH₄ to form Na₃AlH_{6-x}(OH)_x, As the NaOH content increases, the Na₃AlH_{6-x}(OH)_x further decomposes to NaH.

The reaction between NaBH₄ and NaOH produces Na-B-O-H intermediates. When ball-milled for 10 hours, the 1:4 NaBH₄:4NaOH mixture can be completely converted into

Na-B-O-H intermediates. Prior to heating to 300°C, these intermediates undergo a phase change at 240 °C-250 °C, and the nature of this phase change varies depending on the molar ratio of NaOH added. For instance, ball-milled (2h) 1:3 NaBH₄:NaOH yields Na₃BO₃, Na, NaOH, and H₂ when heated to 400°C, while ball-milled (2h) 1:4 NaBH₄:NaOH produces Na₃BO₃, Na₂O, NaOH, and H₂ under the same conditions.

For the Ca₄Mg₃H₁₄-NaH system, ball milling a 1:1 Ca₄Mg₃H₁₄:NaH mixture at 400 rpm for 2 hours enables NaH to alter the reaction pathway, leading to the formation of Ca₄Mg₂H₁₄ and NaMgH₃. Upon heating to 348 °C, the interaction between NaMgH₃ and Ca₄Mg₃H₁₄ results in a significant reduction of the overall dehydrogenation peak temperature by 102 °C (from 450 °C to 348 °C). This interaction not only facilitates the earlier decomposition of Ca₄Mg₃H₁₄ but also promotes the premature decomposition of NaMgH₃ (from 400 °C to 348 °C).

For the NaAlH₄/MgH₂-Guanidine (CH₅N₃) system, the thermal decomposition of CH₅N₃ alone follows the reaction:

$$3CH_5N_3 \rightarrow C_3H_6N_6 + 3NH_3$$
 $T = 179 \, ^{\circ}C$

Subsequently, C₃H₆N₆ primarily evaporates at approximately 300 °C, with a minor fraction undergoing decomposition. In the NaAlH₄-CH₅N₃ system, a reaction occurs at 150 °C, resulting in the release of hydrogen gas and the formation of Al and an amorphous Na-C-N compound. In contrast, the reaction between MgH₂ and CH₅N₃ is significantly more complex, and at present, only the possible reaction pathways can be proposed based on available data.

Table of Content

Abstract	2
List of Tables	10
List of Figures	11
Acknowledgement	24
Definitions and Abbreviation	25
1. Introduction	26
1.1 The Current Status of Hydrogen	26
1.1.1 Environment Benefits	26
1.1.2 Environment Challenges	28
1.2 Hydrogen Storage Methods	29
1.2.1 Compressed Hydrogen	29
1.2.2 Liquefied Hydrogen	30
1.2.3 Cryo-Compressed Hydrogen	30
1.2.4 Metal Hydrides	31
1.2.5 Complex Metal Hydrides	31
1.2.6 Physical Adsorption	31
1.2.7 Liquid Organic Hydrogen Carriers (LOHCs)	31
1.3 Solid-State Hydrogen Storage	32
1.3.1 Metal Hydrides	32
1.3.2 Complex Hydrides for Hydrogen Storage	34
1.3.3 Borohydrides	37
1.3.4 Modification and Optimisation Strategies for Solid State I Materials	
1.4 Hydride – Hydroxide Hydrogen Release Systems	39
1.5 Aim of Thesis	42
1.6 References	44

2.]	Experimental	51
	2.1 Sample Handling	51
	2.1.1 Gloveboxes	51
	2.2 Preparation methods and technique	53
	2.2.1 Mechanochemistry	53
	2.2.2 Schlenk Line	56
	2.2.3 Pot Furnaces	57
	2.2.4 Glassblowing	58
	2.3 Characterisation Techniques	60
	2.3.1 Crystallography and Diffraction	61
	2.3.2 Raman Spectrometry	67
	2.3.3 Thermal Analysis	69
	2.4 References	75
3.]	Dehydrogenation of NaOH-NaH with Various Catalysts	78
	3.1 Introduction	78
	3.1.1 Sodium Hydride and Sodium Hydroxide system	78
	3.1.2 Aim	79
	3.2 Experimental	79
	3.2.1 Preparation of the System	79
	3.2.2 Ball-milling of NaOH-NaH	79
	3.2.3 TG-DTA-MS Studies	80
	3.2.4 Powder X-ray Diffraction (PXD)	80
	3.2.5 Catalyst Preparation	81
	3.3 Result and Discussion	82
	3.3.1 Thermal Treatment of the Individual NaOH and NaH Components	82
	3.3.2 Dehydrogenation of NaOH-NaH and Mechanism	89
	3.3.3 Different factors that affect the dehydrogenation	93
	3.3.4 Activation Energy	99

3.3.5 Additives and Catalysts	102
3.4 Conclusion	123
3.5 References	125
4. Dehydrogenation in the NaAlH4-NaOH System	128
4.1 Introduction	128
4.1.1 Sodium alanate, NaAlH ₄	128
4.1.2 Aims and objectives of this work	130
4.2 Experimental	131
4.2.1 Mixing and milling of NaOH-NaAlH ₄	131
4.2.2 TG-DTA-MS Studies	131
4.2.3 Powder X-ray Diffraction (PXD)	132
4.2.4 Raman spectroscopy	132
4.3 Results and discussion	132
4.3.1 Thermal Treatment of NaAlH ₄	132
4.3.2 Thermal Treatment of Al and NaOH	137
4.3.3 Thermal Treatment of Hand-mixed NaAlH ₄ -NaOH and Research	
4.3.4 Ball-milling NaAlH ₄ with Differenct Molar Ratios of NaOH	147
4.3.5 Dehydrogenation reaction of ball-milled Na ₃ AlH ₆ -NaOH	with different
molar ratio	158
4.3.6 Synthesis of Na ₅ AlO ₄	166
4.4 Conclusion	168
4.5 References	170
5. Dehydrogenation in the NaBH4-NaOH system	171
5.1 Introduction	171
5.1.1 Sodium borohydride (NaBH ₄) as a solid-state hydrogen store	171
5.1.2 Purpose	172
5.2 Experimental	173
5.2.1 Milling of NaOH-NaBH ₄	173

	5.2.2 Powder X-ray Diffraction (PXD)	173
	5.3 Results and Discussion	174
	5.3.1 Thermal Treatment of NaBH ₄	174
	5.3.2 Mechanism of Ball-milled NaBH ₄ -xNaOH (x = 1, 2, 3, 4)	175
	5.4 Conclusion	187
	5.5 References	189
6.	Dehydrogenation of Ca ₄ Mg ₃ H ₁₄ -NaH	190
	6.1 Introduction	190
	6.1.1 Ternary Hydrides of the s-block Metals	190
	6.1.2 Purpose	192
	6.2 Experimental	193
	6.3 Results and Discussion	194
	6.3.1 Synthesis of Ca ₁₉ Mg ₈ H ₅₄ and Ca ₄ Mg ₃ H ₁₄	194
	6.3.2 Thermal Treatment of Ca ₄ Mg ₃ H ₁₄	195
	6.3.3 Investigations in the Ca ₄ Mg ₃ H ₁₄ -NaH system	197
	6.3.4 Improvement: Milling time, Rotation Speed and Mole Ra Ca ₄ Mg ₃ H ₁₄ -NaH	
	6.4 Conclusion	208
	6.5 References	210
7.	Dehydrogenation of Guanidine-NaAlH ₄ /MgH ₂ system	212
	7.1 Introduction	212
	7.1.1 Guanidine and its role in hydrogen release systems	212
	7.1.2 Aim	213
	7.2 Experimental	213
	7.2.1 Milling of guanidine and metal hydrides (either MgH ₂ or NaAlH ₄)	214
	7.2.2 Powder X-ray Diffraction (PXD)	214
	7.2.3 Synthesis of Guanidine	214
	7.3 Results and Discussion	215

9. Appendices	233
8. Conclusion and Future Work	230
7.5 References	228
7.4 Conclusions	226
7.3.3 Investigation of hydrogen release in the MgH ₂ -CH ₅ N ₃ system	220
7.3.2 Investigation of hydrogen release in the NaAlH ₄ -CH ₅ N ₃ system	218
7.3.1 Thermal Treatment of Guanidine	215

List of Tables

Table 1-1: Molecular weight, gravimetric capacity and decomposition temperatures for
LiH, NaH, MgH ₂ and CaH ₂ 32
Table 1-2: Molecular weight, theoretical gravimetric and temperatures of decomposition
for selected alanate. 35
Table 2-1: Basic crystallography notation and symmetry information for the seven crystal
systems63
Table 3-1: Crystallographic Data Obtained from the Rietveld Refinement for NaH(90%) as-received.
Table 3-2: Reaction condition, peak temperature and weight loss of NaOH-NaH samples ball milled for different durations.
Table 3-3: Reaction conditions, DTA peak temperatures and weight losses of the
NaOH-NaH samples with varying molar ratios, NaOH:NaH
Table 3-4: Reaction condition, peak temperature and weight loss of the NaOH-NaH
sample with the varying mole ratio of NaOH: NaH99
Figure 3-5: Reaction conditions and DTA peak temperatures of the NaOH-NaH samples
with varying wt.% rGO
Table 3-6: DTA peak temperatures and weight losses of the NaOH-NaH samples with varying wt.% Mg ₂ Si
Table 3-7: Activation energy of NaOH-NaH system with and without additives of rGO and Mg ₂ Si
Table 3-8: Activation energy of NaOH-NaH system with various additives
Table 4-1: Comparison of Sodium Alanate (NaAlH ₄) Storage Performance with and
without Ti Doping129
Table 4-2: Comparison of NaAlH ₄ As-received and As-reported Storage Performance 134
Table 4-3: Activation energies (determined by the Kissinger method) of NaAlH ₄ ,
hand-mixed Na AlH 4-NaOH and hand-mixed Na AlH 4-4NaOH 147

List of Figures

Figure 1-1: Schematic of a sustainable hydrogen energy cycle
Figure 2-1: Images of the: (a) a Saffron Scientific Omega gloveboxes employed for sample storage in this thesis, and (b) a mBraun UniLab glovebox employed for sample preparation and for housing the STA.
Figure 2-2: The simple schematic diagram of the cross section of the milling jar 54
Figure 2-3: Configuration of the milling jar in the Retsch PM100 planetary ball mill 56
Figure 2-4: Schlenk line used in the experiment
Figure 2-5: The pot furnace used in the experiment
Figure 2-6: Glassblowing used in the experiment
Figure 2-7: Simplified representation of the electromagnetic spectrum60
Figure 2-8 Schematic diagram of basic cubic unit cell
Figure 2-9: Schematic diagram of Bragg Diffraction path of X-rays on crystal planes. dhkl is the lattice spacing. θ is the angle between the lattice plane. 62
Figure 2-10: Bragg-Brentano reflection geometry used in X'Pert and Miniflex measurements
Figure 2-11: Air-sensitive sample holder for the: (a) X'Pert and (b) Miniflex powder X-ray diffractometers.
Figure 2-12: Schematic diagram of energy changes associated with Raman scattering 68
Figure 2-13: Schematic diagram of the optical path configuration of the micro-Raman spectroscopy system
Figure 2-14:Schematic of the STA instrument employed in this work71
Figure 2-15: Diagram of STA crucible arrangement
Figure 2-16: Faraday Cup detector used in the EGA employed in this work74
Figure 3-1: TG(red) and DTA(blue) profiles for as-received NaOH on heating from 35-400 °C at 5 °C min ⁻¹ under flowing Ar(g). The TGA profile is shown in red (right hand y-axis) and the DTA profile is shown in blue (left hand y-axis)
Figure 3-2: Mass spectrometry output for water (m/z = 18; black) and hydrogen (m/z = 2;red) as a function of temperature for as-received NaOH on heating from 35-400 °C at 5 °C min ⁻¹ under flowing Ar gas.

Figure 3-3: PXD patterns of NaOH as-received (I) and NaOH after drying (II). (1 represent NaOH)
Figure 3-4: TG(red) and DTA(blue) profiles for NaOH after drying on heating from 35-400 °C at 5 °C min ⁻¹ under flowing Ar(g).
Figure 3-5: Mass spectrometry output for water (m/z = 18; black) and hydrogen (m/z = 2;red) as a function of temperature for NaOH after drying on heating from 35-400 °C at 5 °C min ⁻¹ under flowing Ar gas.
Figure 3-6: TG(red) and DTA(blue) profiles for ball-milled NaOH (2h, 400rpm) on heating from 35-400 °C at 5 °C min ⁻¹ under flowing Ar(g)
Figure 3-7: TG(red) and DTA(blue) profiles for as-received NaH (purity: 90%) on heating from 35-400 °C at 5 °C min ⁻¹ under flowing Ar(g)
Figure 3-8: PXD patterns of ball-milled NaOH (dry, 1h, 400rpm; II) and as-received NaH (90 at.%; I). NaH pattern is experimental data taken for the as-received starting materials. (The arrows indicate NaOH in the NaH sample pattern.)
Figure 3-9: Profile plot from Rietveld refinement of as-received NaH (90%). (Purple represent NaOH; Blue represent NaH; Black represent observed line; Red represent calcualted line; Green represent background line)
Figure 3-10: TG(red) and DTA(blue) profiles for ball-milled 1:1.15 NaOH:NaH (2h, 400rpm) on heating from 35-420 °C at 5 °C min ⁻¹ under flowing Ar(g)
Figure 3-11: Mass spectrometry output for water (m/z = 18; black) and hydrogen (m/z = 2; red) as a function of temperature for a ball-milled 1:1.15 NaOH:NaH (2h, 400rpm) on heating from 35-420 °C at 5 °C min ⁻¹ under flowing Ar gas
Figure 3-12: PXD patterns of ball-milled NaOH-NaH before (I) and after heating to 170 (II), 210 (III), 240 (IV) °C under flowing Ar(g) (and cooling), respectively. (1 represent Na2O; 2 represent NaOH; 3 represent NaH)
Figure 3-13: PXD patterns of ball-milled NaOH-NaH (I) and after heating to 170 (II), 210 (III), 240 (IV) °C at 2θ 30-33° under flowing Ar(g) (and cooling), respectively. (1 represent NaH; 2 represent NaOH; 3 represent Na ₂ O)
Figure 3-14:TG(red) and DTA(blue) profiles for (a) ball-milled (b) "hand mixed" NaOH-NaH on heating from 35-420(500) °C at 5 °C min ⁻¹ under flowing Ar(g)93
Figure 3-15: Mass spectrometry output for water (m/z = 18; black) and hydrogen (m/z = 2; red) as a function of temperature for (a) ball-miled (b) hand mixed NaOH-NaH on heating from 35-420(500) $^{\circ}$ C at 5 $^{\circ}$ C min ⁻¹

Figure 3-16: TG(red) and DTA(blue) profiles for ball-milled 1:1.1 NaOH:NaH with milling time (a) 1h (b) 2h (c) 4h on heating 35-400 °C at 5 °C min ⁻¹ under flowing Ar(g)95
Figure 3-17: PXD patterns of 1:1.1 NaOH:NaH with varying milling time(1h, I; 2h, II; 4h, III) after heating to 400 °C under flowing Ar(g). (1 represent Na ₂ O; 2 represent NaOH) 95
Figure 3-18: TG(red) and DTA(blue) profiles for ball-milled NaOH-NaH (2h, 400rpm) with the different molar ratio of NaOH:NaH (a) 1:1.1(b) 1:1.15 (c) 1:1.20 (d) 1:1.25 on heating from 35-400 °C at 5 °C min ⁻¹ under flowing Ar(g)
Figure 3-19: PXD patterns of ball-milled NaOH:NaH (2h, 400rpm) with varying molar ratio of NaOH:NaH (1:1.1, I; 1:1.2, II;1:1.25 III) after heating to 400 °C under flowing Ar(g). (1 represent Na ₂ O; 2 represent NaOH; 3 represent Na)
Figure 3-20: TG(red) and DTA(blue) profiles for ball-milled 1:1.1 NaOH:NaH (2h) with the varing rotation speed (a) 300 rpm (b) 400 rpm on heating from 35-400 °C at 5 °C min ⁻¹ under flowing Ar(g)
Figure 3-21: TG(red) and DTA(blue) profiles for ball-milled 1:1.15 NaOH:NaH (2h, 400rpm) on heating from 35-400 °C at different heating rate (a) 2 °C min ⁻¹ (b) 5 °C min ⁻¹ (c) 10 °C min ⁻¹ (d) 20 °C min ⁻¹ under flowing Ar(g)
Figure 3-22: Mass spectrometry output for water (m/z = 18; black) and hydrogen (m/z = 2;red) as a function of temperature for a ball-milled 1:1.15 NaOH:NaH (2h, 400rpm) on heating from 35-400 °C at 2 °C min ⁻¹ under flowing Ar gas
Figure 3-23: Kissinger plots for dehydrogenation of ball-milled 1:1.15 NaH:NaOH (2h, 400r) on heating from 35-400 °C at heating rate 2, 5, 10, 20 °C min ⁻¹ under flowing Ar(g). Ea = 75.85 ± 3.41 kJ mol ⁻¹ .
Figure 3-24: PXD pattern of as-synthesis rGO
Figure 3-25: DTA profiles for ball-milled 1:1.15 NaOH:NaH (2h, 400rpm) with varying amounts of rGO additives (0 wt.%, purple; 2 wt.% black; 5 wt.%, red; 10 wt.%, blue; 20 wt.%, green) on heating from 35-450 °C at 5 °C min ⁻¹ under flowing Ar(g)
Figure 3-26: Kissinger plots for dehydrogenation of ball-milled 1:1.15 NaH:NaOH (2h, 400r) with 10 wt.% rGO on heating from 35-400 °C at heating rate 2, 5, 10, 20 °C min ⁻¹ under flowing Ar(g). Ea = 73.06 ± 3.32 kJ mol ⁻¹
Figure 3-27: PXD patterns of standard (I) and as-synthesised Mg ₂ Si (II)109
Figure 3-28: TG(red) and DTA(blue) profiles for as-synthesised Mg ₂ Si on heating from 35-600 °C at 10 °C min ⁻¹ under flowing Ar(g)
Figure 3-29: TG(red) and DTA(blue) profiles for ball-milled 1:1.15 NaOH:NaH (2h,

400rpm) with 5 wt.% Mg ₂ Si on heating from 35-450 °C at 5 °C min ⁻¹ under flowing Ar(g).110
Figure 3-30: Mass spectrometry output for water (m/z = 18; black) and hydrogen (m/z = 2;red) as a function of temperature for ball-milled 1:1.15 NaOH:NaH (2h, 400rpm) with 5 wt.% Mg ₂ Si on heating from 35-450 °C at 5 °C min ⁻¹ under flowing Ar(g)
Figure 3-31: TG(red) and DTA(blue) profiles for ball-milled 1:1.15 NaOH:NaH (2h, 400rpm) with 10 wt.% Mg ₂ Si on heating from 35-450 °C at 5 °C min ⁻¹ under flowing Ar(g).
Figure 3-32: Mass spectrometry output for water (m/z = 18; black) and hydrogen (m/z = 2;red) as a function of temperature for ball-milled 1:1.15 NaOH:NaH (2h, 400rpm) with 10 wt.% Mg ₂ Si on heating from 35-450 °C at 5 °C min ⁻¹ under flowing Ar(g)
Figure 3-34: PXD patterns for ball-milled 1:1.15 NaOH:NaH with 10 wt.% Mg ₂ Si after heating to 450 °C under flowing Ar(g). (and cooling to room temperature). (1 represent Na ₂ O; 2 represent Mg ₂ Si; 3 represent Na; 4 represent NaOH) Appendix A3-3 show the PXD patterns for the sample compared to stardard patterns from ICSD
Figure 3-35: Kissinger plots for dehydrogenation of ball-milled 1:1.15 NaH:NaOH (2h, 400r) with 5 wt.% Mg ₂ Si on heating from 35-400 °C at heating rate 2, 5, 10 and 20 °C min ⁻¹ under flowing Ar(g). Ea = 60.08 ± 6.95 kJ mol ⁻¹ . Peak temperature of dehydrogenation of sample on heating from 35-400 °C at heating rate 2, 10 and 20 °C min ⁻¹ was shown on the Appendix 3-4.
Figure 3-36: Kissinger plots for dehydrogenation of ball-milled 1:1.15 NaH:NaOH (2h, 400r) with 10 wt.% Mg ₂ Si on heating from 35-400 °C at heating rate 2, 5, 10 and 20 °C min ⁻¹ under flowing Ar(g). Ea = 48.52 ± 7.60 kJ mol ⁻¹ . Peak temperature of dehydrogenation of sample on heating from 35-400 °C at heating rate 2, 10 and 20 °C min ⁻¹ was shown on the Appendix 3-5.
Figure 3-37: DTA profiles for ball-milled 1:1.15 NaOH:NaH (2h, 400rpm) with various catalyst/additives on heating from 35-400 °C at 5 °C min ⁻¹ under flowing Ar(g)
Figure 3-39: Kissinger plots for dehydrogenation of ball-milled 1:1.15 NaH:NaOH (2h, 400r) with 5 wt.% Ni on heating from 35-400 °C at heating rate 2, 5, 10 and 20 °C min ⁻¹

sample on heating from 35-400 °C at heating rate 2, 10 and 20 °C min ⁻¹ was shown on the
Appendix 3-6
Figure 3-40: Kissinger plots for dehydrogenation of ball-milled 1:1.15 NaH:NaOH (2h, 400r) with 5 wt.% Ti on heating from 35-400 °C at heating rate 2, 5, 10 and 20 °C min ⁻¹ under flowing Ar(g). Ea = 55.99 ± 2.82 kJ mol ⁻¹ . Peak temperature of dehydrogenation of sample on heating from 35-400 °C at heating rate 2, 10 and 20 °C min ⁻¹ was shown on the Appendix 3-7.
Figure 3-41: Kissinger plots for dehydrogenation of ball-milled 1:1.15 NaH:NaOH (2h, 400r) with 5 wt.% TiF ₃ on heating from 35-400 °C at heating rate 2, 5, 10 and 20 °C min ⁻¹ under flowing Ar(g). Ea = 58.62 ± 4.15 kJ mol ⁻¹ .Peak temperature of dehydrogenation of sample on heating from 35-400 °C at heating rate 2, 10 and 20 °C min ⁻¹ was shown on the Appendix 3-8.
Figure 3-42: Kissinger plots for dehydrogenation of ball-milled 1:1.15 NaH:NaOH (2h, 400r) with 5 wt.% MoS ₂ on heating from 35-400 °C at heating rate 2, 5, 10 and 20 °C min ⁻¹ under flowing Ar(g). Ea = 56.33 ± 4.72 kJ mol ⁻¹ . Peak temperature of dehydrogenation of sample on heating from 35-400 °C at heating rate 2, 10 and 20 °C min ⁻¹ was shown on the Appendix 3-9.
Figure 3-43: Kissinger plots for dehydrogenation of ball-milled 1:1.15 NaH:NaOH (2h, 400r) with 5 wt.% SiC on heating from 35-400 °C at heating rate 2, 5, 10 and 20 °C min ⁻¹ under flowing Ar(g). Ea = 46.79 ± 1.77 kJ mol ⁻¹ . Peak temperature of dehydrogenation of sample on heating from 35-400 °C at heating rate 2, 10 and 20 °C min ⁻¹ was shown on the Appendix 3-10.
Figure 4-1: PXD pattern of ball-milled NaAlH ₄ (24 h; I) and NaAlH ₄ as-received (II)133
Figure 4-2: TG(red) and DTA(blue) profiles for ball-milled NaAlH ₄ (24h, 400rpm) on heating from 35-400 °C at 5 °C min ⁻¹ under flowing Ar(g).
Figure 4-3: Mass spectrometry output for water (m/z = 18; black) and hydrogen (m/z = 2;red) as a function of temperature for ball-milled NaAlH ₄ (24h, 400rpm) on heating from $35-400$ °C at 5 °C min ⁻¹ under flowing Ar(g).
Figure 4-4: PXD patterns of ball-milled NaAlH ₄ (24h, 400rpm) after heating to 180 (I), 200 (II) and 220 (III) °C under flowing Ar(g). (1 represent NaAlH ₄ ; 2 represent Na ₃ AlH ₆ ; 3 represent Al)
Figure 4-5: PXD patterns of ball-milled NaAlH ₄ (24h, 400rpm) after heating to 220 (I) and 250 (II) under flowing Ar(g) (1 represent NaAlH ₄ : 2 represent NaAlH ₄ : 3 represent Al)136

Figure 4-6: TG(red) and DTA(blue) profiles for hand mixed 1:1 NaOH:Al on heating from 35-450 °C at 5 °C min ⁻¹ under flowing Ar(g)
Figure 4-7: Mass spectrometry output for water (m/z = 18; black) and hydrogen (m/z = 2;red) as a function of temperature for hand mixed 1:1 Al:NaOH on heated from 35-450 °C at 5 °C min ⁻¹ under flowing Ar(g)
Figure 4-8: PXD patterns of hand mixed 1:1 NaOH:Al before (II) and after (I) heating to 450 °C under flowing Ar(g). (1 represent NaOH; 2 represent Al)
Figure 4-9: TG(red) and DTA(blue) profiles for hand mixed 1:1 NaAlH ₄ :NaOH on heating from 35-450 °C at 5 °C min ⁻¹ under flowing Ar(g)
Figure 4-10: Mass spectrometry output for water (m/z = 18; black) and hydrogen (m/z = 2;red) as a function of temperature for hand mixed 1:1 NaAlH ₄ :NaOH on heating from $35-450$ °C at 5 °C min ⁻¹ under flowing Ar(g)
Figure 4-11: PXD patterns of hand mixed 1:1 NaAlH ₄ :NaOH after heating to 175 (I), 185 (II) and 300 (III) °C under flowing Ar(g). (and cooling to room temperature). (1 represent NaAlH ₄ ; 2 represent NaOH; 3 represent Na ₃ AlH ₆ ; 4 represent NaH; 5 represent Al) 141
Figure 4-12: PXD pattern of hand mixed 1:1 NaAlH ₄ :NaOH after heating to 450 °C under flowing Ar(g) (and cooling to room temperature). (1 represent Al; 2 represent Na). Appendix A4-1 show the PXD patterns for the sample compared to stardard patterns from ICSD.
Figure 4-13: TG(red) and DTA(blue) profiles for hand mixed 1:4 NaAlH4:NaOH on heating from 35-400 °C at 5 °C min ⁻¹ under flowing Ar(g)
Figure 4-14: Mass spectrometry output for water (m/z = 18; black) and hydrogen (m/z = 2; red) as a function of temperature for hand mixed 1:4 NaAlH ₄ :NaOH on heating from $35-400$ °C at 5 °C min ⁻¹ under flowing Ar(g)
Figure 4-15: PXD pattern of hand mixed 1:4 NaAlH ₄ :NaOH after heating to 200 °C under flowing Ar(g) (and cooling to room temperature). (1 represent Na ₃ AlH ₆ ; 2 represent NaOH; 3 represent Al)Appendix A4-2 show the PXD patterns for the sample compared to stardard patterns from ICSD.
Figure 4-16: PXD pattern of hand mixed 1:4 NaAlH ₄ :NaOH after heating to 300 °C under flowing Ar(g) (and cooling to room temperature). (1 represent NaOH; 2 represent Na ₅ AlO ₄) Appendix A4-3 show the PXD patterns for the sample compared to stardard patterns from ICSD.
Figure 4-17: PXD pattern of hand mixed 1:4 NaAlH::NaOH after heating to 400 °C under

flowing Ar(g) (and cooling to room temperature). (1 represent Al; 2 represent NaOH; 3
represent NaH; 4 represent Na ₅ AlO ₄) Appendix A4-4 show the PXD patterns for the
sample compared to stardard patterns from ICSD
Figure 4-18: PXD patterns of ball-milled 1:0.5 NaAlH ₄ :NaOH(10h, 400rpm; IV) and 1:1
NaAlH ₄ :NaOH (2h, III; 4h, II; 10h, I). (1 represent NaOH; 2 represent NaAlH ₄ ; 3 represent
Na ₃ AlH ₆)
Figure 4-19: Raman spectra of NaAlH ₄ (III), NaOH (II) and ball-milled 1:1 NaAlH ₄ :NaOH
(10h, 400 rpm; I)
Figure 4-20: PXD patterns of 1:0.3 NaAlH ₄ :NaOH after ball-milling (2h, 400rpm; I) and
heating to 185 (II) and 300 (III) °C under flowing Ar(g). (and cooling to room temperature)
(1 represent NaAlH ₄ ; 2 represent NaOH; 3 represent Na ₃ AlH ₆ ; 4 represent NaH; 5
represent A1)
Figure 4-21: PXD pattern of 1:2 NaAlH ₄ :NaOH after ball-milling (2h,I; 4h II). (1 represent
NaAlH ₄ ; 2 represent NaOH; 3 represent NaH; 4 represent Na ₃ AlH ₆)151
Figure 4-22: TG(red) and DTA(blue) profiles for ball-milled 1:1 NaAlH ₄ :NaOH (10h,
400rpm) on heating from 35-400 °C at 5 °C min ⁻¹ under flowing Ar(g)
Figure 4-23: PXD pattern of ball-milled 1:1 NaAlH ₄ :NaOH (4h, 400rpm) after heating to
400 °C under flowing Ar(g). (1 represent Al; 2 represent Na ₂ O; 3 represent Na; 4 represent
Na ₅ AlO ₄)
Figure 4-24: PXD patterns of ball-milled 1:3 NaAlH ₄ :NaOH (2h, I; 4h II). (1 represent
NaOH; 2 represent NaH; 3 represent NaAlH ₄ ; 4 represent Na ₃ AlH ₆)
Figure 4-25: PXD patterns of ball-milled 1:4 NaAlH ₄ :NaOH (2h, I; 4h II). (1 represent
NaAlH ₄ ; 2 represent NaOH; 3 represent NaH; 4 represent Na ₃ AlH ₆)
Figure 4-26: TG(red) and DTA(blue) profiles for ball-milled NaAlH ₄ :NaOH (1h, 300rpm)
with molar ratio of (a)1:0.1 NaAlH ₄ :NaOH (b)1:0.2 NaAlH ₄ :NaOH (c)1:0.3
NaAlH ₄ :NaOH on heating from 35-400(300) °C at 5 °C min ⁻¹ under flowing Ar(g) 157
Figure 4-27: Mass spectrometry output for water ($m/z = 18$; black) and hydrogen ($m/z = 2$;
red) as a function of temperature for ball-milled NaAlH ₄ :NaOH (1h, 300rpm) with molar
ratio of (a)1:0.1 NaAlH ₄ :NaOH (b)1:0.2 NaAlH ₄ :NaOH (c)1:0.3 NaAlH ₄ :NaOH on heating
from 35-400(300) °C at 5 °C min ⁻¹ under flowing Ar(g)
Figure 4-28: PXD pattern of ball-milled NaAlH ₄ -2NaH (20h, 400rpm)159
Figure 4-29: TG(red) and DTA(blue) profiles for as-synthesised Na ₃ AlH ₆ on heating from
35-400 °C at 5 °C min ⁻¹ under flowing Ar(g)

Figure 4-30: Mass spectrometry output for water ($m/z = 18$; black) and hydrogen ($m/z = 2$;
red) as a function of temperature for as-synthesised Na_3AlH_6 on heating from 35-400 °C at
5 °C min ⁻¹ under flowing Ar(g)
Figure 4-31: PXD patterns of ball-milled Na ₃ AlH ₆ :NaOH (2h, 400rpm) with molar ratio (1:1 Na ₃ AlH ₆ :NaOH, I; 1:3 Na ₃ AlH ₆ :NaOH, II; 1:4 Na ₃ AlH ₆ :NaOH, III). (1 represent NaOH; 2 represent Na ₃ AlH ₆ ; 3 represent NaH)
Figure 4-32: PXD patterns of ball-milled 1:1 Na ₃ AlH ₆ :NaOH (2h, I; 10h, II)162
Figure 4-33: TG(red) and DTA(blue) profiles for ball-milled 1:3 Na ₃ AlH ₆ :NaOH (2h, 400rpm) on heating from 35-400 °C at 5 °C min ⁻¹ under flowing Ar(g)
Figure 4-34: Mass spectrometry output for water (m/z = 18; black) and hydrogen (m/z = 2; red) as a function of temperature for ball-milled 1:3 Na ₃ AlH ₆ :NaOH (2h, 400rpm) on heating from 35-400 °C at 5 °C min ⁻¹ under flowing Ar(g)
Figure 4-35: PXD pattern of ball-milled 1:3 Na ₃ AlH ₆ :NaOH (2h, 400rpm) after heating to 400 °C under flowing Ar(g) (and cooling to room temperature). (1 represent NaOH; 2 represent Na ₂ O; 3 represent Na ₅ AlO ₄)
Figure 4-36: TG(red) and DTA(blue) profiles for ball-milled 1:4 Na ₃ AlH ₆ :NaOH (2h, 400rpm) on heating from 35-400 °C at 5 °C min ⁻¹ under flowing Ar(g)
Figure 4-37: Mass spectrometry output for water (m/z = 18; black) and hydrogen (m/z = 2; red) as a function of temperature for ball-milled 1:4 Na ₃ AlH ₆ :NaOH (2h, 400rpm) on heating from 35-400 °C at 5 °C min ⁻¹ under flowing Ar(g)
Figure 4-38: PXD pattern of ball-milled 1:4 Na ₃ AlH ₆ :NaOH (2h, 400rpm) after heating to 400 °C under flowing Ar(g) (and cooling to room temperature). (1 represent NaOH; 2 represent Na ₂ O; 3 represent Na ₅ AlO ₄)
Figure 4-39: TG(red) and DTA(blue) profiles for ball-milled 4:1:1 NaOH:Al:NaH (2h, 400rpm) on heating from 35-400 °C at 5 °C min ⁻¹ under flowing Ar(g)
Figure 4-40: Mass spectrometry output for water (m/z = 18; black) and hydrogen (m/z = 2; red) as a function of temperature for ball-milled 4:1:1 NaOH:Al:NaH (2h, 400rpm) on heating from 35-400 °C at 5 °C min ⁻¹ under flowing $Ar(g)$
Figure 4-41: PXD patterns of ball-milled 4:1:1 NaOH:Al:NaH (2h, 400rpm) after heating to 400 °C under flowing Ar(g). (and cooling to room temperature). (1 represent Na ₅ AlO ₄ ; 2 represent Na ₂ O; 3 represent Al; 4 represent NaOH)
Figure 5-1: PXD patterns of standard NaBH ₄ (II) and ball-milled commercial NaBH ₄ (I).174
Figure 5-2: TG (red) and DTA (blue) profiles for ball-milled NaBH ₄ (2h, 400rpm) on

heating from room temperature to 400 °C at 2 °C min ⁻¹ under flowing Ar(g)174
Figure 5-3: TG (red) and DTA (blue) profiles for ball-milled 1:1 NaBH ₄ :NaOH (2h, 400rpm) on heating from 35-400 °C at 2 °C min ⁻¹ under flowing Ar(g)
Figure 5-4: Mass spectrometry output for water (m/z = 18; blue) and hydrogen (m/z = 2; red) as a function of temperature for ball-milled 1:1 NaBH ₄ :NaOH (2h, 400rpm) on heating from 35-400 °C at 2 °C min ⁻¹ under flowing $Ar(g)$
Figure 5-5: PXD patterns of ball-milled NaBH ₄ :NaOH (2h, 400rpm) with varing molar ratio (1:1 I; 1:2 II; 1:3 III; 1:4 IV). (1 represent NaBH ₄ , 2 represent NaOH)
Figure 5-6: PXD patterns of ball-milled 1:4 NaBH ₄ :NaOH (10h; III) and 1:3 NaBH ₄ :NaOH(4h, I; 10h, II)
Figure 5-7: TG (red) and DTA (blue) profiles for ball-milled NaBH ₄ :NaOH (2h, 400rpm) with varing molar ratio (a)1:2 NaBH ₄ :NaOH (b)1:3 NaBH ₄ :NaOH (c)1:4 NaBH ₄ :NaOH on heating from 35-400 °C at 2 °C min ⁻¹ under flowing Ar(g).
Figure 5-8: Mass spectrometry output for water (m/z = 18; blue) and hydrogen (m/z = 2; red) as a function of temperature for ball-milled NaBH ₄ :NaOH (2h, 400rpm) with varying molar ratio (a)1:2 NaBH ₄ :NaOH (b)1:3 NaBH ₄ :NaOH (c)1:4 NaBH ₄ :NaOH on heating from 35-400 $^{\circ}$ C at 2 $^{\circ}$ C min ⁻¹ under flowing Ar(g).
Figure 5-9: PXD patterns of ball-milled 1:3 NaBH ₄ :NaOH (2h, 400rpm) after heating to 300 (I), 400 (II), 430 (III) and 500 (IV) °C under flowing Ar(g). (and cooling to room temperature)
Figure 5-10: PXD pattern of ball-milled 1:3 NaBH ₄ :NaOH (2h, 400rpm) after heating to 400 °C (and cooling to room temperature). (1 represent Na ₃ BO ₃ ; 2 represent Na; 3 represent NaOH)
Figure 5-11: PXD pattern of ball-milled 1:4 NaBH ₄ :NaOH (2h, 400rpm) after heating to 400 °C(and cooling to room temperature). (1 represent Na ₃ BO ₃ ; 2 represent Na ₂ O; 3 represent NaOH)
Figure 5-12:PXD pattern of ball-milled 1:4 NaBH ₄ :NaOH (2h, 400rpm) after heating to 320 °C and keeping for 1h (cooling to room temperature). (1 represent NaH; 2 represent Na ₃ BO ₃ ; 3 represent NaOH)
Figure 5-13: TG(red) and DTA(blue) profiles for ball-milled 1:3 NaBH ₄ :NaOH (2h, 400rpm) on heating from room temperature to different temperature
Figure 5-14: TG(red) and DTA(blue) profiles for ball-milled 1:4 NaBH ₄ :NaOH (2h, 400rpm) on heating from room temperature to different temperature185

Figure 5-15: Photographs showing the appearance of the TG-DTA thermobalance crucible and thermocouple after heating. (1:1 NaBH ₄ :NaOH, 1:2 NaBH ₄ :NaOH and 1:3
NaBH ₄ :NaOH)
Figure 5-16: Raman patterns of ball-milled 1:4 NaBH ₄ :NaOH after heating to 300 °C, 340 °C, 360 °C and 400 °C
Figure 6-1: The PXD pattern of as-synthesised Ca ₁₉ Mg ₈ H ₅₄ (10h ball-milling, 500rpm, 5
min run and 2 min rest periods;II) and standard Ca ₁₉ Mg ₈ H ₅₄ (I)194
Figure 6-2: TG (red) and DTA (blue) profiles for as-synthesised Ca ₁₉ Mg ₈ H ₅₄ on heating from 35-350 °C at 5 °C min ⁻¹ under flowing Ar(g)
Figure 6-3: The PXD pattern of as-synthesised Ca ₄ Mg ₃ H ₁₄ (II)compared to standard Ca ₄ Mg ₃ H ₁₄ .(I)
Figure 6-4: TG (red) and DTA (blue) profiles for as-synthesised Ca ₄ Mg ₃ H ₁₄ on heating from 35-500 °C at 5 °C min ⁻¹ under flowing Ar(g).
Figure 6-5: Mass spectroscopy output for water (m/z = 18) and hydrogen (m/z = 2) as a function of temperature for as-synthesised $Ca_4Mg_3H_{14}$ on heating from 35-500 °C at 5 °C min ⁻¹ under flowing $Ar(g)$.
Figure 6-6: PXD pattern of as-synthesised Ca ₄ Mg ₃ H ₁₄ after heating to 450 °C (and cooling to room temperature). (1 represent CaH ₂ ; 2 represent Mg; 3 represent Ca ₄ Mg ₃ H ₁₄) 197
Figure 6-7:The PXD pattern of ball-milled 1:1 Ca ₄ Mg ₃ H ₁₄ :NaH (2h, 400rpm). (1 represent Ca ₄ Mg ₃ H ₁₄ ; 2 represent NaMgH ₃)
Figure 6-8: TG (red) and DTA (blue) profiles for ball-milled 1:1 Ca ₄ Mg ₃ H ₁₄ :NaH (2h, 400rpm) on heating from 35-400 °C at 5 °C min ⁻¹ under flowing Ar(g)
Figure 6-9: Mass spectroscopy output for water (m/z = 18) and hydrogen (m/z = 2) as a function of temperature for ball-milled 1:1 $Ca_4Mg_3H_{14}$:NaH (2h, 400rpm) on heating from 35-400 °C at 5 °C min ⁻¹ under flowing Ar(g)
Figure 6-10: The PXD patterns of ball-milled 1:1 Ca ₄ Mg ₃ H ₁₄ :NaH (2h, 400rpm;I) and after heating to 150 (II), 200 (III) and 280 (IV) °C (and cooling to room temperature). (1 represent Ca ₄ Mg ₃ H ₁₄ ; 2 represent NaMgH ₃)
Figure 6-11: The PXD patterns of ball-milled 1:1 $Ca_4Mg_3H_{14}$: NaH (2h, 400rpm) after heating to 280 (I) 320 (II), 360 (III) and 400 (IV) °C (and cooling to room temperature). (1 represent $Ca_4Mg_3H_{14}$; 2 represent NaMgH ₃ ; 3 represent Mg; 4 represent CaH_2 ; 5 represent Na)
Figure 6-12:The PXD pattern of ball-milled 1:1 Ca ₄ Mg ₃ H ₁₄ :NaH (2h, 400rpm) after

heating to 330 °C (and cooling to room temperature). (1 represent Ca ₄ Mg ₃ H ₁₄ ; 2 represent Mg; 3 represent CaH ₂ ; 4 represent Na; 5 represent NaH)201
Figure 6-13: The PXD pattern of ball-milled 1:1 Ca ₄ Mg ₃ H ₁₄ :NaH (10h, 400rpm). (1 represent CaH ₂ ; 2 represent NaMgH ₃ ; 3 represent Mg)
Figure 6-14: TG (red) and DTA (blue) profiles for ball-milled 1:1 Ca ₄ Mg ₃ H ₁₄ :NaH (10h, 400rpm) on heating from 35-400 °C at 5 °C min ⁻¹ under flowing Ar(g)
Figure 6-15: Mass spectroscopy output for water (m/z = 18) and hydrogen (m/z = 2) as a function of temperature for ball-milled 1:1 Ca ₄ Mg ₃ H ₁₄ :NaH (10h, 400rpm) on heating from 35-400 °C at 5 °C min ⁻¹ under flowing Ar(g).
Figure 6-16: The PXD pattern of ball-milled 1:1 Ca ₄ Mg ₃ H ₁₄ :NaH (10h, 400rpm) after heating to 400 °C (and cooling to room temperature). (1 represent CaH ₂ ; 2 represent Mg; 3 represent Na)
Figure 6-17: The PXD pattern of ball-milled 1:1 Ca ₄ Mg ₃ H ₁₄ :NaH (2h, 300rpm). (1 represent Ca ₄ Mg ₃ H ₁₄ ; 2 represent NaH)
Figure 6-18: The PXD pattern of ball-milled 1:2 Ca ₄ Mg ₃ H ₁₄ :NaH (2h, 300rpm). (1 represent Ca ₄ Mg ₃ H ₁₄ ; 2 represent NaH; 3 represent MgH ₂)
Figure 6-19: TG (red) and DTA (blue) profiles for ball-milled 1:2 Ca ₄ Mg ₃ H ₁₄ :NaH (2h, 300rpm) on heating from 35-400 °C at 5 °C min ⁻¹ under flowing Ar(g)
Figure 6-20: Mass spectroscopy output for water (m/z = 18) and hydrogen (m/z = 2) as a function of temperature for ball-milled 1:2 $Ca_4Mg_3H_{14}$:NaH (2h, 400rpm) on heating from 35-400 °C at 5 °C min ⁻¹ under flowing Ar(g)
Figure 6-21: The PXD pattern of ball-milled 1:2 Ca ₄ Mg ₃ H ₁₄ :NaH (2h, 400rpm) after heating to 400 °C (and cooling to room temperature). (1 represent CaH ₂ ; 2 represent Mg; 3 represent Na)
Figure 7-1: Schematic representation of the guanidine synthesis
Figure 7-2: PXD patterns of the synthesis product (I) as compared to the standard diffraction pattern of guanidine(II).
Figure 7-3: TG (red) and DTA (blue) profiles for as-synthesised guanidine, CH ₅ N ₃ , on heating from 35-400 °C at 5 °C min ⁻¹ under flowing Ar(g)
Figure 7-4: Mass spectroscopy output as a function of temperature for: (a) ammonia (m/z = 17), methane (m/z = 16) and hydrogen (m/z = 2) and (b) ammonia (m/z = 17), methane (m/z = 13/16), nitrogen (m/z = 28), hydrogen (m/z = 2) for CH ₅ N ₃ on heating from 35-400 °C at 5 °C min ⁻¹ under flowing Ar(g)
55-400 Cat 5 Chilli under howing Ar(g)

Figure 7-5: PXD pattern of as-synthesised guanidine (I) and after heating to 200 °C (II).218
Figure 7-6: TG (red) and DTA (blue) profiles for ball-milled 1:1 CH ₅ N ₃ :NaAlH ₄ (1h, 200rpm) on heating from 35-400 °C at 5 °C min ⁻¹ under flowing Ar(g)
Figure 7-7: Mass spectroscopy output for ammonia (m/z = 17), methane (m/z = 13/16), nitrogen (m/z = 28), hydrogen (m/z = 2) as a function of temperature for ball-milled 1:1 $CH_5N_3:NaAlH_4$ (1h, 200rpm) on heating from 35-400 °C at 5 °C min ⁻¹ under flowing Ar(g).
Figure 7-8: PXD patterns of 1:1 CH ₅ N ₃ :NaAlH ₄ after ball-milling (1h, 200rpm;I) and heating to 150 (II), 170 (III) and 300 (IV) °C.
Figure 7-9: TG (red) and DTA (blue) profiles for ball-milled (1h, 200rpm) (a) 1:1 CH ₅ N ₃ :MgH ₂ (b) 1:2 CH ₅ N ₃ :MgH ₂ on heating from 35-400 °C at 5 °C min ⁻¹ under flowing Ar(g).
Figure 7-10: Mass spectroscopy output for ammonia (m/z = 17), methane (m/z = 13/16), nitrogen (m/z = 28), hydrogen (m/z = 2) as a function of temperature for ball-milled (1h, 200rpm) (a) 1:2 CH ₅ N ₃ :MgH ₂ (b) 1:1 CH ₅ N ₃ :MgH ₂ on heating from 35-400 °C at 5 °C min ⁻¹ under flowing Ar(g).
Figure 7-11: PXD patterns of 1:1 CH ₅ N ₃ :MgH ₂ after ball-milling (1h, 200rpm;I) and heating to 150 (II), 240 (III) and 400 (IV) °C. (and cooling to room temperature)
Figure 7-12: PXD patterns of 1:2 CH ₅ N ₃ :MgH ₂ after ball-milling (1h, 200rpm) and heating to 160 (I) and 400 (II) °C. (and cooling to room temperature)
Figure 7-13: TG (red) and DTA (blue) profiles for ball-milled 4:1 CH ₅ N ₃ :MgH ₂ (1h, 200rpm) on heating from 35-400 °C at 5 °C min ⁻¹ under flowing Ar(g)
Figure 7-14: Mass spectroscopy output for ammonia (m/z = 17), methane (m/z = 13/16), nitrogen (m/z = 28), hydrogen (m/z = 2) as a function of temperature for ball-milled 4:1 $CH_5N_3:MgH_2$ (1h, 200rpm) on heating from 35-400 °C at 5 °C min ⁻¹ under flowing Ar(g).226
Figure 7-15: PXD patterns of 4:1 CH ₅ N ₃ :MgH ₂ after heating to 150 (I), 240 (II) and 400 (III) °C. (and cooling to room temperature)

AI Statement

I used AI in the process of writing my thesis. However, its function was limited to improving grammar and making the whole article more fluent. All the results analysis in the thesis were my own thoughts.

Acknowledgement

I am deeply grateful to my supervisor, Prof. Duncan H. Gregory, for giving me the opportunity to study in the UK. It is thanks to his guidance and support that I have gained so much knowledge and successfully completed my project. I would also like to express my thanks to all the members of the Gregory group. Their assistance made my research journey enjoyable and smooth.

I am thankful to my parents, whose unwavering support and care made my life in the UK truly wonderful.

I also want to thank my wife, Yunjia Hu, who even gave up her job to join me in the UK for graduate studies. We shared two years of happiness in the UK and later married after returning home.

I am also grateful to all the staff in the Joseph Black Building. Their warm assistance made it easy for me to learn how to use the lab equipment. Lastly, I want to thank the University of Glasgow for its great campus atmosphere, which made my time there even more fulfilling.

Definitions and Abbreviation

BM: Ball-milling

DOE: Department of Energy

DTA: Differential Thermal Analysis

HM: Hand-mixed

ICDD: International Centre for Diffraction Data

ICSD: Inorganic Crystal Structure Database

LOHC: Liquid Organic Hydrogen Carriers

MOF: Metal Organic Framework

MS: Mass Spectrometry

MW: Microwave

PXD: Powder X-ray Diffraction

RHC: Reactive Hydride Composites

STA: Simultaneous Thermogravimetric Analysis

TG: Thermogravimetry

XRD: X-Ray Diffraction

GO: Graphene Oxide

rGO: Reduced Graphene Oxide

1. Introduction

1.1 The Current Status of Hydrogen

The global demand for energy continues to grow due to increasing human populations and industrial activities. Currently, about 90% of the world's energy needs are met by fossil fuels, which are finite and contribute to environmental degradation. As a result, there is an urgent need to develop alternative energy sources that are renewable, sustainable, and environmentally benign. Hydrogen, with its potential for high energy density and clean combustion, has emerged as a leading candidate to meet these criteria. 2,3

Hydrogen, the lightest and most abundant element in the universe, has long been recognized as a promising energy carrier for a sustainable and environmentally friendly future.⁴ With its highest energy content per unit mass (120 MJ/kg), hydrogen offers a viable alternative to fossil fuels, which are both non-renewable and highly polluting.⁵ The combustion of hydrogen produces only water, making it a clean energy source that can significantly reduce greenhouse gas emissions and air pollution.

1.1.1 Environment Benefits

Hydrogen, as an energy carrier, offers several significant environmental benefits, making it a promising candidate for a sustainable and low-carbon future. When hydrogen is used as a fuel, its combustion produces only water (H₂O) as a byproduct.⁶ This is in stark contrast to fossil fuels, which release carbon dioxide (CO₂), nitrogen oxides (NO_x), sulfur oxides (SO_x), and particulate matter when burned.^{7,8} These pollutants contribute to air pollution, smog, and respiratory health issues.⁹ Hydrogen fuel cells, which convert hydrogen into electricity, emit no greenhouse gases during operation.^{10,11,12} This is particularly important for reducing the overall carbon footprint and mitigating climate change.

Hydrogen is the most abundant element in the universe. While it is not found in its pure form on Earth, it can be produced from a variety of sources, including water (H₂O) through electrolysis, biomass, and natural gas reforming. Among the various approaches, hydrogen production from biomass is regarded as a renewable and environmentally friendly pathway. The most common thermochemical methods include gasification and pyrolysis. Gasification involves the partial oxidation of biomass at high temperatures (700 - 1000 °C) in a limited oxygen or steam atmosphere, producing syngas (H₂+CO). The hydrogen yield can be further enhanced through the water–gas shift reaction 1. Typical feedstocks for this process include lignocellulosic residues, agricultural wastes, and forestry by-products. ^{13,14}

$$CO + H_2O \rightarrow CO_2 + H_2 \tag{1}$$

For comparison, natural gas reforming is another widely used industrial route, in which methane reacts with water steam to produce hydrogen.^{13,14} The reaction 2 was shown below:

$$CH_4 + 2H_2O \rightarrow CO_2 + 4H_2$$
 (2)

According to figure 1-1, hydrogen can be produced from renewable energy sources such as solar, wind, and hydroelectric power.¹⁵ Electrolysis powered by renewable electricity can produce "green hydrogen," which is a truly sustainable and carbon-free energy carrier.¹⁶ Hydrogen can serve as an effective energy storage medium, allowing excess renewable energy to be stored and used when needed. This helps to address the intermittent nature of renewable energy sources like solar and wind, ensuring a stable and reliable energy supply.¹⁷ Hydrogen can be used to balance the grid by storing excess electricity during periods of low demand and releasing it during peak demand, thereby enhancing grid stability and reliability.¹⁸ By replacing fossil fuels with hydrogen in various applications, such as transportation, heating, and industrial processes, the dependence on non-renewable and polluting energy sources can be significantly reduced. Hydrogen fuel cell vehicles offer a zero-emission alternative to internal combustion engine vehicles.^{19,20} They have the potential to significantly reduce greenhouse gas emissions and air pollution in the transportation sector.

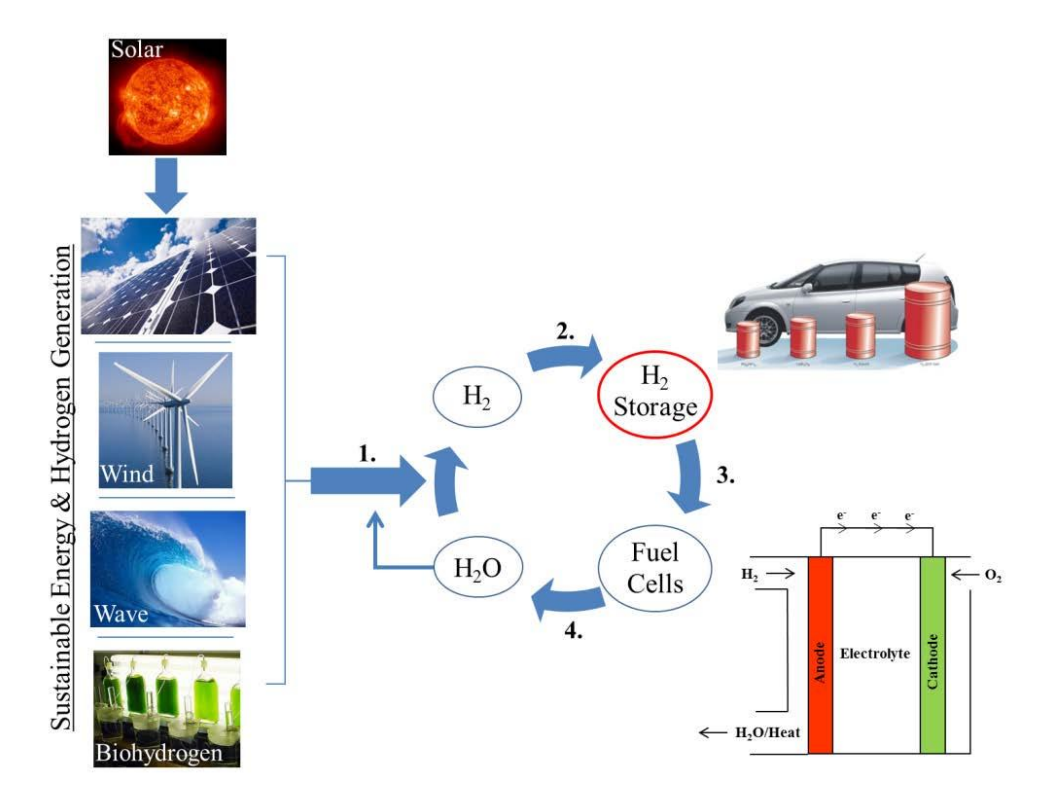


Figure 1-1: Schematic of a sustainable hydrogen energy cycle²¹

Hydrogen can also be used in industrial processes that currently rely on fossil fuels, such as steel production and chemical manufacturing.²² This can lead to substantial reductions in

industrial emissions. Hydrogen can be used in fuel cells or turbines to generate electricity, providing a clean alternative to traditional power plants.²³ In some cases, hydrogen can be produced from natural gas through steam methane reforming combined with carbon capture and storage technologies.²⁴ This process can significantly reduce the carbon footprint of hydrogen production. Hydrogen can also be used in combination with captured CO₂ to produce synthetic fuels or chemicals, effectively recycling carbon and reducing emissions.²⁵ The only byproduct of hydrogen combustion or fuel cell operation is water, which can be captured and reused, contributing to water conservation efforts.²⁶ The use of hydrogen can support the expansion of renewable energy infrastructure by providing a storage solution that complements intermittent renewable sources.

1.1.2 Environment Challenges

However, producing green hydrogen, which is hydrogen generated through electrolysis using renewable energy sources (such as solar, wind, or hydroelectric power), faces several significant challenges. These challenges are primarily related to cost, efficiency, infrastructure, and scalability. Electrolysers, which split water into hydrogen and oxygen using electricity, are expensive to manufacture and install. The high initial capital costs of electrolysers are a major barrier to widespread adoption.¹⁰ The cost of renewable energy itself, although decreasing, still adds to the overall expense of producing green hydrogen.

Additionally, integrating renewable energy sources with electrolysis systems requires significant investment in infrastructure.²⁷ The operational and maintenance costs of electrolysis systems can be high, further increasing the overall cost of green hydrogen production. Current electrolysis technologies, such as proton exchange membrane and alkaline electrolysis, are not yet fully optimized for efficiency.²⁸ Energy losses during the electrolysis process mean that a significant amount of the input energy is not converted into hydrogen. Solar and wind energy are intermittent sources, meaning they are not always available. This intermittency can affect the efficiency and consistency of hydrogen production, as electrolysers need a stable power supply to operate efficiently.²⁹ The existing energy infrastructure is largely designed for fossil fuels and is not optimized for hydrogen. Developing a new infrastructure for hydrogen production, storage, and distribution requires significant investment and time. Hydrogen is challenging to store and transport due to its low volumetric energy density. Effective storage solutions, such as high-pressure tanks or liquid hydrogen, are expensive and complex.

Also, transporting hydrogen requires specialized pipelines or vehicles, which are not yet widely available. The current global production capacity for green hydrogen is relatively small compared to the demand for hydrogen in various industries.³⁰ Scaling up production

to meet future demands will require significant advancements in technology and infrastructure.³¹ While electrolysis technologies are improving, they are not yet mature enough to support large-scale industrial applications. Further research and development are needed to enhance the performance and reliability of electrolysers. There is a lack of standardized regulations and policies for green hydrogen production, storage, and use. This can create uncertainty and hinder investment and innovation. Governments need to provide incentives and subsidies to encourage the adoption of green hydrogen technologies. Without adequate support, the high costs of green hydrogen production can be a significant barrier.

Green hydrogen is currently more expensive than hydrogen produced from fossil fuels or hydrogen produced using natural gas with carbon capture and storage. This makes it less competitive in the market. There is a need to raise awareness among consumers and businesses about the benefits of green hydrogen. Lack of understanding and familiarity with hydrogen technologies can slow down market adoption. Research is needed to develop more efficient and cost-effective electrolysis technologies. This includes improving the performance of catalysts, membranes, and overall system design. Exploring alternative methods for producing green hydrogen, such as biological processes or advanced thermochemical methods, is essential for diversifying production options and reducing costs.

1.2 Hydrogen Storage Methods

Despite its many advantages, the widespread adoption of hydrogen as an energy carrier faces significant challenges, particularly in terms of storage. Hydrogen's low volumetric energy density and gaseous nature at ambient conditions make it difficult to store and transport efficiently.³⁴ Effective hydrogen storage solutions are crucial for the practical implementation of hydrogen-based energy systems, especially for on-board applications in vehicles.³⁵ Various hydrogen storage methods have been developed, each with its own set of advantages and disadvantages. Currently, there are seven main hydrogen storage methods.

1.2.1 Compressed Hydrogen

Compressed hydrogen is the most widely used method for hydrogen storage. This method involves storing hydrogen at high pressures, typically up to 700 bar, in cylindrical vessels.^{2,36} The technology for compressing hydrogen is well-developed and offers high rates of hydrogen filling and release.^{37,38} However, the compression process consumes a

significant amount of energy, accounting for about 13–18% of the lower heating value of hydrogen.^{39,40} This energy consumption impacts the overall economics of hydrogen storage. Four types of vessels are commonly used for compressed hydrogen storage:

Type I: These are the cheapest and are made of metallic materials, capable of withstanding pressures up to 30 bar. ^{41,42} They are typically made of steel or aluminium alloy. ^{41,43}

Type II: These vessels have a metallic wall wrapped with fiber resin composite on the cylindrical part, offering a 30–40% weight reduction compared to Type I vessels. 41,44

Type III: Made of carbon fiber composite materials lined with metal (e.g., aluminium), these vessels are strong and lightweight, suitable for pressures up to 700 bar., ^{37,44}

Type IV: Similar to Type III, these vessels are entirely made of composite materials, with a polymeric liner such as high-density polyethylene.^{41,42}

Compressed hydrogen storage is practical for stationary applications and has shown promise for on-board applications, with vehicles like the Toyota Mirai and Hyundai Nexo using this method. However, safety concerns and the need for complex valve technology to manage high pressures remain challenges. 46

1.2.2 Liquefied Hydrogen

Liquefied hydrogen offers a higher volumetric energy density compared to compressed hydrogen, as hydrogen is stored at cryogenic temperatures (-253 °C).⁴⁷ The density of liquid hydrogen reaches around 71 g/L, with an energy density of 8 MJ/L.⁷ This method is well-established and allows for high rates of hydrogen release.

However, liquefaction is energy-intensive, consuming about 30–40% of the net heating value of hydrogen.⁴⁸ Additionally, liquid hydrogen storage requires expensive insulation to prevent boil-off, where hydrogen vaporizes due to heat from the surroundings. Boil-off losses can be significant, with about 1.5-3% of hydrogen lost per day.^{49,50} These challenges, along with the need for specialized infrastructure, limit the practicality of liquefied hydrogen for on-board applications.

1.2.3 Cryo-Compressed Hydrogen

Cryo-compressed hydrogen combines the aspects of both compressed gaseous hydrogen and cryogenic hydrogen. Hydrogen is stored at cryogenic temperatures and under high pressures (250–350 bar).^{51,52} This method offers higher densities and reduced boil-off losses compared to liquefied hydrogen.^{41,42} However, it requires more expensive double-walled vessels and increased energy input for storage.⁴¹

1.2.4 Metal Hydrides

Metal hydrides store hydrogen by chemically bonding hydrogen atoms to metal atoms, forming solid compounds.⁵³ This method offers higher hydrogen storage capacities and operates at moderate temperatures and pressures, making it safer than compressed or liquefied hydrogen.^{54,55} Metal hydrides such as magnesium hydride (MgH₂) and intermetallic hydrides (e.g., LaNi₅) are widely studied for their potential in hydrogen storage. MgH₂, in particular, has gained attention due to its high hydrogen content (7.6 wt.%) and relatively low hydrogen release temperature (350-400 °C).⁵⁶ However, the kinetics of hydrogenation and dehydrogenation are slow, and the hydrogen release temperature is still too high for practical applications. Research focuses on improving these properties through methods such as ball milling, alloying, and the addition of catalysts.^{57,58,59}

1.2.5 Complex Metal Hydrides

Complex metal hydrides involve hydrogen atoms covalently bonded to central atoms in coordination complexes, stabilized by cations such as lithium, sodium and magnesium. These hydrides, including alanates (e.g., NaAlH₄) and borohydrides (e.g., LiBH₄), offer higher storage densities due to their light element composition.^{60,61} NaAlH₄, for example, can release up to 5.6 wt.% of hydrogen through a two-step reaction. However, it requires high temperatures for hydrogen release and has poor reversibility.^{62,63,64} Research has shown that doping NaAlH₄ with titanium catalysts can significantly improve its thermodynamics and kinetics.^{65,66,67} Similarly, LiBH⁴ has a high hydrogen capacity (18.5 wt.%), but its high decomposition temperature and poor reversibility limit its practical use.^{68,69} Recent studies have explored destabilization techniques and the addition of catalysts to enhance its performance.^{70,71}

1.2.6 Physical Adsorption

Physical adsorption involves hydrogen molecules being adsorbed onto the surface of solid materials through van der Waals forces.^{72,73} Materials such as activated carbon, metal-organic frameworks (MOFs), and zeolites are commonly used for this purpose. While these materials offer high surface areas and reversible hydrogen storage, their room-temperature capacities are low, making them more suitable for cryogenic temperatures and higher pressures.^{74,75,76,77,78}

1.2.7 Liquid Organic Hydrogen Carriers (LOHCs)

LOHCs store hydrogen chemically by reacting hydrogen with organic molecules. The hydrogen is released by dehydrogenating the organic compound in a reactor.⁷⁹ LOHCs

such as methylcyclohexane/toluene systems offer high hydrogen capacities (6.2 wt.%) and can utilize existing gasoline infrastructure for storage and transportation.⁸⁰ However, the dehydrogenation process requires high temperatures and enthalpies, posing challenges for practical applications.

1.3 Solid-State Hydrogen Storage

Hydrogen storage technologies can be broadly categorized into conventional methods (compressed gas and liquefied hydrogen) and solid-state methods (metal hydrides, complex hydrides and physical adsorption).⁸¹ Conventional methods, although simple, have limitations in terms of storage density and energy efficiency. In contrast, solid-state hydrogen storage can offers higher storage densities and better safety profiles.⁸² Solid-state hydrogen storage materials can be divided into three main categories: metal hydrides, complex hydrides and physical adsorption.⁸³ Metal hydrides store hydrogen through the formation of metal-hydrogen bonds only, while complex hydrides store hydrogen through the formation of complex hydride anions.^{83,84}

1.3.1 Metal Hydrides

Light metal hydrides are binary or complex compounds formed between hydrogen and light metals such as Li, Na, Mg, Ca, and Al. They are typically solid at room temperature and can store hydrogen chemically. Light metal hydrides, such as LiH, NaH, MgH₂ play a crucial role in solid-state hydrogen storage due to their high gravimetric hydrogen densities.⁸⁵ Table 1-1 shows the properties of hydrogen storage of these materials.

Table 1-1: Molecular weight, gravimetric capacity and decomposition temperatures for LiH, NaH, MgH_2 and CaH_2

Parameter/metal hydrides	Molecule weight/g·mol ⁻¹	Theoretical gravimetric hydrogen capacity/ wt.%	T _d /°C
LiH	7.95	12.59	900
NaH	23.99	4.17	425
MgH ₂	26.31	7.60	327
CaH ₂	42.09	4.75	600

Lithium hydride (LiH) has the capacity to store up to 12.59 wt.% hydrogen, whereas sodium hydride (NaH) can only store 4.17 wt.% hydrogen. Both LiH and NaH exhibit high chemical reactivity, which not only necessitates stringent handling and reaction conditions but also poses challenges for achieving reversible hydrogen cycling.⁸⁶ Moreover, the high

decomposition temperature of LiH (900 °C) renders it unsuitable as a standalone candidate for practical solid-state hydrogen storage applications.⁸⁷ However, LiH has been extensively studied as a component in Li-N-H systems for both direct and indirect hydrogen storage, as well as in hydride-hydroxide modular hydrogen release systems.⁸⁸ The calcium hydride (CaH₂) can store 4.75 wt.% hydrogen and also has high decomposition temperatures. Like magnesium hydride (MgH₂), the dehydrogenation process for calcium hydride is reversible, and it is typically synthesized by reacting calcium metal with high-pressure hydrogen at elevated temperatures.⁸⁹

$$CaH_2 \rightarrow Ca + H_2 \Delta H^{\circ}(298K) = 171 \text{ kJ} \cdot \text{mol}^{-1} H_2$$
 (3)

Similar to lithium hydride (LiH), calcium hydride (CaH₂) can only be utilized within complex composite hydrogen storage systems, where it interacts with other components, due to its high decomposition temperature (600 °C). In recent years, its interactions with amides, borohydrides and ammonia borane have been extensively studied.⁹⁰

Therefore, NaH, LiH, and CaH₂ each possess inherent limitations that make them unsuitable for use as single hydrogen storage materials. Effective hydrogen storage with these hydrides typically requires interaction with other components in composite systems to improve thermodynamic and kinetic properties. In contrast, magnesium hydride (MgH₂) stands out due to its relatively high gravimetric hydrogen capacity (7.60 wt%) and the lowest decomposition temperature (327 °C) among the four light metal hydrides. Additionally, the abundance and low cost of magnesium further enhance its appeal as a promising candidate for solid-state hydrogen storage.⁹¹ However, the decomposition temperature of MgH₂ (327 °C) is still relatively high, and its decomposition enthalpy (76.2 kJ mol⁻¹) indicates considerable thermodynamic stability under ambient conditions.^{91,92} The corresponding endothermic decomposition reaction is as follows:

$$MgH_2 \rightarrow Mg + H_2 \quad \Delta H^{\circ}(298K) = 76.2 \text{ kJ} \cdot \text{mol}^{-1} H_2$$
 (4)

To reduce the decomposition temperature and enthalpy of decomposition of MgH₂, current strategies primarily focus on nanostructuring the material (such as ball milling) to reduce particle size, create unique nanostructures, or introduce suitable additives. ^{94,95} According to Wu et al.'s article, the hydrogen storage performance of MgH₂/single-walled carbon nanotube (SWNT) composites prepared via ball milling was systematically investigated. The study revealed that both the SWNT content and milling time significantly influenced the hydrogen capacity and the absorption/desorption kinetics of the composite. Optimal performance was achieved with 5 wt% SWNT addition: the composite absorbed 6.7 wt% H₂ within 2 minutes at 300 °C, and released 6 wt% H₂ within 5 minutes at 350 °C. ⁹⁶ In addition to carbon-based additives, transition metal-based catalysts such as nickel, niobium,

and titanium compounds have also been extensively explored for their catalytic effects. 97,98,99,100 Thus, the synergistic combination of nanostructuring and catalytic additives is considered a key direction for advancing solid-state hydrogen storage materials. 101,102

1.3.2 Complex Hydrides for Hydrogen Storage

1.3.2.1 Introduction to Complex Hydrides for Hydrogen Storage

Hydrogen storage is a critical technology for the transition to a sustainable energy economy, and complex hydrides have emerged as promising materials due to their high gravimetric and volumetric hydrogen capacities. Complex hydrides include metal borohydrides, alanates, and amides, which are characterized by covalent bonding of hydrogen to metals or non-metals to form complex anions (e.g., [BH₄]-, [AlH₄]-, [NH₂]-). ^{103,104} These materials have been extensively studied for their potential in hydrogen storage applications, particularly for mobile and stationary energy systems. However, despite their high hydrogen capacities, complex hydrides face significant challenges related to the thermodynamics and kinetics of hydrogen uptake and release. Hydrogen release often requires high temperatures (above 200 °C), and hydrogen uptake typically occurs at high pressures (above 50 bar). ¹⁰⁵ These conditions are impractical for many applications, especially in the automotive sector. Additionally, the reversibility of hydrogen absorption and desorption is often poor, leading to limited cyclability.

1.3.2.2 Alanates for Hydrogen Storage

Alanates, specifically metal alanates (MAlH₄, where M is an alkali or alkaline earth metal), are considered promising candidates for solid-state hydrogen storage. These materials can store up to 10.5 mass% of hydrogen, making them one of the highest capacity hydrogen carriers. However, their practical application has been hindered by slow hydrogen kinetics, poor reversibility, and high thermodynamic stability.¹⁰⁶

According to Table 1-2, alanates are characterized by their rich hydrogen content and moderate desorption temperatures. For example, LiAlH₄ can release hydrogen at temperatures as low as 150 °C, while NaAlH₄ releases hydrogen at around 170-230 °C.^{107,108,109} The hydrogen release process typically involves multiple steps, with the formation of intermediate phases such as M₃AlH₆. The thermodynamic properties of alanates, including their enthalpy of formation and decomposition, have been extensively studied to understand their hydrogen storage behaviour.^{100,111}

Table 1-2: Molecular weight, theoretical gravimetric and temperatures of decomposition for selected alanate. 112,113

Alanate	Molecular weight/g·mol-1	Theoretical gravimetric hydrogen capacity/ wt.%	T _d / °C
	weight g mor	capacity/ wt./0	
LiAlH ₄	37.95	10.54	170, 270
NaAlH ₄	54.00	7.41	190, 230
Mg(AlH ₄) ₂	86.30	9.27	110-200, 310

Lithium Alanate (LiAlH4)

LiAlH₄ is typically prepared by reacting LiH with AlBr₃ in an ether solution or through ball milling. It has a monoclinic cubic crystal structure with a $P2_1/c$ space group. 114 The [AlH₄] anion forms tetrahedral units, and lithium ions are surrounded by hydrogen atoms in a distorted geometry. It has a theoretical hydrogen storage capacity of 10.54 wt.%. As shown in reaction 5, 6 and 7, LiAlH₄ decomposes in two steps, releasing hydrogen at temperatures of approximately 170°C and 270°C, respectively. 115 Lithium aluminium hydride (LiAlH₄) is known for its kinetic stability, yet it exhibits significant thermodynamic instability for hydrogen storage applications, as it tends to decompose easily below room temperature. However, research has shown that doping LiAlH₄ with Ti-based or V-based catalysts can effectively reduce the decomposition temperature of the hydrides. 116 For instance, Srinivasa et al. demonstrated that the addition of Ti-based catalysts could lower the decomposition temperature, thereby improving the material's thermal stability and hydrogen release efficiency. 117 Furthermore, a previous study indicated that ball-milling LiAlH₄ with Ti compounds could achieve reversible hydrogen storage capacities of up to 1.8 wt.%, highlighting the potential of such modifications to enhance the practicality of LiAlH₄ for hydrogen storage. 118

$$3 \text{ LiAlH}_4 \rightarrow \text{Li}_3 \text{AlH}_6 + 2 \text{ Al} + 3 \text{ H}_2 \quad 5.3 \text{ wt.} \% \text{H}_2$$
 (5)

$$Li_3AlH_6 \rightarrow 3 LiH + Al + 3/2 H_2 2.6 wt.\%H_2$$
 (6)

$$3 \text{ LiH} + 3 \text{ Al} \rightarrow 3 \text{ LiAl} + 3/2 \text{ H}_2 \quad 2.6 \text{ wt.}\%\text{H}_2$$
 (7)

Sodium Alanate (NaAlH₄)

Sodium alanate can be synthesized by direct synthesis from the elements under stringent conditions, ball milling of the elements under an inert atmosphere, or wet chemical synthesis using NaH and Al. It has a tetragonal crystal structure with a space group of $I4_1/a$. The $[AlH_4]^-$ anion forms isolated tetrahedral units, and sodium atoms are surrounded by eight nearest $[AlH_4]^-$ tetrahedra in a distorted square anti-prismatic

geometry. Its theoretical hydrogen storage capacity is 7.41 wt.%, but the practical capacity is around 3.70 wt.%. ¹²⁰ As shown in reaction 8, 9 and 10, NaAlH₄ decomposes in two steps. The first step at around 190 °C releases hydrogen and forms Na₃AlH₆, while the second step at around 230 °C releases more hydrogen and forms NaH. ^{121,122} Previous research has demonstrated that sodium alanate doped with titanium catalysts exhibits reversible hydrogen storage capabilities at moderate operating temperatures. ¹²³ Moreover, the hydrogen storage density of NaAlH₄ doped with titanium catalysts can reach up to 4.5 wt.%, which is significantly higher than that of undoped counterparts. This enhancement is attributed to the improved thermodynamic and kinetic properties of the doped material during the hydrogenation and dehydrogenation processes. ¹²⁴ The addition of titanium catalysts not only lowers the decomposition temperature but also accelerates the hydrogen absorption and release rates, making NaAlH₄ a promising candidate for practical hydrogen storage applications. ¹²⁵ The addition of Ti-based catalysts, such as TiCl₃, can significantly improve the reversibility and kinetics of hydrogen release, lowering the desorption temperature from 220°C to 160°C. ¹²⁶

3 NaAlH₄
$$\rightleftharpoons$$
 Na₃AlH₆ + 2 Al + 3 H₂ 3.7 wt.%H₂ (8)
Na₃AlH₆ \rightleftharpoons 3 NaH + Al + 3/2 H₂ 1.9 wt.%H₂ (9)
NaH \rightleftharpoons Na + 1/2H₂ 1.9 wt.%H₂ (10)

Magnesium Alanate (Mg(AlH₄)₂)

Mg(AlH₄)₂ can be synthesized by reacting MgH₂ with AlH₃ in a solvent-free environment or through ball milling. It forms a trigonal sheet-like structure with distorted and isolated [AlH₄]⁻ tetrahedra. The theoretical hydrogen storage capacity is 9.27 wt.%. As shown in reaction 11 and 12, the initial dehydrogenation step of magnesium alanate occurs within the temperature range of 110–200 °C, releasing approximately 7 wt.% of hydrogen.¹²⁷ Subsequently, the dissociation of magnesium hydride takes place around 310 °C, resulting in the evolution of an additional 2.3 wt.% of hydrogen. Meanwhile, the intermetallic compound Al₃Mg₂ is formed through the reaction between magnesium and aluminium at approximately 400 °C.¹²⁸ Several studies have been conducted to achieve reversibility in magnesium alanate systems. However, due to the exothermic nature of the first dehydrogenation step and the underlying thermodynamic constraints, reversibility has not been successfully attained.¹²⁹

$$Mg(AlH_4)_2 \rightarrow MgH_2 + 2 Al + 3 H_2 \quad 7.0 \text{ wt.}\%H_2$$
 (11)
 $MgH_2 + 2 Al \rightarrow 1/2 Al_3Mg_2 + 1/2 Al + H_2 \quad 2.3 \text{ wt.}\%H_2$ (12)

1.3.3 Borohydrides

1.3.3.1 Introduction of Borohydrides

Borohydrides such as lithium borohydride (LiBH₄), sodium borohydride (NaBH₄), magnesium borohydride (Mg(BH₄)₂), and calcium borohydride (Ca(BH₄)₂) exhibit significant hydrogen storage potential. For example, lithium borohydride (LiBH₄) has a high theoretical hydrogen storage capacity of up to 18.5 wt.%, but it has a high decomposition temperature and slow hydrogenation kinetics. Sodium borohydride (NaBH₄) offers a high hydrogen storage density (10.7 wt.%) but undergoes an irreversible hydrolysis reaction, producing hydrogen gas and sodium metaborate as a byproduct. ^{130,131,132} Magnesium borohydride (Mg(BH₄)₂) provides good hydrogen storage capabilities, but its slow hydrogen absorption and desorption kinetics limit practical applications. Calcium borohydride (Ca(BH₄)₂) is another viable candidate with an 8.3 wt.% hydrogen capacity, though it also faces challenges related to high desorption temperatures. ¹³³

Despite their advantages, borohydrides face several critical challenges such as: (a) High decomposition temperatures, as most borohydrides decompose at temperatures exceeding 200 °C, making them unsuitable for low-temperature applications; (b) slow kinetics, where the rate of hydrogen absorption and desorption is often too slow for practical use. Modifications such as doping with catalysts or reducing particle sizes through nanoconfinement have been explored to improve kinetics; ¹³⁴ (c) thermodynamic stability, given that, many borohydrides are highly stable, requiring high temperatures to release hydrogen. Strategies like destabilization through alloying have been employed to lower the hydrogen release temperature and (d) Reversibility, some borohydrides undergo irreversible reactions, such as NaBH₄ in hydrolysis, making their reusability a challenge. ¹³⁵

1.3.4 Modification and Optimisation Strategies for Solid State Hydrogen Storage Materials

To overcome the limitations of alanates and borohydride, various strategies have been explored, including doping with catalysts, forming reactive hydride composites, and nanoconfinement.

1.3.4.1 Nanostructuring and Nanoconfinement

Nanostructuring and nanoconfinement have been identified as effective strategies to address these challenges. By reducing the particle size and/or confining the hydrides within nanostructured scaffolds, the hydrogen absorption and desorption kinetics can be significantly improved. Nanoconfinement can also alter the thermodynamic properties of the hydrides, making hydrogen release and uptake more feasible at lower temperatures and

pressures. ¹³⁶ For example, nanoconfinement in carbon scaffolds has been widely used, with materials such as mesoporous carbons, graphene derivatives, and carbon nanotubes providing high surface area and thermal stability, which enhance the hydrogen storage performance of complex hydrides. ¹³⁷ Metal-organic frameworks (MOFs) offer another platform for nanoconfinement, providing tunable pore sizes and high surface areas. MOFs can stabilize complex hydrides and improve their hydrogen storage properties through enhanced kinetics and reduced activation energies. ¹³⁸ For example, LiAlH₄ and NaAlH₄ confined within porous carbon materials have shown lower hydrogen desorption temperatures and faster kinetics compared to their bulk counterparts. Core-shell structures, where alanate nanoparticles are encapsulated within a metallic shell, offer a unique approach to stabilising alanates. ¹³⁹ These structures can prevent particle agglomeration and maintain the nanosizing effects during hydrogen cycling. Recent studies have demonstrated the successful synthesis of core-shell alanate structures with improved hydrogen storage properties.

1.3.4.2 Catalysts and Additives

The addition of catalysts and other additives has been shown to significantly enhance the hydrogen storage properties of complex hydrides. Transition metals, such as Ti, Co, and Ni, are commonly used to improve the kinetics of hydrogen absorption and desorption. These catalysts can be added in the form of nanoparticles or incorporated into the scaffold material to enhance the overall performance. Detailed studies have shown that the catalytic effects can be attributed to the formation of intermediate phases and the stabilization of reaction products. For example, Ti-doped NaAlH₄ has been shown to form a Ti-Al alloy that facilitates hydrogen release by lowering the activation energy. 124

1.3.4.3 Reactive Hydride Composites (RHCs)

Formation of a reactive hydride composite, a concept which involves the mixing of two or more hydrides, has also been investigated to improve the hydrogen storage properties of alanates and borohydrides. These composites can alter the decomposition pathway and reduce the desorption temperature. RHCs utilize a synergistic effect between different hydrides, leading to modified thermodynamic stability and reaction enthalpy.¹⁴¹

For instance, mixing NaAlH₄ with LiBH₄ has been shown to improve the hydrogen release properties of both materials. Some notable examples include 2LiBH₄–MgH₂, which reduces hydrogen release temperature compared to pure LiBH₄, offering reversibility under moderate conditions.¹⁴² NaBH₄–MgH₂ demonstrates improved hydrogen cycling performance and stability over multiple cycles. LiNH₂–LiH can be reversibly operated at temperatures around 250°C with a hydrogen capacity of about 6.5 wt.%.¹⁴³

Despite their promise, reversible hydrogen carriers face several challenges in their practical implementation. One significant issue is the high operating temperatures required for efficient hydrogen release. Many RHC systems still necessitate temperatures above 200°C to achieve optimal performance in hydrogen release, which can be a major limitation for certain applications due to the energy input and potential safety concerns associated with such high temperatures. Another challenge is the slow kinetics of hydrogen absorption and desorption. The rates at which RHCs absorb and release hydrogen need to be significantly improved to be viable for practical applications. These slow kinetics can result in longer processing times and reduced overall efficiency. Additionally, structural stability is a major concern for some RHCs.¹⁴⁴ Over multiple cycles of hydrogen absorption and desorption, certain RHCs experience degradation, which in turn reduces their effectiveness and longevity. This instability can lead to increased costs and maintenance requirements, further complicating their widespread adoption.

1.4 Hydride – Hydroxide Hydrogen Release Systems

Hydride–Hydroxide systems represent promising approaches for hydrogen storage and generation, leveraging the reversible reactions between metal hydrides and metal hydroxides. This system is particularly relevant for applications where hydrogen needs to be generated on-demand, such as in fuel cells. Light metal hydroxides are considered attractive candidates for solid-state hydrogen storage due to their low cost. Unlike nitrogen- or boron-containing systems, they do not produce by-products that could poison fuel cells. 146

Numerous hydride–hydroxide systems have been extensively studied, including LiBH₄–LiOH, NaOH–NaH, and LiH–LiOH. These systems are of great interest due to their high theoretical hydrogen capacities, low dehydrogenation temperatures, or in some cases, reversible hydrogen release and uptake. A key theoretical basis underpinning these systems is the concept proposed by Chen et al., which involves H⁺-H⁻ coupling between protons from hydroxide (OH⁻) groups and hydride (H⁻) ions, thereby facilitating the dehydrogenation process. ¹⁴⁷ According to Chen et al.'s study, the interaction between LiNH₂ and LiH significantly lowers the hydrogen release temperature compared to the decomposition temperatures of the individual components. While pure LiNH₂ decomposes above 300 °C to form lithium imide and ammonia, and LiH releases hydrogen only above 550 °C, their mixture generates hydrogen at approximately 150 °C. Techniques such as TG, XRD, and IR spectroscopy revealed that LiNH₂ reacts with LiH to produce hydrogen and lithium imide (or lithium-rich imide), with an enthalpy of reaction around 45 kJ mol⁻¹,

which is substantially lower than the 83.68 kJ mol⁻¹ required for pure LiNH₂ decomposition. Furthermore, isotopic labelling experiments indicated proton–deuteron exchange, providing deeper insights into the reaction mechanism. This work offered a new perspective on the chemical behaviour of metal amides and hydrides and laid the groundwork for the design of novel hydrogen storage materials.

Subsequently, Vajo et al. investigated solid-state reactions between ionic hydrides and alkali metal hydroxides, which can produce hydrogen and metal oxides. He hydrolysis of ionic hydrides, yet remain kinetically stable at room temperature when hydrides and hydroxides are mixed and processed via mechanochemical methods. Several systems were evaluated, including LiH + LiOH, 2LiH + NaOH, LiBH₄ + 4LiOH, and 3LiBH₄ + 4LiOH·H₂O. Notably, the reaction of 3LiBH₄ + 4LiOH·H₂O releases approximately 10 wt.% H₂, with more than 5 wt.% evolving below 100 °C. The LiH + LiOH mixture produced around 5.73 wt.% hydrogen at 250 °C, achieving 91% of the theoretical yield (6.27 wt.%). The addition of 10 mol% TiCl₃ increased hydrogen evolution at 100 °C but slightly reduced the final yield. Other systems, such as LiH + NaOH and 2LiH + NaOH, yielded 1.92 wt.% and 3.20 wt.% H₂ at 250 °C, respectively. The LiBH₄ + 4LiOH mixture released 6.64 wt.% hydrogen at 350 °C with a 98% yield, while the hydrated 3LiBH₄ + 4LiOH·H₂O system achieved 10.05 wt.% total hydrogen with 98% efficiency.

LiBH₄, in particular, has gained widespread attention as a solid-state hydrogen storage material due to its high gravimetric (18.5 wt.%) and volumetric (121 kg H₂/m³) hydrogen densities. However, its practical use is limited by its high dehydrogenation temperature (>380 °C) and poor reversibility. According to Li et al.'s article, various strategies have been explored to overcome these limitations, including catalyst addition and nanostructuring.¹⁴⁹ For instance, the incorporation of MgH₂ in the 2LiBH₄–MgH₂ system significantly reduced the dehydrogenation enthalpy and lowered the hydrogen release temperature from 500 °C to 340 °C. The use of TiCl₃ and MgCl₂ catalysts enabled hydrogen release at 60 °C and reversible uptake of 4.5 wt.% H₂ at 600 °C under 7 MPa. Confined LiBH₄ within mesoporous carbon also significantly improved performance, lowering the dehydrogenation temperature to *ca.* 150 °C and enabling reversible hydrogen storage up to 8 wt.% under 600 °C and 7 MPa.

More recently, light metal borohydride–hydroxide systems, such as LiBH₄–Mg(OH)₂, have emerged as promising candidates. According to Drozd et al.'s work, hydrogen release from NaBH₄ + Mg(OH)₂ is influenced by particle size and mixing homogeneity, with activation energies around 155.9 kJ mol⁻¹.¹⁵⁰ Ball-milled mixtures released 87-92% of hydrogen within the 240-318 °C range. In Varin et al.'s study, nanostructured NaBH₄ and

LiBH₄–Mg(OH)₂ composites enhanced with nano-Ni showed performance. LiBH₄–Mg(OH)₂ began dehydrogenation at 200 °C with a low activation energy of 38-47 kJ/mol, but with a two-stage hydrogen release mechanism. 151 According to Liu et al.'s article, LiBH₄-0.3Mg(OH)₂ composites exhibited the best dehydrogenation behaviour, releasing up to 9.6 wt.% hydrogen between 100-450 °C through three distinct steps, and demonstrated reversible uptake of 4.7 wt.% H₂ under 100 bar at 450 °C.(superior to pure LiBH₄)¹⁵² Cai et al.'s study investigated LiBH₄ composites with alkali metal hydroxides (LiOH, NaOH, KOH) to reduce dehydrogenation temperatures. H⁺-H⁻ interactions significantly lowered onset temperatures and enhanced hydrogen release rates. 153 For instance, LiBH₄-LiOH released 6.5 wt.% H₂ within 10 minutes at 250 °C, and the onset dehydrogenation temperatures dropped from 280 °C (pure LiBH₄) to 207 °C, 221 °C, and 230 °C for LiBH₄–LiOH, 2LiBH₄–NaOH, and 2LiBH₄–KOH, respectively. These trends were attributed to the increasing acidity of [OH] sites due to the electronegativity of the alkali metals (Li > Na > K), enhancing their interaction with [LiBH₄]. Additionally, higher LiOH content improved dehydrogenation kinetics, with LiBH₄–4LiOH releasing 6.5 wt.% hydrogen in 10 minutes at 250 °C.

To address challenges such as poor cyclability and high dehydrogenation temperatures, light metal hydride-hydroxide systems have been developed. According to Lu et al.'s study, a novel hybrid approach was proposed for hydrogen storage in solid inorganic hydride materials, as well as for hydrogen production from water. 154 This method is based on the reaction between LiOH (or LiOH·H2O) and LiH, which exhibits favourable kinetics and enables hydrogen release and uptake within a practically viable temperature range (<350 °C). The system demonstrates a reversible hydrogen storage capacity of 6–8.8 wt.%. As a hydrogen production pathway, this reaction yields hydrogen entirely derived from water, through its reaction with alkali metal oxides. Experimental studies validated the dehydrogenation, hydrogen uptake, and regeneration of LiH. For example, a mixture of LiOH·H₂O and LiH released up to 8.5 wt.% H₂ at 350 °C, while LiOH and LiH released 6.0 wt.% H₂ at 300 °C. The regeneration step involves the reaction Li₂O + H₂O \rightarrow 2LiOH (or LiOH·H₂O), enabling reformation of the hydroxide and thus facilitating reversible hydrogen cycling. Despite its promising performance, this system still faces several scientific and technical challenges, including a deeper understanding and precise control of the reaction mechanisms, as well as improving the overall energy efficiency of the full cycle.

Mao *et al* probed the mechanism of the NaOH-NaH system. According to previous research, Na₂O can easily absorb the H₂ at low temperature (about 60 °C) to form NaOH and NaH. In the contrast, the NaOH and NaH mixed can form Na₂O and H₂ in reaction

13.¹⁵⁵ Therefore, reversibility is the biggest advantage of the NaOH-NaH system. Both LiH and NaH are Group I light metal hydrides. Although the gravimetric hydrogen capacity of NaH is less than LiH, the LiH-LiOH system is not reversible, and the dehydrogenation temperature of the NaH-NaOH system is lower than LiH-LiOH. The dehydrogenation reaction is endothermic.¹⁵⁶

$$Na_2O + H_2 = NaOH + NaH \quad \Delta H = +55.65 \text{ kJ/mol}$$
 (13)

1.5 Aim of Thesis

This thesis focuses on developing new complex RHCs and understanding their fundamental mechanisms of hydrogen storage. Beginning with the NaOH-NaH system, the purpose of this work was to develop sodium-based metal and complex hydride systems combing sodium hydrides with hydroxides and with hydride previously not considered for RHC-type storage. Advances in nanostructuring and catalysis have led to significant improvements in the kinetics performance. Five different systems were fully investigated.

- NaH NaOH system
- NaAlH₄ NaOH system
- NaBH₄ NaOH system
- Ca₄Mg₃H₁₄ NaH system
- NaAlH₄/MgH₂ Guanidine(CH₅N₃) system

The selection of these systems was guided by several considerations. Sodium-based hydrides and hydroxides are inexpensive, lightweight, and possess relatively high theoretical hydrogen capacities, making them attractive for large-scale storage. The NaH - NaOH, NaAlH₄ - NaOH, and NaBH₄ - NaOH systems were chosen to investigate the effect of hydroxide incorporation on the hydrogen release properties of simple and complex sodium hydrides. The Ca₄Mg₃H₁₄ - NaH system represents a mixed alkaline composite with potential synergistic effects arising from multicomponent interactions. Finally, the NaAlH₄/MgH₂ - Guanidine(CH₅N₃) system was introduced as organic-molecular-based hydrogen storage, offering the possibility of modifying dehydrogenation pathways through organic molecular.

The aim of the thesis was to research the hydrogen release performance of all the systems and to investigate gravimetric capacity, dehydrogenation temperatures, and the kinetics of dehydrogenation (including activation energies) systematically. Mechanochemical nanostructuring and the use of catalysts/additives were the two main methods employed in order to attempt to improve the kinetic behaviour of the five systems. Powder X-ray

diffraction was used to try and identify any intermediate species forming during the dehydrogenation reactions and to propose and validate a mechanism of hydrogen release for each system.

1.6 References

- 1. N. A. Rusman and M. Dahari, International Journal of Hydrogen Energy, 2016, 41, 12108-12126.
- 2. M. S. Dresselhaus and I. L. Thomas, Nature, 2001, 414, 332.
- 3. B. D. Shakya, L. Aye and P. Musgrave, International Journal of Hydrogen Energy, 2005, 30, 9.
- 4. N. Abas, A. Kalair and N. Khan, Futures, 2015, 69, 31-49.
- 5. M. R. Usman, Renewable and Sustainable Energy Reviews, 2022, 167, 112743.
- 6. F. P. Martins, S. De-León Almaraz, A. B. Botelho Junior, C. Azzaro-Pantel and P. Parikh, *Renewable and Sustainable Energy Reviews*, 2024, **204**, 114796.
- 7. D. Peyerl and B. van der Zwaan, Discover Sustainability, 2024, 5, 199.
- 8. W. Lubitz and B. Tumas, Chemical Reviews Editorial, 2007, 107, 3900.
- 9. A. Züttel, A. Remhof, A. Borgschulte and O. Friedrichs, *Philosophical Transactions of the Royal Society A*, 2010, **368**, 3329.
- 10. M. M. Hossain Bhuiyan and Z. Siddique, *International Journal of Hydrogen Energy*, 2025, **102**, 1026-1044.
- 11. M. Winter and R. J. International Journal of Hydrogen Energy Brodd, Chemical Reviews, 2004, 104, 4245.
- 12. P. Pei and H. Chen, Applied Energy, 2014, 125, 60.
- 13. T. Abbasi and S. A. Abbasi, Renewable and Sustainable Energy Reviews, 2011, 15, 3034-3040.
- 14. M. Marquevich, G. W. Sonnemann, F. Castells, et al., Green Chem., 2002, 4, 414-423.
- 15. I. Staffell, D. Scamman, A. V. Abad, P. Balcombe, P. E. Dodds, P. Ekins, N. Shah, and K. R. Ward, *Energy Environ. Sci.*, 2019, **12**, 463-491.
- 16. B. Pivovar, N. Rustagi, and S. Sutyapal, Electrochem. Soc. Interface, 2018, 27, 47-52.
- 17. I. A. Hassan, H. S. Ramadan, M. A. Saleh, and D. Hissel, *Renew. Sustain. Energy Rev.*, 2021, **149**, 111311.
- 18. S. B. Walker, U. Mukherjee, M. Fowler, and A. Elkamel, *Int. J. Hydrogen Energy*, 2016, 41, 7717-7731.
- 19. R. Ding and X. J. Sun, Catal. Sci. Technol., 2020, 10, 1567-1581.
- 20. B. Tanc, H. T. Arat, E. Baltacioglu, and K. Aydın, Int. J. Hydrogen Energy, 2019, 44, 10120-10128.
- 21. V. Vogl, M. Åhman, and L. J. Nilsson, *J. Cleaner Prod.*, 2018, **203**, 736-745.
- 22. L. Schlapbach and A. Zuttel, *Nature*, 2001, 414. 353–358.
- 23. L. Lombardi, E. Carnevale, and A. Corti, Int. J. Energy Environ. Eng., 2011, 2, 63-78.
- 24. U. I. Amran, A. Ahmad, and M. R. Othman, Aust. J. Basic Appl. Sci., 2017, 11, 43-50.
- 25. E. Cetinkaya, I. Dincer, and G. F. Naterer, Int. J. Hydrogen Energy, 2012, 37, 2071-2080.
- 26. P. Colomban, Fuel Cells, 2013, 13, 6.

- 27. M. M. Rampai, C. B. Mtshali, N. S. Seroka and L. Khotseng, RSC Adv, 2024, 14, 6699-6718.
- 28. A. Z. Arsad, M. A. Hannan, A. Q. Al-Shetwi, M. Mansur, K. M. Muttaqi, Z. Y. Dong and F. Blaabjerg, *International Journal of Hydrogen Energy*, 2022, **47**, 17285-17312.
- 29. Z. X. Guo, C. Shang and K. F. Aguey-Zinsou, *Journal of the European Ceramic Society*, 2008, 28, 1467-1473.
- 30. M. Jayachandran, R. K. Gatla, A. Flah, A. H. Milyani, H. M. Milyani, V. Blazek, L. Prokop and H. Kraiem, *IEEE Access*, 2024, **12**, 23363-23388.
- 31. J. Breternitz and D. Gregory, *Crystals*, 2015, **5**, 617-633.
- 32. N. Ma, W. Zhao, W. Wang, X. Li and H. Zhou, *International Journal of Hydrogen Energy*, 2024, **50**, 379-396.
- 33. M. Felderhoff, C. Weidenthaler, R. von Helmolt and U. Eberle, *Phys Chem Chem Phys*, 2007, 9, 2643-2653.
- 34. P. Preuster, A. Alekseev and P. Wasserscheid, Annu Rev Chem Biomol Eng, 2017, 8, 445-471.
- 35. D. J. Durbin and C. Malardier-Jugroot, *International Journal of Hydrogen Energy*, 2013, **38**, 14595-14617.
- 36. F. Zhang, P. Zhao, M. Niu and J. Maddy, *International Journal of Hydrogen Energy*, 2016, 41, 14535-14552.
- 37. S. W. Jorgensen, Current Opinion in Solid State and Materials Science, 2011, 15, 39-43.
- 38. E. Rivard, M. Trudeau and K. Zaghib, Materials (Basel), 2019, 12, 1973.
- J. O. Jensen, A. P. Vestbø, Q. Li and N. J. Bjerrum, *Journal of Alloys and Compounds*, 2007, 446-447, 723-728.
- 40. K. T. Møller, T. R. Jensen, E. Akiba and H.-w. Li, *Progress in Natural Science: Materials International*, 2017, **27**, 34-40.
- 41. H. Barthelemy, M. Weber and F. Barbier, *International Journal of Hydrogen Energy*, 2017, **42**, 7254-7262.
- 42. A. M. Abdalla, S. Hossain, O. B. Nisfindy, A. T. Azad, M. Dawood and A. K. Azad, *Energy Conversion and Management*, 2018, **165**, 602-627.
- 43. J. O. Abe, A. P. I. Popoola, E. Ajenifuja and O. M. Popoola, *International Journal of Hydrogen Energy*, 2019, 44, 15072-15086.
- 44. R. Moradi and K. M. Groth, International Journal of Hydrogen Energy, 2019, 44, 12254-12269.
- 45. Y. Wang, H. Yuan, A. Martinez, P. Hong, H. Xu and F. R. Bockmiller, *Advances in Applied Energy*, 2021, **2**, 100011.
- 46. P. Prachi R, W. Mahesh M and G. Aneesh C, Advances in Energy and Power, 2016, 4, 11-22.
- 47. A. Zuttel, Naturwissenschaften, 2004, 91, 157-172.
- 48. IEA, *Hydrogen production and storage: R&D priorities and gaps*, 2006, https://www.iea.org/reports/hydrogen-production-and-storage. (accessed 2 January 2025).

- 49. A. Züttel, P. Wenger, S. Rentsch, P. Sudan, P. Mauron and C. Emmenegger, *Journal of Power Sources*, 2003, **118**, 1-7.
- 50. R. K. Ahluwalia, T. Q. Hua, J. K. Peng, S. Lasher, K. McKenney, J. Sinha and M. Gardiner, *International Journal of Hydrogen Energy*, 2010, **35**, 4171-4184.
- 51. S. M. Aceves, F. Espinosa-Loza, E. Ledesma-Orozco, T. O. Ross, A. H. Weisberg, T. C. Brunner and O. Kircher, *International Journal of Hydrogen Energy*, 2010, **35**, 1219-1226.
- 52. G. G. Libowitz, Journal of Physics and Chemistry of Solids, 1994, 55, 1461.
- 53. B. Sakintuna, F. Lamari-Darkrim and M. Hirscher, *International Journal of Hydrogen Energy*, 2007, **32**, 1121.
- 54. L. George and S. K. Saxena, International Journal of Hydrogen Energy, 2010, 35, 5454.
- 55. I. P. Jain, C. Lal and A. Jain, International Journal of Hydrogen Energy, 2010, 35, 5133-5144.
- 56. B. Peng, J. Liang, Z. Tao and J. Chen, Journal of Materials Chemistry, 2009, 19, 2877.
- 57. K. F. Aguey-Zinsou, J.-R. Ares-Fernández, Energy and Environmental Science, 2010, 3, 526.
- 58. F. Cheng, Z. Tao, J. Liang and J. Chen, Chemical Communications, 2012, 48, 7334.
- 59. C. Milanese, T. R. Jensen, B. C. Hauback, C. Pistidda, M. Dornheim, H. Yang, L. Lombardo, A. Zuettel, Y. Filinchuk, P. Ngene, P. E. de Jongh, C. E. Buckley, E. M. Dematteis and M. Baricco, *International Journal of Hydrogen Energy*, 2019, 44, 7860-7874.
- 60. J. Graetz, Chem Soc Rev, 2009, 38, 73-82.
- 61. A. Zaluska, L. Zaluski and J. O. Strom-Olsen, Journal of Alloys and Compounds, 2000, 298, 125.
- 62. J. W. Lauher, Acta Crystallographica B-Structural Science, 1979, B35, 1454.
- 63. H. Yukawa, N. Morisaku, Y. Li, K. Koyima, R. Rong, Y. Shinzato, R. Sekine and M. Morinaga, *Journal of Alloys and Compounds*, 2007, **446-447**, 242.
- 64. B. Bogdanovic and M. Schwickardi, Journal of Alloys and Compounds, 1997, 253-254, 1.
- 65. C. Rongeat, I. L. Jansa, S. Oswald, L. Schultz and O. Gutfleisch, Acta Materialia, 2009, 57, 5563.
- 66. X. Xiao, K. Yu, X. Fan, Z. Wu, X. Wang, C. Chen, Q. Wang and L. Chen, *International Journal of Hydrogen Energy*, 2011, **36**, 539.
- 67. Y. Kojima, Y. Kawai, T. Haga, M. Matsumoto and A. Koiwai, *Journal of Alloys and Compounds*, 2007, 441, 189.
- 68. X. Liu, H. W. Langmi, S. D. Beattie, F. F. Azenwi, G. S. McGrady and C. M. Jensen, *Journal of the American Chemical Society*, 2011, **133**, 15593.
- 69. J. R. Ares, K.-F. Aguey-Zinsou, M. Porcu, J. M. Sykes, M. Dornheim, T. Klassen and R. Bormann, *Materials Research Bulletin*, 2008, **43**, 1263.
- 70. I. P. Jain, P. Jain and A. Jain, Journal of Alloys and Compounds, 2010, 503, 303.
- 71. K. Gandhi, D. Kumar Dixit and B. Kumar Dixit, Physica B: Condensed Matter, 2010, 405, 3075-3081.
- 72. L. Zhou, Renewable and Sustainable Energy Reviews, 2005, 9, 395-408.

- 73. H. W. Langmi, D. Book, A. Walton, S. R. Johnson, M. M. Al-Mamouri, J. D. Speight, P. P. Edwards, I. R. Harris and P. A. Anderson, *Journal of Alloys and Compounds*, 2005, **404-406**, 637-642.
- 74. K.-H. Chung, Energy, 2010, 35, 2235-2241.
- 75. H. W. Langmi, J. Ren, B. North, M. Mathe and D. Bessarabov, Electrochimica Acta, 2014, 128, 368-392.
- 76. O. K. Farha, A. O. Yazaydin, I. Eryazici, C. D. Malliakas, B. G. Hauser, M. G. Kanatzidis, S. T. Nguyen, R. Q. Snurr and J. T. Hupp, *Nat Chem*, 2010, **2**, 944-948.
- 77. B. L. Huang, A. J. H. McGaughey and M. Kaviany, *International Journal of Heat and Mass Transfer*, 2007, **50**, 393-404.
- 78. Q.-L. Zhu and Q. Xu, Energy & Environmental Science, 2015, 8, 478-512.
- 79. T. He, Q. Pei and P. Chen, Journal of Energy Chemistry, 2015, 24, 587-594.
- 80. M. R. Usman and D. L. Cresswell, International Journal of Green Energy, 2013, 10, 177-189.
- 81. M. Becherif, H. S. Ramadan, K. Cabaret, F. Picard, N. Simoncini and O. Bethoux, *Energy Procedia*, 2015, **74**, 371-380.
- 82. M. Kamran and M. Turzyński, Journal of Energy Storage, 2024, 96, 112601.
- 83. S. G. Nnabuife, A. K. Hamzat, J. Whidborne, B. Kuang and K. W. Jenkins, *International Journal of Hydrogen Energy*, 2025, **107**, 218-240.
- 84. M. Y. Song, S. H. Baek, J.-L. Bobet and S.-H. Hong, *International Journal of Hydrogen Energy*, 2010, **35**, 10366.
- 85. L. George and S. K. Saxena, International Journal of Hydrogen Energy, 2010, 35, 5454-5470.
- 86. T. He, H. Cao and P. Chen, Adv Mater, 2019, 31, e1902757.
- 87. M. Simanullang and L. Prost, International Journal of Hydrogen Energy, 2022, 47, 29808-29846.
- 88. H. Li, Z. Li, M. Luo, H. Yuan, Y. Wu, X. Guo and L. Hao, *Journal of Materials Science*, 2023, 58, 16269-16296.
- 89. A. C. M. Griffond, M. V. Sofianos, D. A. Sheppard, T. D. Humphries, A.-L. Sargent, M. Dornheim, K.-F. Aguey-Zinsou and C. E. Buckley, *Journal of Alloys and Compounds*, 2021, **858**, 158229.
- 90. S. Balakrishnan, T. D. Humphries, M. Paskevicius and C. E. Buckley, *International Journal of Hydrogen Energy*, 2023, **48**, 30479-30488.
- 91. B. Peng, J. Liang, Z. Tao and J. Chen, Journal of Materials Chemistry, 2009, 19, 2877.
- 92. K. F. Aguey-Zinsou, J.-R. Ares-Fernández, Energy and Environmental Science, 2010, 3, 526.
- 93. F. Cheng, Z. Tao, J. Liang and J. Chen, Chemical Communications, 2012, 48, 7334.
- 94. A. Denis, E. Sellier, C. Aymonier and J.-L. Bobet, Journal of Alloys and Compounds, 2009, 476, 152.
- 95. H. Gasan, O. N. Celik, N. Aydinbeyli and Y. M. Yaman, *International Journal of Hydrogen Energy*, 2012, 37, 1912.
- 96. C. Z. Wu, P. Wang, X. Yao, C. Liu, D. M. Chen, G. Q. Lu and H. M. Cheng, *Journal of Alloys and Compounds*, 2006, **420**, 278-282.

- 97. C. R. Luna, C. E. Macchi, A. Juan and A. Somoza, *International Journal of Hydrogen Energy*, 2010, **35**, 12421.
- 98. W. N. Yang, C. X. Shang and Z. X. Guo, International Journal of Hydrogen Energy, 2010, 35, 4534.
- 99. Z. S. Wronski, G. J. C. Carpenter, T. Czujko and R. A. Varin, *International Journal of Hydrogen Energy*, 2011, **36**, 1159.
- 100. L. Xie, Y. Liu, X. Zhang, j. Qu, Y. Wang and X. Li, Journal of Alloys and Compounds, 2009, 482, 388.
- 101. H. Wang, J. Zhang, J. W. Liu, L. Z. Ouyang and M. Zhu, *International Journal of Hydrogen Energy*, 2013, 38, 10932-10938.
- 102. R. Sahoo, M. Singh and T. N. Rao, ChemElectroChem, 2021, 8, 2358-2396.
- 103. E. M. Dematteis, M. B. Amdisen, T. Autrey, J. Barale, M. E. Bowden, C. E. Buckley, Y. W. Cho, S. Deledda, M. Dornheim, P. de Jongh, J. B. Grinderslev, G. Gizer, V. Gulino, B. C. Hauback, M. Heere, T. W. Heo, T. D. Humphries, T. R. Jensen, S. Y. Kang, Y.-S. Lee, H.-W. Li, S. Li, K. T. Møller, P. Ngene, S.-i. Orimo, M. Paskevicius, M. Polanski, S. Takagi, L. Wan, B. C. Wood, M. Hirscher and M. Baricco, *Progress in Energy*, 2022, **4**, 032009.
- 104. S. Orimo, Y. Nakamori, J. R. Eliseo, A. Züttel and C. M. Jensen, Chemical Reviews, 2007, 107, 4111.
- 105. J. Jepsen, J. M. Bellosta con Colbe, T. Klassen and M. Dornheim, *International Journal of Hydrogen Energy*, 2012, **37**, 4202.
- 106. S. McWhorter, C. Read, G. Ordaz and N. Stetson, *Current Opinion in Solid Sate and Materials Science*, 2011, **15**, 29.
- 107. D. S. Easton, J. H. Schneibel and S. S. Speakman, Journal of Alloys and Compounds, 2005, 398, 245.
- 108. Z. Xueping, L. Ping and Q. Xuanhui, Rare Metal Materials and Engineering, 2009, 38, 766.
- 109. S. McWhorter, C. Read, G. Ordaz and N. Stetson, *Current Opinion in Solid Sate and Materials Science*, 2011, **15**, 29.
- 110. Y. Kim, E.-K. Lee, J.-H. Shim, Y. W. Cho and K. B. Yoon, *Journal of Alloys and Compounds*, 2006, 422, 283.
- 111. M. S. L. Hudson, D. Pukazhselvan, G. Irene Sheeja and O. N. Srivistava, *International Journal of Hydrogen Energy*, 2007, **32**, 4933.
- 112. C. M. Andrei, J. Walsmsley, D. Blanchard, H. W. Brinks, R. Holmestad and B. C. Hauback, *Journal of Alloys and Compounds*, 2005, **395**, 307.
- 113. D. S. Easton, J. H. Schneibel and S. S. Speakman, Journal of Alloys and Compounds, 2005, 398, 245.
- 114. N. Sklar and B. Post, Inorganic Chemistry, 1967, 6, 669.
- 115. M. Ismail, N. A. Sazelee, N. A. Ali and S. Suwarno, *Journal of Alloys and Compounds*, 2021, **855**, 157475.
- 116. N. A. Sazelee and M. Ismail, International Journal of Hydrogen Energy, 2021, 46, 9123-9141.
- 117. M. Ismail, N. A. Ali, N. A. Sazelee and S. Suwarno, *International Journal of Hydrogen Energy*, 2022, 47, 31903-31910.

- 118. N. Z. Abd.Khalim Khafidz, Z. Yaakob, K. L. Lim and S. N. Timmiati, *International Journal of Hydrogen Energy*, 2016, 41, 13131-13151.
- 119. B. C. Hauback, Zeitschrift für Kristallographie, 2008, 223, 636-648.
- 120. A. Zaluska, L. Zaluski and J. O. Strom-Olsen, Journal of Alloys and Compounds, 2000, 298, 125.
- 121. H. Yukawa, N. Morisaku, Y. Li, K. Koyima, R. Rong, Y. Shinzato, R. Sekine and M. Morinaga, *Journal of Alloys and Compounds*, 2007, **446-447**, 242.
- 122. C. P. Balde, B. P. C. Hereijgers, J. H. Bitter and K. P. de Jong, *Journal of the American Chemical Society*, 2008, **130**, 6761.
- 123. J. M. Bellosta von Colbe, B. Bogdanovic, M. Felderhoff, A. Pommerin and F. Schüth, *Journal of Alloys and Compounds*, 2004, **370**, 104.
- 124. M. Fichtner, P. Canton, O. Kircher, A. Leon, Journal of Alloys and Compounds, 2005, 404-406, 732.
- 125. X. Xiao, K. Yu, X. Fan, Z. Wu, X. Wang, C. Chen, Q. Wang and L. Chen, *International Journal of Hydrogen Energy*, 2011, **36**, 539.
- 126. C. Rongeat, I. L. Jansa, S. Oswald, L. Schultz and O. Gutfleisch, Acta Materialia, 2009, 57, 5563.
- 127. A. Fossdal, H. W. Brinks, M. Fichtner and B. C. Hauback, *Journal of Alloys and Compounds*, 2005, 404-406, 752.
- 128. M. S. L. Hudson, H. Raghubanshi, D. Pukazhselvan and O. N. Srivastava, *International Journal of Hydrogen Energy*, 2010, **35**, 2083.
- 129. M. Fichtner, J. Engel, O. Fuhr, A. Glöss, O. Rubner and R. Alrichs, *Inorganic Chemistry*, 2003, 42, 7060.
- 130. E. Rönnebro, Current Opinion in Solid Stae and Materials Science, 2011, 15, 44.
- 131. H. Hagemann and R. Černý, Dalton Transactions, 2010, 39, 6006.
- 132. T. Umegaki, J.-M. Yan, X.-B. Zhang, H. Shioyama, N. Kuriyama and Q. Xu, *International Journal of Hydrogen Energy*, 2009, **34**, 2303.
- 133. C. Comanescu, Energies, 2023, 16, 4536.
- 134. B. Long, J. Chen, S. W. Sharshir, L. Ibrahim, W. Zhou, C. Wang, L. Wang and Z. Yuan, *Journal of Materials Chemistry A*, 2024, **12**, 5606-5625.
- 135. I. Merino-Jiménez, C. Ponce de León, A. A. Shah and F. C. Walsh, *Journal of Power Sources*, 2012, 219, 339-357.
- 136. D. J. Han, K. R. Bang, H. Cho and E. S. Cho, Korean Journal of Chemical Engineering, 2020, 37, 1306-1316.
- 137. A. Schneemann, J. L. White, S. Kang, S. Jeong, L. F. Wan, E. S. Cho, T. W. Heo, D. Prendergast, J. J. Urban, B. C. Wood, M. D. Allendorf and V. Stavila, *Chem Rev*, 2018, 118, 10775-10839.
- 138. D. J. Han, K. R. Bang, H. Cho and E. S. Cho, Korean Journal of Chemical Engineering, 2020, 37, 1306-1316.
- 139. M. B. Gawande, A. Goswami, T. Asefa, H. Guo, A. V. Biradar, D. L. Peng, R. Zboril and R. S. Varma,

- Chem Soc Rev, 2015, 44, 7540-7590.
- 140. R. A. Varin, L. Zbroniec, M. Polanski and J. Bystrzycki, Energies, 2010, 4, 1-25.
- 141. N. A. Ali, N. A. Sazelee and M. Ismail, *International Journal of Hydrogen Energy*, 2021, 46, 31674-31698.
- 142. K. Wang, X. Kang, Q. Kang, Y. Zhong, C. Hu and P. Wang, J. Mater. Chem. A, 2014, 2, 2146-2151.
- 143. P. Plerdsranoy, P. Dansirima, T. R. Jensen and R. Utke, *International Journal of Hydrogen Energy*, 2023, 48, 28435-28444.
- 144. F. J. Desai, M. N. Uddin, M. M. Rahman and R. Asmatulu, *International Journal of Hydrogen Energy*, 2023, 48, 29256-29294.
- 145. V. C. Y. Kong, F. R. Foulkes, D. W. Kirk and J. T. Hinatsu, *International Journal of Hydrogen Energy*, 1999, **24**, 665.
- 146. M. H. Sun, S. Z. Huang, L. H. Chen, Y. Li, X. Y. Yang, Z. Y. Yuan and B. L. Su, *Chem Soc Rev*, 2016, 45, 3479-3563.
- 147. P. Chen, Z. Xiong, J. Luo, J. Lin, K. L. Tan, *The Journal of Physical Chemistry B*, 2003, **107**, 10967-10970.
- 148. J. J. Vajo, S. L. Skeith, F. Mertens and S. W. Jorgensen, *Journal of Alloys and Compounds*, 2005, **390**, 55-61.
- 149. C. Li, P. Peng, D. W. Zhou and L. Wan, *International Journal of Hydrogen Energy*, 2011, **36**, 14512-14526.
- 150. V. Drozd, S. Saxena, S. V. Garimella and A. Durygin, *International Journal of Hydrogen Energy*, 2007, **32**, 3370-3375.
- 151. R. A. Varin and R. Parviz, International Journal of Hydrogen Energy, 2012, 37, 1584-1593.
- 152. Y. Liu, Y. Zhang, H. Zhou, Y. Zhang, M. Gao and H. Pan, *International Journal of Hydrogen Energy*, 2014, **39**, 7868-7875.
- 153. W. Cai, H. Wang, D. Sun, Q. Zhang, X. Yao and M. Zhu, RSC Adv., 2014, 4, 3082-3089.
- 154. J. Lu, Z. Z. Fang and H. Y. Sohn, *Journal of Power Sources*, 2007, 172, 853-858.
- 155. J. Mao, Z. Guo, H. K. Liu and S. X. Dou, Journal of Materials Chemistry A, 2013, 1, 2806-2811.
- 156. J. Mao, Q. Gu and D. Gregory, Materials, 2015, 8, 2191-2203.

2. Experimental

In this study, most of the chemical reagents employed are highly sensitive to air and moisture. Consequently, all sample storage and handling procedures were conducted under an inert atmosphere, primarily within an argon-filled glovebox. To achieve nanostructured hydrogen storage materials, the majority of samples were prepared via ball milling. For comparative analysis of dehydrogenation behaviour, the NaOH–NaH and NaAlH₄–NaOH systems were also manually ground and studied alongside their ball-milled counterparts.

Following synthesis, the materials were subjected to a series of characterization techniques. Simultaneous thermogravimetric and differential thermal analysis (STA; TG-DTA) was employed to assess the thermal behaviour of the samples. When coupled with mass spectrometry (MS), this technique allows for the real-time detection of gaseous species evolved during thermal decomposition. Structural analysis was carried out using powder X-ray diffraction (PXD), while Raman spectroscopy was utilized to identify the functional groups present in the materials, thereby aiding in the analysis of potential chemical compositions.

The purpose of this chapter is to provide a detailed overview of the working principles and operational protocols of these analytical instruments. By applying these techniques systematically, experimental parameters can be optimized to guide the development of hydrogen storage materials with desirable performance characteristics.

2.1 Sample Handling

2.1.1 Gloveboxes

To effectively reduce the risk of oxidation and hydrolysis during the handling of air-sensitive and pyrophoric substances, gloveboxes were extensively employed in this study for chemical preparations. The two different gloveboxes was shown in Figure 2-1. These controlled environments provided ideal conditions for the safe manipulation of highly reactive materials, preparation of chemical reactions, and storage of samples under an inert atmosphere. The light metals, complex hydrides, and hydroxides used in this research were highly sensitive to air exposure. Metals hydrides being pyrophoric, while many of the hydroxides exhibited strong hygroscopic behaviour. As a result, the majority of the experimental work presented in this thesis was carried out within recirculating gloveboxes filled with dry inert gases such as argon (Ar) or nitrogen (N₂). To facilitate the transfer of tools and materials into and out of the glovebox, antechambers capable of

evacuation were used. These chambers underwent a triple evacuation and refill cycle with inert gas before the inner door was opened, minimizing the introduction of oxygen and moisture. Inside the main chamber, the inert atmosphere was continuously purified by a circulation system consisting of a molecular sieve and catalyst, driven by a recirculation blower, to ensure a clean environment. In the mBraun glovebox used for thermogravimetric and differential thermal analysis (TG-DTA) experiments, oxygen and moisture levels were strictly controlled, typically maintained below 0.5 ppm. During regular operations such as manual mixing or sample handling, O₂ levels remained under 10 ppm, and H₂O concentrations consistently stayed below 0.5 ppm. By comparison, the Saffron Scientific gloveboxes maintained O₂ and H₂O concentrations within the 0–10 ppm range.

To sustain these environmental conditions, periodic regeneration of the molecular sieve and catalyst systems was necessary. Regeneration was usually performed every two months, though the frequency could be adjusted based on glovebox usage intensity or after long periods of inactivity. In the mBraun system, the catalyst (activated carbon) was regenerated in situ using a 5% H₂ in Ar gas mixture, matching the Ar-based glovebox environment. This method simplified the process and improved efficiency. In contrast, the Saffron Scientific gloveboxes required off-box regeneration. The catalyst and molecular sieve chambers had to be physically removed from the glovebox and treated externally. These chambers were exposed to a controlled flow of regeneration gas (either 5% H₂ in Ar or 5% H₂ in N₂, according to the glovebox atmosphere) for at least 12 hours to eliminate absorbed oxygen, moisture, and other contaminants. Both glovebox systems were equipped with integrated analysers for real-time monitoring of O₂ and H₂O levels. In the event of rising values, operational checks were initiated, and regeneration schedules were adjusted accordingly to maintain optimal experimental conditions.





a b

Figure 2-1: Images of the: (a) a Saffron Scientific Omega gloveboxes employed for sample storage in this thesis, and (b) a mBraun UniLab glovebox employed for sample preparation and for housing the STA.

2.2 Preparation methods and technique

2.2.1 Mechanochemistry

2.2.1.1 Introduction to Mechanochemistry

Mechanochemistry is a branch of chemistry that involves the initiation and promotion of chemical reactions through the direct application of mechanical energy, such as grinding, shearing, or milling.^{1,2} According to International Union of Pure and Applied Chemistry (IUPAC), It is formally defined as: "The branch of chemistry which is concerned with chemical and physico-chemical changes of substances of all states of aggregation due to the influence of mechanical energy."³

A key advantage of mechanochemical synthesis is its significantly reducing particle sizes compared to conventional thermochemical methods.^{4,5} This efficiency is achieved through the continuous generation of fresh solid surfaces during milling and the subsequent reduction of diffusion path lengths due to the persistent pulverization of particles.⁶

Mechanochemistry has gained significant attention in recent years for its broad applications in organic synthesis, materials chemistry, pharmaceutical co-crystals, and metal-organic frameworks (MOFs).⁷ It enables reactions that are often faster, cleaner, and more selective than traditional solution-based methods, while its solvent-free or solvent-minimized nature aligns with green chemistry principles by reducing waste and

energy consumption.^{8,9} As a result, mechanochemistry plays a pivotal role in developing sustainable synthesis routes for functional solids, including those used in energy applications and pharmaceuticals. 10 It has also emerged as a valuable tool in addressing environmental challenges, such as the degradation of persistent organic pollutants. 11,12 In addition, mechanochemistry is one of the principal preparative techniques for solid-state hydrogen storage materials, facilitating the synthesis of novel hydrides, catalysed and composite hydrogen release systems. The hydrogen desorption properties of mechanochemically synthesized materials have been demonstrated to be comparable to, or even superior to, those produced via conventional thermochemical solid-state methods. This enhancement is attributed to the shorter hydrogen diffusion paths within the reduced particle sizes.¹³ As shown in the Figure 2-2, It represents cross section of the milling jar of planetary ball-milling machine. The large circles represent milling balls, and the small black dots represent powder particles (reactants). The centrifugal force, indicated by an arrow radiating from the centre of the jar's rotation, causes the milling balls and powder to be pressed against the inner wall of the jar. Meanwhile, the milling jar stage moves along a larger circular path, creating a combined rotational and translational motion.¹⁴

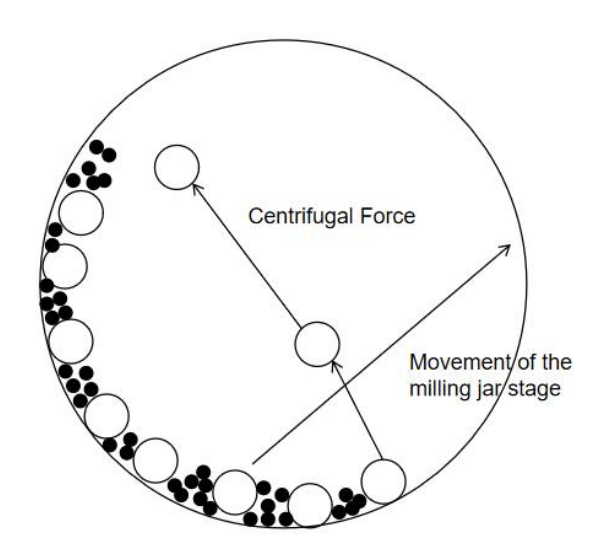


Figure 2-2: The simple schematic diagram of the cross section of the milling jar.

To enhance the grinding efficiency in practical applications, there are many aspects that can be improved, with the type of grinding equipment being the primary consideration. Several types of ball milling equipment are commonly used in mechanochemistry, each offering distinct advantages depending on the application. Planetary ball mills are among the most widely used due to their high energy input and dual rotational motion, making them ideal for organic synthesis, metal-organic frameworks (MOFs), and nanomaterial preparation. Vibratory ball mills (such as Retsch MM 400) operate through high-frequency oscillations and are suitable for small-scale, rapid reactions and solvent-assisted grinding. Tumbler ball mills, with their simpler construction and lower energy input, are better suited

for powder mixing and large-scale sample pretreatment. High-energy ball mills (such as SPEX 8000 or Simoloyer systems) provide intense mechanical energy and are commonly used in mechanical alloying and the production of nanoscale powders.¹⁵ Then, the conditions of ball milling reactions, such as rotation speed, the type of milling jar and balls, milling time, and ball-to-powder mass ratio, are also crucial. Once the experimental mill is selected, these parameters can be adjusted to control the intensity and nature of the mechanical stress applied to the material. Structural changes in the crystal lattice are an inherent outcome of mechanochemical processing, as the applied stress can induce strain, structural defects, and dislocations. Moreover, crystal polymorphic transformations and chemical reactions (such as decomposition reactions, alloying, and redox reactions) may occur.¹⁶

2.2.1.2 Milling Machine, Procedure and Conditions

The Figure 2-3 shows the internal structure of a planetary ball mill (Retsch PM100 model), with key components labelled to illustrate its mechanical setup and operational design. The milling jar is set securely onto the milling jar stage, which is in turn fixed to a larger rotating platform known as the sun wheel. The jar is clamped in place using clamp fixtures and a jar clamp, while a counterweight on the opposite side helps balance the system during high-speed rotation, reducing vibration on the instrument. A safety closure device ensures secure operation, especially during high-energy grinding. During milling, the sun wheel rotates in one direction, while the milling jar itself counter-rotates due to its mounting on the rotating platform. This counterrotation creates a dynamic environment where the milling balls inside the jar are subjected to intense centrifugal and Coriolis forces. The relative motion between the grinding balls and the milling jar creates a combination of frictional and impact forces, which together generate the intense dynamic energy necessary for the milling process.¹⁷ This energy input effectively breaks down the sample, leading to a significant reduction in particle size.

To conduct ball milling under an inert gas atmosphere, the materials(s), milling jar, stainless steel milling balls, and safety closure device will be transferred into a glove box filled with inert gas. Subsequently, the metal balls and materials will be placed into the milling jar and sealed with a rubber ring and the safety closure device. The milling jar will then be set onto the rotating platform inside the grinding chamber, and the milling variables will be adjusted. As mentioned above, these variables include: rotation speed (100-500 rpm), the type of milling jar and balls, milling time, rotation direction (clockwise/anti-clockwise), and ball-to-powder mass ratio. In this project, the type of milling jar and balls and the rotation direction are fixed. The milling jar and balls are made

of stainless steel, and the rotation direction alternates between clockwise and anti-clockwise. The remaining variables are different for each experiment. By adjusting these experimental parameters, the intensity of the ball milling process can be systematically controlled to tailor the grinding environment to different energy levels, depending on the specific material under investigation. The detailed milling conditions for each experiment will be described in the experimental sections of the subsequent chapters.

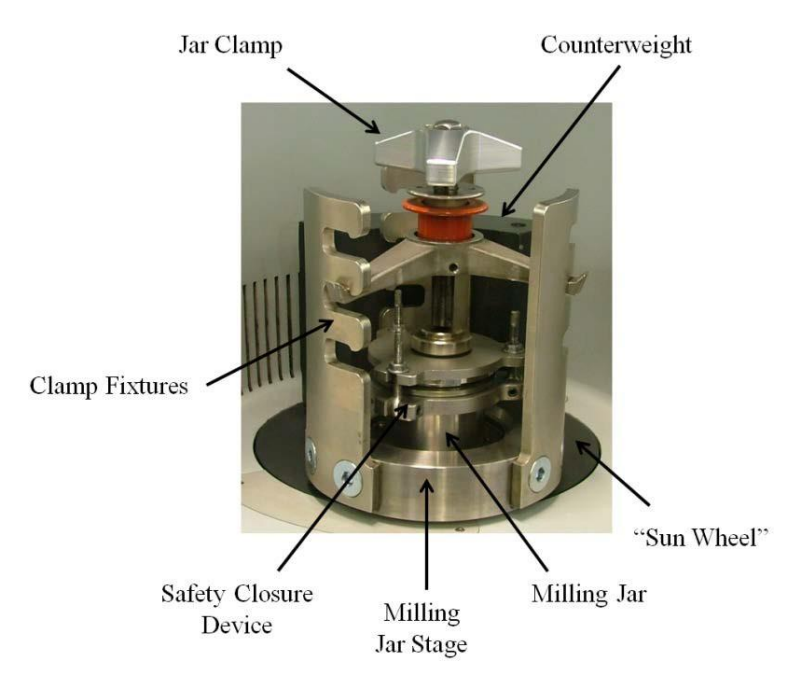


Figure 2-3: Configuration of the milling jar in the Retsch PM100 planetary ball mill.

2.2.2 Schlenk Line

In this work, the Schlenk line was primarily employed to dry NaOH, graphene oxide (GO), and guanidine under vacuum conditions. Figure 2-4 shows the setup of the Schlenk line that consists of a double crossover manifold with multiple ports: one end is connected to the atmosphere, and the other end is connected to a vacuum pump. When in use, the valve connected to the atmosphere is closed, and the vacuum pump is activated to evacuate the entire system. To prevent volatile reaction products and solvent vapours from entering the vacuum pump, a cold trap (liquid nitrogen) is employed to condense liquids and vapours. Schlenk glassware (two-necked round bottom flask) is similar to standard glassware but includes an additional side arm with a tap, which is connected to the Schlenk line via PVC tubing secured with O-rings.

To avoid contamination from air and moisture, and guarantee airtightness, all joints and taps must be properly greased with a thin layer of vacuum grease, ensuring even distribution. Additionally, all connections are wrapped with Parafilm to maintain vacuum integrity, with a target vacuum pressure of ca. 2×10^{-3} mbar. If this pressure is not

achieved, it indicates a leak, and the system must be re-inspected and re-configured. After the experiment, the extra side arm with a tap on the Schlenk glassware is closed, and the glassware is removed and transferred to a glovebox. The pressure is then released through the upper valve, and the contents of the cold trap are disposed of after returning to ambient temperature.

Sodium hydroxide (NaOH) is highly hygroscopic and may contain hydrated forms such as NaOH·H₂O. To ensure dryness, the Schlenk glassware containing NaOH is placed on a hot plate and stirrer in an oil bath to facilitate uniform heating and heated to 100 °C. Under vacuum conditions, the crystallization water is removed to yield anhydrous NaOH. Graphene oxide (GO) is condensed into a solid under vacuum using liquid nitrogen, while guanidine is dried at ambient temperature.

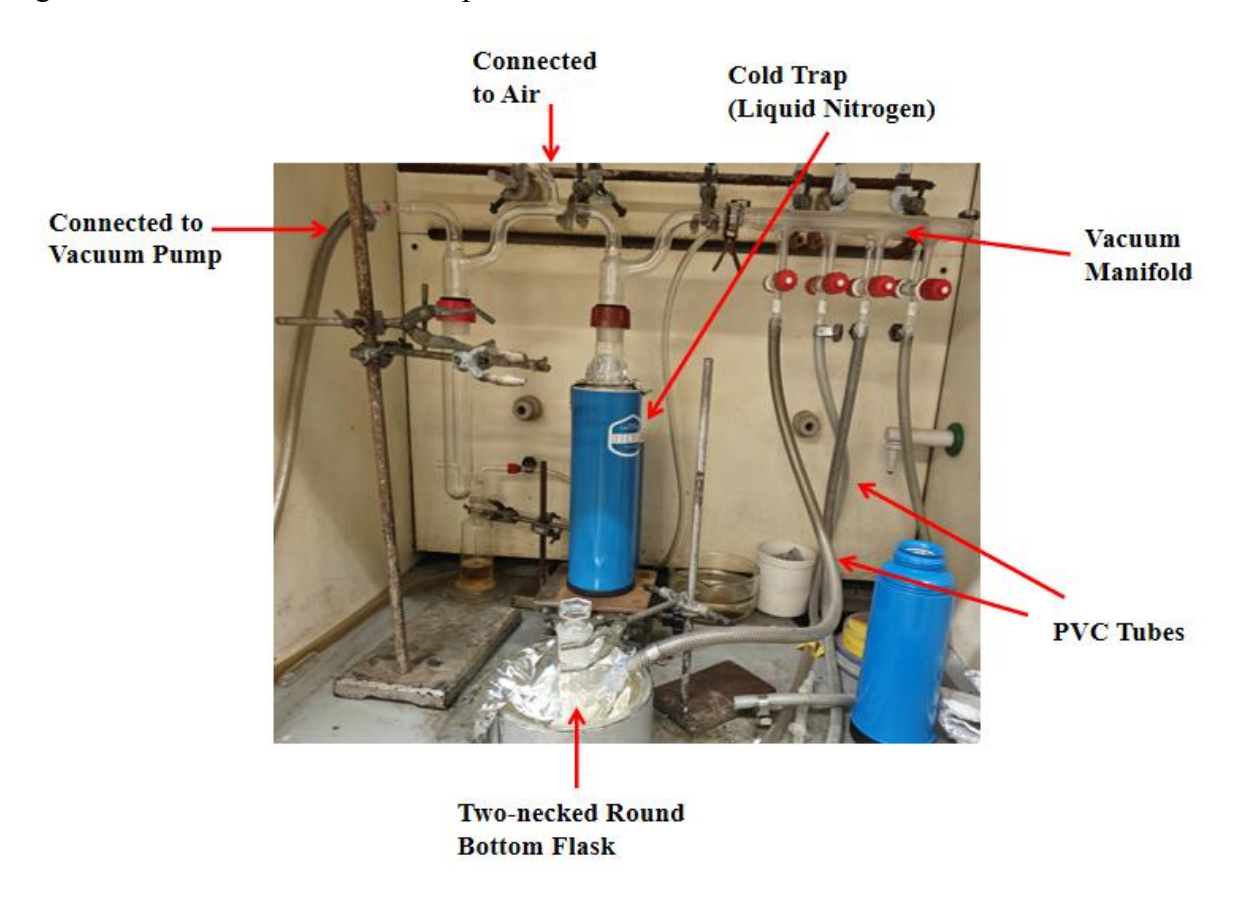


Figure 2-4: Schlenk line used in the experiment.

2.2.3 Pot Furnaces

A pot furnace was employed for thermal desorption experiments and conventional thermal synthesis. The furnace was equipped with programmable temperature controllers (Eurotherm), which permitted precise control over heating parameters such as ramp rate, dwell time, and heating temperature. This degree of precision ensured the reproducibility of the applied thermal conditions. The pot furnace used in this study is illustrated in Figure

2-5. The furnace was utilized for material synthesis under a flowing argon (Ar) or nitrogen (N₂) atmosphere, for heating samples for simulating the conditions required for simultaneous thermal analysis (STA) prior to conducting experiments in the thermobalance. Some strongly exothermic reactions may require reducing the amount of starting material to ensure that the overall reaction proceeds safely and controllably within the crucible.

To maintain controlled gas flow conditions, the reaction tube was sealed with a Suba-Seal rubber septum, and gas inlet and outlet pathways were established using syringes and tubing. The junction between the syringe and the rubber septum was wrapped with Parafilm to prevent air ingress. The outlet gas flow was directed through an empty Dreschel bottle, followed by a second Dreschel bottle containing an appropriate bubbler fluid, such as paraffin oil. The empty Dreschel bottle served as a safety measure to prevent backflow of the bubbler fluid into the reaction vessel. Subsequently, the gas flow rate was regulated by adjusting the valve on the Argon or Nitrogen cylinder. An appropriate flow rate was established by monitoring the bubbling rate of paraffin oil in the Drechsel bottle. When the reaction in the pot furnace was complete, the sample vessels were cooled to room temperature before removing. The samples were collected inside a glovebox to ensure that the products were not exposed to air contamination.

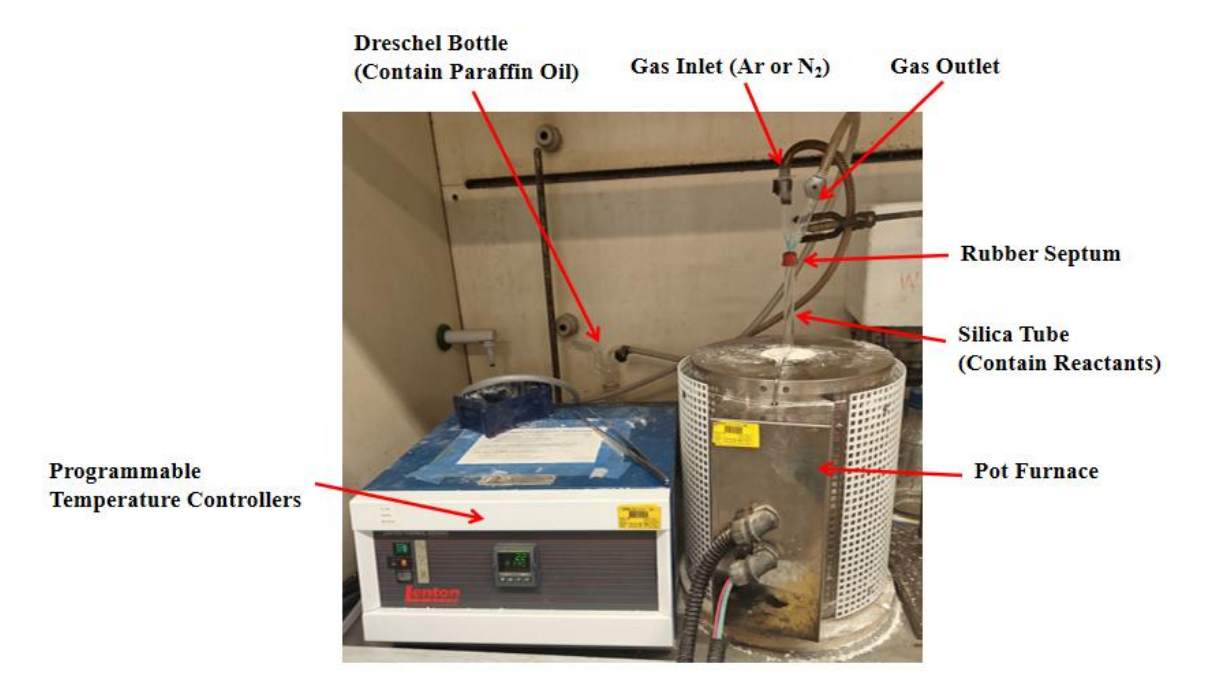


Figure 2-5: The pot furnace used in the experiment.

2.2.4 Glassblowing

Custom glass tubes (quartz glass tubes) were fabricated using glassblowing equipment under high-temperature furnace conditions. Quartz glass tubing is an amorphous material formed by the fusion of high-purity silicon dioxide (SiO₂), characterized by exceptional

thermal stability and chemical inertness. With a softening point of approximately 1665 °C, it maintains excellent structural integrity even under high-temperature conditions, making it suitable for applications involving elevated temperatures, vacuum systems, corrosive environments, or ultra-high purity requirements. Quartz glass is typically shaped and sealed using high-temperature sources such as oxyhydrogen flames; once softened, it can be precisely formed or sealed, and is widely employed in gas sampling tubes, high-temperature reactors, and related apparatus. Due to its extremely low coefficient of thermal expansion, quartz glass is highly resistant to thermal shock and cracking, making it one of the most dimensionally stable and durable glass materials available for demanding scientific and industrial applications.¹⁹

As shown in the Figure 2-6, The glassblowing torch was equipped with two gas inlet pipes for natural gas and O₂. Prior to ignition, a low flow rate of natural gas was introduced and subsequently ignited with an open flame. The ratio of natural gas to oxygen was then adjusted to achieve the optimal flame conditions required for the splitting of quartz glass tubes and sealing operations. Didymium glassblowing safety glasses should be worn to protect the eyes from intense light exposure during the process. During heating, the quartz tubing must be continuously rotated to ensure uniform heating at the fracture site, which facilitates even softening and prevents structural stress. Given the air sensitivity of the materials in this study, the sample tubes were initially prepared inside a glove box and sealed with Suba-Seal rubber septum and parafilm to prevent exposure to atmospheric contaminants. This procedure ensured that the samples remained in an oxygen-free environment during subsequent Raman spectroscopy measurements.

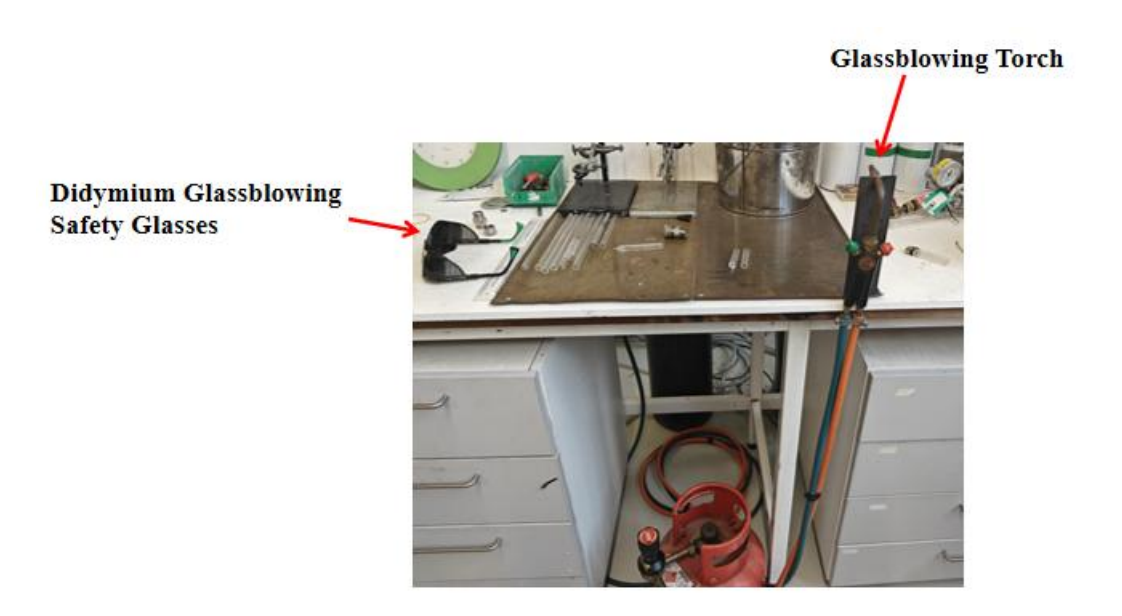


Figure 2-6: Glassblowing used in the experiment.

2.3 Characterisation Techniques

To effectively discuss the analytical techniques and instruments utilized in this study, it is essential to first present a concise overview of the fundamental principles of atomic quantum theory, which serve as the theoretical foundation for these methods. Previous researchers, based on their fundamental understanding of the nature of light, have developed a range of analytical tools. From a basic chemical perspective, light exhibits both particle-like and wave-like properties, a concept known as wave-particle duality. The equation is shown in 2-1.

$$E = hv$$
 Eq. 2-1

The energy of a photon, denoted as E (in J). v represents the frequency of the light wave in hertz (Hz). h is Planck's constant $(6.63 \times 10^{-34} \text{ J} \cdot \text{s})$. The electromagnetic spectrum, as illustrated in Figure 2-7, encompasses the full range of electromagnetic radiation, characterized by variations in both frequency (v) and wavelength (λ) of the oscillating light waves. The speed of the light c is equal to $3.00 \times 10^8 \text{ m s}^{-1}$. The equation is shown in 2-2.

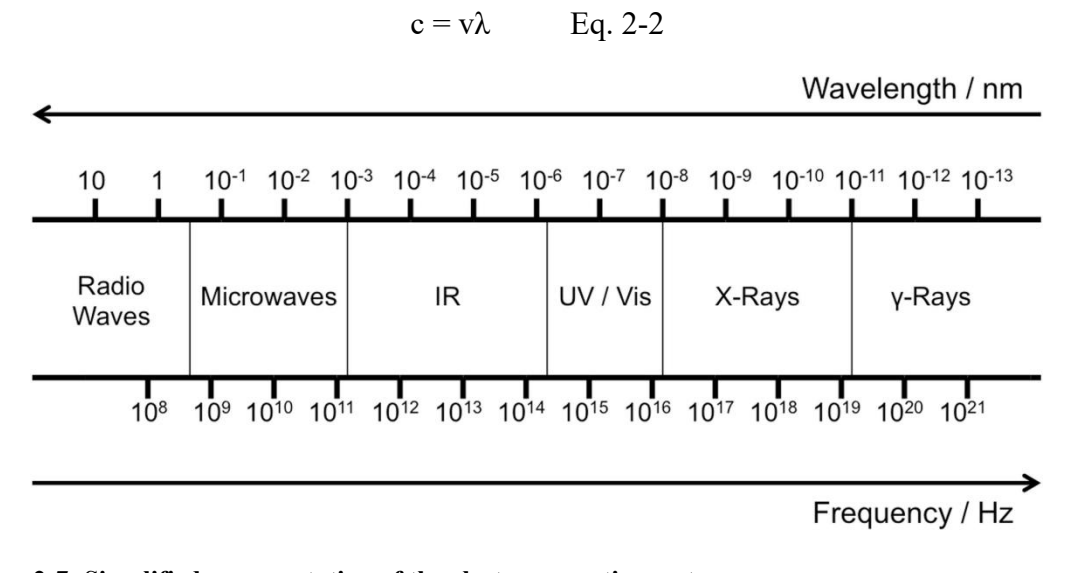


Figure 2-7: Simplified representation of the electromagnetic spectrum.

Based on the understanding of wave-particle duality, electromagnetic radiation has become an essential tool for conducting experiments that fundamentally reveal the nature of matter. Scientists and engineers have designed and fabricated various instruments targeting specific regions of the electromagnetic spectrum, enabling precise detection of materials at the subatomic level. In this study, a combination of multiple analytical methods has been employed, each utilizing a different portion of the electromagnetic spectrum to comprehensively characterize the properties of the synthesized materials. The following sections will provide a detailed introduction to these analytical techniques and their theoretical foundations.

2.3.1 Crystallography and Diffraction

Crystallography is a scientific discipline that studies the structure and properties of crystals. ²⁰ By analysing the ordered arrangement of atoms or molecules within a material, it reveals the internal structure and symmetry of the material. ^{21,22} The core of crystallography involves using X-ray, neutron, or electron diffraction techniques to measure and analyse the diffraction patterns produced when radiation passes through a crystal, thereby determining the precise positions and arrangements of atoms within the crystal. ²³ Crystalline solids consist of atoms arranged in a highly ordered and periodic manner, forming a lattice structure that repeats in three dimensions. This periodicity can be captured by a fundamental building block known as the unit cell. As shown in Figure 2-8, a unit cell is defined by three edge vectors (a, b, and c) along with the interaxial angles α , β , and γ , which describe the geometry and orientation of the cell in space.

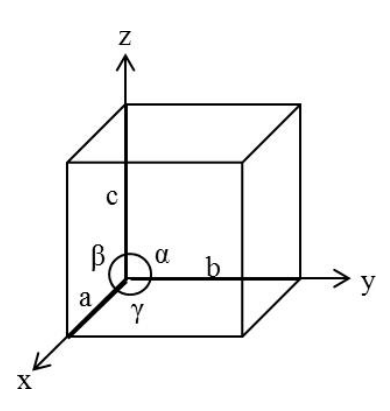


Figure 2-8 Schematic diagram of basic cubic unit cell

To establish a foundational understanding, the basic principles of diffraction theory in relation to crystallography will be introduced. These principles are fundamental to experimental investigations in solid-state chemistry. As illustrated in Figure 2-9, diffraction arises when waves, such as X-rays or other forms of electromagnetic radiation, encounter a material and are scattered by its internal structure.²⁴ In the Figure 2-9, A and B represent two incident X-ray beams striking different crystallographic planes and undergoing reflection. Points X and Z correspond to the points of incidence (and reflection) for beams A and B on the upper and lower planes, respectively, while point Y denotes the reflection point of beam B on the adjacent lower plane. The segments XY and YZ form a path perpendicular to the interplanar spacing and are used to calculate the optical path difference between the two beams. Depending on the phase relationship of the interacting waves, they can interfere either constructively or destructively, resulting in an increase or decrease in intensity, respectively. In the context of crystallographic studies, the key information is derived from constructive interference. Bragg's law (Equation 2-3) provides the fundamental mathematical framework for understanding diffraction phenomena. The

equation 2-3 is shown as below:

$$n\lambda = 2d \sin \theta$$
 Eq. 2-3

In this equation, λ is the wavelength of the incident radiation, d is the interplanar spacing within the crystal. θ is the angle at which constructive interference, and thus a diffraction peak, is observed. The integer n indicates the order of reflection. In this study, only first-order diffraction (n = 1) is considered, simplifying the equation accordingly.

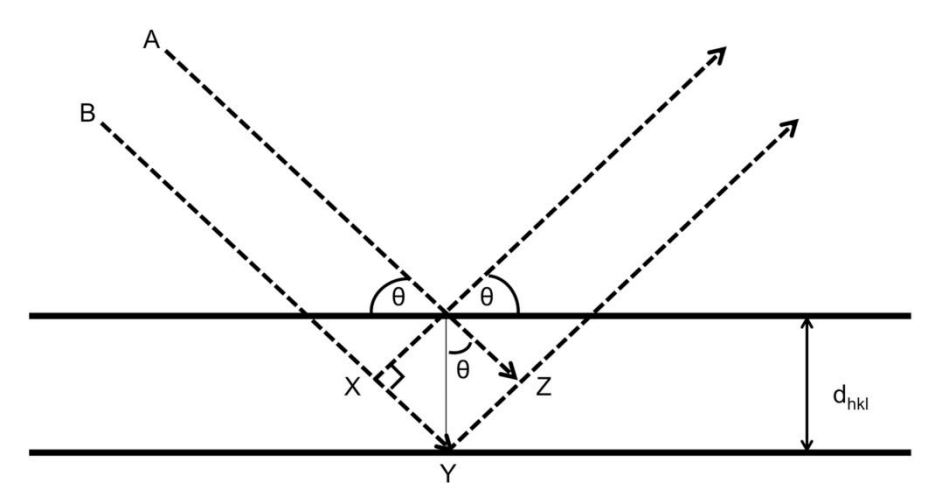


Figure 2-9: Schematic diagram of Bragg Diffraction path of X-rays on crystal planes. dhkl is the lattice spacing. θ is the angle between the lattice plane.

The information regarding the crystal structure is obtained by collecting data across a range of diffraction angles (θ). The diffraction pattern of the incident radiation, such as X-rays, reveals diffraction maxima (peaks) that correspond to the specific Bragg angles (θ) at which Constructive interference occurs. The shape, position, and intensity of each peak collectively provide critical information about the crystal structure.

The crystal system of a solid material can be identified based on the interplanar spacing (d-spacing) obtained from diffraction measurements. The orientation of atomic planes is described using Miller indices (h, k, l), which serve as the basis for determining unit cell dimensions. To further refine the description of a crystal's geometry, the Bravais lattice classification is applied. This framework combines the seven fundamental crystal systems (as outlined in Table 2-1) with five possible lattice centrings: primitive (P), body-centred (I), face-centred (F), base-centred (C), and rhombohedral (R), resulting in 14 unique lattice types. From this structural information, a specific space group (one of the 230 recognized symmetries) can be assigned to the crystal. These space groups will be used throughout this study to describe the crystal structures of the synthesized compounds.²⁶

Table 2-1: Basic crystallography notation and symmetry information for the seven crystal systems.²⁷

Crystal System	Unit Cell Parameters	Bravais Lattices	Point Groups
Triclinic	$\alpha \neq \beta \neq \gamma \neq 90^{\circ}$ $a \neq b \neq c$	P	1, -1 (C1, Ci)
Monoclinic	$\alpha = \gamma = 90^{\circ}$ $\beta \neq 90^{\circ}$ $a \neq b \neq c$	P, C	2, m, 2/m (C ₂ , C _S , C _{2h})
Orthorhombic	$\alpha = \beta = \gamma = 90^{\circ}$ $a \neq b \neq c$	P, C, I, F	222, mm2, mmm (D_2, C_{2v}, D_{2h})
Trigonal/ Rhombohedral	$\alpha = \beta = \gamma \neq 90^{\circ}$ $a = b = c$	R	3, -3, 32, 3 <i>m</i> , -3 <i>m</i> (C3, C3i, D3, C3v, D3d)
Tetragonal	$\alpha = \beta = \gamma = 90^{\circ}$ $a = b \neq c$	P, I	4, -4, 4/ <i>m</i> ,422, 4 <i>mm</i> , 4-2 <i>m</i> , 4/ <i>mmm</i> (C4, S4, C4h, D4, C4v, D2d, D4h)
Hexagonal	$\alpha = \beta = 90^{\circ} \gamma = 120^{\circ}$ $a = b \neq c$	P	6, -6, 6/m, 622, 6mm, 6-m2, 6/mmm (C6, C3h, C6h, D6, C6v, D3h, D6h)
Cubic	$\alpha = \beta = \gamma = 90^{\circ}$ $a = b = c$	P, I, F	23, m3, 432, -43m, m3m (T, Th, O,Td, Oh)

2.3.1.1 Powder X-Ray Diffraction

X-rays have shorter wavelengths than visible light within the electromagnetic spectrum. W. H. Bragg and his son, L. Bragg, pioneered the study of X-ray interactions with crystals,

recognising their potential for structural analysis.^{28,29,30} Their groundbreaking research established X-ray diffraction as a widely applicable and essential analytical technique for determining crystal structures.^{31,32} Currently, X-rays play an extremely important and wide-ranging role in science and technology, particularly in the fields of materials science, physics, chemistry, biology, and medicine.

The radiation source employed in diffraction experiments plays a crucial role in determining the quality of the data obtained, which in turn influences the precision of crystal structure determination. In conventional laboratory diffractometers, a fixed source generates X-rays by directing high-energy electrons towards a metal target (such as copper used in the Panalytical X'Pert Pro and Miniflex instruments). The incident electrons excite the metal atoms, causing electrons within the metal to transition from higher-energy to lower-energy state, thereby releasing a specific amount of energy in the form of photons. Laboratory X-ray diffractometers are typically equipped with a monochromator, often a germanium crystal, which is specifically designed to select photons within the X-ray region of the electromagnetic spectrum. In this work, the strongest $K\alpha_1$ radiation from copper (λ = 1.54 Å) was utilised.

The sample holders used in this study were selected based on the nature of the samples. For non-air-sensitive samples, a 10 mm pre-sample slit was installed on the X'Pert Pro instrument. The Bragg-Brentano reflection geometry was applied as shown in Figure 2-10. In this setup, the sample is tilted around an axis by an angle θ , while the detector is positioned to rotate by an angle of 2θ to capture the reflected radiation. Samples for the X'Pert Pro were prepared on a quartz sample holder (slide), while those for the Miniflex were prepared on an aluminium alloy sample holder. Both sample holders featured a recess on the surface. After filling the recess with the sample, a glass slide was pressed over it to ensure the sample was evenly distributed within the recess, thereby maximizing the quantity of sample used for analysis. The Miniflex instrument is equipped with an automatic sample changer and so has the advantage of being able to test six samples consecutively and automatically, whereas the X'Pert Pro can only analyse one sample at a time.

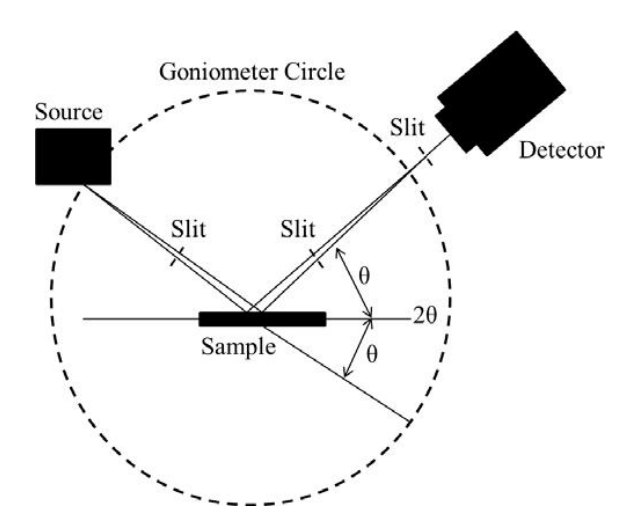


Figure 2-10: Bragg-Brentano reflection geometry used in X'Pert and Miniflex measurements.

For air-sensitive samples, an air-sensitive sample holder was used on the X'Pert instrument, as shown in Figure 2-11a. The sample preparation procedure was similar to that for non-air-sensitive samples, with the material being loaded onto a quartz sample slide. However, all preparation steps were conducted within a glovebox to prevent exposure to air. Once the sample was loaded, an airtight cover was fitted onto the outer holder, and the joints were sealed with high-vacuum grease and Parafilm. During PXD testing, the X-ray beam passes through the window of transparent polymer film to reach the sample. The polymer film exhibited a broad peak between 15° and 20°, which can easily be distinguished from the diffraction peaks of the samples used in this work. For the Miniflex instrument, an alternative air-sensitive sample holder was also employed, as depicted in Figure 2-11b. The preparation process was likewise conducted within a glovebox, with the sample loaded onto an aluminium alloy holder. After loading, a specially designed tightening device was used to secure the airtight cover onto the sample holder. The advantage of this holder is that it does not introduce any additional peaks and provides enhanced sealing, ensuring the integrity of air-sensitive samples during analysis.



a



b

Figure 2-11: Air-sensitive sample holder for the: (a) X'Pert and (b) Miniflex powder X-ray diffractometers.

Diffraction data for this work were obtained using two different laboratory diffractometers: the Rigaku Miniflex and the Panalytical X'Pert Pro. The samples were analysed using Cu K α_1 radiation over the angular ranges of $5^{\circ} \le 2\theta \le 85^{\circ}$ (ca. 1 hour duration). The step size was set at 0.0167° and the scanning speed at 1.57° min⁻¹. The diffraction data were compared to standard patterns in the ICSD database via PowderCell or the ICDD PDF database via PANalytical HighScore Plus software. 33,34,35,36

When the particle size of a product decreases, PXD peaks usually become noticeably broader. This broadening arises from the inverse relationship between crystallite size and peak width, as described by the Scherrer equation 2-4.³⁷

D=
$$K\lambda/\beta\cos\theta$$
 Eq. 2-4

In this context, D represents the crystallite size, K is the shape factor (typically ranging from 0.89 to 0.94), λ denotes the X-ray wavelength, β corresponds to the full width at half maximum (FWHM) of the diffraction peak, and θ is the diffraction angle. From the equation, it is evident that the peak width β is inversely proportional to the crystallite size D; smaller crystallites result in broader peaks. Smaller crystallites reduce the number of coherently scattering planes, leading to an increase in the full width at half maximum (FWHM) of diffraction peaks. Additionally, factors such as lattice distortion and structural disorder, which are common in nanomaterials, can further contribute to peak broadening. Therefore, PXD peak width is a valuable indicator of particle size reduction, especially in the characterization of nanostructured materials.

2.3.1.2 Structure Refinement and Rietveld Method.

The Rietveld method is a full-profile structural refinement technique, and in this work, the GSAS-EXPGUI software was utilised to implement this method. 38,39 The fundamental principle of the Rietveld method is to, not only merely performing profile fitting, extract detailed crystallographic structure information. 40 This method requires prior knowledge of the material's composition. A suitable structural model is then selected from the Inorganic Crystal Structure Database (ICSD). By iteratively refining the fitting parameters, the profile fitting can be optimized to closely match the experimental data. This process yields structural information that closely approximates the actual material. Moreover, when multiple phases are present, the method allows for the determination of the weight percentage of each individual component.

2.3.2 Raman Spectrometry

Raman spectroscopy is a non-destructive vibrational spectroscopic technique that is widely used in chemistry, materials science, physics, and biology to analyse the molecular structure, chemical composition, crystal structure, and phase transitions of solid, liquid, and gaseous samples. 41,42 Its fundamental principle is based on the phenomenon of Raman scattering, first discovered by C. V. Raman in 1928.⁴³ When a monochromatic laser is directed onto a sample, most photons undergo elastic scattering (Rayleigh scattering), retaining the same energy as the incident light. However, a very small fraction of photons (ca. one in a million) interacts with the vibrational modes of molecules, leading to a change in photon energy. This inelastic scattering is known as Raman scattering. As shown in the Figure 2-12, two types of Raman scattering may occur: Stokes scattering, where the scattered photon has lower energy than the incident photon, corresponding to a transition from the molecular ground state to an excited vibrational state (this is the more common and stronger signal); anti-Stokes scattering, where the scattered photon has higher energy than the incident photon, due to the molecule being in an excited vibrational state before interaction.⁴⁴ This signal is typically weaker due to the lower population of thermally excited molecules. The energy difference, known as the Raman shift, is expressed in wavenumbers (cm⁻¹) and is equal to the difference between the frequencies of the incident and scattered photons, corresponding to the energy of a specific molecular vibrational mode. For a vibrational mode to be Raman active, it must be accompanied by a change in the polarizability of the molecule, which refers to the ease with which the electron cloud is distorted under an external electric field.⁴⁵

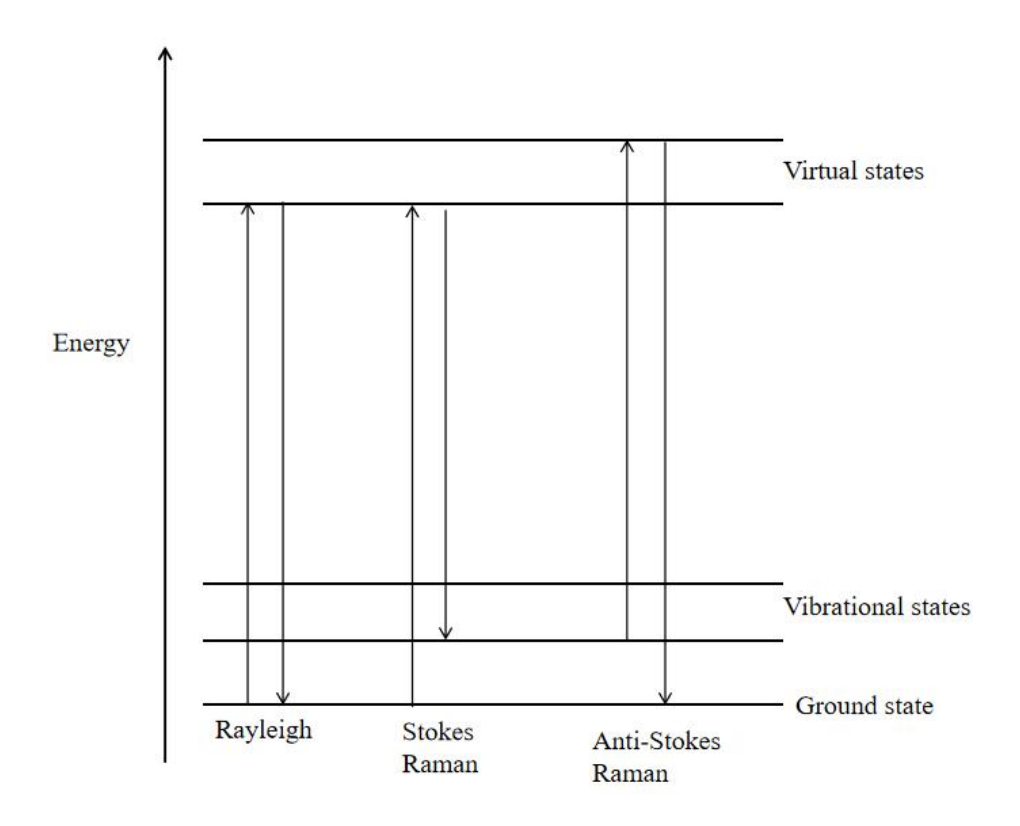


Figure 2-12: Schematic diagram of energy changes associated with Raman scattering.

A typical Raman spectrum plots Raman shift (x-axis) against scattered intensity (y-axis), where each peak corresponds to a specific vibrational mode of the material. The peak position reflects the type of chemical bond, molecular symmetry, or lattice structure, while the peak intensity and width provide insight into factors such as concentration, crystallinity, structural order, and internal stress.⁴⁶ For example, highly crystalline materials often exhibit sharp and strong Raman peaks, while amorphous or defect-rich materials show broadened and weaker peaks. Shifts in Raman peak positions can also indicate changes in structure caused by doping, stress, temperature fluctuations, or phase transitions. Owing to these advantages, Raman spectroscopy is widely used to investigate the structure and properties of a variety of functional materials, including carbon-based materials (e.g., graphene, carbon nanotubes, diamond), inorganic oxides, semiconductors, two-dimensional materials, and polymers. Its specific applications include functional group identification, phase analysis, stress/strain detection, doping monitoring, compositional mapping, and in situ monitoring of chemical reactions, making it a highly valuable analytical tool.⁴⁷

All analyses conducted in this study utilized a Horiba Jobin Yvon LabRam instrument, equipped with a confocal microscope, 600/1200 grooves/mm grating (1 mm⁻¹), a 100 μm pinhole aperture, and a Synapse CCD detector. The instrument employed either a green (532 nm) or ultraviolet (325 nm) laser. The Figure 2-13 illustrates a typical optical setup of a micro-Raman spectroscopy system, based on the principle of Raman scattering. A stable, monochromatic laser source serves as the excitation light, which is directed by a beam

splitter toward the sample through a microscope objective. The objective lens focuses the laser onto the sample surface, where Raman scattering occurs. Among the scattered photons, a small fraction undergoes inelastic scattering, generating Raman signals that carry vibrational information about the sample. These scattered signals are collected by the same objective and pass back through the beam splitter. A notch filter is placed in the return path to efficiently suppress the intense Rayleigh (elastically scattered) light while allowing the weaker Raman-shifted light to pass. The filtered Raman signal is then focused by a lens and directed into a spectrometer, where it is dispersed into its component wavelengths using a diffraction grating. Finally, the dispersed light is detected by a CCD (charge-coupled device), which converts the optical signals into electronic data to produce the Raman spectrum.⁴⁸

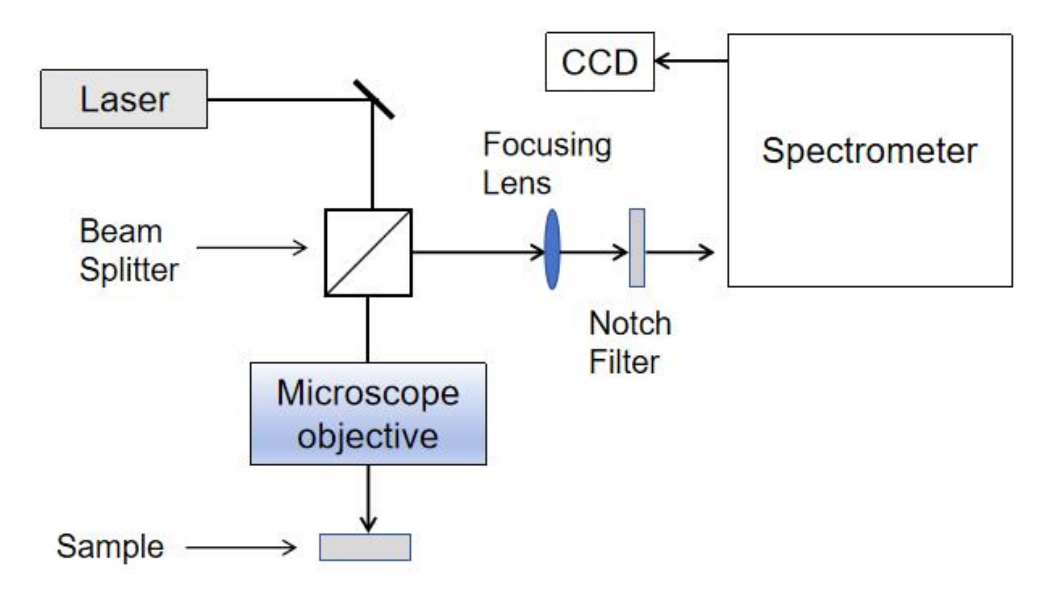


Figure 2-13: Schematic diagram of the optical path configuration of the micro-Raman spectroscopy system.⁴⁹

2.3.3 Thermal Analysis

Thermal analysis techniques have undergone decades of refinement and development, becoming key methods for investigating thermodynamic processes during sample heating. Common thermal analysis methods include Differential Scanning Calorimetry (DSC), Thermogravimetric Analysis (TGA), Differential Thermal Analysis (DTA), and Dynamic Mechanical Analysis (DMA). DSC is widely used to determine the glass transition temperature, melting point, crystallization temperature, and reaction enthalpy changes of materials, making it an important tool for studying phase transitions and thermal processes. TGA reveals the thermal stability, decomposition behaviour, and volatile content of materials by measuring mass changes as a function of temperature. DTA is employed for

qualitative analysis of endothermic or exothermic reaction processes. DMA evaluates the mechanical property changes of polymer materials under thermal loading. Thermal analysis techniques offer advantages such as high sensitivity, comprehensive information, and relatively straightforward operation. However, results are significantly influenced by conditions such as atmosphere and heating rate, often necessitating combination with other characterization methods. Through thermal analysis, deeper insights into material thermal behaviour can be gained, providing critical guidance for new material development, product performance optimization, and process condition design. 50,51,52 In this study, Simultaneous Thermal Analysis (STA) was employed, which combines Thermogravimetric Analysis (TGA) and Differential Thermal Analysis (DTA).

Gibbs free energy and Hess's law are fundamental and core thermodynamic principles. To determine the enthalpy change of a specific chemical reaction, the principle of energy conservation embodied in Hess's law can be applied.⁵³ This method is based on the difference in standard enthalpies of formation between reactants and products, allowing the calculation of the heat change involved in the reaction process. Equation 2-5 presents the mathematical expression of Hess's law. ΔH_f represent the standard enthalpy of each component. The n and m represent the stoichiometric coefficients of the products and reactants in the balanced reaction, respectively.

$$\Delta H^{\circ} = \Sigma n \Delta H_{f^{\circ}} \text{ (products)} - \Sigma m \Delta H_{f^{\circ}} \text{ (reactants)}$$
 Eq. 2-5

Once the enthalpy and entropy changes associated with a reaction are determined, the thermodynamic feasibility of the reaction can be evaluated using the Gibbs free energy equation 2-6:

$$\Delta G^{\circ} = \Delta H^{\circ} - T \Delta S^{\circ}$$
 Eq. 2-6

When the value of ΔG is significantly positive, it indicates that the reaction is thermodynamically non-spontaneous under standard conditions, tending to maintain an equilibrium state between reactants and products. Conversely, if ΔG is significantly negative, the reaction can proceed spontaneously under standard conditions, favoring complete formation of the products. When ΔG is close to zero, the system tends to establish an equilibrium coexistence of reactants and products.

Prior to subjecting the materials to Simultaneous Thermal Analysis (STA), preliminary heating experiments were conducted using a pot furnace under an inert atmosphere (Ar) to evaluate the thermal properties of the samples. This pretreatment step was designed to prevent potential damage to the STA equipment caused by the release of large amounts of heat during the reaction.

2.3.3.1 Simultaneous Thermal Analysis (STA; TG-DTA)

In this study, Simultaneous Thermal Analysis (STA) combines Thermogravimetric Analysis (TGA) and Differential Thermal Analysis (DTA). The instrument used was the Netzsch STA 409 PC, as shown in Figure 2-14. The instrument features a multi-channel gas flow system: green arrows indicate the purge gas (Ar; 60 ml/min) that flows through the sample chamber to maintain an inert atmosphere; blue arrows represent protective gas (Ar) that shields sensitive components like the balance; and black dashed lines indicate the vacuum pathway used to control the pressure environment.

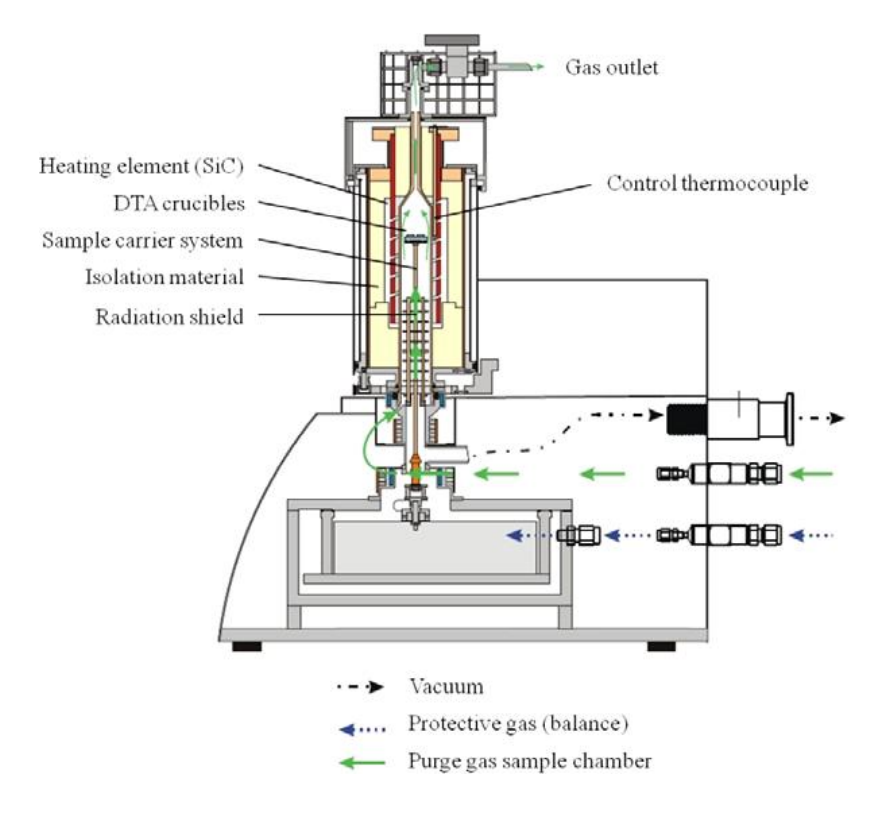


Figure 2-14: Schematic of the STA instrument employed in this work.⁵⁷

Differential Thermal Analysis is a technique that involves heating two alumina crucibles under the same conditions: one containing the sample to be tested and the other serving as an empty reference. As described in Figure 2-15, the arrangement of the crucibles on the sample holder ensures that both are subjected to the same thermal treatment. The key measurement in DTA is the temperature difference (ΔT) between the sample crucible and the reference crucible. Under normal circumstances, without thermal events such as decomposition reaction or phase change in the sample, the temperatures of the two crucibles should be the same. The DTA curve, which plots this temperature difference, can distinguish between exothermic and endothermic processes, offering valuable information into the thermal properties of materials.

In TGA measurements, the masses of the sample and reference crucibles cannot be exactly identical. Therefore, before placing the sample, the empty sample crucible and reference

crucible must be calibrated using the balance system to equalize their relative masses. The sample is then added. The sample mass depends on the total amount of synthesized material available, typically ranging from 15 to 30 mg. By combining the weight change data from TGA with the thermal events observed in DTA, an initial assessment of whether a reaction has occurred can be made.

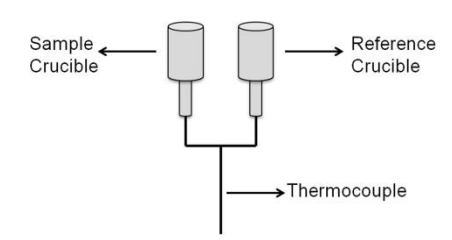


Figure 2-15: Diagram of STA crucible arrangement.⁵⁴

Prior to the experiment, empty alumina crucibles are heated to the target experimental temperature at predetermined heating rates (1, 2, 5, 10, and 20 °C/min) to create calibration files. In the initial trials, approximately 15-30 mg of sample is loaded into the sample crucible. The preliminary experiments typically follow a procedure in which the sample is heated from room temperature to the desired temperature at a rate of 5 °C/min, followed by natural cooling. Subsequent experiments can be adjusted based on the TG-DTA data by modifying the heating rate and sample mass accordingly. The relevant data are acquired using the Proteus analysis software provided with the Netzsch TA4_5 series instruments and can also be exported to external software (e.g., Origin) for further data visualization. The TG-DTA experiments provide critical parameters such as the onset temperature of thermal events, peak temperature, and mass loss during the heating process.

After the experiment, some residue is likely to remain in the crucible. The alumina crucibles can be reused after proper cleaning. The cleaning process involves exposing the used crucibles to air for 24 hours to allow any remaining residues to react with atmospheric oxygen. The crucibles are then soaked in aqua regia (3:1 HCl:HNO₃) for approximately 24 hours. Afterward, they are heated at 1100 °C for 6 hours to ensure complete removal of any remaining residues. Residues may also accumulate on the thermocouple, particularly if the reaction is highly intense. To clean these deposits, the STA system is heated to 1100 °C under vacuum and held for 3 hours to allow for the evaporation of residual materials.

Beyond the basic evaluation of the onset temperatures, peak temperatures and enthalpy of thermal performance occurring in a sample, activation energy of the reaction can be calcuated through the Kissinger plots.^{55,56} These plots can be used to determine the activation energy (E_a) for dehydrogenation reaction. The Kissinger plots equation 2-7 is shown as below:

$$ln(\beta/T_m^2) = -E_a/RT$$
 Eq. 2-7

 β is the heating rate. In this study, the heating rate chosen were 2, 5, 10, 20 °C/min. T_m is the DTA peak temperature (K). E_a is the activation energy. $R=8.314~\rm J\cdot K^{-1}\cdot mol^{-1}$. A straight line is obtained by plotting $In(\beta/T_m^2)$ on the y-axis against $1/T_m$ on the x-axis (fitted line based on 4 peak temperature points). The simplified equation for this linear fit is shown in Equation 2-8, where m represent the slope. The activation energy (E_a) is calculated from this slope according to Equation 2-9, $E_a=-R$ m

$$y = mx + c$$
 Eq. 2-8
 $m = -E_a/R$ Eq. 2-9

2.3.3.2 Mass spectrometry

Mass spectrometry (MS) is a highly sensitive analytical technique widely used to determine the molecular weight, structural composition, and distribution of compounds. Its fundamental principle involves ionizing the sample via an ion source to generate charged particles, which are then separated based on their mass-to-charge ratio (m/z) under the influence of electric or magnetic fields. These ions are subsequently detected by a detector, and the resulting signals are recorded to produce a mass spectrum.⁵⁷ In this study, mass spectrometry (MS) is coupled with STA to enable simultaneous evolved gas analysis (EGA). The MS instrument used was a Hiden Analytical HPR20, and data acquisition was carried out using MASsoft Professional mass spectrometer control software.

This MS system features two gas detection modes, each associated with a specific detector. The first is line mode, which uses a Faraday cup detector and is commonly employed for targeted ion monitoring. In this mode, specific ions are detected based on known m/z values. For example, hydrogen (H₂) is typically monitored using m/z = 2 in this study. When the ion beam collides with the metal surface (see Figure 2-16), the ions are neutralized by gaining or losing electrons through interaction with the metal wall, generating an electric current. This current, after amplification, provides a signal corresponding to the presence of specific ions.⁵⁸ This mode is best suited when the possible gas species released are known in advance. However, in cases where the gaseous products are unknown or multiple gas species may be present, the second mode, bar mode, is employed. This mode utilizes a secondary electron multiplier detector, which is capable of scanning a wide m/z range (0 - 200 atomic mass units, amu). In this mode, weak ion signals are amplified through a cascade process to generate measurable current. Specifically, the incident ions strike the initial dynode of the multiplier, releasing

secondary electrons. These electrons are accelerated and sequentially impact additional dynode stages, releasing more electrons at each stage.⁵⁹ This cascading effect culminates in a strong detectable signal at the collector.

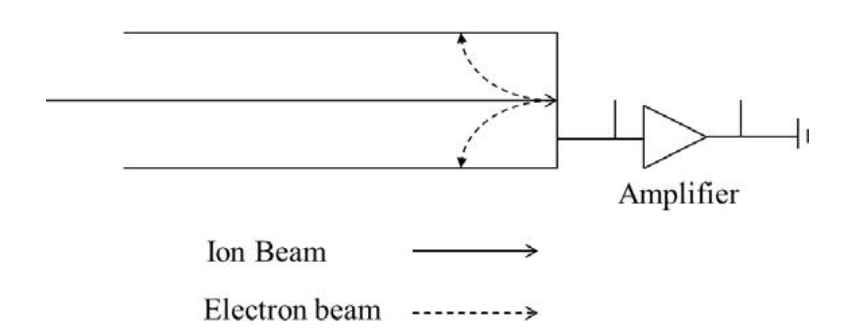


Figure 2-16: Faraday Cup detector used in the EGA employed in this work. (Adapted from reference 60)

By analyzing the changes in the TG and DTA curves, the time window during which a reaction occurs can be determined. Then, by examining the m/z signal variation within that time frame, the atomic masses of the released gases can be inferred. Based on this, the likely gas species can be proposed and subsequently confirmed by targeted detection using line mode.

2.4 References

- 1. C. Suryanarayana, E. Ivanov and V. V. Bolyrev, *Materials Science and Engineering A-Structural Materials Properties*, 2001, **304-306**, 151.
- 2. Q. Zhang and F. Saito, Advanced Powder Technology, 2012, 23, 523.
- 3. "Mechanochemistry in Nanoscience and Minerals Engineering", P. Baláž, Springer-verlag, 2008.
- 4. V. Šepelák and K.-D. Becker, Journal of the Korean Ceramic Society, 2012, 49, 19.
- 5. C. Suryanarayana, Progress in Materials Science, 2001, 46, 1.
- 6. J. Huot, D. B. Ravinsbaek, J. Zhang, F. Cuevas, M. Latroche and T. R. Jensen, *Progress in Materials Science*, 2013, **58**, 30.
- 7. D. Tan and T. Friščić, Eur. J. Org. Chem., 2018, 2018, 18-33.
- 8. A. Calka and A. P. Radlinski, *Materials Science and Engineering A-Structural Materials Properties*, 1991, **134**, 1350.
- 9. T. E. Fischer, Annual Review of Material Science, 1988, 18, 303.
- 10. G.Kaupp, CrystEngComm, 2009, 11, 388–403.
- 11. "Environmental Chemistry: Green Chemistry and Pollutants in Ecosystems", E. Lichtfouse, J.Schwarzbauer and D. Robert, Springer-verlag, 2005; M. Aresta, A. Dibenedetto, T. Pastore, Chapter 50, Part IV, pp 553-559.
- 12. I. Pri-Bar and B. R. James, Journal of Molecular Catalysis A-Chemical, 2007, 264, 135.
- 13. J. F. Fernandez-Bertan, Pure and Applied Chemistry, 1999, 71, 581.
- 14. W. Peukert, International Journal of Mineral Processing, 2004, 74S, S3.
- 15. S. L. James, C. J. Adams, C. Bolm, D. Braga, P. Collier, T. Friscic, F. Gregioni, K. D. M. Harris, G. Hyett, W. Jones, A. Krebs, J. Mack, L. Maini, A. G. Orpen, I. P. Parkin, W. C. Shearouse, J. W. Steed and D. C. Wadell, *Chemical Society Reviews*, 2012, **41**, 413.
- 16. L. Tacaks, Progress in Materials Science, 2002, 47, 355.
- 17. Retsch, http://www.retsch.com/products/milling/ball-mills/pm-100 (accessed 7/12/2024).
- 18. T. Chandra, J. P. Zebrowski, Journal of Chemical Health and Safety, 2014, 21, 22-28.
- 19. A. V. Shiyanov, E. A. Abramov and S. V. Nasyrov, Glass and Ceramics, 2022, 79, 3-4, 96-99.
- 20. "Oxford Dictionary of Chemistry", J. Daintith, Oxford University Press, 2008.
- 21. M. I. Aroyo, ed., *International Tables for Crystallography, International Union of Crystallography*, Chester, 2016.
- 22. B. E. Warren, X-ray Diffraction, Dover Publications, New York, 1990.
- 23. C. Giacovazzo, H. Guagliardi, G. Artioli, R. Camalli, G. Gilli, G. Ferraris, G. Magnani and R. Poloni, *Fundamentals of Crystallography*, 3rd edn, Oxford University Press, Oxford, 2011.
- 24. Crystal Structure Analysis; Principles and Practice, Book Series 6, W. Clegg, A. J. Blake, R. O. Gould and P Main, Oxford University Press, 2006.

- 25. "Solid State Chemistry; An introduction", L. Smart and E. Moore, CRC Press Taylor & Francis Group LLC, 1995.
- 26. "International Tables for X-Ray Crystallography", N. F. M. Henry and K. Lonsdale, D. Reidel Pub. Co., 1976.
- 27. "Crystal Structure Analysis for Chemists and Biologists", J. P. Glusker, M. Lewis and M. Rossi, VCH Publishers Inc., 1994.
- 28. W. H. Bragg, Nature, 1912, 90, 219.
- 29. L. Bragg, Nature, 1912, 90, 410.
- 30. W. H. Bragg, Nature, 1913, 91, 477.
- 31. W. H. Bragg, Nature, 1914, 93, 124.
- 32. L. Bragg, Proceedings of the Royal Society A, 1961, 262, 145.
- 33. G. Nolze and W. Kraus, *PowderCell for Windows*, Version 2.4, BAM, Berlin, 2000; ICSD, Inorganic Crystal Structure Database, FIZ Karlsruhe, Germany.
- 34. ICDD PDF-4+ 2024, International Centre for Diffraction Data, Newtown Square, PA, USA; *PANalytical HighScore Plus*, Version 4.9, Malvern Panalytical.
- 35. *HighScore Plus*; http://www.panalytical.com/Xray-diffraction-software/HighScore-Plus.htm; accessed 20/12/2024.
- 36. Inorganic Crystal Structure Database (ICSD), http://icsd.cds.rsc.org/ (accessed 18/12/2024).
- 37. P. Scherrer, Nachr. Ges. Wiss. Göttingen, 1918, 26, 98-100.
- 38. "The Rietveld Method", R. A. Young, IUCr Book Series 5, Oxford University Press, 1993.
- 39. B. H. Toby, Journal of Applied Crystallography, 2001, 34, 210.
- 40. L. B. McCusker, R. B. Von Dreele, D. E. Cox, D. Louër and P. Scardi, *Journal of Applied Crystallography*, 1999, **32**, 36.
- 41. "Molecular Symmetry and Group Theory", A. Vincent, J. Wiley & Sons, 1983.
- 42. "Fundamentals of Fourier Transform Infrared Spectroscopy", B. C. Smith, CRC Press LLC, 1996.
- 43. C. V. Raman and K. S. Krishnan, Nature, 1928, 121, 501.
- 44. A. C. Ferrari and J. Robertson, *Philos. Trans. R. Soc. A*, 2004, **362**, 2477–2512.
- 45. "Fourier Transform Infrared Spectrometry", P. R. Griffiths and J. A. de Haseth, J. Wiley & Sons, 2007.
- 46. "Modern Raman Spectroscopy A Practical Approach", W. E. Smith and G. Dent, J. Wiley & Sons, 2005.
- 47. J. R. Ferraro, K. Nakamoto and C. W. Brown, *Introductory Raman Spectroscopy*, Academic Press, 2nd edn., 2003.
- 48. E. Smith and G. Dent, *Modern Raman Spectroscopy A Practical Approach*, John Wiley & Sons, Chichester, 2005.
- 49. "Atkins' Physical Chemistry", P. Atkins and J. de Paula, Oxford University Press, 2023.

- 50. G. W. H. Höhne, W. F. Hemminger and H. J. Flammersheim, *Differential Scanning Calorimetry: An Introduction for Practitioners*, Springer, Berlin, 2nd edn., 2003.
- 51. M. E. Brown and P. K. Gallagher, *Handbook of Thermal Analysis and Calorimetry: Principles and Practice*, Elsevier, Amsterdam, Vol. 1, 2008.
- 52. S. Vyazovkin, A. K. Burnham, J. M. Criado, L. A. Pérez-Maqueda, C. Popescu and N. Sbirrazzuoli, *Thermochim. Acta*, 2011, **520**, 1-19.
- 53. I. V. Parkin, Chemical Society Reviews, 1996, 25, 199.
- 54. Netzsch, http://www.netzsch-thermal-analysis.com/en/home.html (accessed 24/12/2024).
- 55. H. E. Kissinger, Journal of Research of the National Bureau of Standards, 1956, 57, 217.
- 56. H. E. Kissinger, Analytical Chemistry, 1957, 29, 1702.
- 57. R. G. Cooks, Z. Ouyang, Z. Takats and J. M. Wiseman, Science, 2006, 311, 1566–1570.
- 58. D. J. Douglas and J. B. French, *J. Am. Soc. Mass Spectrom.*, 2002, **13**, 444-453.
- 59. J. H. Gross, Mass Spectrometry: A Textbook, 2nd edn, Springer, 2011.
- 60. "Mass Spectrometry Principles and Applications", E de Hoffman and V. Stroobant, J. Wiley and Sons, 2007.

3. Dehydrogenation of NaOH-NaH with Various Catalysts

3.1 Introduction

3.1.1 Sodium Hydride and Sodium Hydroxide system

Among various hydrogen storage materials, sodium-based compounds have emerged as promising candidates for stationary hydrogen storage applications because sodium is one of the most abundant elements on Earth (2.64 wt.%) and cost-effectiveness.¹ Additionally, sodium resources are widely distributed across the globe, being readily available from both seawater and underground deposits.² Recent studies by Xu *et al* have demonstrated that sodium oxide (Na₂O) exhibits a high capacity for hydrogen absorption at near-ambient temperatures (~60 °C), forming sodium hydride (NaH) and sodium hydroxide (NaOH).³ Moreover, the hydrogenated products, NaH and NaOH, can be efficiently reverted to Na₂O through thermal treatment, highlighting the material's potential for reversible hydrogen storage.⁴

$$Na_2O + H_2 = NaH + NaOH \Delta H = \pm 55.65 \text{ kJ/mol H}_2$$
 (3.2 wt.%)

Dehydrogenation in the NaH–NaOH system occurs at a lower temperature than that of NaH alone. This reduction in dehydrogenation temperature is likely attributed to the interaction between the distinct hydrogen species present in NaOH and NaH, namely, protonic hydrogen (H^δ) and hydridic hydrogen (H^δ), respectively. However, the precise dehydrogenation mechanism remains unclear. Notably, early investigations of the Na–O–H system have suggested that alkali metal hydrides and their corresponding hydroxides may exhibit miscibility. More recently, studies exploring the effect of NaOH as an additive in the NaH system have revealed that approximately 10 mol% of NaOH can be incorporated into the NaH structure, enhancing hydrogen mobility above 150 °C.^{3,4} These findings indicate that hydroxide ions (OH⁻) can substitute for hydride ions (H⁻) within the NaH lattice at elevated temperatures. Given the strong correlation between proton conduction and hydrogen uptake/release kinetics, a detailed investigation into the structural and phase evolution of the Na–O–H system upon heating is expected to provide crucial insights into the desorption mechanism, ultimately guiding strategies for performance optimization.

According to Mao *et al*'s research, Na₂O begins to absorb hydrogen at slightly above ambient temperatures (30–50 °C) under relatively low hydrogen pressure (18 bar).⁵ The hydrogenated products, NaH and NaOH, release hydrogen at lower temperatures compared to pure NaH. Furthermore, differential thermal analysis (DTA) has identified an

endothermic event near 170 °C in the NaH–NaOH system, which cannot be attributed to either the dehydrogenation reaction of the mixture or the phase transitions of the individual components. *In-situ* synchrotron powder X-ray diffraction (PXD) analysis confirms the formation of a solid solution between NaOH and NaH, which remains stable up to 240 °C. Within the temperature range of 160–240 °C, both NaH and Na(H,OH) cubic phases exhibit significant volume expansion. This pronounced intraphase interaction between protonic and hydridic hydrogen species is proposed as the primary driving force facilitating dehydrogenation in the hydride–hydroxide system.

3.1.2 Aim

The purpose is to validate the mechanism proposed by the NaOH-NaH system and to probe the dehydrogenation reaction pathway in more detail. The kinetics of NaH-NaOH systems might be further improved by the choice of suitable catalysts.

3.2 Experimental

3.2.1 Preparation of the System

NaH (Sigma Aldrich, dry, 90%), MoS₂ (Sigma Aldrich, powder, 98%), SiC (Sigma Aldrich, 400 mesh, \geq 97.5%), Ni (Sigma Aldrich, powder, 99.7%), Ti (Sigma Aldrich, 325 mesh, \geq 99.5%), TiF₃ (Sigma Aldrich, 5g), KMnO₄ (Sigma Aldrich, ACS reagent, \geq 99%), H₂SO₄ (Fisher Scientific, \geq 95%), Mg (Alfa Aesar, 325 mesh, 99.8%) and Si (Sigma Aldrich, 325 mesh, 99.5%) were used as received. NaOH (Alfa Aesar, pellet, 99.99%) was dried prior to synthesis experiment through use of the Schlenk line. (100 °C; -2×10⁻³ bar)

Because of the air and moisture sensitivity of NaOH (Alfa Aesar, pellet, 99.99%), Na₂O and NaH (Sigma Aldrich, dry, 90%), all operations were conducted in a recirculating Argon or N₂-filled (BOC, 99.998%) glovebox (MBraun LABstar, O₂ < 10 ppm, H₂O < 0.5 ppm). NaOH (Alfa Aesar, pellet, 99.99%) was ball-milled for 1 hour to reduce the particle size of the powder. After ball-milling, the NaOH was sent to Schlenk line to dry overnight. (100 °C; -2×10^{-3} bar)

3.2.2 Ball-milling of NaOH-NaH

About 0.5 g of various NaOH-NaH mixtures (discussed in more detail in following sections) were weighed and then transferred to a stainless steel grinding jar that was filled with eight stainless steel balls (10 mm diameter), each of which weighed *ca.* 4 g. The grinding jar was sealed under argon before removal from the glovebox. Unless otherwise stated, ball milling was conducted at a 400 rpm rotation speed with a ball-to-powder ratio

of 60:1 in a planetary ball mill (Retsch PM100) over 5-minute milling periods (reverse rotation) followed by 5-minute rest periods. Milling durations are specified in subsequent sections.

3.2.3 TG-DTA-MS Studies

Compositions in hydroxide-hydride the system characterized using was thermogravimetric-differential thermal analysis (TG-DTA) coupled with mass spectrometry (MS) to investigate their respective thermal behaviour. These experiments aimed to determine the onset and peak temperatures of thermal events during heating, to quantify the weight loss, and to identify the nature and quantity of gaseous species evolved during the reaction. TG-DTA measurements were conducted using a Netzsch STA 409 PC instrument, which was coupled to a Hiden HPR20 mass spectrometer. All analyses were performed under an argon flow, and sample handling was carried out exclusively in inert atmosphere glove boxes to prevent contamination or unwanted reactions.

Prior to analysis, correction files were generated, followed by the examination of the materials. Initial experiments involved heating the samples from room temperature to 500 °C at a rate of 5 °C/min. Based on the results of these preliminary TG-DTA measurements, subsequent experiments were designed to investigate intermediate temperature points, enabling the identification of any transient species formed and facilitating the elucidation of the hydrogen release mechanism. For each experiment, approximately 15–30 mg of sample was subjected to thermal treatment.

TG-DTA analysis was further employed to determine the activation energy of compositions in the Na-H-OH system using the Kissinger method. Samples were heated to 500 °C at varying heating rates of 2, 5, 10, and 20 °C min⁻¹, and Kissinger plots were constructed to extract kinetic parameters associated with the dehydrogenation process.

3.2.4 Powder X-ray Diffraction (PXD)

All starting materials and hydride–hydroxide hydrogen release systems were characterized using PXD. All the materials used in this study were air-sensitive. Therefore, all the samples were prepared using the air-sensitive sample holder under inert atmosphere.(glovebox) All the materials were characterized by PANalytical X'Pert. Diffraction data was collected over a 2θ range of 5–85° for 1 h to facilitate phase identification. The obtained diffraction data were compared with appropriate reference patterns using the ICSD database via PowderCell or the ICDD PDF database via PANalytical HighScore Plus software.^{6,7} Rietveld refinements were performed using the General Structure Analysis System (GSAS) with the EXPGUI interface.⁸

3.2.5 Catalyst Preparation

In addition to the catalysts mentioned previously in 3.2.1: MoS₂, SiC, Ni, Ti, and TiF₃, two other catalysts were synthesised prior to ues. These were rGO and Mg₂Si.

Graphene oxide (GO) was synthesized following Tour's method. Briefly, a mixture of 360 mL of sulfuric acid (H₂SO₄) and 40 mL of phosphoric acid (H₃PO₄; Fisher Scientific, ≥ 95%) was prepared and cooled in an ice bath (0 °C, a mixture of ice and water). Once the solution reached the desired temperature, 18 g of potassium permanganate (KMnO₄; Sigma Aldrich, ACS reagent, $\geq 99\%$) was gradually added to 3 g of graphene agglomerates. The resulting powder was then slowly introduced into the acid mixture while ensuring that the solution did not overheat. The reaction mixture was allowed to warm naturally to room temperature upon removal from the ice bath and subsequently heated to 50 °C for 16 h. During heating, the initially black solution transitioned to a brown colour. Then, the reaction mixture was poured into 400 mL of cold deionized (DI) water, maintained in an ice bath (0 °C, a mixture of ice and water), followed by the addition of 7 mL of hydrogen peroxide (H₂O₂, 30%, Sigma-Aldrich). The final mixture was then allowed to warm naturally to room temperature. Centrifugation was employed to separate the dispersed GO, and the supernatant was exchanged with DI water through repeated washing. A minimum of ten such washing cycles were performed to ensure the removal of residual reactants. Once a purified GO dispersion was obtained, it was adjusted to a concentration between 14 mg mL⁻¹ and 20 mg mL⁻¹. The dispersion was sonicated using an Elma S30 Elmasonic bath and subsequently transferred into a syringe equipped with a needle. The concentrated dispersion was carefully dispensed dropwise into liquid nitrogen, forming solid, saturated beads. The frozen beads were then freeze-dried using a Schlenk line under a vacuum of approximately 3.10⁻¹ mbar, with temperatures ranging from –198 °C to room temperature. The resulting materials (GO) were loaded into a crucible and heated in a furnace at a rate of 2 °C min⁻¹ until 250 °C, and dwelled at this temperature for 3 h before cooling down. This was in order to eliminate CO/CO₂ via their release in subsequent heating cycles of this material. After heating, the reduced graphene oxide, rGO, was collected from the crucible.

Magnesium silicide (Mg₂Si) was synthesized following the method reported by Fan *et al.*¹⁰ A total of 70 mg (2.88 mmol) of magnesium powder (Mg, 99.8%, 325 mesh, Alfa Aesar) was thoroughly mixed with 35 mg (1.25 mmol) of silicon powder (Si, 99.5%, 325 mesh, Sigma-Aldrich). To compensate for the volatilization of Mg, an excess of Mg powder (15 wt.%) was employed, corresponding to a Mg:Si molar ratio of 2.3:1. The mixed powders were transferred into an alumina crucible, which is considered microwave (MW)-transparent. The crucible containing the reactants was placed inside a quartz tube,

which was subsequently sealed and connected to a vacuum line outside the glovebox. A modified single-mode MW cavity reactor (CEM Discovery, 2.45 GHz) with an adjustable input power of 0–300 W was used for synthesis. The powder mixture was subjected to MW irradiation at an incident power of 200 W under a static vacuum of P < 10⁻⁴ mbar. The irradiation was maintained for 120 s to facilitate Mg₂Si formation. Following MW treatment, the quartz tube was allowed to cool naturally to room temperature. The synthesized Mg₂Si samples were then ground and stored in an inert atmosphere within a glovebox to prevent oxidation before further characterization.

3.3 Result and Discussion

3.3.1 Thermal Treatment of the Individual NaOH and NaH Components

To investigate the thermal behaviour of NaOH itself, samples were heated under flowing argon from room temperature to 400 °C at a heating rate of 5 °C min⁻¹. From Figure 3-1 and 3-2, the TG results indicate that mass loss begins at approximately 55 °C and reaches 8.74 wt.% by 140 °C, followed by a gradual decrease to 8.81 wt.% at 420 °C. If the loss is entirely due to H₂O, calculations show that the NaOH sample contains approximately 21.978 at.% NaOH·nH₂O (n = 1).The DTA analysis reveals five distinct thermal events at 66.22 °C, 137.21 °C, 288.10 °C, 295.63 °C, and 312.80 °C. Notably, only two of these peaks (those occurring at lower temperatures) coincide with the primary mass loss, suggesting that the remaining thermal events correspond to processes occurring post-dehydration.

The latter three peaks will be analysed in a subsequent section. From the MS data in Figure 3-2, the presence of an H₂O signal, along with the PXD pattern in Figure 3-3 showing additional NaOH·H₂O peaks besides those of NaOH in the as-received sample, indicates that the mass loss observed in Figure 3-1 from 55 to 140 °C is due to H₂O. The DTA peak at 66.22 °C in Figure 3-1 represents the gradual evaporation of water partially adsorbed on the surface. When the temperature reaches 110 °C, the MS signal for H₂O increases and a significant total mass loss begins, suggesting the evaporation of H₂O from NaOH·H₂O impurities. This also corresponds to the DTA peak at 137.21 °C in Figure 3-1.¹¹

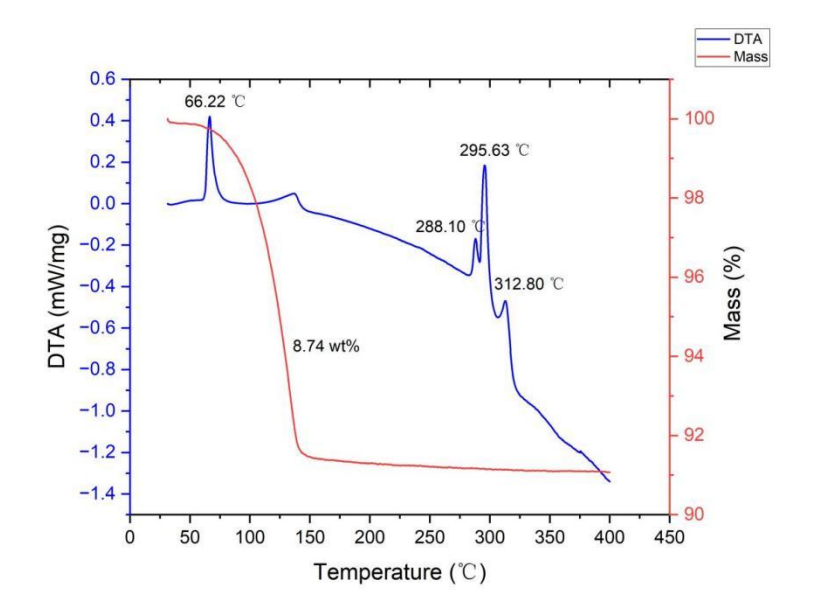


Figure 3-1: TG(red) and DTA(blue) profiles for as-received NaOH on heating from 35-400 °C at 5 °C min⁻¹ under flowing Ar(g). The TGA profile is shown in red (right hand y-axis) and the DTA profile is shown in blue (left hand y-axis).

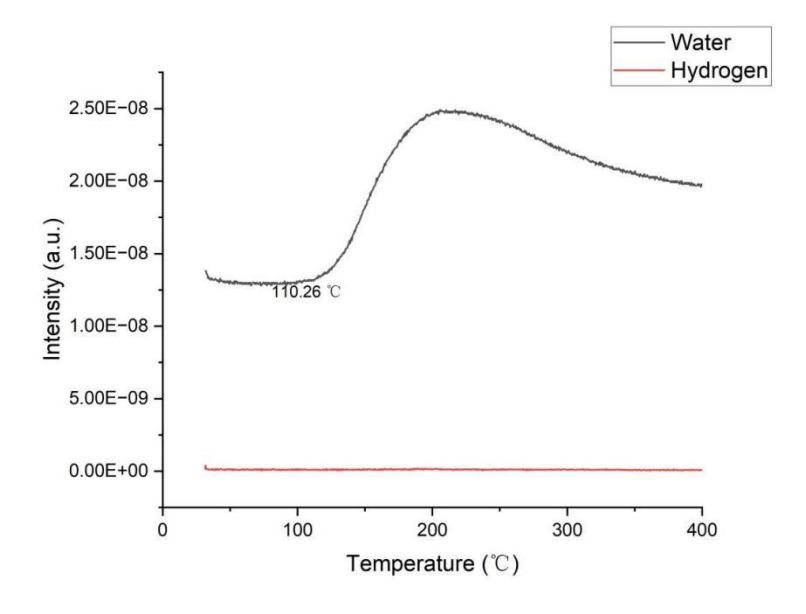


Figure 3-2: Mass spectrometry output for water (m/z = 18; black) and hydrogen (m/z = 2;red) as a function of temperature for as-received NaOH on heating from 35-400 $^{\circ}$ C at 5 $^{\circ}$ C min⁻¹ under flowing Ar gas.

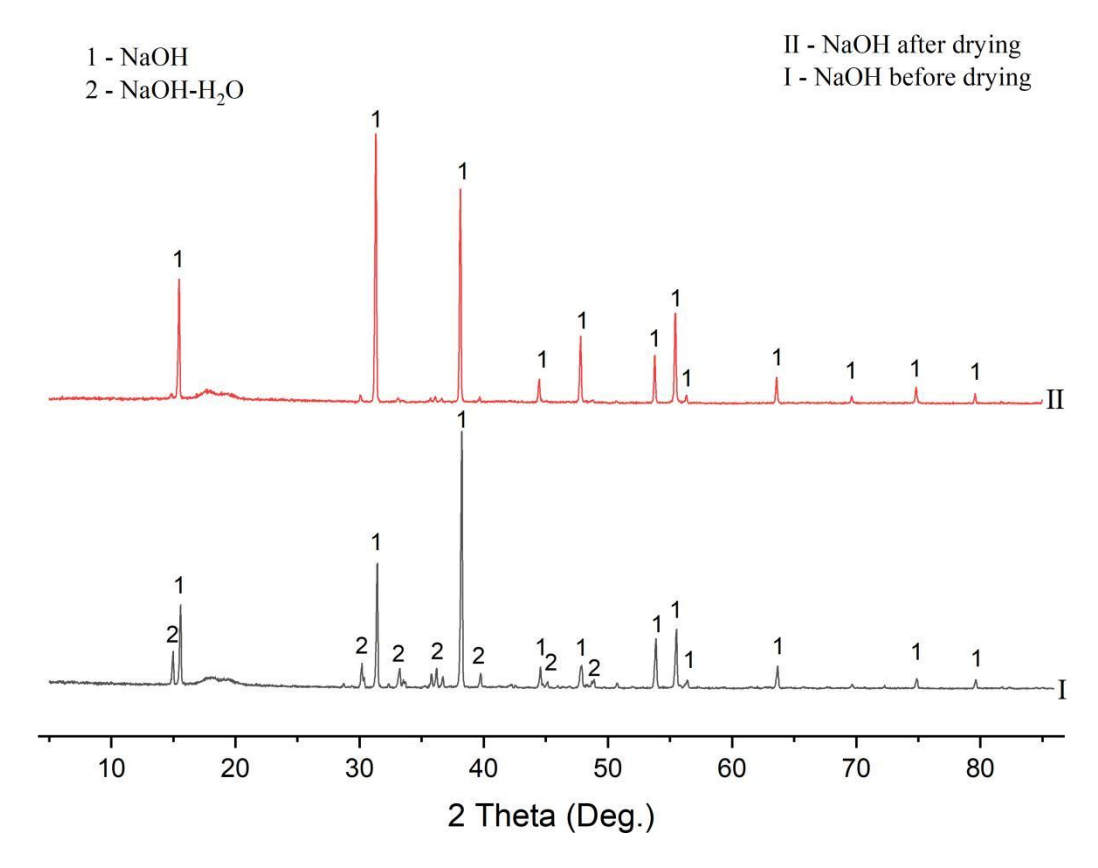


Figure 3-3: PXD patterns of NaOH as-received (I) and NaOH after drying (II). (1 represent NaOH)

To remove the crystallised water from NaOH·H₂O, the NaOH monohydrate was dried on the Schlenk line under 2x10⁻² Pa vacuum at 100 °C. After drying, no H₂O signal is observed in the MS data of Figure 3-5, and there is almost no mass loss between 55–140 °C. Therefore, after drying using the Schlenk line, the NaOH·nH₂O (n = 1) peaks in the PXD pattern of Figure 3-3 have nearly completely disappeared. Once analysis had established that the process at 137 °C was due to the loss of one equivalent of water from NaOH·H₂O. By comparison with the TG-DTA results for the undried NaOH sample, this confirms that the initial NaOH contained approximately 9 wt.% water before drying which is 21.978 At. % NaOH-nH₂O (n=1). Figure 3-4 presents two peaks at 297.18 °C, and 315.44 °C without mass loss. Figure 3-4 shows that there is no water and hydrogen released during heating. Also, The first peak at 297.18 °C corresponds to the α-β (orthorhombic-to-monoclinic) phase transition of NaOH, which is closed to 299 °C as reported in the literature.⁵ The second peak is attributed to the melting of NaOH because the melting point of the NaOH should be 318 °C. 12,13 To investigate the thermal behaviour of dry NaOH after ball-milling for comparision, the NaOH was ball-milled for 2 h and heated to 400 °C at 5 °C min⁻¹. In Figure 3-6, the ball-milled NaOH does not show any mass change, and the temperature maxima of the two main DTA peaks are close to those of the unmilled sample. Furthermore, NaOH is highly stable. Even after ball milling and subsequent heating to 900°C, NaOH does not undergo decomposition. (Appendix 3-1)

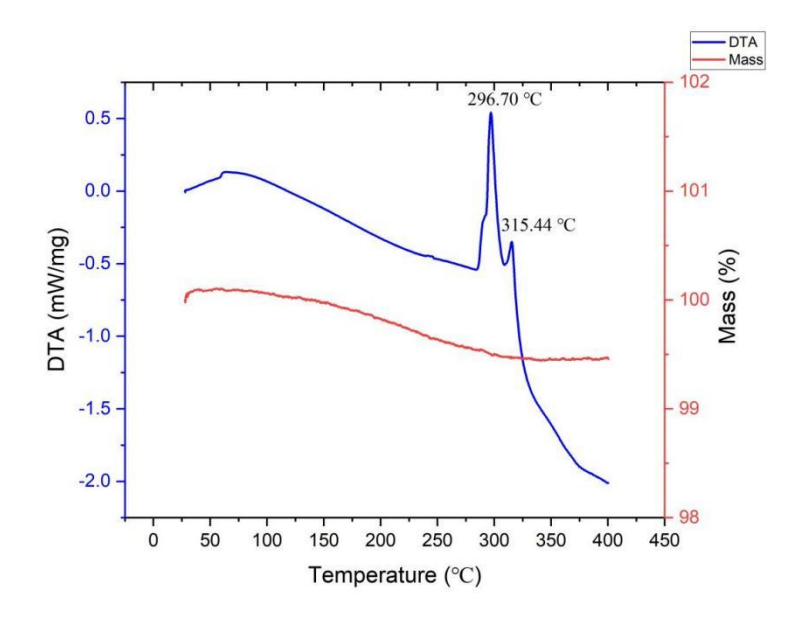


Figure 3-4: TG(red) and DTA(blue) profiles for NaOH after drying on heating from 35-400 °C at 5 °C min⁻¹ under flowing Ar(g).

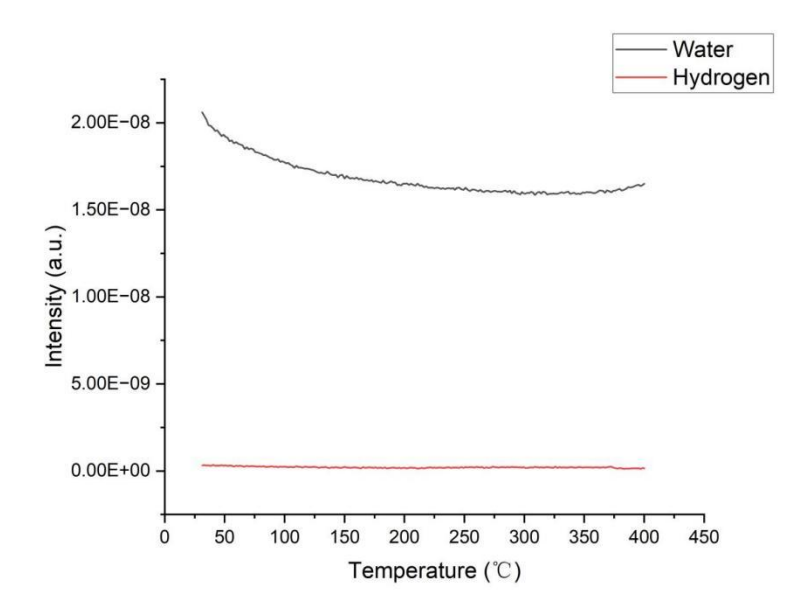


Figure 3-5: Mass spectrometry output for water (m/z = 18; black) and hydrogen (m/z = 2;red) as a function of temperature for NaOH after drying on heating from 35-400 $^{\circ}$ C at 5 $^{\circ}$ C min⁻¹ under flowing Ar gas.

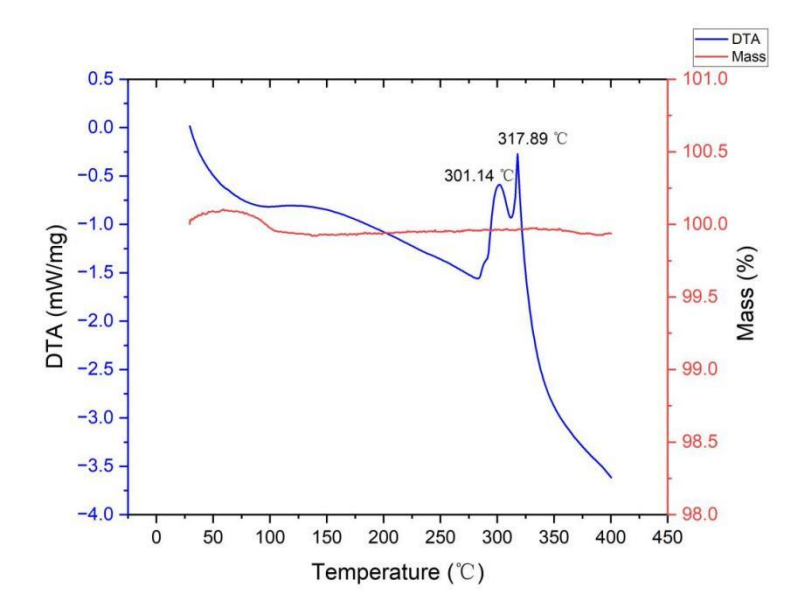


Figure 3-6: TG(red) and DTA(blue) profiles for ball-milled NaOH (2h, 400rpm) on heating from 35-400 °C at 5 °C min⁻¹ under flowing Ar(g).

High purity NaH was not available online. The 90 at.% NaH from sigma was the only commercial NaH available at the time the experiments were performed. From Figure 3-7, the DTA profile only has one peak at 380 °C that represents the decomposition of unmilled NaH.

$$2NaH = 2Na + H_2$$
 Eq. 1

The theoretical mass loss for this decomposition reacton is *ca.* 4.17 wt.%. The experimental mass loss of about 3.59 wt.% was therefore unexpected. There are (at least) two possible reasons for this. The first reason may be that 10 at.% of the sample is an impurity (or impurities) that does decompose or react with NaH below 450 °C. This "inert" impurity mass thus reduces the overall mass loss of the NaH sample. However, in theory, the mass loss should reach 3.75 wt.%. One other possible reason for the mass difference is if the impurity is NaOH. This could arise because NaH is sensitive to water (air) - to form NaOH. The presence of NaOH is confirmed in Figure 3-8. If the 10 at.% of impurities are NaOH, the theoretical mass loss should be 3.64 wt.%, which is closer to the experimental value of 3.59 wt.%. Therefore, based on the mass loss, the 10 at.% impurity is most likely NaOH, and it likely reacts with NaH.

$$NaOH+NaH = Na_2O + H_2$$
 Eq. 2

In addition to the above-mentioned similarity in mass, from Figure 3-8, the peak of NaH at 32° is close to the peak of NaOH at the same position. Due to the amount of NaOH being quite small, the peak of NaOH may be covered by NaH at 32°. The peak of NaH at about 38° is the same as the peak in NaOH. It also didn't show the peak of Na. The possible impurity in NaH is about the NaOH because the water in the air cannot be avoided

completely. After structure refinement as shown in Table 3-1, the purity of the new NaH can be confirmed. Therefore, to provide a real molar ratio of 1:1 NaOH:NaH the amount of the 9.69 wt.% NaOH impurity in NaH should be factored into reaction calculations. Therefore, if all the impurity in the NaH is assumed to be NaOH, and the moles of NaOH and NaH are 1 and X respectively, then the calculation equation can be made as below:

$$(40+24*0.0969X)/40 = 0.9031X$$
 X= 1.19

Therefore, the ideal molar NaH:NaOH ratio is approximately 1.19:1 when using the NaH (90%) starting material.

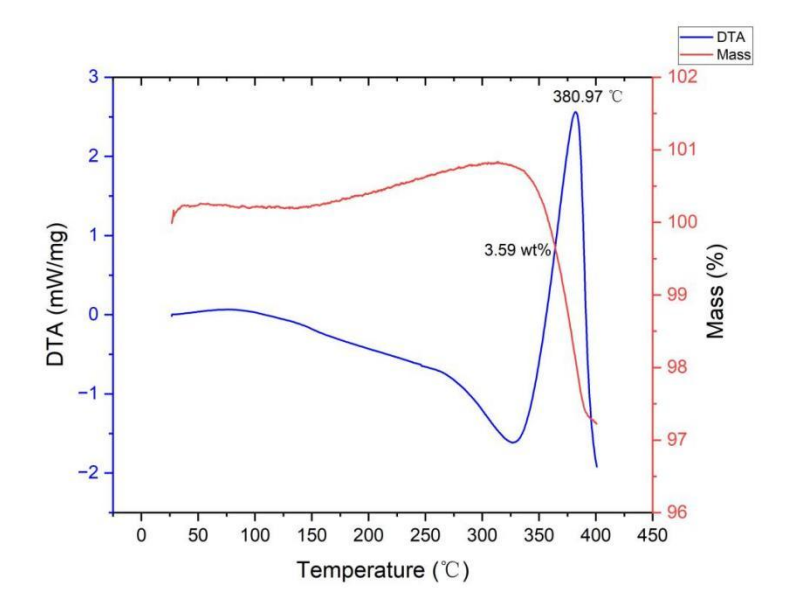


Figure 3-7: TG(red) and DTA(blue) profiles for as-received NaH (purity: 90%) on heating from 35-400 °C at 5 °C min⁻¹ under flowing Ar(g).

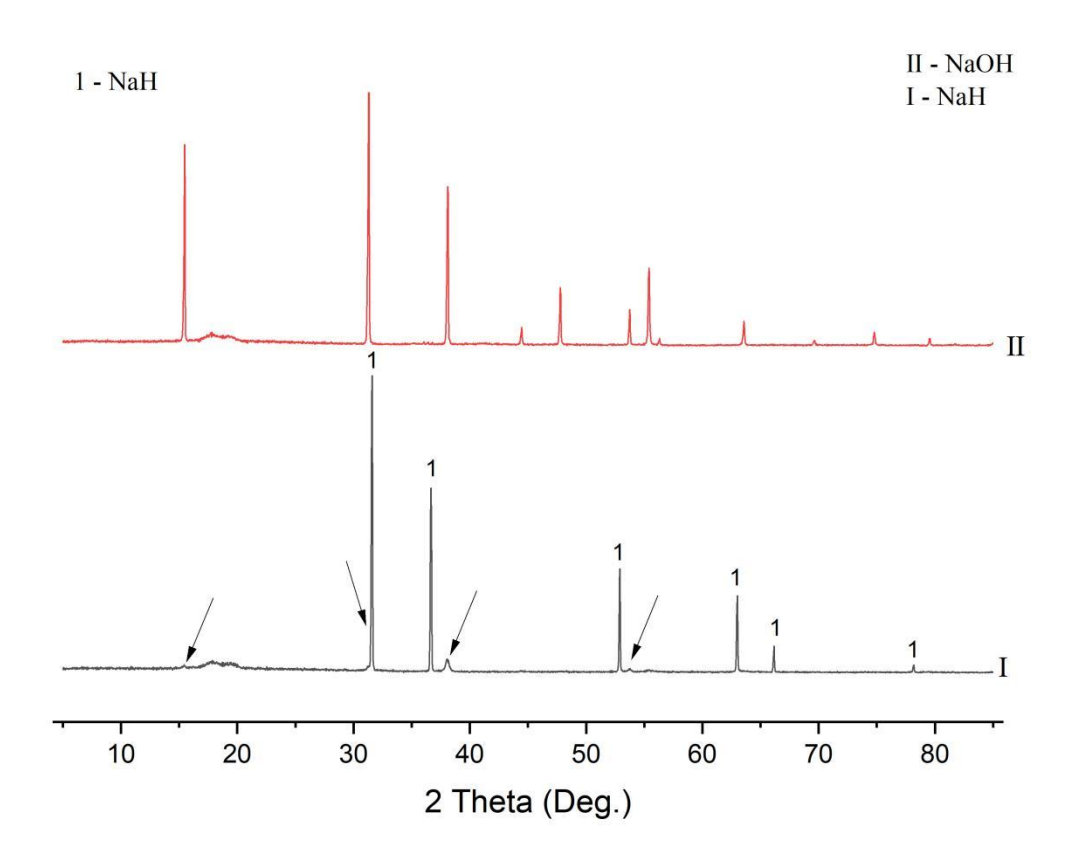


Figure 3-8: PXD patterns of ball-milled NaOH (dry, 1h, 400rpm; II) and as-received NaH (90 at.%; I). NaH pattern is experimental data taken for the as-received starting materials. (The arrows indicate NaOH in the NaH sample pattern.)

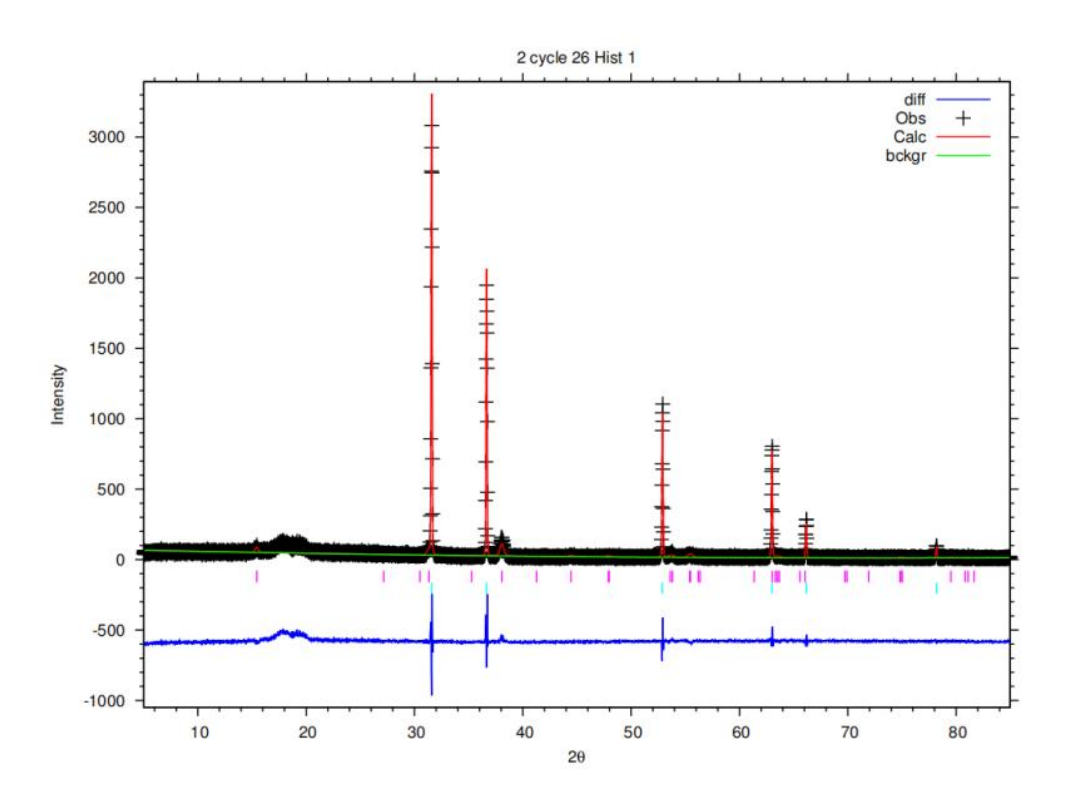


Figure 3-9: Profile plot from Rietveld refinement of as-received NaH (90%). (Purple represent NaOH; Blue represent NaH; Black represent observed line; Red represent calcualted line; Green represent background line).

Table 3-1: Crystallographic Data Obtained from the Rietveld Refinement for NaH(90%) as-received.

Chemical formula	NaH	NaOH		
Crystal system	cubic	orthorhombic		
Space group	Fm-3m(225)	Bmmb(63)		
a/Å	4.8789(1)	3.403(3)		
b/Å	4.8789(1)	11.354(5)		
c/Å	4.8789(1)	3.398(3)		
V/ų	116.14(1)	131.34(7)		
Formula weight/ g mol-1	23.998	39.997		
Calculated density/ g cm-3	2.27	2.13		
Formula unit/ Z	4 4			
Weight percentage/ wt.%	84.824	15.176		
Purity/ at.%	90.31 9.69			
No. Of observation	4786			
R _{wp}	0.2650			
Rp	0.2002			
χ²	3.039			

3.3.2 Dehydrogenation of NaOH-NaH and Mechanism

To investigate the reaction pathway and mechanism of NaOH-NaH dehydrogenation, the hydroxide-hydride mixture was first ball-milled for 2 h (400rpm and mass ratio of ball:powder 80:1) and then heated from 35 °C - 420 °C. According to calculation shown above, the ideal NaOH:NaH molar ratio should be *ca.* 1:1.19 to achieve the optimal hydrogen weight loss percentage in TG-DTA experiments when using this NaH (90%) starting material (only). In Figures 3-10 and 3-11, the molar ratio used is 1:1.19, and the hydrogen weight loss percentage is 3.08 wt.%, which is close to the ideal value of 3.12 wt.%. This further confirms that NaH contains approximately 10% NaOH. In Figure 3-10, there are two peaks: one at 173 °C and another at 346 °C. There is also a hint of a shoulder on the leading edge of the peak at *ca.* 290 °C. This same feature seems to appear in other DTA traces. This also match up to the first peaks in the individual NaOH DTA trace. It suggests that there is a small amount of NaOH remaining to transform before reacting with remaining NaH.

Since the MS graph shows a hydrogen peak at 348 °C, which is very close to 346 °C, then

the endothermic DTA peak at 346 °C can be assigned to the dehydrogenation process. The peak at 173 °C will be analysed in next paragraph.

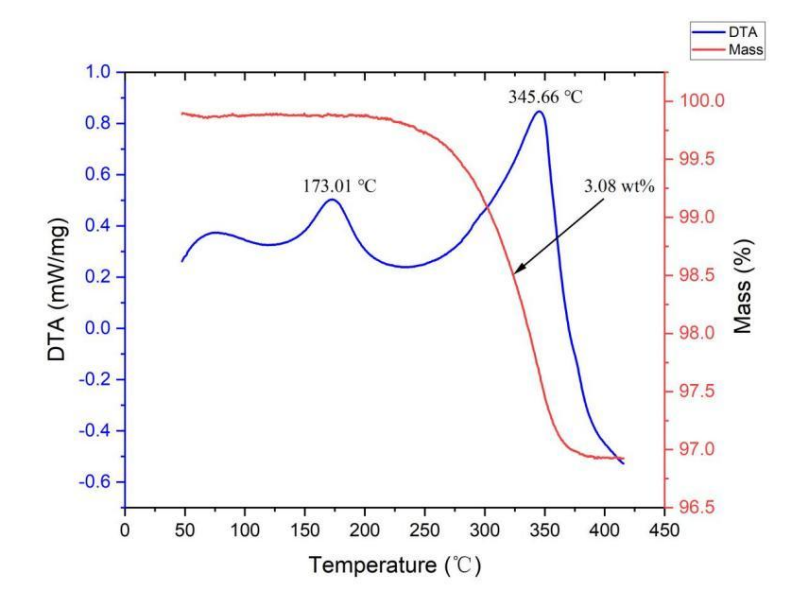


Figure 3-10: TG(red) and DTA(blue) profiles for ball-milled 1:1.15 NaOH:NaH (2h, 400rpm) on heating from 35-420 °C at 5 °C min⁻¹ under flowing Ar(g).

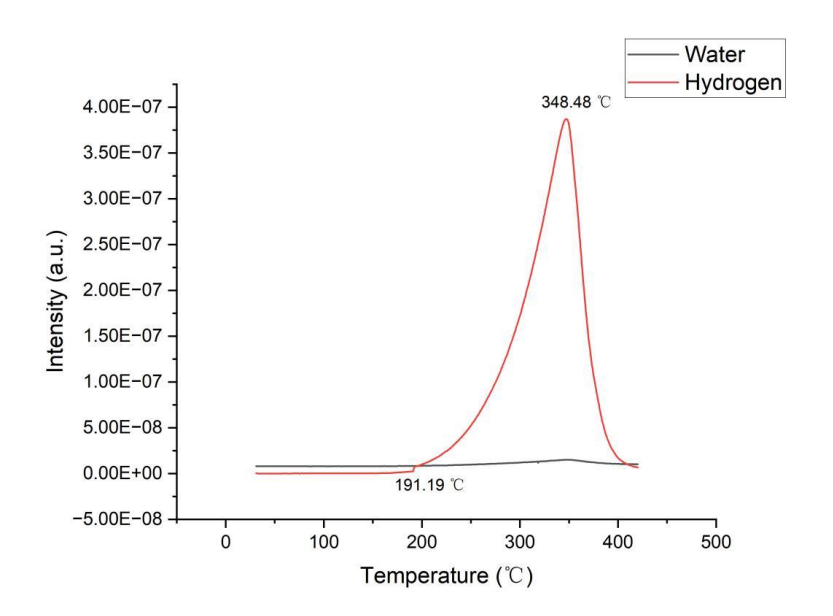


Figure 3-11: Mass spectrometry output for water (m/z = 18; black) and hydrogen (m/z = 2; red) as a function of temperature for a ball-milled 1:1.15 NaOH:NaH (2h, 400rpm) on heating from 35-420 °C at 5 °C min⁻¹ under flowing Ar gas.

Figure 3-12 and 3-13 presents the PXD patterns of the ball milled NaH-NaOH sample before and after heating to 170 °C, 210 °C, and 240 °C respectively in the TG-DTA (each followed by turning the TG-DTA furnace off and cooling to room temperature). The as-milled NaH-NaOH sample shows clear peaks for both NaH and NaOH, indicating that NaH and NaOH do not react during the ball milling process. The most noticeable change in

the PXD pattern after heating to 170 °C occurs at approximately 32° 2θ, where Figure 3-13 shows that the NaH peak shifts to lower 2θ, and an additional peak appears at almost the same position. Additionally, the NaOH peak at 15° 2θ splits into two, and extra peaks emerge around *ca.* 49° 2θ and 56° 2θ. By comparing the relative intensities of the NaH peak at *ca.* 37° 2θ and the NaOH peak at 38° 2θ before and after heating to 170 °C, it is evident that the amount of NaH decreases. From 170°C-210°C, the NaOH peak at 31.2° gradually diminishes, while the newly formed split peak of NaH at *ca.* 31.8° starts to increase. Additionally, a small amount of Na₂O at 32.2° and 210 °C begins to form. The NaOH peak at 56° also starts to broaden. From 210 °C-240 °C, the NaH peak at 32° significantly decreases, while the Na₂O peaks become more pronounced.

Towards confirming the possible formation of an intermediate phase, several conclusions can be drawn based on the above observations. First, at 170 °C, the NaH peak shifts at lower 31.5°, and a new unidentified peak appears near the original NaH position. This shift suggests a possible interaction between NaH and NaOH, potentially forming a solid solution or inducing lattice distortion. Such structural changes could alter the interplanar spacing, thereby explaining the observed shift in the peak position and the appearance of the new feature. The leftward shift of the NaH peak from 31.6°-31.5° at 170 °C and 210 °C likely results from lattice expansion, indicating the incorporation of OH- into the NaH lattice. Furthermore, from 210 °C to 240 °C, the NaH peak at 32° decreases in intensity significantly compared to NaOH, accompanied by Na₂O formation at 32.2°. This suggests that NaH does not react with NaOH in a simple 1:1 ratio to form Na₂O, more specifically that process does not happen in one step. From the ball-milled NaH-NaOH sample up to 210 °C, the NaH-like peak continuously decreases and shifts. This indicates that the substitution of H⁻ with OH⁻ gradually causes lattice distortion, leading to systematic peak shifts. Additionally, the peak splitting at 15° 20 and broadening at 56° 20 for NaOH at 170°C and 210°C strongly suggest an interaction between NaH and NaOH during heating, leading to the formation of a solid solution NaH_{1-x}(OH)_x. Moreover, this is quite similar to the findings of Mao et al., where the NaH-like phase also continuously shifts and decreases.5

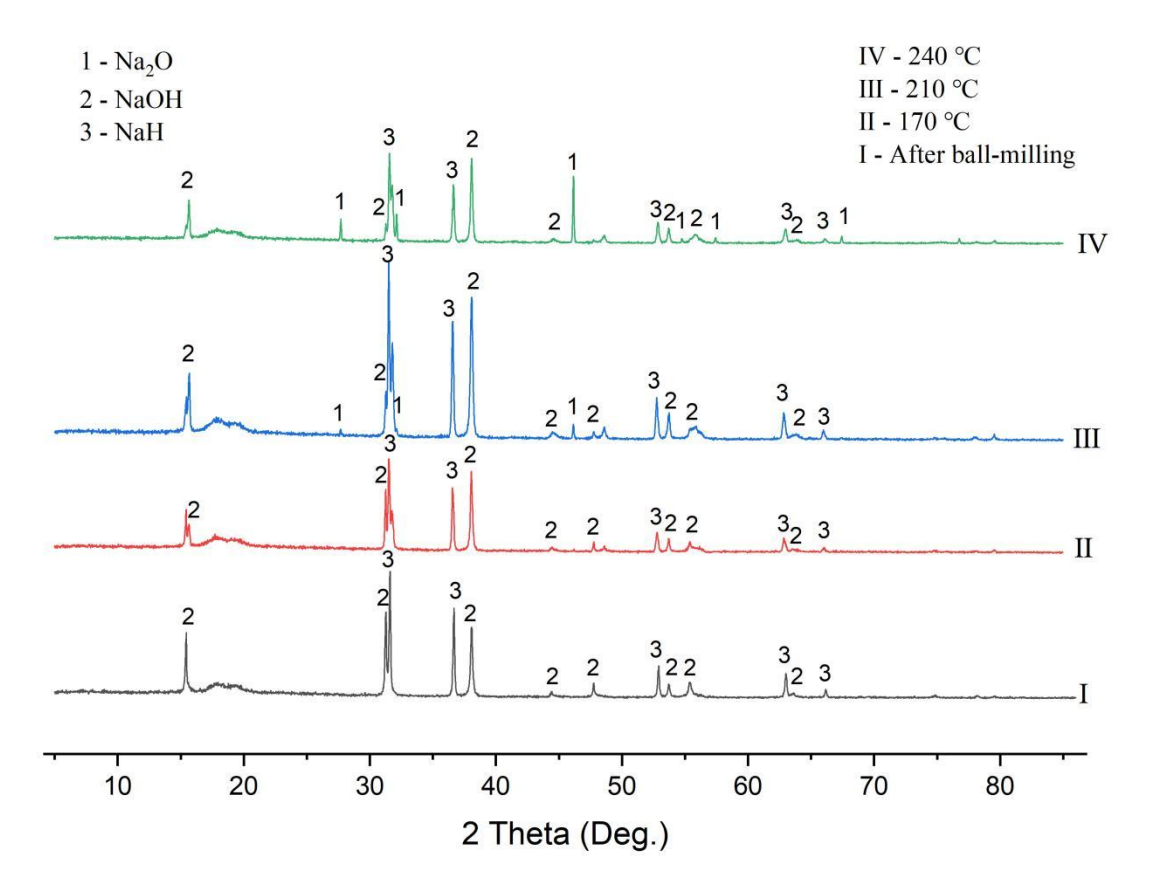


Figure 3-12: PXD patterns of ball-milled NaOH-NaH before (I) and after heating to 170 (II), 210 (III), 240 (IV) °C under flowing Ar(g) (and cooling), respectively. (1 represent Na₂O; 2 represent NaOH; 3 represent NaH)

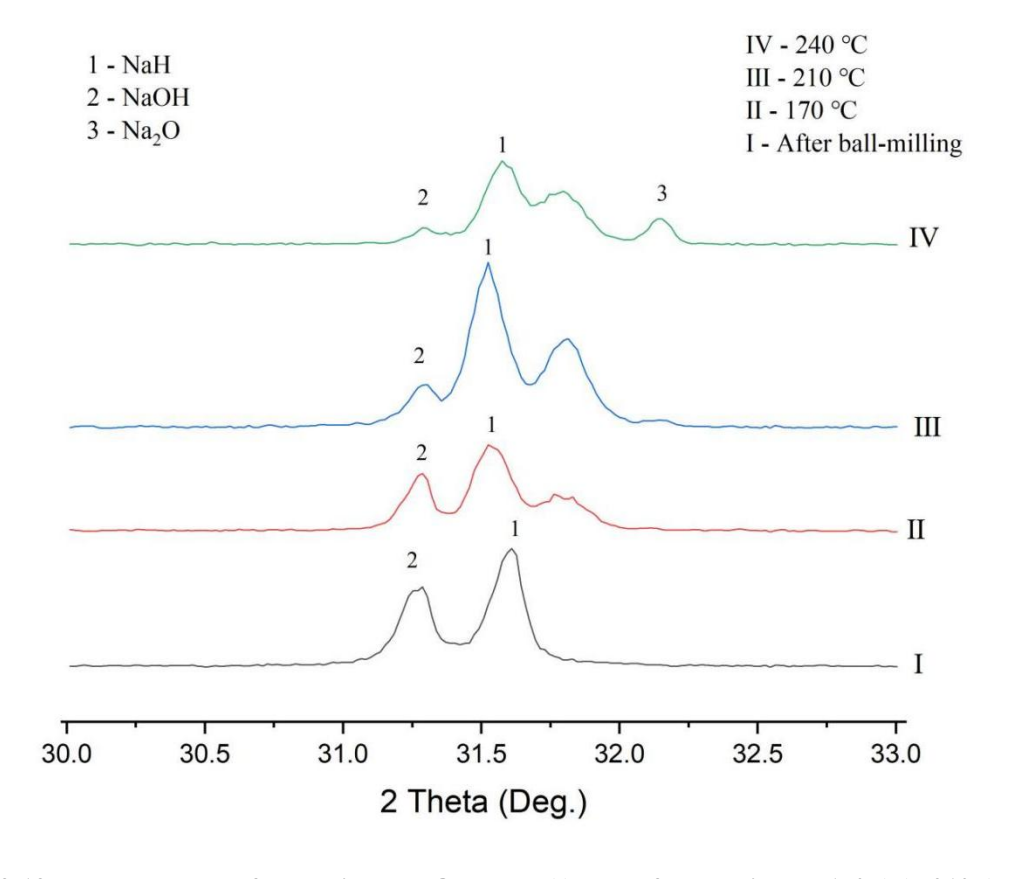


Figure 3-13: PXD patterns of ball-milled NaOH-NaH (I) and after heating to 170 (II), 210 (III), 240 (IV) $^{\circ}$ C at 20 30-33 $^{\circ}$ under flowing Ar(g) (and cooling), respectively. (1 represent NaH; 2 represent NaOH; 3 represent Na₂O)

3.3.3 Different factors that affect the dehydrogenation

3.3.3.1 Milling Time

Figures 3-14 and 3-15 show the thermal behaviour of ball-milled and "hand-mixed" (ground with a pestle and mortar; 20 mins) NaOH-NaH. From the Figure 3-14(b), it can be seen that the "hand-mixed" NaOH-NaH does not show an endothermic DTA peak at *ca*. 175 °C. Compared to the ball-milled NaOH-NaH sample, the "hand-mixed" NaOH-NaH exhibits higher initial hydrogen release temperatures (191 °C vs. 208 °C) and peak temperatures of the dehydrogenation reaction (345 °C vs. 350 °C) according to the MS data. Therefore, ball milling the starting materials results in a better hydrogen release performance compared to hand-mixing in the NaOH-NaH system.

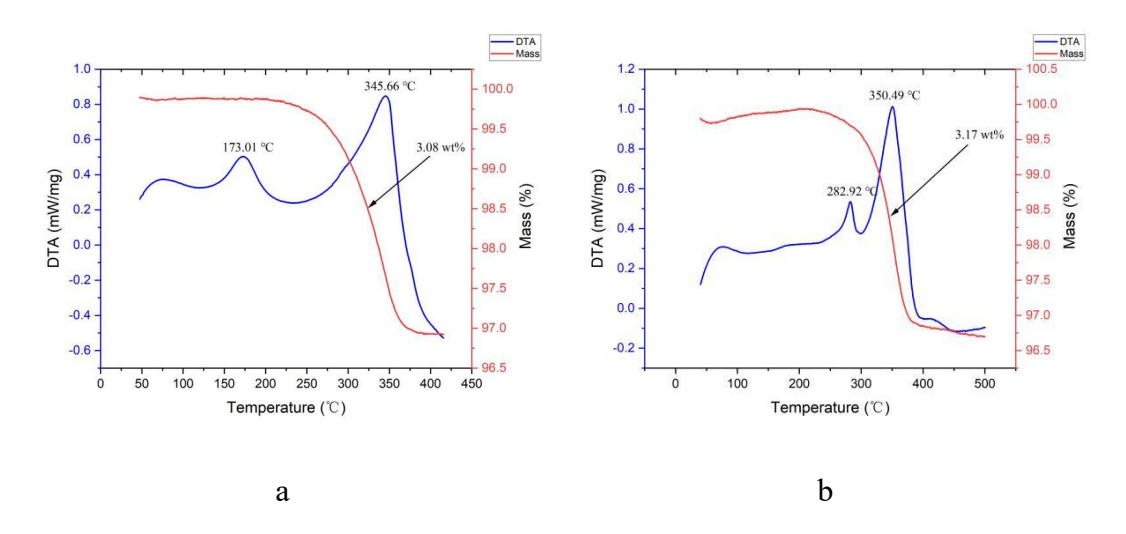


Figure 3-14:TG(red) and DTA(blue) profiles for (a) ball-milled (b) "hand mixed" NaOH-NaH on heating from 35-420(500) °C at 5 °C min⁻¹ under flowing Ar(g).

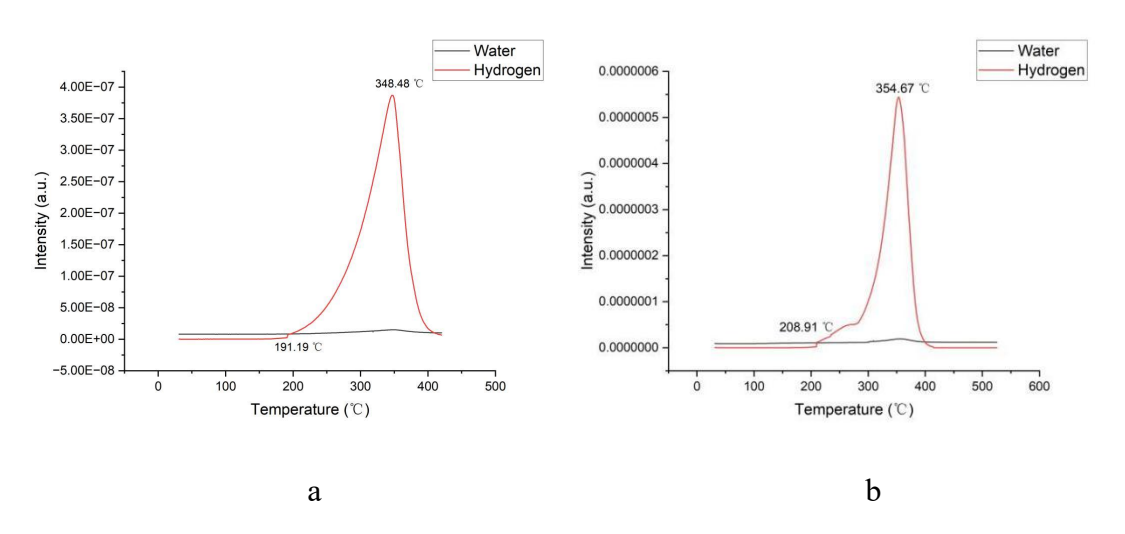


Figure 3-15: Mass spectrometry output for water (m/z = 18; black) and hydrogen (m/z = 2; red) as a function of temperature for (a) ball-miled (b) hand mixed NaOH-NaH on heating from 35-420(500) $^{\circ}$ C at 5 $^{\circ}$ C min⁻¹.

The above experiments having established that milling is a beneficial process, the next objective is to see how these milling conditions, such as milling time, molar ratio and rotation speed, makes a difference to the progress of the reaction.

From Table 3-2 and Figure 3-16, the mass loss of hydrogen and the DTA peak 1 (173 °C) of (intermediate) ternary (hydride-hydroxide) phase for different milling time samples are close to each other. However, the peak temperature of the dehydrogenation reaction significantly decreases by 10 °C to 348 °C when the NaH-NaOH sample is ball-milled for 4 hours. From the PXD patterns of the milled samples (Figure 3-17), it can be seen that NaOH phase shows a distinct peak at in the NaH-NaOH sample after 1 hour of ball milling. As the ball milling time increases, the relative intensity of the NaOH peak gradually decreases. This is also reflected in Figure 3-16, where the DTA curve in figure 3-16(a) a shows that between 359 °C and 400 °C, the slope is not a smooth line; there is a slight change in slope around 380 °C. According to previous Figure 3-7, the peak temperature of NaH is also close to 380 °C. This suggests that a small amount of NaH may be reacting alone. Therefore, ball milling for just 1 hour is insufficient for a complete mixing of NaH and NaOH; 2 hours of ball milling is needed at least.

Table 3-2: Reaction condition, peak temperature and weight loss of NaOH-NaH samples ball milled for different durations.

Sample	Rotation	Milling	molar	ratio	DTA Peak		Total
numbers	speed /	time / h	NaOH:NaH		temperature /°C		mass loss
	rpm						/ wt.%
1	400	1	1:1.1		174.50	359.43	2.93
2	400	2	1:1.1		172.86	358.81	2.89
3	400	4	1:1.1		171.43	348.01	2.81

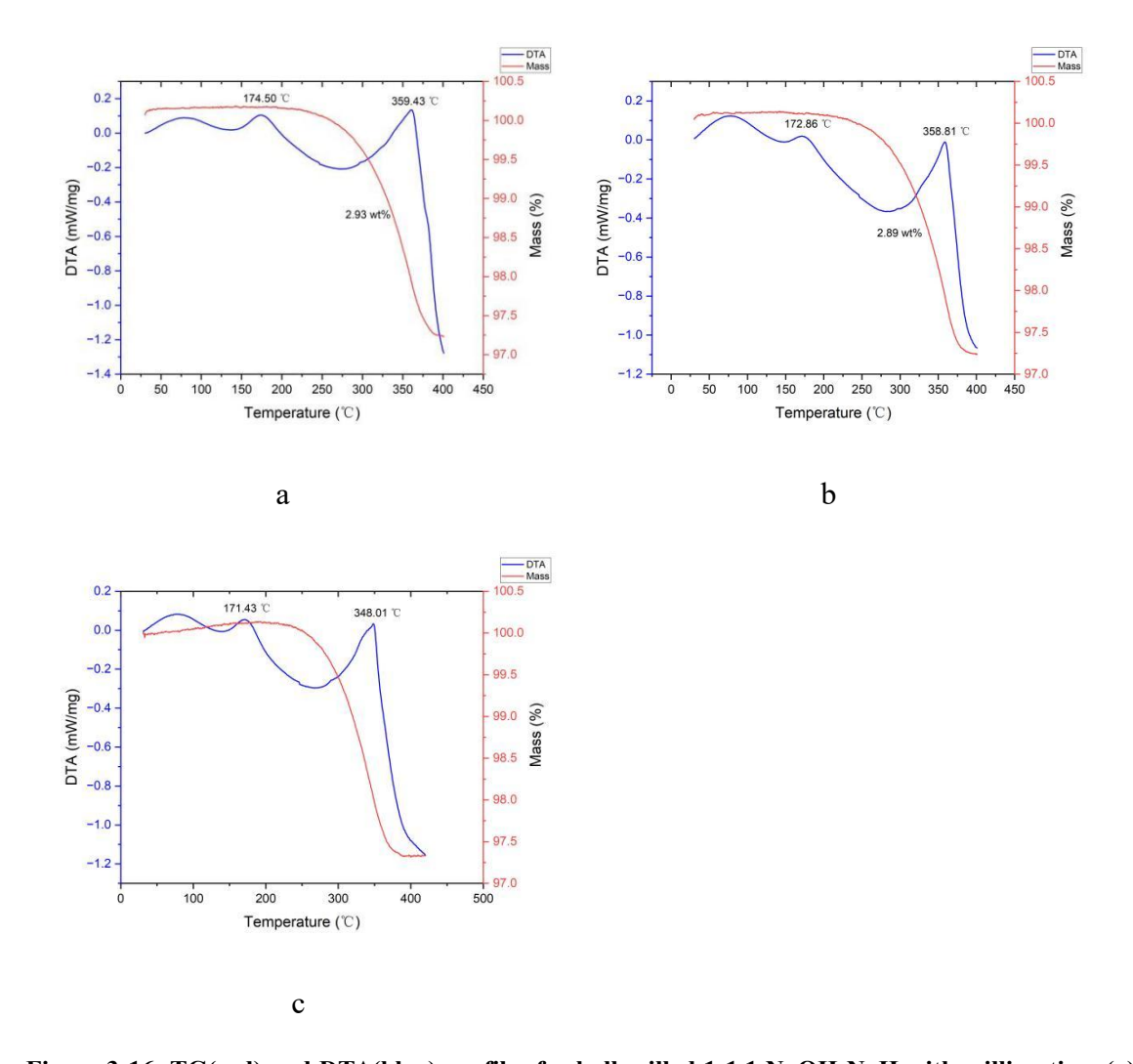


Figure 3-16: TG(red) and DTA(blue) profiles for ball-milled 1:1.1 NaOH:NaH with milling time (a) 1h (b) 2h (c) 4h on heating 35-400 °C at 5 °C min⁻¹ under flowing Ar(g).

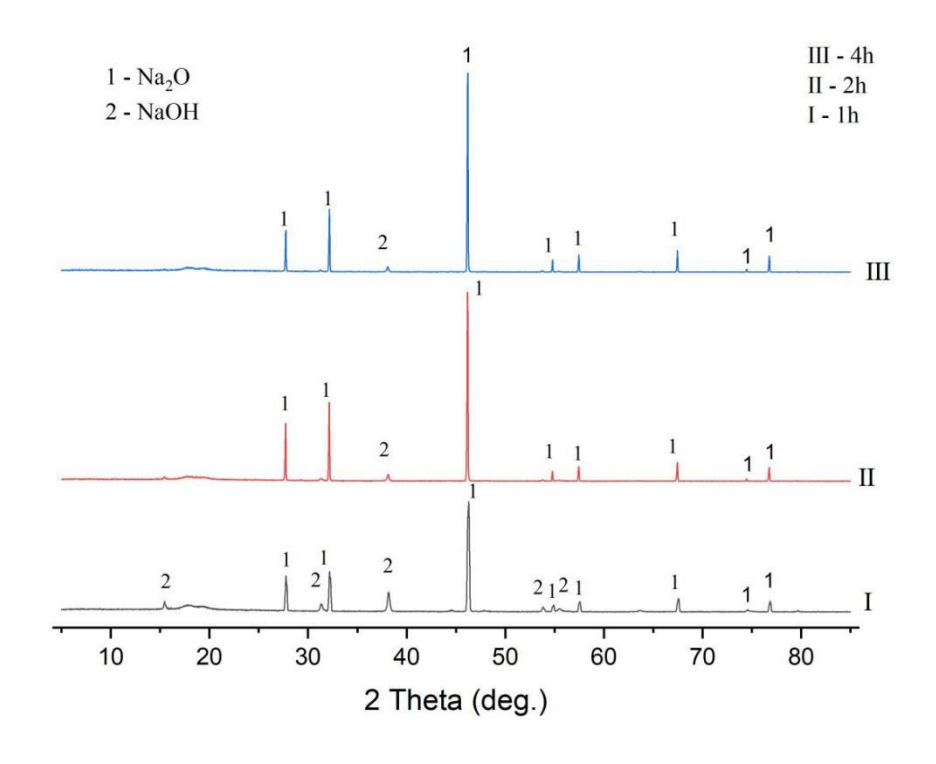


Figure 3-17: PXD patterns of 1:1.1 NaOH:NaH with varying milling time(1h, I; 2h, II; 4h, III) after

3.3.3.2 Molar Ratio

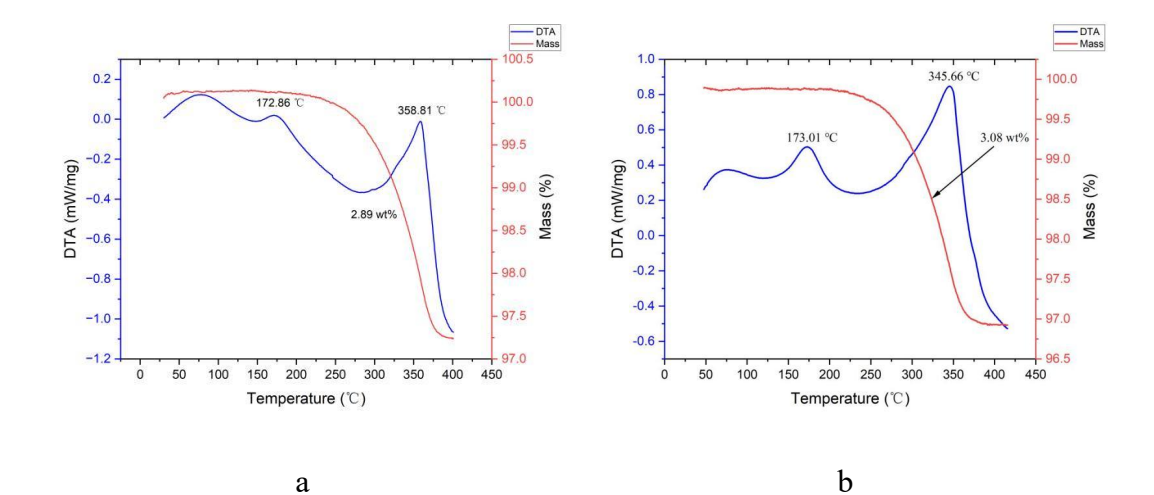
The main purpose of this section is to investigate the effect of the molar ratio of NaOH:NaH on the thermal behaviours of the dehydrogenation of the NaOH–NaH system. It also aims to examine whether adding more NaH can improve the reaction. From Table 3-3, it can be seen that samples with different molar ratios of NaOH:NaH (from 1:1.1 -1:1.25) have essentially the first DTA peak has a maximum at approx the same temperature. However, according to Figure 3-18, the DTA peak temperatures for dehydrogenation are different. The sample with a NaOH:NaH molar ratio of 1:1.15 has the lowest peak temperature. When the NaOH-NaH mole ratio reaches 1:1.2, a second DTA peak appears in the dehydrogenation temperature region, which is close to 380 °C; similar to the decomposition temperature of NaH according to the previous Figure 3-7. This indicates that at this point, the molar amount of NaH is greater than that of NaOH. Because only when NaH is in excess of NaOH can the remaining NaH potentially undergo a separate reaction after fully reacting with NaOH. Between 1:1.1-1:1.15, and from 1:1.2 to 1:1.25, the DTA peak associated with Na-H-OH dehydrogenation decreases in temperature as molar ratio increase. However, from the molar ratio of 1:1.15 to 1:1.2, the peak temperature for dehydrogenation increases. The only possible reason for this is that the excess NaH affects the interaction between protic hydrogen (H^{δ^+}) and hydridic hydrogen (H^{δ}) . Since the decomposition reaction of NaH is endothermic and begins at 325 °C, as shown in 3-7, between 325-360 °C, two reactions may occur simultaneously. Interference may occur during the thermal decomposition of NaH and the dehydrogenation reaction of NaH_{1-x}(OH)_x. Therefore, more energy is required to overcome the energy barrier. As a result, the peak temperature of dehydrogenation will also increase accordingly. In addition, the mass loss of hydrogen remains a critical indicator. When the molar ratio of NaOH:NaH reaches 1:1.15 and 1:1.25, the mass loss (3.08 wt.%) is nearly the ideal value (3.12 wt.%). However, in the case of 1:1.25 NaOH:NaH, part of the hydrogen mass loss originates from the reaction of NaH alone. In conclusion, these data suggest that the most suitable mole ratio for NaH (90%) in this experiment is ca. 1.15.

From PXD patterns in Figure 3-19, it can be seen that when the molar ratio of NaH:NaOH reaches 1.25:1, a peak for Na at *ca.* 28° after dehydrogenation is observed. According to the ICSD database, Na peak at 28° is the most obvious peak.⁷ However, the only strange point is that the NaOH peak at ca. 15°, 31° and 38° shown in the Figure 3-19 remains small and present regardless of the molar ratio. A possible explanation is that despite the use of

the air-sensitive sample holder, the sample has come into contact with a low concentration of water (air), and Na₂O, being unstable in air, reacts with moisture to generate a small amount of NaOH. Although the phase of NaOH is shown in the PXD figure, its intensity is much stronger than that of Na₂O phase. Moreover, the additional NaOH enhances the intensity of its phase, as illustrated in Figure 3-17. Therefore, this does not impact the final conclusion.

Table 3-3: Reaction conditions, DTA peak temperatures and weight losses of the NaOH-NaH samples with varying molar ratios, NaOH:NaH.

Samples	Rotation	Milling	NaOH: NaH	DTA peak		Mass
number	speed / rpm	time / h	molar ratio	temperatures /°C		loss /
						wt.%
4	400	2	1: 1.1	172.86	358.81	2.89
5	400	2	1:1.15	173.01	345.66	3.08
6	400	2	1: 1.2	172.30	358.31	3.00
					377.56	
7	400	2	1: 1.25	172.06	354.51	3.08
					376.71	



97

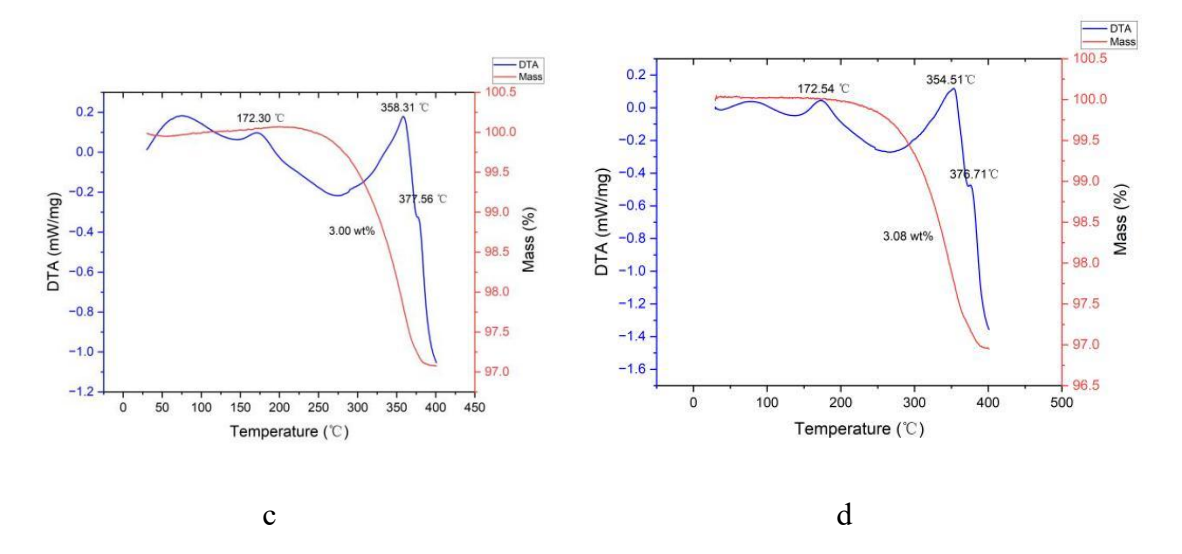


Figure 3-18: TG(red) and DTA(blue) profiles for ball-milled NaOH-NaH (2h, 400rpm) with the different molar ratio of NaOH:NaH (a) 1:1.1(b) 1:1.15 (c) 1:1.20 (d) 1:1.25 on heating from 35-400 °C at 5 °C min-1 under flowing Ar(g).

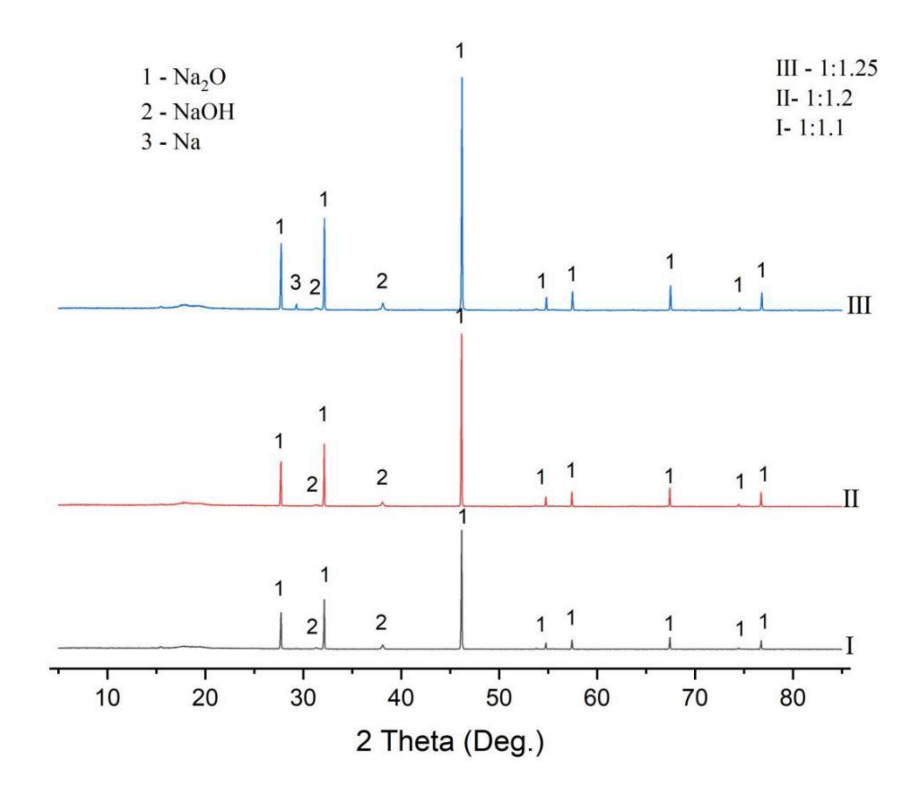


Figure 3-19: PXD patterns of ball-milled NaOH:NaH (2h, 400rpm) with varying molar ratio of NaOH:NaH (1:1.1, I; 1:1.2, II;1:1.25 III) after heating to 400 °C under flowing Ar(g). (1 represent Na₂O; 2 represent NaOH; 3 represent Na)

3.3.3.3 Rotation Speed

The main purpose of this chapter is to investigate the effect of rotation speed on the thermal behaviour of dehydrogenation of NaOH-NaH. From Figure 3-20 and Table 3-4, it can be seen that for the NaH-NaOH samples milled for 2 hours, samples milled at 300 rpm or 400 rpm have similar DTA profiles and peak temperatures and similar mass profiles and

total weight losses. A lower rotation speed may lead to the same effect as the samples milled for 1 hour, as shown in Table 3-4, where cannot achieve complete mixing.

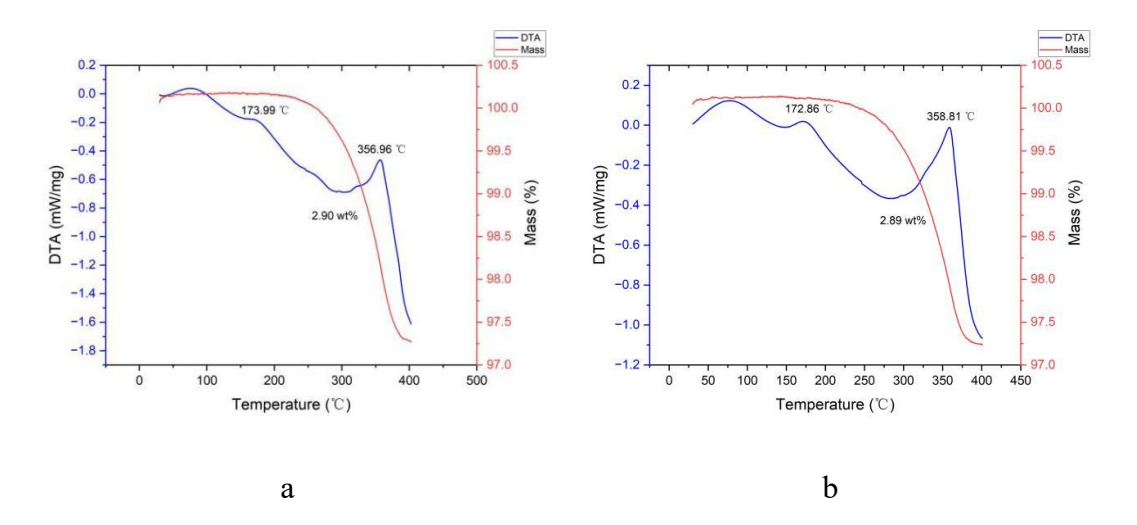


Figure 3-20: TG(red) and DTA(blue) profiles for ball-milled 1:1.1 NaOH:NaH (2h) with the varing rotation speed (a) 300 rpm (b) 400 rpm on heating from 35-400 °C at 5 °C min⁻¹ under flowing Ar(g).

Table 3-4: Reaction condition, peak temperature and weight loss of the NaOH-NaH sample with the varying mole ratio of NaOH: NaH.

Samples	Rotation	Milling	NaOH: NaH	DTA peak		Mass
number	speed / rpm	time / h	molar ratio	temperatures /°C		loss /
						wt.%
8	300	2	1: 1.1	173.99	356.96	2.90
9	400	2	1: 1.1	172.86	358.81	2.89

3.3.4 Activation Energy

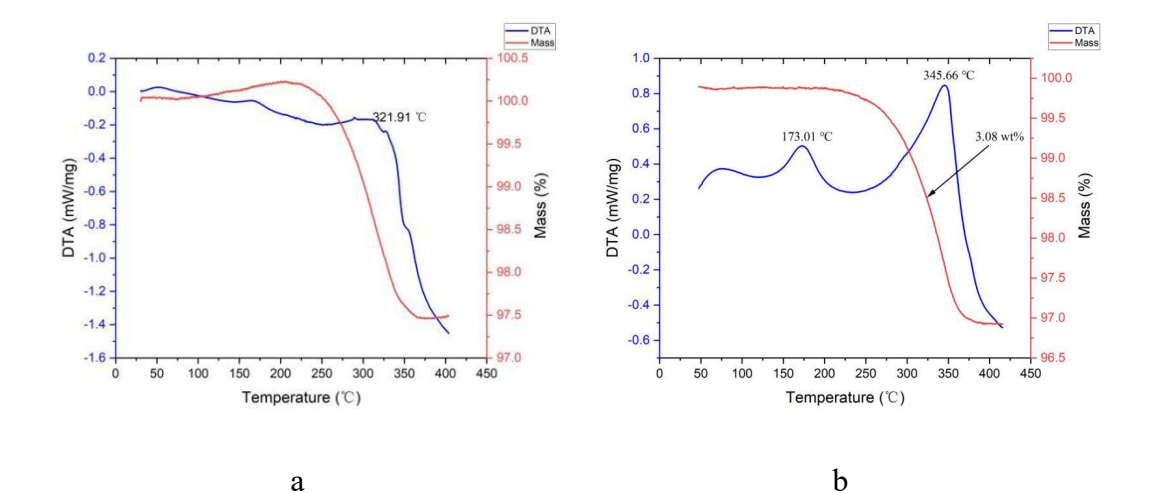
Activation energy (E_a) is the minimum amount of energy needed to overcome the energy barrier and initiate a chemical reaction.¹⁴ In simple terms, activation energy is the energy needed for reacting molecules to collide with sufficient force to undergo a chemical change. The mathematical equation is shown below.

$$In(\beta/T_m^2) = - E_a/RT_m \qquad Eq. 3$$

 β is the heating rate. T_m is the peak temperature (K). E_a is the activation energy. R=8.314 J·K⁻¹·mol⁻¹. A straight line is obtained by plotting $In(\beta/T_m^2)$ on the y-axis against $1/T_m$ on the x-axis. Then $E_a=-Rm$. m is the slope of the straight line. Heating rates of 2, 5, 10 and 20 °C min⁻¹ were employed in the experiments described here.

According to Figures 3-21 and 3-22, as expected, we can observe that the DTA peak

temperatures in the NaH-NaOH system vary at different heating rates. At a heating rate of 2 °C min⁻¹ in Figure 3-21(a), the peaks appear broad and weak in intensity. To determine a precise and accurate peak temperature for dehydrogenation under such conditions, it is necessary to analyse the MS data. However, the temperature of MS cannot be used directly. Because the peak temperature of MS is higher than that of TG-DTA and has hysteresis. As can be seen from Figure 3-22 of MS figure, its main peak is 322.84°C, which just corresponds to 321.91°C in the TG-DTA figure. Based on this, the NaH-NaOH peak temperatures (T_m) are determined to be 321.91 °C, 345.66 °C, 372.06 °C, and 413.59 °C. According to the above formula 3, four points can be drawn on the graph and a trend line can be drawn at the same time. The slope of the trend line multiplied by the constant R value can be obtained as the activation energy. After calculation, the activation energy for the dehydrogenation of $NaH_{1-x}(OH)_x$ is found to be 75.85 kJ mol⁻¹. The article reports that the activation energy for the thermal decomposition of NaH (95 at.%) is 115.5 kJ mol⁻¹.15 The activation energy for the dehydrogenation of NaOH-NaH ball-milled at 200 rpm for 1 hour (with a 10-minute run and 5-minute pause; ball-to-powder ratio of 20:1) is 114.8 kJ mol⁻¹. In comparison, under higher ball-milling conditions (400 rpm, 2 hours; 5-minute run and 5-minute pause; ball-to-powder ratio of 80:1) and a more suitable molar ratio of NaH:NaOH (1.15:1), the activation energy for the dehydrogenation of NaH_{1-x}(OH)_x is significantly reduced because the improved ball-milling condition can make the NaOH-NaH have fully reaction.



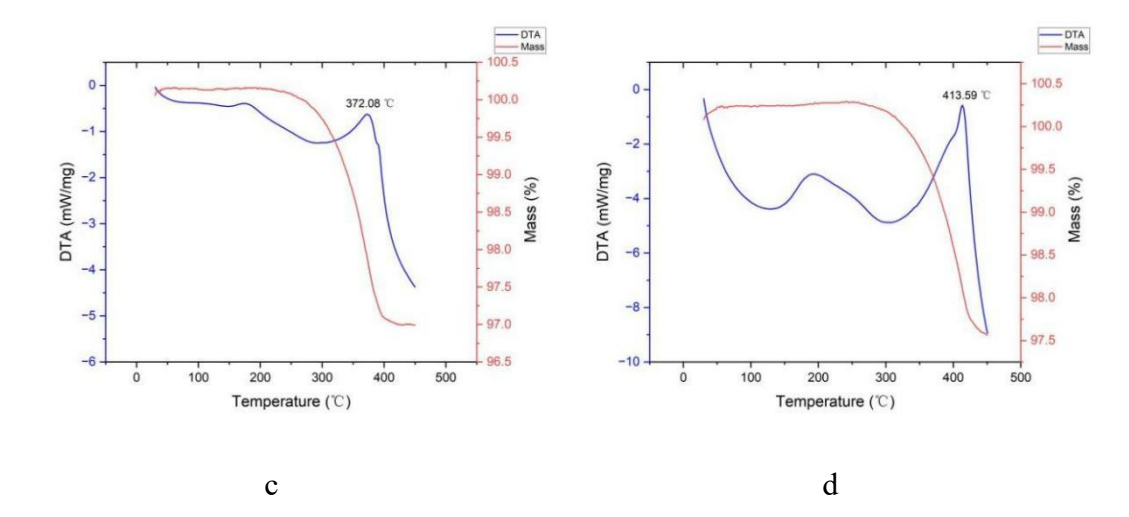


Figure 3-21: TG(red) and DTA(blue) profiles for ball-milled 1:1.15 NaOH:NaH (2h, 400rpm) on heating from 35-400 °C at different heating rate (a) 2 °C min⁻¹(b) 5 °C min⁻¹(c) 10 °C min⁻¹ (d) 20 °C min⁻¹ under flowing Ar(g).

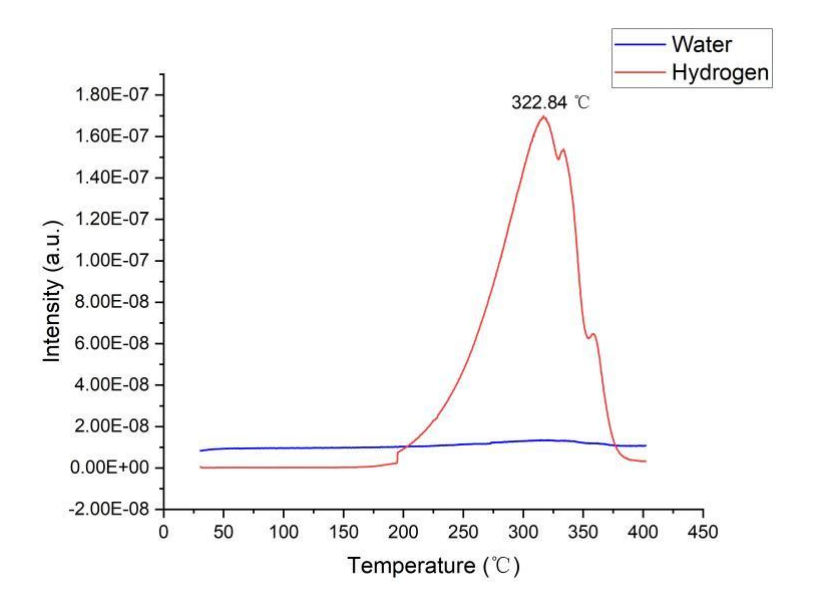


Figure 3-22: Mass spectrometry output for water (m/z = 18; black) and hydrogen (m/z = 2;red) as a function of temperature for a ball-milled 1:1.15 NaOH:NaH (2h, 400rpm) on heating from 35-400 °C at 2 °C min⁻¹ under flowing Ar gas.

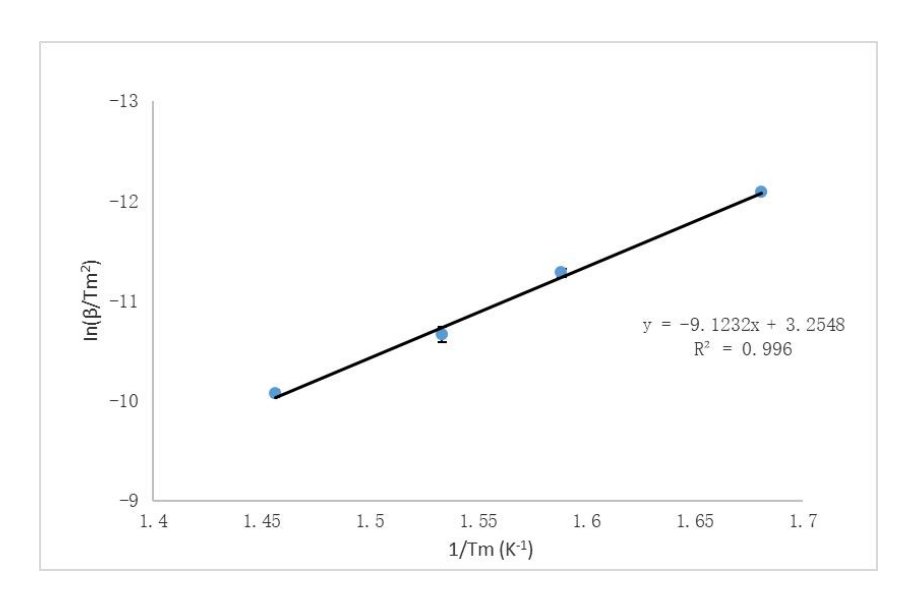


Figure 3-23: Kissinger plots for dehydrogenation of ball-milled 1:1.15 NaH:NaOH (2h, 400r) on heating from 35-400 °C at heating rate 2, 5, 10, 20 °C min⁻¹ under flowing Ar(g). Ea = 75.85 ± 3.41 kJ mol⁻¹.

3.3.5 Additives and Catalysts

3.3.5.1 Introduction

Adding catalysts and other additives can significantly enhance the hydrogen storage performance of some complex hydrides. The purpose of this chapter is to understand the roles of different catalysts based on previous studies. At the same time, experiments will be conducted to explore the effects of different catalysts/additives in the Na-H-OH system.

3.3.5.2 Graphene

Graphene is a material composed of a single layer of carbon atoms arranged in a two-dimensional honeycomb lattice, which gives it an extremely high specific surface area (approximately 2630 m² g⁻¹) and exceptional physical and chemical properties.¹⁷ These unique characteristics make graphene highly promising in a variety of fields, particularly in hydrogen storage. One of the key challenges in hydrogen storage is the efficient adsorption and release of hydrogen, and the high surface area of graphene provides abundant space for hydrogen adsorption, significantly increasing its hydrogen storage capacity.^{18,19} Additionally, the excellent electrical and thermal conductivity of graphene enables effective thermal management during hydrogen storage, preventing difficulties in hydrogen release caused by heat effects during the adsorption process.¹⁹

To further enhance graphene's hydrogen adsorption capacity, researchers have optimised its structure through chemical modification or doping with other elements.^{20,21,22} For example, doping with nitrogen and boron can adjust graphene's electronic structure,

improve its hydrogen adsorption ability, and effectively lower the temperature at which hydrogen is released, thus increasing the efficiency of the hydrogen storage process. ^{23,24,25} These modifications not only improve graphene's hydrogen storage capacity but also enable it to release hydrogen at lower temperatures, enhancing the operability of the storage process. According to Chen *et al*'s article, it investigates the hydrogen storage capabilities of twin T-graphene (TTG) doped with nitrogen and boron. The study reveals that pristine TTG can store hydrogen with a capacity of 7.69 wt.%, while N-doped and B-doped TTG achieve capacities of 9.88 wt.% and 10.06 wt.%, respectively. These values exceed the U.S. Department of Energy's target of 6.5 wt.%. The desorption temperature is predicted to be -32.15 °C, indicating that these materials can serve as reversible hydrogen storage media.²³

In addition to its adsorption properties, graphene's lightweight and high-strength characteristics also provide unique advantages for hydrogen storage materials.²⁶ Compared to traditional hydrogen storage materials, graphene has a lower density and stronger mechanical properties, making it highly promising for the development of efficient and portable hydrogen storage devices.²⁷ For example, Ti-doped porous graphene achieved a hydrogen storage capacity of 6.5 wt.% at room temperature (27 °C), with a volumetric capacity of 55 g H₂/L. Ca-doped graphene achieved a hydrogen storage capacity of 8.38 wt.% at room temperature (27 °C). ^{28,29} Furthermore, graphene can be combined with other materials, such as metal-organic frameworks or carbon nanotubes, to further enhance its hydrogen storage capacity and release rate, enabling more efficient hydrogen storage under high-pressure or low-temperature conditions. 30,31,32,33 For instance, according to Gangu et al's article, the hydrogen release temperature of LiBH₄ combined with 3D fluorinated graphene is reduced to 204 °C. At room temperature, the hydrogen storage capacity of Graphene Oxide-Multiwalled Carbon Nanotubes composite (GO-MWCNTs) can reach 2.6 wt.%, while the thermally reduced rGO-MWCNTs have a storage capacity of 2.1 wt.% under the same conditions.³⁴

Overall, with its ultra-high specific surface area, excellent electrical conductivity, and thermal conductivity, graphene shows immense potential in the field of hydrogen storage. By continually optimizing its structure and surface properties, graphene is expected to become an important hydrogen storage material in the future hydrogen energy industry, driving the development and progress of hydrogen energy technologies.

This chapter primarily focus on reduced graphene oxide (rGO). There are differences in structure and properties between graphene and rGO. rGO is a material obtained by chemically reducing graphene oxide (GO), and its surface contains a small amount of oxygen-containing functional groups. These functional groups enhance its chemical

reactivity, enabling it to react with a variety of molecules. This makes rGO suitable for applications that require high chemical reactivity, such as hydrogen storage. The preparation process of rGO is relatively simple and cost-effective, making it suitable for large-scale production. These active sites on rGO can interact more strongly with hydrogen molecules, thereby improving the efficiency of hydrogen adsorption and desorption. For example, in experiments, the hydrogen adsorption capacity of rGO can reach 1.34 wt.%, a value higher than that of graphene, which is only 0.1 wt.%. The oxygen-containing functional groups on the surface of rGO can serve as active sites for catalysts, promoting the adsorption and desorption of hydrogen. These functional groups can adsorb hydrogen molecules through chemical bonding or van der Waals forces, thus enhancing the efficiency of hydrogen adsorption. For instance, in electrochemical hydrogen storage, rGO exhibits higher hydrogen adsorption capacity and better cycling stability. In contrast, graphene lacks these active sites on its surface, and hydrogen adsorption mainly relies on physical adsorption, which is relatively weak. Therefore, in terms of catalytic performance, graphene is not as effective as rGO.

In addition to its catalytic role in hydrogen storage, rGO also plays a catalytic role in the dehydrogenation of MgH₂.³⁹ For example, Yao et al. prepared a composite of nickel nanoparticles uniformly dispersed on reduced graphene oxide (Ni@rGO) via mechanical ball milling and incorporated it into MgH₂.⁴⁰ The results showed that the Ni@rGO composite significantly reduced the initial hydrogen desorption temperature of MgH₂ from 251 °C to 190 °C. Moreover, the composite could absorb 5.0 wt.% of hydrogen within 20 minutes at 100 °C and desorb 6.1 wt.% of hydrogen within 15 minutes at 300 °C. It was also found that when the nickel loading was 45 wt.%, rGO could prevent the reaction between nickel and magnesium, thereby maintaining better catalytic performance. The synergistic effect of in situ formed Mg₂Ni/Mg₂NiH₄ and rGO achieved efficient hydrogen storage catalysis, with activation energies for hydrogenation and dehydrogenation of 47.6 \pm 3.4 kJ mol⁻¹ and 117.8 \pm 3.4 kJ mol⁻¹, respectively, lower than those reported for other MgH₂ systems.³⁹

Similarly, Ji et al. synthesized a composite of iron-nickel alloy supported on reduced graphene oxide (FeNi/rGO) via hydrothermal and carbonization methods and introduced it into MgH₂ powder.⁴¹ The results showed that 5 wt.% FeNi/rGO-modified MgH₂ began to release hydrogen at 230 °C and released 6.5 wt.% of hydrogen within 10 minutes at 300 °C, significantly better than pure MgH₂ (355-410 °C). At 125 °C, the composite absorbed 5.4 wt.% of hydrogen within 20 minutes, while pure MgH₂ required a higher temperature to begin hydrogen absorption. After 50 cycles, the hydrogen storage capacity of MgH₂ + 5 wt.% FeNi/rGO remained at 6.9 wt.% without a decline in kinetic performance. FeNi/rGO

significantly reduced the reaction energy barrier of MgH_2 , with activation energies for dehydrogenation and hydrogenation of 93.6 ± 7.3 kJ mol⁻¹ and 42.3 ± 3.3 kJ mol⁻¹, respectively, much lower than those of pure MgH_2 . The synergistic effect of FeNi nanoparticles and rGO achieved efficient hydrogen storage catalysis and significantly improved cycling stability. Therefore, rGO has a catalytic effect in MgH_2 , and its function may also influence the dehydrogenation of NaH-NaOH, potentially promoting the dehydrogenation process.

The PXD figure of the synthesized rGO is shown in Figure 3-24. In Figure 3-24, we observe that rGO exhibits only a board peak because its structure is amorphous. When compared with literature data, the 2θ angle of this peak is found to be similar.⁴² Figure 3-25 illustrates the DTA behaviour at different weight percentages of rGO as an additive. The ball-milling conditions were 2h, 400rpm, ball:powder 80:1, and molar ratio of 1:1.15 NaOH:NaH. When the weight percentage of rGO increases from 0-2 wt.%, the peak temperature for dehydrogenation does not decrease. However, when the weight percentage increases from 2 -10 wt.%, the peak temperature for dehydrogenation begins to decrease significantly. From 10 -20%, the peak temperature for dehydrogenation remains almost unchanged. It does seem to suggest that no further advantage is reached beyond 10 wt.%. However, the effective gravimetric capacity decreases as more rGO is added.

After calculation, the activation energy of the sample with 10 wt.% rGO is approximately 73.06 kJ/mol, while the activation energy of the sample without a catalyst is approximately 75.85 kJ/mol. Hence, although the addition of 10% rGO significantly reduces the peak temperature for dehydrogenation, its effect on the activation energy is relatively minor.

Figure 3-5: Reaction conditions and DTA peak temperatures of the NaOH-NaH samples with varying wt.% rGO.

Sample Number	NaOH: NaH molar ratio	wt.% rGO	Milling condition	Peak temperature/°C
5	1:1.15	0	400rpm, 2h	345.66
11	1:1.15	2	400rpm, 2h	348.22
12	1:1.15	5	400rpm, 2h	342.71
13	1:1.15	10	400rpm, 2h	331.92
14	1:1.15	20	400rpm, 2h	331.45

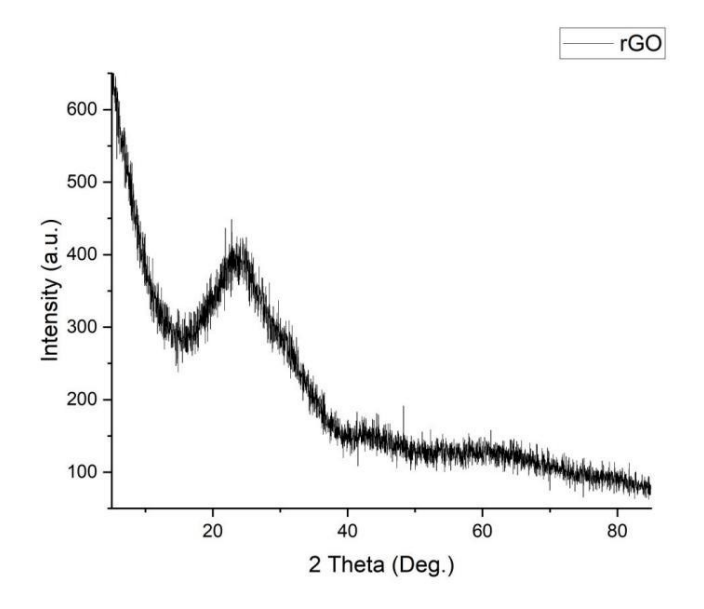


Figure 3-24: PXD pattern of as-synthesis rGO

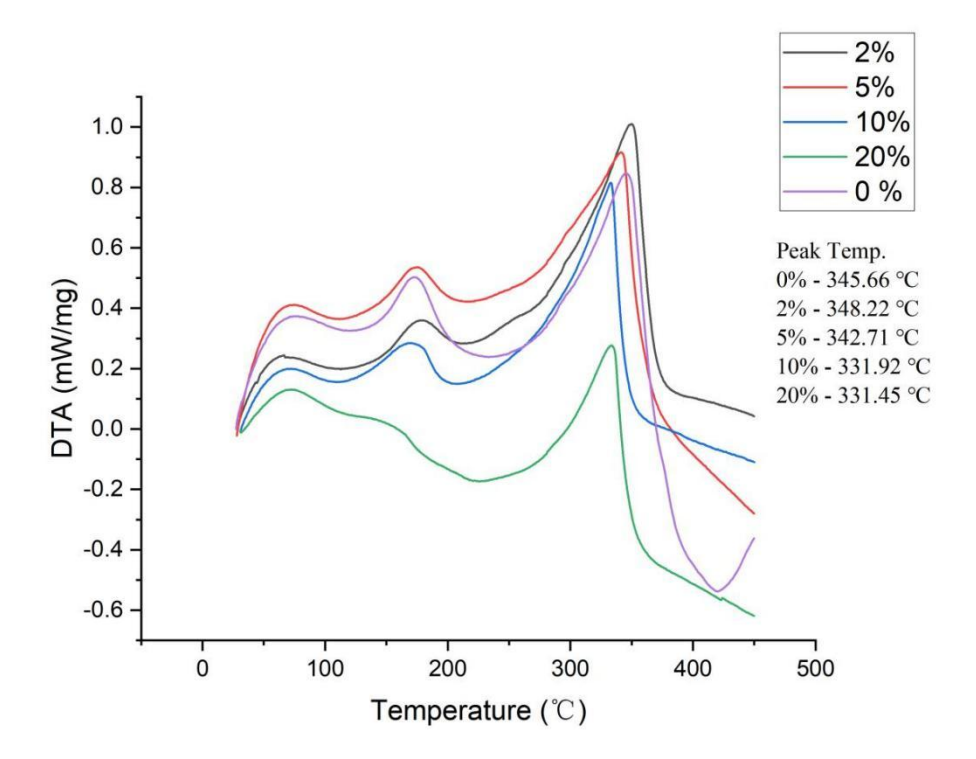


Figure 3-25: DTA profiles for ball-milled 1:1.15 NaOH:NaH (2h, 400rpm) with varying amounts of rGO additives (0 wt.%, purple; 2 wt.% black; 5 wt.%, red; 10 wt.%, blue; 20 wt.%, green) on heating from 35-450 $^{\circ}$ C at 5 $^{\circ}$ C min⁻¹ under flowing Ar(g).

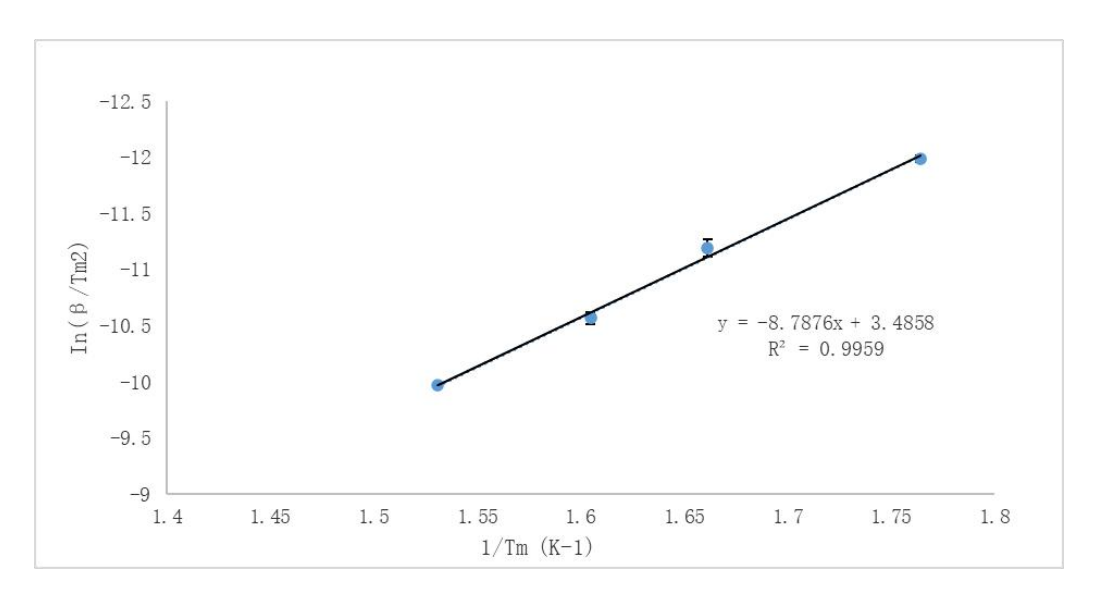


Figure 3-26: Kissinger plots for dehydrogenation of ball-milled 1:1.15 NaH:NaOH (2h, 400r) with 10 wt.% rGO on heating from 35-400 °C at heating rate 2, 5, 10, 20 °C min⁻¹ under flowing Ar(g). Ea = 73.06 ± 3.32 kJ mol⁻¹.

3.3.5.3 Magnesium Silicide

Mg₂Si (magnesium silicide) is an intermetallic compound composed of magnesium and silicon, with a range of exceptional physical and chemical properties, making it highly promising for applications in materials science, energy storage, and electronic devices.⁴³ As a material with high hardness and melting point, Mg₂Si demonstrates excellent electrical and thermal conductivity, while its relatively low density has attracted significant attention for use in aerospace, automotive industries, and lightweight materials research.⁴⁴ In particular, Mg₂Si is favored in thermoelectric materials due to its high thermoelectric performance, enabling efficient conversion of thermal energy into electrical energy, which makes it suitable for thermoelectric power generation devices.⁴⁵ By adjusting the structure of Mg₂Si or doping it with other elements such as Sn to form Mg₂Si_{1-x}Sn_x, researchers have found that its thermoelectric effect can be significantly enhanced, improving thermoelectric conversion efficiency. 46 Additionally, magnesium silicide exhibits good corrosion resistance, maintaining stable performance even in harsh environments, making it durable and reliable for industrial applications. In terms of energy storage, the potential of Mg₂Si as a negative electrode material for lithium-ion batteries is also being recognized, as its large specific capacity and high electrical conductivity help improve battery capacity and cycling stability.⁴⁷ Overall, Mg₂Si, as a versatile material with unique physical and chemical properties, demonstrates enormous potential in various fields such as thermoelectrics, lightweight structural materials, and energy storage, offering significant research and industrial value, especially in enhancing energy conversion efficiency and storage performance.

In the field of hydrogen storage, Mg₂Si has shown considerable potential, mainly due to its excellent chemical stability, high thermal conductivity, and low density. In hydrogen storage technology, the efficient adsorption and release of hydrogen are key challenges, and Mg₂Si, as a promising hydrogen storage material, has become a focus of research. The chemical structure of Mg2Si provides good thermal management during hydrogen adsorption and release, which is critical for improving hydrogen storage efficiency.⁴⁸ Specifically, Mg2Si can chemically react with hydrogen to form hydrides, releasing hydrogen at appropriate temperatures, and this adsorption-release process is essential for the storage and recycling of hydrogen energy.⁴⁹ Furthermore, Mg₂Si's low density and relatively high hydrogen absorption capacity make it a promising candidate for hydrogen storage. By optimizing the microstructure of Mg₂Si and doping it with other elements, researchers can further enhance its hydrogen absorption capacity and release rate, improving the overall performance of hydrogen storage materials.⁵⁰ The corrosion resistance of Mg₂Si is another significant advantage in hydrogen storage applications, as it can maintain stable performance over multiple adsorption and release cycles, which is crucial for long-term use in hydrogen storage devices.⁵¹ Overall, Mg₂Si, with its unique physical and chemical properties, shows great potential in the hydrogen storage field.

According to Fan et al's article, Mg₂Si could be successfully synthesised by MW.^{10,52} During the synthesis of Mg₂Si under microwave irradiation, a plasma was almost immediately formed (within about 2 seconds), initially appearing light purple in colour and then turning green. After the reaction was completed, a fine black powder was obtained. (microwave irradiation) is that the microwave-induced metal The reason for using MW plasma (MIMP) method can complete the reaction in an extremely short time (only 60 seconds), which is much faster than the traditional high-temperature solid-state reaction method (usually requiring more than 10 hours). This rapid reaction kinetics is attributed to the formation of plasma in the microwave field, where the charged particles in the plasma experience enhanced motion under the influence of the 2.45 GHz electromagnetic field, thereby greatly accelerating the reaction rate. From Figure 3-27, it can also be observed that the peak positions of the experimental Mg₂Si are very similar to those of the standard Mg₂Si. Figure 3-27 suggest that the Mg₂Si synthesized by this method is relatively pure and no impurity peak is shown. Moreover, the products synthesized by this method still remain small powder at the end.

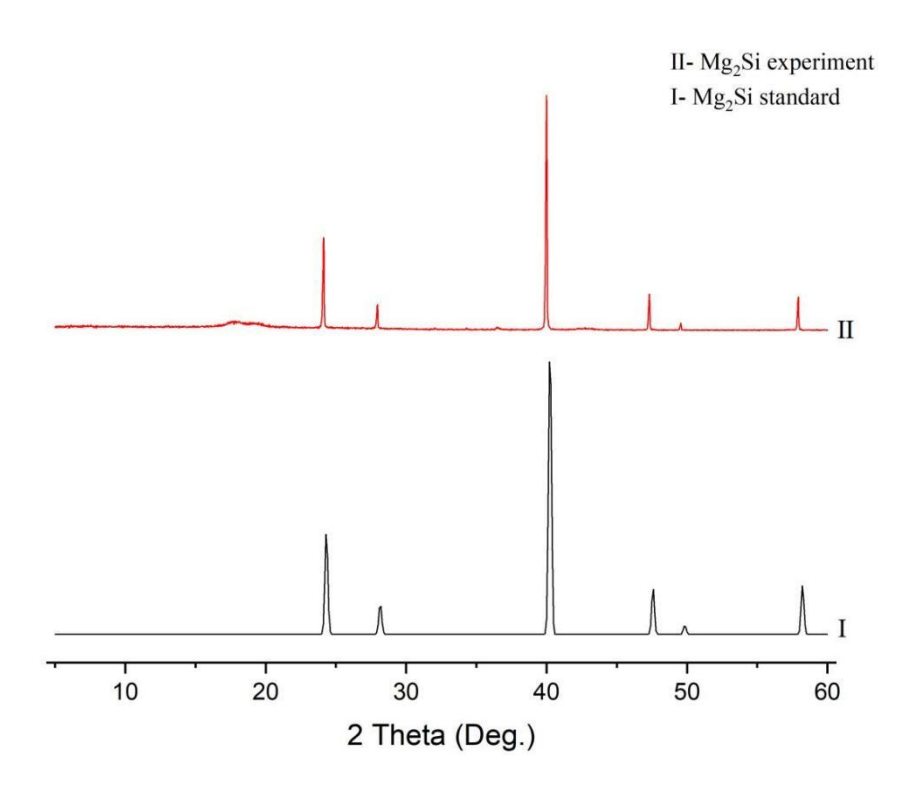


Figure 3-27: PXD patterns of standard (I) and as-synthesised Mg₂Si (II).

Figure 3-28 illustrates the thermal behaviour of Mg₂Si when Mg₂Si is heated to 600 with 10 °C min⁻¹. The figure demonstrates that Mg₂Si exhibits no mass change and undergoes no reactions below 600 °C. Therefore, the reaction of Mg₂Si does not influence the dehydrogenation of the NaOH-NaH system.

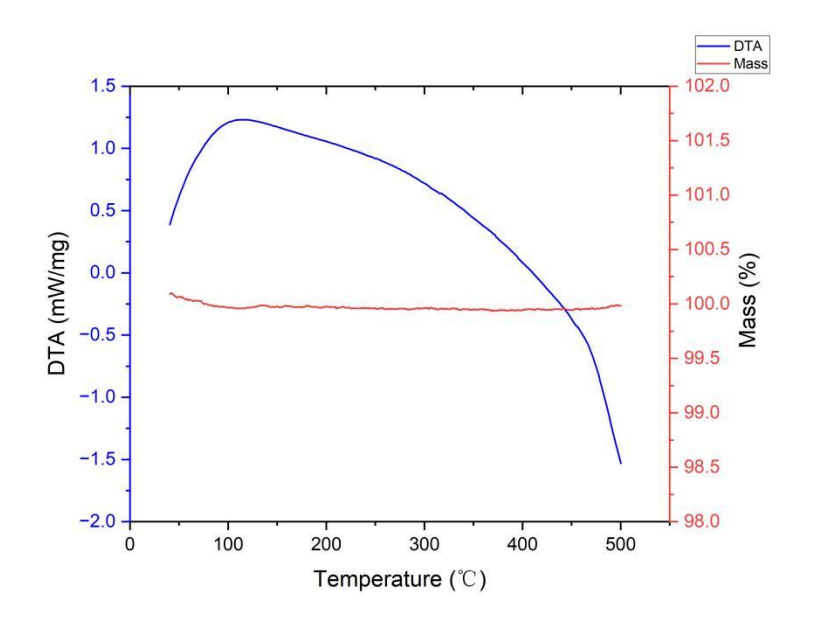


Figure 3-28: TG(red) and DTA(blue) profiles for as-synthesised Mg₂Si on heating from 35-600 °C at 10 °C min⁻¹ under flowing Ar(g).

Figures 3-29 to 3-32 illustrate the thermal performance of 1:1.15 NaOH:NaH with the addition of 5 wt.% and 10 wt.% Mg₂Si, respectively. From Figures 3-29 and 3-31, it can be observed that NaOH-NaH with 5 wt.% Mg₂Si exhibits two peaks between 320 °C -380 °C,

specifically at 322.46 °C and 364.83 °C. However, when the Mg₂Si content is increased to 10 wt.%, three peaks appear between 320 °C - 380 °C. The first peak at 323.60 °C and the third peak at 361.50 °C are very close to the two peaks observed with 5 wt.% Mg₂Si, suggesting that the additional peak between 320 °C - 380 °C is likely due to a reaction between Mg₂Si and NaOH-NaH.

From the MS data in Figures 3-30 and 3-32, it can be seen that the main hydrogen release peak of 5 wt.% Mg₂Si (322.17 °C) and 10 wt.% Mg₂Si (322.78 °C) corresponds to the DTA peak at approximately 322 °C, which is significantly lower than the 346 °C for sample 5 in Figure 3-9. Although it can significantly reduce the peak temperature of dehydrogenation reaction (from 346 °C to 322 °C), the occurrence of reactions involving Mg₂Si is potentially a major drawback of this additive, as it introduces uncertainties in the overall reaction mechanism. In addition, the peak temperature of 10 wt.% Mg₂Si can be seen from the three peak temperatures, indicating that there may be more than one reaction, which may occur together. Moreover, the mass loss of hydrogen is significantly reduced.

Table 3-6: DTA peak temperatures and weight losses of the NaOH-NaH samples with varying wt.% Mg₂Si.

Sample Number	Wt.% Mg ₂ Si	Peak temperature/°C		Mass loss /
				wt.%
15	5	173.30	322.42 364.83	2.83
16	10	172.06	323.60 346.25	2.60
			361.50	
5	0	173.01	345.66	3.08

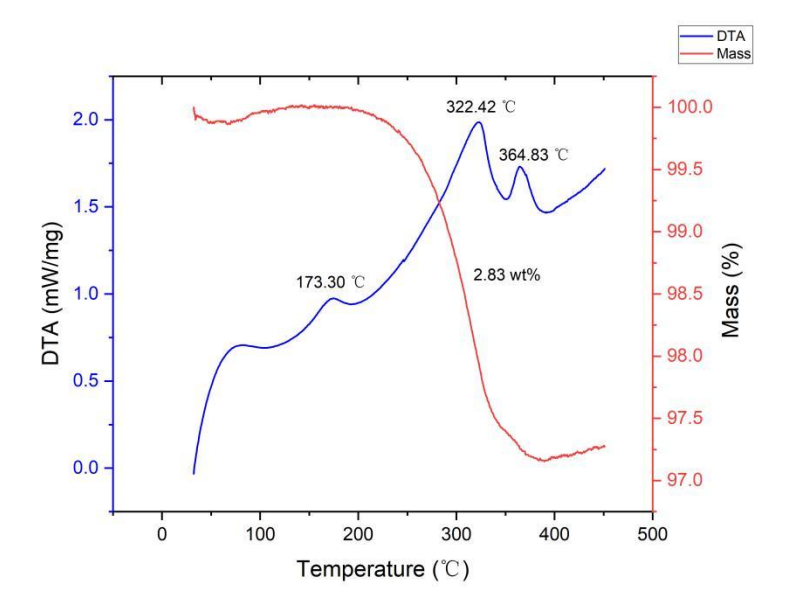


Figure 3-29: TG(red) and DTA(blue) profiles for ball-milled 1:1.15 NaOH:NaH (2h, 400rpm) with 5

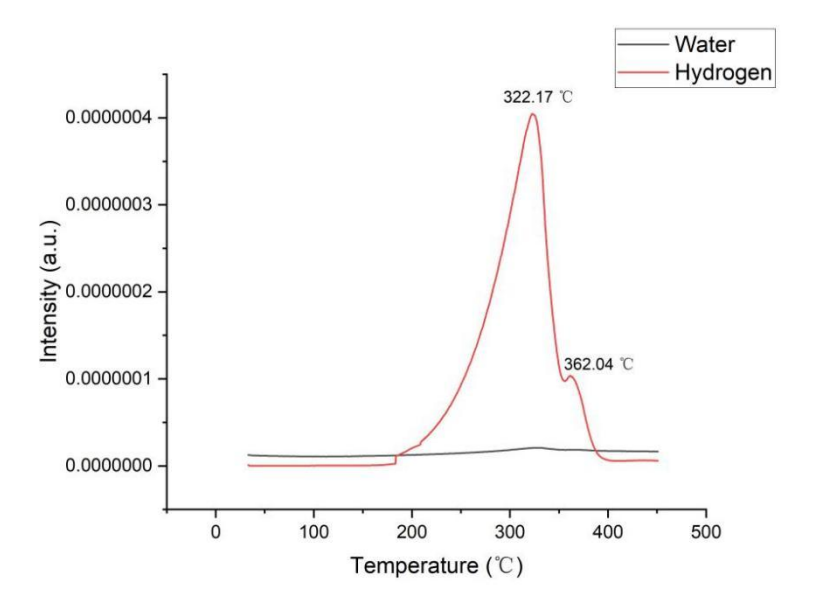


Figure 3-30: Mass spectrometry output for water (m/z = 18; black) and hydrogen (m/z = 2;red) as a function of temperature for ball-milled 1:1.15 NaOH:NaH (2h, 400rpm) with 5 wt.% Mg_2Si on heating from 35-450 °C at 5 °C min⁻¹ under flowing Ar(g).

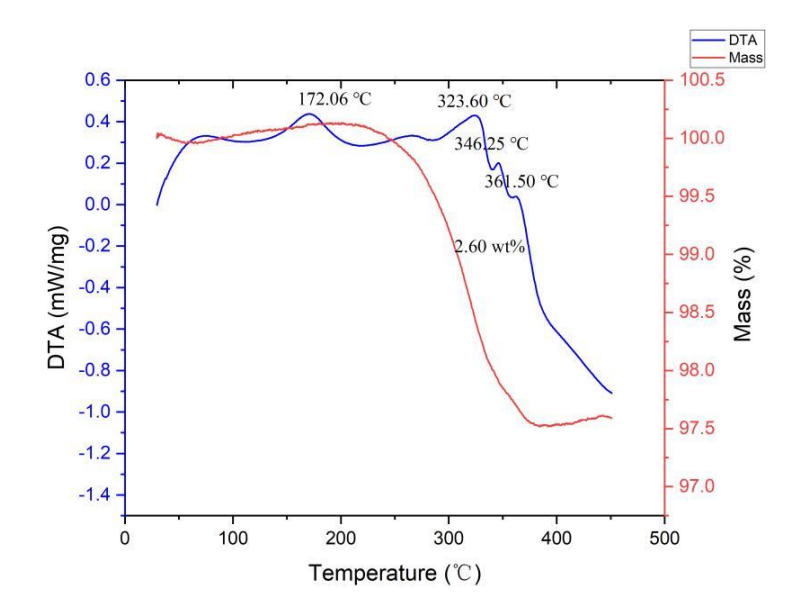


Figure 3-31: TG(red) and DTA(blue) profiles for ball-milled 1:1.15 NaOH:NaH (2h, 400rpm) with 10 wt.% Mg_2Si on heating from 35-450 °C at 5 °C min⁻¹ under flowing Ar(g).

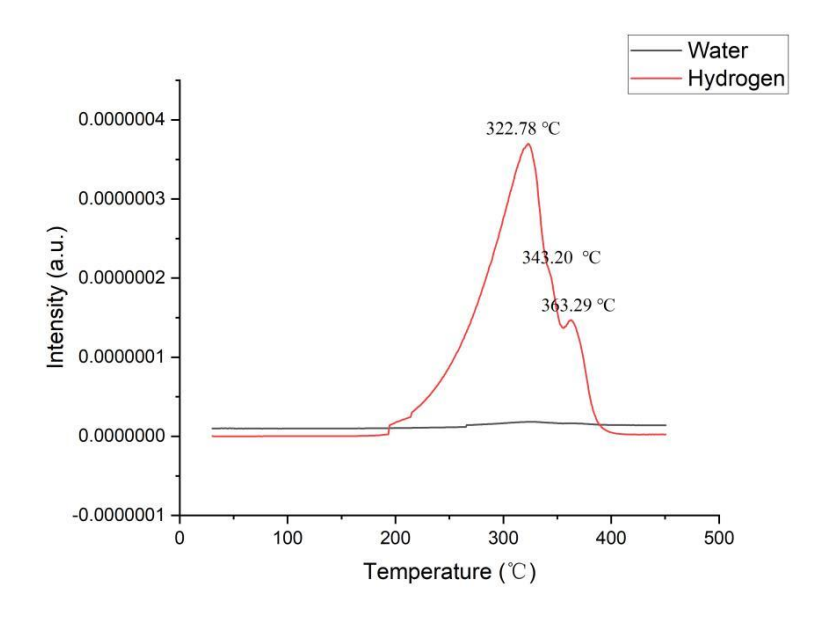


Figure 3-32: Mass spectrometry output for water (m/z = 18; black) and hydrogen (m/z = 2;red) as a function of temperature for ball-milled 1:1.15 NaOH:NaH (2h, 400rpm) with 10 wt.% Mg_2Si on heating from 35-450 °C at 5 °C min⁻¹ under flowing Ar(g).

To investigate the reactions occurring between Mg₂Si and components of the NaOH-NaH system, Figures 3-33 and 3-34 present PXD patterns of the reaction products of the NaOH-NaH-10 wt.% Mg₂Si sample heated to 330 °C and 450 °C, respectively. The 10 wt.% Mg₂Si sample is selected for discussion here because the peaks in the 5 wt.% Mg₂Si sample were too small to be clearly identified, whereas the 10 wt.% sample exhibited more distinguishable peaks. As shown in Figure 3-33, a significant amount of Na₂O was already present at 330 °C, indicating that the peak temperature of 323 °C observed in the DTA corresponds to the dehydrogenation reaction of NaOH-NaH. Compared to the peak temperature of 346 °C in the sample without Mg₂Si, This peak decreased by *ca.* 24 °C to 322 °C. Additionally, the NaOH-NaH-10 wt.% Mg₂Si sample at 330 °C contains NaH, NaOH, and Mg₂Si. The presence of NaOH may result from the reaction of Na₂O with trace amounts of air and reaction of NaH.

At 450 °C, metallic Na appears in the sample, which very likely originates from the decomposition of NaH. However, in the NaOH-NaH system with a molar ratio of 1:1.15 without Mg₂Si (sample 5), neither metallic Na nor additional peaks were observed in previous Figure 3-19. This further confirms that NaH has undergone a decomposition reaction to become Na, and its peak temperature is 362 °C. It is also close to the 380 °C of NaH decomposition reaction shown in Figure 3-7. Therefore, the amount of NaOH is expected to be less than before without Mg₂Si.

This suggests that some NaOH may have reacted with Mg₂Si and was consumed in the process. Furthermore, the relatively intensity of the Mg₂Si peak at 330 °C is stronger than

at 450 °C, supporting the conclusion that the first peak between 320 - 380 °C at 323.60 °C corresponds to the dehydrogenation of NaOH-NaH, while the third peak at 361.50 °C represents the decomposition of NaH into Na and H₂. The second peak at 346.25 °C is likely associated with the reaction between NaOH and Mg₂Si. However, due to the broad and weak nature of the corresponding peaks, the exact reaction products cannot be definitively identified.

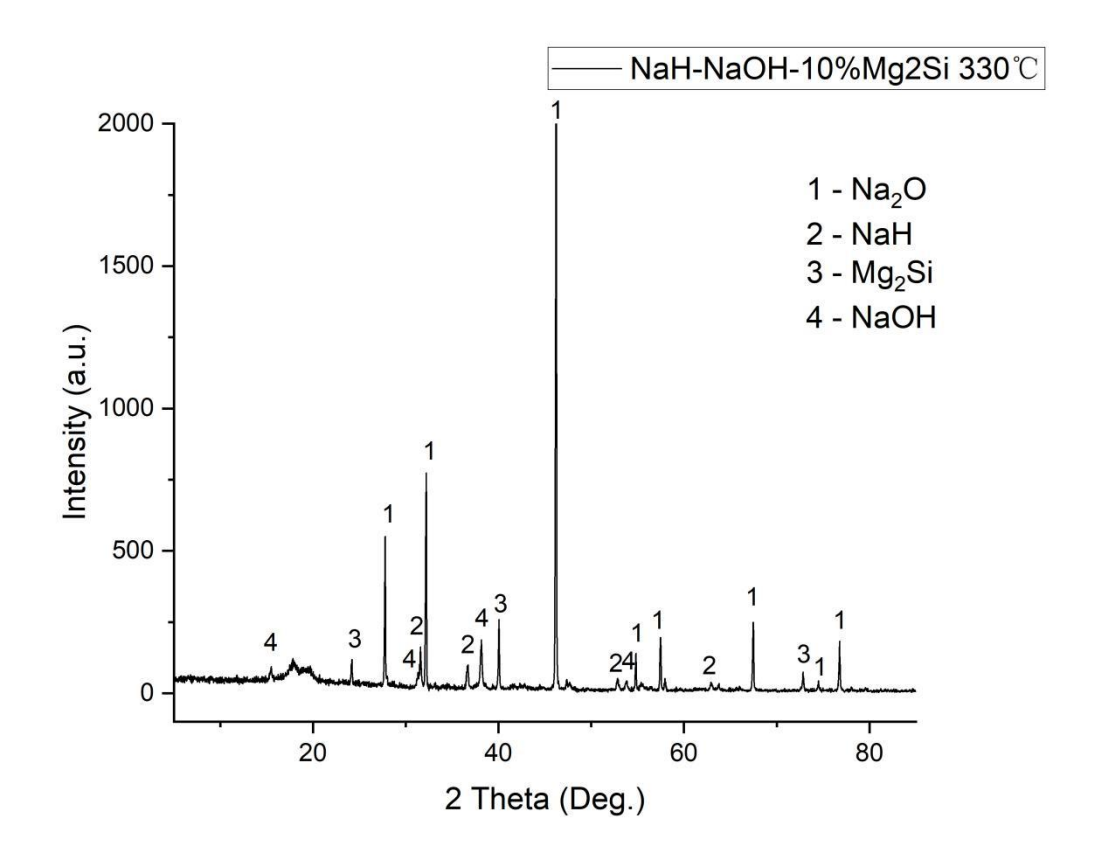


Figure 3-33: PXD patterns for ball-milled 1:1.15 NaOH:NaH with 10 wt.% Mg₂Si after heating to 330 °C under flowing Ar(g). (and cooling to room temperature). (1 represent Na₂O; 2 represent NaH; 3 represent Mg₂Si; 4 represent NaOH) Appendix A3-2 show the PXD patterns for the sample compared to stardard patterns from ICSD.

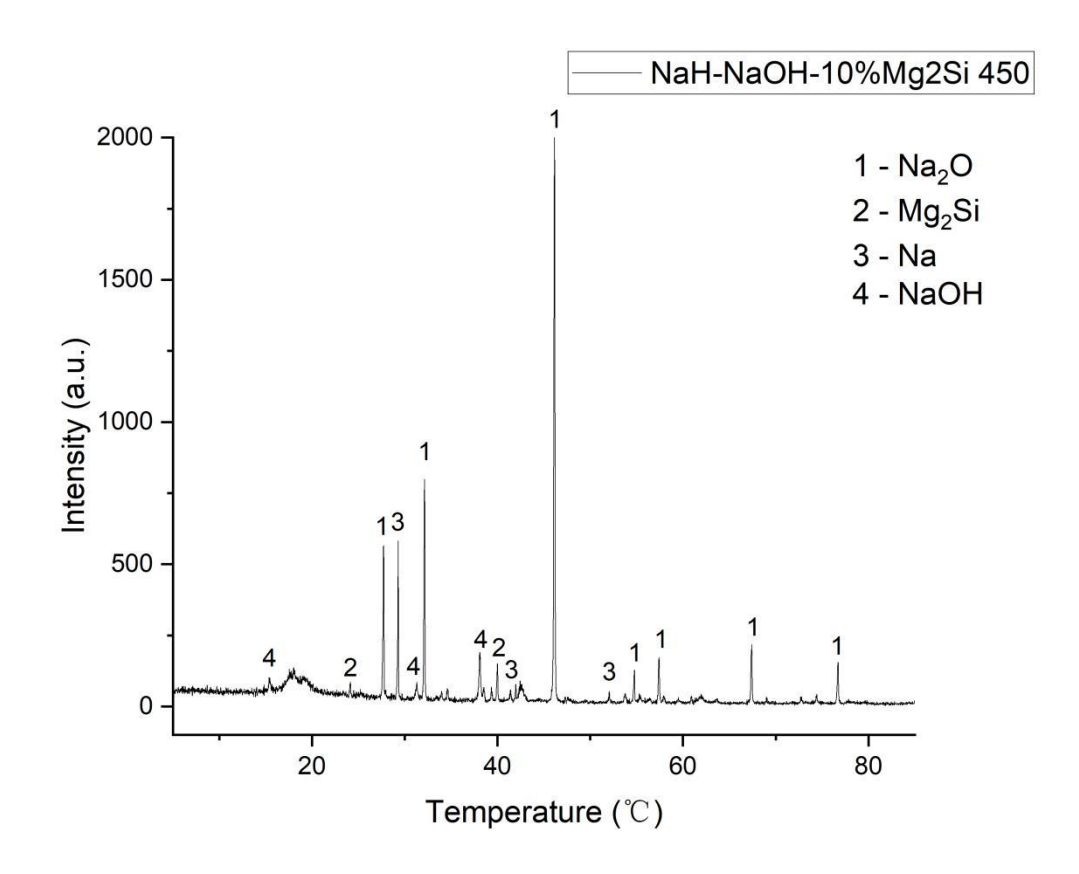


Figure 3-34: PXD patterns for ball-milled 1:1.15 NaOH:NaH with 10 wt.% Mg₂Si after heating to 450 °C under flowing Ar(g). (and cooling to room temperature). (1 represent Na₂O; 2 represent Mg₂Si; 3 represent Na; 4 represent NaOH) Appendix A3-3 show the PXD patterns for the sample compared to stardard patterns from ICSD.

The activation energies for dehydrogenation for samples with different additives are presented in Table 3-7. The activation energy does not change appreciably when adding rGO. On the other hand, if 10 wt.% or 5 wt.% Mg₂Si are added, the activation energy can be significantly reduced, with E_a decreasing further when 10 wt.% Mg₂Si is added. However, the Mg₂Si may not be the most suitable catalyst in the NaH-NaOH system given that the Mg₂Si have reaction during heating, and these reaction will decrease the hydrogen mass loss. According to the article by Cermak *et al.*, Mg₂Si can also reduce the activation energy in the MgH₂ system, lowering the dehydrogenation temperature of MgH₂ by about 5 °C.⁵³ However, this effect is limited compared to other catalysts. Additionally, since Mg₂Si occupies 10 wt.% in the MgH₂ system, the overall gravimetric capacity is reduced, although no reaction occurs. Therefore, Mg₂Si can lower the activation energy without undergoing a reaction.

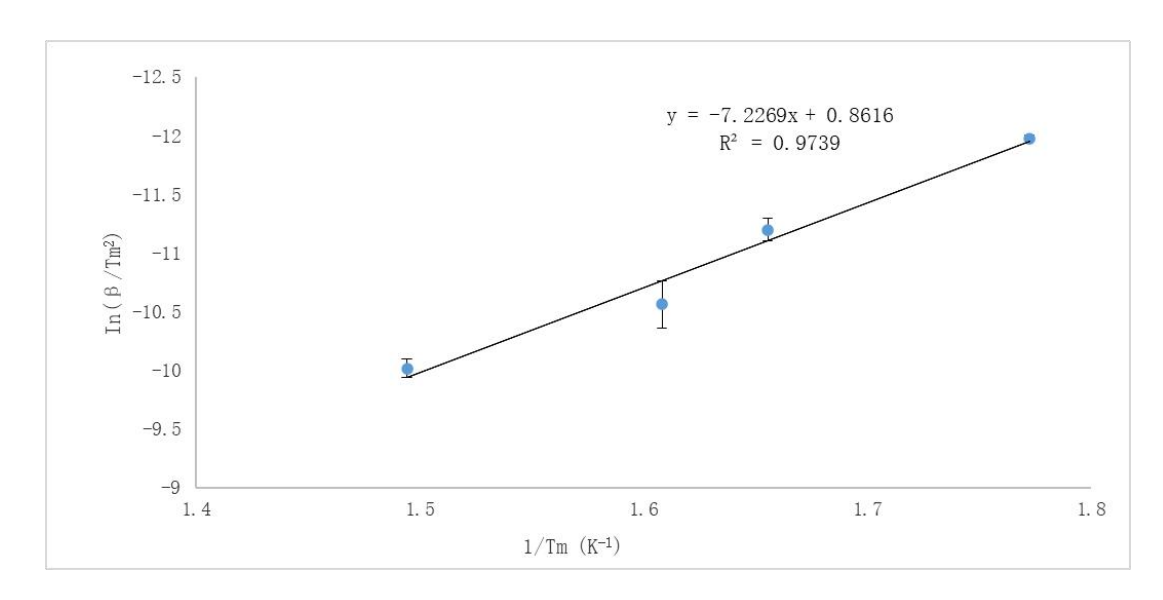


Figure 3-35: Kissinger plots for dehydrogenation of ball-milled 1:1.15 NaH:NaOH (2h, 400r) with 5 wt.% Mg₂Si on heating from 35-400 °C at heating rate 2, 5, 10 and 20 °C min⁻¹ under flowing Ar(g). Ea = 60.08 ± 6.95 kJ mol⁻¹. Peak temperature of dehydrogenation of sample on heating from 35-400 °C at heating rate 2, 10 and 20 °C min⁻¹ was shown on the Appendix 3-4.

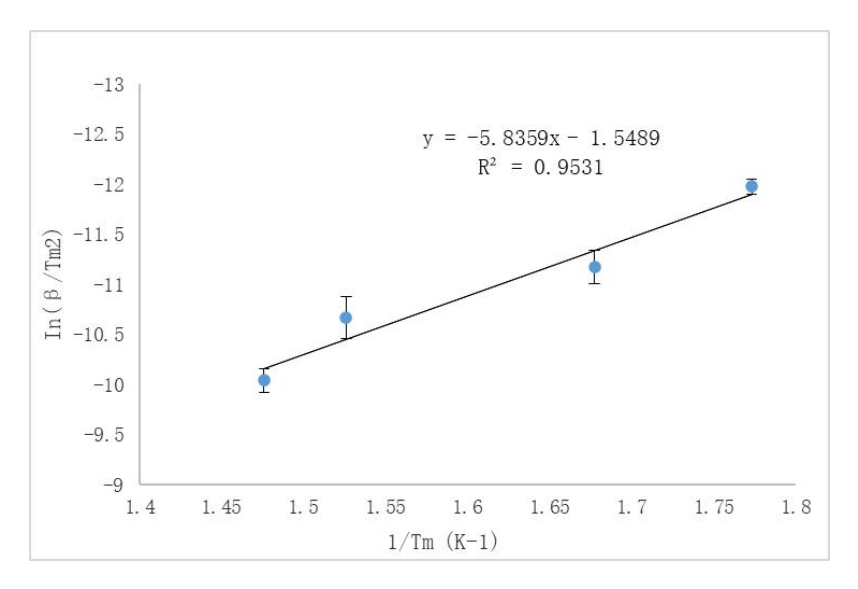


Figure 3-36: Kissinger plots for dehydrogenation of ball-milled 1:1.15 NaH:NaOH (2h, 400r) with 10 wt.% Mg₂Si on heating from 35-400 °C at heating rate 2, 5, 10 and 20 °C min⁻¹ under flowing Ar(g). Ea = 48.52 ± 7.60 kJ mol⁻¹. Peak temperature of dehydrogenation of sample on heating from 35-400 °C at heating rate 2, 10 and 20 °C min⁻¹ was shown on the Appendix 3-5.

Table 3-7: Activation energy of NaOH-NaH system with and without additives of rGO and Mg2Si.

Chemicals	Activation energy / kJ mol ⁻¹	
NaOH+NaH	75.85 ± 3.41	
NaOH+NaH+10 wt.%rGO	73.06 ± 3.32	
NaOH+NaH+5 wt.% Mg ₂ Si	60.08 ± 6.95	
NaOH+NaH+10 wt.% Mg ₂ Si	48.52 ± 7.60	

3.3.5.4 Other Additives in the NaOH-NaH system: Ti, TiF₃, MoS₂, Ni and SiC.

Titanium (Ti), titanium trifluoride (TiF₃), molybdenum disulfide (MoS₂), nickel (Ni), and silicon carbide (SiC) each play distinct roles in hydrogen storage, significantly enhancing storage efficiency, catalytic performance, and system stability. Titanium, while having a low hydrogen adsorption capacity itself, is commonly used as an alloying element with other metals such as magnesium and aluminium to form metal hydrides, which play a key role in hydrogen storage.⁵⁴ Titanium-based alloys (e.g., Ti-Mg) can store large amounts of hydrogen at low temperatures and pressures, and titanium's high strength and excellent corrosion resistance further enhance the stability of these alloys.⁵⁵ Additionally, titanium acts as a catalyst to promote hydrogen adsorption and desorption reaction by lowering the energy barrier for hydrogen adsorption, thereby improving storage efficiency.⁵⁶ For example, according to Wang *et al.*'s article, titanium has a significant catalytic effect on MgH₂, reducing its initial dehydrogenation temperature from 308 °C to 257 °C and its activation energy from 161.3 kJ mol⁻¹ to 104.2 kJ mol⁻¹.⁵⁷ The reason is that Ti reacts with MgH₂ during ball milling to form TiH_{1.971}, which acts as an active species and plays a catalytic role in the dehydrogenation process.

Titanium trifluoride (TiF₃), has a unique electronic structure, that makes it a potent catalyst for enhancing hydrogen storage. The unique electronic structure of TiF₃ arises from the Ti³⁺ (3d¹) configuration stabilized by highly electronegative F⁻ ligands, which generates partially filled d-states capable of mediating electron transfer with hydrogen species.⁵⁸ This feature enhances the dissociation and recombination of H-H bonds, thereby making TiF₃ a highly effective catalyst for dehydrogenation and hydrogenation reactions. For example, according to Kang et al.'s article, TiCl₃ and TiF₃ absorbed very little hydrogen (0.1-0.2 wt.%) even after long exposure at a hydrogen pressure of up to 120 bar and a temperature of 200 °C, and their vibrational spectra and electronic structure remained almost unchanged after hydrogen exposure, indicating that they do not chemically react with hydrogen under these conditions.⁵⁹ Moreover, H₂/D₂ isotope exchange experiments showed that TiF₃ has very limited ability to promote hydrogen dissociation, even after ball milling. This article provides possible insight into the role of Ti-containing additives in promoting hydrogen-coupled electron transfer when placed at the interface with another active material that can act as an electron source. The structure of the TiF₆ octahedron in TiF₃ may facilitate hydrogen dissociation via a hydrogen-coupled electron transfer (HCET) mechanism. Wang et al.'s article exihibit that TiF₃ has a significant catalytic effect on MgH₂, reducing its initial dehydrogenation temperature from 308 °C to 173 °C and its

activation energy from 161.3 kJ mol⁻¹ to 75 kJ mol⁻¹.⁵⁷ The reason is that during ball milling, TiF₃ reacts with MgH₂ to form TiH_{1.971} and TiH₂, which act as active species and play a catalytic role in the dehydrogenation process. The F⁻ ions in TiF₃ have high catalytic activity, which significantly reduces the dehydrogenation temperature and activation energy of MgH₂.

Molybdenum disulfide (MoS₂), a layered transition metal sulfide with a hexagonal crystal structure (space group P6₃/mmc), is widely used for hydrogen storage owing to its excellent catalytic properties. Its edge sites are considered active sites, particularly the sulfur (S) edge sites, which exhibit higher activity than the molybdenum (Mo) edge sites. These edge sites can adsorb and dissociate hydrogen atoms, thereby facilitating the production of hydrogen gas.⁶⁰ In some hydride materials, MoS₂ also acts as a catalyst when combined with other metal hydrides, helping to increase the hydrogen absorption rate and facilitate its desorption. For instance, according to Wang *et al.*'s article, the study found that the MgH₂-5 wt.% MoS₂ composite material, after 5 hours of ball milling, began releasing hydrogen at 259 °C and could desorb 4.0 wt.% of hydrogen within 20 minutes at 280 °C.⁶¹ After PXD, XPS, and TEM characterization, it was determined that the reason for this phenomenon is the coexistence of Mo and MoS₂ in the MgH₂-5 wt.% MoS₂ sample after ball milling. After dehydrogenation and re-hydrogenation, only Mo remains in the sample, which significantly weakens the Mg-H bond and promotes the dissociation of MgH₂ on the Mo surface.

Nickel (Ni), a common transition metal catalyst, is widely used in hydrogen adsorption and desorption reactions. In hydrogen storage, nickel is typically added to other metals (such as magnesium and sodium) to form alloys, which can lower the energy barrier for hydrogen adsorption, speeding up the adsorption/desorption rate. Nickel not only improves the kinetics of hydrogen storage materials but also enhances the thermal stability of the alloys, ensuring high efficiency in long-term use. For example, according to Liang et al.'s article, Ni-Mg absorbed 7.5 wt.% of hydrogen within 10 minutes under a hydrogen pressure of 2.0 MPa and at 200 °C, and desorbed 6.9 wt.% of hydrogen within 40 minutes at 220 °C. 62 The hydrogen adsorption and desorption activation energies for Ni-Mg were 59 kJ mol⁻¹ H₂ and 68.5 kJ mol⁻¹ H₂, respectively, both lower than those of pure Mg (87 kJ mol⁻¹ H₂ for adsorption and 108.3 kJ mol⁻¹ H₂ for desorption). The Ni-Mg system maintained stable capacity after multiple absorption/desorption cycles at 200 °C/220 °C, demonstrating good reversible cycling performance. According to Xie et al.'s article, the dehydrogenation activation energy of MgH₂ doped with 10 wt.% Ni was significantly reduced from 191 kJ mol⁻¹ for undoped MgH₂ to 118 kJ mol⁻¹ after ball milling for 2 hours at 300 rpm.⁶³ This reduction is attributed to the uniform dispersion of Ni nanoparticles on the surface of MgH₂, which created more active sites favourable for hydrogen atom combination and desorption.

Silicon carbide (SiC), a material known for its high temperature tolerance and chemical stability, plays a crucial structural role in hydrogen storage systems, even though it does not directly participate in hydrogen adsorption and desorption.⁶⁴ Therefore, unlike other catalysts that promote dehydrogenation reactions through chemical catalytic effects, SiC reduces the activation energy mainly through physical effects. According to the Arrhenius equation (equation 4), k is the rate constant that reflects the reaction rate at a given temperature; A is the pre-exponential factor (or frequency factor), representing the effective collision frequency of reactant molecules; E_a is the activation energy; R is the gas constant (8.314 J·mol⁻¹·K⁻¹); and T is the absolute temperature (K).⁶⁵ During ball milling, SiC acts as a "milling aid" to reduce the powder particle size, which increases the contact area of the reactants and shortens the hydrogen diffusion pathways, thereby facilitating the reaction. From the perspective of the Arrhenius relationship, this process effectively increases the pre-exponential factor (A) and enhances the probability of successful molecular interactions, which in turn manifests as an apparent reduction in the activation energy.

$$k = Aexp(-E_a/RT)$$
 Eq. 4

According to the Ranjbar et al's article, with the increase in SiC content, the particle size of MgH₂ decreases after ball milling for 24 hours.⁶⁶ The particle size of the 5 wt.% SiC sample was 17.6 nm, while that of the 20 wt.% SiC sample was 9.2 nm. This indicates that SiC helps to reduce the grain size of MgH₂. Moreover, the desorption temperature of the 20 wt.% SiC sample was approximately 20 °C lower than that of the undoped sample. The 5 wt.% SiC sample exhibited the best hydrogen absorption/desorption performance, with an absorption rate of 0.15 wt.%/s.

Overall, Ti, TiF₃, MoS₂, Ni, and SiC each play important roles in MgH₂ hydrogen storage system. Titanium and its alloys efficiently store hydrogen, TiF₃ and MoS₂ enhance hydrogen adsorption and desorption through catalytic actions, nickel improves the kinetics of hydrogen storage materials, and SiC provides structural support and enhances thermal stability. Therefore, the purpose of this chapter is to apply these catalysts in Na-H-OH systems. By optimally combining these materials, the overall performance of hydrogen storage systems can be significantly improved.

All the NaOH-NaH with these catalyst/additives were under the same milling condition (2h, 400rpm; 1:1.15 NaOH:NaH). The amount of these catalysts/additives is 5 wt.% in the NaOH-NaH system. From Figures 3-37 and 3-38, it can be observed that the sample with 5

wt.% SiC has the lowest peak temperature (320 °C) for the dehydrogenation reaction at a heating rate of 5 °C min⁻¹. For the remaining samples, the addition of 5 wt.% additives resulted in lower peak temperatures compared to the product without additives (345.66 °C). In terms of hydrogen mass loss, the sample with the additive rGO exhibited significantly lower mass loss than the other additives. The remaining samples were close to the theoretical mass loss (2.96 wt.%). From the table 3-8, after calcualtion by using Kissinger plots(Figure 3-39 to 3-43), it indicated that 5 wt. % Ni and SiC significantly reduce the activation energy of the NaOH-NaH dehydrogenation reaction compared to other catalysts. The activation energy is 41.24 and 46.79 kJ mol⁻¹ respectively. Based on the previous information, 5 wt.% SiC can reduce the particle size of the powder. Therefore, in the Na-H-OH system, a smaller particle size of the powder can significantly lower its activation energy. Compared to 5 wt.% SiC, 5 wt.% Ni has an even lower activation energy. According to the previous information, Ni nanoparticles may be uniformly dispersed on the surface of NaOH-NaH, forming active sites that are more favourable for the desorption of hydrogen atoms.

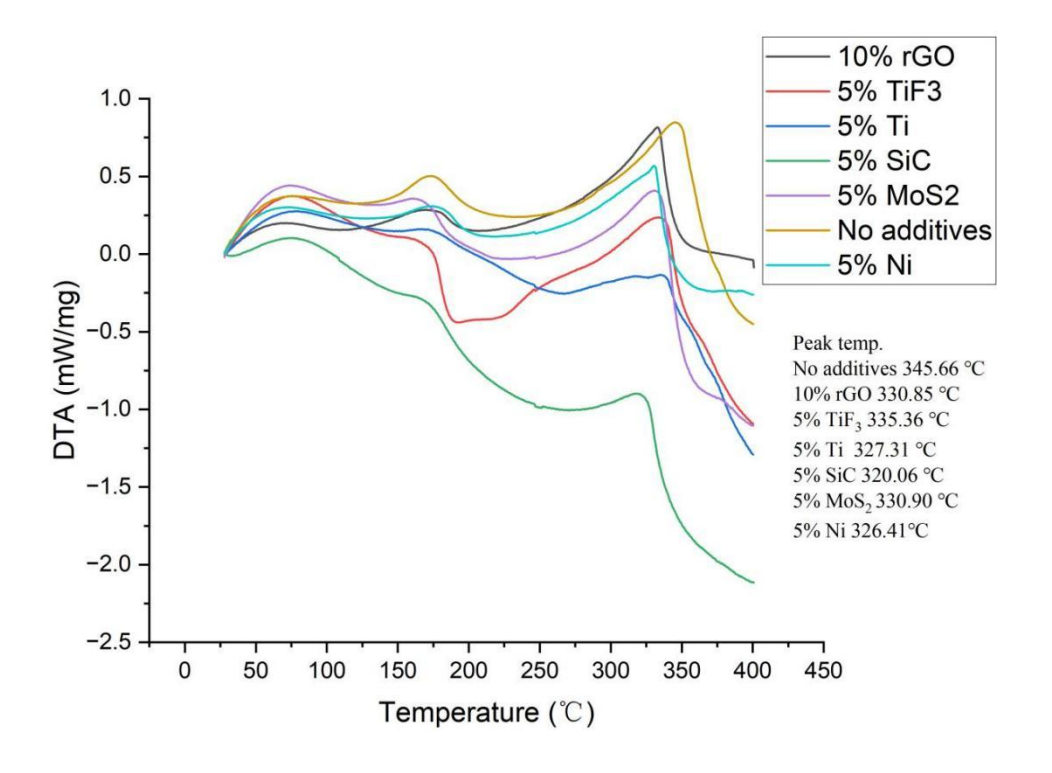


Figure 3-37: DTA profiles for ball-milled 1:1.15 NaOH:NaH (2h, 400rpm) with various catalyst/additives on heating from 35-400 $^{\circ}$ C at 5 $^{\circ}$ C min⁻¹ under flowing Ar(g).

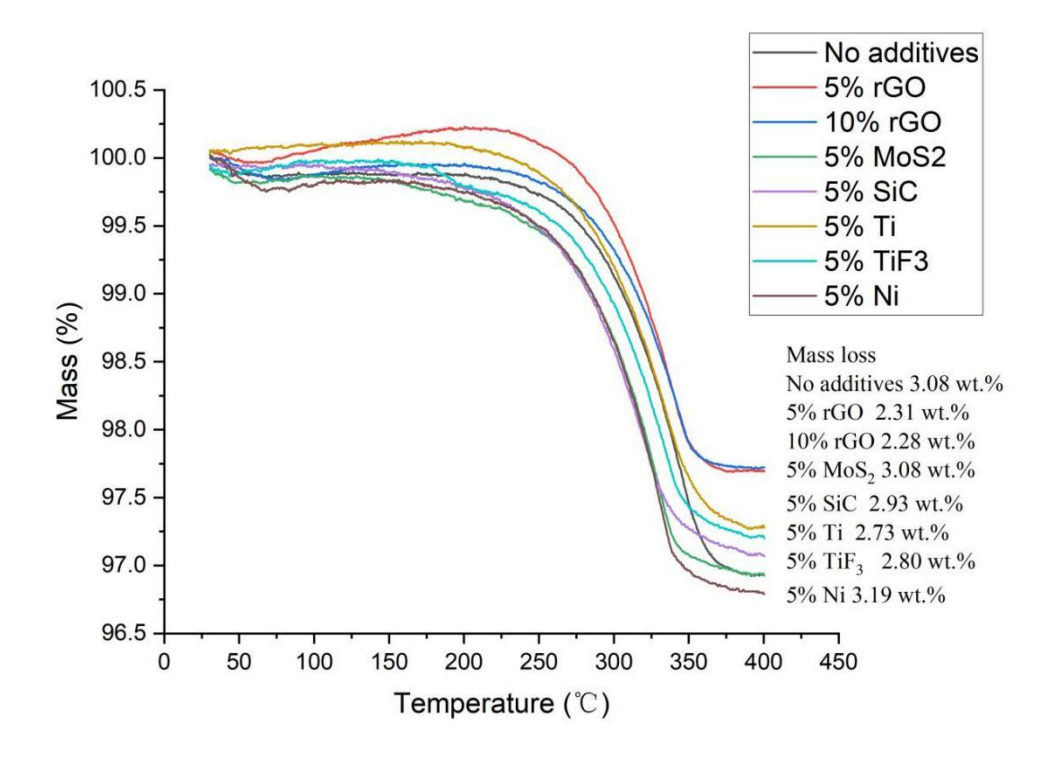


Figure 3-38: TG profiles for ball-milled 1:1.15 NaOH:NaH (2h, 400rpm) with various catalyst/additives on heating from 35-400 °C at 5 °C min⁻¹ under flowing Ar(g).

Table 3-8: Activation energy of NaOH-NaH system with various additives.

Sample	Activation energy/kJ mol ⁻¹	Peak temperature of dehydrogenation reaction with 5 °C min ⁻¹ /°C
NaH-NaOH	75.85 ± 3.41	345.66
+5 wt.%MoS ₂	56.33 ± 4.72	330.90
+5 wt.%SiC	46.79 ± 1.77	320.06
+5wt. %Ni	41.24 ± 2.64	326.41
+10 wt.%rGO	73.06 ± 3.32	330.85
+5 wt.%Ti	55.99 ± 2.82	327.31
+5 wt.%TiF ₃	58.62 ± 4.15	335.36

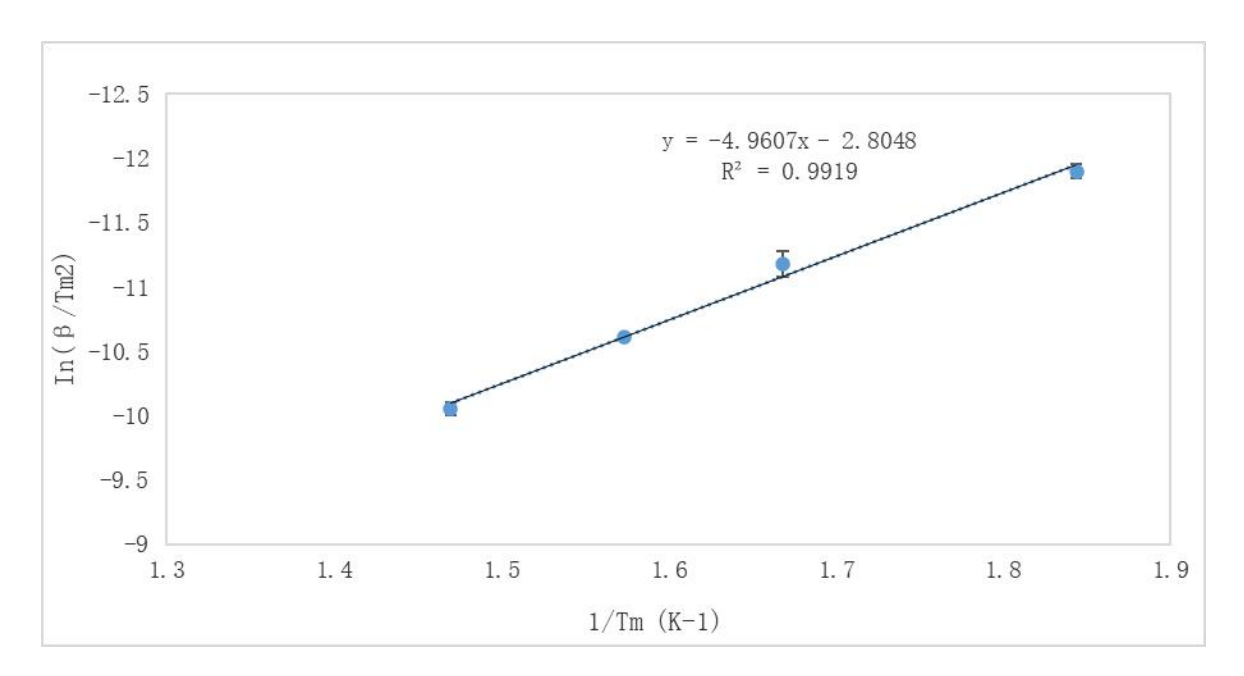


Figure 3-39: Kissinger plots for dehydrogenation of ball-milled 1:1.15 NaH:NaOH (2h, 400r) with 5 wt.% Ni on heating from 35-400 °C at heating rate 2, 5, 10 and 20 °C min⁻¹ under flowing Ar(g). Ea =41.24 \pm 2.64 kJ mol⁻¹. Peak temperature of dehydrogenation of sample on heating from 35-400 °C at heating rate 2, 10 and 20 °C min⁻¹ was shown on the Appendix 3-6.

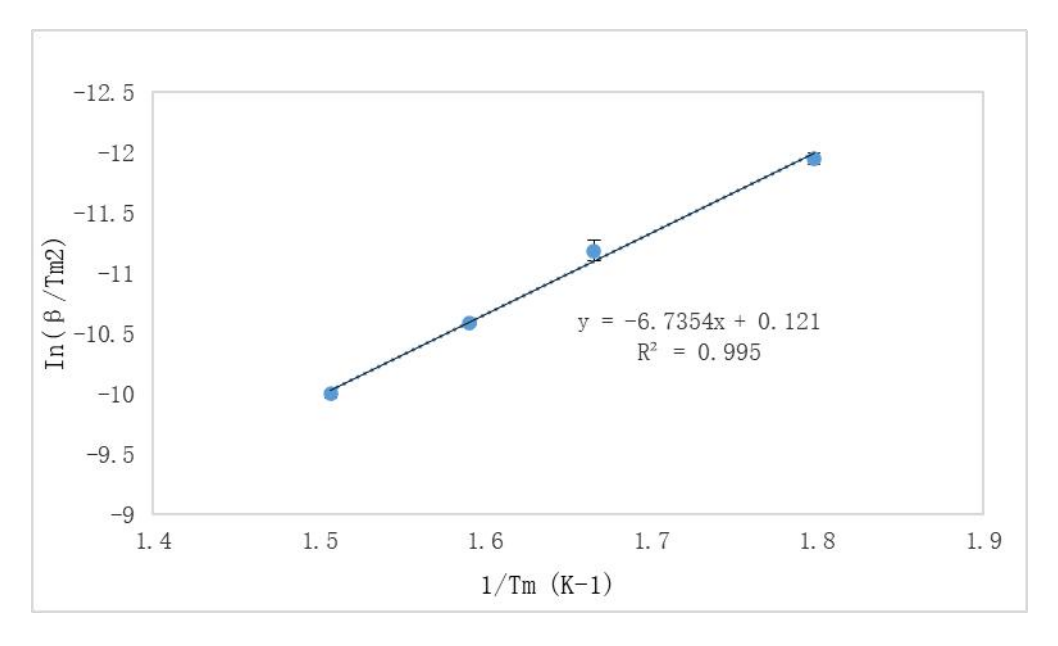


Figure 3-40: Kissinger plots for dehydrogenation of ball-milled 1:1.15 NaH:NaOH (2h, 400r) with 5 wt.% Ti on heating from 35-400 °C at heating rate 2, 5, 10 and 20 °C min⁻¹ under flowing Ar(g). Ea = 55.99 ± 2.82 kJ mol⁻¹. Peak temperature of dehydrogenation of sample on heating from 35-400 °C at heating rate 2, 10 and 20 °C min⁻¹ was shown on the Appendix 3-7.

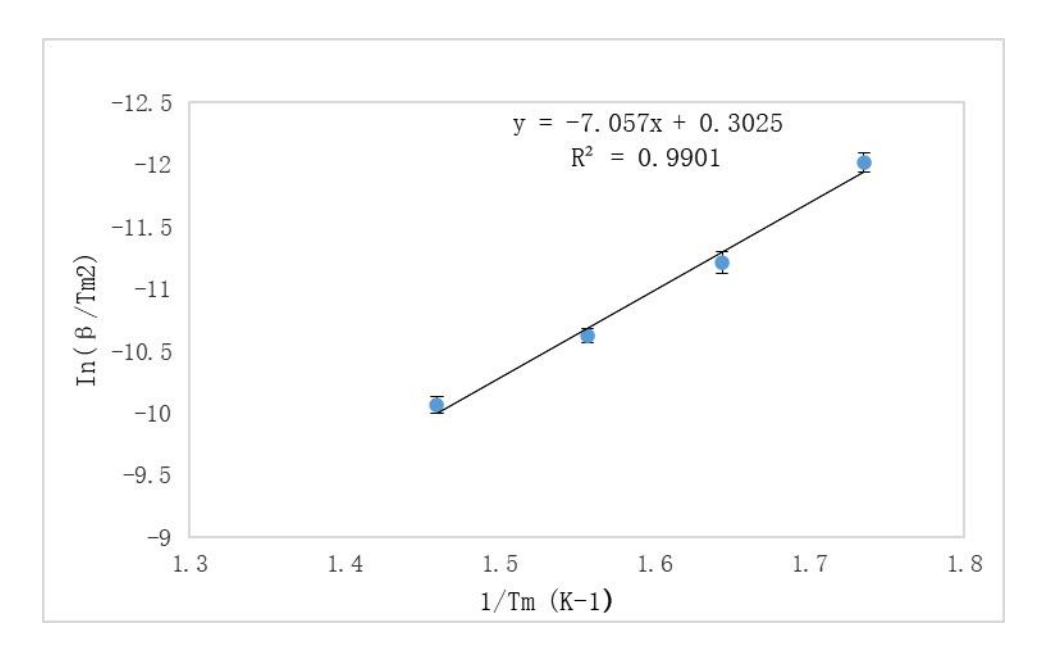


Figure 3-41: Kissinger plots for dehydrogenation of ball-milled 1:1.15 NaH:NaOH (2h, 400r) with 5 wt.% TiF₃ on heating from 35-400 °C at heating rate 2, 5, 10 and 20 °C min⁻¹ under flowing Ar(g). Ea = 58.62 ± 4.15 kJ mol⁻¹.Peak temperature of dehydrogenation of sample on heating from 35-400 °C at heating rate 2, 10 and 20 °C min⁻¹ was shown on the Appendix 3-8.

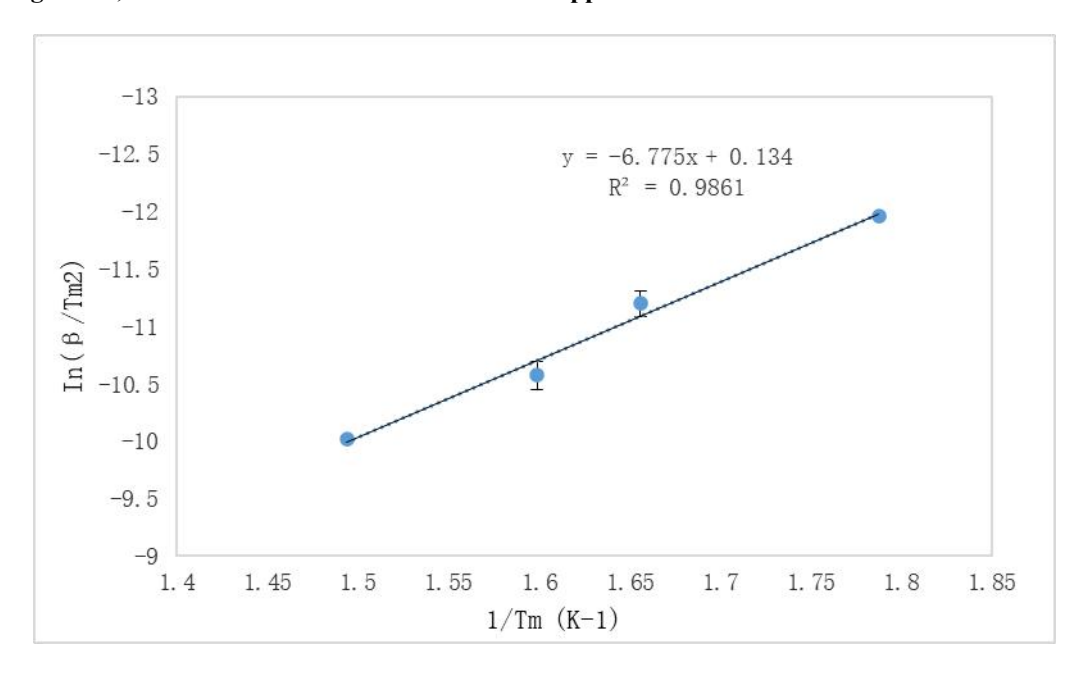


Figure 3-42: Kissinger plots for dehydrogenation of ball-milled 1:1.15 NaH:NaOH (2h, 400r) with 5 wt.% MoS₂ on heating from 35-400 °C at heating rate 2, 5, 10 and 20 °C min⁻¹ under flowing Ar(g). Ea = 56.33 ± 4.72 kJ mol⁻¹. Peak temperature of dehydrogenation of sample on heating from 35-400 °C at heating rate 2, 10 and 20 °C min⁻¹ was shown on the Appendix 3-9.

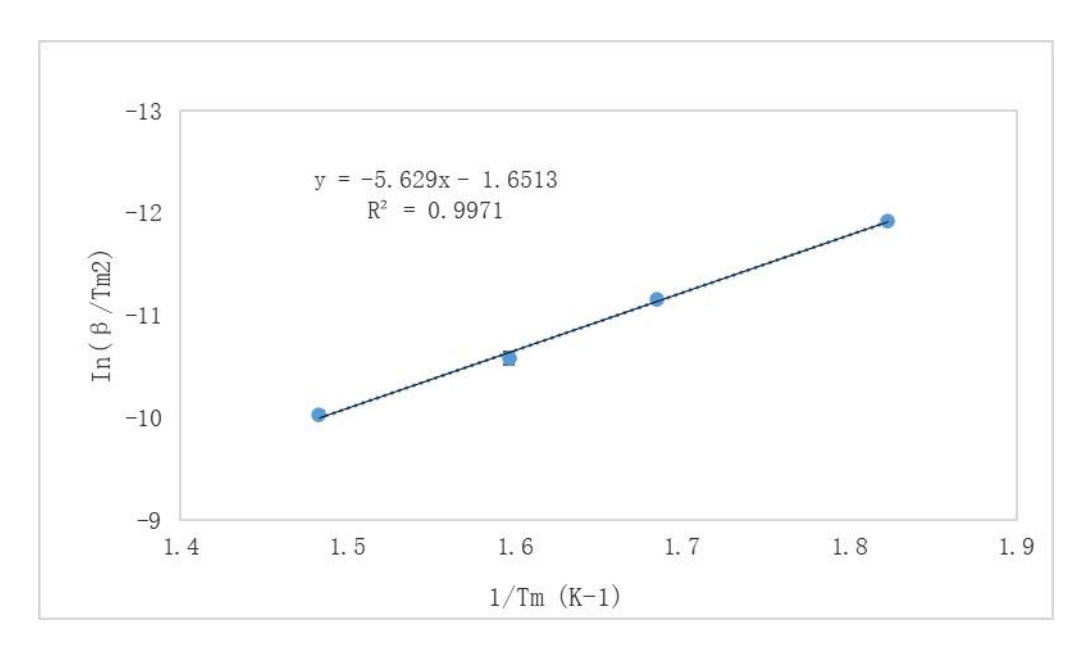


Figure 3-43: Kissinger plots for dehydrogenation of ball-milled 1:1.15 NaH:NaOH (2h, 400r) with 5 wt.% SiC on heating from 35-400 °C at heating rate 2, 5, 10 and 20 °C min⁻¹ under flowing Ar(g). Ea = 46.79 ± 1.77 kJ mol⁻¹. Peak temperature of dehydrogenation of sample on heating from 35-400 °C at heating rate 2, 10 and 20 °C min⁻¹ was shown on the Appendix 3-10.

3.4 Conclusion

The NaOH–NaH system demonstrates significantly enhanced dehydrogenation kinetics following ball milling. The reaction proceeds via a two-step mechanism. The first step, occurring around 175 °C, involves the gradual substitution of hydride (H⁻) with hydroxide (OH⁻), which induces lattice distortion, as evidenced by systematic peak shifts. The observed peak splitting at 15° 2 θ and peak broadening at 56° 2 θ in NaOH at 170 °C and 210 °C, respectively, indicate a pronounced interaction between NaH and NaOH upon heating, leading to the formation of a solid solution, NaH_{1-x}(OH)_x.

The second step, taking place between 320 °C and 350 °C, corresponds to the decomposition of this intermediate phase, resulting in the formation of Na₂O and the release of hydrogen gas. Optimal ball milling conditions (400 rpm, 2 hours) ensure homogeneous mixing and sufficient mechanochemical activation of NaH and NaOH. Under these conditions, the optimal molar ratio of NaH to NaOH lies between 1.15:1 and 1.2:1, with the 1.15:1 ratio yielding the lowest dehydrogenation peak temperature and the highest mass loss. When the molar ratio exceeds 1:1.2, excess NaH undergoes independent side reactions, diminishing overall efficiency. Regarding catalyst selection, both nickel (Ni) and silicon carbide (SiC) significantly reduce the activation energy of the NaOH–NaH system. SiC mainly functions as a physical milling aid. By reducing particle size, increasing the contact area of reactants, SiC facilitates hydrogen release. This physical effect is manifested in the Arrhenius relationship as an enhancement of the pre-exponential

factor and an apparent reduction in the activation energy. Ni nanoparticles may become uniformly dispersed over the NaOH-NaH surface, creating active sites that promote hydrogen atom desorption. Although Mg₂Si also effectively lowers activation energy, it reacts with NaOH as show in Figure 3-29 and 3-31(more peaks between 300°C-400°C), making it unsuitable as a recommended catalyst.

3.5 References

- 1. A. Altuntepe, S. Erkan, M. A. Olgar, S. Çelik and R. Zan, *Journal of Solid State Chemistry*, 2024, 330, 124438.
- 2. Z. Xu and J. Wang, Advanced Energy Materials, 2022, 12, 2201692.
- 3. Q. Xu, R. Wang, T. Kiyobayashi, N. Kuriyama and T. Kobayashi, *Journal of Power Sources*, 2006, **155**, 167-171.
- 4. P. Yu, Y. S. Chua, H. Cao, Z. Xiong, G. Wu and P. Chen, Journal of Energy Chemistry, 2014, 23, 414-419.
- 5. J. Mao, Q. Gu and D. Gregory, *Materials*, 2015, **8**, 2191-2203.
- 6. G. Nolze and W. Kraus, *PowderCell for Windows*, Version 2.4, BAM, Berlin, 2000; ICSD, Inorganic Crystal Structure Database, FIZ Karlsruhe, Germany.
- 7. ICDD PDF-4+ 2024, International Centre for Diffraction Data, Newtown Square, PA, USA; *PANalytical HighScore Plus*, Version 4.9, Malvern Panalytical.
- 8. A. C. Larson and R. B. Von Dreele, *General Structure Analysis System (GSAS)*, Los Alamos National Laboratory Report LAUR 86–748, 2004; B. H. Toby, *J. Appl. Crystallogr.*, 2001, **34**, 210–213.
- 9. D. C. Marcano, D. V. Kosynkin, J. M. Berlin, A. Sinitskii, Z. Sun, A. Slesarev, L. B. Alemany, W. Liu and J. M. Tour, ACS nano, 2010, 4, 4806-4814.
- 10. Z. Fan, M. D. Cappelluti and D. H. Gregory, ACS Sustainable Chemistry & Engineering, 2019, 7, 19686-19698.
- 11. K. Stephan, M. Schmitt, D. hebecker and T. Bergmann, Int J. Refrig., 1997, 20(7), 483-495.
- 12. E. G. Sorte, E. H. Majzoub, T. Ellis-Caleo, B. A. Hammann, G. Wang, D. Zhao, R. C. Bowman and M. S. Conradi, *The Journal of Physical Chemistry C*, 2013, **117**, 23575-23581.
- 13. Q. Li, H. Xu, F. Li, P. Li, L. Shen and J. Zhai, Fuel, 2012, 97, 366-372.
- 14. S. Vyazovkin, Phys Chem Chem Phys, 2016, 18, 18643-18656.
- 15. M. Kawaguchi, *The Journal of Physical Chemistry C*, 2021, **125**, 11813-11819.
- 16. F. Tanaka, Y. Nakagawa, S. Isobe and N. Hashimoto, *International Journal of Energy Research*, 2020, 44, 2941-2951.
- 17. I. Fatma, H. Assad and A. Kumar, *Two-Dimensional Nanomaterials-Based Polymer Nanocomposites*, 2024, **1**, 1-45.
- 18. K. Wang, J. Y. Wu, R. Z. Wang and L. W. Wang, Energy Conversion and Management, 2006, 47, 1902-1912.
- 19. T. Y. Kim, C. H. Park and N. Marzari, Nano Lett, 2016, 16, 2439-2443.
- 20. C. N. R. Rao, K. Gopalakrishnan and A. Govindaraj, Nano Today, 2014, 9, 324-343.
- 21. L. S. Panchakarla, K. S. Subrahmanyam, S. K. Saha, A. Govindaraj, H. R. Krishnamurthy, U. V. Waghmare and C. N. R. Rao, *Advanced Materials*, 2009, **21**, 4726-4730.
- 22. P. Lazar, R. Zboril, M. Pumera and M. Otyepka, Phys Chem Chem Phys, 2014, 16, 14231-14235.

- 23. F. Chen, X. Zhang, X. Guan, S. Gao, J. Hao, L. Li, Y. Yuan, C. Zhang, W. Chen and P. Lu, *Applied Surface Science*, 2023, **622**, 156895.
- 24. N. Sathishkumar, S. Y. Wu and H. T. Chen, *International Journal of Energy Research*, 2019, 43, 4867-4878.
- 25. X. Tan, H. A. Tahini and S. C. Smith, ACS Appl Mater Interfaces, 2016, 8, 32815-32822.
- 26. V. Jain and B. Kandasubramanian, Journal of Materials Science, 2019, 55, 1865-1903.
- 27. T. Kopac, International Journal of Hydrogen Energy, 2024, 69, 777-803.
- 28. E. Beheshti, A. Nojeh and P. Servati, Carbon, 2011, 49, 1561-1567.
- 29. E. Tylianakis, G. M. Psofogiannakis and G. E. Froudakis, *The Journal of Physical Chemistry Letters*, 2010, 1, 2459-2464.
- 30. S. H. Aboutalebi, S. Aminorroaya-Yamini, I. Nevirkovets, K. Konstantinov and H. K. Liu, *Advanced Energy Materials*, 2012, **2**, 1439-1446.
- 31. M. P. Suh, H. J. Park, T. K. Prasad and D. W. Lim, Chem Rev, 2012, 112, 782-835.
- 32. Y. Liu, D. Shen, Z. Tu, L. Xing, Y. G. Chung and S. Li, *International Journal of Hydrogen Energy*, 2022, 47, 41055-41068.
- 33. S. S. Han, W. Q. Deng and W. A. Goddard, Angewandte Chemie, 2007, 119, 6405-6408.
- 34. K. K. Gangu, S. Maddila, S. B. Mukkamala and S. B. Jonnalagadda, *Journal of Energy Chemistry*, 2019, **30**, 132-144.
- 35. H. Yang, H. Hu, Z. Ni, C. K. Poh, C. Cong, J. Lin and T. Yu, Carbon, 2013, 62, 422-429.
- 36. N. Pourmoghaddam and N. Ayas, International Journal of Hydrogen Energy, 2024, 82, 1422-1434.
- 37. H. Jindal, A. S. Oberoi, I. S. Sandhu, M. Chitkara and B. Singh, *International Journal of Energy Research*, 2020, **45**, 5815-5826.
- 38. R. S. Rajaura, S. Srivastava, V. Sharma, P. K. Sharma, C. Lal, M. Singh, H. S. Palsania and Y. K. Vijay, *International Journal of Hydrogen Energy*, 2016, 41, 9454-9461.
- 39. C. Dun, S. Jeong, D.-H. Kwon, S. Kang, V. Stavila, Z. Zhang, J.-W. Lee, T. M. Mattox, T. W. Heo, B. C. Wood and J. J. Urban, *Chemistry of Materials*, 2022, **34**, 2963-2971.
- 40. P. Yao, Y. Jiang, Y. Liu, C. Wu, K.-C. Chou, T. Lyu and Q. Li, *Journal of Magnesium and Alloys*, 2020, 8, 461-471.
- 41. L. Ji, L. Zhang, X. Yang, X. Zhu and L. Chen, Dalton Trans, 2020, 49, 4146-4154.
- 42. A. Jana and D. H. Gregory, Chemistry, 2020, 26, 6703-6714.
- 43. L. Lu, K. K. Thong and M. Gupta, Composites Science and Technology, 2003, 63, 627-632.
- 44. P. P. Seth, O. Parkash and D. Kumar, RSC Adv, 2020, 10, 37327-37345.
- 45. X. Cheng, N. Farahi and H. Kleinke, Jom, 2016, 68, 2680-2687.
- 46. M. B. A. Bashir, S. Mohd Said, M. F. M. Sabri, D. A. Shnawah and M. H. Elsheikh, *Renewable and Sustainable Energy Reviews*, 2014, **37**, 569-584.

- 47. N. S. Nazer, R. V. Denys, H. F. Andersen, L. Arnberg and V. A. Yartys, *Journal of Alloys and Compounds*, 2017, **718**, 478-491.
- 48. Z. H. Tan, L. Z. Ouyang, J. M. Huang, J. W. Liu, H. Wang, H. Y. Shao and M. Zhu, *Journal of Alloys and Compounds*, 2019, **770**, 108-115.
- 49. S. T. Kelly, S. L. Van Atta, J. J. Vajo, G. L. Olson and B. M. Clemens, *Nanotechnology*, 2009, **20**, 204017.
- 50. X. F. Tan, M. Kim, Q. Gu, J. Pinzon Piraquive, G. Zeng, S. D. McDonald and K. Nogita, *Journal of Power Sources*, 2022, **538**, 231538.
- 51. G. Ben-Hamu, D. Eliezer and K. S. Shin, *Intermetallics*, 2008, 16, 860-867.
- 52. Z. Fan, H.-N. Ho, R. Szczesny, W.-R. Liu and D. H. Gregory, CrystEngComm, 2022, 24, 5801-5809.
- 53. J. Cermak and L. Kral, Journal of Alloys and Compounds, 2018, 744, 252-259.
- 54. N. A. A. Rusman and M. Dahari, International Journal of Hydrogen Energy, 2016, 41, 12108-12126.
- 55. S. K. Sharma, S. Gajevic, L. K. Sharma, R. Pradhan, S. Miladinovic, A. Asonja and B. Stojanovic, *Materials (Basel)*, 2024, 17.
- 56. J. Mao, Z. Guo, I. P. Nevirkovets, H. K. Liu and S. X. Dou, *The Journal of Physical Chemistry C*, 2011, **116**, 1596-1604.
- 57. Y. Wang, Q. Zhang, Y. Wang, L. Jiao and H. Yuan, Journal of Alloys and Compounds, 2015, 645, S509-S512.
- 58. A. Grzech, U. Lafont, P. C. M. M. Magusin and F. M. Mulder, *The Journal of Physical Chemistry C*, 2012, 116, 26027-26035.
- 59. S. Kang, L. E. Klebanoff, A. A. Baker, D. F. Cowgill, V. Stavila, J. R. I. Lee, M. H. Nielsen, K. G. Ray, Y. S. Liu and B. C. Wood, *International Journal of Hydrogen Energy*, 2018, **43**, 14507-14519.
- 60. C. G. Morales-Guio and X. Hu, Acc Chem Res, 2014, 47, 2671-2681.
- 61. L. Wang, Y. Hu, J. Lin, H. Leng, C. Sun, C. Wu, Q. Li and F. Pan, *Journal of Magnesium and Alloys*, 2023, 11, 2530-2540.
- 62. H. Liang, H. Zhang, Y. Zong, H. Xu, J. Luo, X. Liu and J. Xu, Journal of Alloys and Compounds, 2022, 905, 164279.
- 63. L. Xie, Y. Liu, X. Zhang, J. Qu, Y. Wang and X. Li, *Journal of Alloys and Compounds*, 2009, **482**, 388-392.
- 64. A. Ranjbar, Z. P. Guo, X. B. Yu, D. Attard, A. Calka and H. K. Liu, *International Journal of Hydrogen Energy*, 2009, **34**, 7263-7268.
- 65. F. Jensen, Quality and Reliability Engineering International, 1985, 1, 13-17.
- 66. A. Ranjbar, Z. P. Guo, X. B. Yu, D. Wexler, A. Calka, C. J. Kim and H. K. Liu, *Materials Chemistry and Physics*, 2009, **114**, 168-172.

4. Dehydrogenation in the NaAlH₄-NaOH System

4.1 Introduction

4.1.1 Sodium alanate, NaAlH₄

NaAlH₄ is an efficient solid-state hydrogen storage material that belongs to the family of aluminium hydrides. NaAlH₄ has attracted significant attention in hydrogen energy technology, particularly in the field of hydrogen storage, because it can store hydrogen at relatively low pressures and has a high gravimetric capacity. Theoretically, its hydrogen storage capacity can reach up to 7.5 wt.% by weight, making it a promising candidate for solid-state hydrogen storage.¹ Given that Al is a relatively light element, the high hydrogen content is due to the hydrogen being chemically bound as AlH₄- (aluminium hydride) within the crystal lattice of NaAlH₄, allowing for efficient storage of hydrogen in a stable solid form.²

However, the hydrogen release and absorption processes in NaAlH₄ require relatively high temperatures and/or pressures. When heated, NaAlH₄ undergoes a three-step decomposition process, as shown in reaction 1, 2 and 3. In the first step, hydrogen is released from NaAlH₄ at temperatures between 180-190 to form Na₃AlH₆ and hydrogen gas. In the second step, hydrogen is released from Na₃AlH₆ at temperatures over 260 °C,^{3,4} giving NaH, Al, and additional hydrogen gas.⁵ This decomposition process is reversible. In the third step, NaH decomposes to Na and hydrogen. The temperature for dehydrogenation complete dehydrogenation (and 2NaH to 2Na + H₂) is high (over 425 °C).⁶ The mechanism of NaAlH₄ dehydrogenation reaction is shown below.

$$3\text{NaAlH}_4 = \text{Na}_3\text{AlH}_6 + 2\text{Al} + 3\text{H}_2$$
 (1)
 $T = 180\text{-}190 \,^{\circ}\text{C}$ (3.7 wt.%)
 $\text{Na}_3\text{AlH}_6 + 2\text{Al} = 3\text{Al} + 3\text{NaH} + 1.5\text{H}_2$ (2)
 $T > 260 \,^{\circ}\text{C}$ (1.9 wt.%)
 $3\text{NaH} + 3\text{Al} = 3\text{Al} + 3\text{Na} + 3/2\text{H}_2$ (3)
 $T > 425 \,^{\circ}\text{C}$ (1.9 wt.%)

Total mass loss: 7.5 wt.%

To address the challenges of high release temperature of dehydrogenation and reversibility, various improvement strategies researchers have been explored. One common approach is to enhance the hydrogenation and dehydrogenation rates of NaAlH₄ by adding catalysts or modifying the material. Metals or metal compounds such as Ti and TiCl₃ have been shown

to act as catalysts, improving the hydrogen release and absorption processes of NaAlH₄.⁷ For instance, as reported by Frankcombe et al., the theoretical reversible hydrogen storage capacity of undoped NaAlH₄ is 5.6 wt.% in Table 4-1. However, in practical applications, its hydrogen release temperature is relatively high (above 207 °C), and its cycling stability is poor, with a significant decrease in hydrogen storage capacity after multiple cycles.⁸ In contrast, when NaAlH₄ is doped with Ti, its actual hydrogen storage capacity can reach 5.5–5.7 wt.%, approaching the theoretical value. The hydrogen release temperature is significantly reduced, with the first desorption temperature decreasing from 207 °C to 77 °C, and the second desorption temperature decreasing from 252 °C to 97 °C. Moreover, after 100 cycles, the hydrogen storage capacity of Ti-doped NaAlH₄ only decreases by *ca*. 10%, demonstrating excellent cycling stability. The activation energy is also reduced from over 100 kJ mol⁻¹ to around 60 kJ mol⁻¹. The optimal Ti doping level is found to be 2-4 wt.%. These improvements indicate that Ti doping not only lowers the hydrogen release temperature but also enhances the hydrogen storage capacity and cycling stability while reducing the reaction activation energy.

Table 4-1: Comparison of Sodium Alanate (NaAlH4) Storage Performance with and without Ti Doping

Parameter	Undoped NaAlH4	Ti-Doped NaAlH4	
Reversible Hydrogen Storage Capacity/ wt.%	5.6 (Theoretical)	5.5-5.7 wt% (Experimental)	
First Dehydrogenation Temperature/ °C	207	77	
Second Dehydrogenation Temperature/°C	252	97	
Activation Energy/ kJ mol ⁻¹	>100	60	

Additionally, mixing NaAlH₄ with other hydrides (such as LiAlH₄, MgH₂, etc.) or high surface area materials (such as carbon-based materials) is another approach to improving its performance.⁹ According to Kwak et al., mechanical ball milling was conducted in a hydrogen atmosphere to prepare MgH₂–NaAlH₄ composite materials with varying ratios.¹⁰ Among these, the MgH₂–0.3NaAlH₄ composite exhibited a maximum hydrogen desorption temperature of 319 °C, which is lower than that of pure MgH₂ (365 °C). Additionally, this composite demonstrated the highest hydrogen absorption rate (2.20 wt.% H₂ min⁻¹) and the largest effective hydrogen storage capacity (7.42 wt.% H₂) at 320 °C.

As reported by Ismail et al., the hydrogen storage performance and reaction mechanism of MgH₂–NaAlH₄ composite materials (with a molar ratio of 4:1) were investigated.¹¹ At

320 °C, the composite released 3.5 wt.% hydrogen within 12 minutes, significantly higher than the 0.4 wt.% released by pure MgH₂. The dehydrogenation process of the composite involves four stages: initially, NaAlH₄ reacts with MgH₂ to form NaMgH₃ and Al; subsequently, MgH₂ reacts with Al to form Mg₁₇Al₁₂, while MgH₂ also undergoes self-decomposition; then, NaMgH₃ decomposes into NaH and Mg; finally, NaH decomposes into Na and H₂. PXD analysis revealed the formation of phases such as NaMgH₃, Al, and Mg₁₇Al₁₂ during these reaction stages. The formation of these phases contributes to the enhanced dehydrogenation performance of MgH₂. These composite materials can lower the temperature required for hydrogen release and improve reaction kinetics.

4.1.2 Aims and objectives of this work

Based on previous chapter with the NaH-NaOH system, the interaction between protonic hydrogen (H^δ) and hydridic hydrogen (H^δ) can significantly enhance the dehydrogenation reaction kinetics. ¹² This includes reducing reaction barriers, lowering activation energy, enabling earlier hydrogen release at lower temperatures, and accelerating the release rate. Therefore, the addition of NaOH to NaAlH₄ may potentially lower the dehydrogenation temperature of the reaction (1) and (2). Furthermore, if NaOH remains unreacted during the first two steps, it can react with NaH in the third step of the NaAlH₄ dehydrogenation reaction, thereby making the overall reaction fully reversible. This "ideal" dehydrogenation reaction scheme is shown as below:

NaAlH₄ + NaOH
$$\rightleftharpoons$$
 1/3Na₃AlH₆ + 2/3Al + H₂ + NaOH (4)
T < 180-190 °C (2.13 wt.%)
1/3Na₃AlH₆ + NaOH \rightleftharpoons 1/3Al + NaH + 1.5H₂ + NaOH (5)
T < 260 °C (1.09 wt.%)
NaH + NaOH + Al \rightleftharpoons 1/2Na₂O + H₂ + Al (6)
T= 320 - 350 °C (1.78 wt.%)

Total mass loss: 5.00 wt.%

The purpose is to learn from the NaH-NaOH system to apply the addition of NaOH to NaAlH₄. By changing the dehydrogenation pathway by adding NaOH, it might be possible to reduce the dehydrogenation temperature and make the system fully reversible. The mechanism of NaAlH₄-NaOH dehydrogenation reaction should also be researched.

4.2 Experimental

NaH (Sigma Aldrich, dry, 90%), NaAlH₄ (Sigma Aldrich, powder, 93%) and Al (Sigma Aldrich, powder, 99.99%) was used as received. NaOH (Alfa Aesar, pellet, 99.99%) was dried prior to synthesis experiment through use of the Schlenk line. (100 °C; -2×10⁻² bar)

Because of the air and moisture sensitivity of NaOH (Alfa Aesar, pellet, 99.99%), NaAlH₄ and NaH (Sigma Aldrich, dry, 90%), all operations were carried out in a recirculating Argon or N₂-filled (BOC, 99.998%) glovebox (MBraun LABstar, O₂ < 10 ppm, H₂O < 0.5 ppm). NaOH (Alfa Aesar, pellet, 99.99%) was ball-milled for 1 hour to reduce the particle size of the powder. After ball-milling, the NaOH was sent to Schlenk line to dry overnight. (100 °C; -2×10^{-2} bar)

4.2.1 Mixing and milling of NaOH-NaAlH4

This experiment contain hand-mixed. Hand-mixing was conducted for 20 mins in an argon-filled glovebox (MBraun LABstar, $O_2 < 10$ ppm, $H_2O < 0.5$ ppm). For the ball-milling, The NaOH and NaAlH₄ mixtures were weighed in different amounts according to their respective molar ratios. And then transferred to a stainless-steel grinding jar that was filled with eight stainless steel balls (10 mm diameter), each of which weighed about 4 g. The grinding jar was sealed under argon before removal from the glovebox. Ball milling was conducted at various reaction time and a 400 rpm rotation speed with a ball-to-powder ratio of 80:1 in a planetary ball mill (Retsch PM100) in 5-minute milling periods (reverse rotation) followed by 5-minute rest periods.

4.2.2 TG-DTA-MS Studies

NaAlH₄-NaOH samples were characterised using thermogravimetric-differential thermal analysis (TG-DTA) coupled with mass spectrometry (MS) to investigate their thermal behaviour. These experiments aimed to determine the onset and peak temperatures of thermal events during heating, quantify weight loss, and identify the nature and quantity of gaseous species evolved during the reaction. TG-DTA measurements were conducted using a Netzsch STA 409 PC instrument, which was coupled to a Hiden HPR20 mass spectrometer. All analyses were performed under an argon flow, and sample handling was carried out exclusively in inert atmosphere glove boxes to prevent contamination or unwanted reactions.

Prior to analysis, correction files were generated, followed by the examination of the materials. Initial experiments involved heating the samples from room temperature to 400 °C at a rate of 5 °C min⁻¹. Based on the results of these preliminary TG-DTA

measurements, subsequent experiments were designed to investigate intermediate temperature points, enabling the identification of any transient species formed and facilitating the elucidation of the hydrogen release mechanism. For each experiment, approximately 15–30 mg of sample was subjected to thermal treatment. TG-DTA analysis was further employed to determine the activation energy of the system using the Kissinger method. Samples were heated to 400 °C at varying heating rates of 2, 5, 10, and 20 °C min⁻¹, and Kissinger plots were constructed to extract kinetic parameters associated with the dehydrogenation process.

4.2.3 Powder X-ray Diffraction (PXD)

All starting materials and NaAlH₄-NaOH samples were characterized using PXD. All the materials used in this study were air-sensitive. Therefore, all the samples were prepared using the air-sensitive sample holder under inert atmosphere.(glovebox) All the materials were characterized by PANalytical X'Pert and Rigaku Miniflex. Diffraction data was collected over a 2θ range of 5–85° for 1 h to facilitate phase identification. The obtained diffraction data were compared with appropriate reference patterns using the ICSD database via PowderCell or the ICDD PDF database via PANalytical HighScore Plus and Jade 6.5 software.^{13,14} Rietveld refinements were performed using the General Structure Analysis System (GSAS) with the EXPGUI interface.¹⁵

4.2.4 Raman spectroscopy

Raman spectroscopy was conducted at room temperature (Horiba LabRam HR confocal microscope; 325 nm UV laser, 100 µm aperture, 600 grooves/mm grating, Synapse CCD). Sealed glass capillaries were used to contain the sample.

4.3 Results and discussion

4.3.1 Thermal Treatment of NaAlH4

Figure 4-1 illustrates the comparison between NaAlH₄ as received and NaAlH₄ after 24 hours of ball milling. It can be observed that although the purity of the as-received NaAlH₄ is only 93%, no impurity peaks (such as NaOH) are detected in the PXD pattern. The impurity is possible to be inert impurity. Therefore, in subsequent experiments, the NaAlH₄: NaOH molar ratio was determined based on 1:0.93n (n = 1, 2, 3, 4). After 24 hours of ball milling, the NaAlH₄ peaks become broader because the particle size of NaAlH₄ is reduced. However, no additional peaks appear, indicating that no decomposition occurs. This confirms that at a milling speed of 400 rpm, NaAlH₄ remains stable and does not undergo

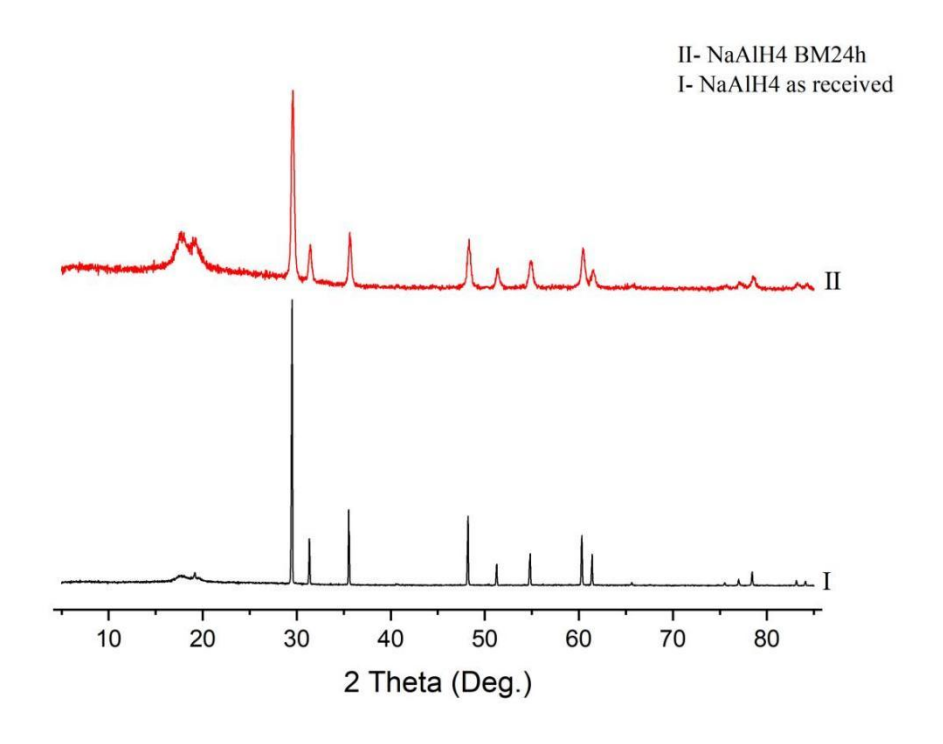


Figure 4-1: PXD pattern of ball-milled NaAlH₄ (24 h; I) and NaAlH₄ as-received (II).

According to Figure 4-2, the thermal decomposition of NaAlH₄ exhibits four DTA peaks at peak temperatures of 186 °C, 256 °C, 293 °C, and 373 °C. The first and third peak temperatures align with those reported in previous literature in Table 4-2. The fourth peak temperature closely matches the peak temperature observed for the decomposition of NaH (see Section 3.3). The total hydrogen mass loss is measured at 6.84 wt.%, which is close to the theoretical hydrogen mass loss of 6.88 wt.% for NaAlH₄ assuming 93 at.% purity. However, compared to NaAlH₄ reported in the previous literature, an additional peak was observed at 256 °C in the DTA analysis. Moreover, in the MS spectrum (Figure 4-3), only three peaks were detected, with the initial peak at 186 °C missing. While the mass loss in the final step is consistent with literature values, the mass losses in the first two steps do not match the reported values (3.7 wt.% and 1.9 wt.%). These discrepancies of mass loss and peak temperature will be analysed in the following sections.

Table 4-2: Comparison of NaAlH₄ As-received and As-reported Storage Performance

Parameter	NaAlH ₄ As-received	NaAlH4 As-reported
First Dehydrogenation Temperature /°C	186	180-190
Second Dehydrogenation Temperature /°C	256, 293	>260
Third Dehydrogenation Temperature /°C	373	>425
First Dehydrogenation Mass loss /wt.%	0.42	3.7
Second Dehydrogenation Mass loss /wt.%	4.84	1.9
Third Dehydrogenation Mass loss /wt.%	1.60	1.9
Total Dehydrogenation Mass loss /wt.%	6.84	7.5

To investigate this discrepancy, Figures 4-4 and 4-5 present PXD patterns of NaAlH₄ After heating in the TG-DTA to 180 °C, 200 °C, 220 °C, and 250 °C. The results indicate that NaAlH₄ remains unchanged up to 180 °C. At 200 °C, a small amount of Na₃AlH₆ begins to form, and at 250 °C, significant decomposition of NaAlH₄ occurs, leading to the formation of Na₃AlH₆. No additional peaks or intermediates are observed between 180 °C and 250 °C. This suggests that although NaAlH₄ begins to decompose around 186 °C, the decomposition and hydrogen release proceed at a very slow rate. The decomposition rate only increases significantly around 250 °C. The melting point of NaAlH₄ is reported to be 185 °C.16 Therefore, it can be inferred that the first peak at 186 °C corresponds to the melting of NaAlH₄, during which NaAlH₄ slowly decomposes into Na₃AlH₆ and Al, releasing hydrogen gas. The second peak at 256 °C represents the dehydrogenation reaction of NaAlH₄, where it decomposes into Na₃AlH₆ and Al. As the temperature increases, the reaction rate accelerates, leading to a faster release of hydrogen gas. A significant increase in the reaction rate is observed around 250 °C. The third peak at 293 °C corresponds to the dehydrogenation reaction of Na₃AlH₆, which decomposes into NaH and Al, releasing hydrogen gas. Additionally, a kink (small change in gradient) appears in the TG curve around 270 °C, indicating that the dehydrogenation reactions of both NaAlH₄ and Na₃AlH₆ are occurring simultaneously at this temperature. The fourth peak at 373 °C represents the dehydrogenation reaction of NaH, which decomposes into Na and H₂. This explains why the hydrogen mass loss in the first two steps of the dehydrogenation of NaAlH₄ differs, while the hydrogen mass loss in the third step is closer to the expected value. In the MS data shown in Figure 4-3, a peak is observed at 275 °C. This peak corresponds to the decomposition of NaAlH₄ into Na₃AlH₆. Therefore, the

decomposition mechanism of as-received NaAlH₄ follows the same pattern as described in the literature, but the decomposition temperatures are significantly higher. This discrepancy also suggests that the decomposition of NaAlH₄ and Na₃AlH₆ may occur simultaneously in the temperature range of 270–300 °C.

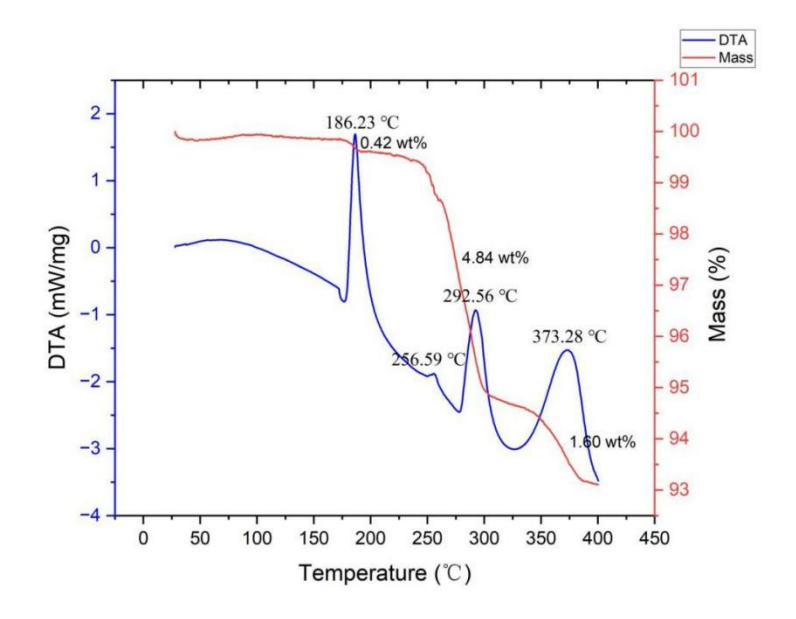


Figure 4-2: TG(red) and DTA(blue) profiles for ball-milled NaAlH₄ (24h, 400rpm) on heating from 35-400 °C at 5 °C min⁻¹ under flowing Ar(g).

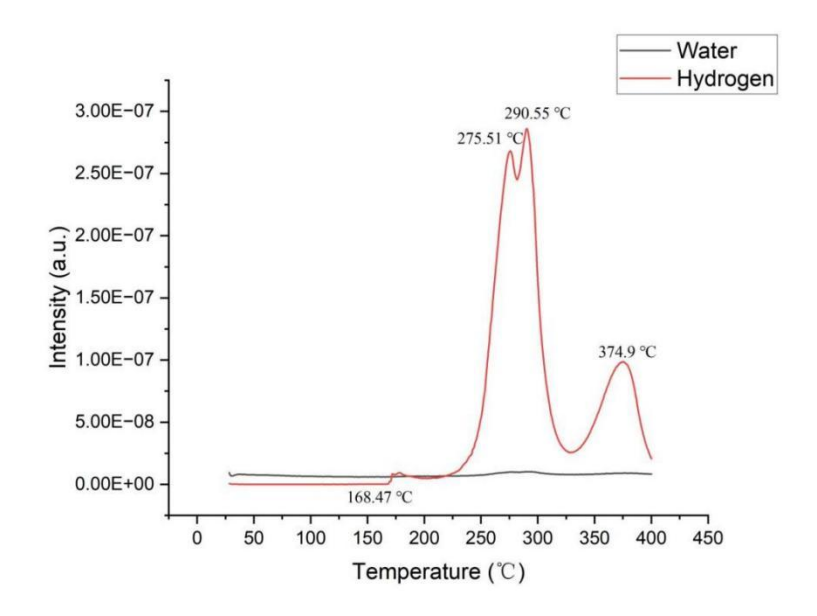


Figure 4-3: Mass spectrometry output for water (m/z = 18; black) and hydrogen (m/z = 2;red) as a function of temperature for ball-milled NaAlH₄ (24h, 400rpm) on heating from 35-400 °C at 5 °C min⁻¹ under flowing Ar(g).

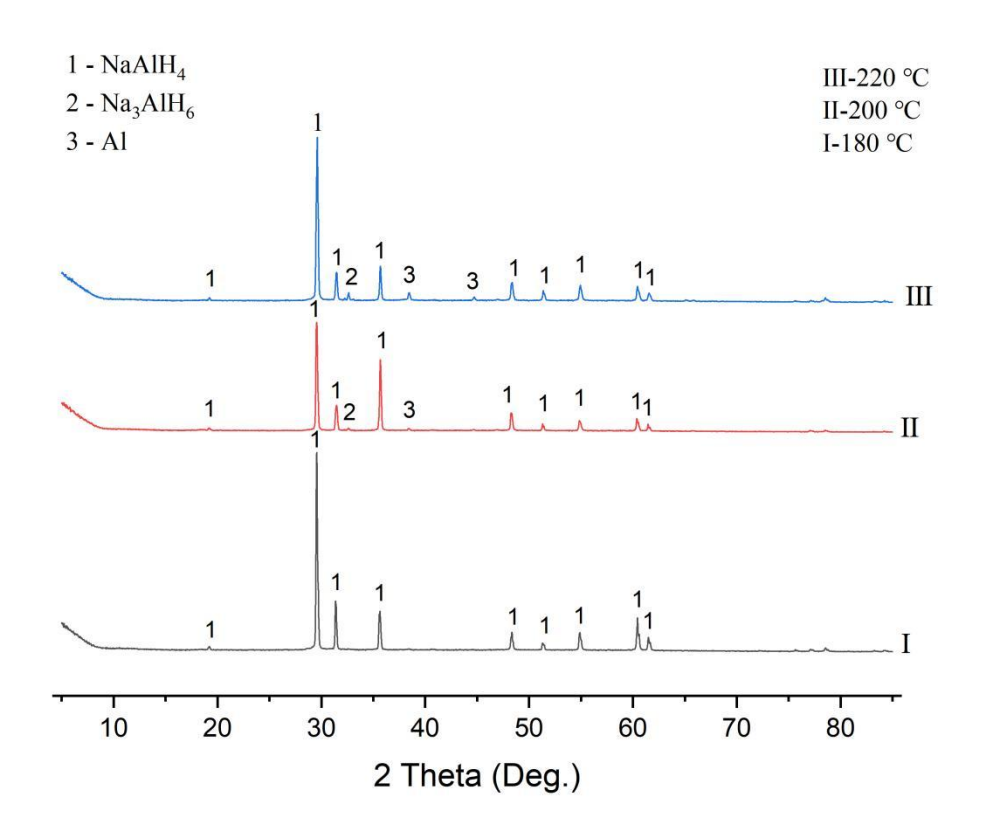


Figure 4-4: PXD patterns of ball-milled NaAlH₄ (24h, 400rpm) after heating to 180 (I), 200 (II) and 220 (III) °C under flowing Ar(g). (1 represent NaAlH₄; 2 represent Na₃AlH₆; 3 represent Al)

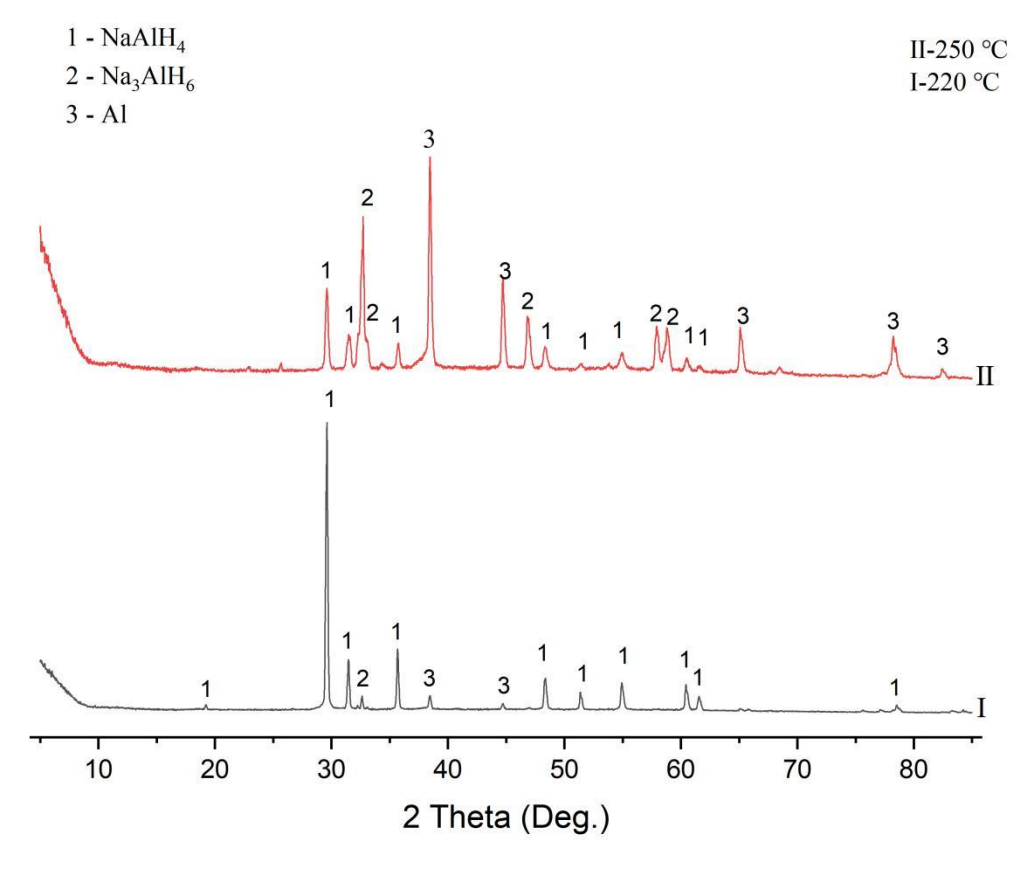


Figure 4-5: PXD patterns of ball-milled NaAlH₄ (24h, 400rpm) after heating to 220 (I) and 250 (II) under flowing Ar(g). (1 represent NaAlH₄; 2 represent Na₃AlH₆; 3 represent Al)

4.3.2 Thermal Treatment of Al and NaOH

To ensure that no side reactions occur throughout the process of NaAlH₄ and NaOH, the interaction between Al (the side product from the alanate dehydrogenation reaction) and the potential starting material, NaOH was investigated. Al and NaOH can react with moisture in the air at room temperature to form NaAlO₂ and H₂.¹⁷ Therefore, it is crucial to confirm that Al and NaOH do not react before 450 °C in an argon atmosphere.

The DTA curve of the "hand mixed" NaOH-Al mixture(Figure 4-6) exhibits peaks similar to those observed for the decomposition of NaOH alone, specifically around 295 °C and 315 °C.(Figure 3-4) According to previous section 3.3.1, this indicates that no additional reactions occur. Furthermore, the MS data in Figure 4-7 show no formation of H₂ or water below 450 °C, and the PXD patterns before and after heating remain similar, with no additional peaks appearing (Figure 4-8). In conclusion, NaOH and Al do not undergo any reaction under these conditions.

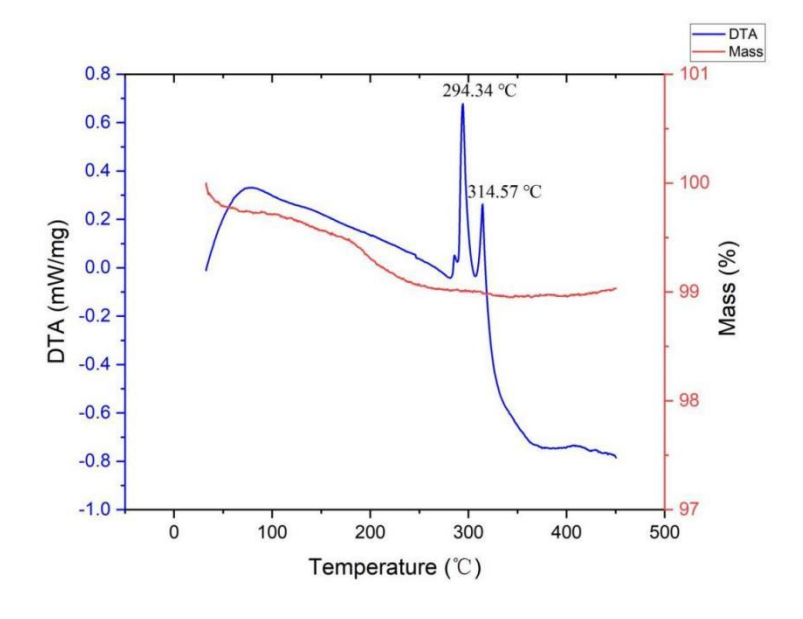


Figure 4-6: TG(red) and DTA(blue) profiles for hand mixed 1:1 NaOH:Al on heating from 35-450 °C at 5 °C min⁻¹ under flowing Ar(g).

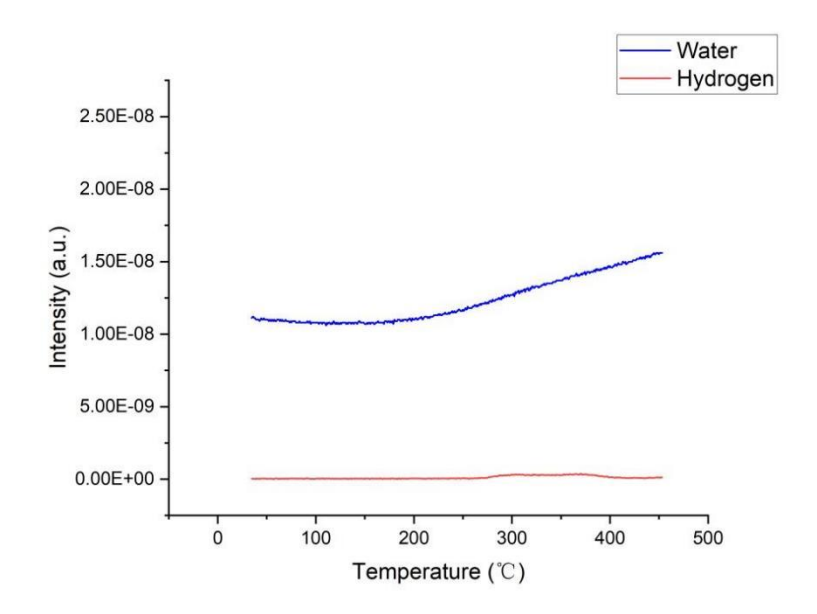


Figure 4-7: Mass spectrometry output for water (m/z = 18; black) and hydrogen (m/z = 2;red) as a function of temperature for hand mixed 1:1 Al:NaOH on heated from 35-450 $^{\circ}$ C at 5 $^{\circ}$ C min⁻¹ under flowing Ar(g).

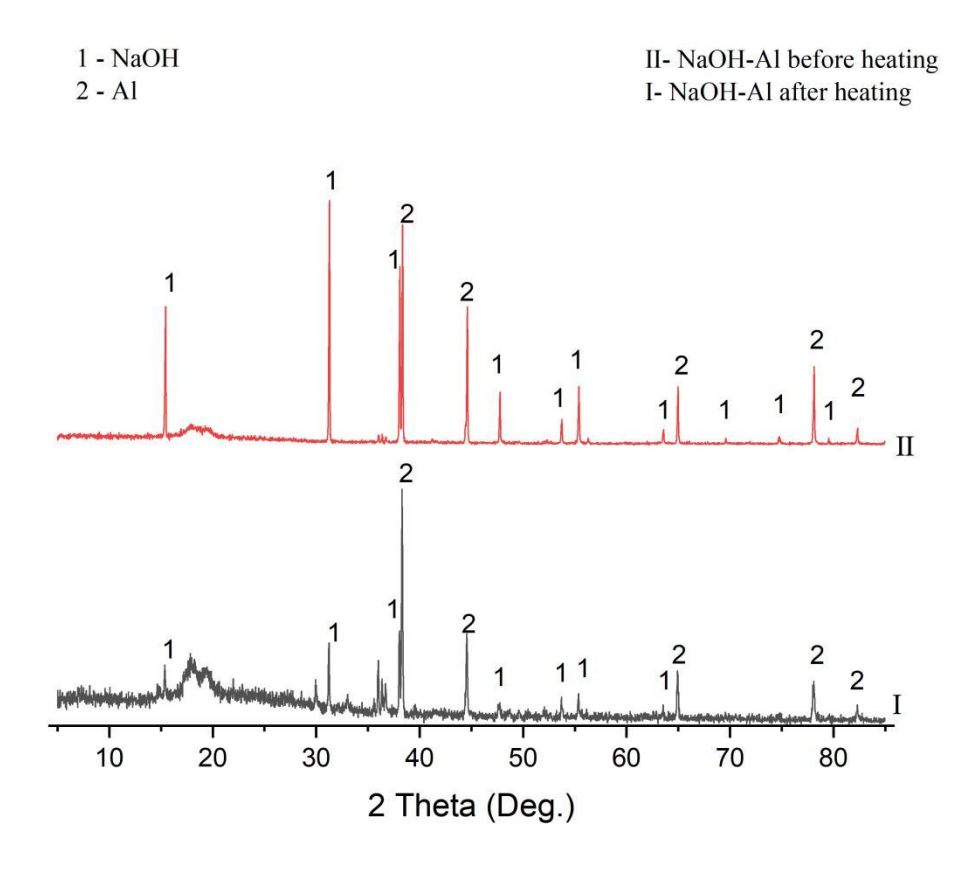


Figure 4-8: PXD patterns of hand mixed 1:1 NaOH:Al before (II) and after (I) heating to 450 °C under flowing Ar(g). (1 represent NaOH; 2 represent Al)

4.3.3 Thermal Treatment of Hand-mixed NaAlH₄-NaOH and Mechanism Research

From Figure 4-9, the TG-DTA data for the hand-mixed NaAlH₄: NaOH mixture show

three peaks at 185 °C, 270 °C, and 386 °C, respectively. Compared to the decomposition of NaAlH₄ alone, the first thermal event has apparently changed from an endothermic to an exothermic process, whereas the temperature of the second event has decreased from 290 °C to 270 °C. However, the temperature of the third reaction has not changed significantly and even increased, with 386 °C being very close to the 380 °C expected for The observation indicates that NaH remains in the sample at high NaH dehydrogenation. temperature. A small inflection is observed at 182 °C on the DTA curve, preceding the first peak at 185°C. This is related to the previously reported melting point of NaAlH₄ at 180 °C. Therefore, it can be inferred that NaAlH₄ first undergoes an endothermic melting process before the exothermic reaction occurs. Additionally, between 320 °C and 380 °C, a small inflection is noted on the DTA curve around 350 °C. It's feasible that some of the NaOH might have reacted with the NaH. The hydrogen mass loss at each step is approximately 3.42 wt.%, 0.49 wt.%, and 1.09 wt.%, respectively, with the total hydrogen mass loss being approximately 5 wt.%. From the MS data in Figure 4-10, the only gas released is hydrogen. The theoretical hydrogen mass loss is also 5.00 wt.%. Therefore, all the hydrogen in NaOH and NaAlH₄ is released as hydrogen gas. However, according to the proposed reactions shown in section 4.1.2 (equations 4, 5, and 6), the theoretical mass losses for the three-step reaction should be 2.13 wt.%, 1.09 wt.%, and 1.78 wt.%, respectively. Although complete dehydrogenation is apparently achieved, the process does not follow the expected reaction mechanism.

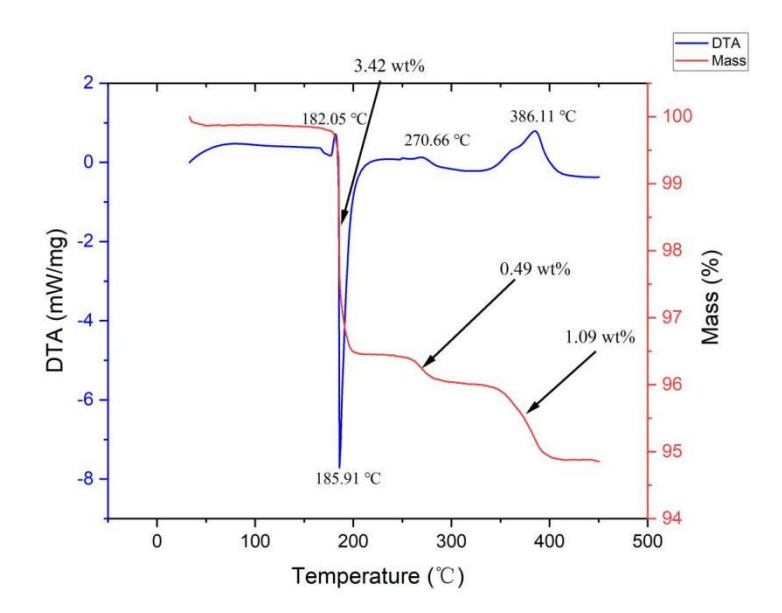


Figure 4-9: TG(red) and DTA(blue) profiles for hand mixed 1:1 NaAlH₄:NaOH on heating from 35-450 °C at 5 °C min⁻¹ under flowing Ar(g).

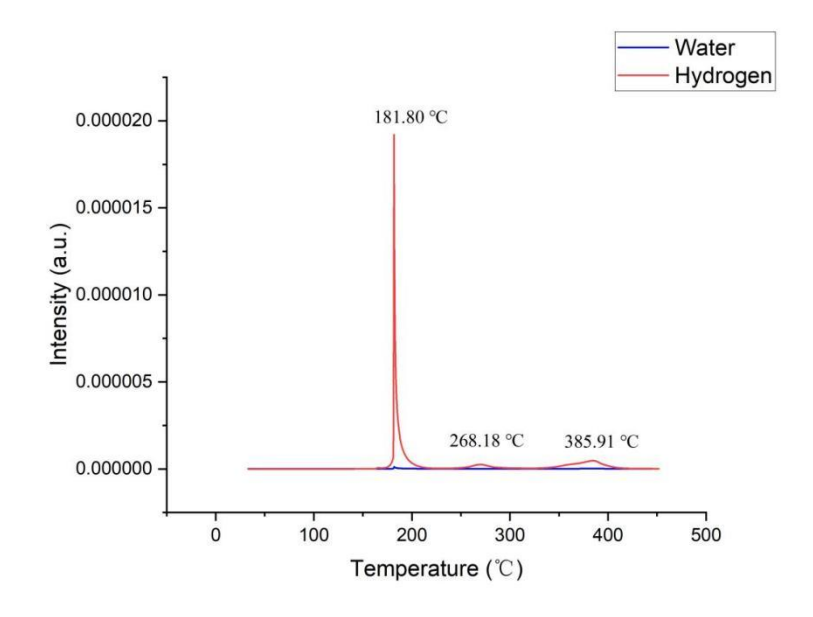


Figure 4-10: Mass spectrometry output for water (m/z = 18; black) and hydrogen (m/z = 2;red) as a function of temperature for hand mixed 1:1 NaAlH₄:NaOH on heating from 35-450 °C at 5 °C min⁻¹ under flowing Ar(g).

Figure 4-11 shows the PXD patterns of the hand-mixed NaAlH₄-NaOH after heating to 175 °C, 185 °C, and 300 °C (and cooling). The DTA line in Figure 4-9 show a sharp peak at 186 °C between 175 °C and 210 °C. From 175 °C to 185 °C, the peaks of NaAlH₄ begin to disappear, and Na₃AlH₆ starts to form in large quantities. The peaks of NaOH do not change, indicating that NaOH did not participate in the reaction of NaAlH₄ decomposing into Na₃AlH₆. However, at 300 °C, the NaOH peaks decreased considerably, suggesting much of the NaOH has probably reacted. When Na₃AlH₆ has apparently completely reacted, NaOH still remains at 300 °C. When the temperature reaches 450 °C in the Figure 4-12, the final products are Na and Al, accompanied by a small amount of unknown peaks, with no Na₂O or NaOH present. Unless the unknown peaks correspond to an oxygen-containing phase, then O must also have been lost in the decomposition (either as O₂ and/or as H₂O), which should increase the mass loss above 5 wt.% if all H is also lost. Therefore, NaOH did not react with NaH as initially expected in reaction (6). However, since NaOH does not remain at 450 °C and has already significantly decreased by ca. 300 °C, and based on previous validation that NaOH does not react with Al alone, it is highly likely that some other combination of NaH, NaOH, and Al are reacting together.

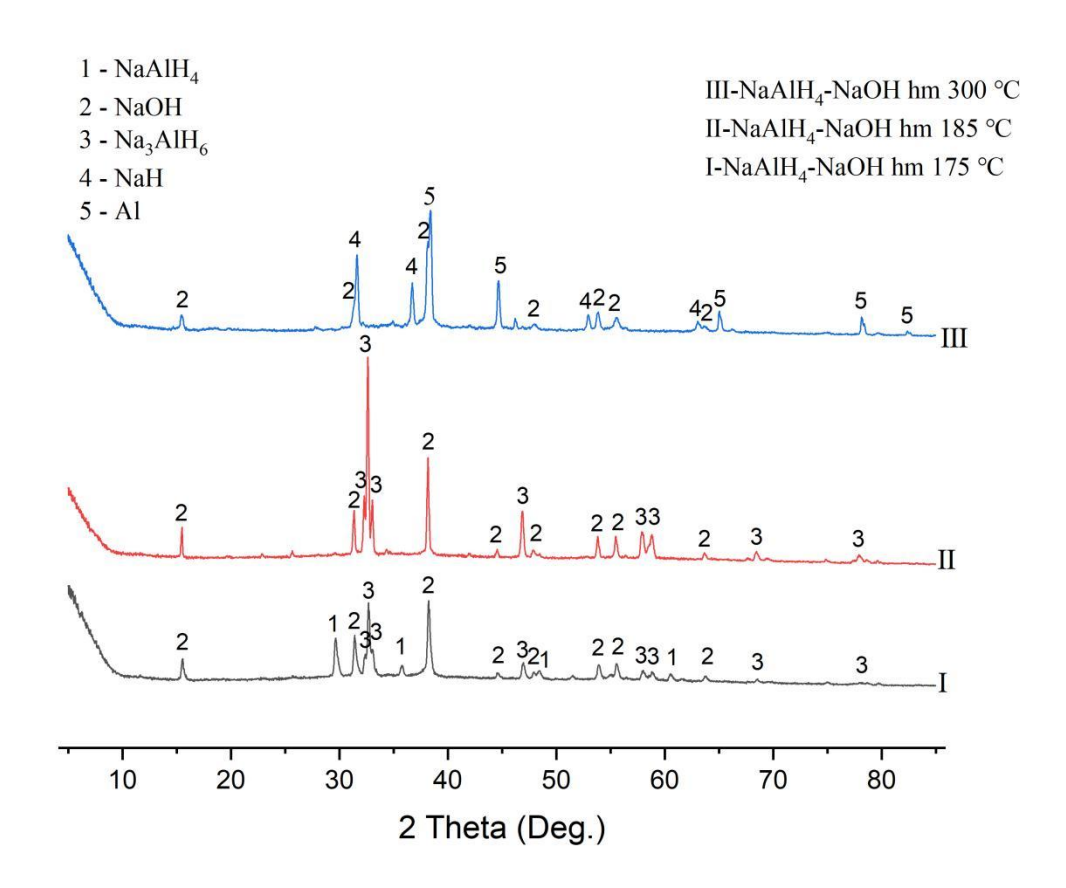


Figure 4-11: PXD patterns of hand mixed 1:1 NaAlH4:NaOH after heating to 175 (I), 185 (II) and 300 (III) °C under flowing Ar(g). (and cooling to room temperature). (1 represent NaAlH₄; 2 represent NaOH; 3 represent Na₃AlH₆; 4 represent NaH; 5 represent Al)

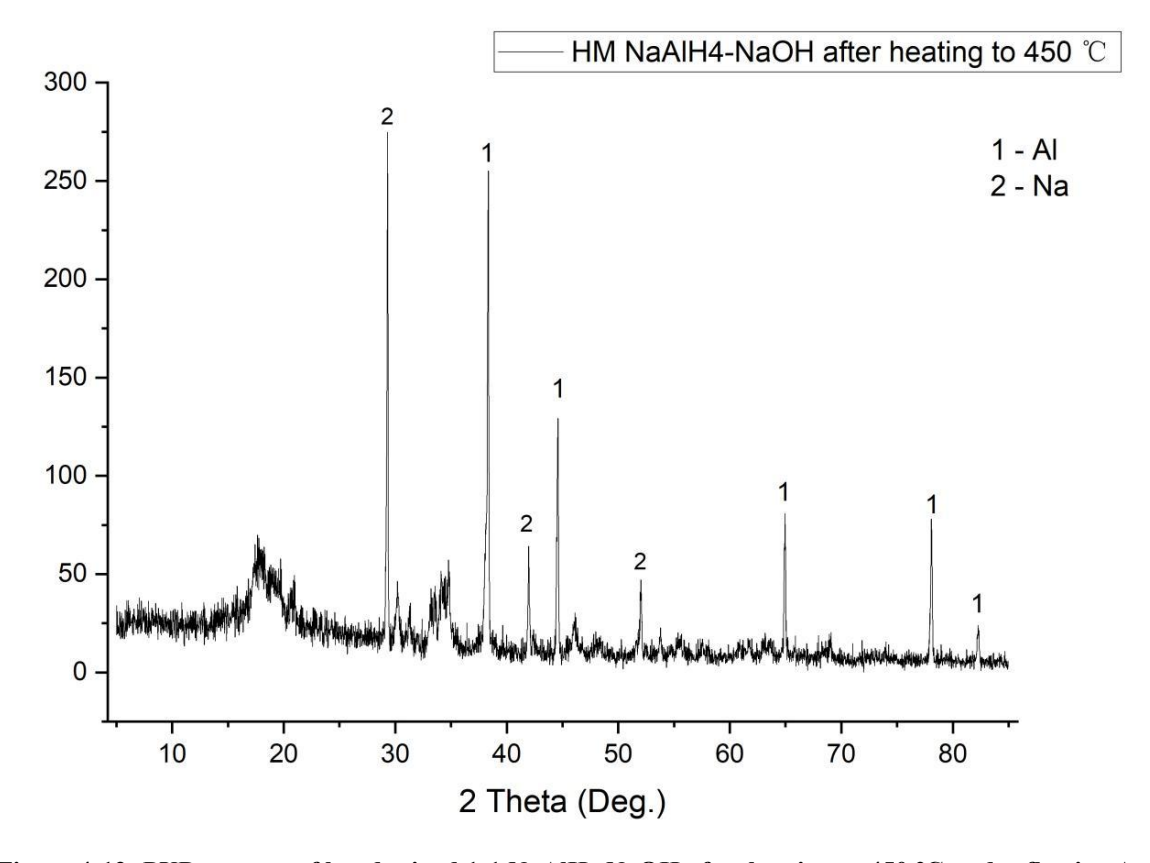


Figure 4-12: PXD pattern of hand mixed 1:1 NaAlH₄:NaOH after heating to 450 $^{\circ}$ C under flowing Ar(g) (and cooling to room temperature). (1 represent Al; 2 represent Na). Appendix A4-1 show the PXD patterns for the sample compared to stardard patterns from ICSD.

Due to the previous individual reaction of NaH, it suggests that the amount of NaOH was insufficient. This suggests that if any NaOH were present in excess, it would react with NaH to form Na₂O. However, no peak corresponding to Na₂O is observed in Figure 4-12. This indicates that the amount of NaOH was insufficient for the reaction. As a result, the molar ratio of NaAlH4 to NaOH in the reaction was not 1:1 due to the complete consumption of NaOH. Therefore, additional NaOH was introduced, and its TG-DTA analysis along with the PXD of the product after heating were conducted to infer the reaction mechanism. Therefore, Figures 4-13 and 4-14 show the thermal performance of NaAlH4:NaOH 1:4 dehydrogenation hand-mixed reaction. dehydrogenation reactions exhibit differences in their exothermic and endothermic characteristics. For the 1:1 NaAlH₄:NaOH mixture, the first dehydrogenation peak at 186 °C is exothermic, while the subsequent two peaks are endothermic. In contrast, all three peaks in the dehydrogenation reaction of the 1:4 NaAlH₄:NaOH mixture are exothermic.

$$NaAlH_4 + 4NaOH = 1/3 Na_3AlH_6 + 2/3Al + H_2 + 4NaOH$$
 (7)

Theoretical mass loss = 0.93 wt.%

The slope of the TG curve undergoes a change between 270 °C and 300 °C. This indicates that the second and third steps of the reaction, which occur within this temperature range, proceed simultaneously.

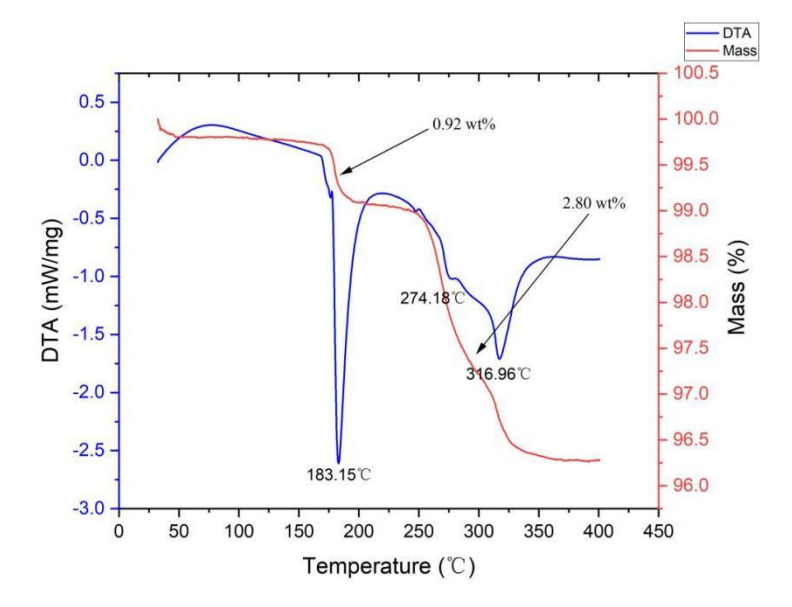


Figure 4-13: TG(red) and DTA(blue) profiles for hand mixed 1:4 NaAlH₄:NaOH on heating from 35-400 °C at 5 °C min⁻¹ under flowing Ar(g).

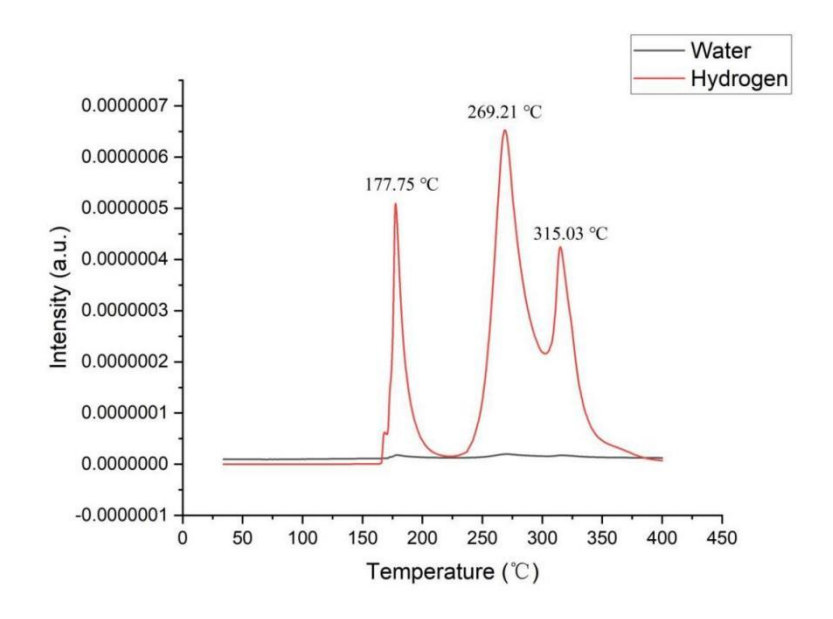


Figure 4-14: Mass spectrometry output for water (m/z = 18; black) and hydrogen (m/z = 2; red) as a function of temperature for hand mixed 1:4 NaAlH₄:NaOH on heating from 35-400 °C at 5 °C min⁻¹ under flowing Ar(g).

To verify the reaction occurring at the third peak temperature in the NaAlH₄-4NaOH mixture, ex situ PXD patterns were taken after heating to 200 °C, 300 °C, and 400 °C (and cooling to room temperature in each case). These are shown in Figures 4-15, 4-16, and 4-17, respectively. When heated to 200 °C, NaAlH₄ decomposes into Na₃AlH₆, and NaOH still remains in large quantities. No additional peaks are generated, indicating that neither NaAlH₄ nor Na₃AlH₆ reacts with NaOH. Upon heating to 300 °C, PXD Figure 4-16 clearly shows the peaks corresponding to Al, NaOH, and NaH. However, there are some additional peaks at approximately 35° and 42° that cannot be readily identified due to their complex and noisy nature, as well as their relatively low intensity. Therefore, the identification of these peaks can only be aided by examining the sample heated to 400°C, as these may correspond to the formation of certain compounds. Upon heating to 400 °C and cooling, the final product, compared with the ICSD database, is identified as Na₅AlO₄. Therefore, the reaction mechanism for the final step is $NaH + Al + 4NaOH \Rightarrow Na_5AlO_4 +$ 5/2H₂. In the previous PXD Figure 4-12, an unidentifiable phase was also observed between 32° and 35°, which closely resembles Na₅AlO₄. Therefore, it is highly likely that the 1:1 NaAlH₄:NaOH and 1:4 NaAlH₄:NaOH mixtures underwent similar reactions. This similarity in reaction pathways likely led to the insufficient amount of NaOH, allowing NaH to undergo its own decomposition reaction at 380 °C. Phase of Na₅AlO₄ in PXD figure is abundant, the small amount of Na₅AlO₄ generated cannot be detected in the PXD Figure 4-16 by software, as seen in the pattern at 300°C, where Na₅AlO₄ is already present but not clearly visible. Therefore, the total mechanism was shown below:

$$NaAlH_4 + 4NaOH = 1/3Na_3AlH_6 + 2/3Al + H_2 + 4NaOH$$
 (7)

Theoretical mass loss = 0.93 wt.%

$$1/3Na_3AlH_6 + 4NaOH = NaH + 1/3Al + 1/2H_2 + 4NaOH$$
 (8)

Theoretical mass loss = 0.46 wt.%

$$NaH + Al + 4NaOH = Na5AlO4 + 5/2H2$$
 (9)

Theoretical mass loss = 2.31 wt.%

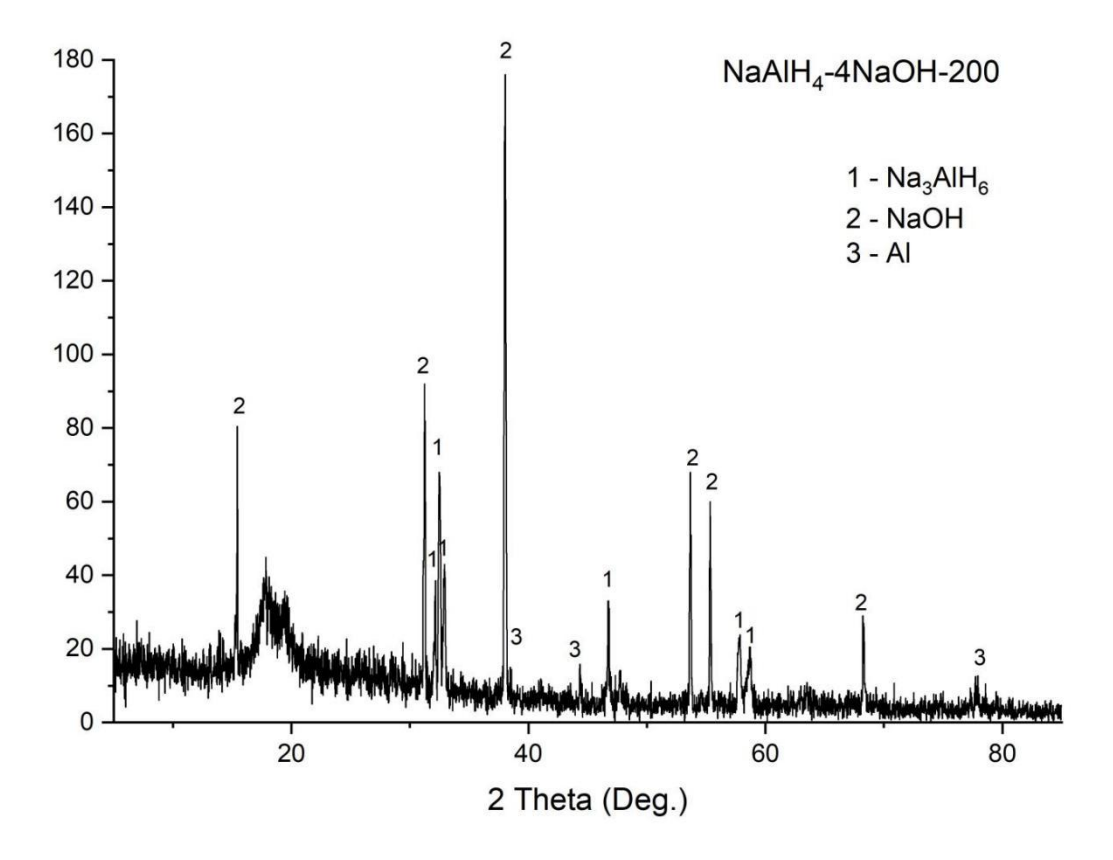


Figure 4-15: PXD pattern of hand mixed 1:4 NaAlH₄:NaOH after heating to 200 °C under flowing Ar(g) (and cooling to room temperature). (1 represent Na₃AlH₆; 2 represent NaOH; 3 represent Al)Appendix A4-2 show the PXD patterns for the sample compared to stardard patterns from ICSD.

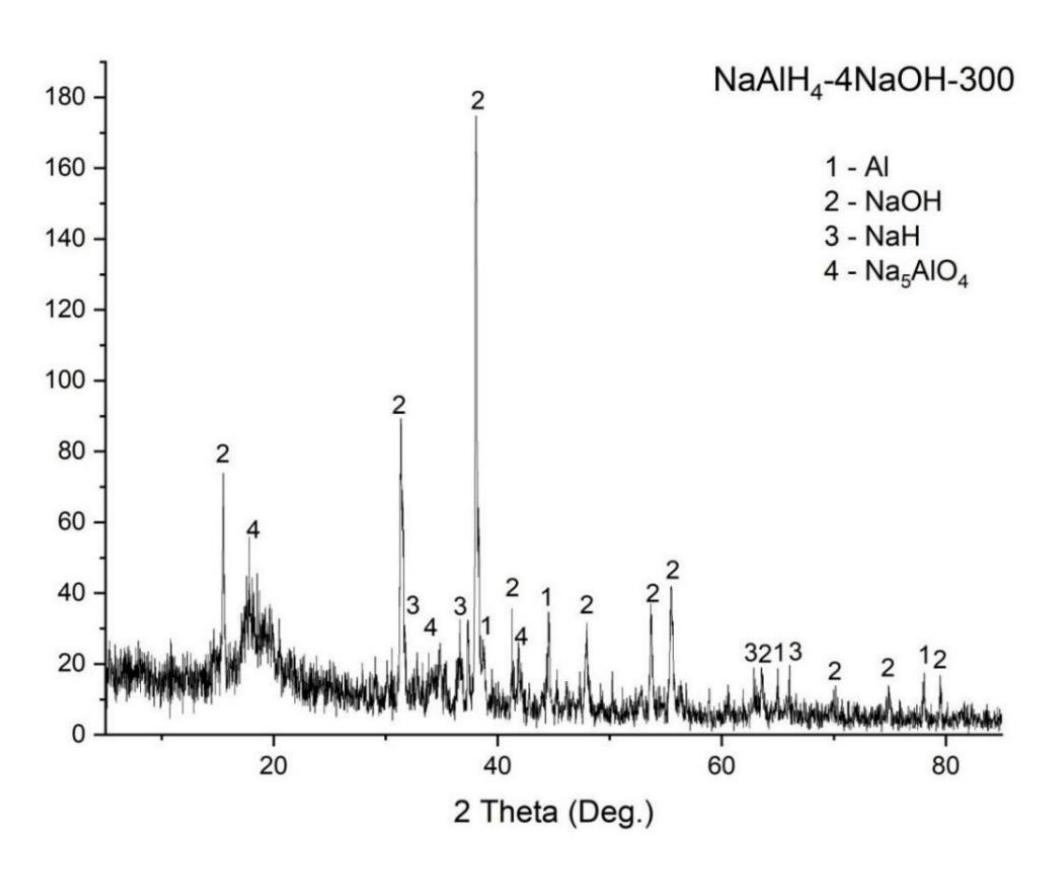


Figure 4-16: PXD pattern of hand mixed 1:4 NaAlH₄:NaOH after heating to 300 °C under flowing Ar(g) (and cooling to room temperature). (1 represent NaOH; 2 represent Na₅AlO₄) Appendix A4-3 show the PXD patterns for the sample compared to stardard patterns from ICSD.

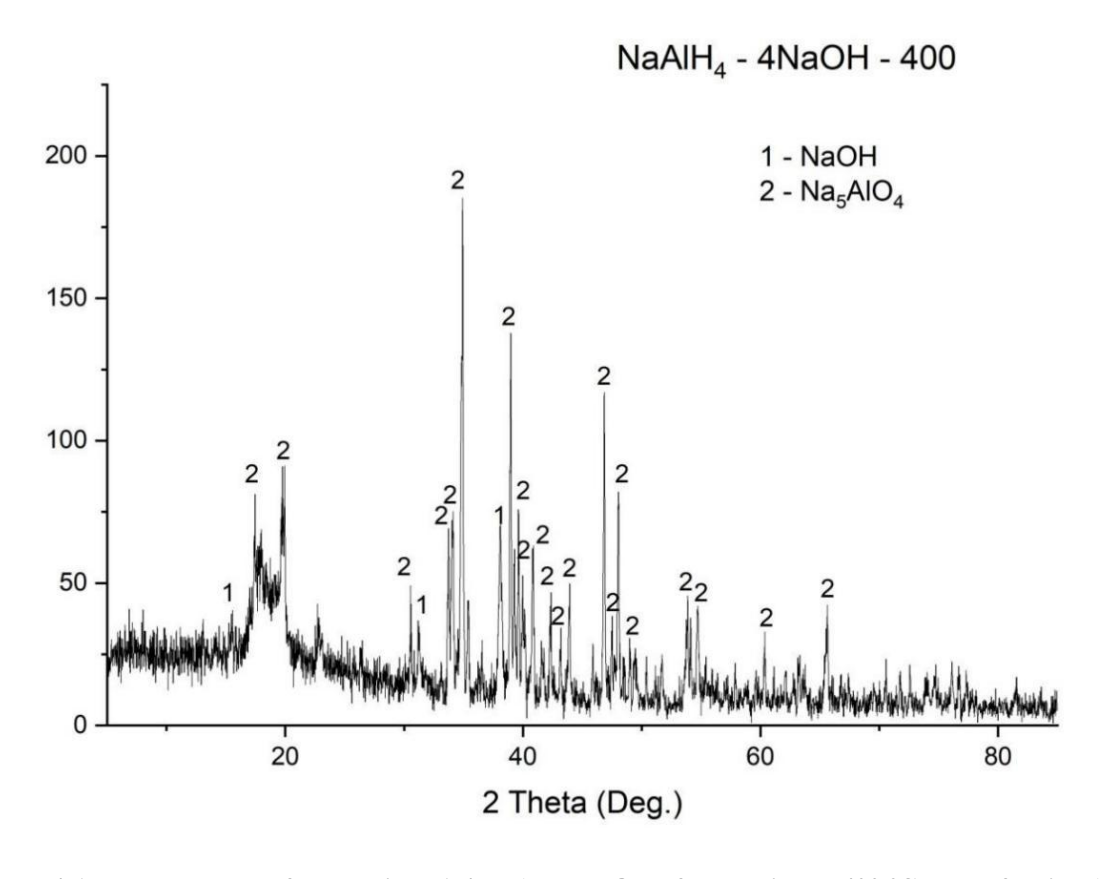


Figure 4-17: PXD pattern of hand mixed 1:4 NaAlH₄:NaOH after heating to 400 °C under flowing Ar(g) (and cooling to room temperature). (1 represent Al; 2 represent NaOH; 3 represent NaH; 4 represent Na₅AlO₄) Appendix A4-4 show the PXD patterns for the sample compared to stardard patterns from

ICSD.

Although the mechanism of the hand-mixed NaAlH₄-NaOH system has been investigated, there remains one unresolved issue: the first reaction step of NaAlH4 with NaOH changes from an endothermic to an exothermic reaction. XRD verification seems to suggest that NaOH does not react directly with NaAlH₄. Therefore, there are three possible explanations. The first is that NaOH acts as a catalyst for NaAlH₄. The second is that NaOH reacts with NaAlH₄ to form an intermediate phase, but this state is unstable or cannot be detected by XRD. The third possibility is that there is an interaction between protonic hydrogen (H^{δ+}) and hydridic hydrogen (H^{δ+}) in NaOH and NaAlH₄, which lowers the energy barrier and activation energy.

Table 4-3 shows the activation energies of the first two steps for NaAlH₄, hand-mixed NaAlH₄-NaOH, and hand-mixed 1:4 NaAlH₄:NaOH. The detailed calcualtion step is present on Appendices from A4-5 to A4-13. From these results, it is clear that after adding 1 mol of NaOH, the activation energy of the first step is reduced by approximately half. Furthermore, the activation energy of the second step is also reduced. In the TG-DTA pattern for the NaAlH₄-4NaOH sample (Figure 4-13), a small concave shape is observed around 270°C, indicating that this reaction has become exothermic.

Based on the activation energy calculations, one cannot be sure with hand mixing that each component is not reacting independently (to some extent) and that milling should remove this possibility. Based on the previous experimental results, we obtained reactions 7, 8 and 9. However, these still fail to explain why the reaction transitions from endothermic to exothermic, despite the reduction in activation energy. This may be due to a reaction occurring between NaOH and NaAlH₄ at around 180 °C. Therefore, the next step is to use ball milling to further validate the potential reactions between NaAlH₄ and NaOH.

Table 4-3: Activation energies (determined by the Kissinger method) of NaAlH₄, hand-mixed NaAlH₄-NaOH and hand-mixed NaAlH₄-4NaOH

DTA heat rate / °C min ⁻¹	First peak / °C	Second peaks	Activation energy / kJ mol ⁻¹
NaAlH4-2 °C/min	182.32	273.51	
5°C/min	186.73	292.56	First: 309.95±12.61
10°C/min	191.28	297.59	Second: 165.65±24.03
20°C/min	194.93	308.23	
1:1 NaAlH ₄ -NaOH-2 °C/min	179.54	255.19	F' 4 140 21 110 14
5 °C/min	185.91	270.66	First: 148.21±18.14 Second: 112.31±7.05
10 °C/min	194.82	288.99	Second. 112.31±7.03
20 °C/min	205.35	301.52	
1:4 NaAlH ₄ -4NaOH- 2 °C/min	176.78	244.86	F' + 124.05+21.46
5°C/min	183.15	269.21	First: 134.85±21.46 Second: 99.10±9.23
10 °C/min	191.65	278.78	Second: 99.10±9.23
20°C/min	204.71	298.18	

4.3.4 Ball-milling NaAlH₄ with Differenct Molar Ratios of NaOH

4.3.4.1 Mechanism Research of Ball-milling with different molar ratio of NaAlH₄:NaOH

In the preceding sections, the reaction mechanism of NaAlH₄ and NaOH when hand-mixed was described. However, under ball-milling conditions, different reactions occur. Therefore, in this chapter, the reaction mechanisms are investigated by comparing the PXD patterns of products obtained from various molar ratios of NaAlH₄:NaOH after ball milling and subsequent heating to 400 °C.

Since the hand-mixed 1:1 NaAlH₄-NaOH system undergoes an exothermic reaction, it is possible that NaAlH₄-NaOH could react that the milling process could provide the

necessary activation energy to initiate the exothermic reaction. To verify this hypothesis, 1:1 NaAlH₄:NaOH samples were ball-milled for 2 hours, 4 hours, and 10 hours. The respective PXD patterns are shown in Figure 4-18. When a 1:1 sample was ball-milled for 2 h, partial decomposition of NaAlH₄ into Na₃AlH₆ was seen to begin. The phases of Na₃AlH₆ at 33°, 47°, and 58° are broad rather than sharp, which is significantly different from the peaks of Na₃AlH₆ observed in the previous PXD Figure 4-15. Additionally, the relative intensity of NaOH is notably weaker compared to that of NaAlH₄. After ball milling for 4 hours, the peaks of NaOH decreased, and the peaks of NaAlH₄ significantly diminished, while Na₃AlH₆ began to form in large quantities. After ball milling for 10 hours, only the peaks of Na₃AlH₆ remained, and they broadened. Since the 1:1 NaAlH₄:NaOH mixture only exhibited the phase of Na₃AlH₆ after 6 hours of ball milling, to investigate whether the amount of NaOH affects NaAlH₄, a mixture of 1:0.5 NaAlH₄:NaOH was also ball-milled for 10 hours. For the 2:1 NaAlH₄:NaOH sample, after ball milling for 10 hours, the NaOH peaks disappeared, but NaAlH₄ was still present. The Na₃AlH₆ phase also broadened.

To identify the compounds or functional groups present in the 1:1 NaAlH₄:NaOH mixture after 10 hours of ball milling, Raman spectra were compared for NaAlH₄ as received, NaOH after drying, and the 1:1 NaAlH₄:NaOH mixture. In the Raman spectra (Figure 4-19), peaks corresponding to Na₃AlH₆ were observed at 1568, 1158, 1060 and 961 cm⁻¹. According to Yukawa et al's article, in the Raman spectrum of Na₃AlH₆, the main peaks are observed at 1556 cm⁻¹ and 1152 cm⁻¹, corresponding to the symmetric and antisymmetric stretching vibrations of the Al–H bonds, respectively.¹⁸ Additionally, peaks around 1562 cm⁻¹, 1114 cm⁻¹, and 987 cm⁻¹ are identified, which are associated with the stretching and bending vibrations of hydrogen in Na₃AlH₆. These results highlight the distinct vibrational characteristics of the six-coordinated [AlH₆]³⁻ complex anion in Na₃AlH₆.

Currently, two issues remain. The first is that the Al phases in Figure 4-18 for reaction 7 of 1:1 NaAlH4:NaOH is absent. The second is that, based on previous PXD analysis in Figure 4-11 and 4-15, NaOH does not react with NaAlH4, but after ball milling for 10h, the NaOH peaks of 1:1 NaAlH4:NaOH disappears. The formation of broad peaks corresponding to Na₃AlH₆ is likely due to the reaction between NaOH and NaAlH₄, resulting in the formation of an intermediate compound Na₃AlH_{6-x}(OH)_x. Further verification is required.

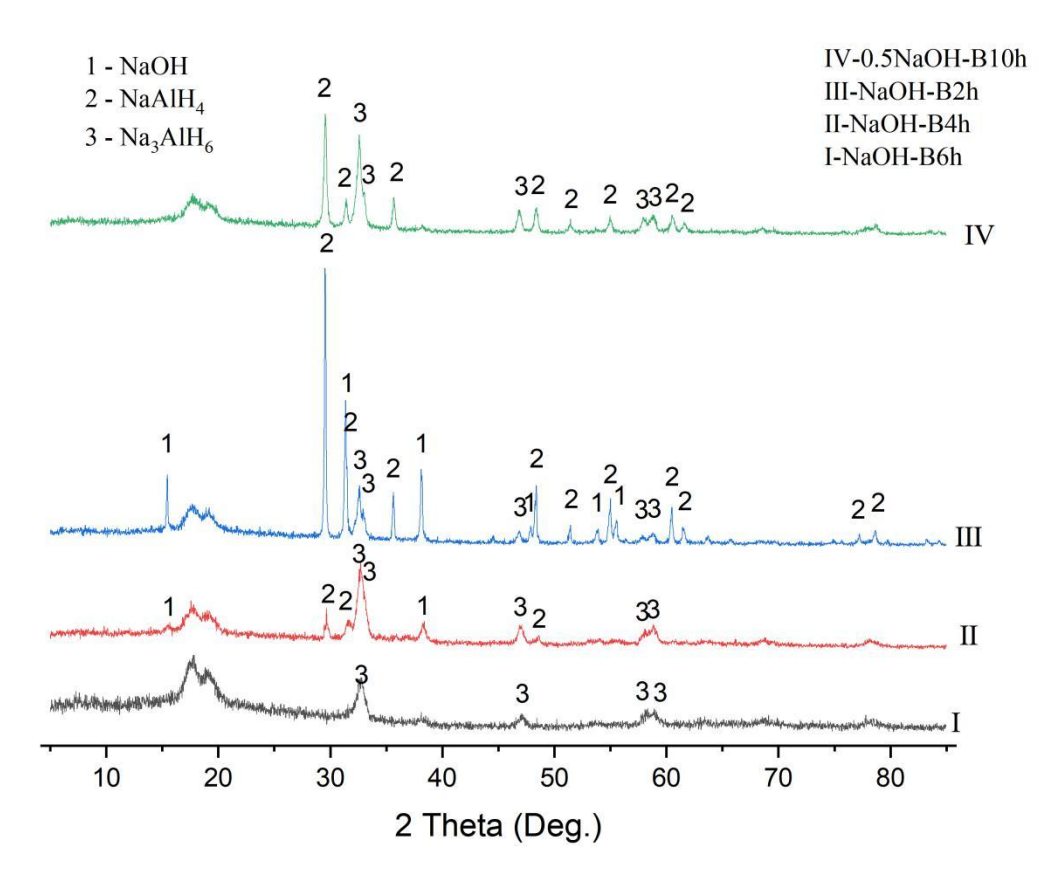


Figure 4-18: PXD patterns of ball-milled 1:0.5 NaAlH₄:NaOH(10h, 400rpm; IV) and 1:1 NaAlH₄:NaOH (2h, III; 4h, II; 10h, I). (1 represent NaOH; 2 represent NaAlH₄; 3 represent Na₃AlH₆)

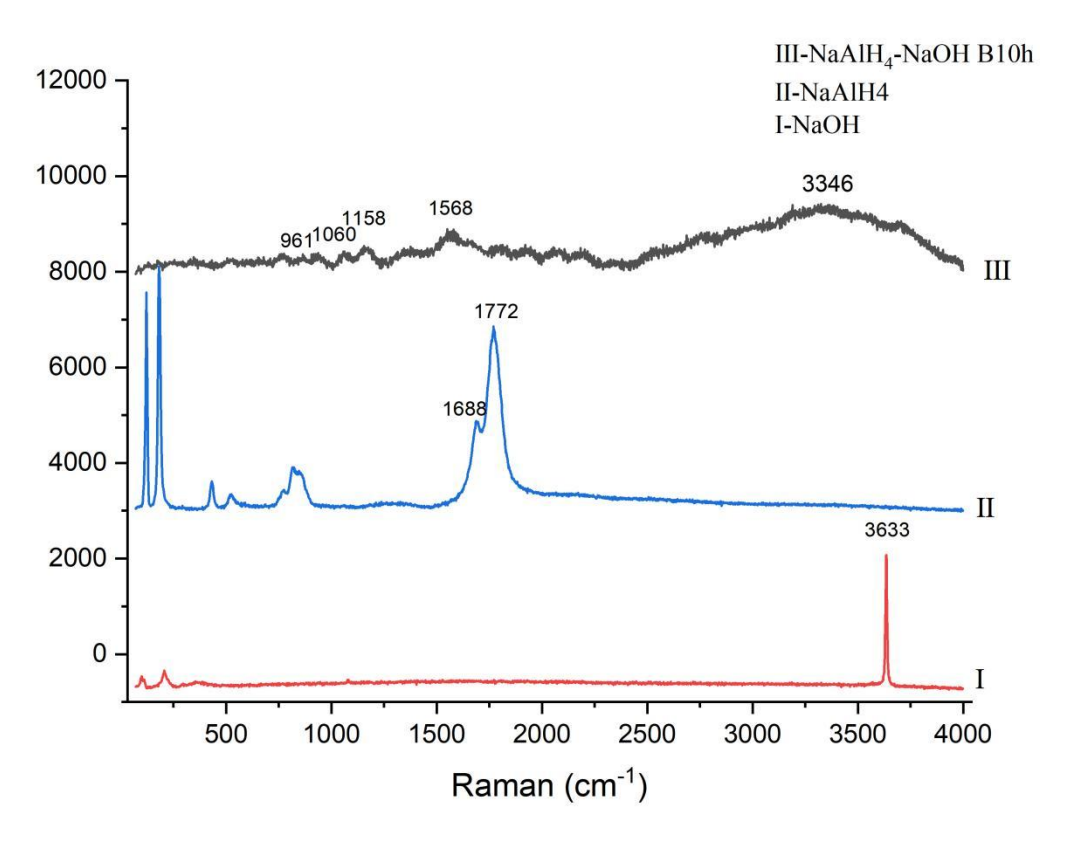


Figure 4-19: Raman spectra of NaAlH₄ (III), NaOH (II) and ball-milled 1:1 NaAlH₄:NaOH (10h, 400 rpm; I).

To investigate whether a small amount of NaOH, acting as an additive, can facilitate the reaction of NaAlH₄. Figure 4-20 shows the PXD patterns of molar ratio of 10:3 NaAlH4:NaOH mixture that has been ball milled for 10 h, and subsequently heated to either 185 °C or 300 °C. From the addition of 0.3NaOH to 1NaOH, it can be observed that the peaks corresponding to NaAlH₄ gradually decrease after ball milling and upon heating to 185 °C and 300 °C, accompanied by the formation and relative intensity increase of the broad Na₃AlH₆ peaks. Based on the previous Figure 4-18, the peaks of NaOH disappeared after 10 hours of ball milling in both the 1:0.5 NaAlH₄:NaOH and 1:1 NaAlH₄:NaOH mixtures. Similarly, in the 1:0.3 NaAlH₄:NaOH mixture after 10 hours of ball milling, the NaOH peaks also vanished. Therefore, the disappearance of NaOH can be attributed to the completion of the reaction between NaAlH4 and NaOH. Given these observations, it is possible that the reaction between NaAlH₄ and NaOH initially forms a Na-Al-H-OH phase, which subsequently decomposes into sodium hydroxide and one or more hydrides. These intermediates then further transform into NaH and Al at higher temperatures, eventually yielding Na and Al. According to the previous Raman Figure 4-19, the intermediate phase is likely to be Na₃AlH_{6-x}(OH)_x, as it exhibits distinct vibrational characteristics of the six-coordinated [AlH₆]³⁻ structure. However, verifying this intermediate phase is challenging due to its broad peaks, which make it difficult to refine using GSAS software to determine its possible content. This situation is similar to the case of NaOH and NaH, where the OH⁻ "dissolves" into the hydride structure, forming a hydride-hydroxide solid solution.

The previous experiments described the effect of a small amount of NaOH on the reaction of NaAlH₄ after ball milling. Next, the aim is to investigate whether a larger quantity of NaOH can further promote the reaction of NaAlH₄ under ball-milling conditions. From Figure 4-21, it is clear that when the molar ratio of NaAlH₄ to NaOH reaches 1:2 and milling time reach 2h and 4h, there is again a noticeable NaOH and NaH peak. This observation differs from the previously described 1:1 NaAlH₄:NaOH case, where the relative intensity of the intermediate phase Na₃AlH_{6-x}(OH)_x begins to decrease gradually from 2 to 4 hours of ball milling. This indicates that Na₃AlH_{6-x}(OH)_x further decomposes into NaH and NaOH with extended ball-milling time. According to the previous Table 4-2, the activation energy for the second reaction step (Reaction 8) is reduced when more NaOH is added. Therefore, the addition of NaOH during ball milling can facilitate the decomposition of Na₃AlH_{6-x}(OH)_x.

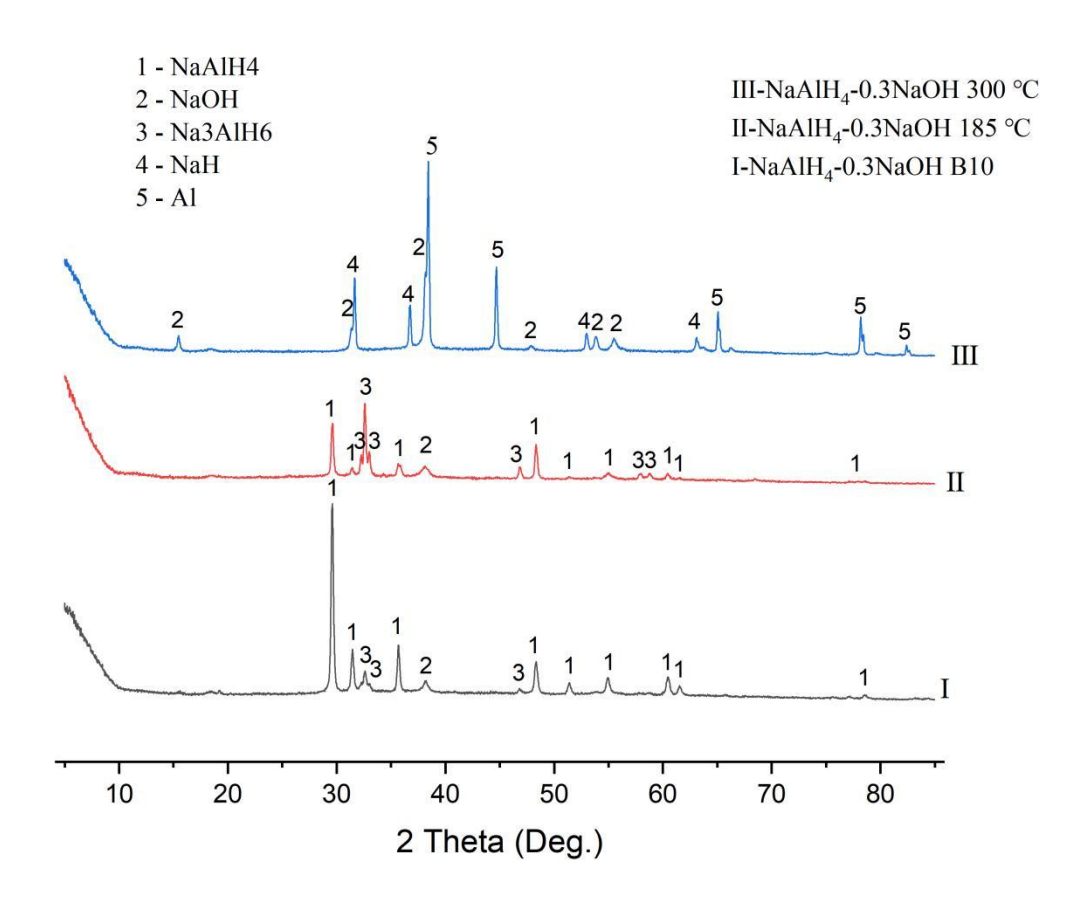


Figure 4-20: PXD patterns of 1:0.3 NaAlH₄:NaOH after ball-milling (2h, 400rpm; I) and heating to 185 (II) and 300 (III) °C under flowing Ar(g). (and cooling to room temperature). (1 represent NaAlH₄; 2 represent NaOH; 3 represent Na₃AlH₆; 4 represent NaH; 5 represent Al)

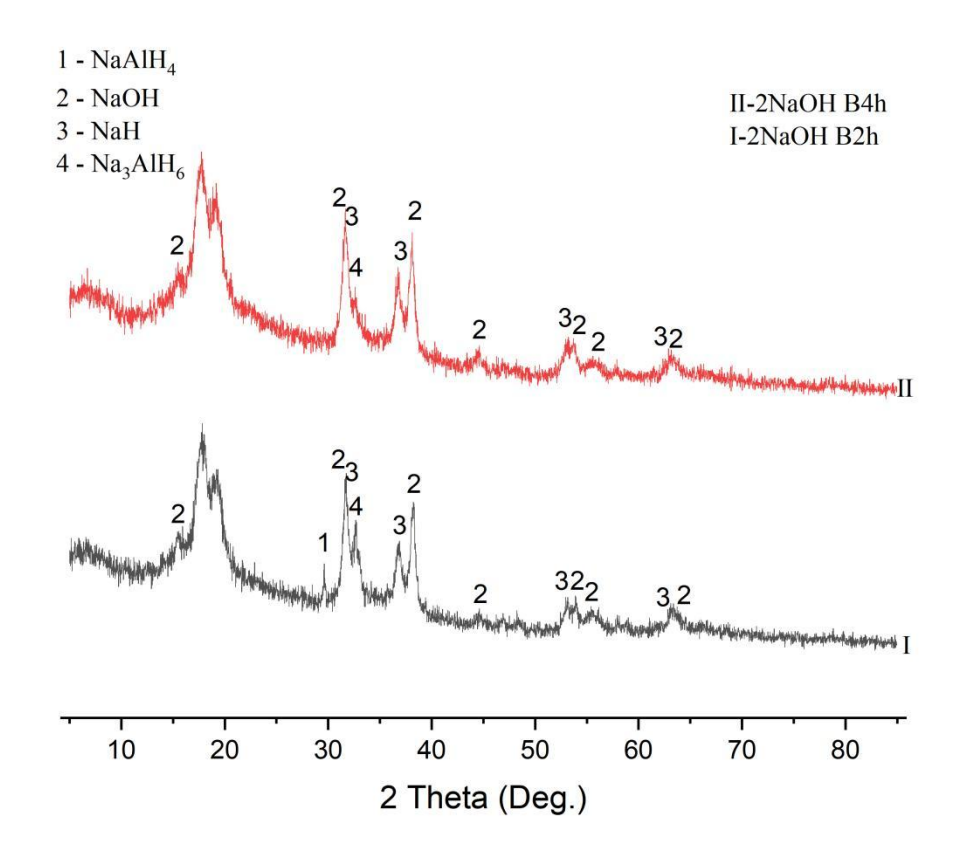


Figure 4-21: PXD pattern of 1:2 NaAlH₄:NaOH after ball-milling (2h,I; 4h II). (1 represent NaAlH₄; 2 represent NaOH; 3 represent NaH; 4 represent Na₃AlH₆)

Figure 4-22 shows the thermal performance of 1:1 NaAlH₄:NaOH after ball milling for 10 hours and heating to 400 °C. It can be observed that, compared to the original hand-mixed sample(1:1 NaAlH₄:NaOH in Figure 4-9), the first step (reaction 7) has completely disappeared. This is because the first step (reaction 7) has already occurred during ball milling, as evidenced by the presence of only the intermediate phase Na₃AlH_{6-x}(OH)_x in PXD Figure 4-18. The first peak of 1:1 NaAlH₄:NaOH samples after ball milling for 10 hours at 255 °C is lower than the previous 270 °C (1:1 NaAlH₄:NaOH in Figure 4-9) and 292 °C (NaAlH₄ in Figure 4-2), and has become an exothermic reaction. Between 255 °C and 300 °C, Na₃AlH_{6-x}(OH)_x may decompose into Al, NaH, and NaOH. The second peak of 1:1 NaAlH₄:NaOH samples after ball milling for 10 hours is at 361°C, and according to PXD in Figure 4-23, peaks corresponding to Na₅AlO₄, Na₂O, and Na are present. As described earlier for the hand-mixed sample (reaction 9), 4NaOH + Al + NaH will react to form Na₅AlO₄. The small amount of Na₅AlO₄ generated shows some small peaks around 35° that is similar to the one in Figure 4-12. As previously analysed, these peaks may correspond to Na₅AlO₄. Compared to the hand-mixed sample of 1:1 NaAlH₄:NaOH, there is an additional peak for Na₂O. In the hand mixed 1:1 NaAlH₄:NaOH on Figure 4-9, at ca. 300 °C, the NaH and NaOH products had not reacted further for the third step (reaction 9), whereas in the ball-milled 1:1 NaAlH4:NaOH, they reacted to form Na₂O and hydrogen at lower temperature. This indicates that ball milling reduces the particle size of the sample, making it easier for 1:1 NaH:NaOH reaction to form Na₂O and hydrogen.

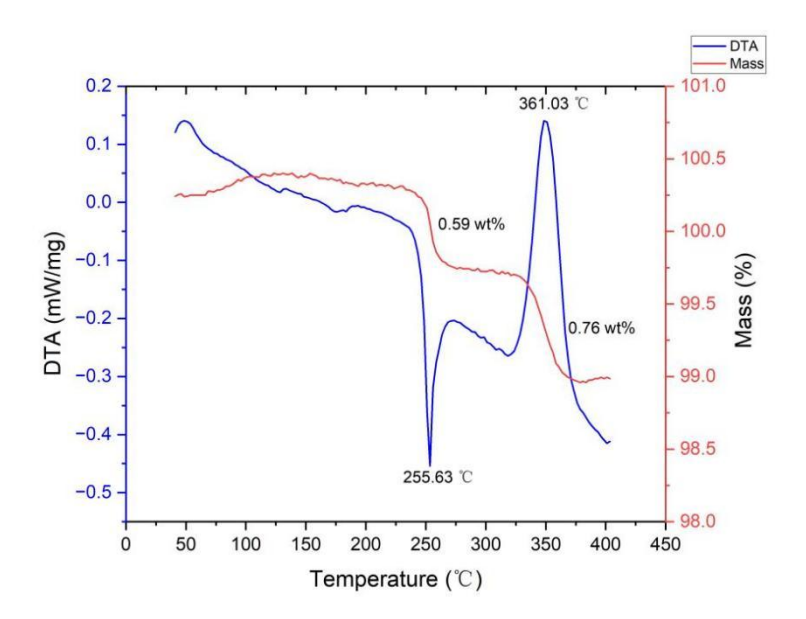


Figure 4-22: TG(red) and DTA(blue) profiles for ball-milled 1:1 NaAlH₄:NaOH (10h, 400rpm) on heating from 35-400 °C at 5 °C min⁻¹ under flowing Ar(g).

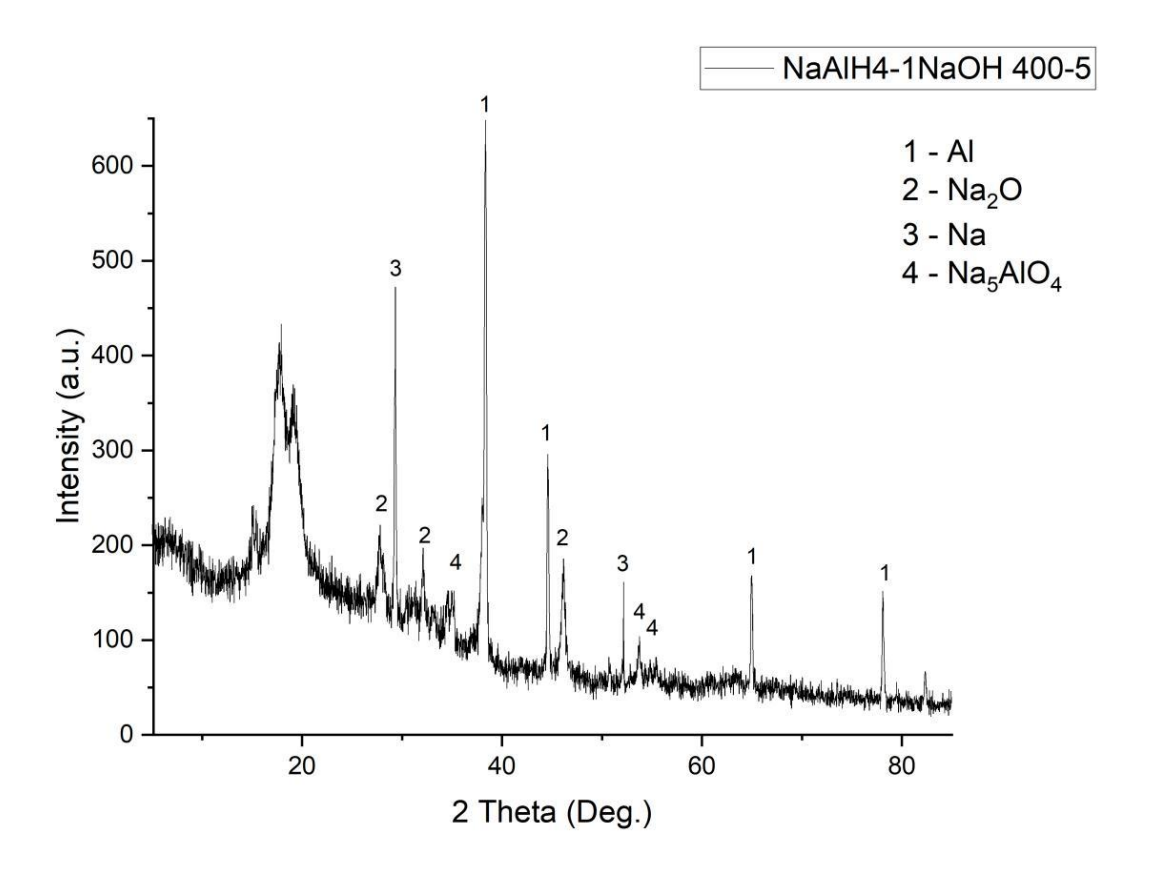


Figure 4-23: PXD pattern of ball-milled 1:1 NaAlH₄:NaOH (4h, 400rpm) after heating to 400 °C under flowing Ar(g). (1 represent Al; 2 represent Na₂O; 3 represent Na; 4 represent Na₅AlO₄)

In Figure 4-21, the 1:2 NaAlH₄:NaOH sample shows the appearance of NaH peaks after ball milling for 2 hours and 4 hours. This indicates that the intermediate may further decomposes into NaH because from 2 hours to 4 hours, the relative intenity of phases of Na₃AlH_{6-x}(OH)_x decrease, and the NaH phases increase. To investigate whether NaH is formed from the decomposition of Na₃AlH_{6-x}(OH)_x and to explore whether the decomposition of Na₃AlH_{6-x}(OH)_x continues upon adding more NaOH, 1:3 NaAlH₄:NaOH and 1:4 NaAlH₄:NaOH mixtures were ball-milled for 2 hours and 4 hours and compared with the previously studied 1:1 NaAlH₄:NaOH and 1:2 NaAlH₄:NaOH mixtures.

From Figure 4-24, it can be observed that when the NaAlH4:NaOH molar ratio reaches 1:3 after 2 hours of milling, compared with the previously reported 1:2 NaAlH4:NaOH sample in PXD Figure 4-21, the relative intensity of NaAlH4 is higher. This finding is somewhat unexpected. After 4 hours of ball milling, the phase of Na₃AlH_{6-x}(OH)_x completely disappears, leaving only the phases of NaH and NaOH. The appearance of the Na₃AlH_{6-x}(OH)_x phase after 2 hours of ball milling suggests that NaH is likely formed from the decomposition of Na₃AlH_{6-x}(OH)_x. However, it is peculiar that the phase of Al cannot still be detected. One possible reason is that the decomposed Al adheres to the stainless steel ball mill jar and cannot be removed. This is likely due to the excellent ductility and high plasticity of Al, which can undergo severe plastic deformation under the impact force

of ball milling and subsequently form cold welds. According to Suryanarayana et al.'s article, different types of ball milling equipment have a significant influence on the cold-welding behaviour of aluminium. For instance, when using high-energy vibration ball mills such as the SPEX 8000 (equivalent rotation speed of about 1725 rpm) or planetary ball mills (rotation speed typically ranging from 300 to 600 rpm), aluminium powders tend to experience cold welding and agglomeration within the first 5 to 30 minutes of ball milling due to severe plastic deformation. Benjamin first observed in his 1970 mechanical alloying experiments that when ball milling aluminium powders using an Attritor mill (with an agitator shaft rotation speed of about 400 rpm), significant cold welding occurred within the first hour, with powders gradually aggregating into lumps and adhering to the grinding balls or the inner wall of the mill jar. Therefore, it is highly probable that the generated Al cold-welds to the ball mill jar during the milling process, making it undetectable.

Figure 4-25 shows that, as in the 1:3 system, when the NaAlH₄:NaOH molar ratio reaches 1:4, after 4 hours of ball milling, only NaH and NaOH peaks are present. After 2 hours of ball milling, the relative intensity of the Na₃AlH_{6-x}(OH)_x phase in the 1:4 NaAlH₄:NaOH mixture is lower than that in the 1:3 NaAlH₄:NaOH mixture. Overall, the PXD pattern of the 1:4 NaAlH₄:NaOH mixture is largely similar to that of the 1:3 NaAlH₄:NaOH mixture. In contrast to the 1:2 NaAlH₄:NaOH mixture, which still exhibits the Na₃AlH_{6-x}(OH)_x phase after 4 hours of ball milling, the 1:1 NaAlH₄:NaOH mixture shows complete disappearance of the NaOH phase after 10 hours of ball milling, as illustrated in Figure 4-18. Thus, when the molar ratio of NaAlH₄:NaOH reaches 1:2, Na₃AlH_{6-x}(OH)_x further decomposes into NaH and NaOH. When the molar ratio reaches 1:3 or 1:4, the decomposition rate of Na₃AlH_{6-x}(OH)_x accelerates, with complete decomposition occurring after 4 hours of ball milling. Due to the absence of Al, the DTA-TG and MS figures of the dehydrogenation of 1:2, 1:3, and 1:4 NaAlH₄:NaOH mixtures after ball milling show no discernible patterns (see Appendix A4-14 and A4-15). In the TG-DTA figure of the 1:2 NaAlH₄:NaOH mixture after 4 hours of ball milling, the total hydrogen mass loss is 0.83 wt.%. A minor peak is observed at 261°C, corresponding to an exothermic reaction with negligible mass loss. The main dehydrogenation reaction peak occurs at 363°C, which is an endothermic reaction. In the TG-DTA figure of the 1:3 NaAlH₄:NaOH mixture after 4 hours of ball milling, the total hydrogen mass loss is 0.82 wt.%, with the main dehydrogenation reaction peak at 345 °C, which is also an endothermic reaction. This indicates that most of the dehydrogenation reaction has already been completed during ball milling. In the TG-DTA figure of the 1:4 NaAlH4:NaOH mixture after 4 hours of ball milling, the total hydrogen mass loss is 1.02 wt.%, with a broad peak observed at 320 °C.

This suggests that the majority of the dehydrogenation reaction has been completed during the ball-milling process.

From the DTA curves of the 1:1 NaAlH₄:NaOH mixture in Figure 4-22 and the 1:2 NaAlH₄:NaOH mixture in Figure A4-1, it can be observed that the reaction corresponding to the second step (reaction 8) is gradually diminishing. When examining the DTA curves of the 1:3 and 1:4 NaAlH₄:NaOH mixtures, this reaction has completely disappeared. The only variable that has been altered in these experiments is the amount of NaOH. According to the previous Kissinger analysis of variable heat rate TG-DTA data (Table 4-2), adding more NaOH in the NaAlH₄-NaOH system reduces the activation energy. Therefore, the possible reason for disappearance of the second step (reaction 8) the energy generated by the exothermic reaction of Na₃AlH_{6-x}(OH)_x after ball milling promotes the occurrence of the second reaction. Additionally, in 1:3 NaAlH₄:NaOH and 1:4 NaAlH₄:NaOH after 2 hours of ball milling, peaks of NaAlH₄, NaH, and Na₃AlH₆ are present, indicating that the synthesis of Na₃AlH_{6-x}(OH)_x and its decomposition occur simultaneously. After 4 hours of ball milling, the 1:2 NaAlH₄:NaOH sample in Figure 4-21 still shows a broad Na₃AlH_{6-x}(OH)_x phase, but NaAlH₄-3NaOH after ball-milling for 4h in Figure 4-24 does not show the same phase. Therefore, more NaOH can make the second step of dehydrogenation reaction of Na₃AlH_{6-x}(OH)_x proceed in ball-milling more quickly.

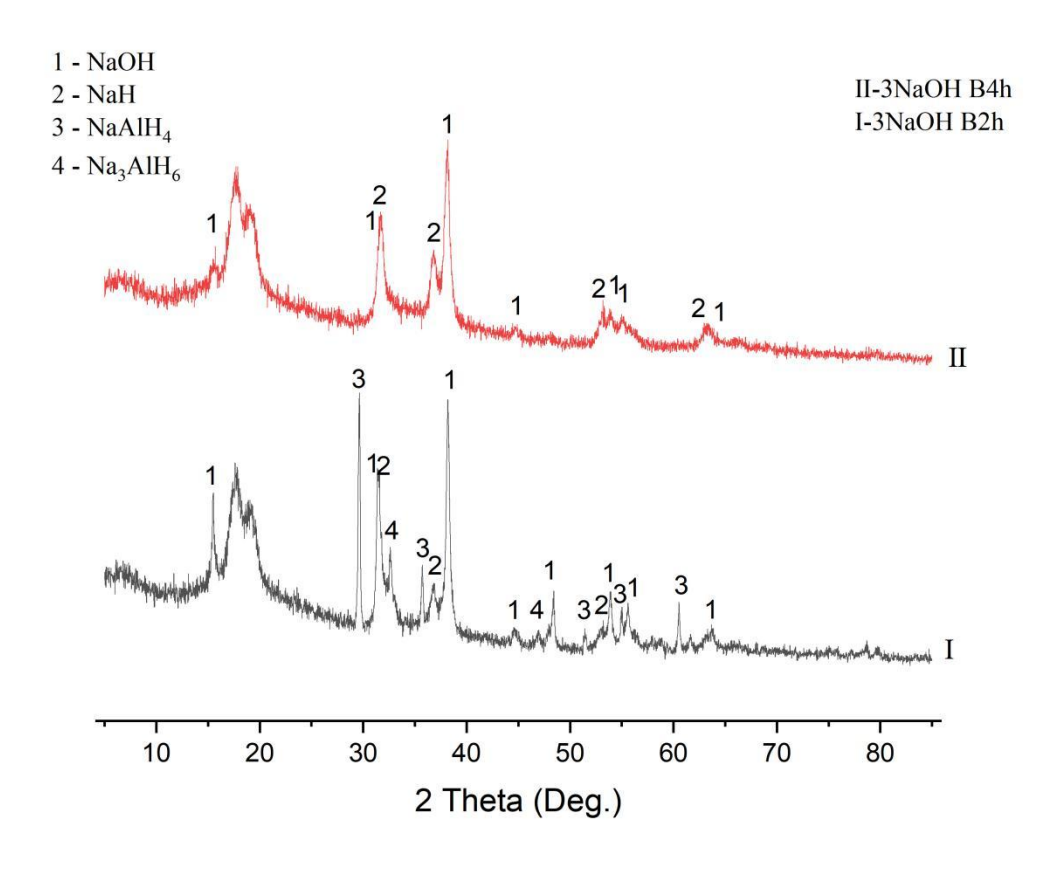


Figure 4-24: PXD patterns of ball-milled 1:3 NaAlH4:NaOH (2h, I; 4h II). (1 represent NaOH; 2

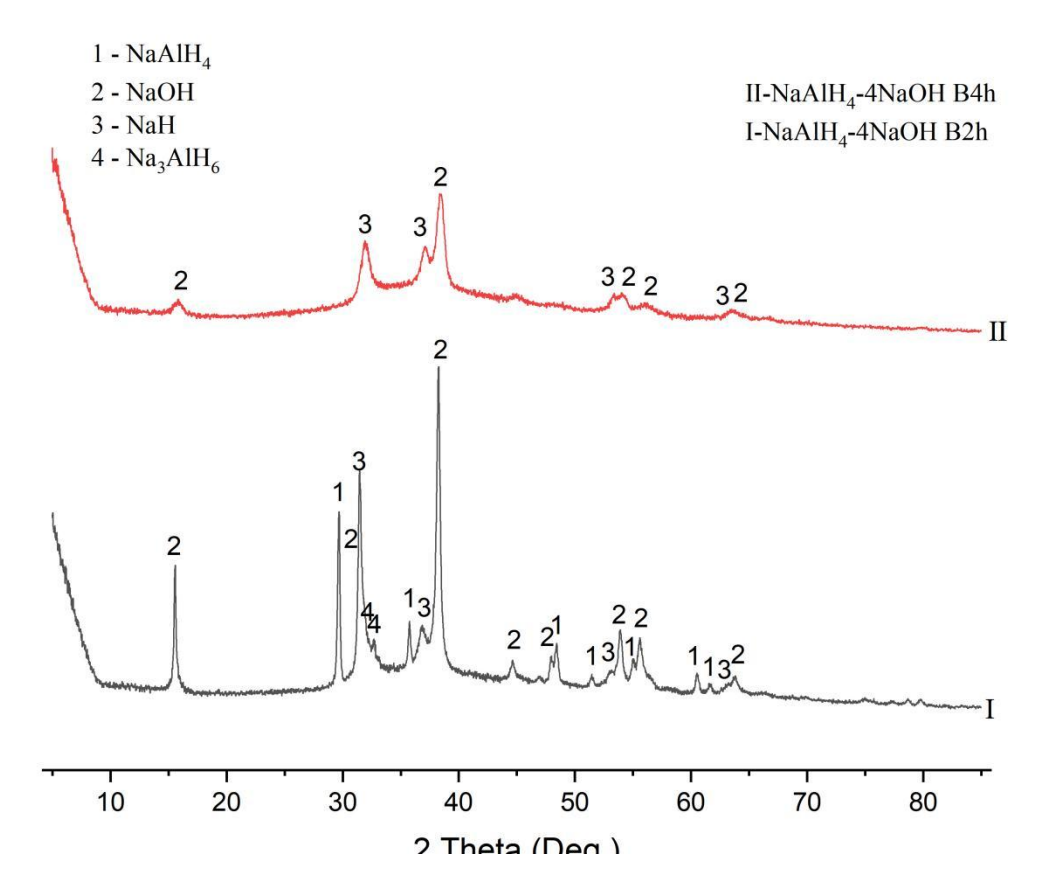


Figure 4-25: PXD patterns of ball-milled 1:4 NaAlH₄:NaOH (2h, I; 4h II). (1 represent NaAlH₄; 2 represent NaOH; 3 represent NaH; 4 represent Na₃AlH₆)

4.3.4.2 Role of NaOH

To investigate whether NaOH acts as a catalyst and how much NaOH is needed to shift the first reaction from an endothermic to an exothermic reaction, dehydrogenation reaction of ball-milled (300 rpm, 1h) 1:0.1 NaAlH4:NaOH, 1:0.2 NaAlH4:NaOH and 1:0.3 NaAlH4:NaOH was performed on heating from 35 °C-400 °C under argon. Figures 4-26 and 4-27 show the thermal behaviour of NaAlH4 with 0.1, 0.2 and 0.3 molar equivalents of NaOH added. To prevent the reaction between a small amount of NaOH and NaAlH4, which previously led to the formation of the solid solution Na₃AlH_{6-x}(OH)_x during ball milling, further modifications to the milling process or reactant ratios should be considered. The ball milling conditions for these samples were milder than the previous samples of 1:1-4 NaAlH4:NaOH (300 rpm for 1 hour, compared to 400 rpm for 2 hours). From Figure 4-26, it can be seen that when the NaOH content reaches 30 mol.%, the reaction shifts from endothermic to exothermic. However, 30 mol.% NaOH might be regarded as excessive for a substance acting as a catalyst. Additionally, a small amount of NaOH (such as 30 mol.% NaOH) does not significantly promote the second and third steps of the reaction. Therefore, it is highly likely that NaOH can only act as a reactive additive in the NaAlH4 system, and

at least 20 mol.% NaOH ratio is necessary to change the reaction pathway of NaAlH₄.

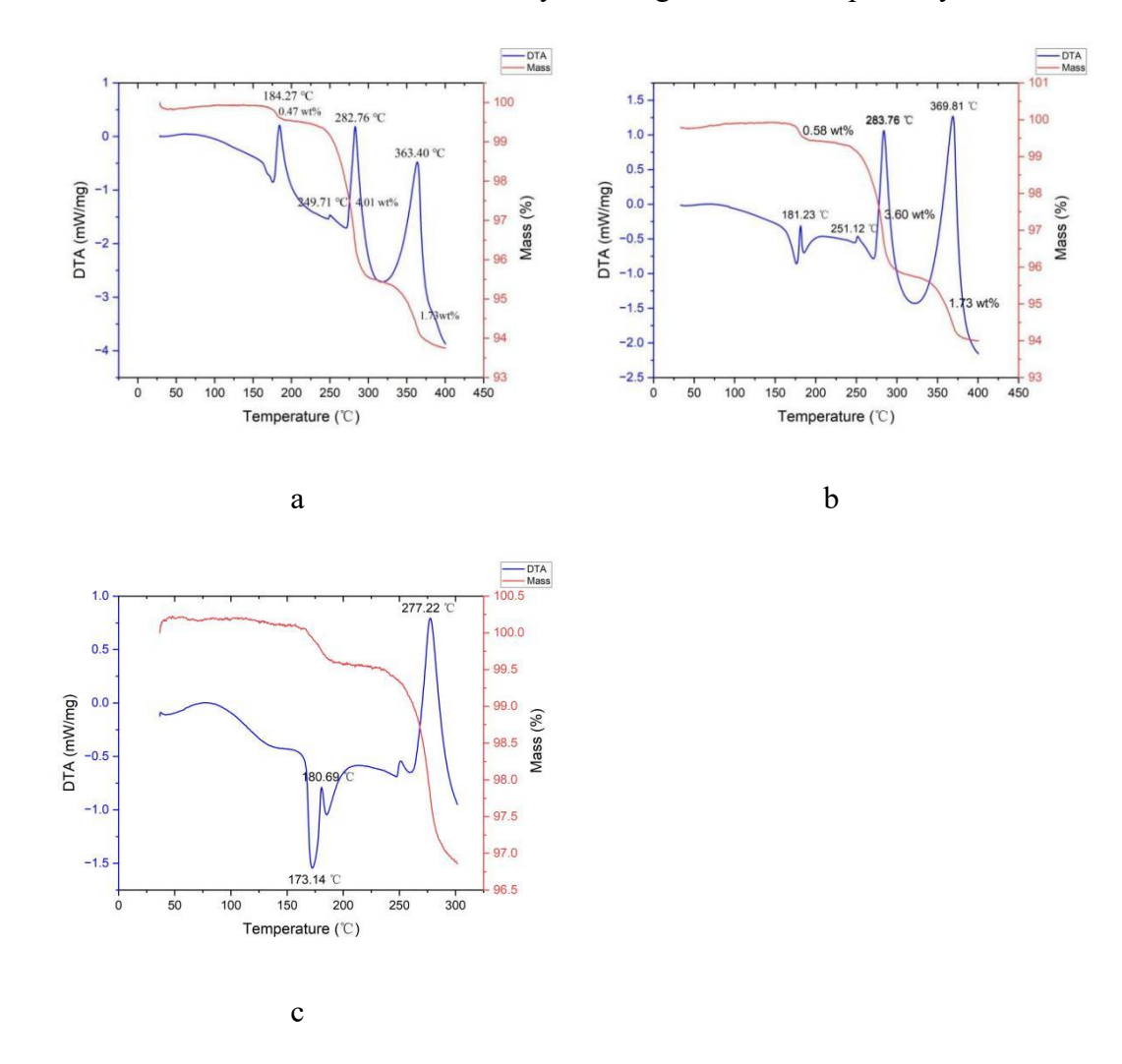
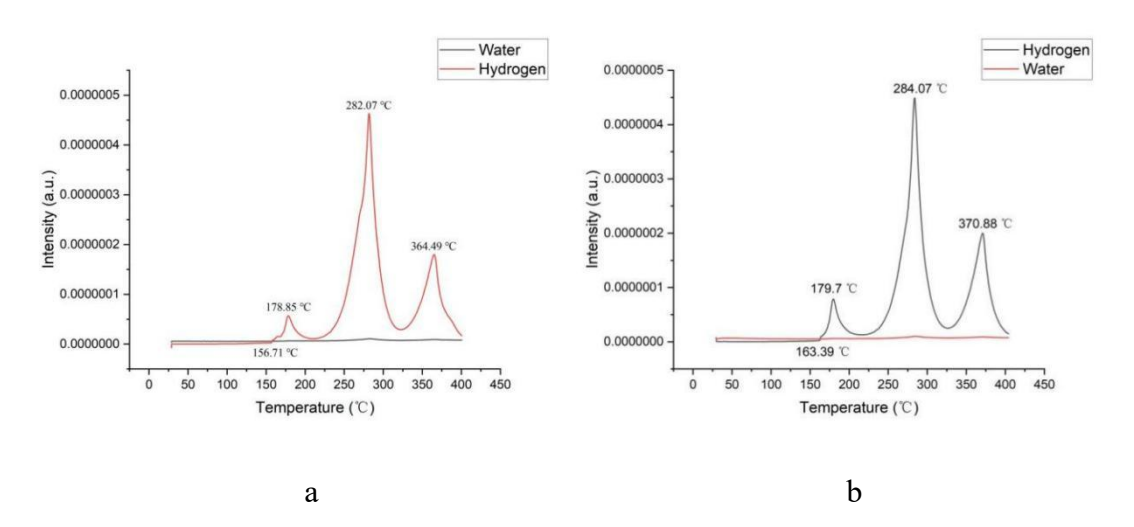


Figure 4-26: TG(red) and DTA(blue) profiles for ball-milled NaAlH₄:NaOH (1h, 300rpm) with molar ratio of (a)1:0.1 NaAlH₄:NaOH (b)1:0.2 NaAlH₄:NaOH (c)1:0.3 NaAlH₄:NaOH on heating from 35-400(300) °C at 5 °C min⁻¹ under flowing Ar(g).



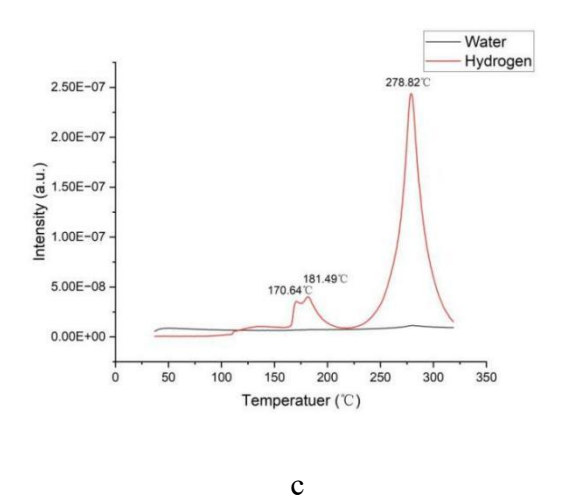


Figure 4-27: Mass spectrometry output for water (m/z = 18; black) and hydrogen (m/z = 2; red) as a function of temperature for ball-milled NaAlH₄:NaOH (1h, 300rpm) with molar ratio of (a)1:0.1 NaAlH₄:NaOH (b)1:0.2 NaAlH₄:NaOH (c)1:0.3 NaAlH₄:NaOH on heating from 35-400(300) °C at 5 °C min⁻¹ under flowing Ar(g).

4.3.5 Dehydrogenation reaction of ball-milled Na₃AlH₆-NaOH with different molar ratio

To investigate the relationship between Na₃AlH₆ and NaOH under ball milling conditions, first Na₃AlH₆ was synthesized by ball milling 1:2 NaAlH₄:NaH at 400 rpm for 20h. Similar ball-milling conditions to those reported by Yap et al. were employed. In Yap et al.'s study, NaH and NaAlH₄ were mixed in a molar ratio of 2:1 and placed into a stainless steel ball mill jar with a ball-to-powder weight ratio of 40:1. Subsequently, the mixture was ball-milled for 20 hours using a planetary ball mill (model NQM-0.4) at a rotation speed of 400 rpm.²¹ All procedures were conducted within a glovebox filled with high-purity argon. The reaction 10 is shown below:

$$NaAlH_4 + 2NaH \rightarrow Na_3AlH_6$$
 (10)

The objective of this chapter is to investigate whether Na₃AlH₆ and NaOH can directly form Na₃AlH_{6-x}(OH)_x. Additionally, it explores the reactions occurring between 300°C and 400°C after ball milling the Na₃AlH₆–NaOH mixture. As shown in Figure 4-28, although small amounts of NaH and NaAlH₄ have not completely reacted, the majority of the product is Na₃AlH₆ after this time.

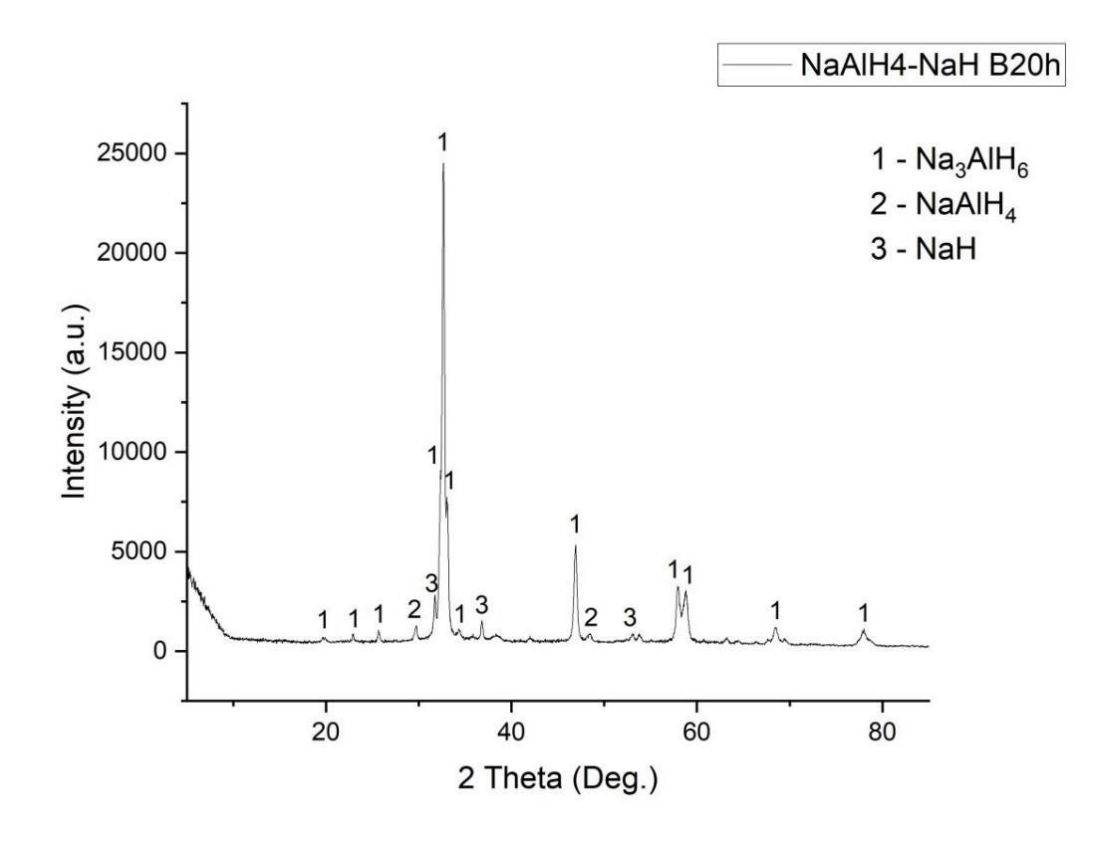


Figure 4-28: PXD pattern of ball-milled NaAlH₄-2NaH (20h, 400rpm).

Figures 4-29 and 4-30 show the thermal behaviour of Na₃AlH₆ (contain small amount of NaOH and NaAlH₄) after heating to 400 °C. There are two endothermic DTA peaks corresponding to the decomposition of Na₃AlH₆ into NaH, and the decomposition of NaH into Na. The first peak temperature (251.60 °C) of dehydrogenation of Na₃AlH₆ is significantly lower than the second peak temperature observed in the previous NaAlH₄ reaction in Figure 4-2, decreasing from ca. 290 °C to ca. 250 °C. This temperature is remarkably close to the 260°C described in the literature within Section 4.1, Introduction. The reason may be attributed to the fact that, as shown in Figure 4-2, the peak temperature for the first step of NaAlH₄ decomposition (formation of Na₃AlH₆) is approximately 275 °C. Consequently, the peak temperature for the subsequently generated Na₃AlH₆ reaches 290 °C. If Na₃AlH₆ were to react independently, its peak temperature would likely be ca. 250 °C. The second DTA peak temperature, 379.6 °C, is close to the third peak observed in the NaAlH₄ reaction at ca. 380 °C in previous Figure 4-2. The theoretical hydrogen mass loss should be 5.88 wt.%. The hydrogen mass loss for both reaction steps is 2.94 wt.%. Experimental hydrogen mass loss was 5.26 wt.% (2.60 wt.% and 2.66 wt.% respectively) which is about 10 wt. % higher than the experimental hydrogen mass loss. This discrepancy may be related to the purity of the Na₃AlH₆ sample because of the purity of NaH (90 at.%) and NaAlH₄ (93 at.%).

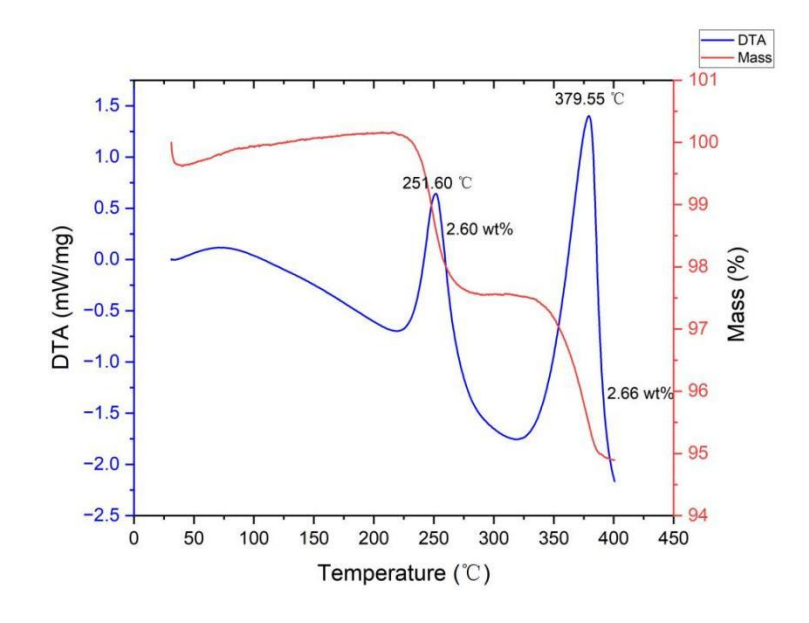


Figure 4-29: TG(red) and DTA(blue) profiles for as-synthesised Na₃AlH₆ on heating from 35-400 °C at 5 °C min⁻¹ under flowing Ar(g).

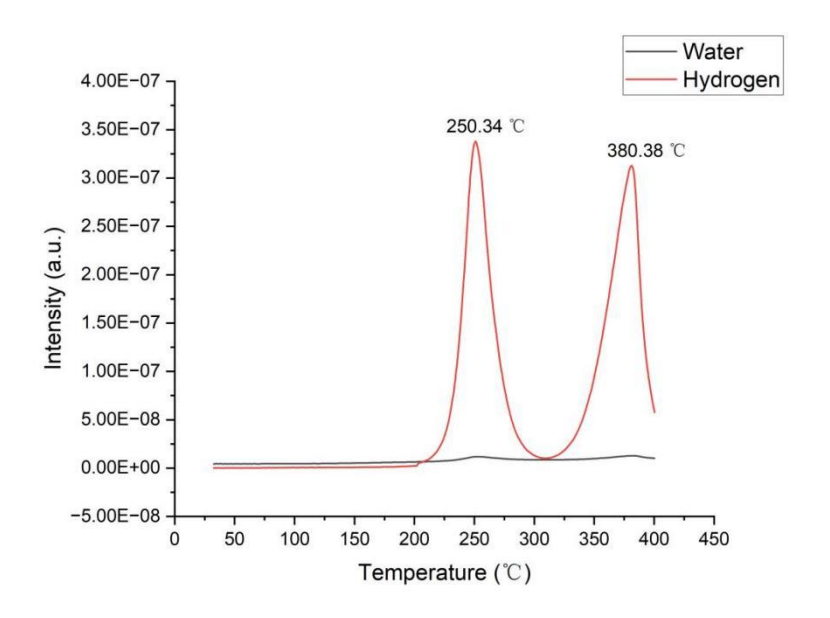


Figure 4-30: Mass spectrometry output for water (m/z = 18; black) and hydrogen (m/z = 2; red) as a function of temperature for as-synthesised Na_3AlH_6 on heating from 35-400 °C at 5 °C min⁻¹ under flowing Ar(g).

In the ball-milling experiments of Na₃AlH₆ with NaOH, molar ratios of 1:1, 1:3, and 1:4 Na₃AlH₆ to NaOH were selected. The reason is that the 1:1 Na₃AlH₆:NaOH ratio corresponds to the original 1:0.33 NaAlH₄:NaOH molar ratio in reaction 7. As shown in Figure 4-26, under relatively mild ball-milling conditions, the dehydrogenation reaction of the 1:0.3 NaAlH₄:NaOH mixture can alter the first step of the NaAlH₄ reaction from endothermic to exothermic. Thus, the 1:1 Na₃AlH₆:NaOH ratio investigates the effect of a small amount of NaOH on Na₃AlH₆ after ball milling. The 1:3 and 1:4 Na₃AlH₆:NaOH ratios correspond to the original 1:1 and 1:1.33 NaAlH₄:NaOH molar ratios, respectively.

Figure 4-31 shows the products from ball milling mixtures of Na₃AlH₆ and NaOH with different molar ratios of 1:1, 1:3 and 1:4 over a period of 2 hours. It can be observed that after adding NaOH to Na₃AlH₆, the peaks of Na₃AlH₆ broaden, similar to observations of 1:1 NaAlH4:NaOH in previous Figure 4-18. The relative intensity of the NaOH phase in the 1:1 Na₃AlH₆:NaOH mixture is relatively low after 2 hours of ball milling. As shown in Figure 4-32, the phases in the 1:1 Na₃AlH₆:NaOH mixture remain almost unchanged after ball milling for both 2 and 10 hours. The NaOH phases at 15° and 38° do not diminish. This indicates that the reaction between Na₃AlH₆ and NaOH to form Na₃AlH_{6-x}(OH)_x was already complete after 2 hours of ball milling. This result is unexpected because, according to Figure 4-18, the NaOH phase disappeared after 6 hours of ball milling in the 1:1 NaAlH₄:NaOH mixture. In other words, it was expected that no NaOH phase would be present in the 1:1 and 1:3 Na₃AlH₆:NaOH mixtures. However, this also suggests that NaAlH₄ directly reacts with NaOH to form Na₃AlH_{6-x}(OH)_x, rather than first decomposing into Na₃AlH₆ and then reacting with NaOH. From the 1:1 Na₃AlH₆:NaOH mixture to the 1:3 and 1:4 Na₃AlH₆:NaOH mixtures, the NaH phase does not increase. In contrast, in the previously reported 1:2 NaAlH₄:NaOH and 1:3 NaAlH₄:NaOH mixtures (Figures 4-21 and 24), the NaH peaks gradually increased. This indicates that the Na₃AlH_{6-x}(OH)_x formed from the reaction of Na₃AlH₆ and NaOH does not decompose further. The possible reason is that the energy generated from the reaction between NaAlH₄ and NaOH previously facilitated the decomposition of the Na₃AlH_{6-x}(OH)_x. Without this energy, the energy barrier cannot be overcome, and therefore Na₃AlH_{6-x}(OH)_x cannot decompose.

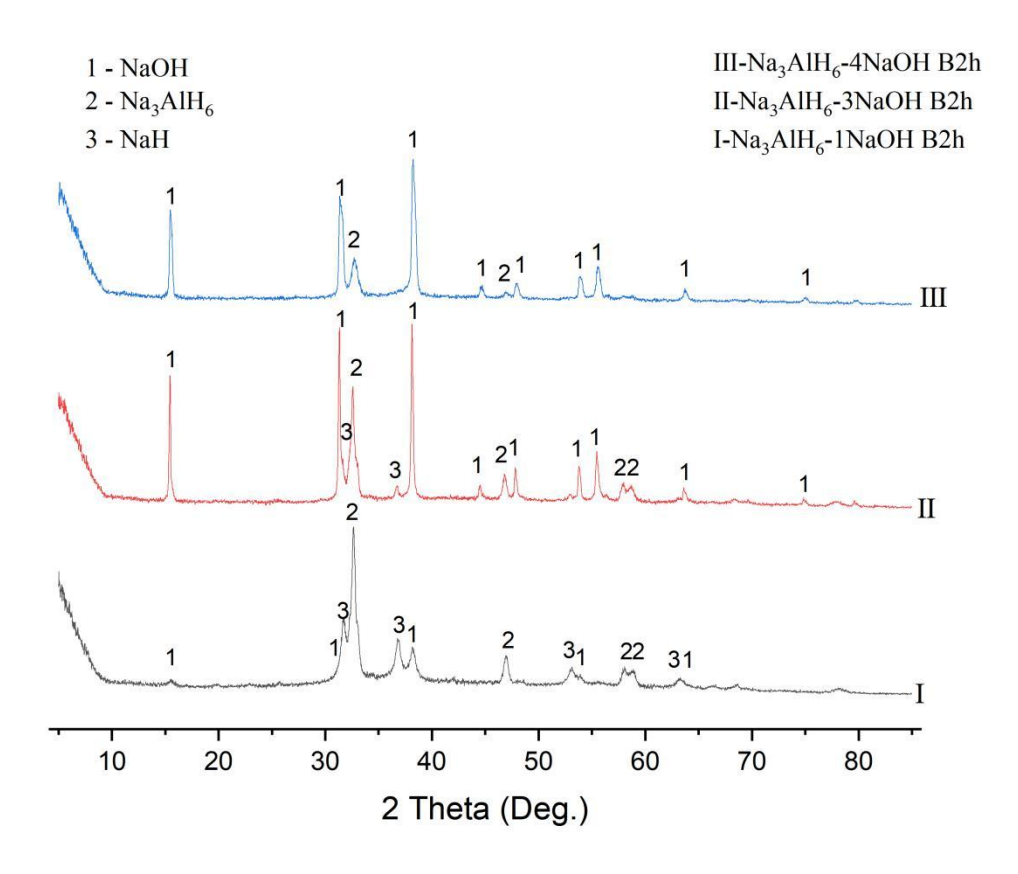


Figure 4-31: PXD patterns of ball-milled Na₃AlH₆:NaOH (2h, 400rpm) with molar ratio (1:1 Na₃AlH₆:NaOH, I; 1:3 Na₃AlH₆:NaOH, II; 1:4 Na₃AlH₆:NaOH, III). (1 represent NaOH; 2 represent Na₃AlH₆; 3 represent NaH)

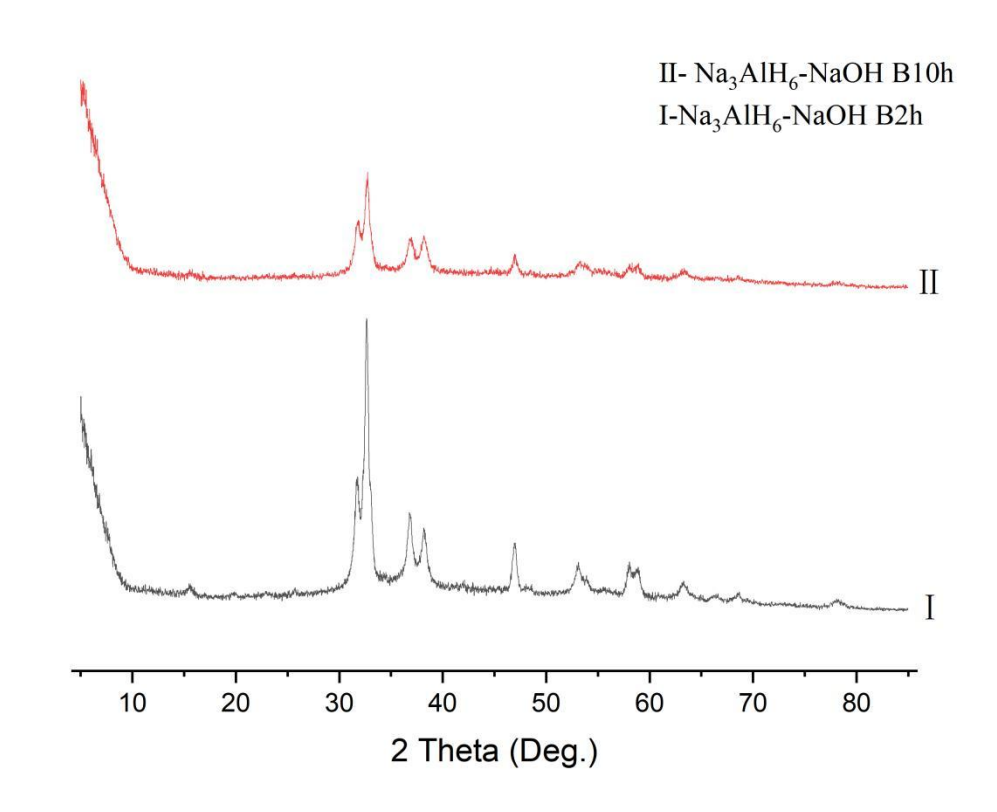


Figure 4-32: PXD patterns of ball-milled 1:1 Na₃AlH₆:NaOH (2h, I; 10h, II).

To investigate the role of NaOH in promoting the dehydrogenation of Na₃AlH₆ and Na₃AlH_{6-x}(OH)_x, a ball-milling process was conducted on a 1:3 molar mixture of Na₃AlH₆ and NaOH for 2 hours at 400 rpm. Subsequently, the ball-milled sample was heated to 400 °C at a rate of 5 °C min⁻¹. Figures 4-33 and 4-34 illustrate that multiple thermal events occurred during the thermal treatment of the ball-milled 1:3 Na₃AlH₆:NaOH mixture within the temperature range of 240-400 °C. Although it is challenging to determine the exact peak temperatures from the DTA curve shown in Figure 4-33, the MS curve in Figure 4-34 exhibits four distinct peaks. By correlating the MS data with the DTA results, the peak temperatures can be identified. The DTA curve reveals two endothermic reaction peaks at 246 °C and 356 °C, as well as two exothermic reaction peaks at 263 °C and 330 °C. The DTA peak at 246 °C may suggest that a portion of Na₃AlH₆ did not form Na₃AlH_{6-x}(OH)_x and underwent independent decomposition at this temperature. This is supported by the fact that, as shown in Figures 4-2 and 4-29, the dehydrogenation reaction of Na₃AlH₆ is endothermic with a first peak temperature around 250 °C, which is close to the observed 246 °C peak. The peak at 263 °C is likely associated with the exothermic decomposition of Na₃AlH_{6-x}(OH)_x. This is consistent with the findings in Figure 4-22, which indicates that the first peak temperature for the dehydrogenation reaction of ball-milled (10 hours) 1:1 NaAlH₄:NaOH is 255 °C and the reaction is exothermic

Between 300-360 °C, there are two peak temperatures. According to the PXD pattern in Figure 4-35, the main peaks are Na₂O, Na₅AlO₄ and NaOH. Therefore, the reactions NaH + Al + 4NaOH \rightleftharpoons Na₅AlO₄ + 2.5H₂ and NaH + NaOH \rightleftharpoons Na₂O + H₂ occur simultaneously between 300 °C and 360 °C, with peak temperatures at approximately 330 °C and 356 °C, respectively, based on previous Figure 4-13 for the peak temperature of reaction 9 (316 °C, exothermic reaction) and peak temperature of dehydrogenation of NaOH-NaH (346-358 °C, endothermic reaction).

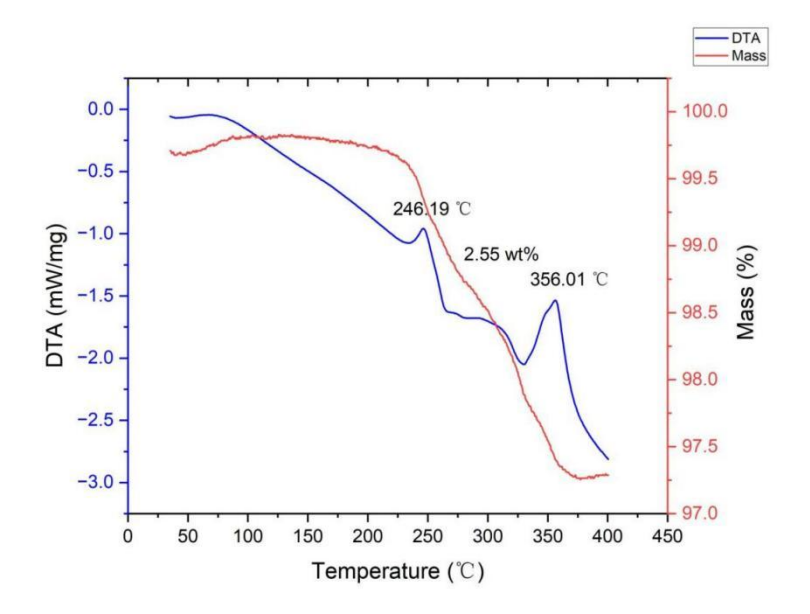


Figure 4-33: TG(red) and DTA(blue) profiles for ball-milled 1:3 Na₃AlH₆:NaOH (2h, 400rpm) on heating from 35-400 °C at 5 °C min⁻¹ under flowing Ar(g).

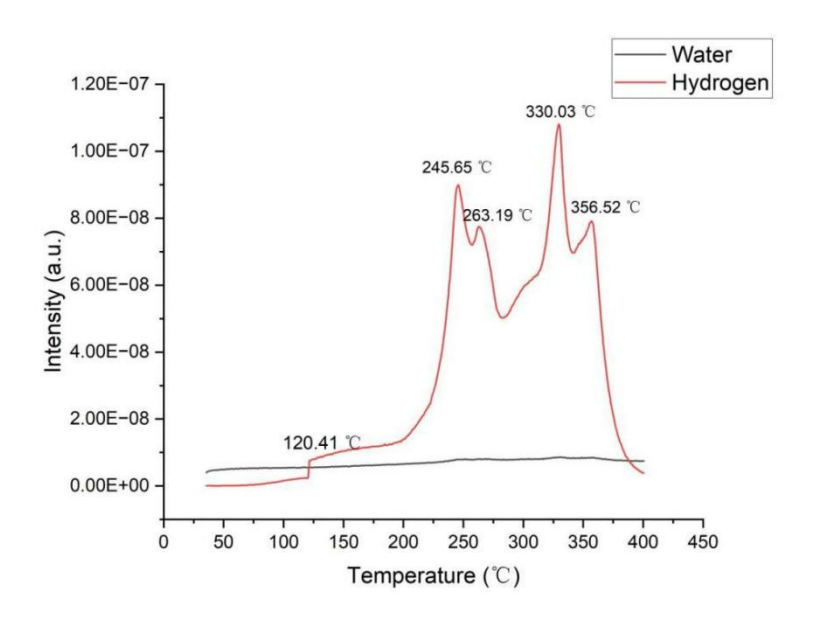


Figure 4-34: Mass spectrometry output for water (m/z = 18; black) and hydrogen (m/z = 2; red) as a function of temperature for ball-milled 1:3 Na₃AIH₆:NaOH (2h, 400rpm) on heating from 35-400 °C at 5 °C min⁻¹ under flowing Ar(g).

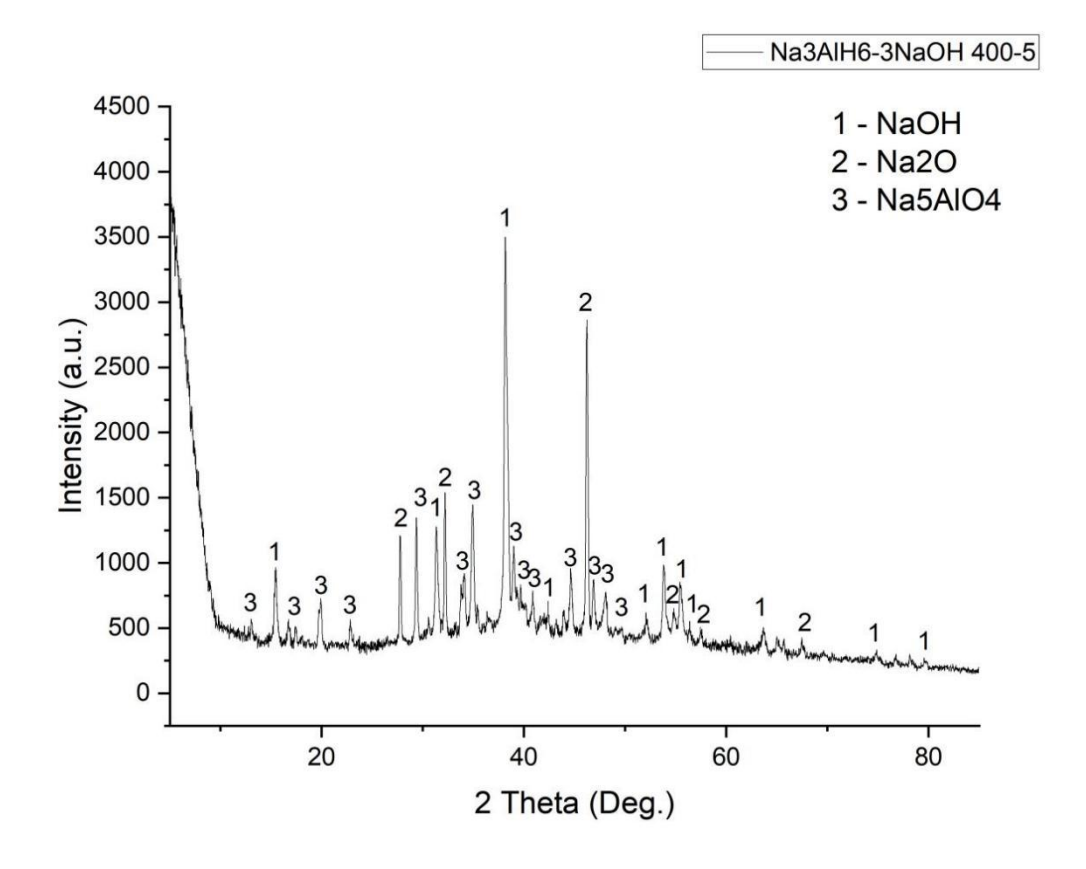


Figure 4-35: PXD pattern of ball-milled 1:3 Na₃AlH₆:NaOH (2h, 400rpm) after heating to 400 °C under flowing Ar(g) (and cooling to room temperature). (1 represent NaOH; 2 represent Na₂O; 3 represent Na₅AlO₄)

To investigate whether the addition of more NaOH can promote the reaction of Na₃AlH₆, Figures 4-36 and 4-37 illustrate the thermal behaviour of the 1:4 Na₃AlH₆:NaOH mixture after heating to 400 °C. The reaction is similar to that of the 1:3 Na₃AlH₆:NaOH mixture. However, the number of peaks in the MS analysis decreased from two peaks to a single broad peak between 300 °C and 400 °C. The possible reason for this observation is that the addition of more NaOH led to a decrease in the peak temperature of the 1:1 NaH:NaOH reaction, which forms Na₂O. This caused the peak temperatures of the two reactions (NaH + Al + 4NaOH \rightleftharpoons Na₅AlO₄ + 2.5H₂ and NaH + NaOH \rightleftharpoons Na₂O + H₂ to become closer, resulting in a broad peak in the MS plot (Figure 4-39). Additionally, the broad peak between 300 °C and 400 °C in the MS plot (Figure 4-39) is not smooth, with a noticeable change in slope. Moreover, the product analysis using PXD (Figure 4-38) confirms that the products remain unchanged, with Na₂O and Na₅AlO₄ being the primary components.

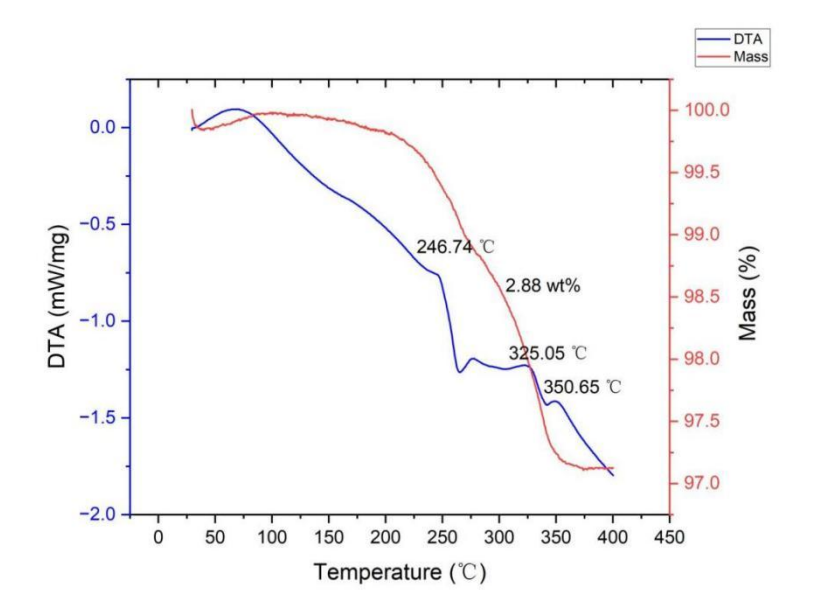


Figure 4-36: TG(red) and DTA(blue) profiles for ball-milled 1:4 Na₃AlH₆:NaOH (2h, 400rpm) on heating from 35-400 °C at 5 °C min⁻¹ under flowing Ar(g).

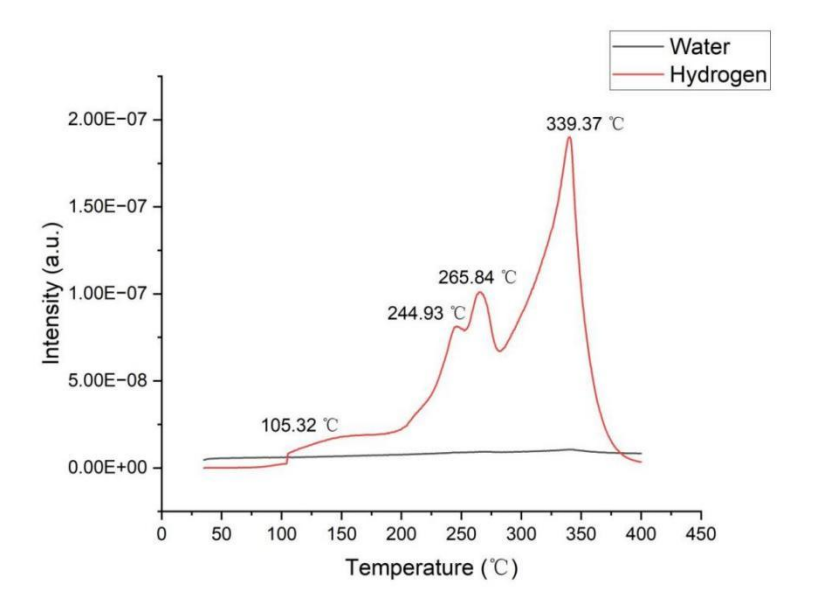


Figure 4-37: Mass spectrometry output for water (m/z = 18; black) and hydrogen (m/z = 2; red) as a function of temperature for ball-milled 1:4 Na₃AlH₆:NaOH (2h, 400rpm) on heating from 35-400 °C at 5 °C min⁻¹ under flowing Ar(g).

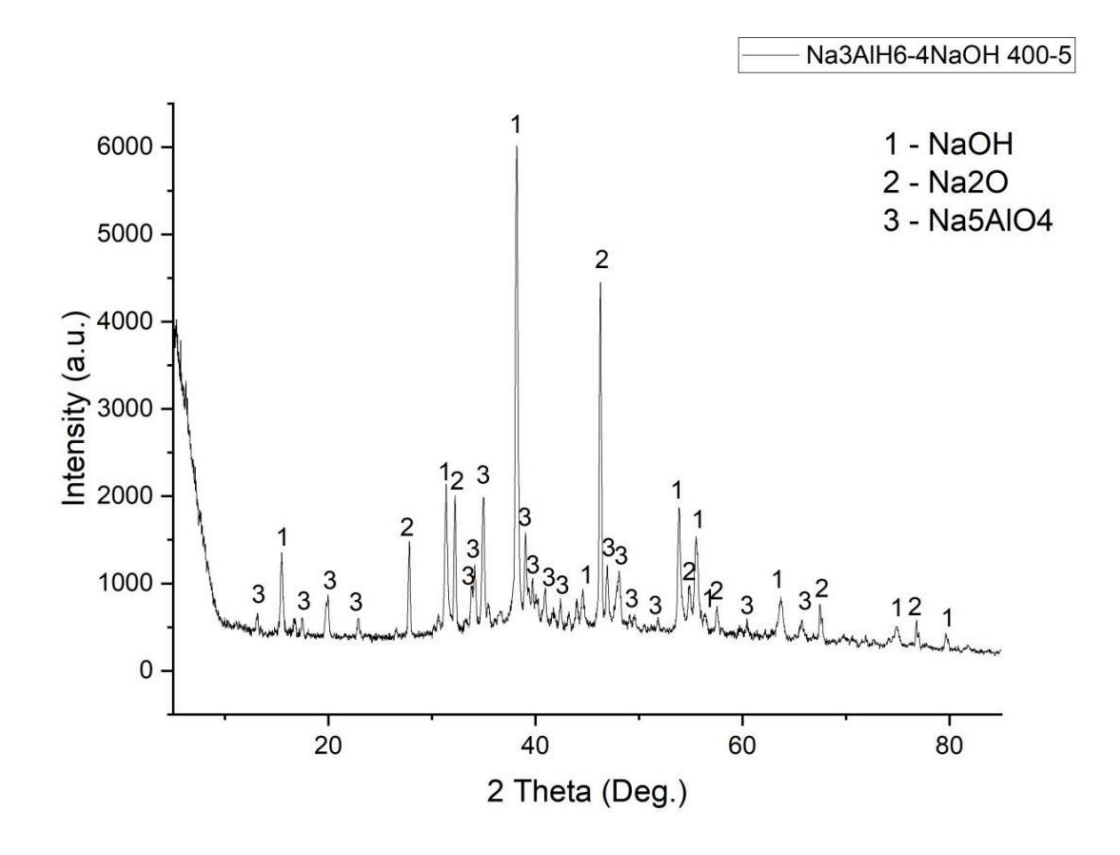


Figure 4-38: PXD pattern of ball-milled 1:4 Na₃AlH₆:NaOH (2h, 400rpm) after heating to 400 °C under flowing Ar(g) (and cooling to room temperature). (1 represent NaOH; 2 represent Na₂O; 3 represent Na₅AlO₄)

4.3.6 Synthesis of Na₅AlO₄

In accordance with the methodology described by Barker et al., Na₅AlO₄ was successfully synthesized by mixing Na₂O and α-Al₂O₃ in a molar ratio of 5:1 and reacting the mixture at 700 °C for 18 hours.²² To further explore alternative synthetic routes for Na₅AlO₄ and to validate the feasibility of Reaction 9, the present study investigates the reaction of NaOH, Al, and NaH in a molar ratio of 4:1:1. This approach is based on the previously established mechanism for the hand-mixed NaOH-NaAlH₄ system, which suggests that the reaction of NaOH, Al, and NaH should yield Na₅AlO₄.

After ball milling 4:1:1 NaOH:Al:NaH for 2 hours and heating it to 400 °C, Figures 4-39 and 4-40 show that two thermal events occur with both releasing hydrogen. From the PXD in Figure 4-41, Na₅AlO₄ and Na₂O are observed. The reaction is clearly similar to the previous ones, but the peak temperatures have decreased significantly. The peak temperature for NaH + Al + 4NaOH \rightarrow Na₅AlO₄ + 2.5H₂ dropped from 325 °C to 304 °C, and the peak temperature for NaH + NaOH \rightarrow Na₂O decreased from 350 °C to 330 °C. As can be seen from Figure 4-43, the Na₅AlO₄ synthesized directly from the 4:1:1 NaOH:Al:NaH mixture is not pure. It contains additional by-products, such as Na₂O, and

some unreacted NaOH. Therefore, further experiments are required to synthesize pure Na₅AlO₄ by varying the ball-milling conditions or the heating conditions.

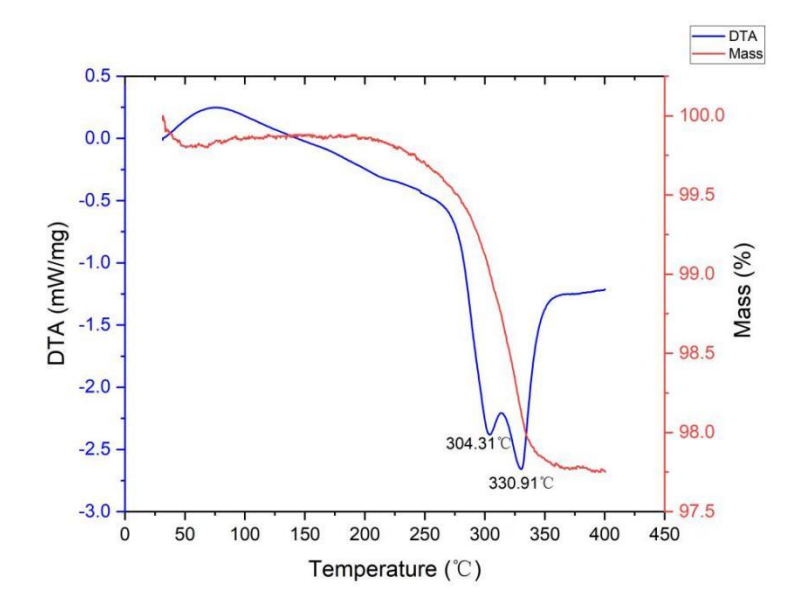


Figure 4-39: TG(red) and DTA(blue) profiles for ball-milled 4:1:1 NaOH:Al:NaH (2h, 400rpm) on heating from 35-400 °C at 5 °C min⁻¹ under flowing Ar(g).

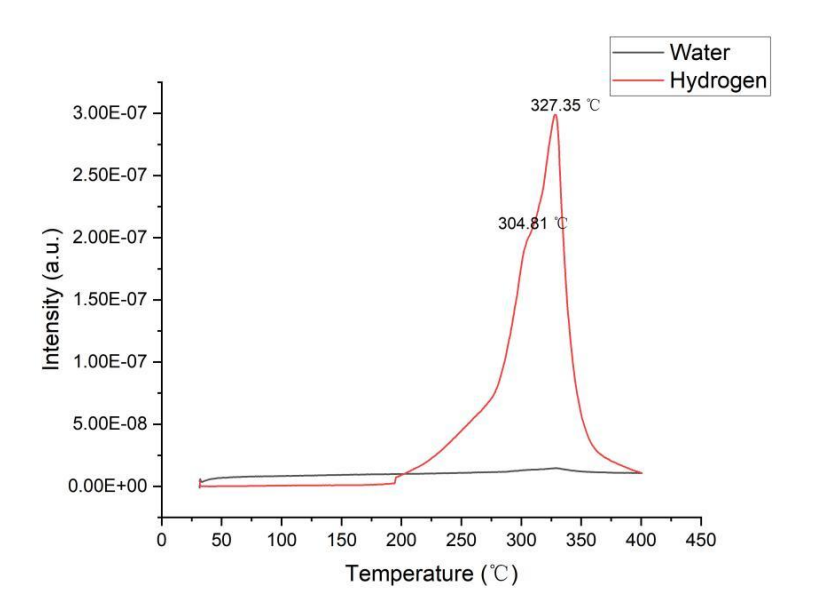


Figure 4-40: Mass spectrometry output for water (m/z = 18; black) and hydrogen (m/z = 2; red) as a function of temperature for ball-milled 4:1:1 NaOH:Al:NaH (2h, 400rpm) on heating from 35-400 °C at 5 °C min⁻¹ under flowing Ar(g).

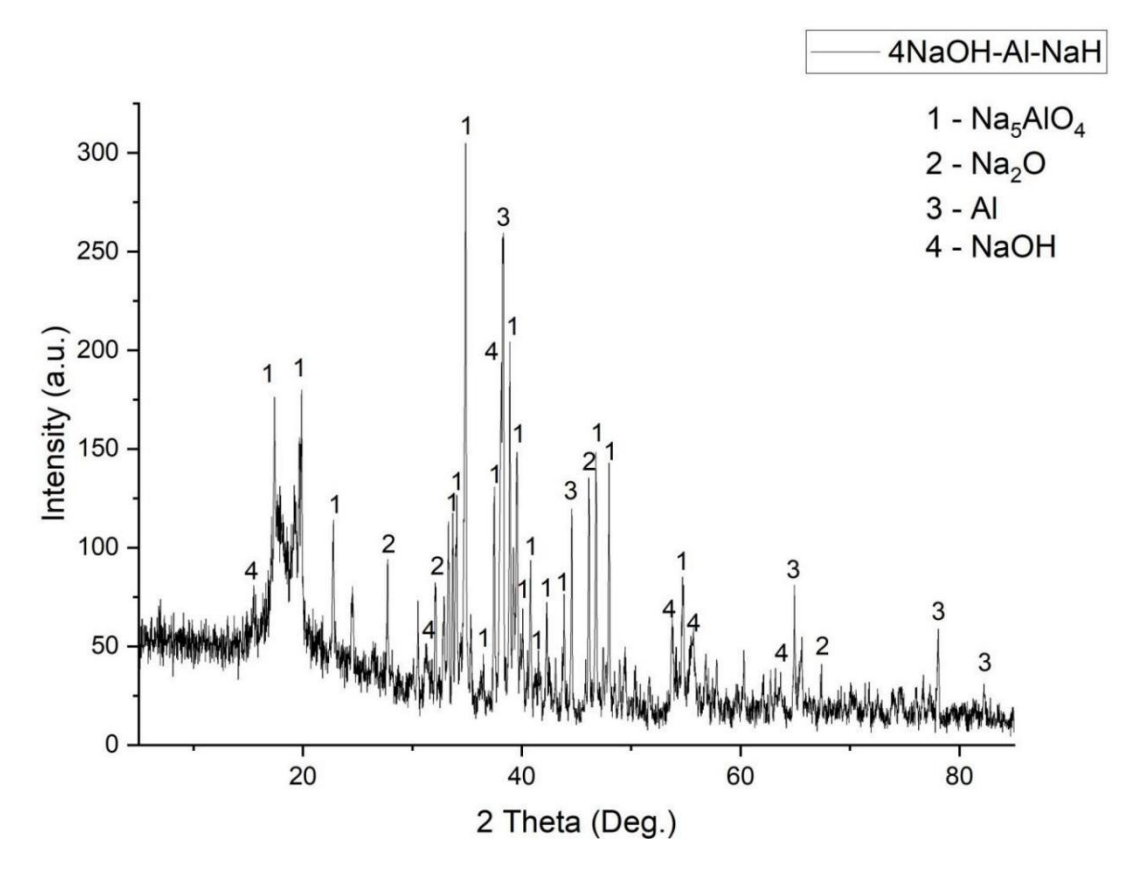


Figure 4-41: PXD patterns of ball-milled 4:1:1 NaOH:Al:NaH (2h, 400rpm) after heating to 400 °C under flowing Ar(g). (and cooling to room temperature). (1 represent Na₅AlO₄; 2 represent Na₂O; 3 represent Al; 4 represent NaOH)

4.4 Conclusion

The addition of NaOH to NaAlH₄ via manual mixing significantly alters the dehydrogenation behaviour of NaAlH₄. PXD analysis confirms the formation of intermediate products, leading to the proposed reactions (Reaction 7, 8, and 9). Specifically, the first step (Reaction 7) and the second step (Reaction 8) of the dehydrogenation process exhibit a substantial reduction in activation energy upon the addition of NaOH, with further decreases observed when higher amounts of NaOH are introduced. Notably, the first step of the dehydrogenation reaction transitions from an exothermic to an endothermic process with the addition of NaOH. When even more NaOH is added (e.g., in a 1:4 NaAlH₄:NaOH ratio), the second step of the dehydrogenation reaction also shifts from exothermic to endothermic. The newly proposed third step (Reaction 9) remains exothermic. During ball-milling of NaAlH₄ with NaOH (2 hours, 400 rpm), an intermediate phase of Na₃AlH_{6-x}(OH)_x is formed, as evidenced by PXD. With increased amounts of NaOH, this intermediate decomposes directly into NaH, NaOH, and Al. Subsequently, the reactions NaH + Al + 4NaOH \rightarrow Na₅AlO₄ + 2.5H₂ and NaH + NaOH \rightarrow Na₂O + H₂ occur within the temperature range of 300-400 °C. Thus, NaOH functions as a

reactive additive in the NaAlH₄ system, modifying the reaction pathways of all steps and facilitating the transition from endothermic to exothermic processes. A NaOH content of 20 - 30 wt.% is required to effectively promote the dehydrogenation of NaAlH₄.

The 1:1 Na₃AlH₆:NaOH ratio, corresponding to the original 1:0.33 NaAlH₄:NaOH ratio, demonstrated that a small amount of NaOH can alter the reaction pathway of Na3AlH6, leading to the formation of Na₃AlH_{6-x}(OH)_x. However, unlike the behaviour observed in the 1:1 NaAlH₄:NaOH mixture, the NaOH phase did not disappear even after prolonged ball milling, suggesting that Na₃AlH₆ reacts directly with NaOH to form Na₃AlH_{6-x}(OH)_x without decomposing into Na₃AlH₆ first. The 1:3 and 1:4 Na₃AlH₆:NaOH ratios, corresponding to the original 1:1 and 1:1.33 NaAlH₄:NaOH ratios, respectively, showed that increasing the amount of NaOH did not lead to further decomposition of Na₃AlH_{6-x}(OH)_x. Instead, the presence of excess NaOH facilitated simultaneous reactions between NaH, Al, and NaOH, forming Na2O and Na5AlO4. The thermal analysis of the ball-milled 1:3 Na₃AlH₆:NaOH mixture revealed multiple thermal events within the 240-400 °C range, with distinct peaks corresponding to the decomposition of Na₃AlH₆, Na₃AlH_{6-x}(OH)_x, and the formation of Na₂O and Na₅AlO₄. The addition of more NaOH in the 1:4 Na₃AlH₆:NaOH mixture led to a broadening of the MS peaks between 300 °C and 400 °C, indicating that the peak temperatures of the reactions involving NaH and NaOH became closer. This suggests that the excess NaOH lowers the reaction temperature for the formation of Na₂O, causing the overlapping of reaction peaks.

Although Na₅AlO₄ can be synthesized from NaOH, Al, and NaH according to reaction 9 under heating conditions, the resulting product is not pure, with the presence of Na₂O. Further experiments are required to attempt the synthesis of pure Na₅AlO₄. For instance, the temperature could be controlled at 300 °C and maintained for 1 hour. The synthesis of a significant amount of Na₅AlO₄ could then be monitored using PXD.

There are still many limitations in the experiments of this chapter. For example, it is possible that Al cannot be removed from the ball-milling jar due to cold welding, but this cannot be proven. The solution is to change the type of ball-milling jar, such as replacing the stainless steel jar with an agate jar, to prevent Al from adhering to the walls of the jar. Secondly, the exact composition of the intermediate Na₃AlH_{6-x}(OH)_x remains undetermined. This can be addressed by adding different molar ratios of NaAlH₄:NaOH into the ball-milling jar and using mild conditions, such as 1:2-2.5 NaAlH₄:NaOH at 200-300 rpm with prolonged ball-milling duration, to synthesize the intermediate Na₃AlH_{6-x}(OH)_x. The specific content of Na₃AlH_{6-x}(OH)_x can then be determined by monitoring the amount of NaOH.

4.5 References

- 1. S. McWhorter, C. Read, G. Ordaz and N. Stetson, *Current Opinion in Solid Sate and Materials Science*, 2011, **15**, 29.
- 2. A. Zaluska, L. Zaluski and J. O. Strom-Olsen, Journal of Alloys and Compounds, 2000, 298, 125.
- 3. H. Yukawa, N. Morisaku, Y. Li, K. Koyima, R. Rong, Y. Shinzato, R. Sekine and M. Morinaga, *Journal of Alloys and Compounds*, 2007, **446-447**, 242.
- 4. C. Rongeat, I. L. Jansa, S. Oswald, L. Schultz and O. Gutfleisch, Acta Materialia, 2009, 57, 5563.
- 5. X. Xiao, K. Yu, X. Fan, Z. Wu, X. Wang, C. Chen, Q. Wang and L. Chen, *International Journal of Hydrogen Energy*, 2011, **36**, 539.
- 6. M. Kumar and T. Das, International Journal of Hydrogen Energy, 2024, 50, 367-378.
- 7. M. Fichtner, P. Canton, O. Kircher, A. Leon, Journal of Alloys and Compounds, 2005, 404-406, 732-737.
- 8. T. J. Frankcombe, Chem Rev., 2012, 112, 2164-2178.
- 9. F. J. Desai, M. N. Uddin, M. M. Rahman and R. Asmatulu, *International Journal of Hydrogen Energy*, 2023, 48, 29256-29294.
- 10. Y.-J. Kwak, M.-Y. Song and K.-T. Lee, Metals, 2024, 14, 227.
- 11. M. Ismail, Y. Zhao, X. B. Yu, J. F. Mao and S. X. Dou, *International Journal of Hydrogen Energy*, 2011, **36**, 9045-9050.
- 12. P. Yu, Y. S. Chua, H. Cao, Z. Xiong, G. Wu and P. Chen, *Journal of Energy Chemistry*, 2014, 23, 414-419.
- 13. G. Nolze and W. Kraus, *PowderCell for Windows*, Version 2.4, BAM, Berlin, 2000; ICSD, Inorganic Crystal Structure Database, FIZ Karlsruhe, Germany.
- 14. ICDD PDF-4+ 2024, International Centre for Diffraction Data, Newtown Square, PA, USA; *PANalytical HighScore Plus*, Version 4.9, Malvern Panalytical.
- 15. A. C. Larson and R. B. Von Dreele, *General Structure Analysis System (GSAS)*, Los Alamos National Laboratory Report LAUR 86–748, 2004; B. H. Toby, *J. Appl. Crystallogr.*, 2001, **34**, 210–213.
- 16. K. J. Gross, S. Guthrie, S. Takara and G. Thomas, Journal of Alloys and Compounds, 2000, 297, 270-281.
- 17. C. B. Porciúncula, N. R. Marcilio, I. C. Tessaro and M. Gerchmann, *Brazilian Journal of Chemical Engineering*, 2012, **29**, 337-348.
- 18. H. Yukawa, N. Morisaku, Y. Li, K. Komiya, R. Rong, Y. Shinzato, R. Sekine and M. Morinaga, *Journal of Alloys and Compounds*, 2007, **446-447**, 242-247.
- 19. C. Suryanarayana, *Prog. Mater. Sci.*, 2001, **46**, 1–184.
- 20. J. S. Benjamin, Metall. Trans., 1970, 1, 2943–2951.
- 21. F. A. H. Yap and M. Ismail, Int. J. Electroactive Mater., 2018, 6, 48-56.
- 22. M. G.Barker, P. G. Gadd and M. J. Begley, J. Chem. Soc. Chem. Comm., 1981, 379–381.

5. Dehydrogenation in the NaBH₄-NaOH system

5.1 Introduction

5.1.1 Sodium borohydride (NaBH₄) as a solid-state hydrogen store

NaBH₄ (sodium borohydride) is a hydride with a high theoretical gravimetric hydrogen content of 10.8 wt.%. Due to its solid state at room temperature and its high chemical stability, it is considered a promising solid-state hydrogen storage material.¹ Sodium borohydride has a molar mass of 37.83 g mol⁻¹ and is an inorganic salt composed of Na⁺ cations and BH₄⁻ anions.² The BH₄⁻ anion adopts a tetrahedral structure with an sp³ hybridized boron atom at the centre of the tetrahedron.^{3,4} It crystallises in cubic space group, *Fm*-3*m*. The B-H bond in NaBH₄ can be cleaved by both hydrolysis and thermolysis to release pure hydrogen gas. Practically, carbon- and nitrogen-free NaBH₄ is low-cost, and does not produce harmful gas-phase contaminants, such as CO and NH₃, during decomposition, which are known to be detrimental to fuel cells.^{5,6} The thermal decomposition and hydrolytic decomposition reactions of NaBH₄ can be described by reactions 1 and 2, respectively.

Thermolysis: NaBH₄
$$\rightarrow$$
 Na + B + 2H₂ \uparrow (10.68 wt.%) (1)
Hydrolysis: NaBH₄ + 2H₂O \rightarrow NaBO₂ + 4H₂ \uparrow (10.94 wt.%) (2)

However, the high decomposition temperature of NaBH₄ (>500°C) limits its practical application. In recent years, researchers have explored various methods to lower its decomposition temperature and improve hydrogen storage performance, achieving significant progress.⁷

The NaBH₄-MgH₂ system has attracted widespread attention due to its relatively low cost and high hydrogen storage capacity. Studies have shown that when NaBH₄ is mixed with MgH₂ in a 2:1 molar ratio, the decomposition of MgH₂ occurs before NaBH₄, and NaBH₄ decomposes at *ca.* 450 °C, forming MgB₂ and NaH while releasing hydrogen. This process significantly lowers the decomposition temperature of NaBH₄, but it is still relatively high.⁸ The reaction is shown below:

$$2NaBH_4 + MgH_2 = 2NaBH_4 + Mg + H_2$$
 (3)

$$2NaBH_4 + Mg \rightleftharpoons 2NaH + MgB_2 + 4H_2 \tag{4}$$

To further reduce the dehydrogenation temperature of the NaBH₄-MgH₂ system and enhance hydrogen storage performance, Mao *et al.* attempted to add various catalysts. TiF₃ was found to be an effective catalyst, significantly lowering the dehydrogenation temperature from 450 °C to 320 °C and increasing the dehydrogenation rate.⁹ Moreover,

the TiF₃-doped NaBH₄-MgH₂ system was able to absorb 5.89 wt.% hydrogen within 12 hours at 600 °C and 4 MPa H₂, showing good reversibility.

Using coupled calorimetric-pressure measurement techniques, Milanese *et al.* found that the dehydrogenation enthalpy of the NaBH₄-MgH₂ system with a 2:1 molar ratio was 90.9 kJ mol⁻¹ H₂, lower than that of pure NaBH₄ (106.8 kJ mol⁻¹ H₂), indicating that the presence of MgH₂ significantly reduced the dehydrogenation enthalpy of NaBH₄.¹⁰ Additionally, using MgF₂ as an additive not only lowered the dehydrogenation temperature and enthalpy of NaBH₄ in the 2:1 system but also increased the dehydrogenation rate.

Kumar *et al.* studied the catalytic effect of ZrCl₄ on the thermal decomposition of NaBH₄. The results showed that ZrCl₄ significantly lowered the decomposition temperature of NaBH₄, allowing hydrogen to be released below 300 °C.¹¹ Furthermore, during ball milling, ZrCl₄ was reduced to ZrCl₂ and metallic zirconium, which exhibited high catalytic activity and reduced the activation energy of NaBH₄ (from 275 kJ mol⁻¹ to 180 kJ mol⁻¹), thus reducing sodium evaporation losses.

Mao *et al.* synthesized NaBH₄·N₂H₄ and NaBH₄·2N₂H₄ by complexing NaBH₄ with hydrazine (N₂H₄). The studies showed that these complexes could release hydrogen at relatively low temperatures (around 50 °C), and the decomposition products contained a large amount of hydrogen and nitrogen, and small amount of ammonia. The structure and decomposition behaviour of these complexes offer new insights for designing novel hydrogen storage materials.¹²

Shin *et al.* investigated the complex of NaBH₄ with oxalic acid dihydrate (OA·2H₂O) and achieved rapid pure hydrogen generation at 50 °C through a thermally induced dry hydrolysis reaction.¹³ This method does not require additional solvents and utilizes the water molecules generated from the decomposition of OA·2H₂O to hydrolyze NaBH₄, offering a highly efficient and safe approach. The total reaction is shown below:

$$NaBH_4 + 2H_2O \rightarrow NaBO_2 + 4H_2 \tag{5}$$

5.1.2 Purpose

By applying the insight gained from studying the NaH-NaOH and NaAlH₄-NaOH systems extended to NaBH₄, this chapter aims to change the thermodynamics of dehydrogenation completely by introducing new reaction pathways by utilizing NaOH. Some methods such as ball-milling and adding an excess of NaOH would be used to improve the dehydrogenation reaction between NaBH₄ and NaOH. Investigating the reaction mechanism between NaBH₄ and NaOH remains a crucial part of the process towards optimising the storage system.

5.2 Experimental

NaBH₄ (Sigma Aldrich, powder, \geq 98%) was used as received. NaOH (Alfa Aesar, pellet, 99.99%) was dried prior to synthesis experiment through use of the Schlenk line. (100 °C; -2×10^{-2} bar)

Because of the air and moisture sensitivity of NaOH and NaBH₄, all operations were carried out in a recirculating Argon or N₂-filled (BOC, 99.998%) glovebox (MBraun LABstar, O₂ < 10 ppm, H₂O < 0.5 ppm). NaOH was ball-milled alone for 1 h to reduce the particle size of the powder before mixtures of NaOH and NaH were subsequently themselves milled. NaOH starting material was (re)dried overnight on the Schlenk line before each subsequent use in synthesis. NaOH (Alfa Aesar, pellet, 99.99%) was ball-milled for 1 hour to reduce the particle size of the powder. After ball-milling, the NaOH was sent to Schlenk line to dry overnight. (100 °C; -2×10⁻² bar)

5.2.1 Milling of NaOH-NaBH₄

NaOH and NaBH₄ mixtures (each *ca.* 0.4 g total mass) were weighed and then transferred to a stainless-steel grinding jar that was filled with eight stainless steel balls (10 mm diameter), each of which weighed approx. 4 g. The grinding jar was sealed under argon before removal from the glovebox. Ball milling was conducted at a rotation speed of 400 rpm with a ball-to-powder ratio of 80: 1 in a planetary ball mill (Retsch PM100) in 5-minute milling periods (reverse rotation) followed by 5-minute rest periods.

5.2.2 Powder X-ray Diffraction (PXD)

All starting materials and NaBH₄-NaOH hydrogen release systems were characterized using powder X-ray diffraction (PXD). All the materials used in this study were air sensitive. Therefore, all the samples were prepared using the air-sensitive sample holder under inert atmosphere. (glovebox) All the materials were characterized by PANalytical X'Pert and Rigaku Miniflex. Diffraction data was collected over a 2θ range of 5–85° for 1 h to facilitate phase identification. The obtained diffraction data were compared with appropriate reference patterns using the ICSD database via PowderCell or the ICDD PDF database via PANalytical HighScore Plus and Jade 6.5 software.^{14,15} Rietveld refinements were performed using the General Structure Analysis System (GSAS) with the EXPGUI interface.¹⁶

5.3 Results and Discussion

5.3.1 Thermal Treatment of NaBH₄

Figure 5-1 shows a comparison between NaBH₄ as received and standard NaBH₄. From the figure, it can be seen that the phase of NaBH₄ as received is pure, with no additional peaks and all the peaks corresponding correctly.

To investigate whether ball-milled NaBH₄ (2 hours, 400 rpm) undergoes an independent decomposition reaction prior to heating to 400 °C. Figure 5-2 shows the thermal behaviour of ball-milled (2h) NaBH₄ when heated to 400 °C. It can be observed that there are no distinct peak temperatures, and no mass change occurs. This indicates that the ball-milled NaBH₄ does not undergo any reactions before 400 °C.

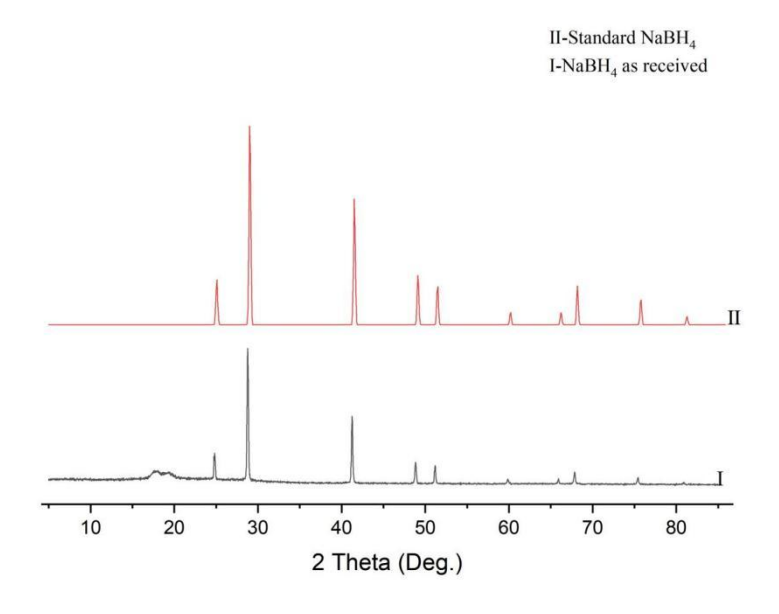


Figure 5-1: PXD patterns of standard NaBH₄ (II) and ball-milled commercial NaBH₄ (I).

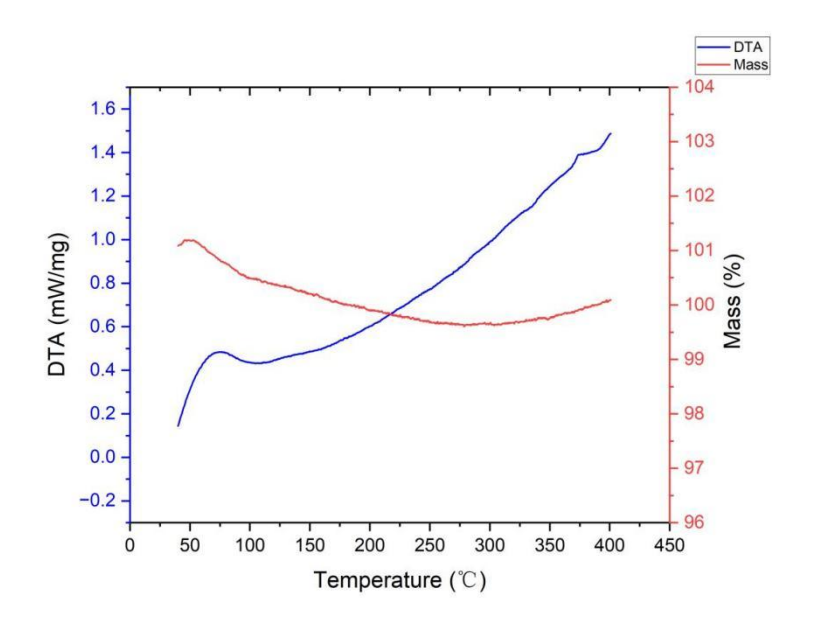


Figure 5-2: TG (red) and DTA (blue) profiles for ball-milled NaBH₄ (2h, 400rpm) on heating from

5.3.2 Mechanism of Ball-milled NaBH₄-xNaOH (x = 1, 2, 3, 4)

Figures 5-3 and 5-4 show the thermal behaviour of a 1:1 mixture of NaBH₄-NaOH after ball milling for 2h. By contrast to NaBH₄ itself, it is evident that the NaBH₄-NaOH mixture starts releasing hydrogen gas ca. 300 °C and peaks ca. 360 °C. However, the observed mass loss (2.64 wt.%) is far from the theoretical hydrogen mass loss of 6.4 wt.% if all the hydrogen element in 1:1 mixture of NaBH₄:NaOH was released. The TG curve is not smooth. The TG curve exhibits fluctuations at ca. 245 °C and 325 °C. The DTA peak at 245 °C is not accompanied by any mass loss in the TG curve without hydrogen evolution. This suggests that the peak may be analogous to the first peak temperature (175 °C) observed for the NaH-NaOH system in Chapter 3, which is indicative of the formation of a solid solution or intermediate. However, the subsequent decrease and sudden increase in the TG curve are highly unusual. One possible explanation is that the formation of the solid solution or intermediate may have led to a volumetric expansion, causing a small portion of the product to leak out of the crucible. This is supported by the overall downward trend in the TG curve following the fluctuations. The fluctuations at 325 °C may be attributed to the simultaneous occurrence of multiple reactions. This is also evident from the MS data (Figure 5-4), which shows two distinct fluctuations between 300 and 360 °C.

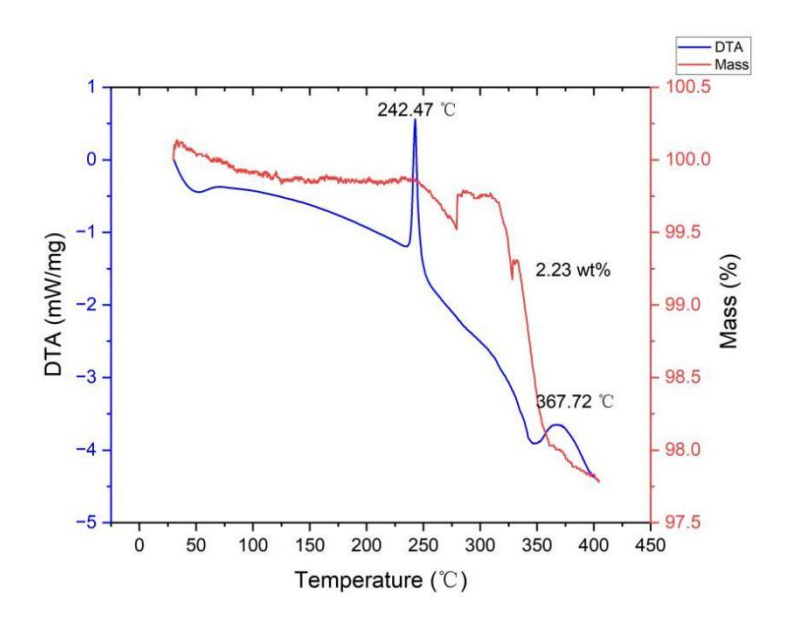


Figure 5-3: TG (red) and DTA (blue) profiles for ball-milled 1:1 NaBH₄:NaOH (2h, 400rpm) on heating from 35-400 °C at 2 °C min⁻¹ under flowing Ar(g).

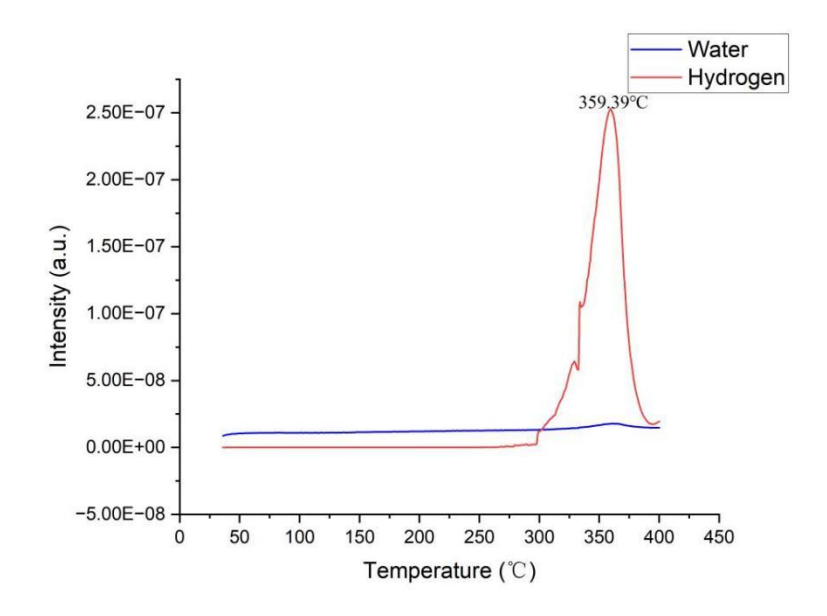


Figure 5-4: Mass spectrometry output for water (m/z = 18; blue) and hydrogen (m/z = 2; red) as a function of temperature for ball-milled 1:1 NaBH₄:NaOH (2h, 400rpm) on heating from 35-400 °C at 2 °C min⁻¹ under flowing Ar(g).

To investigate the thermal reaction mechanism of NaBH₄-NaOH, it is essential to start with the samples after ball milling and before thermal treatment. Figure 5-5 shows the PXD patterns of NaBH₄ with different molar ratios of NaOH after ball milling. It can be seen that, similar to NaAlH₄ in previous Figure 4-18, NaBH₄ reacts with NaOH during ball milling. However, unlike the NaAlH₄-NaOH system, several peaks at 36° in the diffraction pattern of the post-milled sample cannot be matched to patterns in the ICDD PDF using the search-match software. A key difference is that while NaAlH₄-NaOH generates hydrogen gas during ball milling, NaBH₄-NaOH does not. This can be inferred from the change in oxygen levels in the glove box. When NaAlH₄-NaOH sample's milling jar enters the glove box, the oxygen level suddenly increases sharply, but after some time, it dramatically decreases. This is a clear deviation from the normal oxygen intake phenomenon in the glove box. Upon the introduction of O₂ into the glove box, the oxygen level experiences a sharp and sudden increase, followed by a gradual decline, even that may need regeneration. After ruling out the possibility of O₂ contamination, the likelihood of H₂ generation from the ball milling of NaAlH4 and NaOH becomes highly possible. In contrast, the ball milling of NaBH₄ and NaOH does not cause any significant changes in the O₂ and H₂O levels within the glove box. This observation indicates that the hydrogen element in NaBH₄ and NaOH does not evolve as H₂ gas under these conditions.

From Figure 5-5, it can be seen that after 2 hours of ball milling, the NaOH peak in the diffraction pattern for the 1:1 NaBH₄:NaOH sample completely disappears, whereas NaOH peaks are visible in the 1:2 NaBH₄:NaOH sample. The relative intensity of the NaOH phase gradually increases from the 1:2 NaBH₄:NaOH to the 1:4 NaBH₄:NaOH molar ratio.

Moreover, all samples exhibit the formation of a new intermediate phase (Na-B-O-H) within the angular range of 36° to 40°.

To investigate whether NaBH₄ and NaOH react completely, the 1:3 NaBH₄:NaOH mixture was ball milled for 4 hours and 10 hours, and the 1:4 NaBH₄:NaOH mixture was ball milled for 10 hours. As shown in Figure 5-6, after ball milling the 1:3 NaBH₄:NaOH mixture for both 4 and 10 hours, only a minor fraction of NaBH₄ remains in the samples. Compared to the 1:3 NaBH₄:NaOH mixture ball milled for 2 hours, the NaOH phase is completely absent, and the relative intensity of the NaBH₄ phase is significantly reduced. This indicates that both NaBH₄ and NaOH are consumed, leading to the formation of a new intermediate phase (Na-B-O-H). However, it is noteworthy that the 1:3 NaBH₄:NaOH mixture ball milled for 10 hours exhibits substantial differences compared to the 4-hour milled sample. One possible explanation is that after forming the (Na-B-O-H) intermediate with NaOH, NaBH₄ undergoes further phase transformations under the mechanical action of ball milling. In contrast, for the 1:4 NaBH₄:NaOH mixture ball milled for 10 hours, the peaks corresponding to NaBH₄ and NaOH are completely absent.

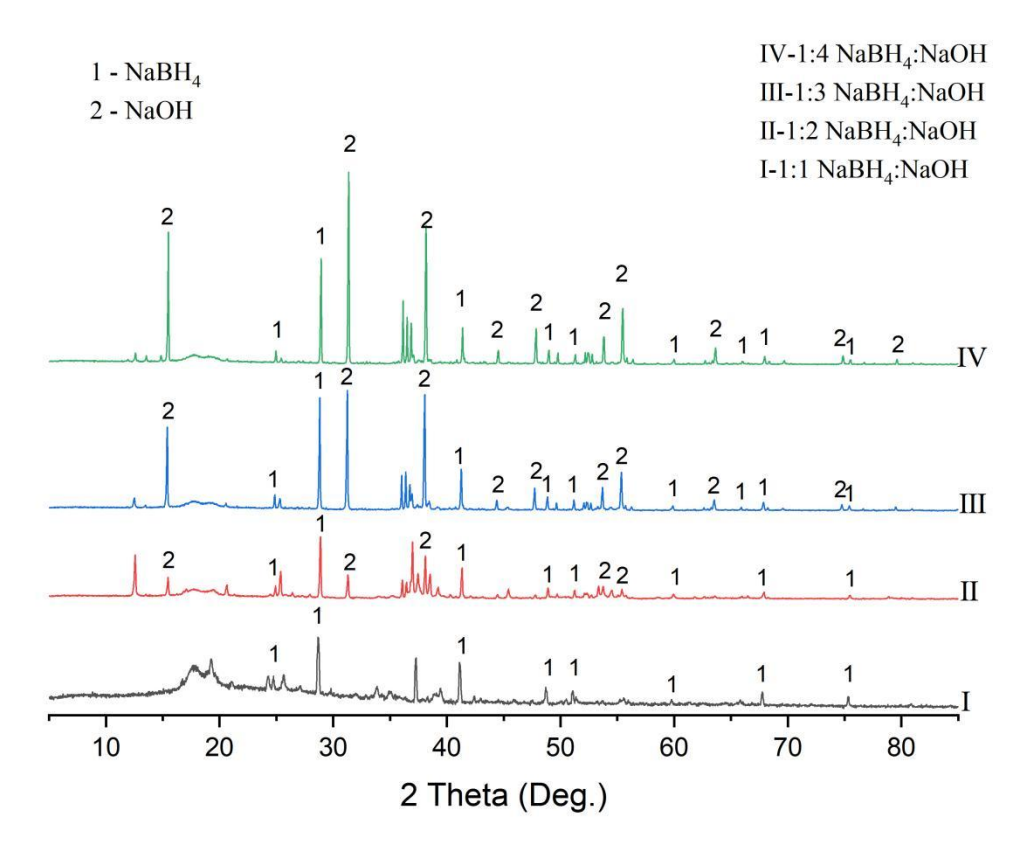


Figure 5-5: PXD patterns of ball-milled NaBH₄:NaOH (2h, 400rpm) with varing molar ratio (1:1 I; 1:2 II; 1:3 III; 1:4 IV). (1 represent NaBH₄, 2 represent NaOH)

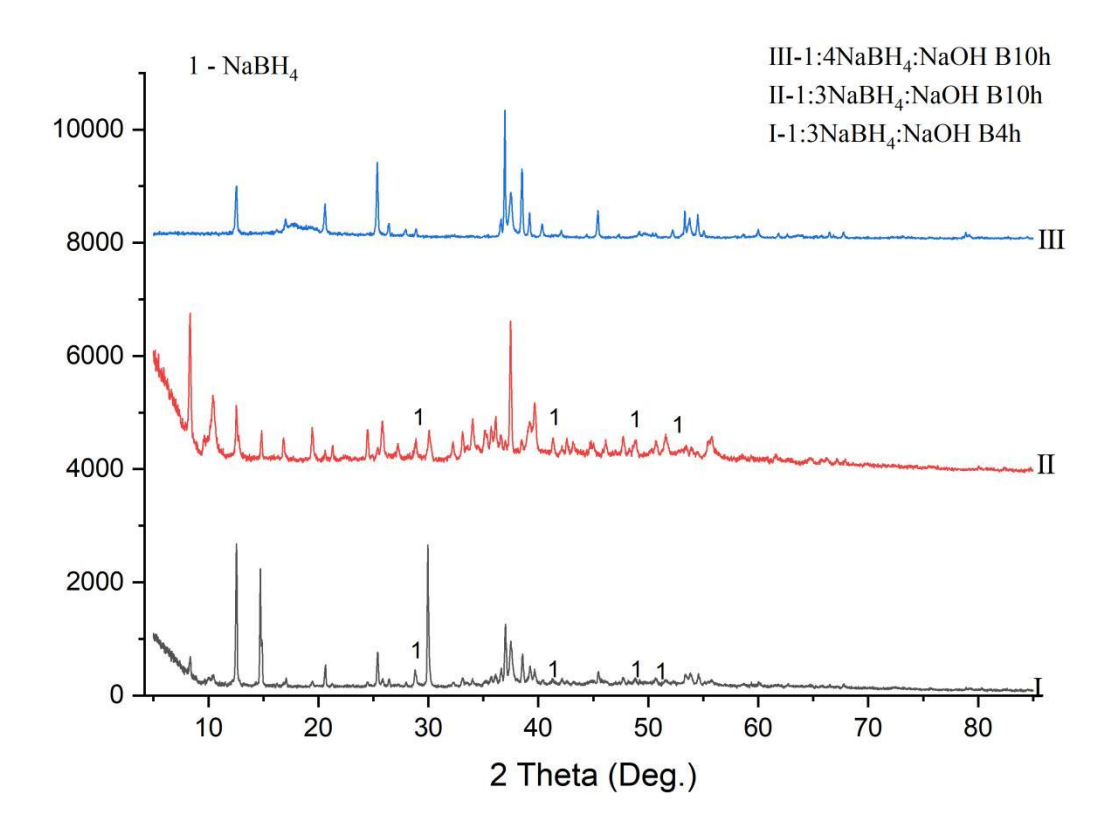


Figure 5-6: PXD patterns of ball-milled 1:4 NaBH₄:NaOH (10h; III) and 1:3 NaBH₄:NaOH(4h, I; 10h, II).

Figures 5-7 and 5-8 display the thermal behaviour of 1:2 NaBH₄:NaOH, 1:3 NaBH₄:NaOH, and 1:4 NaBH4:NaOH after ball-milling for 2h and heating to 400 °C. The TG curves for 1:2 NaBH₄:NaOH and 1:3 NaBH₄:NaOH both show a fluctuating segment around 325 °C, but this is not as apparent in NaBH₄-4NaOH. The first DTA peak temperature for both 1:1 NaBH₄:NaOH and 1:2 NaBH₄:NaOH occurs at ca. 240 °C. However, apparently uniquely for 1:3 NaBH₄:NaOH, two DTA peaks appear between 240-250 °C, whereas 1:4 NaBH₄:NaOH presents a single peak at ca. 250 °C. It seems that 2 reactions occur (from 240-250 °C) that change in emphasis as the NaOH ratio increases; the lower T reaction predominates for the 1:2, both exist in the 1:3 with the higher T peak now more intense, and the higher T one hugely predominates in 1:4. Thus, both thermal events happen in each sample, but the reaction pathways diverge with varying ratio. Furthermore, the second peak temperature for 1:1 NaBH₄:NaOH and 1:2 NaBH₄:NaOH occurs around 370 °C, with the MS peak at 360 °C. However, for 1:3 NaBH₄:NaOH and 1:4 NaBH₄:NaOH, the second peak temperature shifts to around 380 °C, and the MS peak occurs at 370 °C. In conclusion, NaBH₄ with different mole ratios of NaOH undergoes a complex series of reactions, which will need to be further clarified through the PXD analysis in the next steps.

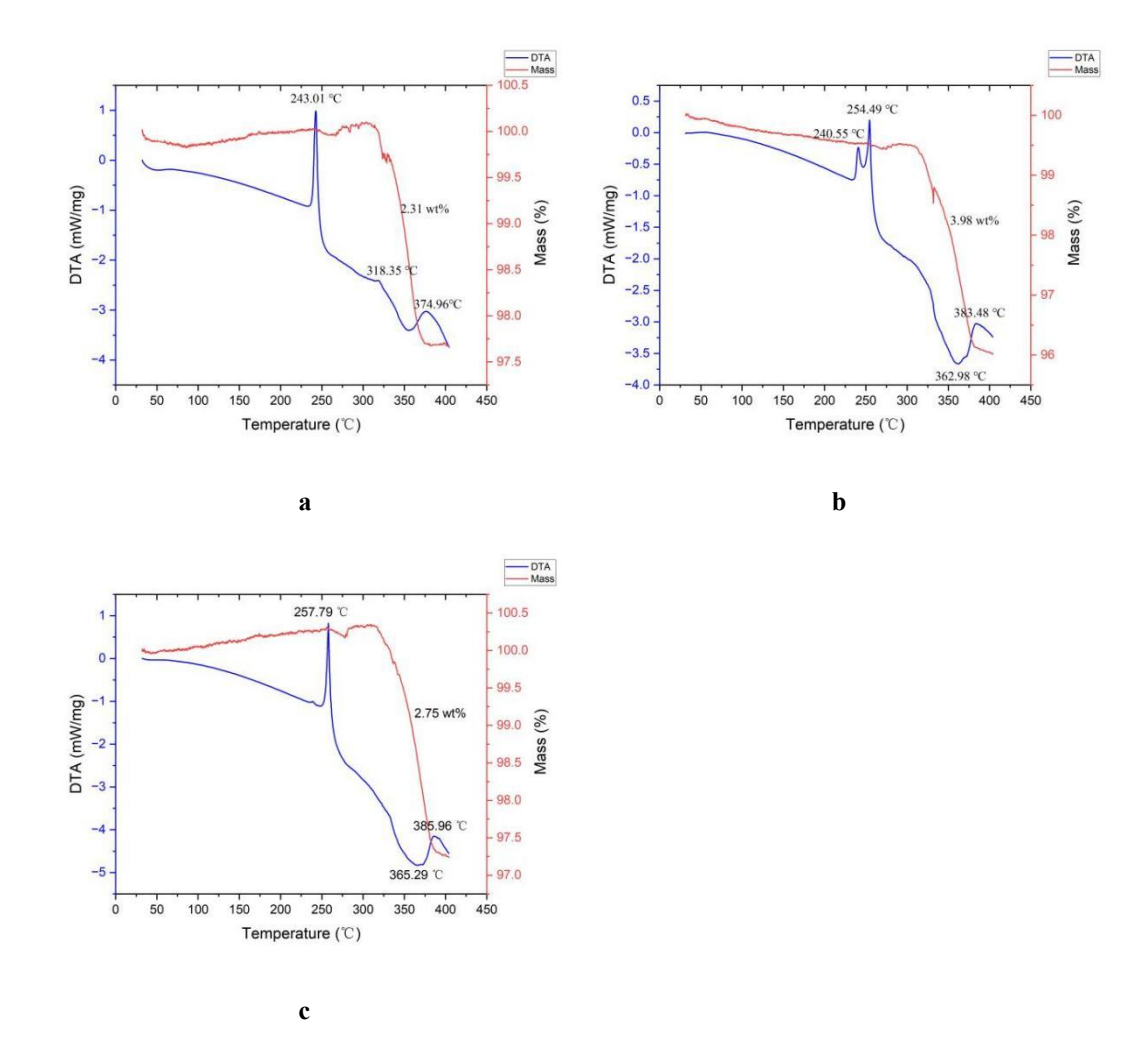
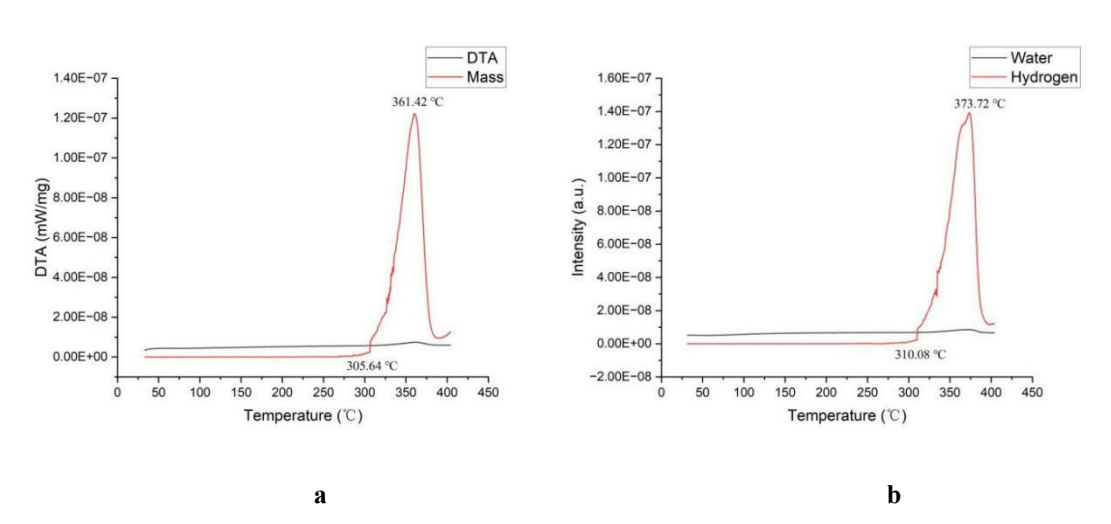


Figure 5-7: TG (red) and DTA (blue) profiles for ball-milled NaBH₄:NaOH (2h, 400rpm) with varing molar ratio (a)1:2 NaBH₄:NaOH (b)1:3 NaBH₄:NaOH (c)1:4 NaBH₄:NaOH on heating from 35-400 °C at 2 °C min⁻¹ under flowing Ar(g).



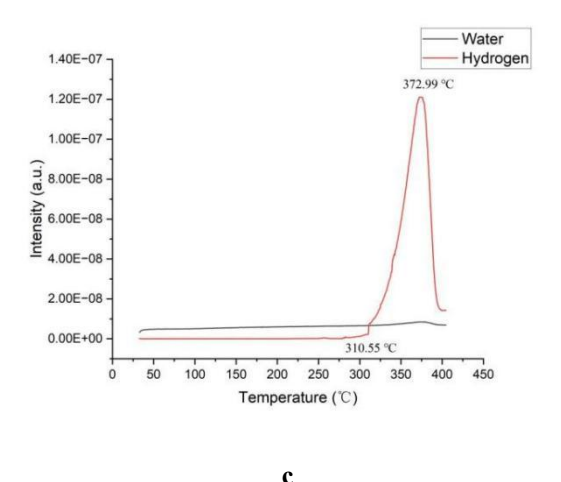


Figure 5-8: Mass spectrometry output for water (m/z = 18; blue) and hydrogen (m/z = 2; red) as a function of temperature for ball-milled NaBH₄:NaOH (2h, 400rpm) with varying molar ratio (a)1:2 NaBH₄:NaOH (b)1:3 NaBH₄:NaOH (c)1:4 NaBH₄:NaOH on heating from 35-400 °C at 2 °C min⁻¹ under flowing Ar(g).

To investigate the potential reactions between NaBH₄ and NaOH, mixtures with molar ratios of 1:3 and 1:4 (NaBH₄:NaOH) were heated to various temperatures and subsequently analysed using PXD. However, regardless of the NaBH₄:NaOH molar ratio, no diffraction peaks can be identified from room temperature to 300 °C when compared to the ICDD PDF. Therefore, the primary focus is on the peaks displayed by 1:3 NaBH₄:NaOH and 1:4 NaBH₄:NaOH at 400 °C.

Figure 5-9 shows that peaks in the diffraction patterns of 1:3 NaBH₄:NaOH remain unidentifiable at 300 °C. However, between 400-500 °C, a notable feature of the patterns is that there are no significant changes to the phase positions present, indicating that most reactions are completed ca. 400 °C. However, Figure 5-10 shows that at 400 °C, 1:3 NaBH₄:NaOH generates a large amount of Na₃BO₃, a small amount of Na and NaOH. Figure 5-11 shows that 1:4 NaBH₄:NaOH at 400 °C generates a large amount of Na₃BO₃, a moderate amount of Na₂O, and contains a small amount of NaOH. The presence of Na, Na₂O, and NaOH in 1:3 NaBH₄:NaOH and 1:4 NaBH₄:NaOH suggests that NaH may be one of product of the dehydrogenation reaction of an intermediate or multiple intermediates. The possible reason is that the initial decomposition temperature of NaH in chapter 3 Figure 3-7 is close to 325 °C, which coincides with the temperature where fluctuations were observed in the TG curves of 1:1 NaBH₄:NaOH, 1:2 NaBH₄:NaOH and 1:3 NaBH₄:NaOH. Moreover, the additional NaOH in 1:4 NaBH₄:NaOH could react with NaH to form Na₂O. To verify this hypothesis, 1:4 NaBH₄:NaOH was heated to 320 °C and maintained at 320 °C for 1 hour. As shown in Figure 5-12, a small amount of Na₃BO₃ and NaH were formed under these conditions. Therefore, we can tentatively propose an outline reaction scheme for 1:3 NaBH₄:NaOH and 1:4 NaBH₄:NaOH (principally between

300-400 °C):

NaBH₄-3NaOH:

$$NaBH_4 + 3NaOH \rightarrow "(Na-B-O-H) intermediate(s)"$$
 ball-milling (6)

"(Na-B-O-H) intermediate(s)"
$$\rightarrow$$
 Na₃BO₃ + NaH + 3H₂ T = 300 - 400 °C (7)

$$Na_3BO_3 + NaH + 3H_2 \rightarrow Na_3BO_3 + Na + 3.5H_2$$
 $T = 325 - 400 \text{ }^{\circ}\text{C}$ (8)

 $(NaH \rightarrow Na + H_2 \quad T \ge 325)$

NaBH₄-4NaOH:

$$NaBH_4 + 4NaOH \rightarrow "(Na-B-O-H) intermediate(s)"$$
 ball-milling (9)

"(Na-B-O-H) intermediate(s)"
$$\rightarrow$$
 Na₃BO₃ + NaH + NaOH + 3H₂ T = 300 - 400 °C (10)

$$Na_3BO_3 + NaH + NaOH + 3H_2 \rightarrow Na_3BO_3 + Na_2O + 4H_2$$
 $T = 325 - 400$ °C (11)

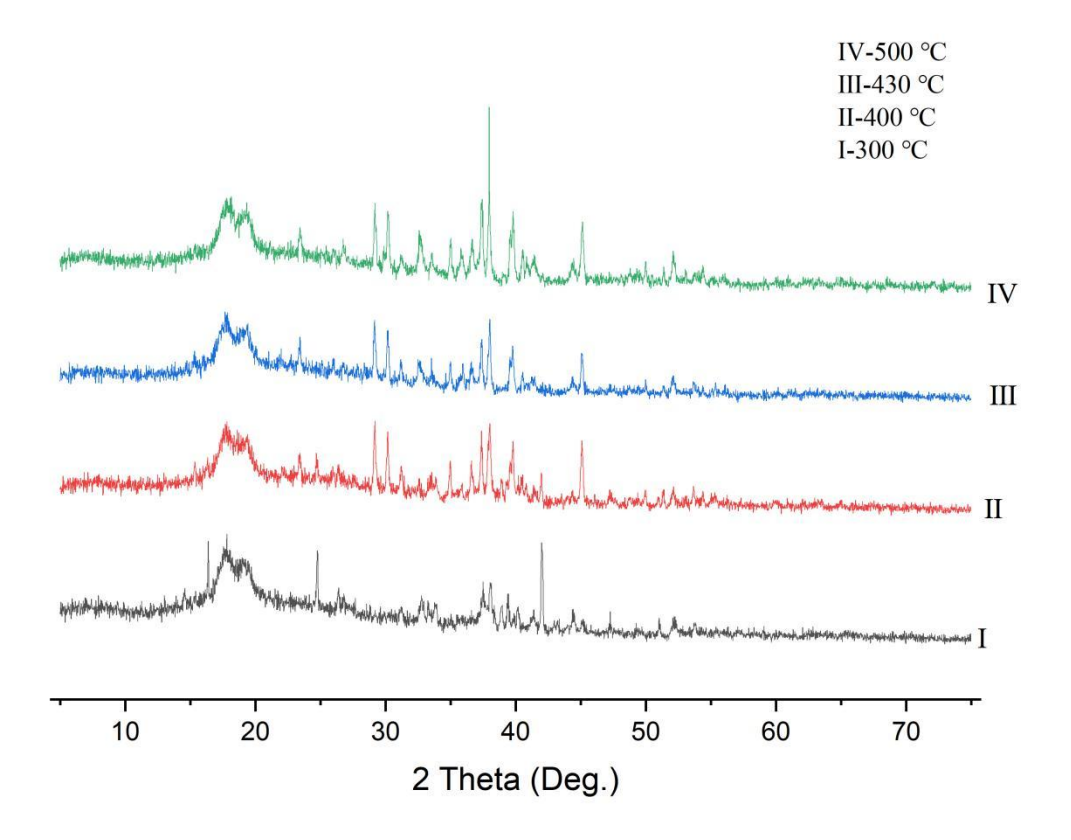


Figure 5-9: PXD patterns of ball-milled 1:3 NaBH₄:NaOH (2h, 400rpm) after heating to 300 (I), 400 (II), 430 (III) and 500 (IV) °C under flowing Ar(g). (and cooling to room temperature)

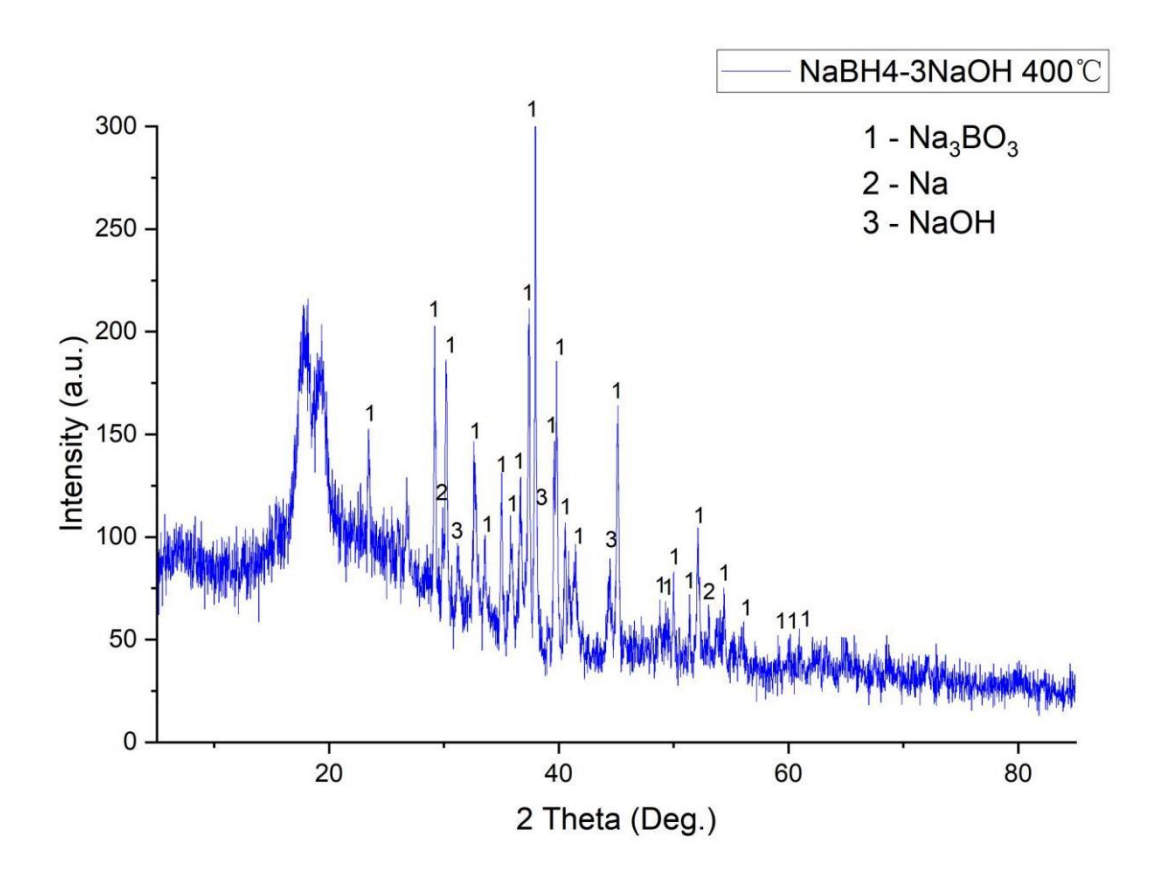


Figure 5-10: PXD pattern of ball-milled 1:3 NaBH₄:NaOH (2h, 400rpm) after heating to 400 °C (and cooling to room temperature). (1 represent Na₃BO₃; 2 represent Na; 3 represent NaOH)

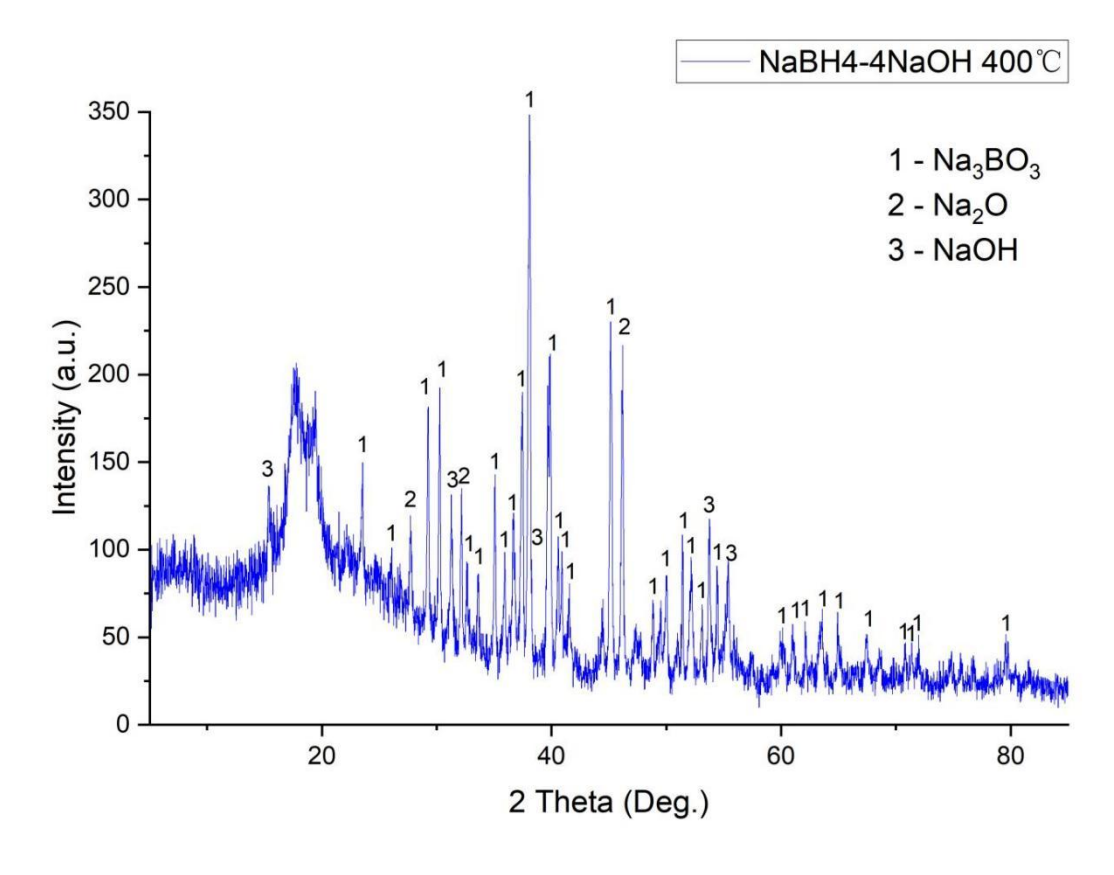


Figure 5-11: PXD pattern of ball-milled 1:4 NaBH₄:NaOH (2h, 400rpm) after heating to 400 °C(and cooling to room temperature). (1 represent Na₃BO₃; 2 represent Na₂O; 3 represent NaOH)

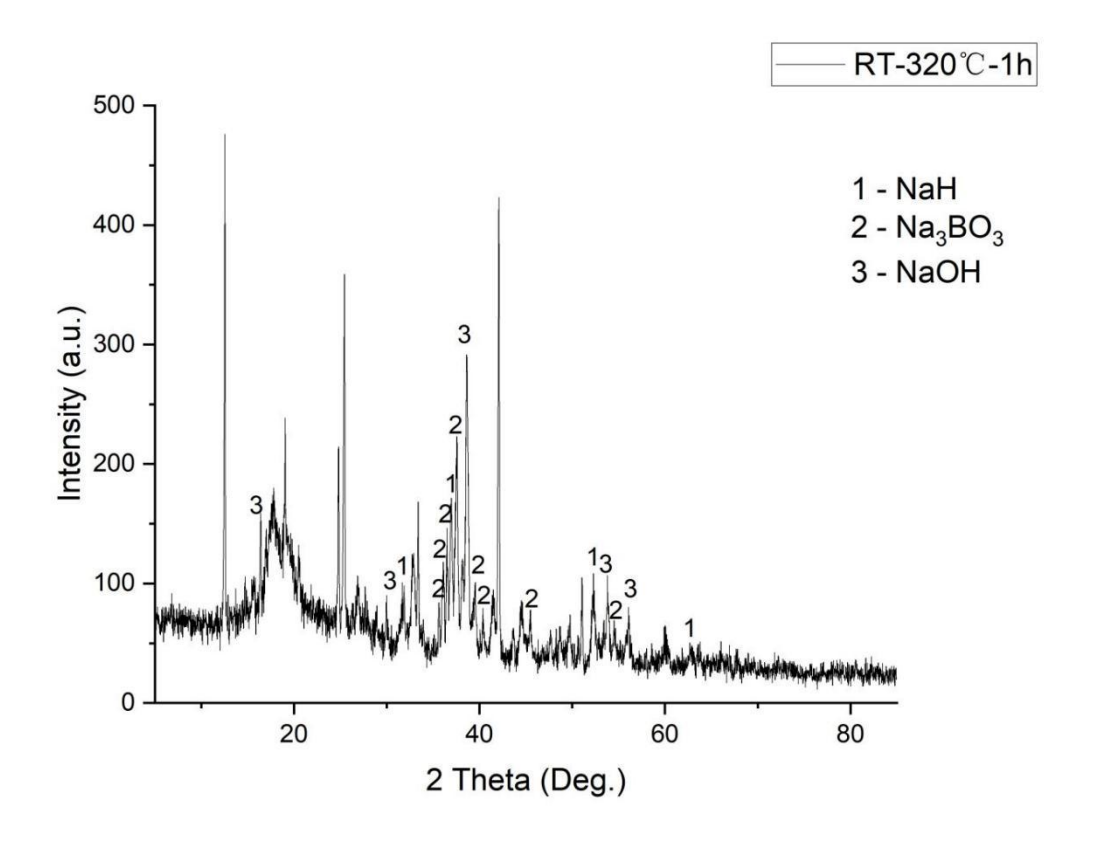


Figure 5-12:PXD pattern of ball-milled 1:4 NaBH₄:NaOH (2h, 400rpm) after heating to 320 °C and keeping for 1h (cooling to room temperature). (1 represent NaH; 2 represent Na₃BO₃; 3 represent NaOH)

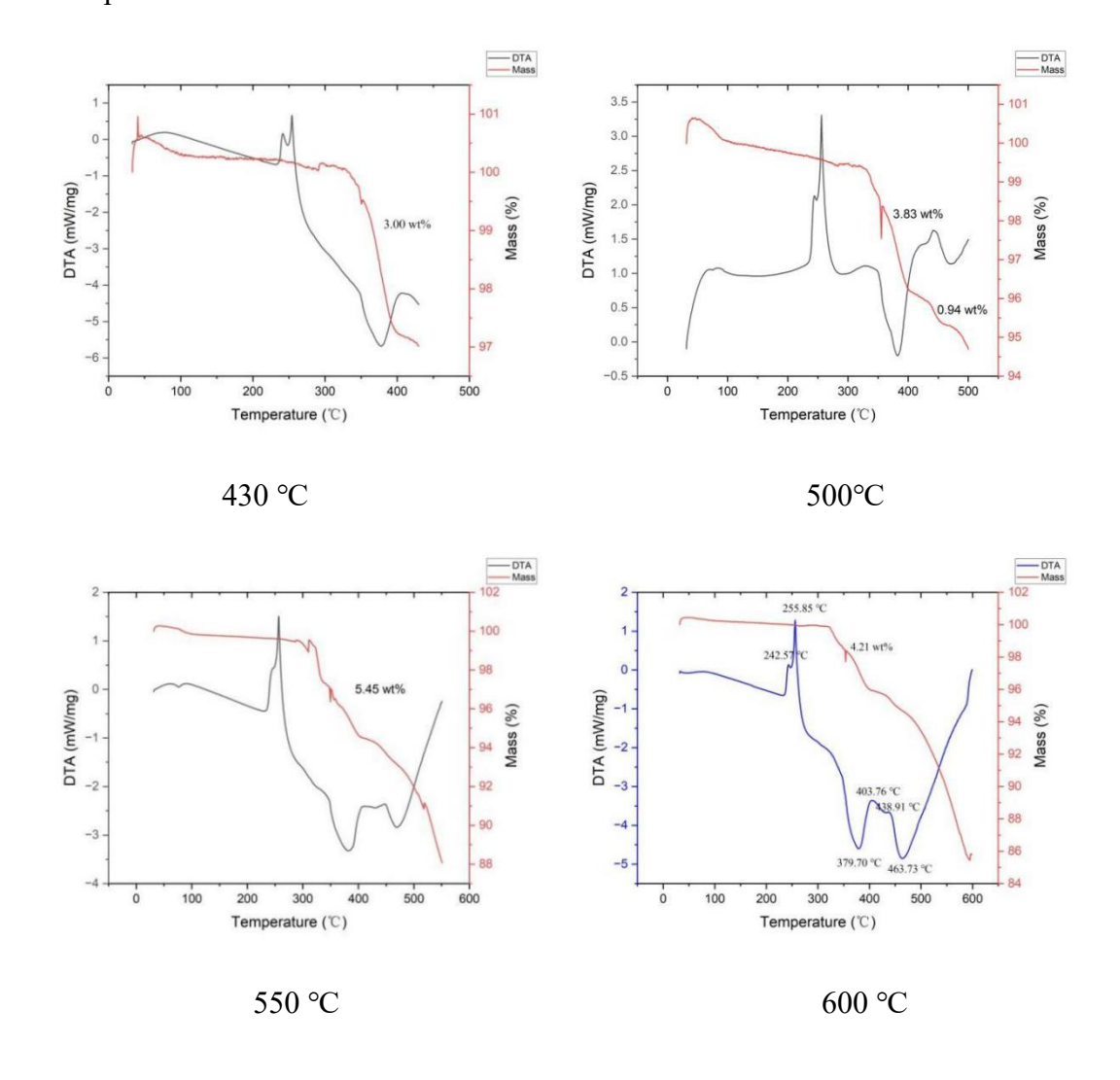
The proposed reaction pathway for the 1:3 NaBH₄:NaOH mixture is summarized by the following overall reaction:

$$NaBH_4 + 3NaOH \rightarrow Na_3BO_3 + Na + 3.5H_2$$
 (11)

The theoretical mass loss for the reaction is 4.41 wt.%. Prior to 300 °C, only phase transitions of (Na-B-O-H) intermediates occur. At *ca.* 310 °C, these intermediates begin to react to form Na₃BO₃ and NaH, with concurrent hydrogen gas evolution, although at a slow reaction rate. As shown in Figure 5-12, when the sample is held at 320 °C for 1 hour, the relative intensities of the final products NaH and Na₃BO₃ are not significant. The reaction rate increases markedly only when the temperature is raised to around 350 °C. Meanwhile, NaH begins to decompose at approximately 325 °C. These two reactions proceed simultaneously between 325 °C and 400 °C. For the 1:4 NaBH₄:NaOH sample, the theoretical mass loss is 4.04 wt.%. The NaH formed around 310°C may potentially react with NaOH to produce Na₂O. However, as indicated in Figure 5-7, the mass losses of both products did not reach the expected values.

To verify the proposed reaction pathways, the thermal treatment of the 1:3 NaBH₄:NaOH and 1:4 NaBH₄:NaOH mixtures was conducted multiple times, heating the samples to temperatures above 400 °C to assess whether the theoretical mass loss could be achieved.

However, the hydrogen mass loss in the experiments never reaches the ideal value, regardless of the number of trials. Figures 5-13 and 5-14 show the TG-DTA results for 1:3 NaBH₄:NaOH and 1:4 NaBH₄:NaOH heated to different temperatures with the 2 °C min⁻¹. It can be observed that the mass loss over 300-400 °C differs each time when heating to different temperature. A further interesting observation is shown in Figure 5-15. It can be seen that the thermocouple, originally white, turns grey-black after heating the 1:x NaBH₄:NaOH mixtures. It was noted that the grey-black colouration of the thermocouple also occurs when either NaH or NaAlH₄-NaOH samples are heated. The most likely substance causing this change is Na, as its melting point is quite low, around 97 °C. Evidently, Na may leak out of the crucible during heating. This can lead to inaccuracies in the mass loss calculations because it is impossible to determine precisely what proportion of Na escapes from the crucible and how much remains.



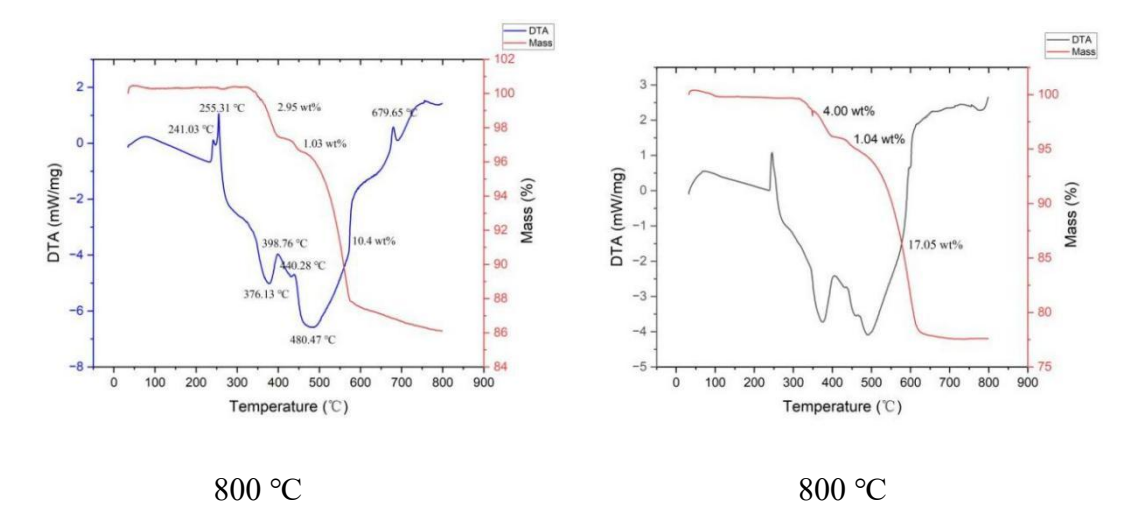


Figure 5-13: TG(red) and DTA(blue) profiles for ball-milled 1:3 NaBH₄:NaOH (2h, 400rpm) on heating from room temperature to different temperature.

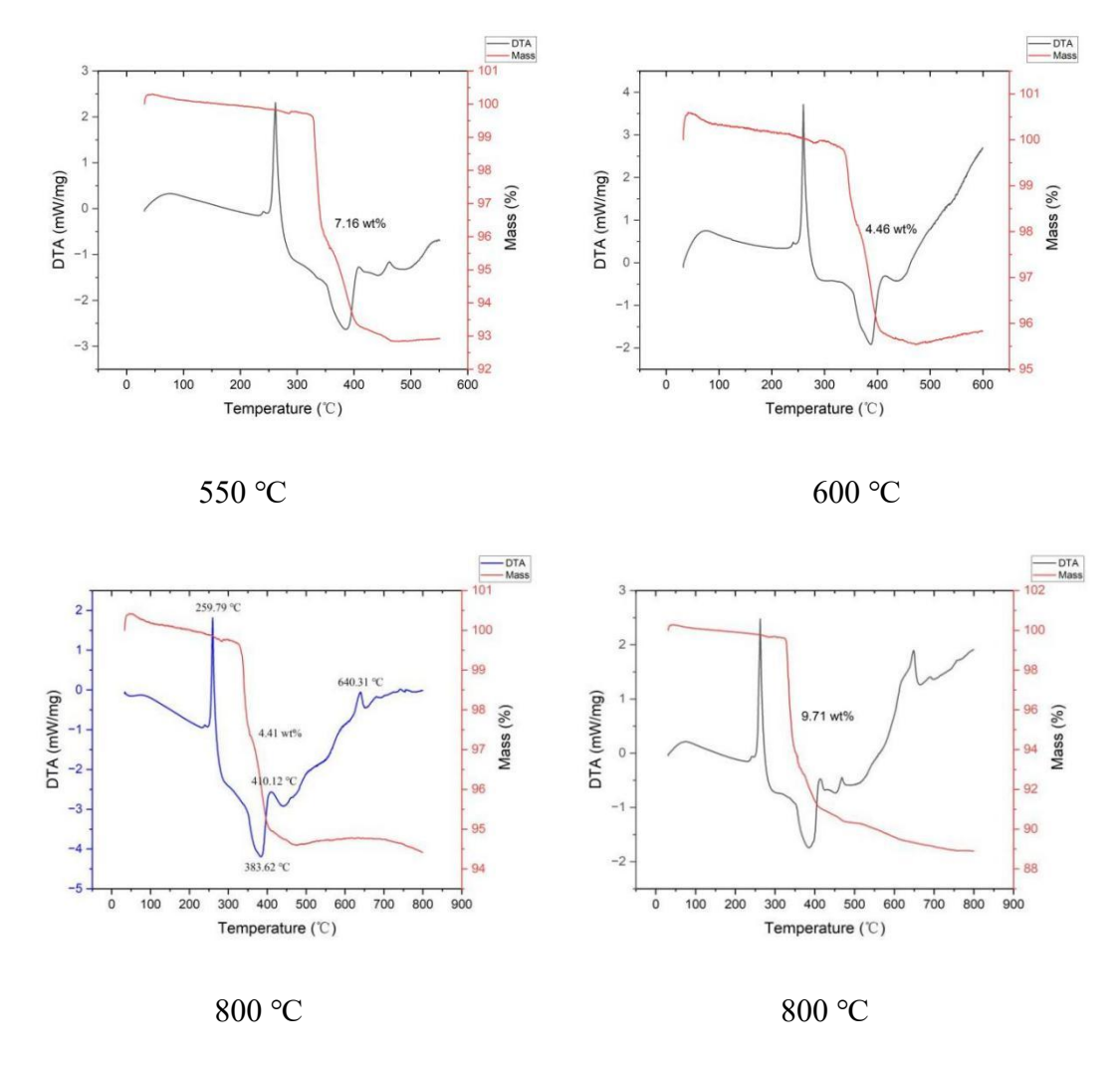


Figure 5-14: TG(red) and DTA(blue) profiles for ball-milled 1:4 NaBH₄:NaOH (2h, 400rpm) on heating from room temperature to different temperature.



Figure 5-15: Photographs showing the appearance of the TG-DTA thermobalance crucible and thermocouple after heating. (1:1 NaBH₄:NaOH, 1:2 NaBH₄:NaOH and 1:3 NaBH₄:NaOH)

To investigate the potential changes that (Na-B-O-H) intermediates may undergo between 300 °C and 400 °C, the 1:4 NaBH₄:NaOH mixture was heated to 300 °C, 340 °C, 360 °C, and 400 °C. After cooling, the samples were analysed using Raman spectroscopy. As shown in Raman Figure 5-16, several peaks were observed, among which the peaks at 3610, 2438, 2299, and 741 cm⁻¹ are particularly noteworthy due to their changes. According to Walrafen et al., the Raman of the hydroxyl group (-OH) indicates that the symmetric stretching vibration of hydroxide ions (OH-) appears at approximately 3620 cm⁻¹ in highly concentrated aqueous solutions and at around 3610 cm⁻¹ in molten NaOH, with significant low-frequency asymmetry.¹⁷ Trudel et al. investigated the Raman of ammonia borane (NH₃BH₃) compounds under high pressure. At zero pressure, the B-H stretching vibrational mode (v_2) of ammonia borane (NH₃BH₃) exhibits a Raman frequency of approximately 2340 cm⁻¹. ¹⁸ Hagemann et al. measured the Raman spectra of the alkali borohydride series MBH₄ (M = Li, Na, K, Rb, Cs) as a function of temperature in the range of 27-270 °C. The symmetric (v₁) B-H stretching vibrations are generally observed in the range of 2200-2300 cm⁻¹, while the asymmetric (v₃) stretching vibrations typically appear between 2350 and 2450 cm⁻¹. ^{19,20} Nakamoto et al. reported that the v₄ bending vibration of the [BO₃]³⁻ ion generally falls within the range of 700-750 cm⁻¹.²⁰

Based on the previous information, when the temperature is raised to 300 °C, both B-H bonds and -OH bonds are present within the (Na-B-O-H) intermediates. Upon heating to 340 °C, the peak corresponding to the [BO₃]³⁻ ion begins to emerge, indicating the formation of Na₃BO₃. When the temperature reaches 360 °C, the vibrational mode of the

B–H bond transitions from symmetric to asymmetric, suggesting that the intermediates start to decompose significantly. However, it is possible that the peak of the -OH bond disappears at this temperature. When the temperature is further increased to 400 °C, the peak of the B-H bond completely vanishes, indicating that the reaction has proceeded to completion. Meanwhile, the peak of the -OH bond reappears. In conjunction with the disappearance of the -OH bond peak at 360 °C, it is likely that NaH reacts with NaOH, consuming the -OH groups. Subsequently, as the intermediates continue to decompose, additional NaOH is generated.

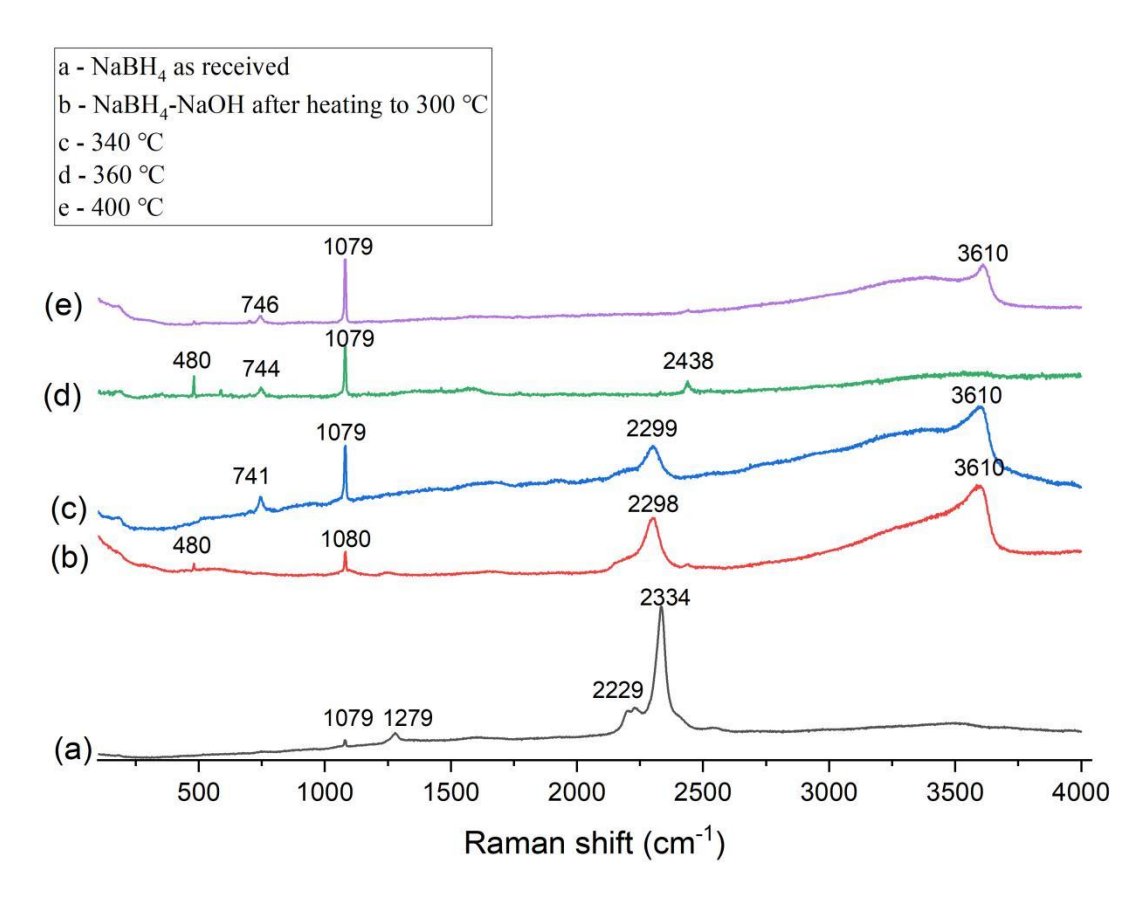


Figure 5-16: Raman patterns of ball-milled 1:4 NaBH₄:NaOH after heating to 300 °C, 340 °C, 360 °C and 400 °C.

5.4 Conclusion

The reaction between NaBH₄ and NaOH produces Na-B-O-H intermediates. When ball-milled for 10 hours, the 1:4 NaBH₄:4NaOH mixture can be completely converted into Na-B-O-H intermediates. Prior to heating to 300°C, these intermediates undergo a phase change at 240 °C-250 °C, and the nature of this phase change varies depending on the molar ratio of NaOH added. For instance, ball-milled (2h) 1:3 NaBH₄:NaOH yields Na₃BO₃, Na, NaOH, and H₂ when heated to 400°C, while ball-milled (2h) 1:4 NaBH₄:NaOH produces Na₃BO₃, Na₂O, NaOH, and H₂ under the same conditions. The

presence of NaH in the PXD pattern of ball-milled (2h) 1:4 NaBH₄:NaOH heated to 320°C and held for 1 hour suggests a reaction scheme between 300 °C and 400 °C (as shown in reactions 6 to 11). Although the theoretical mass loss could not be accurately verified due to Na leakage from the crucible (indicated by the colour change of the thermocouple in STA from white to gray-black), the functional group data obtained from Raman spectroscopy of the 1:4 NaBH₄:4NaOH samples heated between 300 °C and 400 °C support the correctness of reactions 6 to 11.

5.5 References

- 1. L. Ouyang, H. Zhong, H.-W. Li and M. Zhu, Inorganics, 2018, 6, 10.
- 2. Z. Pei, Y. Bai, Y. Wang, F. Wu and C. Wu, ACS Appl Mater Interfaces, 2017, 9, 31977-31984.
- 3. H. X. Nunes, D. L. Silva, C. M. Rangel and A. M. F. R. Pinto, Energies, 2021, 14, 3567.
- 4. Y. Bai, C. Wu, F. Wu, J.-h. Yang, L.-l. Zhao, F. Long and B.-l. Yi, *International Journal of Hydrogen Energy*, 2012, 37, 12973-12979.
- 5. D. M. F. Santos and C. A. C. Sequeira, Renewable and Sustainable Energy Reviews, 2011, 15, 3980-4001.
- 6. J. Urgnani, F. J. Torres, M. Palumbo and M. Baricco, *International Journal of Hydrogen Energy*, 2008, **33**, 3111-3115.
- 7. M. Dragan, Catalysts, 2022, 12, 356.
- 8. Y. Shang, O. Jin, J. A. Puszkiel, F. Karimi, P. Dansirima, C. Sittiwet, R. Utke, S. Soontaranon, T. T. Le, G. Gizer, D. V. Szabó, S. Wagner, C. Kübel, T. Klassen, M. Dornheim, A. Pundt and C. Pistidda, *International Journal of Hydrogen Energy*, 2022, **47**, 37882-37894.
- 9. J. F. Mao, X. B. Yu, Z. P. Guo, H. K. Liu, Z. Wu and J. Ni, *Journal of Alloys and Compounds*, 2009, 479, 619-623.
- 10. C. Milanese, S. Garroni, A. Girella, G. Mulas, V. Berbenni, G. Bruni, S. Suriñach, M. D. Baró and A. Marini, *The Journal of Physical Chemistry C*, 2011, **115**, 3151-3162.
- 11. S. Kumar, A. Jain, H. Miyaoka, T. Ichikawa and Y. Kojima, *International Journal of Hydrogen Energy*, 2017, **42**, 22432-22437.
- 12. J. Mao, Q. Gu, Z. Guo and H. K. Liu, Journal of Materials Chemistry A, 2015, 3, 11269-11276.
- 13. S. Shin, Y. Kim, J. H. Jin and J. Jung, ACS Omega, 2022, 7, 979-986.
- 14. G. Nolze and W. Kraus, *PowderCell for Windows*, Version 2.4, BAM, Berlin, 2000; ICSD, Inorganic Crystal Structure Database, FIZ Karlsruhe, Germany.
- 15. ICDD PDF-4+ 2024, International Centre for Diffraction Data, Newtown Square, PA, USA; *PANalytical HighScore Plus*, Version 4.9, Malvern Panalytical.
- 16. A. C. Larson and R. B. Von Dreele, *General Structure Analysis System (GSAS)*, Los Alamos National Laboratory Report LAUR 86–748, 2004; B. H. Toby, *J. Appl. Crystallogr.*, 2001, **34**, 210–213.
- 17. G. E. Walrafen and R. T. Douglas, *J Chem Phys*, 2006, **124**, 114504.
- 18. S. Trudel and D. F. R. Gilson, Inorg. Chem., 2003, 42, 2814–2816.
- 19. H. Hagemann, S. Gomes, G. Renaudin and K. Yvon, *Journal of Alloys and Compounds*, 2004, 363, 129-132.
- 20. K. Nakamoto, *Infrared and Raman Spectra of Inorganic and Coordination Compounds*, 6th edn., Wiley, Hoboken, 2009.

6. Dehydrogenation of Ca₄Mg₃H₁₄-NaH

6.1 Introduction

6.1.1 Ternary Hydrides of the s-block Metals

Ternary hydrides of the s-block metals have attracted significant research interest in the fields of hydrogen storage and functional materials due to their structural diversity. ^{1,2} These compounds typically consist of one s-block metal (e.g., Li, Na, Mg, Ca), one d- or f-block metal (e.g., Al, Ti, Fe, Ni, La), and hydrogen. They often adopt complex hydride structures characterized by hydrogen atoms coordinated in octahedral or tetrahedral geometries, forming stable three-dimensional crystalline networks via ionic and partially covalent bonding. ^{3,4} It has been reported that reducing particle size to the nanoscale can significantly improve both the thermodynamics and kinetics of hydrogen absorption and desorption. ^{5,6} Among these, ternary hydrides based on MgH₂ and CaH₂ are of particular importance in the development of advanced hydrogen storage materials, offering a valuable platform for tuning hydrogen release temperatures and enhancing reaction reversibility.

Among various hydrogen storage systems, magnesium-based hydrides have attracted considerable attention due to their high theoretical hydrogen capacity (up to 7.6 wt.%), abundant availability, low cost, and environmental benignity.^{7,8} However, pure MgH₂ suffers from high dehydrogenation temperatures (typically exceeding 300 °C) and slow hydrogen sorption kinetics, which severely limit its practical application. 9,10 To overcome these limitations, researchers have developed ternary magnesium-based hydride systems by incorporating transition metals or other metal hydrides (such as Ti, Ni, Fe, Y, etc.) into MgH₂, forming solid solutions, intermetallic compounds, or complex hydrides with enhanced hydrogen storage properties. According to Chaudary et al.'s study, Mg₂FeH₆ is a low-cost, high-capacity cubic ternary hydride (5.47 wt.% H₂, 150 kg/m³), consisting of [FeH₆]⁴⁻ octahedra coordinated with Mg²⁺ cations.¹¹ It demonstrates reversible cycling over 500 times and an enthalpy of formation between 77-98 kJ mol⁻¹ H₂. The deuterated analogue, Mg₂FeD₆, exhibits a dehydrogenation onset at 250 °C, significantly lower than that of MgD₂ (>400 °C), indicating improved thermodynamics. In Alaoui-Belghiti et al.'s work, Mg₂NiH₄ shows a hydrogen capacity of 3.6 wt.% and a formation enthalpy of approximately -72 kJ mol⁻¹ H₂, corresponding to an equilibrium decomposition temperature of 283 °C. 12 Remarkably, applying uniaxial or biaxial compressive strain can lower the decomposition temperature to as low as -13 to 199 °C and reduce the hydrogen diffusion activation energy to 0.38 eV, while enhancing the ionic conductivity up to 25.5 S m⁻¹. These strain-induced effects enable rapid hydrogen release near ambient conditions,

making Mg₂NiH₄ a promising candidate for strain-tunable hydrogen storage systems. Belkoufa et al.'s study systematically investigated Mg₂CoH₅ under various strain conditions.¹³ In its unstrained state, Mg₂CoH₅ exhibits a high formation enthalpy of -94.95 kJ mol⁻¹ H₂ and a decomposition temperature of 457 °C, which is far above the practical threshold. However, under -9% triaxial compressive strain, the formation enthalpy significantly decreases to -40.01 kJ/mol H₂, with the decomposition temperature dropping dramatically to 34 °C, indicating substantial tunability of thermodynamic properties via lattice strain. According to Crivello et al.'s research, Nb₂O₅-catalyzed ball-milled Mg-Al alloys show improved hydrogen storage performance by splitting the traditional single-step hydrogenation/dehydrogenation of MgH₂ into one to three reversible steps. 14 This modification enables the release of up to 4.7 wt.% H₂ at 250 °C, compared to 290 °C for pure MgH₂. Additionally, the reaction enthalpy of each step is reduced from -76.5 to -68.2 kJ mol⁻¹ H₂, indicating decreased thermodynamic stability and more favourable hydrogen release kinetics. These findings underscore the significance of structural engineering, strain modulation, and catalytic enhancement in tailoring the performance of ternary Mg-based hydrides for efficient hydrogen storage.

Compared to the extensively studied magnesium-based hydrides, calcium-based hydrides have received relatively limited attention. Nevertheless, calcium, as a lightweight alkaline-earth metal, is abundant and inexpensive, making it a promising candidate for hydrogen storage applications. The primary challenges in developing calcium hydride (CaH₂) for solid-state hydrogen storage lie in its high thermodynamic stability and the higher molar mass of calcium compared to magnesium, which results in a reduced gravimetric hydrogen capacity. Recent investigations have primarily focused on theoretical evaluations of CaH₂ and related calcium-based compounds to assess their hydrogen storage potential. 15,16,17 According to Surucu et al.'s study, a systematic investigation was conducted on CaXH₃ (X = Mn, Fe, Co), a series of perovskite-type calcium-based hydrides. 18 These compounds crystallize in a cubic *Pm-3m* structure, with lattice constants decreasing from 3.60 Å to 3.48 Å as the atomic number of X increases. The negative formation enthalpies indicate good thermodynamic stability, and these hydrides are considered experimentally synthesizable. Their hydrogen storage capacities, ranging from 2.97 to 3.09 wt.%, exceed those of most other ABH₃-type hydrides, highlighting their potential for further development. In a separate study by Graetz, Ca(AlH₄)₂, a non-reversible calcium-aluminium hydride, was reported to exhibit a high theoretical hydrogen content.¹⁹ However, hydrogen release occurs only at elevated temperatures (400-440 °C). This compound was first synthesized via reaction of CaB₆ or CaH₂ with hydrogen gas at 700 bar and 400-440 °C, but its direct regeneration remains challenging.

Despite its irreversible nature, Ca(AlH₄)₂ is considered a kinetically stabilized hydride, owing to its low decomposition enthalpy and rapid hydrogen release at lower temperatures, offering promise for niche hydrogen storage applications where fast desorption kinetics are critical.

The ternary hydrides Ca₄Mg₃H(D)₁₄ and Ca₁₉Mg₈H(D)₅₄ have been synthesized using high-pressure, high-temperature methods.^{20,21} The former, first reported by Gingl et al., was obtained after six days in an autoclave at 410 °C under 53 bar of hydrogen pressure, while its deuteride required more extreme conditions 465 °C under 95 bar D₂ over seven days. The final hydride contained CaH₂, MgH₂, and unreacted Mg.²² Bertheville and Yvon later characterized another ternary Ca-Mg hydride, Ca₁₉Mg₈H(D)₅₄, which was found to be isostructural to Yb₁₉Mg₈D₅₄.²³ This compound was synthesized by pressing CaH₂ and MgH₂ in a 2:1 molar ratio into pellets, followed by reaction in a multi-anvil pressure cell for three hours. Such methods are commonly employed for synthesizing ternary and quaternary hydrides. The final product included a cubic ternary phase along with CaH₂, αand γ-MgH₂, and MgO impurities. Sartori et al. utilized ball milling in their research on mixed hydride systems, where Ca₄Mg₃H₁₄ and Ca₁₉Mg₈H₅₄ were observed, though not as single-phase materials.²⁴ According to Ma et al.'s study, the hydrogen storage and generation properties of CaMg2-based alloys were systematically investigated, with a particular focus on the effect of nickel (Ni) addition on the alloy's performance.²⁵ The results revealed that the pristine CaMg2 alloy is unable to absorb hydrogen at room temperature but can absorb up to 4.48 wt.% H₂ at 300 °C, forming Ca₄Mg₃H₁₄ and MgH₂ as the main hydride phases. Upon partial substitution of magnesium with nickel, the resulting CaMg_{1.9}Ni_{0.1} alloy exhibits hydrogen absorption capability at room temperature, achieving a maximum hydrogen capacity of 5.65 wt.%. Furthermore, the apparent activation energy for the hydrogenation reaction is significantly reduced to 41.74 mol⁻¹, which is notably lower than that of pure MgH₂ and Mg₂Ni, indicating enhanced kinetics and improved hydrogen storage behaviour induced by Ni doping.

6.1.2 Purpose

This chapter is based on Morris's and Reardon's work.^{26,27} They describes the synthesis of nanoscale ternary hydrides (Ca₁₉Mg₈H₅₄) by using ball-milling. Upon heating to specific temperature (350 °C), nanoscale ternary hydrides such as Ca₁₉Mg₈H₅₄ are converted to Ca₄Mg₃H₁₄. The objective of this chapter is to enhance the hydrogen storage properties of Ca₄Mg₃H₁₄, specifically its hydrogen capacity and dehydrogenation temperature, by incorporating NaH. This study aims to compare the performance of Ca₄Mg₃H₁₄ doped with NaH to that of pure Ca₄Mg₃H₁₄ in order to analyse the potential role of NaH. The

dehydrogenation reactions and the resulting products are analysed using techniques such as PXD and TG-DTA.

6.2 Experimental

MgH₂ (Alfa Aesar, 98%), NaH (Sigma Aldrich, dry, 90%) and CaH₂ (Sigma Aldrich, reagent grade, 95%) was used as received.

Because of the air and moisture sensitivity of NaH, MgH₂ and CaH₂, all operations were carried out in a recirculating Argon or N₂-filled (BOC, 99.998%) glovebox (MBraun LABstar, $O_2 < 10$ ppm, $H_2O < 0.5$ ppm).

6.2.1 Mechanochemical synthesis of Ca₁₉Mg₈H₅₄, Ca₄Mg₃H₁₄ and compositions in the Ca₄Mg₃H₁₄ - NaH system

To synthesise the Ca₁₉Mg₈H₅₄, mixtures of 1:1 CaH₂:MgH₂ (*ca.* 0.4 g total) were weighed and then transferred to a stainless-steel grinding jar that was filled with eight stainless steel balls (10 mm diameter), each of which weighed about 4 g. The grinding jar was sealed under argon before removal from the glovebox. Ball milling was conducted for 10h at a rotation speed of 500 rpm with a ball-to-powder ratio of 80:1 in a planetary ball mill (Retsch PM100) in 5-minute milling periods (reverse rotation) followed by 2-minute rest periods.

6.2.2 Powder X-ray Diffraction (PXD)

All starting materials and samples in the Na-Ca-Mg-H hydrogen release system were characterized using powder X-ray diffraction (PXD). All the materials used in this study were air-sensitive. Therefore, all the samples were prepared using the air-sensitive sample holder under inert atmosphere.(glovebox) All the materials were characterized by PANalytical X'Pert and Rigaku Miniflex. Diffraction data was collected over a 2θ range of 5–85° for 1 h to facilitate phase identification.

The obtained diffraction data were compared with appropriate reference patterns using the ICSD database via PowderCell or the ICDD PDF database via PANalytical HighScore Plus and Jade 6.5 software. Rietveld refinements were performed using the General Structure Analysis System (GSAS) with the EXPGUI interface. 30

6.3 Results and Discussion

6.3.1 Synthesis of Ca₁₉Mg₈H₅₄ and Ca₄Mg₃H₁₄

MgH₂ and CaH₂ was characterized by PXD and compared to the ICSD database and both of the starting materials were phase-pure.(Appendix A6-1 and A6-2) According to the method employed by Reardon's article milling conditions of 10 h milling time and 500 rpm rotation speed were employed with 5 min run and 2 min rest periods.²⁷ A 1:1 MgH₂:CaH₂ molar ratio was used to synthesise the Ca₁₉Mg₈H₅₄. The Ca₁₉Mg₈H₅₄ was successfully synthesized as compared with the ICSD database, as shown in Figure 6-1, and there are no impurity peaks.

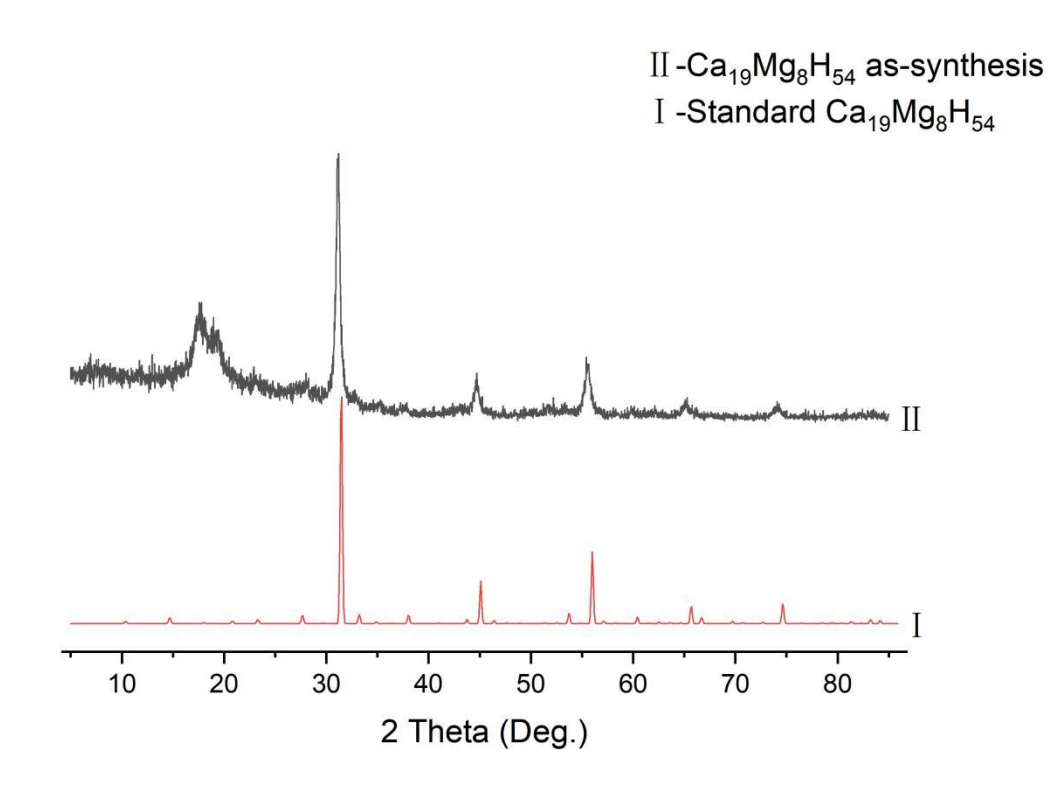


Figure 6-1: The PXD pattern of as-synthesised $Ca_{19}Mg_8H_{54}$ (10h ball-milling, 500rpm, 5 min run and 2 min rest periods; II) and standard $Ca_{19}Mg_8H_{54}(I)$

The second step synthesis of Ca₄Mg₃H₁₄ is to heat Ca₁₉Mg₈H₅₄ to 350 °C (before cooling to room temperature). This will result in the formation of Ca₄Mg₃H₁₄. by reference to Reardon's thesis since the compositions of the 2 phases are different yet there is no mass loss/gain on heating and no apparent generation of impurity phases.²⁷ According to Reardon's study, although the milled product has the Ca₁₉Mg₈H₅₄ structure, it has a composition closer to 3:3:14 (or in principle, 3.5:3.5:14 if the 1:1 ratio of the starting material is retained). Then heating the milled product converts the hydride to the Ca₄Mg₃H₁₄ structure (and the composition - i.e. ratio of Ca:Mg:H - should be unchanged).

Figure 6-2 shows the thermal behaviour of Ca₁₉Mg₈H₅₄. From the appearance of the TG profile, there is no change in mass. However, the DTA curve shows many peaks, which should indicate the phase change from the Ca₁₉Mg₈H₅₄ structure to the Ca₄Mg₃H₁₄ structure

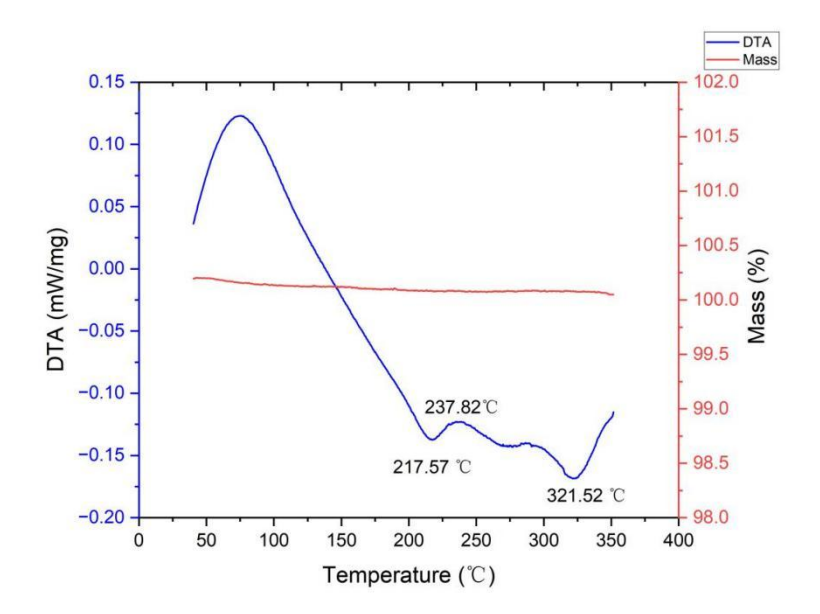
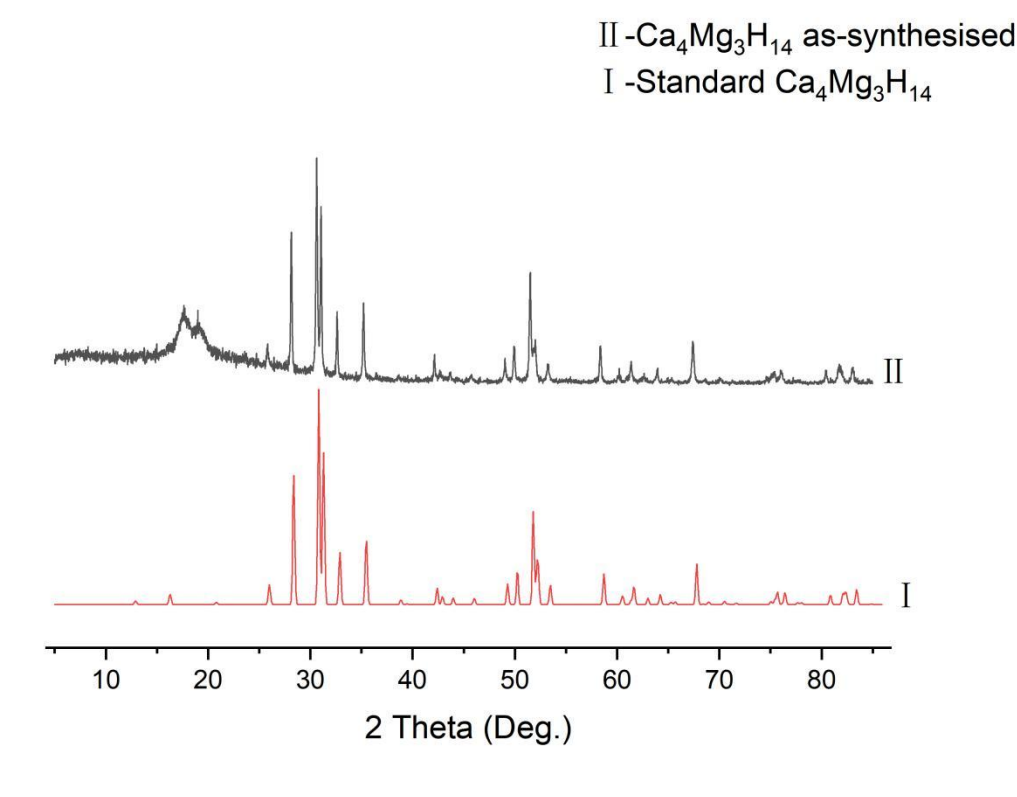


Figure 6-2: TG (red) and DTA (blue) profiles for as-synthesised Ca₁₉Mg₈H₅₄ on heating from 35-350 °C at 5 °C min⁻¹ under flowing Ar(g).



 $Figure~6-3: The~PXD~pattern~of~as-synthesised~Ca_4Mg_3H_{14}~(II) compared~to~standard~Ca_4Mg_3H_{14}.(I)\\$

$6.3.2\ Thermal\ Treatment\ of\ Ca_4Mg_3H_{14}$

Figures 6-4 and 6-5 show the thermal behaviour of Ca₄Mg₃H₁₄ when heated to 500 °C. It can be observed that Ca₄Mg₃H₁₄ begins to decompose and release hydrogen gas at 362 °C, and shows a strong endotherm in the DTA trace with a peak temperature at *ca*. 451 °C. From the PXD pattern in Figure 6-6, it can be seen that Ca₄Mg₃H₁₄ decomposes into CaH₂ and Mg at 450°C. Therefore, the decomposition reaction of Ca₄Mg₃H₁₄ is shown below:

$$Ca_4Mg_3H_{14} \rightarrow 4CaH_2 + 3Mg + 3H_2$$
 T=360-450 °C

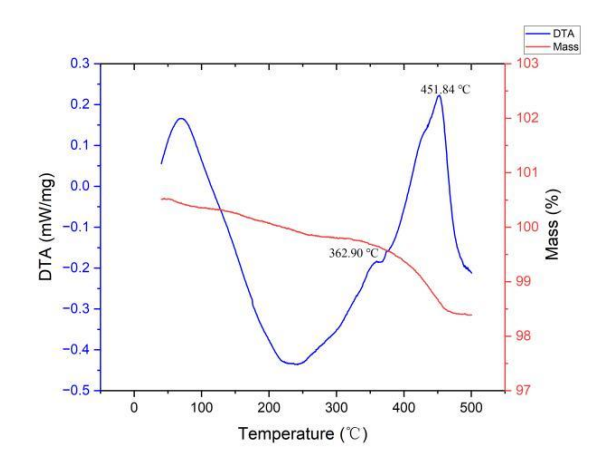


Figure 6-4: TG (red) and DTA (blue) profiles for as-synthesised Ca₄Mg₃H₁₄ on heating from 35-500 °C at 5 °C min⁻¹ under flowing Ar(g).

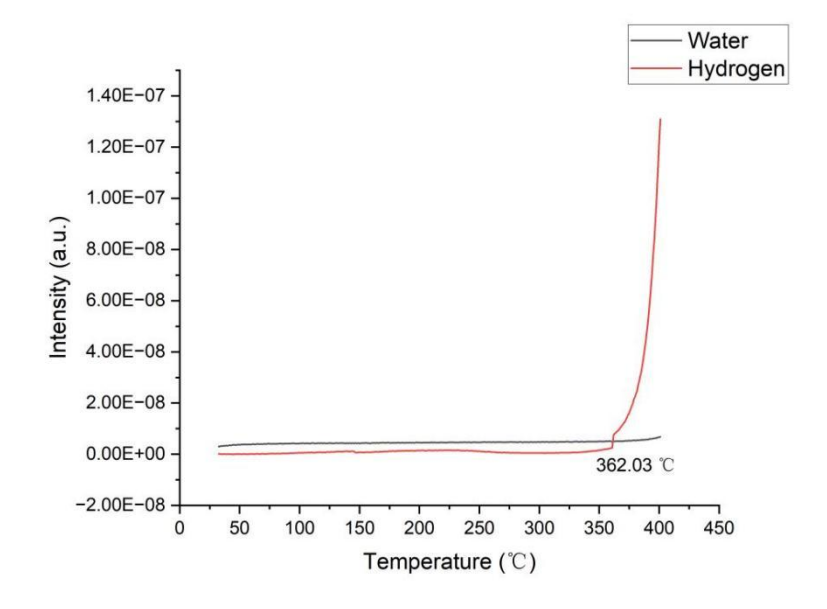


Figure 6-5: Mass spectroscopy output for water (m/z = 18) and hydrogen (m/z = 2) as a function of temperature for as-synthesised $Ca_4Mg_3H_{14}$ on heating from 35-500 °C at 5 °C min⁻¹ under flowing Ar(g).

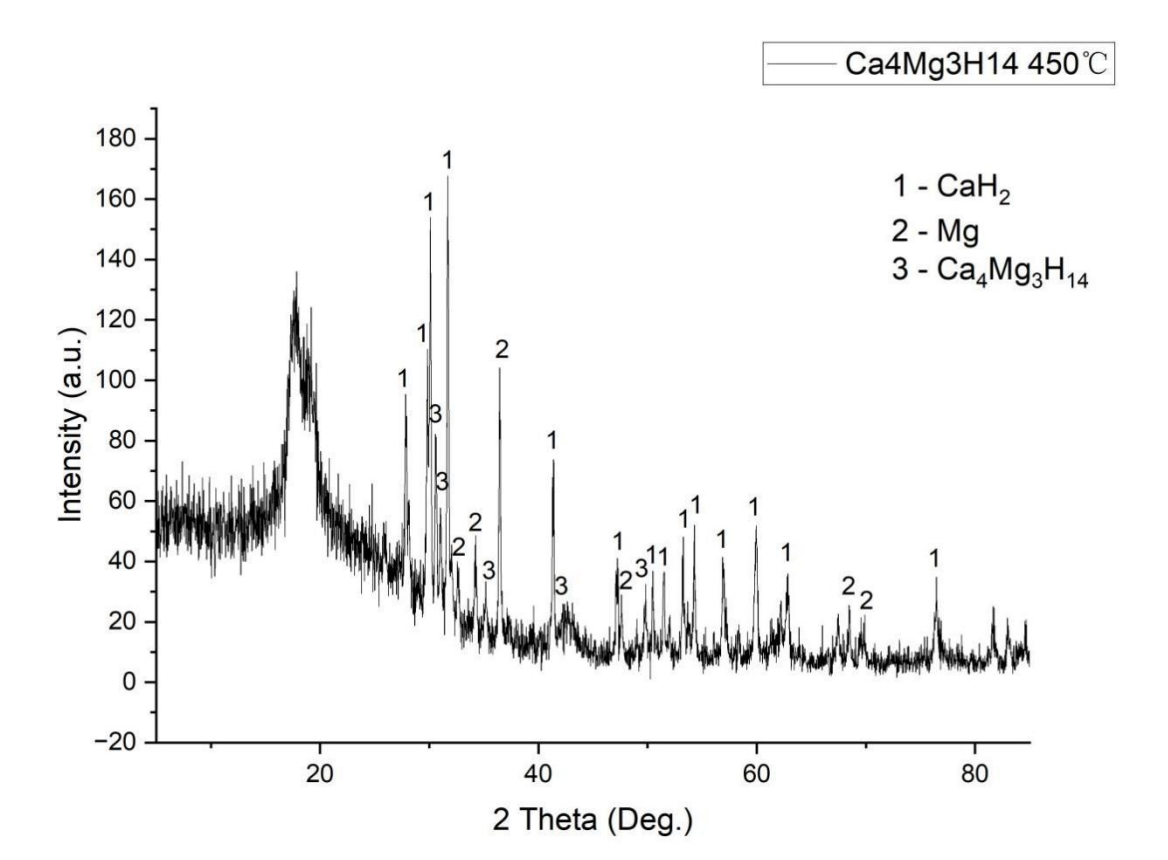


Figure 6-6: PXD pattern of as-synthesised Ca₄Mg₃H₁₄ after heating to 450 °C (and cooling to room temperature). (1 represent CaH₂; 2 represent Mg; 3 represent Ca₄Mg₃H₁₄)

6.3.3 Investigations in the Ca₄Mg₃H₁₄-NaH system

To confirm if the thermodynamics of dehydrogenation could be changed through potentially creating alternative reaction pathways, NaH was added to form reactive hydride composites with Ca₄Mg₃H₁₄. Figure 6-7, shows the diffraction pattern resulting from ball milling a 1:1 molar ratio mixture of Ca₄Mg₃H₁₄:NaH at 400 rpm for 2 h. The final products after milling are Ca₄Mg₃H₁₄ and NaMgH₃. No hydrogen was released during the process as the oxygen content in the glove box did not increase. Consistent with the methodology employed in Chapter 5, the only potential gas released is hydrogen (H₂). NaMgH₃ is clearly formed through the reaction of NaH and MgH₂ or he direct reaction between Ca-Mg-H and NaH.. The peaks of Ca₄Mg₃H₁₄ are noticeably broadened. Therefore, the ratio of Ca and Mg in Ca₄Mg₃H₁₄ may not be strictly 4:3. Although the Ca₄Mg₃H₁₄ phase retains its previous structure, the content of Mg is reduced. NaH may react with some of the Mg and H in Ca₄Mg₃H₁₄ to form NaMgH₃.

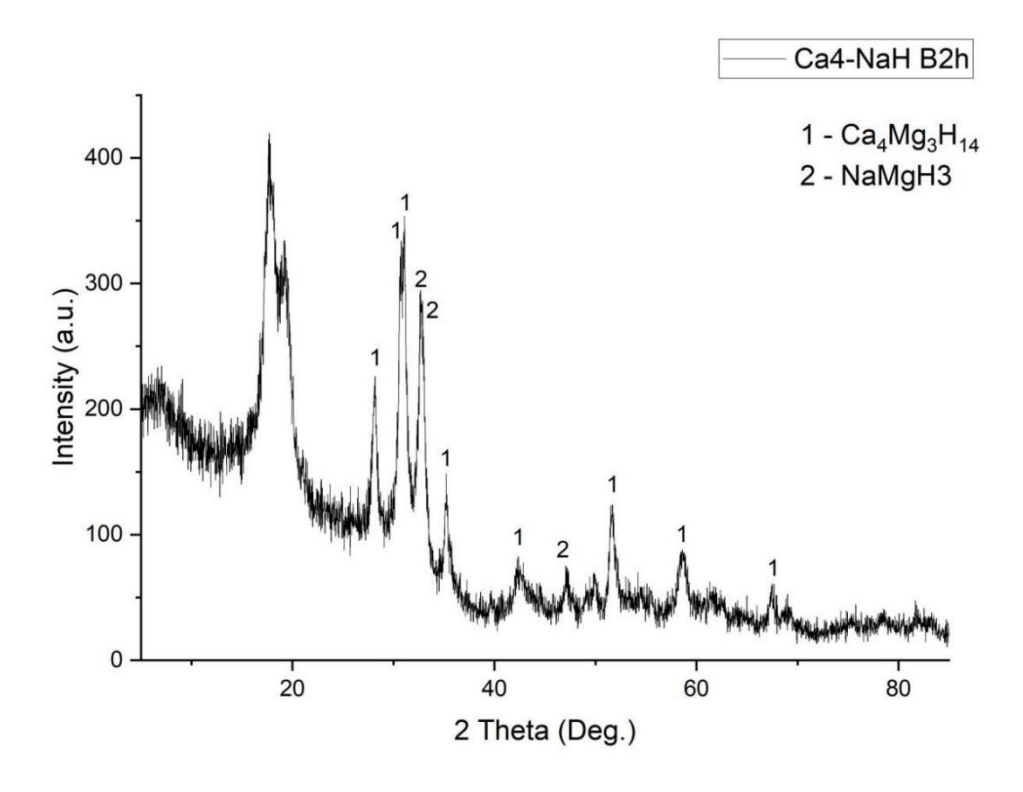


Figure 6-7:The PXD pattern of ball-milled 1:1 Ca₄Mg₃H₁₄:NaH (2h, 400rpm). (1 represent Ca₄Mg₃H₁₄; 2 represent NaMgH₃)

Figures 6-8 and 6-9 show the performance of Ca₄Mg₃H₁₄-NaH after ball milling and heating to 400 °C. It is evident that, when compared to as-synthesised Ca₄Mg₃H₁₄, the dehydrogenation reaction onset temperature of Ca₄Mg₃H₁₄-NaH decreases from *ca.* 360 °C to *ca.* 320 °C from the MS Figure 6-5 and 6-9. Additionally, the DTA endothermic peak temperature has significantly decreased, from 450 °C to 348 °C. The addition of NaH into Ca₄Mg₃H₁₄ can change the reaction pathway, enabling the Ca₄Mg₃H₁₄-NaH system to initiate hydrogen release at lower temperatures compared to as-synthesised Ca₄Mg₃H₁₄.

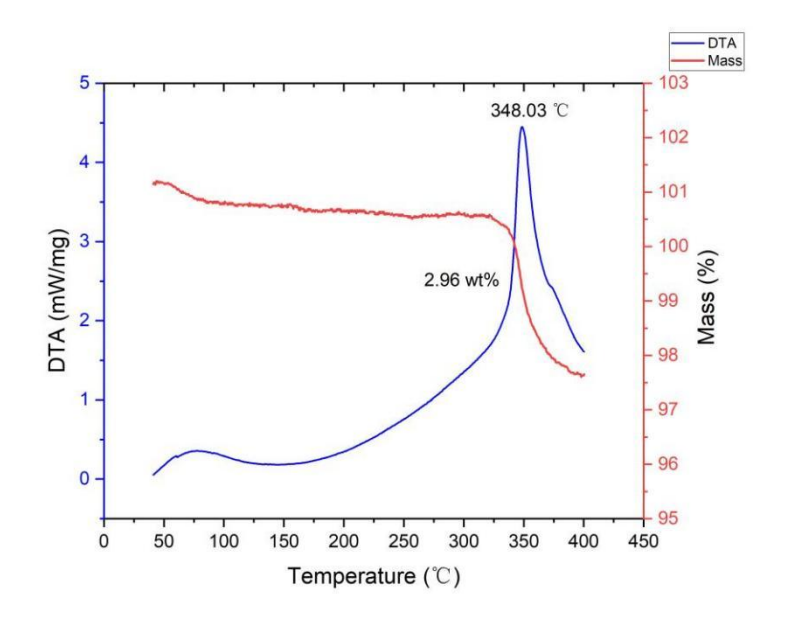


Figure 6-8: TG (red) and DTA (blue) profiles for ball-milled 1:1 Ca₄Mg₃H₁₄:NaH (2h, 400rpm) on

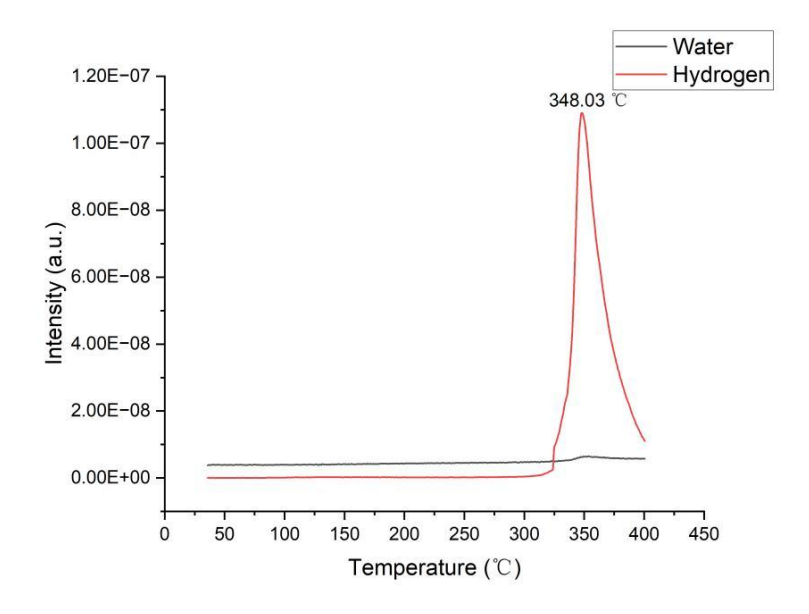


Figure 6-9: Mass spectroscopy output for water (m/z = 18) and hydrogen (m/z = 2) as a function of temperature for ball-milled 1:1 Ca₄Mg₃H₁₄:NaH (2h, 400rpm) on heating from 35-400 °C at 5 °C min⁻¹ under flowing Ar(g).

To investigate the specific reaction(s) occurring, the ball-milled Ca₄Mg₃H₁₄-NaH was heated to various temperatures up to 400 °C. Figure 6-10 shows the behaviour of the system from 150-280 °C, while Figure 6-11 shows the thermal behaviour from 280-400 °C. From Figure 6-10, it can be seen that there are no changes in the Ca₄Mg₃H₁₄-NaH sample from the time it was ball milled until it was heated to 280 °C. From Figure 6-11, however, it is evident that between 280-320 °C, new peaks indicating the formation of Mg begin to appear. When the temperature is increased from 320 °C to 360 °C, the sample starts to decompose fully into Mg, CaH2, and Na and there is little change in these products from 360 °C to 400 °C, indicating that complete decomposition occurs around 360 °C. Excluding the decomposition of CaH₂, as its decomposition temperature is ca. 600 °C.³¹ From Figure 6-12, it is observed that when Ca₄Mg₃H₁₄-NaH is heated to 330 °C, both NaH and Na are present, suggesting that Na comes from the decomposition of NaH. Based on this information, the observed released hydrogen is mainly derived from the H in MgH₂ and NaH. The theoretical hydrogen mass loss of reaction 3 should be 2.60 wt.%, which differs by 0.36 wt.% from the experimental hydrogen mass loss. Therefore, the ratio of Ca to Mg in Ca₄Mg₃H₁₄ may not strictly be 4:3. Additionally, NaMgH₃ appears to decompose into NaH and Mg, releasing hydrogen, between 320 °C and 330 °C. According to the article by Pottmaier et al., experimental results indicate that NaMgH₃ begins to decompose around 400 °C in a two-step process.³² Initially, NaMgH₃ decomposes to form NaH, Mg, and H₂. Subsequently, NaH further decomposes to yield Na and 0.5H₂. Therefore, in the interaction between Ca₄Mg₃H₁₄ and NaMgH₃, the decomposition of NaMgH₃ is initiated

earlier.

The presence of Mg without any MgH₂ peaks suggests that Mg is directly released from the decomposition of Ca₄Mg₃H₁₄ and NaMgH₃, along with the release of hydrogen. Based on the above information, the reaction can be summarized as follows:

$$Ca_4Mg_3H_{14} + NaH \rightarrow Ca_4Mg_2H_{12} + NaMgH_3$$
 Ball-milling (2)
 $Ca_4Mg_2H_{12} + NaMgH_3 \rightarrow 4CaH_2 + Na + 3Mg + H_2$ T = 320 °C - 400°C (3)

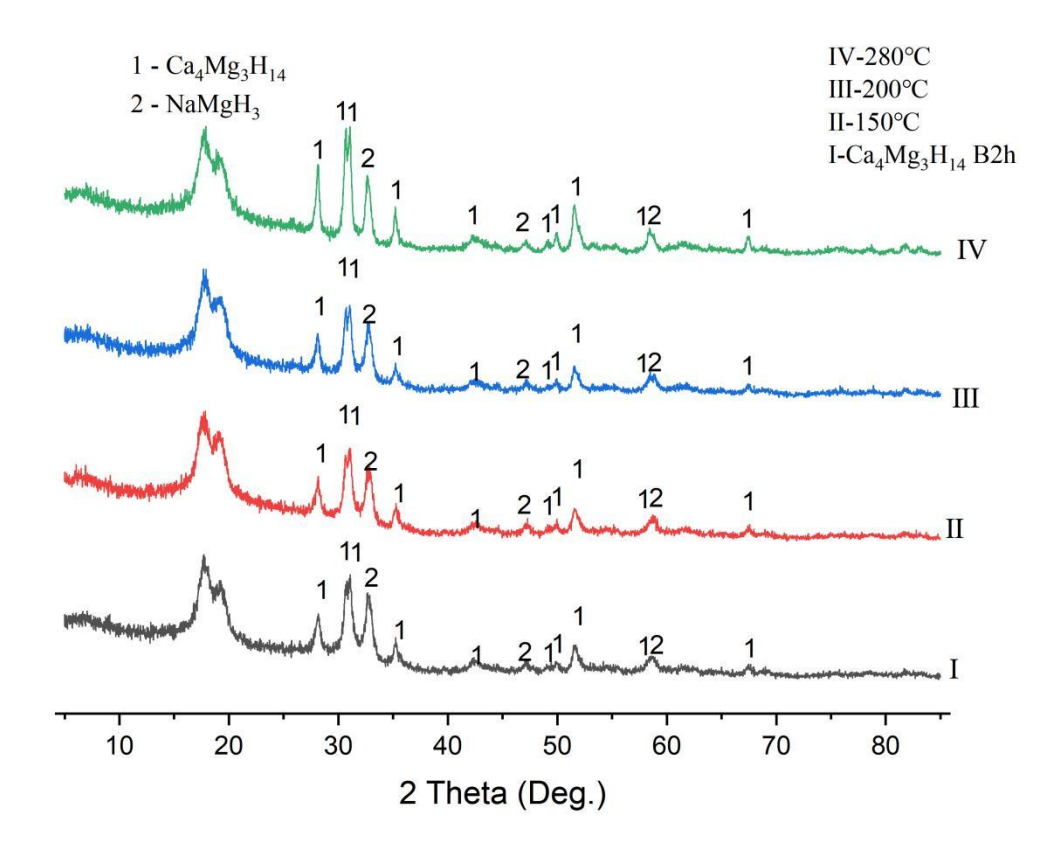


Figure 6-10: The PXD patterns of ball-milled 1:1 $Ca_4Mg_3H_{14}$:NaH (2h, 400rpm;I) and after heating to 150 (II), 200 (III) and 280 (IV) °C (and cooling to room temperature). (1 represent $Ca_4Mg_3H_{14}$; 2 represent NaMgH₃)

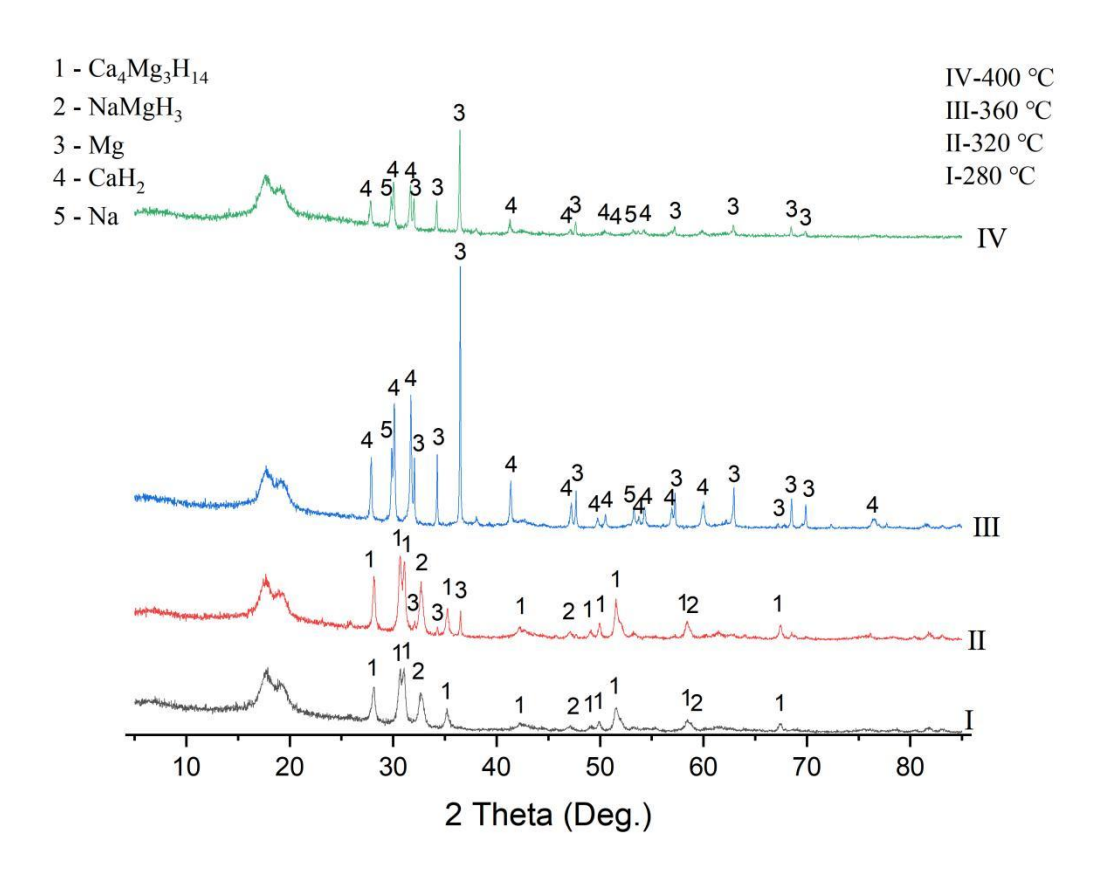


Figure 6-11: The PXD patterns of ball-milled 1:1 Ca₄Mg₃H₁₄:NaH (2h, 400rpm) after heating to 280 (I) 320 (II), 360 (III) and 400 (IV) °C (and cooling to room temperature). (1 represent Ca₄Mg₃H₁₄; 2 represent NaMgH₃; 3 represent Mg; 4 represent CaH₂; 5 represent Na)

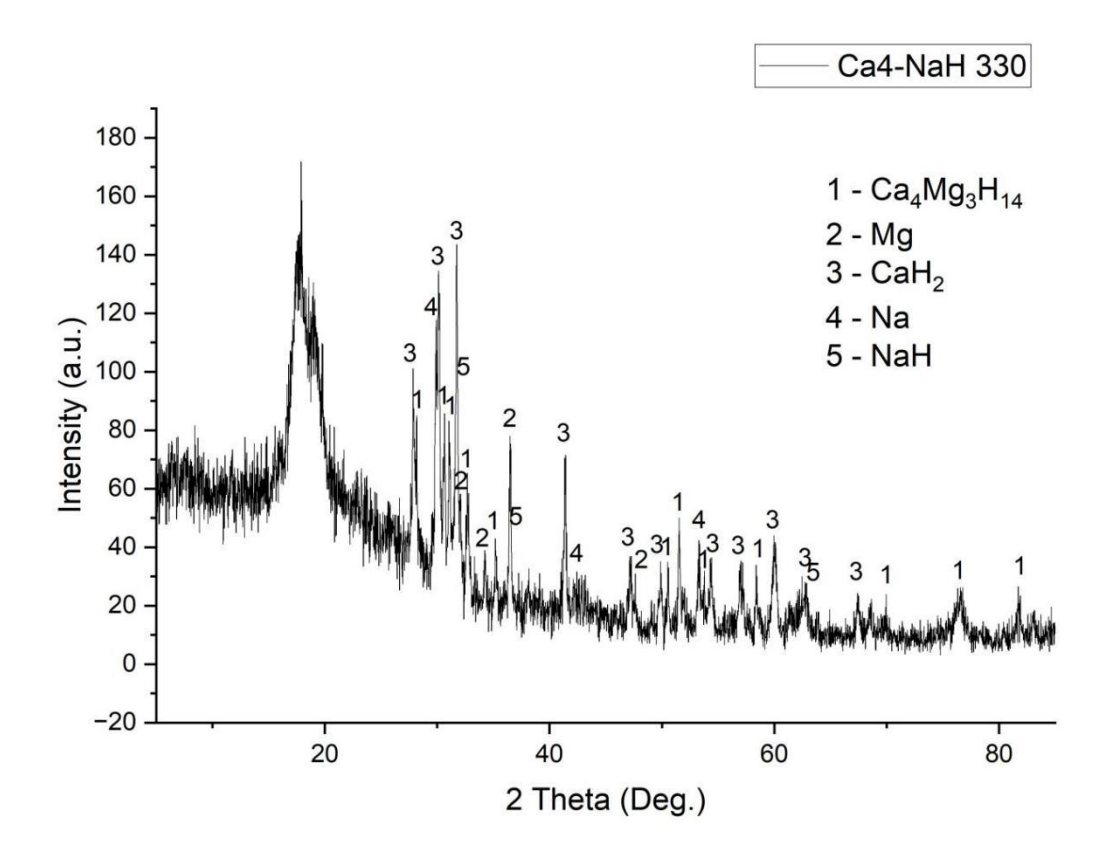


Figure 6-12:The PXD pattern of ball-milled 1:1 Ca₄Mg₃H₁₄:NaH (2h, 400rpm) after heating to 330 °C (and cooling to room temperature). (1 represent Ca₄Mg₃H₁₄; 2 represent Mg; 3 represent CaH₂; 4 represent Na; 5 represent NaH)

Therefore, the addition of NaH indeed improves the dehydrogenation pathway of Ca₄Mg₃H₁₄. The inherent dehydrogenation reaction peak temperature of Ca₄Mg₃H₁₄ is 450 °C. Upon the incorporation of NaH, it reacts with Ca₄Mg₃H₁₄ during ball-milling to form NaMgH₃. As evidenced by DTA Figure 6-8, the overall reaction exhibits a single peak temperature at 348 °C. Therefore, the interaction between NaMgH₃ and Ca₄Mg₃H₁₄ results in a reduction of the overall dehydrogenation reaction peak temperature by 102 °C. This not only causes Ca₄Mg₃H₁₄ to decompose earlier but also induces the premature decomposition of NaMgH₃ (400 °C -348 °C). From the perspective of theoretical mass loss, Ca₄Mg₃H₁₄ decomposes into CaH₂ and Mg, with the decomposition temperature of CaH₂ being *ca*. 600 °C. Thus, before 500 °C, the theoretical mass loss is 2.4 wt.%. The addition of NaH can slightly increase the theoretical mass loss to 2.6 wt.%.

6.3.4 Improvement: Milling time, Rotation Speed and Mole Ratio of Ca₄Mg₃H₁₄-NaH

To explore whether the Ca₄Mg₃H₁₄-NaH system can be further optimized, based on prior experience, varying the rotation speed, the molar ratio of NaH to Ca₄Mg₃H₁₄, and the ball-milling duration may be effective strategies. Additionally, extended ball-milling times will be employed to investigate whether further reactions can occur within the Ca₄Mg₃H₁₄-NaH system.

When the Ca₄Mg₃H₁₄-NaH sample was ball-milled for 10 hours, as shown in Figure 6-13, it can be seen that Ca₄Mg₃H₁₄ has decomposed into CaH₂ and Mg. Furthermore, when the milling jar was opened in the glove box, the oxygen content increased and decreased in a pattern similar to the release of hydrogen, indicating that hydrogen gas was generated again. The presence of NaMgH₃ and the absence of Na or NaH indicate that CaH₂ and Mg must originate from the Ca₄Mg₃H₁₄ phase, but this may not be a simple decomposition process. As shown in the PXD pattern (Figure 6-7), no phases corresponding to CaH₂ and Mg were observed after 2 hours of ball-milling. Therefore, it is likely that Ca₄Mg₃H₁₄ initially reacts with NaH to form Ca₄Mg₂H₁₂. Ca₄Mg₃H₁₄ does not decompose spontaneously during ball-milling; however, the lower Mg-content Ca₄Mg₃H₁₄ (i.e., Ca₄Mg₂H₁₂) is less stable compared to Ca₄Mg₃H₁₄, which may account for its subsequent decomposition.

When the sample was heated, both the peak temperature and onset temperature once again decreased, from 348 °C to 336 °C, and the initial hydrogen release temperature decreased from 325 °C to 297 °C. The decomposition temperature of CaH₂ in the sample is *ca*. 600 °C, so this reaction may involve only the decomposition of NaMgH₃. Upon heating to

400 °C, Na and Mg are produced, as shown in Figure 6-16. By comparing the PXD patterns at 400°C in Figures 6-16 and 6-11, the changes in the content of Mg can be observed. In the 400°C Ca₄Mg₃H₁₄-NaH sample in Figure 6-11, the relative intensity for Mg is larger than that for CaH₂. However, in Figure 6-16, the relative intensity for CaH₂ and Mg are approximately the same. This is consistent with the observation that Mg was generated during ball milling. Since Mg is relatively soft, it easily adheres to the milling jar and balls during the process. As a result, some of the Mg could not be extracted, leading to a reduction in its content.

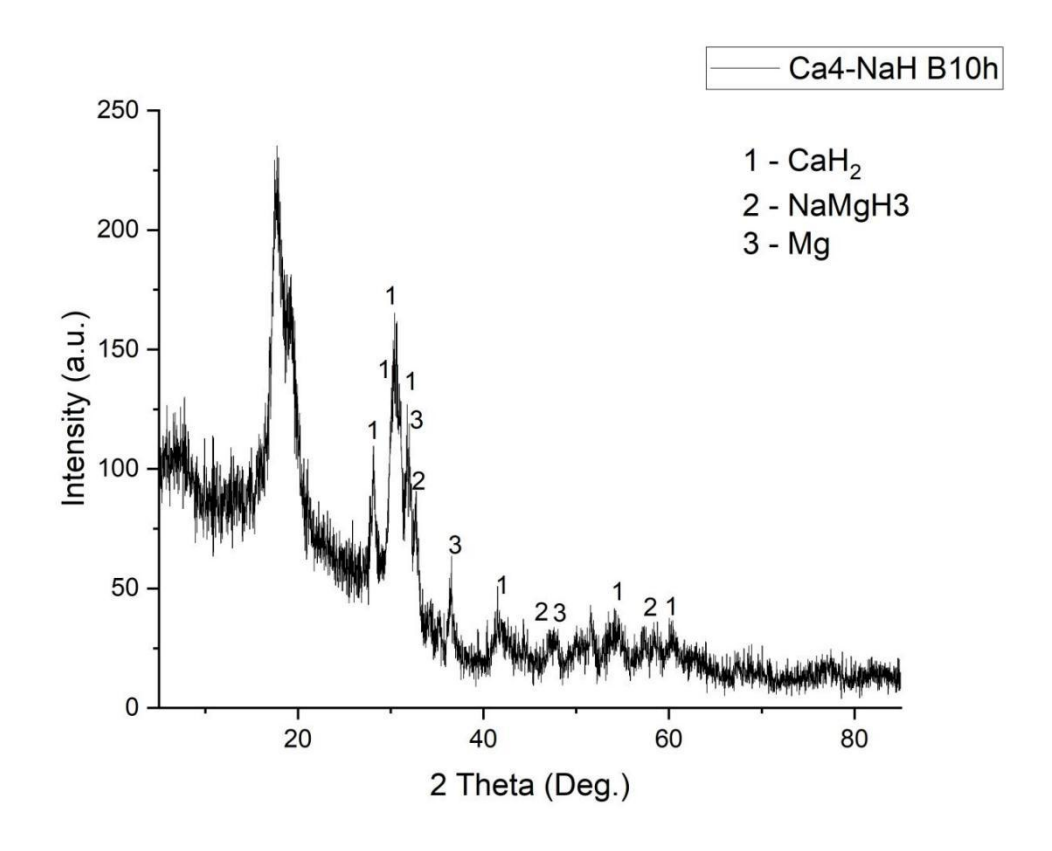


Figure 6-13: The PXD pattern of ball-milled 1:1 Ca₄Mg₃H₁₄:NaH (10h, 400rpm). (1 represent CaH₂; 2 represent NaMgH₃; 3 represent Mg)

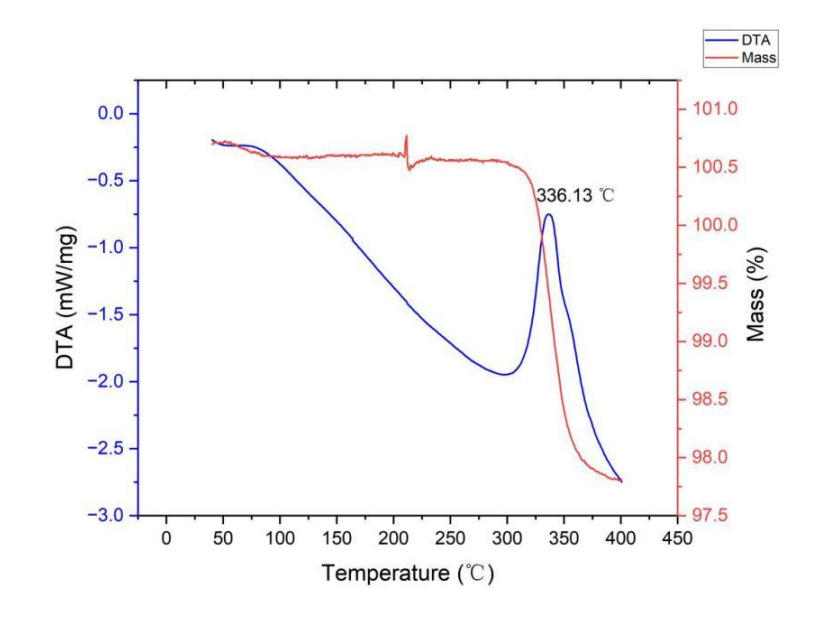


Figure 6-14: TG (red) and DTA (blue) profiles for ball-milled 1:1 Ca₄Mg₃H₁₄:NaH (10h, 400rpm) on heating from 35-400 °C at 5 °C min⁻¹ under flowing Ar(g).

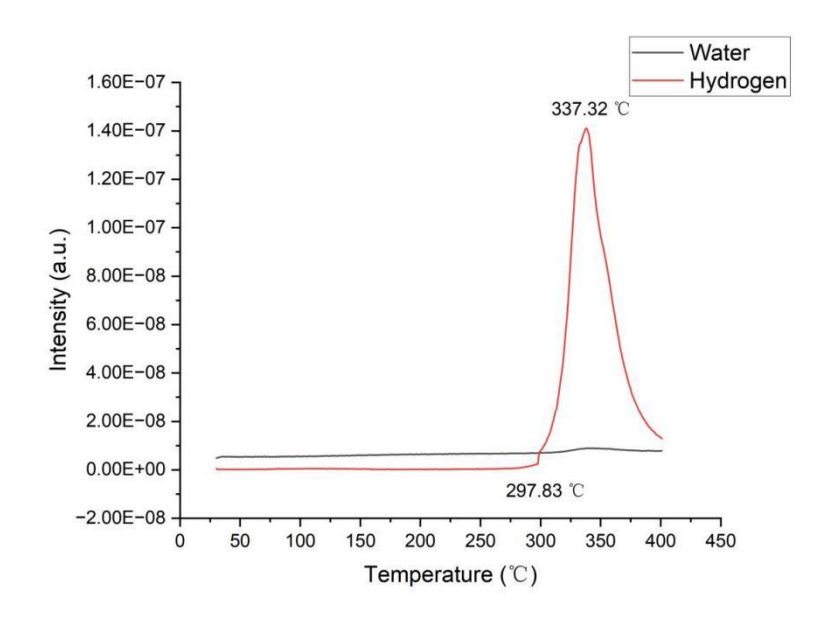


Figure 6-15: Mass spectroscopy output for water (m/z = 18) and hydrogen (m/z = 2) as a function of temperature for ball-milled 1:1 Ca₄Mg₃H₁₄:NaH (10h, 400rpm) on heating from 35-400 °C at 5 °C min⁻¹ under flowing Ar(g).

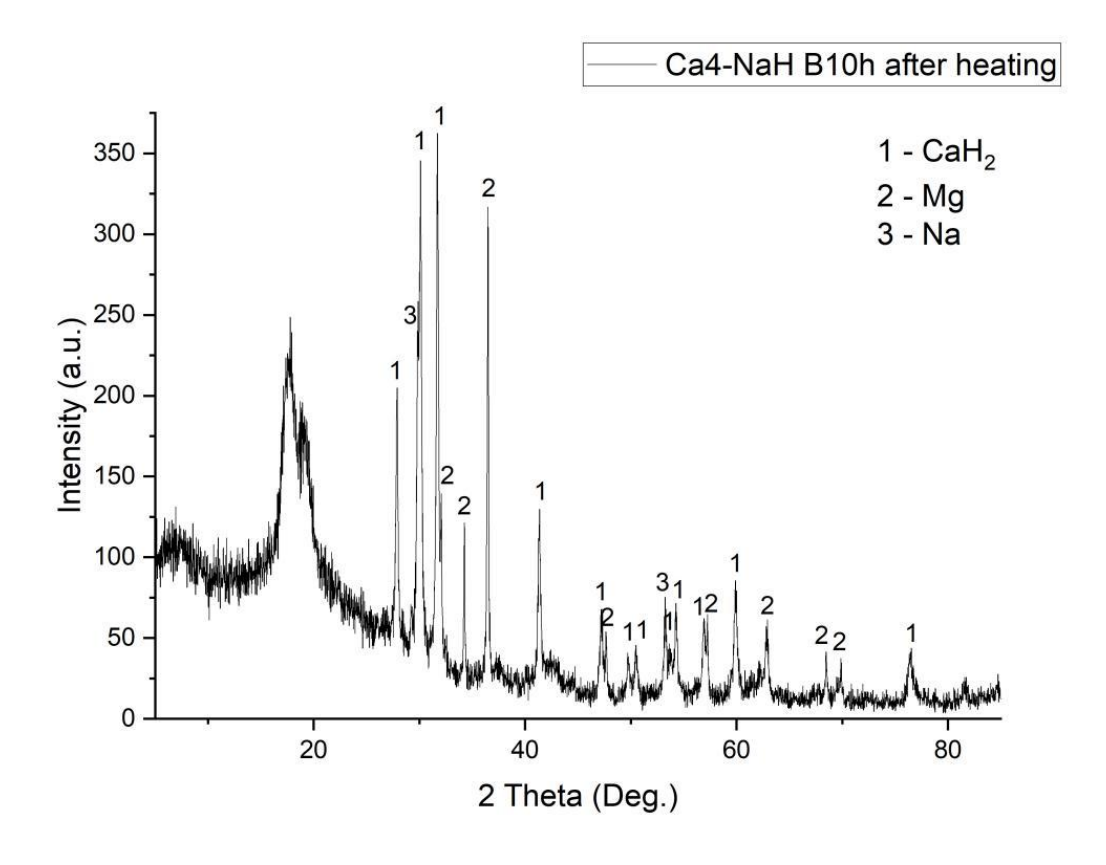


Figure 6-16: The PXD pattern of ball-milled 1:1 Ca₄Mg₃H₁₄:NaH (10h, 400rpm) after heating to 400 °C (and cooling to room temperature). (1 represent CaH₂; 2 represent Mg; 3 represent Na)

To investigate whether Ca₄Mg₃H₁₄ can react similarly under lower ball-milling conditions (300 rpm), a 1:1 molar ratio of Ca₄Mg₃H₁₄:NaH was ball-milled for 2 hours at a rotation speed of 300 rpm. As shown in Figure 6-17, the diffraction peaks of Ca₄Mg₃H₁₄ did not broaden, and only the phases of Ca₄Mg₃H₁₄ and NaH were present. This indicates that at 300 rpm, Ca₄Mg₃H₁₄ and NaH do not react with each other. According to Reardon et al.'s article, NaMgH₃ can be synthesized by ball-milling a 1:1 molar ratio of NaH:MgH₂ for 5 hours at a rotation speed of 450 rpm.³ In conjunction with Figure 6-17, this suggests that at lower rotation speeds (300 rpm), NaH cannot react with MgH₂ to form NaMgH₃. To further explore whether an increased amount of NaH could promote the dehydrogenation of the Ca₄Mg₃H₁₄-NaH system, a 1:2 molar ratio of Ca₄Mg₃H₁₄:NaH was ball-milled for 2 hours at a rotation speed of 300 rpm. As shown in Figure 6-18, the resulting product of the 1:2 Ca₄Mg₃H₁₄:NaH mixture contains Ca₄Mg₃H₁₄, NaH, and MgH₂. Interestingly, under the same ball-milling conditions (300 rpm), the presence of additional MgH₂ in the 1:2 Ca₄Mg₃H₁₄:NaH mixture is notable. The MgH₂ can only originate from the decomposition of Ca₄Mg₃H₁₄.

Figures 6-19 and 6-20 show the thermal performance of ball-milled 1:2 Ca₄Mg₃H₁₄:NaH (2h, 300rpm). Form the DTA trace, the sample has two endothermic peak temperatures at 366 °C and 381 °C. The peak at 381 °C should correspond to the decomposition of NaH

alone, with a peak temperature similar to previous results in chapter 3. The peak at 366 °C may correspond to the dehydrogenation of MgH₂ after ball-milling and the MgH₂ present in Ca₄Mg₃H₁₄. According to Lillo-Ródenas et al.'s article, during ball-milling for 0-2 hours, the peak temperature for the decomposition of MgH₂ is approximately 361 °C, which is close to 366 °C.³³ As shown in Figure 6-21, the main products for the 1:2 Ca₄Mg₃H₁₄:NaH mixture are Na, Mg, and CaH₂. This indicates that H₂ is released from the decomposition of both NaH and MgH₂.

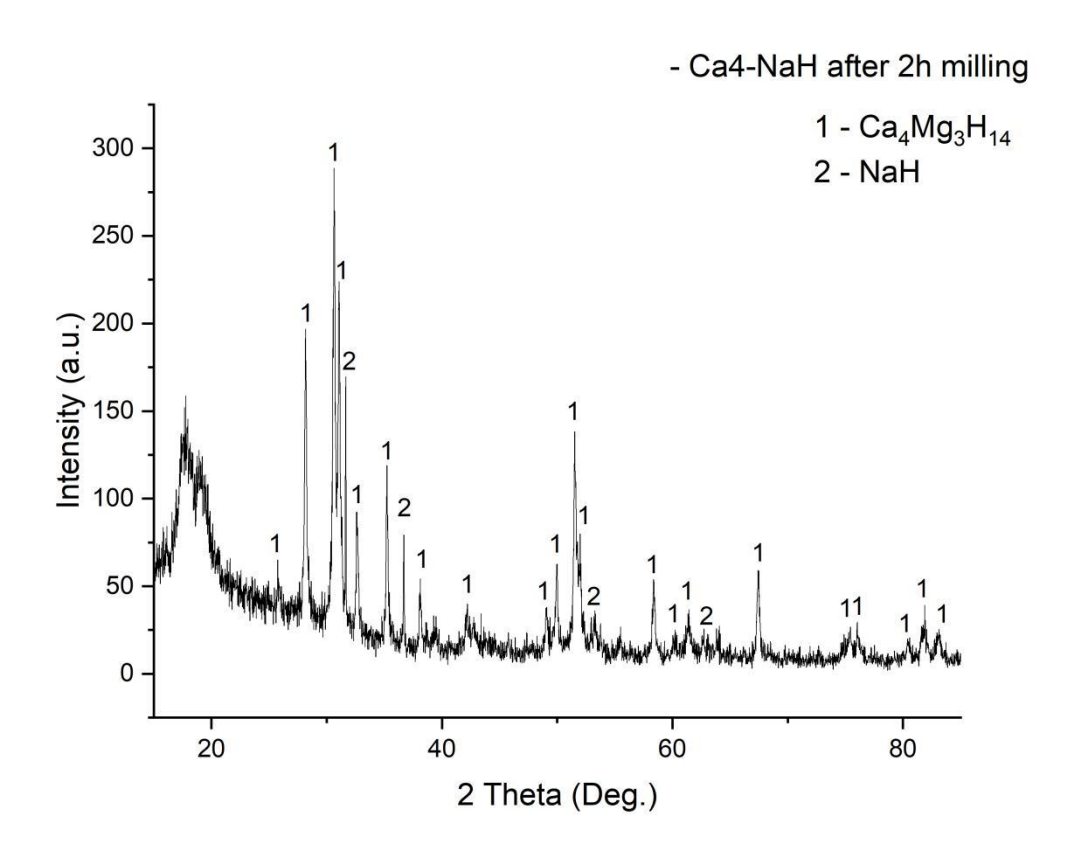


Figure 6-17: The PXD pattern of ball-milled 1:1 Ca₄Mg₃H₁₄:NaH (2h, 300rpm). (1 represent Ca₄Mg₃H₁₄; 2 represent NaH)

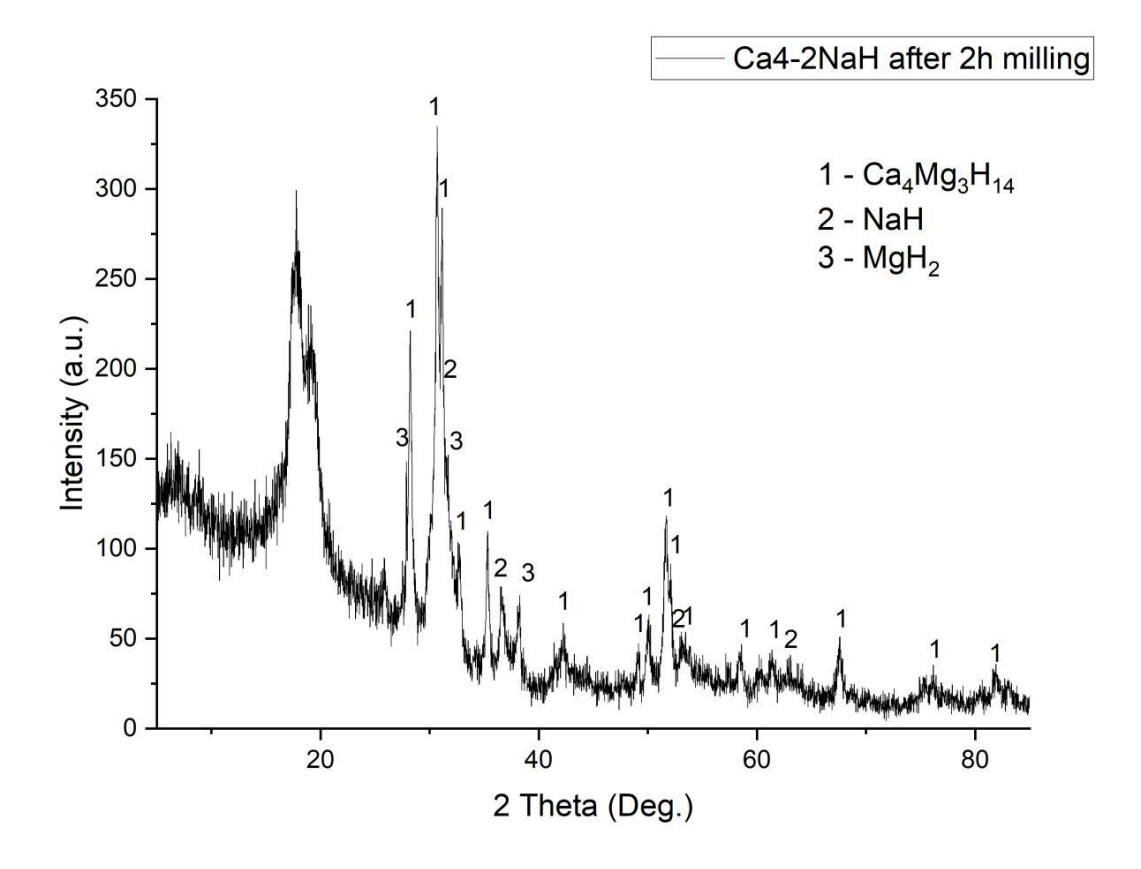


Figure 6-18: The PXD pattern of ball-milled 1:2 Ca₄Mg₃H₁₄:NaH (2h, 300rpm). (1 represent Ca₄Mg₃H₁₄; 2 represent NaH; 3 represent MgH₂)

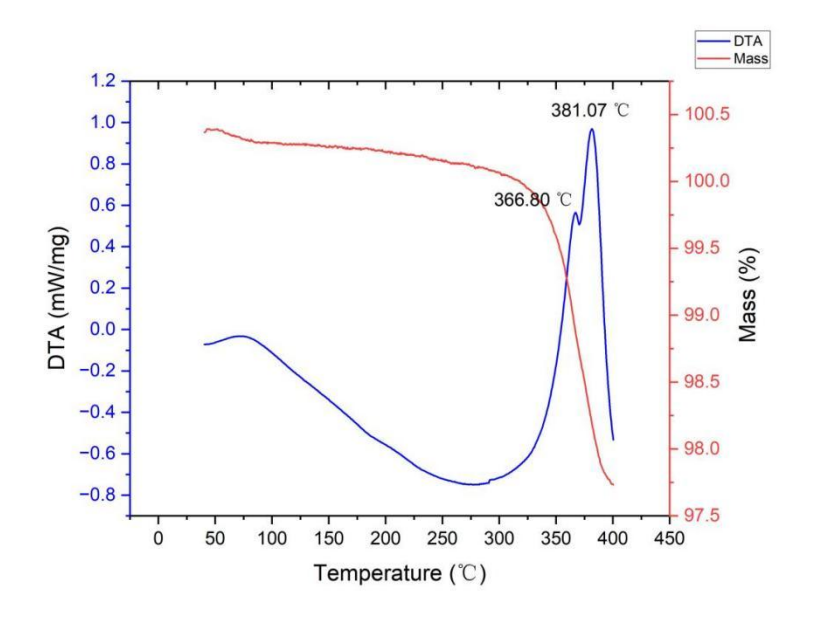


Figure 6-19: TG (red) and DTA (blue) profiles for ball-milled 1:2 $Ca_4Mg_3H_{14}$:NaH (2h, 300rpm) on heating from 35-400 °C at 5 °C min⁻¹ under flowing Ar(g).

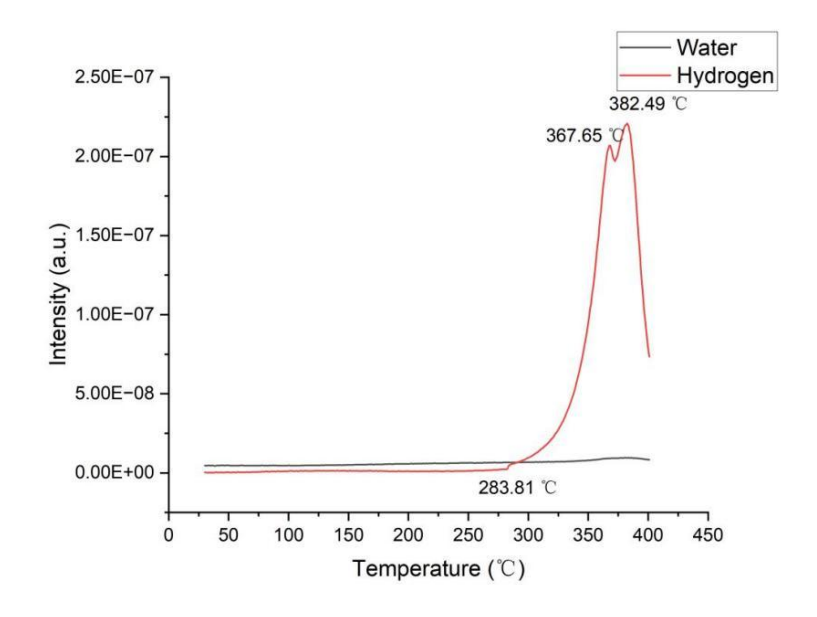


Figure 6-20: Mass spectroscopy output for water (m/z = 18) and hydrogen (m/z = 2) as a function of temperature for ball-milled 1:2 Ca₄Mg₃H₁₄:NaH (2h, 400rpm) on heating from 35-400 °C at 5 °C min⁻¹ under flowing Ar(g).

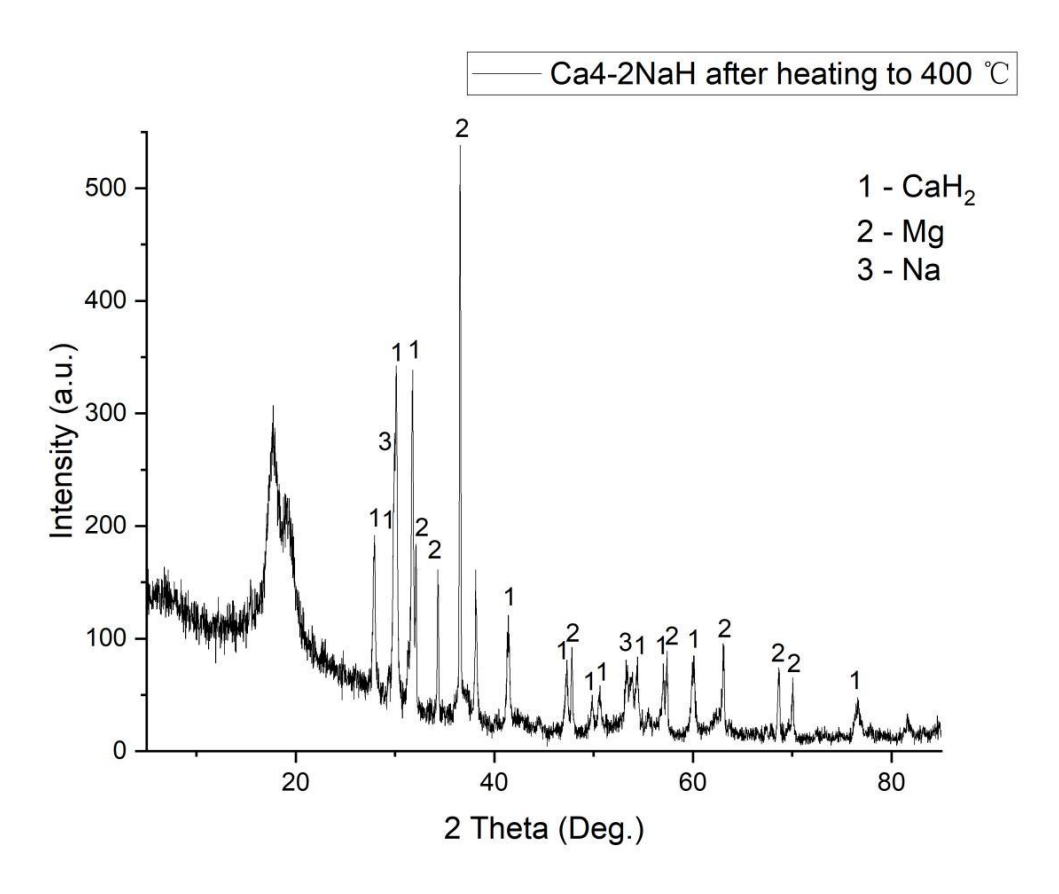


Figure 6-21: The PXD pattern of ball-milled 1:2 Ca₄Mg₃H₁₄:NaH (2h, 400rpm) after heating to 400 °C (and cooling to room temperature). (1 represent CaH₂; 2 represent Mg; 3 represent Na)

6.4 Conclusion

In the case of 1:1 Ca₄Mg₃H₁₄:NaH ball-milled for 2 hours at 400 rpm, NaH can change the reaction pathway to react with Ca₄Mg₃H₁₄, forming Ca₄Mg₂H₁₂ and NaMgH₃. When

heated to 348 °C, the interaction between NaMgH₃ and Ca₄Mg₃H₁₄ results in a decrease of the overall dehydrogenation reaction peak temperature by 102 °C (450 °C - 348 °C), causing not only the earlier decomposition of Ca₄Mg₃H₁₄ but also the premature decomposition of NaMgH₃ (400 °C - 348 °C). The reactions are shown in reactions 2 and 3. For 1:1 Ca₄Mg₃H₁₄:NaH ball-milled for 10 hours at 400 rpm, NaMgH₃, CaH₂, and Mg are formed. The structure of Ca₄Mg₂H₁₂ formed after 2 hours of ball-milling is not stable and decomposes into CaH₂ and Mg. Meanwhile, 1:1 Ca₄Mg₃H₁₄:NaH does not react when ball-milled for 2 hours at 300 rpm. However, 1:2 Ca₄Mg₃H₁₄:NaH ball-milled for 2 hours at 300 rpm generates additional MgH₂, which may act as an intermediate that reacts with NaH to form NaMgH₃ when the ball-milling speed reaches 400 rpm.

6.5 References

- 1. F. Cheng, Z. Tao, J. Liang and J. Chen, Chemical Communications, 2012, 48, 7334.
- 2. A. Zaluska, L. Zaluska and J. O. Strom-Olsen, Journal of Alloys and Compounds, 1999, 288, 217.
- 3. H. Reardon, N. Mazur and D. H. Gregory, *Progress in Natural Science: Materials International*, 2013, **23**, 343.
- 4. K. Yvon, Chimia, 1998, 52, 613.
- 5. C. C. Koch and J. D. Wittenberger, Intermetallics, 1996, 4, 339.
- 6. J. Huot, G. Liang and R. Schulz, Applied Physics, 2001, A72, 187.
- 7. N. Hanada, T. Ichikawa, S.-I. Orimo and H. Fujii, Journal of Alloys and Compounds, 2004, 366, 269-273.
- 8. H. Uesugi, T. Sugiyama, H. Nii, T. Ito and I. Nakatsugawa, *Journal of Alloys and Compounds*, 2011, **509**, S650-S653.
- 9. M. Konarova, A. Tanksale, J. Norberto Beltramini and G. Qing Lu, Nano Energy, 2013, 2, 98-104.
- 10. Z. Weng, I. Retita, Y.-S. Tseng, A. J. Berry, D. R. Scott, D. Leung, Y. Wang and S. L. I. Chan, *International Journal of Hydrogen Energy*, 2021, **46**, 5441-5448.
- 11. A.-L. Chaudhary, S. Dietzel, H.-W. Li, E. Akiba, N. Bergemann, C. Pistidda, T. Klassen and M. Dornheim, *International Journal of Hydrogen Energy*, 2017, **42**, 11422-11428.
- 12. A. Alaoui-Belghiti, A. Assila, I. Belkoufa, M. Rkhis, S. Laasri, M. Tlemçani, E.-k. Hlil and A. Hajjaji, *International Journal of Hydrogen Energy*, 2024, **92**, 1069-1077.
- 13. I. Belkoufa, A. Assila, A. Alaoui-Belghiti, S. Laasri, E. K. Hlil and A. Hajjaji, *International Journal of Hydrogen Energy*, 2025, **105**, 1114-1122.
- 14. J. C. Crivello, T. Nobuki and T. Kuji, International Journal of Hydrogen Energy, 2009, 34, 1937-1943.
- 15. J. Bergsma and B. O. Loopstra, Acta Crystallographica, 1962, 15, 92.
- 16. C. Ataca, E. Aktürk and S. Ciraci, *Physical Review B*, 2009, 79, 041406(R).
- 17. D. K. Dixit, K. Gandhi and B. K. Dixit, International Journal of Hydrogen Energy, 2012, 37, 3767.
- 18. G. Surucu, A. Gencer, A. Candan, H. H. Gullu and M. Isik, *International Journal of Energy Research*, 2019, 44, 2345-2354.
- 19. J. Graetz, Chem Soc Rev, 2009, 38, 73-82.
- 20. B. Huang, K. Yvon and P. Fischer, Journal of Alloys and Compounds, 1992, 190, 65.
- 21. D. Lupu, A. Biris, E. Indrea and R. V. Bucur, *International Journal of Hydrogen Energy*, 1983, 8, 701.
- 22. F. Gingl, F. Bonhomme and K. Yvon, Journal of Alloys and Compounds, 1992, 185, 273.
- 23. B. Bertheville and K. Yvon, Journal of Alloys Compounds, 1999, 290, L8-L10.
- 24. S. Sartori, A. Leon, O. Zabara, J. Muller, M. Fichtner, B. C. Hauback, *Journal of Alloys and Compounds*, 2009, **476**, 639.
- 25. M. Ma, R. Duan, L. Ouyang, X. Zhu, Z. Chen, C. Peng and M. Zhu, Journal of Alloys and Compounds,

- 2017, **691**, 929-935.
- 26. R. Morris, *Synthesis and characterisation of Ca–Mg hydrides for solid-state hydrogen storage*, MSc(R) thesis, University of Glasgow, 2024.
- 27. H. Reardon, Synthesis, structure and characterisation of novel lightweight energy materials based on group I & II metal compounds, PhD thesis, University of Glasgow, 2014.
- 28. G. Nolze and W. Kraus, *PowderCell for Windows*, Version 2.4, BAM, Berlin, 2000; ICSD, Inorganic Crystal Structure Database, FIZ Karlsruhe, Germany.
- 29. ICDD PDF-4+ 2024, International Centre for Diffraction Data, Newtown Square, PA, USA; *PANalytical HighScore Plus*, Version 4.9, Malvern Panalytical.
- 30. A. C. Larson and R. B. Von Dreele, *General Structure Analysis System (GSAS)*, Los Alamos National Laboratory Report LAUR 86–748, 2004; B. H. Toby, *J. Appl. Crystallogr.*, 2001, **34**, 210–213.
- 31. R. Kalamkar, V. Yakkundi and A. Gangal, *International Journal of Hydrogen Energy*, 2020, **45**, 30792-30804.
- 32. D. Pottmaier, E. R. Pinatel, J. G. Vitillo, S. Garroni, M. Orlova, M. D. Baró, G. B. M. Vaughan, M. Fichtner, W. Lohstroh and M. Baricco, *Chemistry of Materials*, 2011, **23**, 2317-2326.
- 33. M. A. Lillo-Ródenas, Z. X. Guo, K. F. Aguey-Zinsou, D. Cazorla-Amorós and A. Linares-Solano, *Carbon*, 2008, **46**, 126-137.

7. Dehydrogenation of Guanidine-NaAlH₄/MgH₂ system

7.1 Introduction

7.1.1 Guanidine and its role in hydrogen release systems

Guanidine (CN₃H₅) is a small organic molecule that has garnered significant attention due to its immense potential in hydrogen storage. Widely studied in the fields of chemistry and biochemistry, guanidine serves as a fundamental building block for many biomolecules and plays a crucial role in supramolecular chemistry.¹ Containing approximately 8.5% hydrogen, all of which are in the form of protons located on amino (–NH₂) or imino (–NH) groups, guanidine's strong basicity allows it to readily protonate and form a stable guanidinium cation (CN₃H₆+), making it an attractive material for hydrogen storage.² Guanidine has a unique molecular structure with a central imino group (–NH) flanked by two amino groups (–NH₂).³ This structure enables guanidine to form stable guanidinium cations through protonation and further interact with metal hydrides or other compounds to create complex hydrides. The crystal structure of guanidine was only recently elucidated, revealing its potential for application in hydrogen storage systems.⁴

Guanidine can be synthesized through various methods. For example, high-purity guanidine can be obtained by reacting guanidinium carbonate with sodium metal in anhydrous ethanol, followed by further purification through sublimation.^{5,6} Guanidine can also form metal guanidinates (MCN₃H₄) through metallation with alkali-metal hydrides (e.g., LiH, NaH) or amides (e.g., LiNH₂). These metal guanidinates exhibit enhanced thermal stability compared to pure guanidine, preserving carbon atoms and reducing the extent of C–N bond breaking during thermal decomposition.^{7,8}

Wu *et al.* report on the development of a novel class of metal borohydride guanidinate complexes (MBH₄·nCN₃H₅, where M = Li, Mg, and Ca; n = 1, 2) and their potential for hydrogen storage. These complexes were synthesized using solid-state methods and characterized through X-ray diffraction, first-principles calculations, and neutron vibrational spectroscopy. The study revealed that these compounds can release approximately 10% hydrogen by weight at moderate temperatures with minimal impurities such as ammonia and diborane. The structures of Mg(BH₄)₂·6CN₃H₅ and Ca(BH₄)₂·2CN₃H₅ were determined, showing unique arrangements of metal cations and ligands. Mg(BH₄)₂·6CN₃H₅ exhibited particularly favourable hydrogen storage properties, including nearly thermally neutral dehydrogenation and high-purity hydrogen release. The research concludes that by adjusting the metal cation (such as Mg²⁺), the hydrogen storage performance of these complexes can be optimized, making them promising candidates for

practical hydrogen storage applications.¹¹

Zhou *et al.* investigated guanidine (CN₃H₅) and its metal guanidinates (MCN₃H₄) as potential hydrogen carriers.¹² Guanidine was reacted with alkali-metal hydrides or amides to form metal guanidinates, which were then characterized in term of their crystal structures and thermal decomposition properties. The study found that metallation significantly improves the thermal stability of guanidine, shifting the decomposition mechanism from C–N bond breaking to N–H bond breaking. For instance, LiCN₃H₄ showed reduced weight loss and ammonia release compared to pure guanidine during thermal decomposition.¹³ By pairing guanidine with metal hydrides like LiH, the resulting composites could release hydrogen primarily through the combination of H⁺ and H⁻, minimizing ammonia generation.¹⁴ The research suggests that these organic molecule-based complexes could pave a new way for developing high-capacity and reversible hydrogen storage systems, with future work focusing on further enhancing hydrogenation properties through strategies such as weakening N–H bonds and introducing more reactive hydrides.^{15,16}

Despite its potential, guanidine-based hydrogen storage systems face several challenges. The dehydrogenation process often involves multiple steps and can be influenced by other compounds, such as ammonia.¹⁷ Additionally, the rehydrogenation of these materials remains a significant challenge, requiring further research to develop effective reversible hydrogen storage methods.^{9,12} Future studies should focus on enhancing the hydrogenation properties of guanidine-based materials by weakening N–H bonds, improving the mobility of metal ions, and introducing more reactive hydrogen carriers.¹⁸ These advancements could pave the way for the development of high-capacity, reversible hydrogen storage technologies based on organic molecules like guanidine.

7.1.2 Aim

The aim of this work is to develop new hydrogen release systems comprising CH₅N₃ with either NaAlH₄ or MgH₂. The research experience gained from the previous studies on the NaAlH₄-NaOH system can also be applied to the investigation of the mechanism of this new system.

7.2 Experimental

MgH₂ (Alfa Aesar, 98%), NaAlH₄ (Sigma Aldrich, powder, 93%), Sodium (Sigma Aldrich, ACS reagent, dry) and Guanidinium carbonate (Sigma Aldrich, for synthesis) was used as received.

Because of the air and moisture sensitivity of MgH₂, NaAlH₄ and Guanidine, all operations were carried out in a recirculating Argon or N₂-filled (BOC, 99.998%) glovebox (MBraun LABstar, $O_2 < 10$ ppm, $H_2O < 0.5$ ppm).

7.2.1 Milling of guanidine and metal hydrides (either MgH₂ or NaAlH₄)

Since the melting point of guanidine is very low, only approximately 50 °C, only mild ball milling conditions were employed. Mixtures of *ca.* 0.2 g in total of guanidine and MgH₂(NaAlH₄) were weighed and then transferred to a stainless-steel grinding jar that was filled with 4 stainless steel balls (10 mm diameter), each of which weighed *ca.* 4 g. The grinding jar was sealed under argon before removal from the glovebox. Ball milling was conducted for various durations (described further below) at 200 rpm rotation speed with a ball-to-powder ratio of 80 : 1 in a planetary ball mill (Retsch PM100) in 2-minute milling periods (reverse rotation) followed by 2-minute rest periods.

7.2.2 Powder X-ray Diffraction (PXD)

All starting materials and Ca-Mg-H hydrogen release systems were characterised using powder X-ray diffraction (PXD). All the materials used in this study were air-sensitive. Therefore, all the samples were prepared using the air-sensitive sample holder under inert atmosphere.(glovebox) All the materials were characterized by PANalytical X'Pert and Rigaku Miniflex. Diffraction data was collected over a 2θ range of 5–85° for 1 h to facilitate phase identification. The obtained diffraction data were compared with appropriate reference patterns using the ICSD database via PowderCell or the ICDD PDF database via PANalytical HighScore Plus and Jade 6.5 software.^{19,20} Rietveld refinements were performed using the General Structure Analysis System (GSAS) with the EXPGUI interface.²¹

7.2.3 Synthesis of Guanidine

Guanidine was synthesised based on the method developed by Wu et al. and Zhou et al.'s article. 9,12 All operations were conducted within a glovebox to maintain an inert atmosphere. Guanidinium carbonate (0.9 g) was dissolved in 80 mL of ethanol with stirring for 12-24 hours. Separately, sodium metal (0.23 g) was dissolved in 20 mL of ethanol, with stirring for 1 hour, until the reaction with sodium was complete (i.e. no sodium metal was visible in the solution). The two resulting solutions were then combined and stirred for 18 hours. Subsequent filtration was performed using one of two methods: centrifugation for 10 minutes or allowing the mixture to stand for 20 minutes. (The later proved more effective). The upper layer (colourless solution) of the resulting biphasic solution was collected into a two-necked round-bottom flask. The collected and colourless solution was

subjected to drying and evaporation using a Schlenk line overnight. This process yielded a viscous, oil-like product. Crystallization of this product directly under high vacuum on the Schlenk line was challenging. Therefore, the oil-like intermediate was transferred into the glovebox transition port (small) and subjected to vacuum drying overnight, enabling its crystallization.

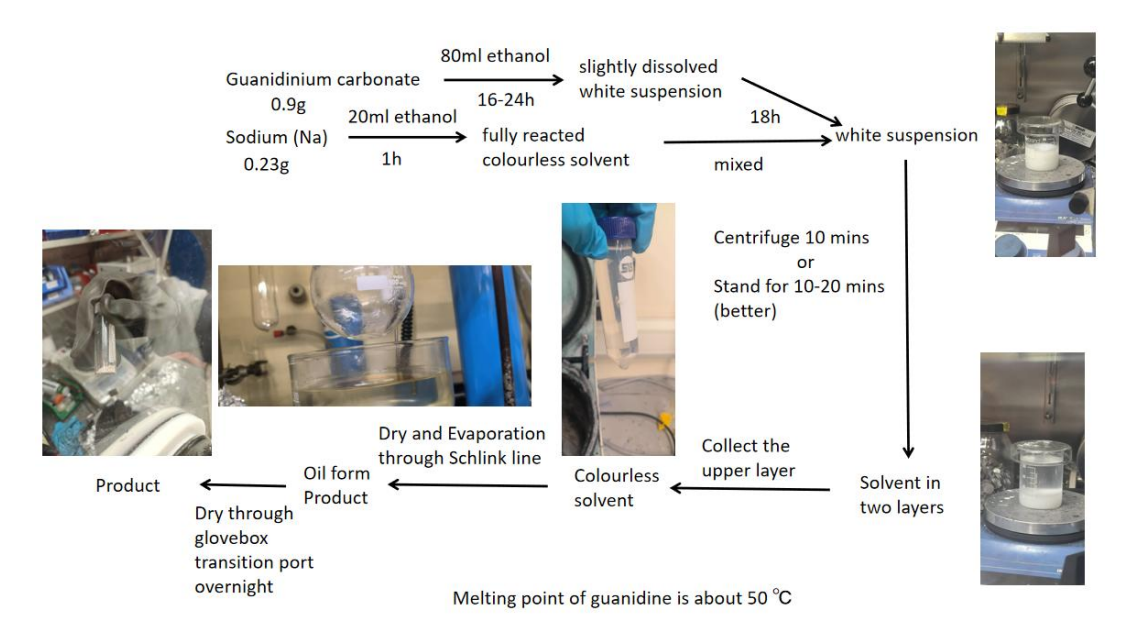


Figure 7-1: Schematic representation of the guanidine synthesis.

7.3 Results and Discussion

7.3.1 Thermal Treatment of Guanidine

After synthesis, guanidine was successfully synthesised as shown in Figure 7-2, and is a pink-white coloured material. Figures 7-3 and 7-4 display the thermal performance of guanidine when heated to 400 °C. There are three DTA peaks observed. The first peak occurs at 58 °C, with no mass change or gas release. The melting point of guanidine is 50 °C, which is close to the observed 58 °C.²² Combined with the absence of any mass loss, this strongly suggests that the first thermal event corresponds to the melting of guanidine. The second peak appears at 179 °C, which is exothermic reaction, and from the MS spectrum, it can be seen that the second peak corresponds to the release of NH₃. Both NH₃ and CH₄ are gases that may be released according to the literature. ^{9,12} In Figure 7-4(a), NH₃ is measured at m/z=17, while CH₄ is measured at m/z=16. It can be observed that both NH₃ and CH₄ are released simultaneously, but their profiles are near-identical, which is unusual. A possible reason is that NH₃ exhibits a strong signal at m/z = 16, which can interfere with or contribute to the signal intensity attributed to CH₄ at the same m/z value. Therefore, in Figure 7-4(b), to avoid mutual interference of NH₃ and CH₄, NH₃ is also measured at m/z

=17, while CH₄ is measured at m/z=13 and m/z=12. No CH₄ release is observed in Figure 7-4(b). Figure 7-4(b) should be correct because the signal intensities of gases are mutually independent.

The mass loss analysis also indicates that if all NH₃ were released, the theoretical mass loss would be 28.81 wt.%, which closely aligns with the observed value of 28.92 wt.%. This suggests that NH₃ is predominantly released at approximately 179 °C. The powder patterns in Figure 7-5 demonstrate that upon heating CH₅N₃ to 200 °C, the resulting product is melamine (C₃H₆N₆). Therefore, the reaction corresponding to the second thermal event can be expressed as:

$$3CH_5N_3 \rightarrow C_3H_6N_6 + 3NH_3$$
 (1)

A third DTA peak appears at 343 °C. According to Costa et al.'s paper, most melamine undergoes evaporation at 315-380 °C, leading to a significant mass reduction.²³ Therefore, the peak at 343 °C corresponds to the evaporation of C₃H₆N₆. This is consistent with the literature, which reports that after evaporation, C₃H₆N₆ undergoes a condensation reaction between 380 °C and 480 °C to form the highly condensed polymer such as melem. This reaction accounts for the remaining 6 wt.% residue.

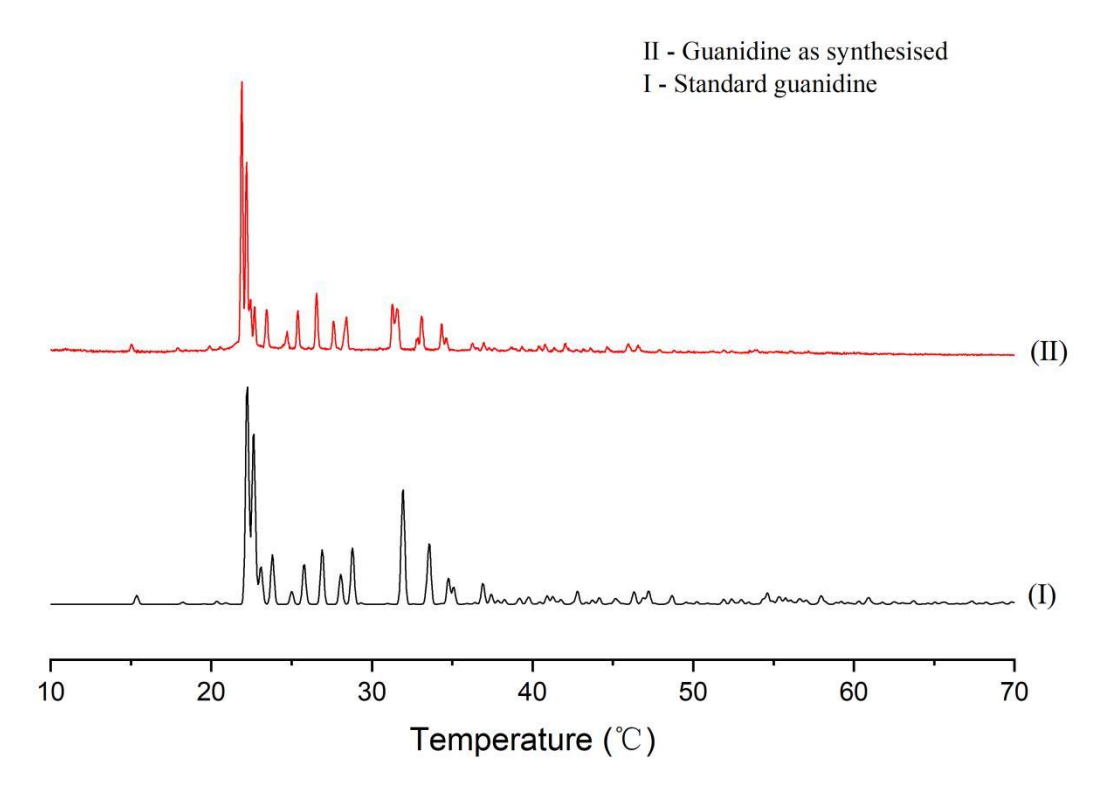


Figure 7-2: PXD patterns of the synthesis product (I) as compared to the standard diffraction pattern of guanidine(II).

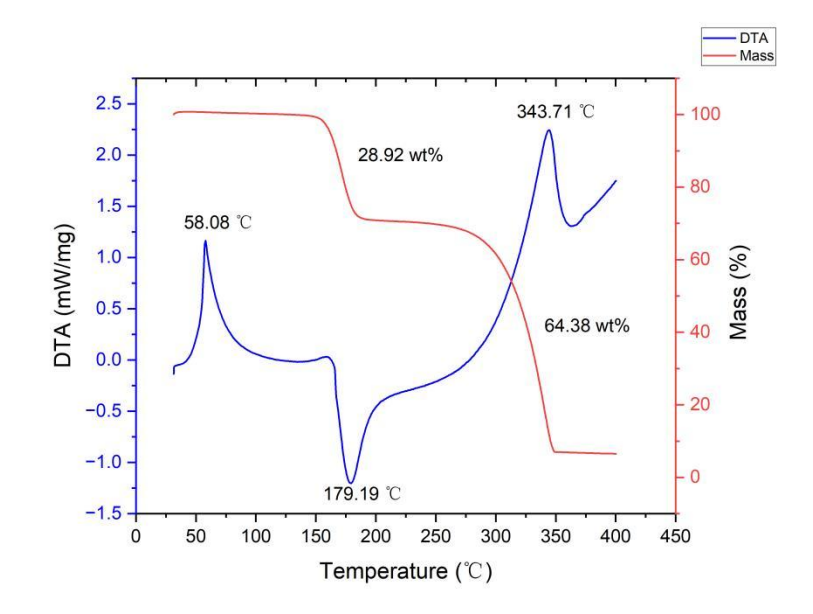


Figure 7-3: TG (red) and DTA (blue) profiles for as-synthesised guanidine, CH_5N_3 , on heating from 35-400 °C at 5 °C min⁻¹ under flowing Ar(g).

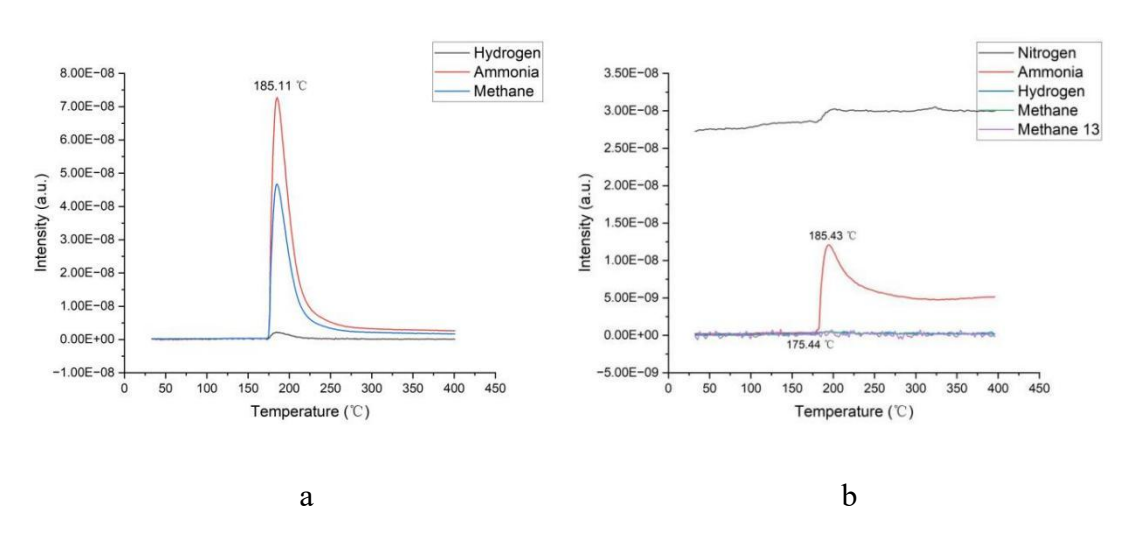


Figure 7-4: Mass spectroscopy output as a function of temperature for: (a) ammonia (m/z = 17), methane (m/z = 16) and hydrogen (m/z = 2) and (b) ammonia (m/z = 17), methane (m/z = 13/16), nitrogen (m/z = 28), hydrogen (m/z = 2) for CH_5N_3 on heating from 35-400 °C at 5 °C min⁻¹ under flowing Ar(g).

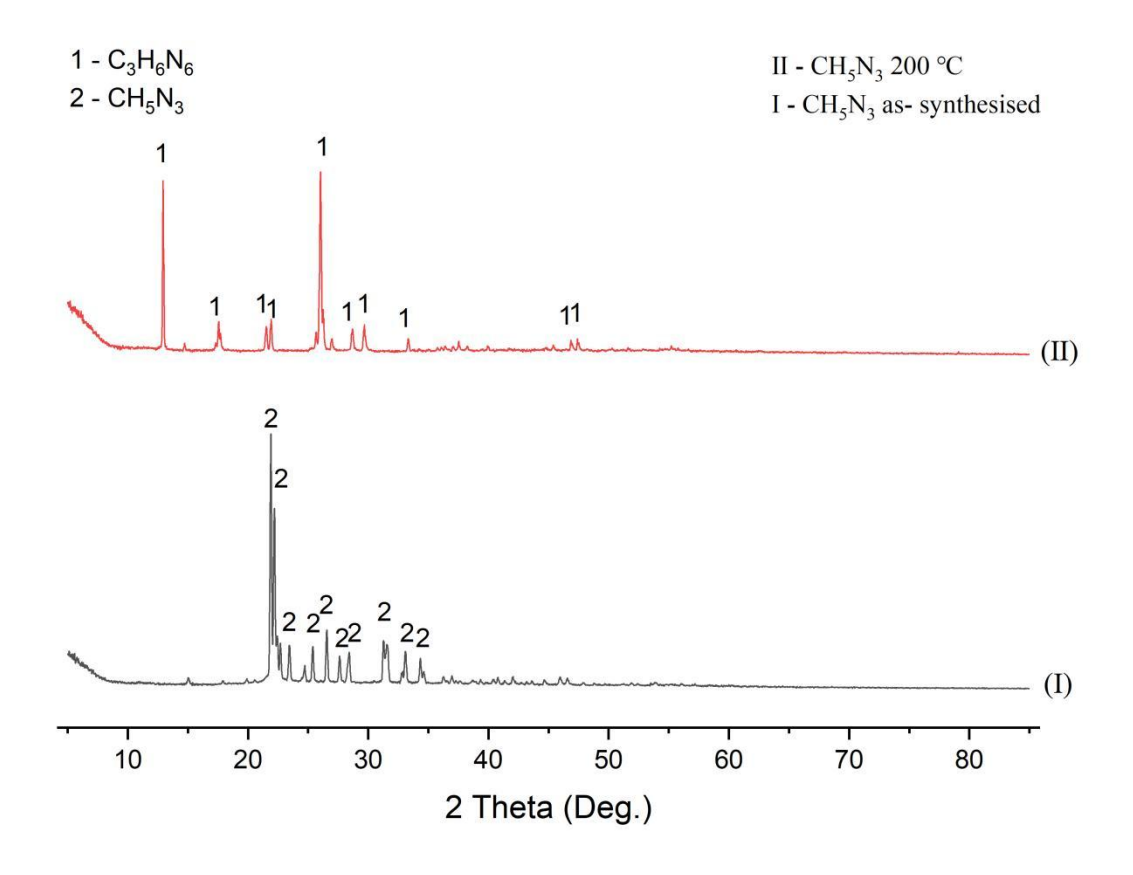


Figure 7-5: PXD pattern of as-synthesised guanidine (I) and after heating to 200 °C (II).

7.3.2 Investigation of hydrogen release in the NaAlH₄-CH₅N₃ system

Due to the low melting point of guanidine, the ball milling parameters were set at a relatively low rotation speed of 200 rpm for 1 hour. Figures 7-6 and 7-7 illustrate the thermal performance of the NaAlH₄-CH₅N₃ system. The DTA results exhibit two peaks: the first peak corresponds to the melting of CH₅N₃, consistent with previous observations, while the second peak at 157 °C represents an exothermic reaction. This reaction occurs rapidly and intensely, with hydrogen being the only detected gaseous product, indicating that NaAlH₄ reacts with CH₅N₃ to release hydrogen.

However, if only hydrogen were released, the theoretical mass loss would be 7.96 wt%, which is significantly lower than the observed 32.81 wt%. Additionally, the mass loss of gases varies at different temperatures.(Appendix 7-1 to 7-3) This discrepancy is attributed to the rapid release of hydrogen, which likely causes some reaction mixtures to be expelled from the crucible into the thermocouple, leading to additional mass loss. The expelled material appears black and is in a clumped form, resembling the products in the crucible but differing from the sodium leakage observed in the NaBH₄-NaOH system, as depicted in Chapter 5, Figure 5-15. In the NaBH₄-NaOH reaction, leaked sodium adheres to the thermocouple with a sticky texture and cannot be removed without high-temperature evaporation. In contrast, the expelled product from the NaAlH₄-CH₅N₃ reaction is

non-adhesive and can be physically removed, suggesting that the leaked material is not sodium.

PXD analysis (Figure 7-8) indicates that no reaction occurs between NaAlH₄ and CH₅N₃ during ball milling. Even when the temperature reaches 150 °C, NaAlH₄ remains present without decomposition. Additionally, once CH₅N₃ melts and solidifies upon cooling, it was hard to be removed from the crucible, further confirming that NaAlH₄ does not form an intermediate compound with CH₅N₃. At 170 °C, the reaction of NaAlH₄ and CH₅N₃ is complete, producing aluminium and unidentified broad peaks at approximately 30° and 35° 20. The unidentified peaks do not match any known materials in the ICSD database and the ICDD PDF. As the heating continues to 400 °C, the product remains unchanged from that at 170 °C. Therefore, the unidentified peaks are likely associated with a Na-C-N-based compound.

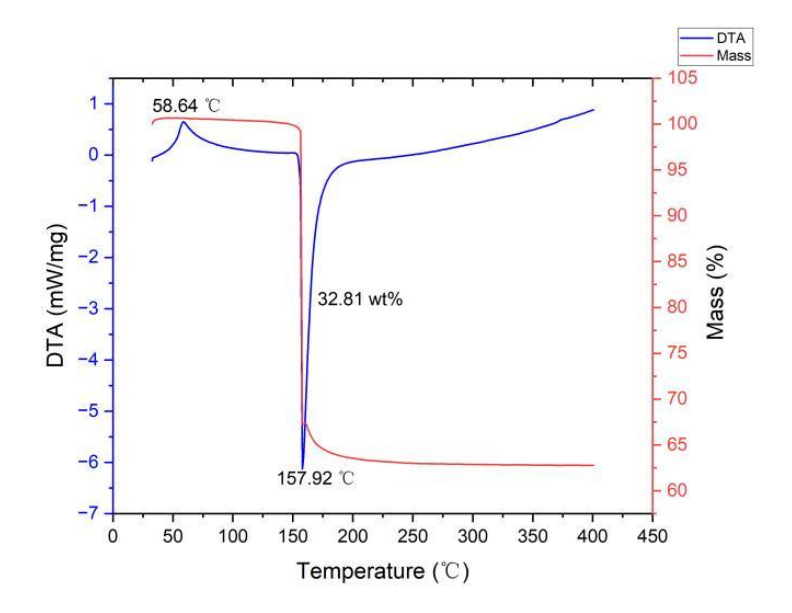


Figure 7-6: TG (red) and DTA (blue) profiles for ball-milled 1:1 CH₅N₃:NaAlH₄ (1h, 200rpm) on heating from 35-400 °C at 5 °C min⁻¹ under flowing Ar(g).

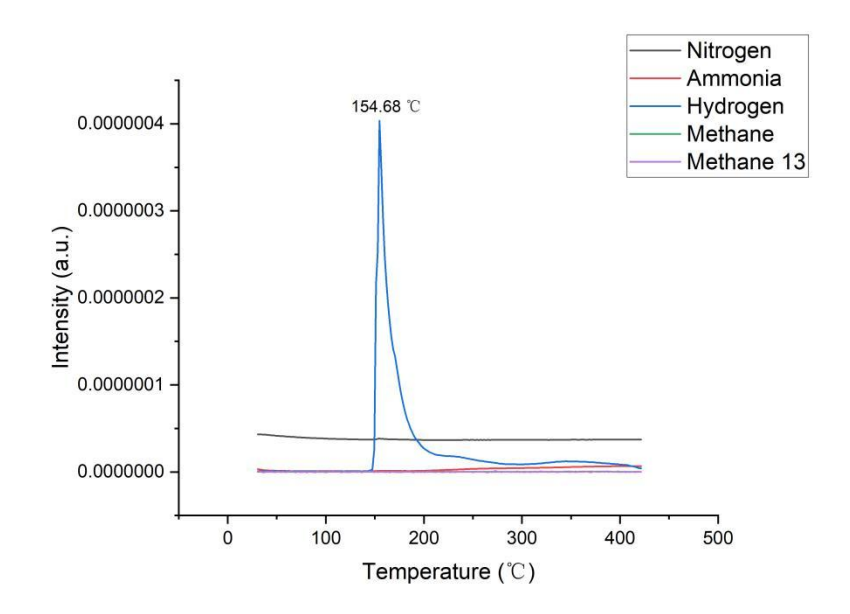


Figure 7-7: Mass spectroscopy output for ammonia (m/z = 17), methane (m/z = 13/16), nitrogen (m/z = 28), hydrogen (m/z = 2) as a function of temperature for ball-milled 1:1 CH₅N₃:NaAlH₄ (1h, 200rpm) on heating from 35-400 °C at 5 °C min⁻¹ under flowing Ar(g).

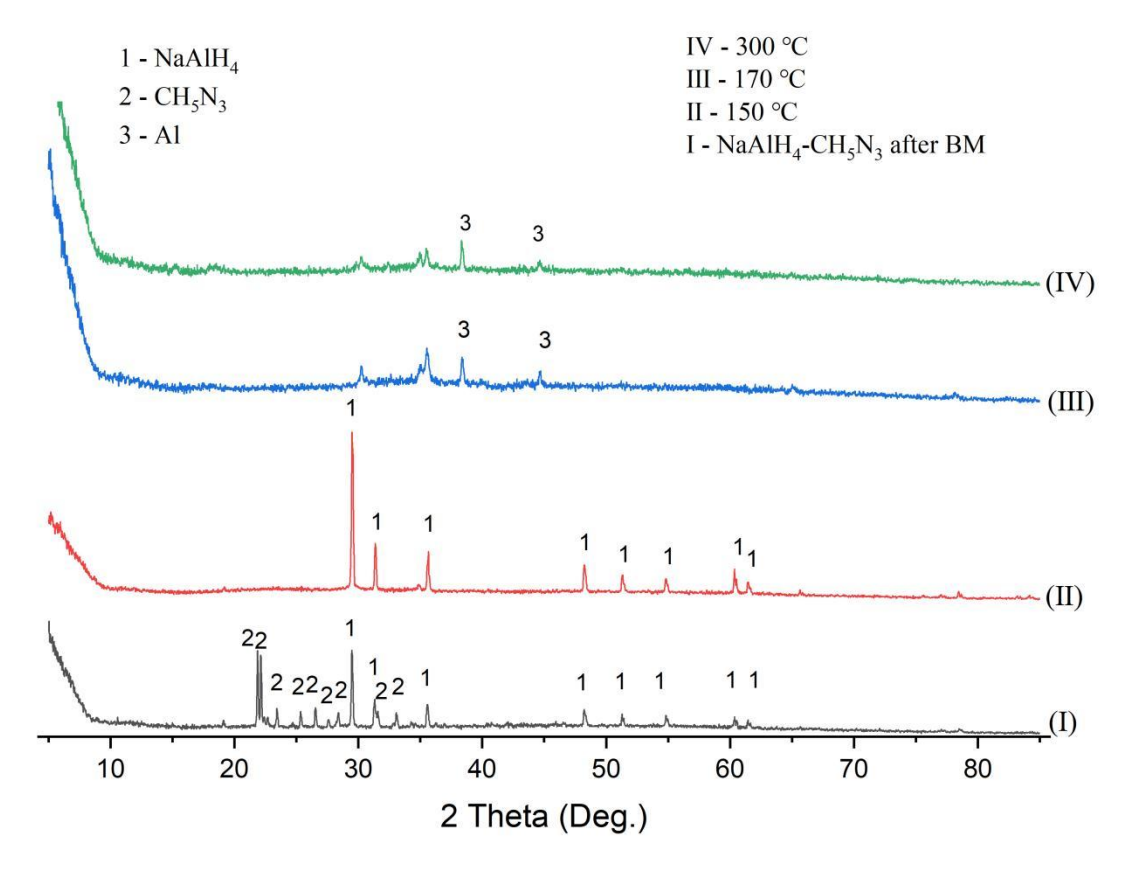


Figure 7-8: PXD patterns of 1:1 CH₅N₃:NaAlH₄ after ball-milling (1h, 200rpm;I) and heating to 150 (II), 170 (III) and 300 (IV) °C.

7.3.3 Investigation of hydrogen release in the MgH₂-CH₅N₃ system

Figures 7-9 and 7-10 illustrate the thermal behaviour of the 1:1 CH₅N₃:MgH₂ and 1:2 CH₅N₃:MgH₂ systems. The DTA peak temperatures of both samples are closely aligned,

with the second (exothermic) peak of CH₅N₃-MgH₂ occurring at 135 °C, slightly higher than that of the second DTA peak for CH₅N₃-2MgH₂ at 128 °C. Additionally, both samples exhibit similar thermal profiles otherwise. MS analysis indicates that hydrogen is released at 128 °C and 200 °C, followed by a minor release of NH₃. According to the PXD pattern shown in Figure 7-11, no reaction between CH₅N₃ and MgH₂ was observed during ball milling. When the temperature was raised to 150 °C, which marks the completion of the first reaction step, the PXD pattern displayed phases corresponding to MgH₂ and an unidentified product. This unidentified phase partially matches CH₅N₃, particularly at diffraction angles of approximately 22°, 26°, 27°, and two peaks above 55°. Upon further heating to 240 °C and 400 °C, the reaction was completed, yielding products that included MgH₂ phases and broad peaks at 18° and 34° that could not be identified by the software or the ICSD database. As depicted in Figure 7-9(a), the mass loss continuously decreased between 240 °C and 400 °C, while the PXD pattern remained unchanged, suggesting that a condensation reaction may have occurred after 240 °C. Figure 7-12 also shows that in the 1:2 CH₅N₃:MgH₂ sample, the CH₅N₃ phase completely disappeared at 160 °C. Given that the reaction between MgH₂ and CH₅N₃ may produce amorphous products that are undetectable by PXD, the exact reaction mechanism is difficult to deduce based solely on the available data. Therefore, insights from the literature are necessary to propose potential reaction pathways, which can then be validated by mass loss analysis. According to the articles by Wu et al. and Zhou et al., LiH reacts with CH₅N₃ to form LiCN₃H₄ and hydrogen gas at relatively low temperatures (around 90 °C).^{9,12} This is an irreversible reaction, indicating that LiCN₃H₄ is highly stable once formed. The reaction is shown below:

$$CH_5N_3 + LiH \rightarrow LiCN_3H_4 + H_2$$
 (2)

The hydride ion (H⁻) in LiH reacts with a proton (H⁺) from CN₃H₅ (originating from the amino or imino group) to generate hydrogen gas and form LiCN₃H₄. This process is analogous to the previously described NaH-NaOH system and can be regarded as a proton transfer reaction, where H⁺ combines with H⁻ to produce H₂. According to Zhang's article, MgH₂ powder and guanidine can react to form Mg(CN₃H₄)₂.²⁴ The synthesis procedure involves depositing MgH₂ powder and guanidine in an autoclave at a 1:2 molar ratio. Subsequently, dry ammonia (15 mL) is condensed into the autoclave, which is then placed in an oven at 50 °C for one month. The reaction is shown below:

$$MgH_2 + 2CH_5N_3 \rightarrow Mg(CN_3H_4)_2 + 2H_2$$
 (3)

This suggests that MgH₂ has the potential to react with CH₅N₃ to form Mg(CN₃H₄)₂. Reaction 3 may correspond to the MS peak observed at approximately 130 °C. As shown

in MS Figure 7-10, the peak temperature at 200 °C is associated with the initial release of hydrogen gas, followed by the release of NH₃ at 220 °C. According to the article by Schwamm et al., Mg(CN₃H₃)₂ can be synthesized stably.²⁵ Therefore, the reaction pathway may be as follows:

$$Mg(CN_3H_4)_2 \rightarrow Mg(CN_3H_3)_2 + H_2$$
 (4)

$$Mg(CN_3H_3)_2 \rightarrow Mg(CN_2)_2 + 2NH_3$$
 (5)

Therefore, the total reaction may be as follows:

$$MgH_2 + 2CH5N_3 \rightarrow Mg(CN_2)_2 + 2NH_3 + 3H_2$$
 (6)

Given the molar ratio of MgH₂ to CH₅N₃ is 1:2, both the 1:1 MgH₂:CH₅N₃ and 2:1 MgH₂:CH₅N₃ mixtures have an excess of MgH₂. This explains the persistent presence of MgH₂ phases observed in PXD patterns shown in Figures 7-11 and 7-12. If the proposed reaction indeed occurs in the 1:1 MgH₂:CH₅N₃ sample, the theoretical mass loss before reaching 240 °C would be 24.70 wt.%, which closely matches the experimental mass loss of 25.51 wt.% as depicted in Figure 7-9. Similarly, for the reaction occurring in the 2:1 MgH₂:CH₅N₃ sample, the theoretical mass loss is 18.92 wt.%, which is close to the experimental mass loss of 19.27 wt.%. For the sample with a molar ratio of 2.5:1 MgH₂:CH₅N₃, the theoretical mass loss is 16.13 wt.%, which closely aligns with the experimentally observed mass loss of 17.26 wt.%.(Appendix 7-4) Moreover, the mass loss of the 1:2 CH₅N₃:MgH₂ mixture at 128 °C reaches 1.73 wt.%, indicating that approximately 2 moles of hydrogen are released from the mixture, which initially contained 9 moles of hydrogen. This suggests that the hydrogen release is primarily through Reaction 3.

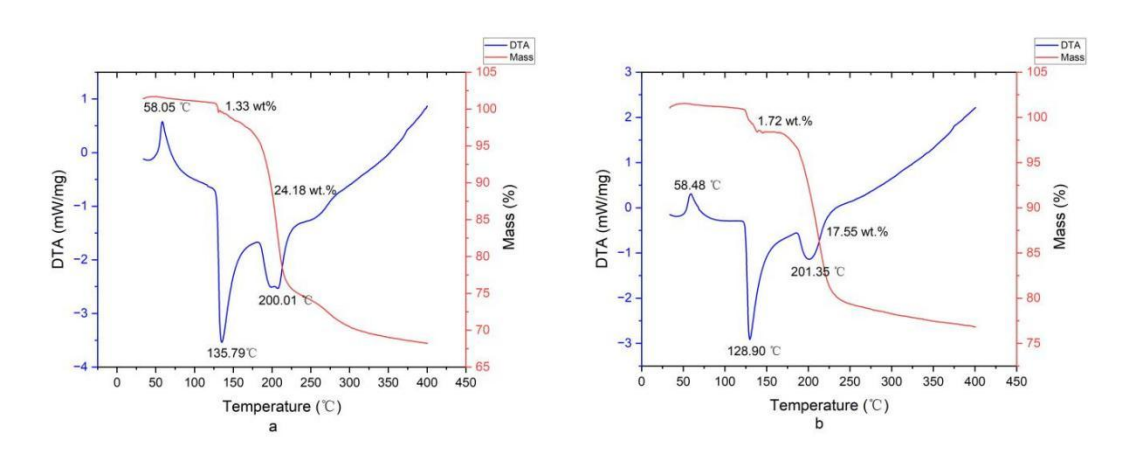


Figure 7-9: TG (red) and DTA (blue) profiles for ball-milled (1h, 200rpm) (a) 1:1 CH $_5$ N $_3$:MgH $_2$ (b) 1:2 CH $_5$ N $_3$:MgH $_2$ on heating from 35-400 °C at 5 °C min $^{-1}$ under flowing Ar(g).

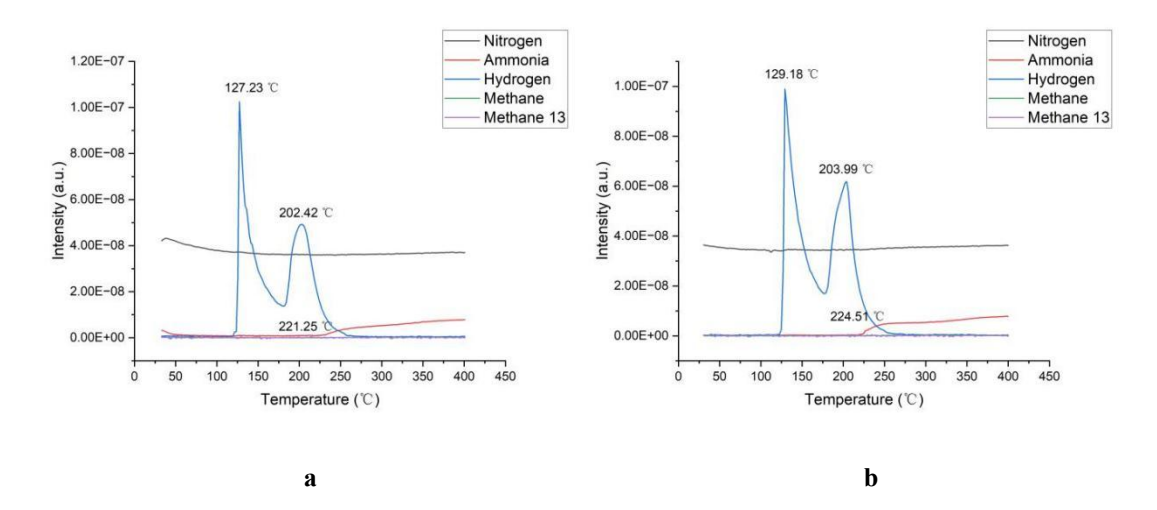


Figure 7-10: Mass spectroscopy output for ammonia (m/z = 17), methane (m/z = 13/16), nitrogen (m/z = 28), hydrogen (m/z = 2) as a function of temperature for ball-milled (1h, 200rpm) (a) 1:2 CH₅N₃:MgH₂ (b) 1:1 CH₅N₃:MgH₂ on heating from 35-400 °C at 5 °C min⁻¹ under flowing Ar(g).

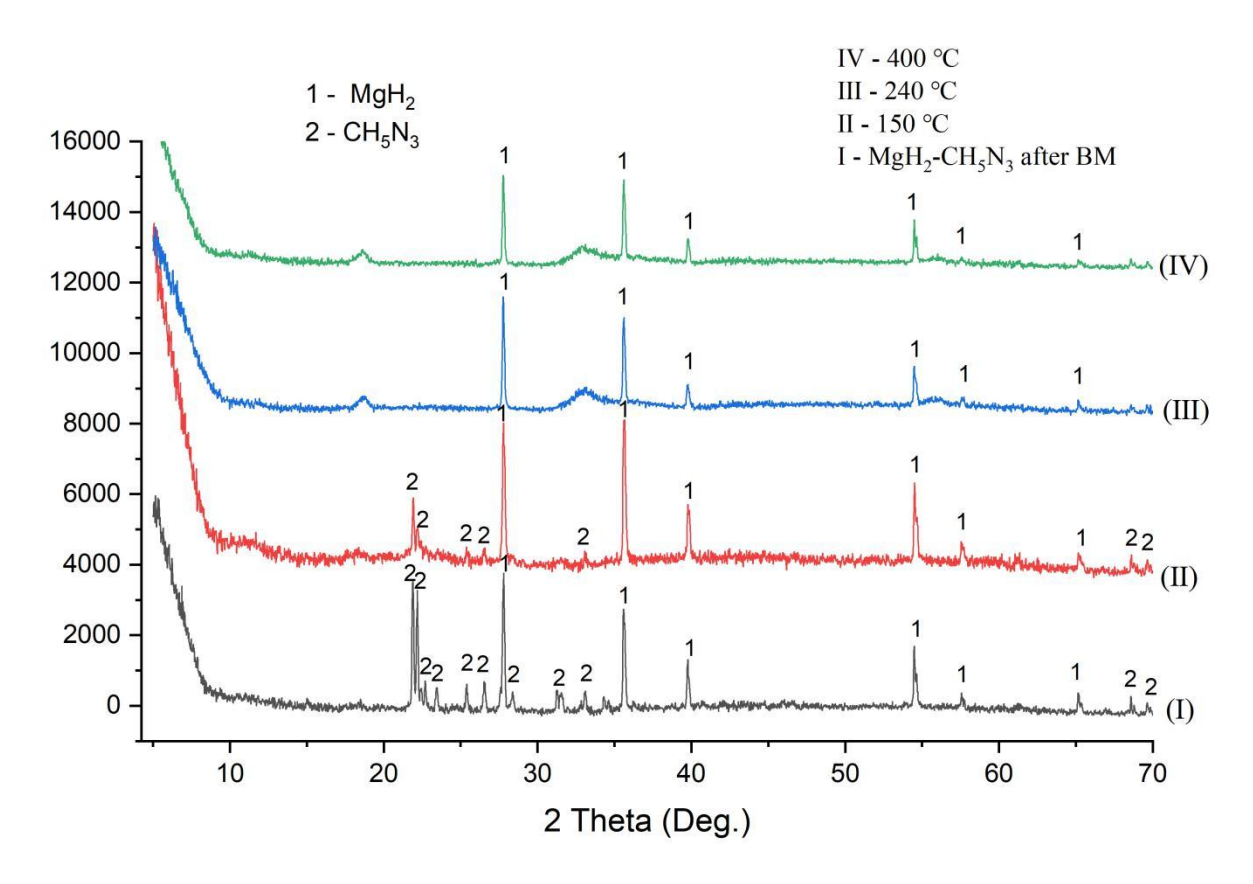


Figure 7-11: PXD patterns of 1:1 CH_5N_3 :MgH₂ after ball-milling (1h, 200rpm;I) and heating to 150 (II), 240 (III) and 400 (IV) °C. (and cooling to room temperature)

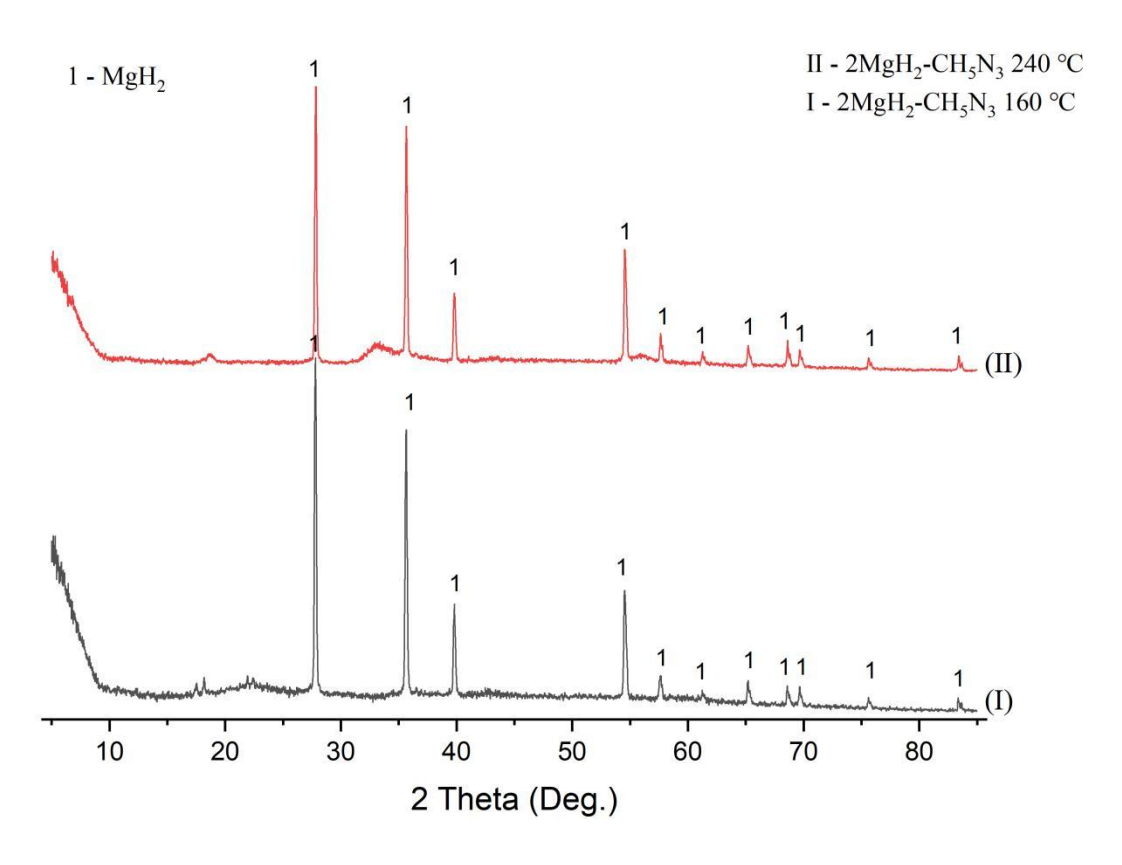


Figure 7-12: PXD patterns of 1:2 CH₅N₃:MgH₂ after ball-milling (1h, 200rpm) and heating to 160 (I) and 400 (II) °C. (and cooling to room temperature)

Based on the previous information, the reactions between 1:1 MgH₂:CH₅N₃ and 2:1 MgH₂:CH₅N₃ involve an excess of MgH₂. To investigate whether MgH₂ could be completely consumed by an excess of CH₅N₃, a ball-milled 4:1 CH₅N₃:MgH₂ mixture (1 hour, 200 rpm) was heated to 400 °C. As shown in Figures 7-13 and 7-14, the thermal behaviour was similar to previous observations, with hydrogen release and mass loss occurring at 138 °C. However, an additional hydrogen release peak appeared at 149 °C. At 200 °C, consistent with the previous MS Figure 7-10, hydrogen gas was released first, followed by NH₃. Notably, a significant mass loss was observed between 200 °C and 300 °C. According to Figure 7-3, this temperature range corresponds to the decomposition of C₃H₆N₆ (melamine).

As depicted in Figure 7-15, upon heating to 150 °C, additional phases appeared between 10° and 20° in the PXD pattern, in addition to the phases corresponding to MgH₂ and CH₅N₃. When heated to 240 °C, the MgH₂ phases disappeared, and peaks corresponding to C₃H₆N₆ emerged. Comparing Figures 7-13, 7-14, and 7-15 with Figures 7-9, 7-10, and 7-11, it is evident that the 4:1 CH₅N₃:MgH₂ mixture exhibited an additional hydrogen release at 149 °C and the formation of C₃H₆N₆ at 240 °C. Therefore, C₃H₆N₆ likely originated from the condensation of excess CH₅N₃. The proposed reaction is as follows:

$$2CH_5N_3 \rightarrow 2/3 C_3H_6N_6 + 3H_2$$
 (7)

However, according to Reaction 1, the condensation of CH₅N₃ would release ammonia gas. The presence of Mg²⁺ in Mg(CH₄N₃)₂ might be a contributing factor. According to Zhou's article, the introduction of Mg²⁺ can enhance the polarity of the N-H bonds in guanidine molecules, thereby reducing their bond energy and making the N-H bonds more susceptible to cleavage. Therefore, under the influence of Mg²⁺, the N-H bonds in guanidine may break more readily, leading to the formation of H₂.

To verify this hypothesis, the theoretical mass loss should be calculated. If we consider the previous Reactions 3, 4, and 5, along with the current Reaction 7, and assume that guanidine remains at 7 wt.% as shown in Figure 7-3, the theoretical mass loss should be 55.51 wt.%. This value is higher than the experimentally observed mass loss, which suggests that there may be uncertainty regarding the residual mass after the condensation of C₃H₆N₆.(Appendix 7-5) In Figure 7-15, when the temperature is raised to 400 °C, the product exhibits two strong peaks corresponding to MgH₂, while the other weaker peaks are absent. This may indicate that the structure of MgH₂ was disrupted at 240 °C, but it subsequently reformed and recrystallized through a reaction with C₃H₆N₆ or products derived from the thermal decomposition of C₃H₆N₆. However, further experiments would be necessary to confirm this hypothesis.

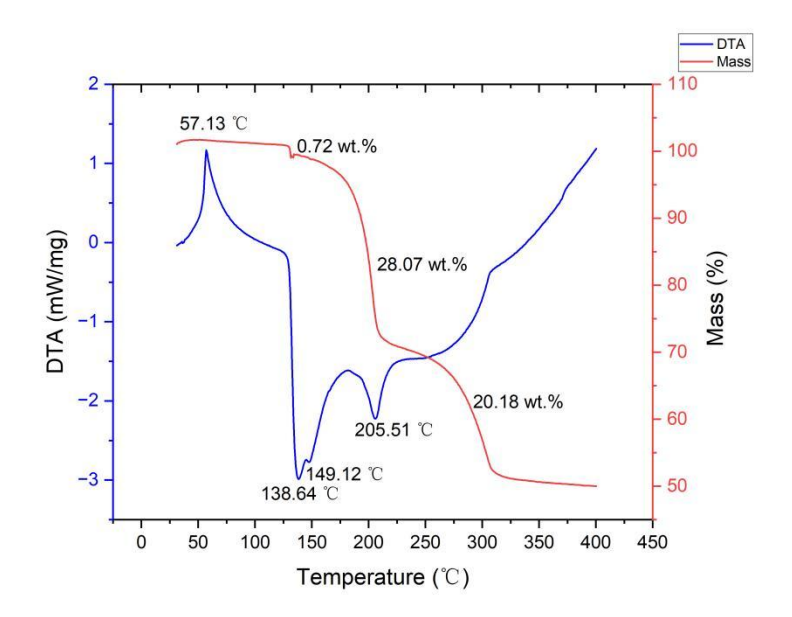


Figure 7-13: TG (red) and DTA (blue) profiles for ball-milled 4:1 CH₅N₃:MgH₂ (1h, 200rpm) on heating from 35-400 °C at 5 °C min⁻¹ under flowing Ar(g).

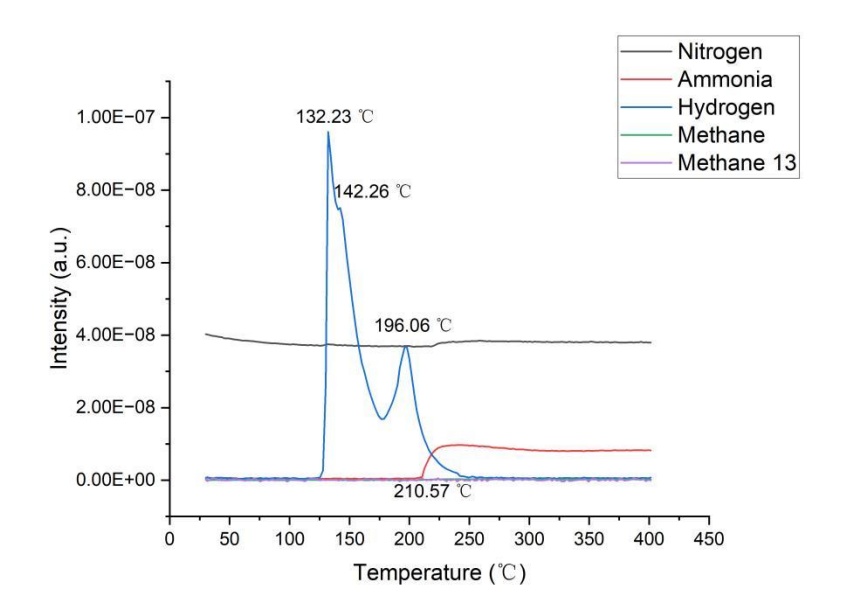


Figure 7-14: Mass spectroscopy output for ammonia (m/z = 17), methane (m/z = 13/16), nitrogen (m/z = 28), hydrogen (m/z = 2) as a function of temperature for ball-milled 4:1 CH₅N₃:MgH₂ (1h, 200rpm) on heating from 35-400 °C at 5 °C min⁻¹ under flowing Ar(g).

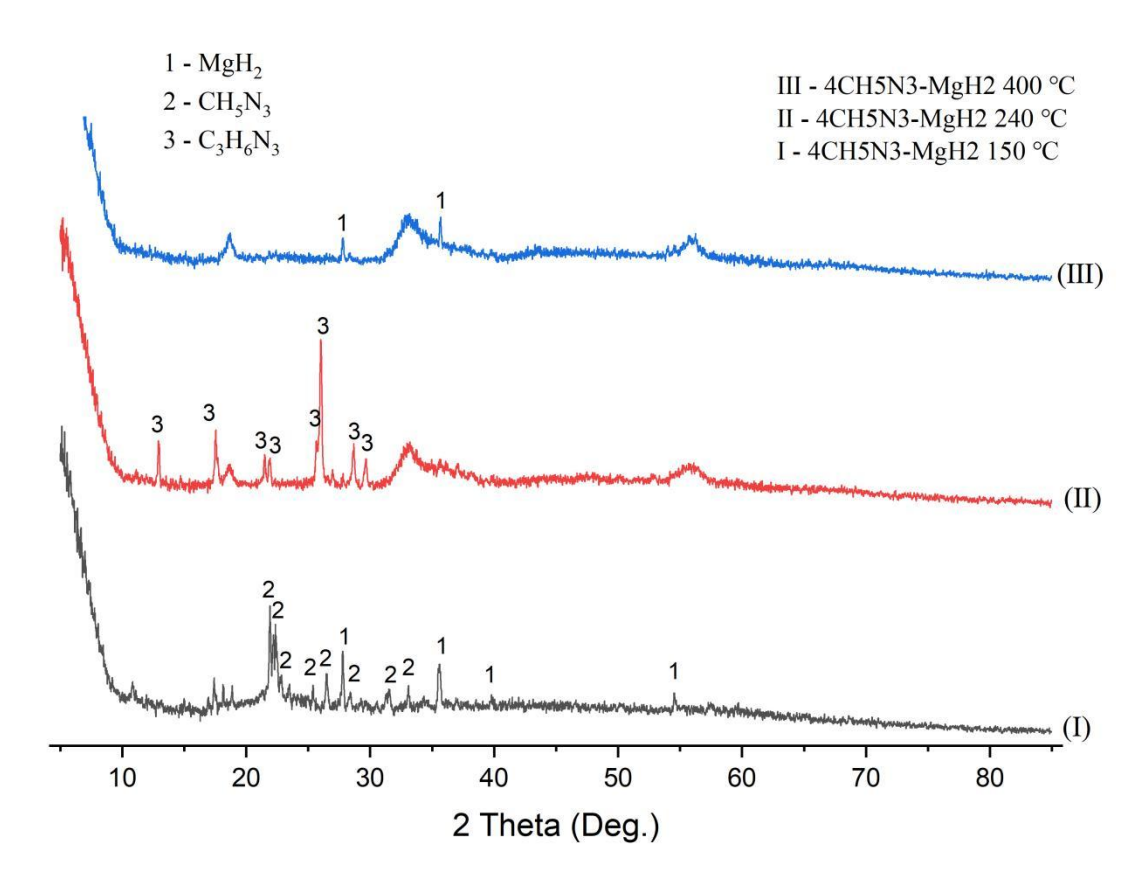


Figure 7-15: PXD patterns of 4:1 CH₅N₃:MgH₂ after heating to 150 (I), 240 (II) and 400 (III) °C. (and cooling to room temperature)

7.4 Conclusions

In conclusion, the behaviour of CH_5N_3 is characterized by its melting at 58 °C and subsequent decomposition into $C_3H_6N_6$ and NH_3 at higher temperatures (180 °C), with

C₃H₆N₆ further evaporating at even higher temperatures (250-350 °C), as described in Reaction 1. In contrast to the single reaction between CH₅N₃ and NaAlH₄ (Reaction 2) occurring at 150 °C, the reactions involving MgH₂ and CH₅N₃ are significantly more complex. Based on mass loss data and relevant literature, it is hypothesized that Reactions 3, 4, 5, and 6 occur in the 1:2 MgH₂:CH₅N₃ system; however, these reactions require further experimental validation. When an excess of CH₅N₃ is introduced to MgH₂, an additional Reaction 7 is proposed, supported by mass loss data but still necessitating additional experimental confirmation.

Future work should include PXD analysis at multiple temperatures, such as 200 °C, 180 °C, and 140 °C, as well as investigations of the reactions between MgH₂ and CH₅N₃ at various molar ratios, including the 1:2 MgH₂:CH₅N₃ system. Both mass loss and PXD analyses should be employed to identify potential products.

7.5 References

- 1. Y. Izato and A. Miyake, Sci. Tech. Energetic Mater, 2018, 79, 80-88.
- 2. V. Hoepfner, U. Englert and R. Dronskowski, Zeitschrift für Naturforschung B, 2011, 66, 975-978.
- 3. T. Yamada, X. Liu, U. Englert, H. Yamane and R. Dronskowski, Chemistry, 2009, 15, 5651-5655.
- 4. Iris M. Müller and D. Möller, European Journal of Inorganic Chemistry, 2005, 2005, 257-263.
- 5. Z. Tang, Y. Tan, H. Wu, Q. Gu, W. Zhou, C. M. Jensen and X. Yu, Acta Materialia, 2013, 61, 4787-4796.
- 6. A. Doroodian, J. E. Dengler, A. Genest, N. Rosch and B. Rieger, *Angew Chem Int Ed.*, 2010, 49, 1871-1873.
- 7. A. E. Shilov, G. B. Shul'pin, Chemical Reviews, 1997, 97, 2879-2932.
- 8. J. Chen, H. Wu, G. Wu, Z. Xiong, R. Wang, H. Fan, W. Zhou, B. Liu, Y. Chua, X. Ju and P. Chen, *Chemistry*, 2014, **20**, 6632-6635.
- 9. H. Wu, X. Zhou, E. E. Rodriguez, W. Zhou, T. J. Udovic, T. Yildirim and J. J. Rush, *Journal of Solid State Chemistry*, 2016, **242**, 186-192.
- 10. G. L. Soloveichik, M. Andrus, Y. Gao, J. C. Zhao and S. Kniajanski, *International Journal of Hydrogen Energy*, 2009, **34**, 2144-2152.
- 11. M. Chong, A. Karkamkar, T. Autrey, S. Orimo, S. Jalisatgi and C. M. Jensen, *Chem Commun (Camb)*, 2011, 47, 1330-1332.
- 12. X. Zhou, W. Zhou, T. J. Udovic, T. Yildirim, J. J. Rush, E. E. Rodriguez and H. Wu, *International Journal of Hydrogen Energy*, 2016, **41**, 18542-18549.
- 13. G. Meisner, M. Scullin, M. Balogh, F. Pinkerton and M. Meyer, J. Phys. Chem. B, 2006, 110 4186-4192.
- 14. H. Wu, W. Zhou, T. J. Udovic, J. J. Rush and T. Yildirim, Chem. Mater., 2008, 20, 1245–1247.
- 15. H. Chu, Z. Xiong, G. Wu, J. Guo, T. He and P. Chen, Dalton Trans., 2010, 39, 10585–10587.
- 16. H. Wu, W. Zhou, K. Wang, T. J. Udovic, J. J. Rush, T. Yildirim, L. Bendersky, A. F. Gross, S.L.V. Atta, J. J. Vajo, F. E. Pinkerton and M. S. Meyer, *Nanotechnology*, 2009, **20**, 204002.
- 17. P. K. Sawinski, M. Meven, U. Englert and R. Dronskowski, *Crystal Growth & Design*, 2013, 13, 1730-1735.
- 18. S. Dong, X. Feng and X. Liu, *Chem Soc Rev*, 2018, 47, 8525-8540.
- 19. G. Nolze and W. Kraus, *PowderCell for Windows*, Version 2.4, BAM, Berlin, 2000; ICSD, Inorganic Crystal Structure Database, FIZ Karlsruhe, Germany.
- 20. ICDD PDF-4+ 2024, International Centre for Diffraction Data, Newtown Square, PA, USA; *PANalytical HighScore Plus*, Version 4.9, Malvern Panalytical.
- 21. A. C. Larson and R. B. Von Dreele, *General Structure Analysis System (GSAS)*, Los Alamos National Laboratory Report LAUR 86–748, 2004; B. H. Toby, *J. Appl. Crystallogr.*, 2001, **34**, 210–213.
- 22. D. R. Lide, CRC Handbook of Chemistry and Physics, CRC Press, Boca Raton, FL, 90th edn, 2009.
- 23. L. Costa and L. G. Camino, J. Therm. Anal., 1988, 34, 423-429.

- 24. J. Zhang, Synthesis, Crystal Structures and Physical Properties of Metal Guanidinate and Cyanoguanidine Coordination Compound, PhD thesis, RWTH Aachen University, 2022.
- 25. R. J. Schwamm, B. M. Day, N. E. Mansfield, W. Knowelden, P. B. Hitchcock and M. P. Coles, *Dalton Trans*, 2014, **43**, 14302-14314.

8. Conclusion and Future Work

In summary, this thesis investigated five composite complex hydride systems.

In the NaH-NaOH system, it was demonstrated that an intermediate NaH-like phase forms between 170 °C and 210 °C, facilitating the interaction between protonic hydrogen (H^{δ^-}) and hydridic hydrogen (H^{δ^-}) to form solid solution NaH_{1-x}(OH)_x and thereby promoting the dehydrogenation of NaOH-NaH at lower temperatures. The total activation energy of the ball-milled NaOH-NaH system was determined to be 75.85 \pm 3.41 kJ/mol. The introduction of various catalysts reduced this activation energy, with Ni exhibiting the most significant effect, lowering it to 41.24 \pm 3.25 kJ/mol. In the future, Mg₂Si with NaOH in mole ratio 1 : 1 could be explored to know the mechanism. Also, additional catalysts such as Co, Pd, and Zr could be explored to further enhance the system's performance.

For the hand-mixed NaAlH₄-NaOH system, insights gained from the NaOH-NaH system were applied to improve the kinetics of NaAlH₄ decomposition. This resulted in modifications to the third step of NaAlH₄ decomposition, which is crucial for enhancing overall reaction kinetics. In the hand-mixed NaAlH₄-NaOH system, the following reactions were observed:

 $NaAlH_4 + 4NaOH = 1/3Na_3AlH_6 + 2/3Al + H_2 + 4NaOH$

 $1/3Na_3AlH_6 + 4NaOH = NaH + 1/3Al + 1/2H_2 + 4NaOH$

 $NaH + Al + 4NaOH = Na_5AlO_4 + 5/2H_2$

During ball-milling of NaAlH₄ with NaOH (2 hours, 400 rpm), an intermediate phase of Na₃AlH_{6-x}(OH)_x is formed, as evidenced by PXD. With increased amounts of NaOH, this intermediate decomposes directly into NaH, NaOH, and Al. Subsequently, the reactions NaH + Al + 4NaOH \rightarrow Na₅AlO₄ + 2.5H₂ and NaH + NaOH \rightarrow Na₂O + H₂ occur within the temperature range of 300-400 °C. Thus, NaOH functions as a reactive additive in the NaAlH₄ system, modifying the reaction pathways of all steps and facilitating the transition from endothermic to exothermic processes. A NaOH content of 20 wt.% - 30 wt.% is required to effectively promote the dehydrogenation of NaAlH₄.

In the future, the hand-mixed NaAlH₄-NaOH system could be enhanced by introducing catalysts, such as those used in the NaH-NaOH system, to improve reaction kinetics. A comparative study of activation energies could help identify the most effective catalyst for this system. Additionally, advanced techniques such as Synchrotron X-ray Diffraction could be employed to analyse intermediate structures in the ball-milled NaAlH₄-NaOH system. Further research could also explore whether hydrogenation of Na₅AlO₄ is reversible or if the conditions required for reversibility are too stringent.

For the NaBH₄-NaOH system, the reaction temperature is typically above 500 °C. However, after two hours of ball milling, the NaBH₄-NaOH system can release hydrogen at approximately 300 °C. The ball-milled NaBH₄-NaOH forms an intermediate that undergoes the following reactions:

NaBH₄ + 3NaOH
$$\rightarrow$$
 "(Na-B-O-H) intermediate(s)" ball-milling
"(Na-B-O-H) intermediate(s)" \rightarrow Na₃BO₃ + NaH + 3H₂ T = 300 - 400 °C
Na₃BO₃ + NaH + 3H₂ \rightarrow Na₃BO₃ + Na + 3.5H₂ T = 325 - 400 °C
(NaH \rightarrow Na + H₂ T \geq 325 °C)

In future studies, infrared spectroscopy could be utilized to analyse the characteristic peaks of NaBH₄ and investigate its intermediates. Additionally, due to Na leakage from the Al₂O₃ crucible at high temperatures, alternative crucible materials, such as Pd crucibles, should be considered. Lowering the heating rate could help prevent Na leakage and allow for a more accurate determination of hydrogen mass loss, which is critical for understanding the system's structural changes. Advanced techniques such as X-ray Photoelectron Spectroscopy (XPS) could further elucidate the composition of reaction products. The introduction of appropriate catalysts could also lower the peak temperature and activation energy.

For the Ca₄Mg₃H₁₄ system, the addition of NaH results in the formation of reactive hydride composites, reducing the decomposition temperatures of both components. Ball milling of Ca₄Mg₃H₁₄ and NaH leads to the formation of NaMgH₃, which decomposes at approximately 300 °C, yielding CaH₂, Na, and Mg as final products. In future research, additional additives such as NaOH and LiH could be introduced to further decrease the decomposition temperature.

For the CH₅N₃-NaAlH₄/MgH₂ system, the independent decomposition of CH₅N₃ follows the reaction:

$$3CH_5N_3 \rightarrow C_3H_6N_6 + 3NH_3$$
 T = 179 °C

Subsequently, C₃H₆N₆ primarily evaporates around 300 °C, with a minor portion undergoing decomposition. In the NaAlH₄-CH₅N₃ system, a reaction at 150 °C releases hydrogen gas and forms Al and an unidentified Na-C-N product. For the MgH₂-CH₅N₃, according to MS, TG and DTA, the following reaction can be inferred. However, the reaction path cannot be confirmed by PXD.

$$MgH_2 + 2CH_5N_3 \rightarrow Mg(CN_3H_4)_2 + 2H_2 \quad T = 140 \text{ °C}$$

 $Mg(CN_3H_4)_2 \rightarrow Mg(CN_3H_3)_2 + H_2 \quad T = 140 - 220 \text{ °C}$

$$Mg(CN_3H_3)_2 \rightarrow Mg(CN_2)_2 + 2NH_3$$
 T > 220 °C

Future work should include PXD analysis at multiple temperatures, such as 200 °C, 180 °C, and 140 °C, as well as investigations of the reactions between MgH₂ and CH₅N₃ at various molar ratios, including the 1:2 MgH₂:CH₅N₃ system. Both mass loss and PXD analyses should be employed to identify potential products. Future research on this system could involve combining CH₅N₃ with additional materials, such as CaH₂ and NaMgH₃, to explore new reaction pathways and improve hydrogen storage performance.

9. Appendices

3. NaH-NaOH dehydrogenation system

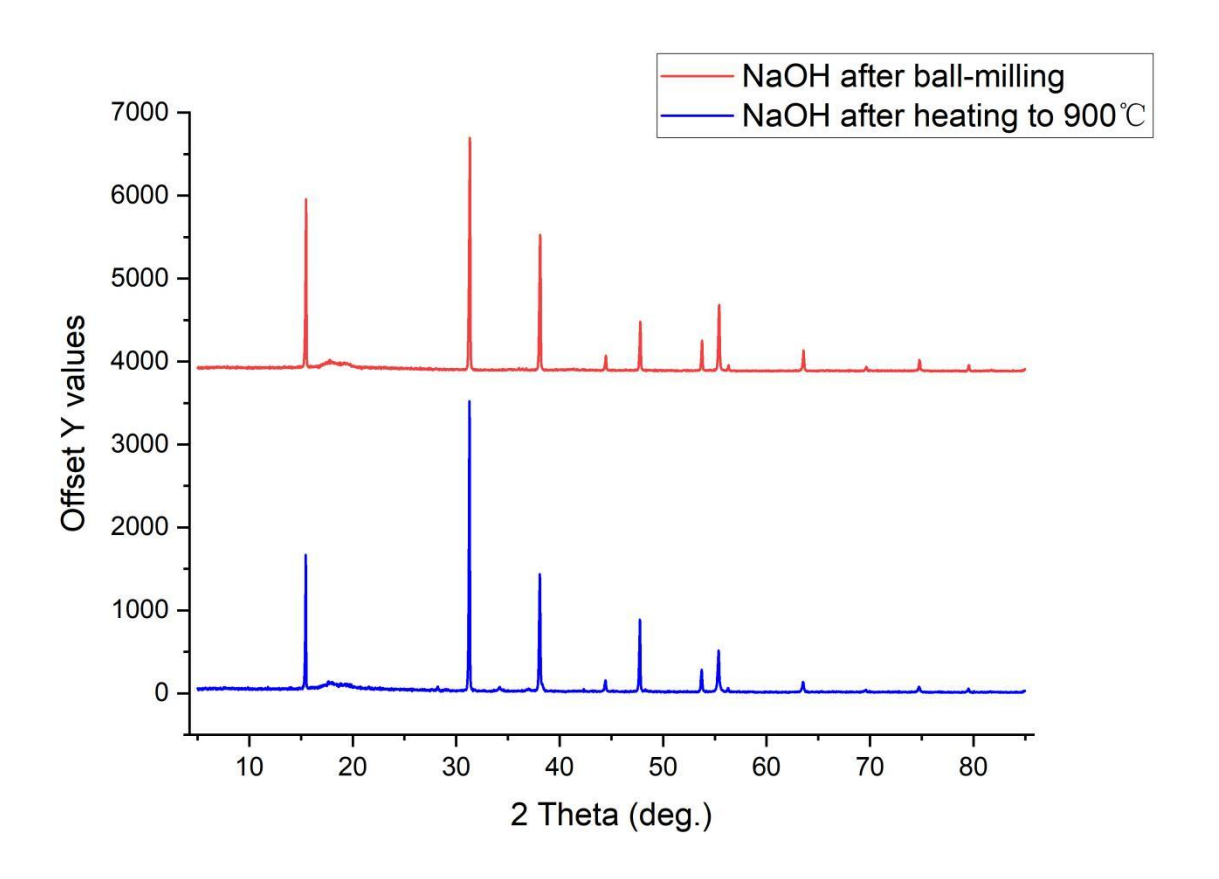


Figure A3-1: PXD patterns of NaOH after ball-milling and heating to 900 °C.

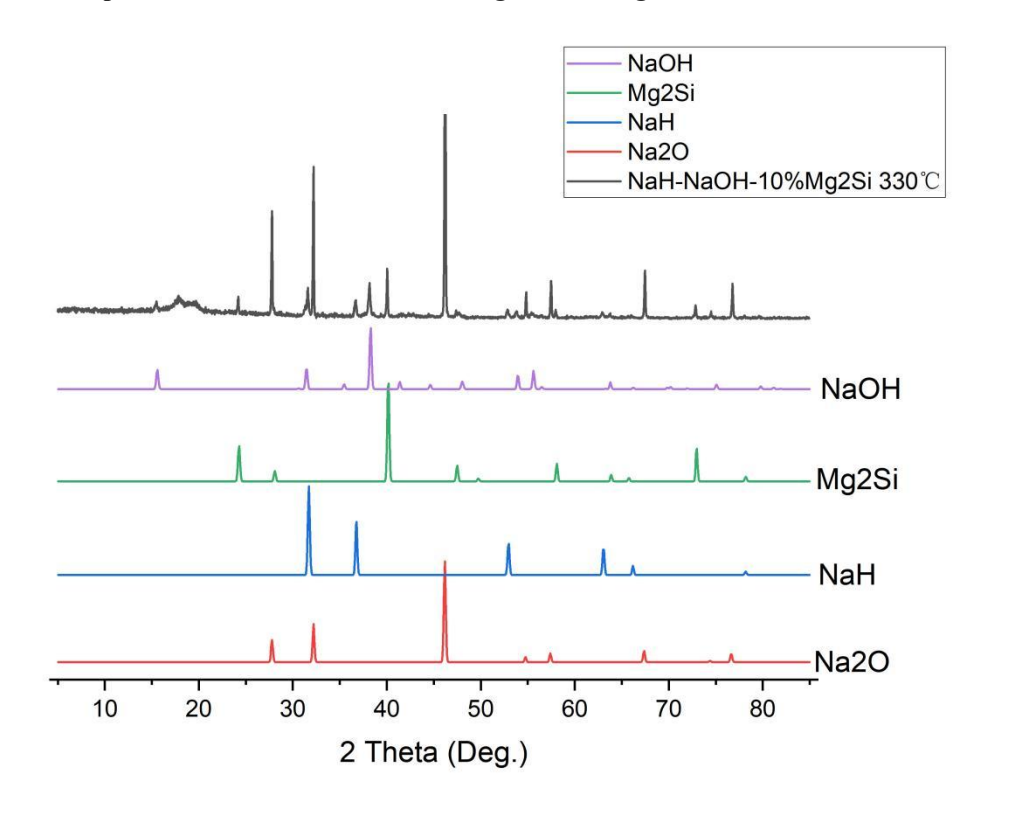


Figure A3-2: PXD patterns for ball-milled 1:1.15 NaOH:NaH with 10 wt.% Mg₂Si after heating to 330 °C under flowing Ar(g)

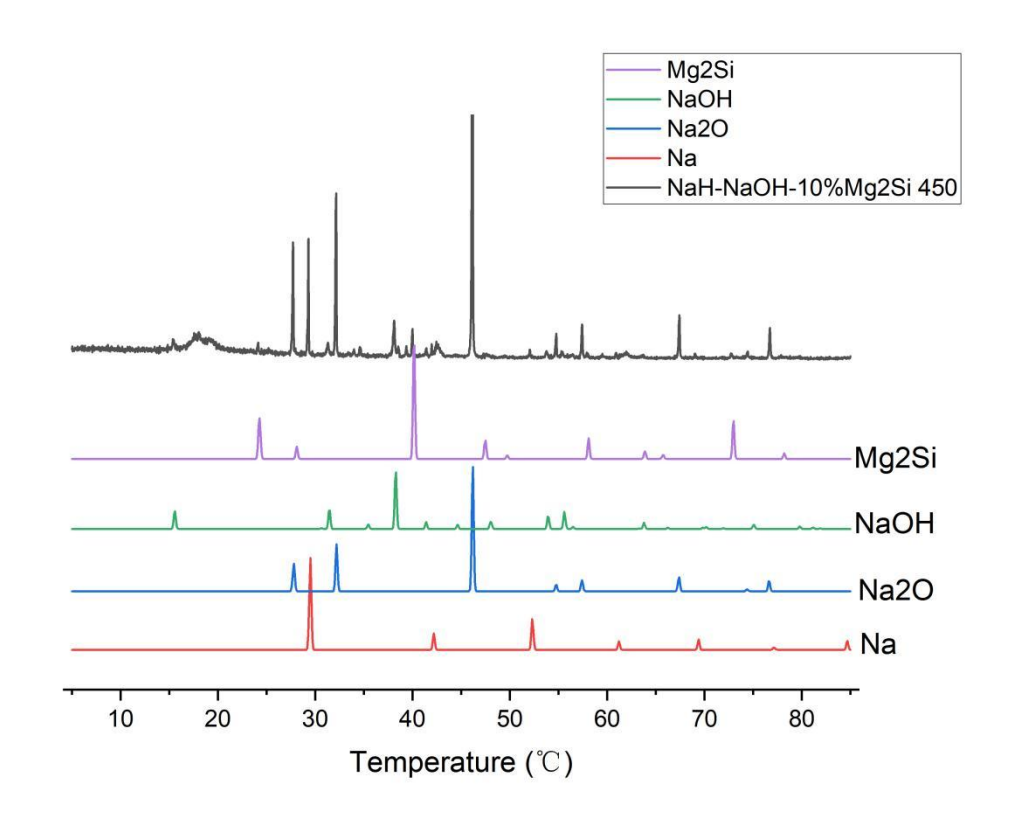


Figure A3-3: PXD patterns for ball-milled 1:1.15 NaOH:NaH with 10 wt.% Mg_2Si after heating to 450 °C under flowing Ar(g).

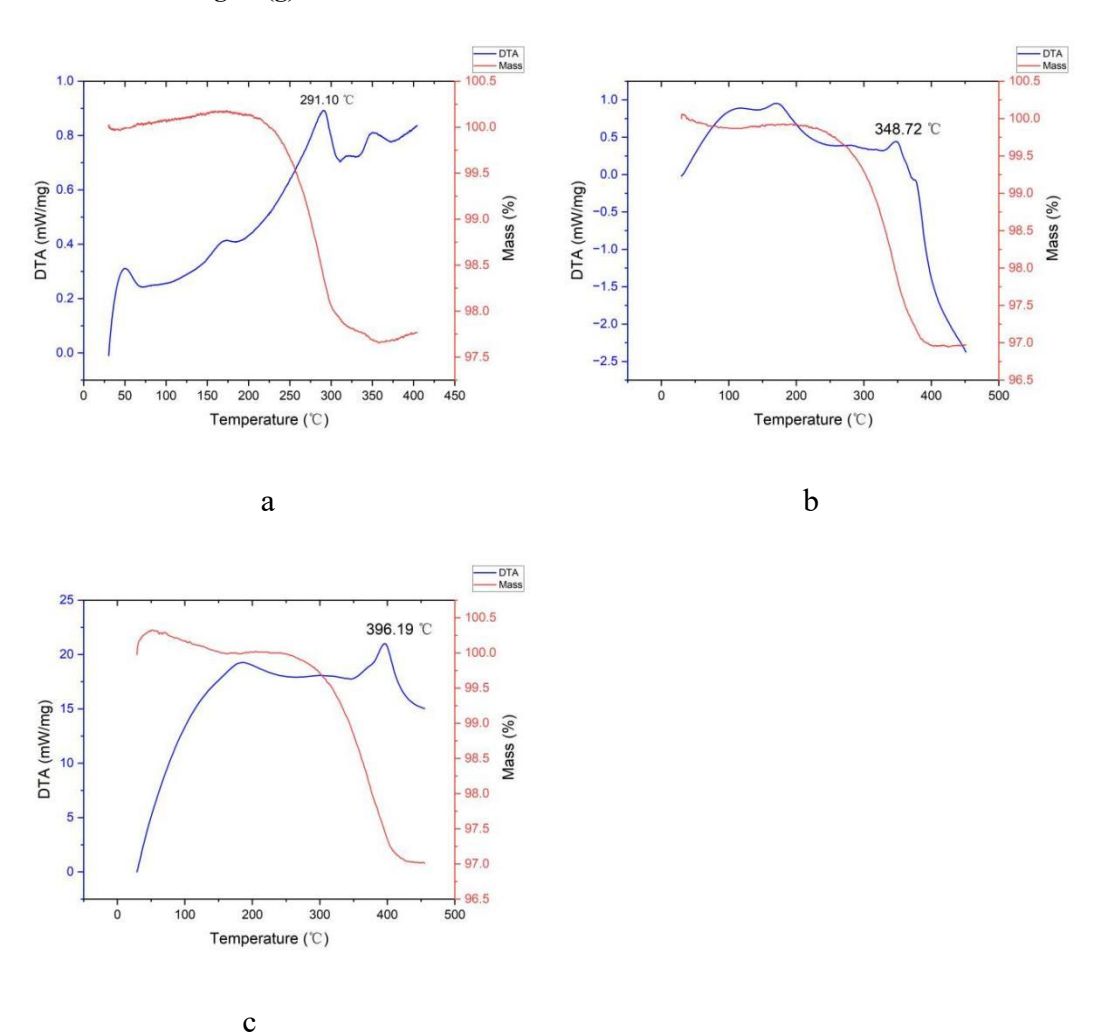


Figure A3-4: TG(red) and DTA(blue) profiles for ball-milled 1:1.15 NaOH:NaH (2h, 400rpm) with 5 wt.% Mg₂Si on heating from 35-400 °C at different heating rate (a) 2 °C min⁻¹(b) 10 °C min⁻¹(c) 20 °C min⁻¹ under flowing Ar(g).

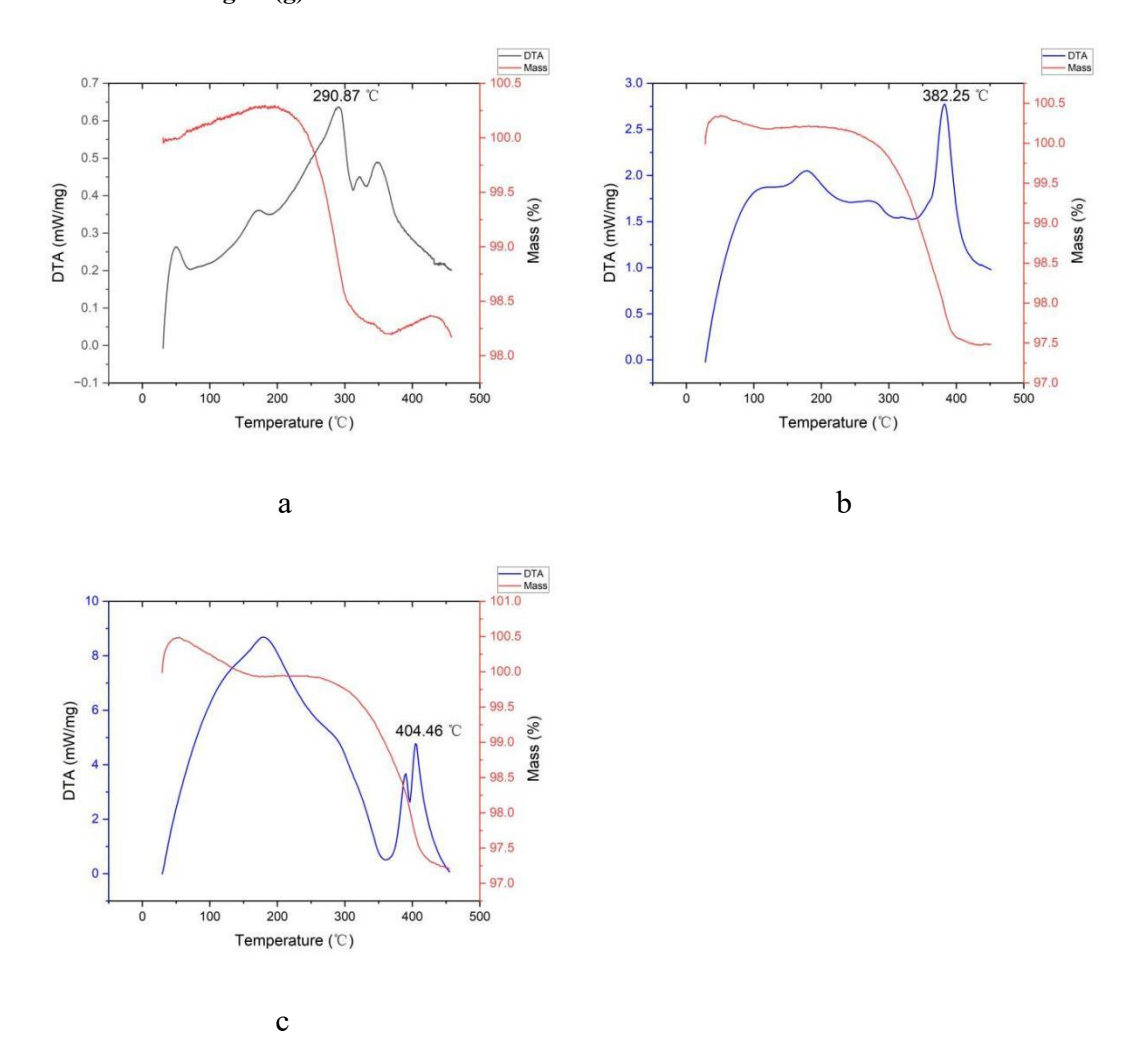
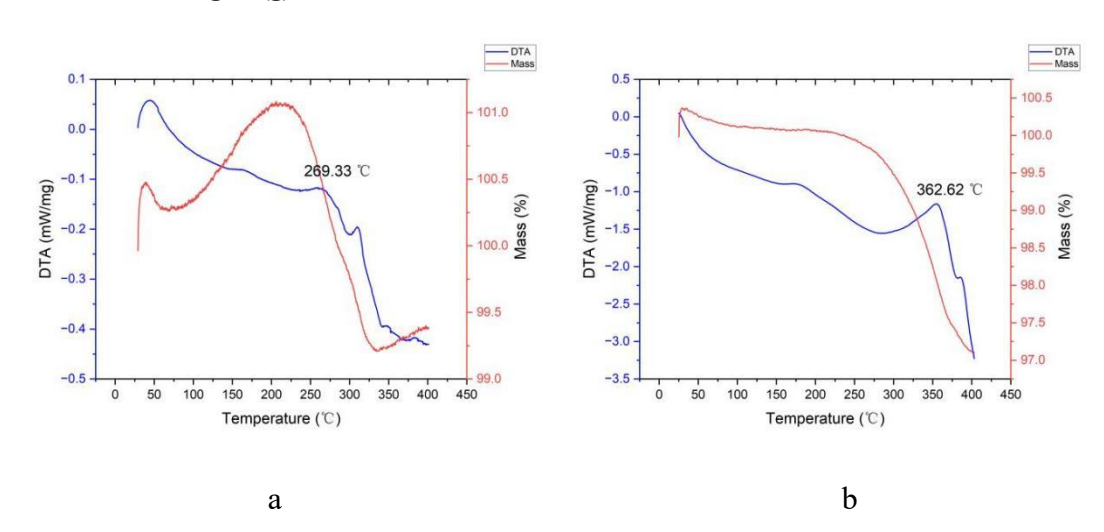


Figure A3-5: TG(red) and DTA(blue) profiles for ball-milled 1:1.15 NaOH:NaH (2h, 400rpm) with 10 wt.% Mg2Si on heating from 35-400 °C at different heating rate (a) 2 °C min⁻¹(b) 10 °C min⁻¹(c) 20 °C min⁻¹ under flowing Ar(g).



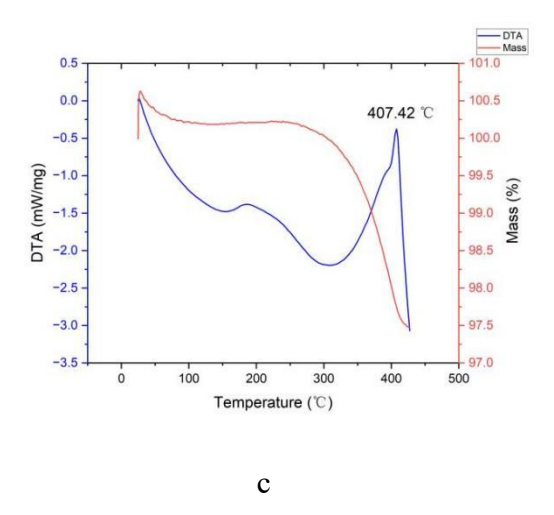


Figure A3-6: TG(red) and DTA(blue) profiles for ball-milled 1:1.15 NaOH:NaH (2h, 400rpm) with 5 wt.% Ni on heating from 35-400 °C at different heating rate (a) 2 °C min⁻¹(b) 10 °C min⁻¹(c) 20 °C min⁻¹ under flowing Ar(g).

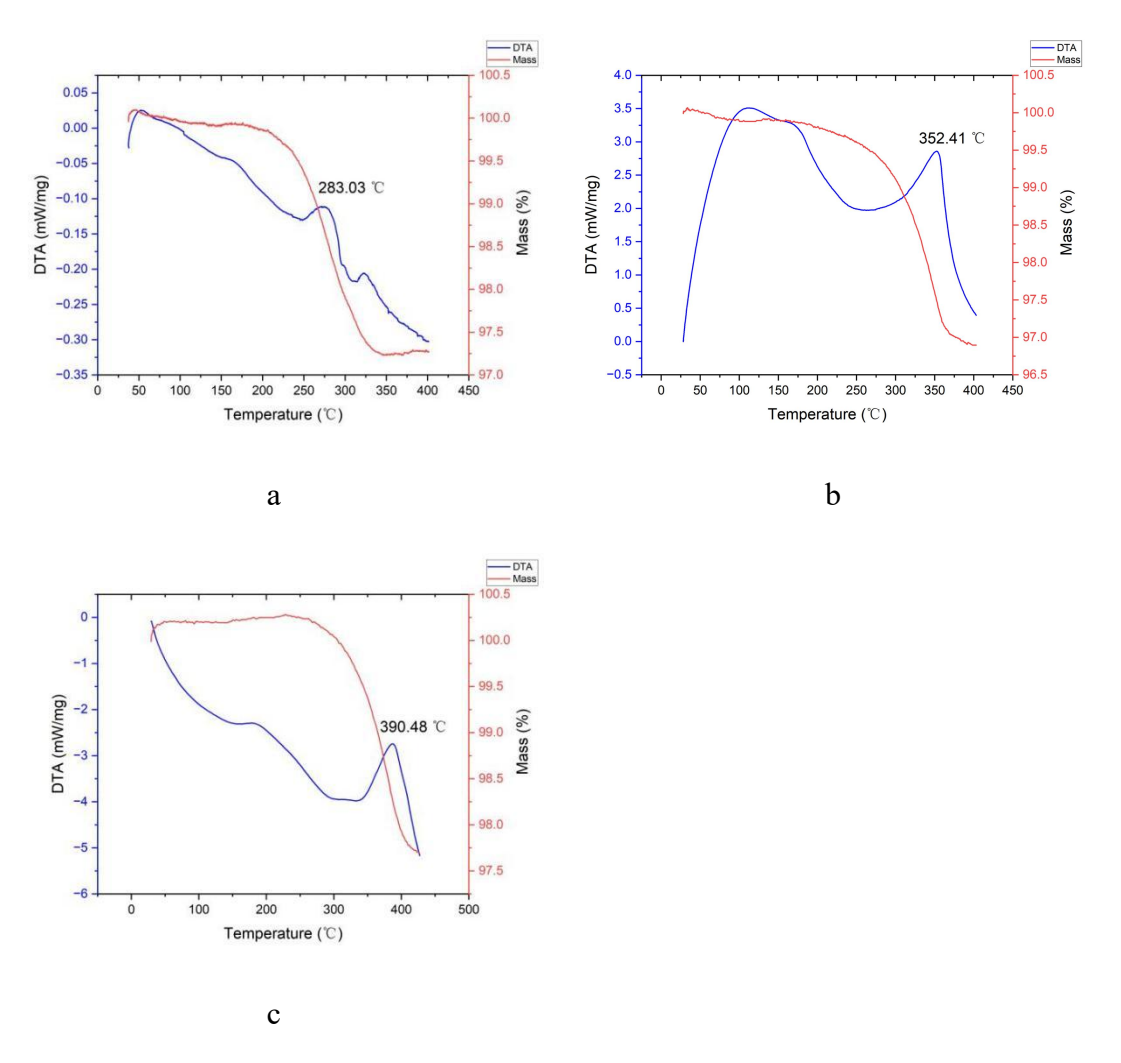


Figure A3-7: TG(red) and DTA(blue) profiles for ball-milled 1:1.15 NaOH:NaH (2h, 400rpm) with 5 wt.% Ti on heating from 35-400 °C at different heating rate (a) 2 °C min⁻¹(b) 10 °C min⁻¹(c) 20 °C min⁻¹ under flowing Ar(g).

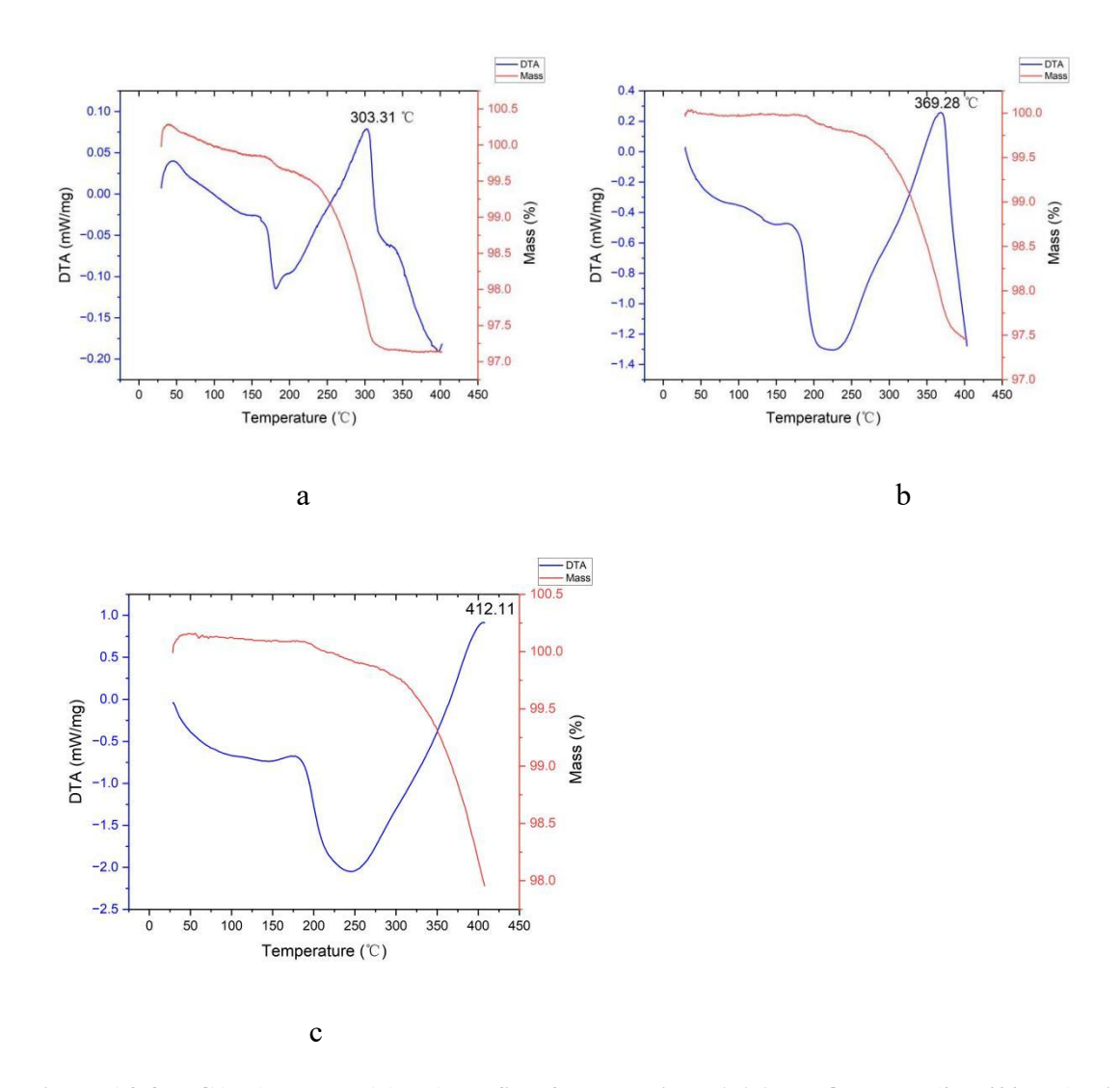
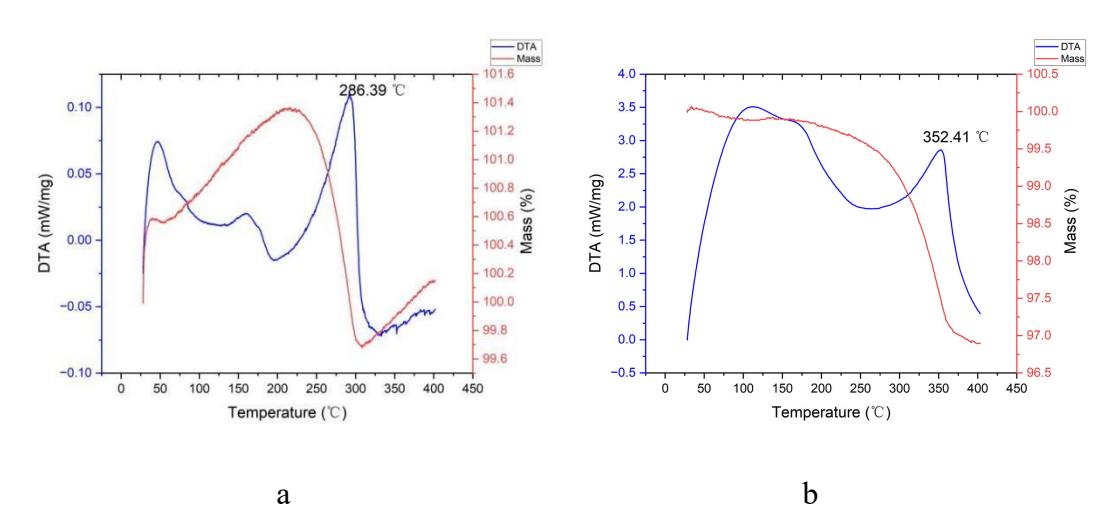


Figure A3-8: TG(red) and DTA(blue) profiles for ball-milled 1:1.15 NaOH:NaH (2h, 400rpm) with 5 wt.% TiF₃ on heating from 35-400 °C at different heating rate (a) 2 °C min⁻¹(b) 10 °C min⁻¹(c) 20 °C min⁻¹ under flowing Ar(g).



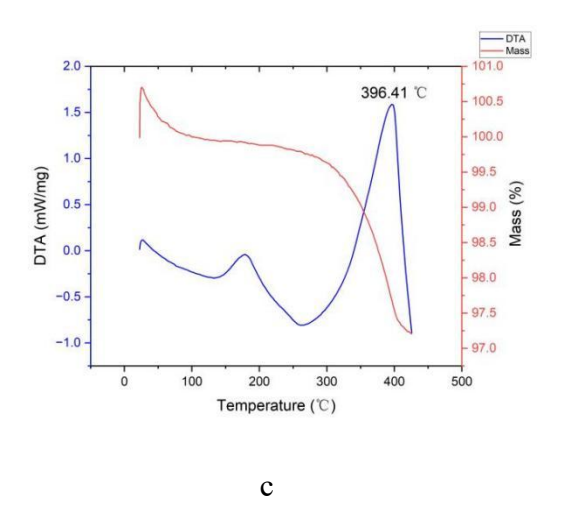


Figure A3-9: TG(red) and DTA(blue) profiles for ball-milled 1:1.15 NaOH:NaH (2h, 400rpm) with 5 wt.% MoS₂ on heating from 35-400 °C at different heating rate (a) 2 °C min⁻¹(b) 10 °C min⁻¹(c) 20 °C min⁻¹ under flowing Ar(g).

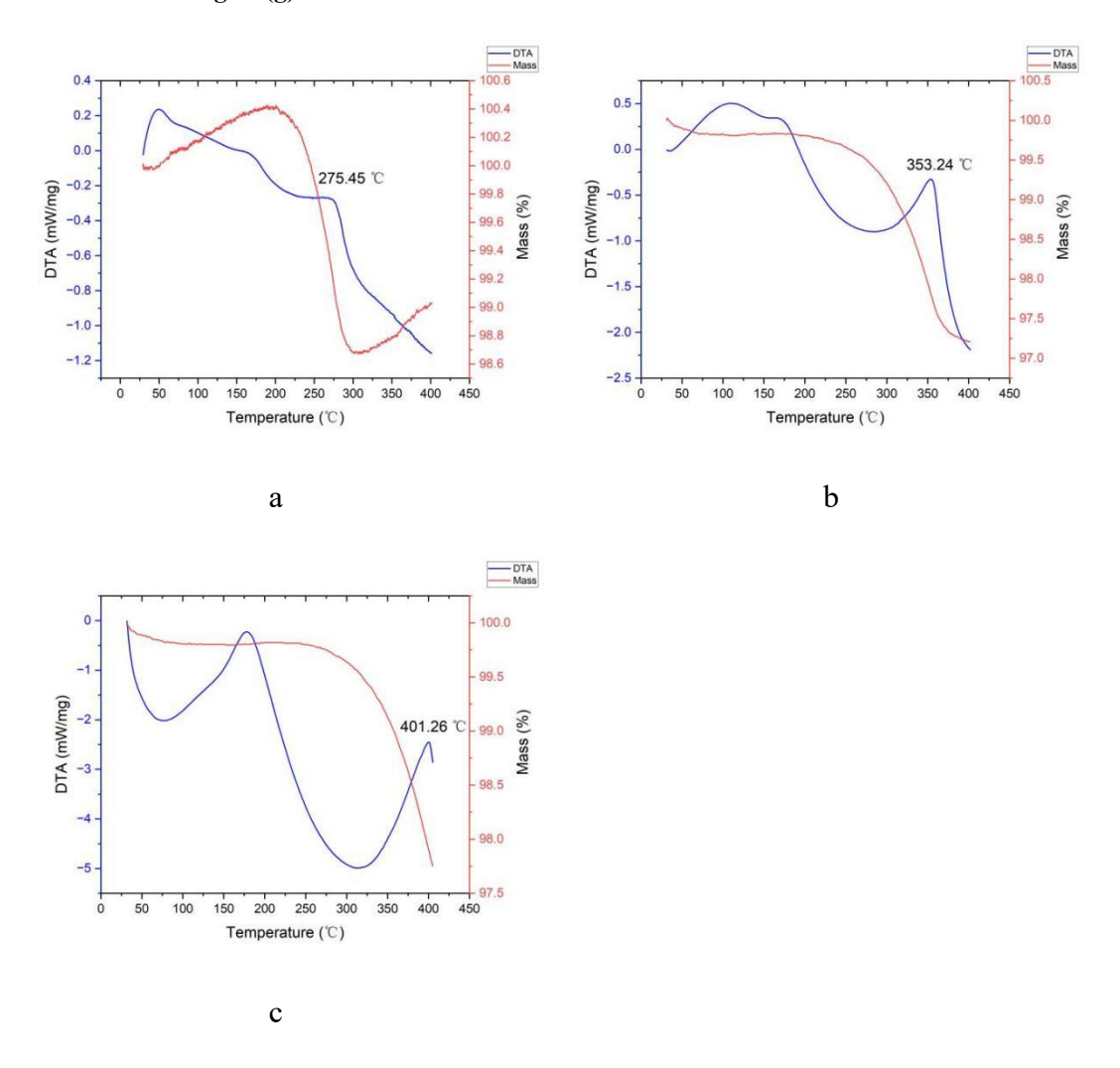


Figure A3-10: TG(red) and DTA(blue) profiles for ball-milled 1:1.15 NaOH:NaH (2h, 400rpm) with 5 wt.% SiC on heating from 35-400 °C at different heating rate (a) 2 °C min⁻¹(b) 10 °C min⁻¹(c) 20 °C min⁻¹ under flowing Ar(g).

4. NaAlH₄-NaOH Dehydrogenation reaction

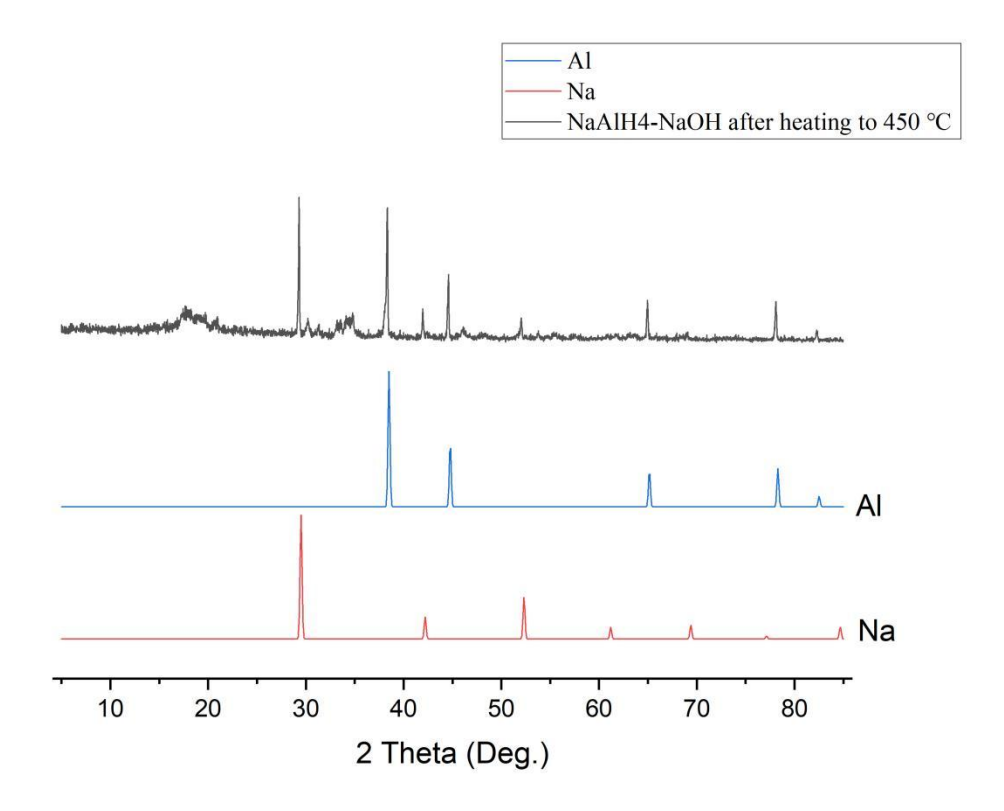


Figure A4-1: PXD pattern of hand mixed 1:1 NaAlH₄:NaOH after heating to 450 °C under flowing Ar(g).

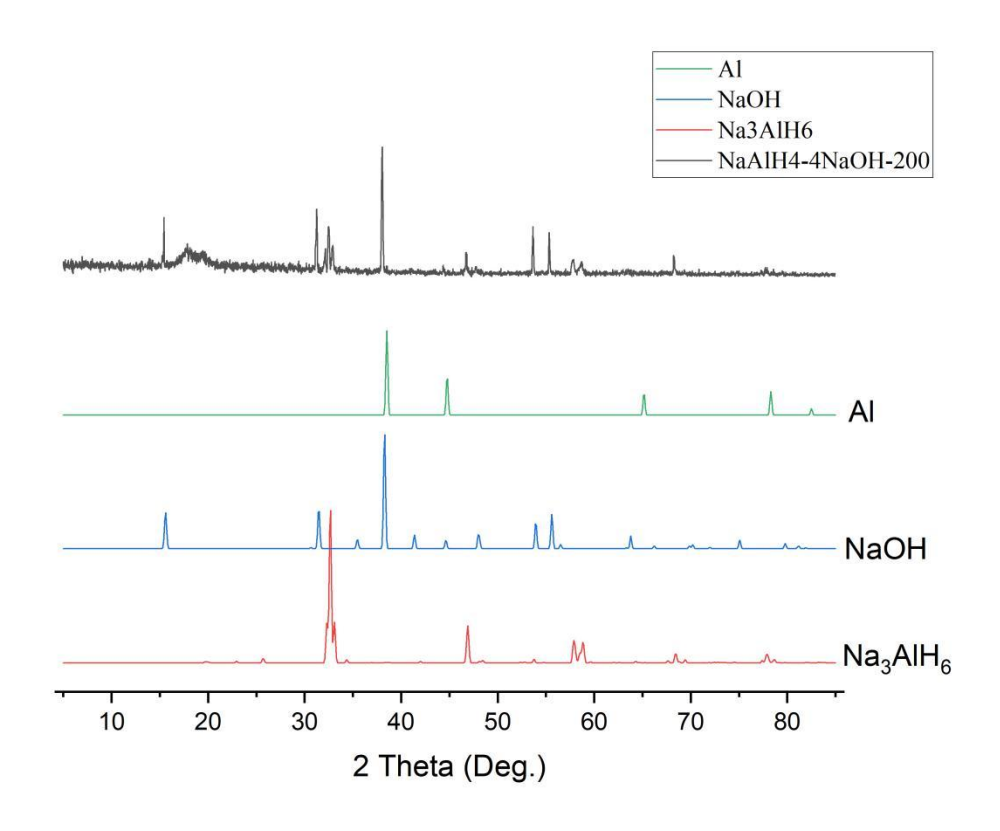


Figure A4-2: PXD pattern of hand mixed 1:4 NaAlH₄:NaOH after heating to 200 °C under flowing Ar(g).

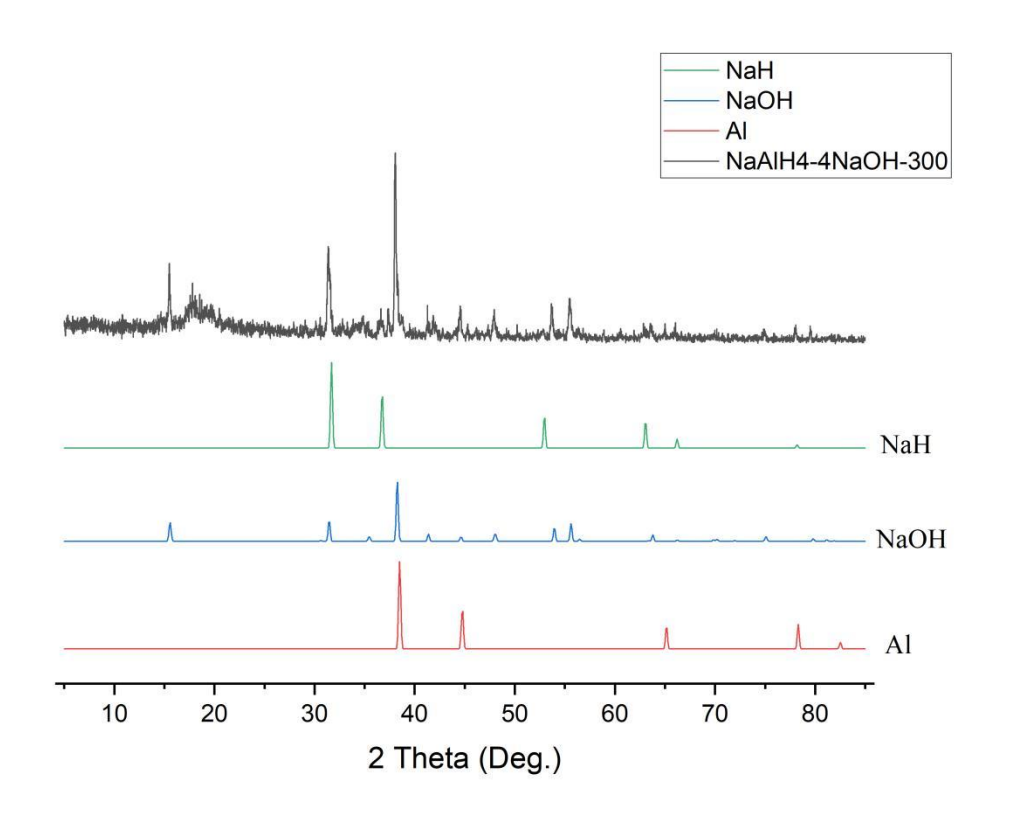


Figure A4-3: PXD pattern of hand mixed 1:4 NaAlH₄:NaOH after heating to 300 °C under flowing Ar(g).

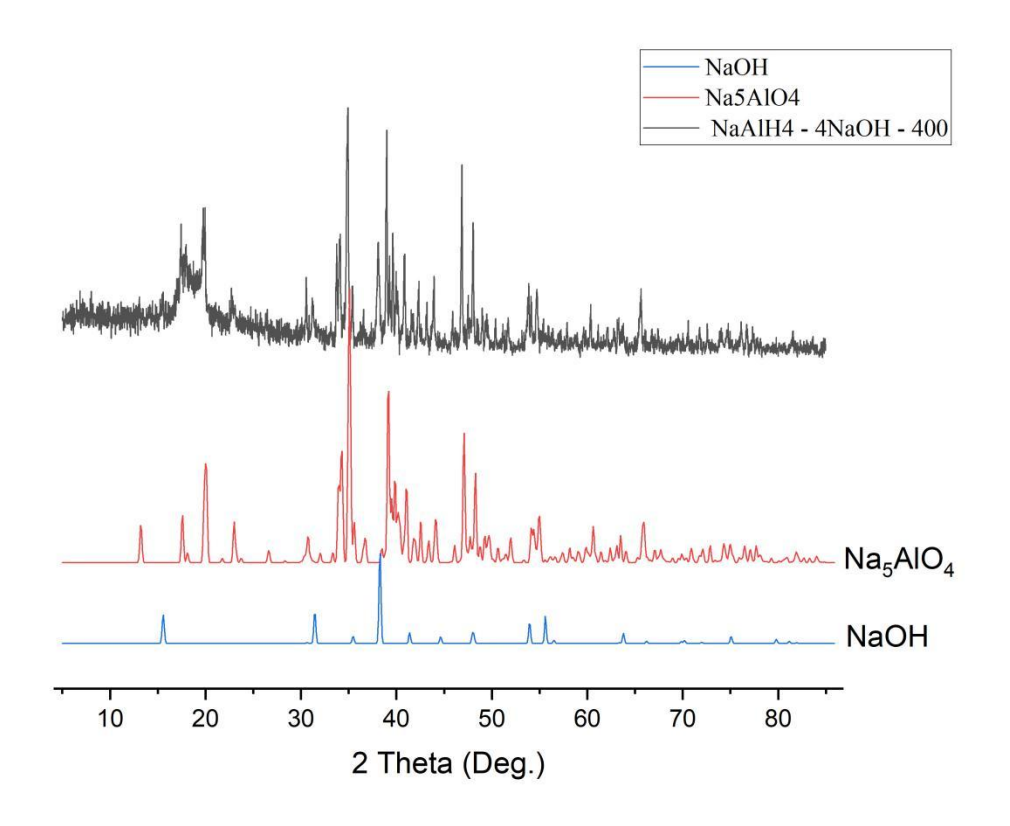


Figure A4-4: PXD pattern of hand mixed 1:4 NaAlH₄:NaOH after heating to 400 $^{\circ}$ C under flowing Ar(g).

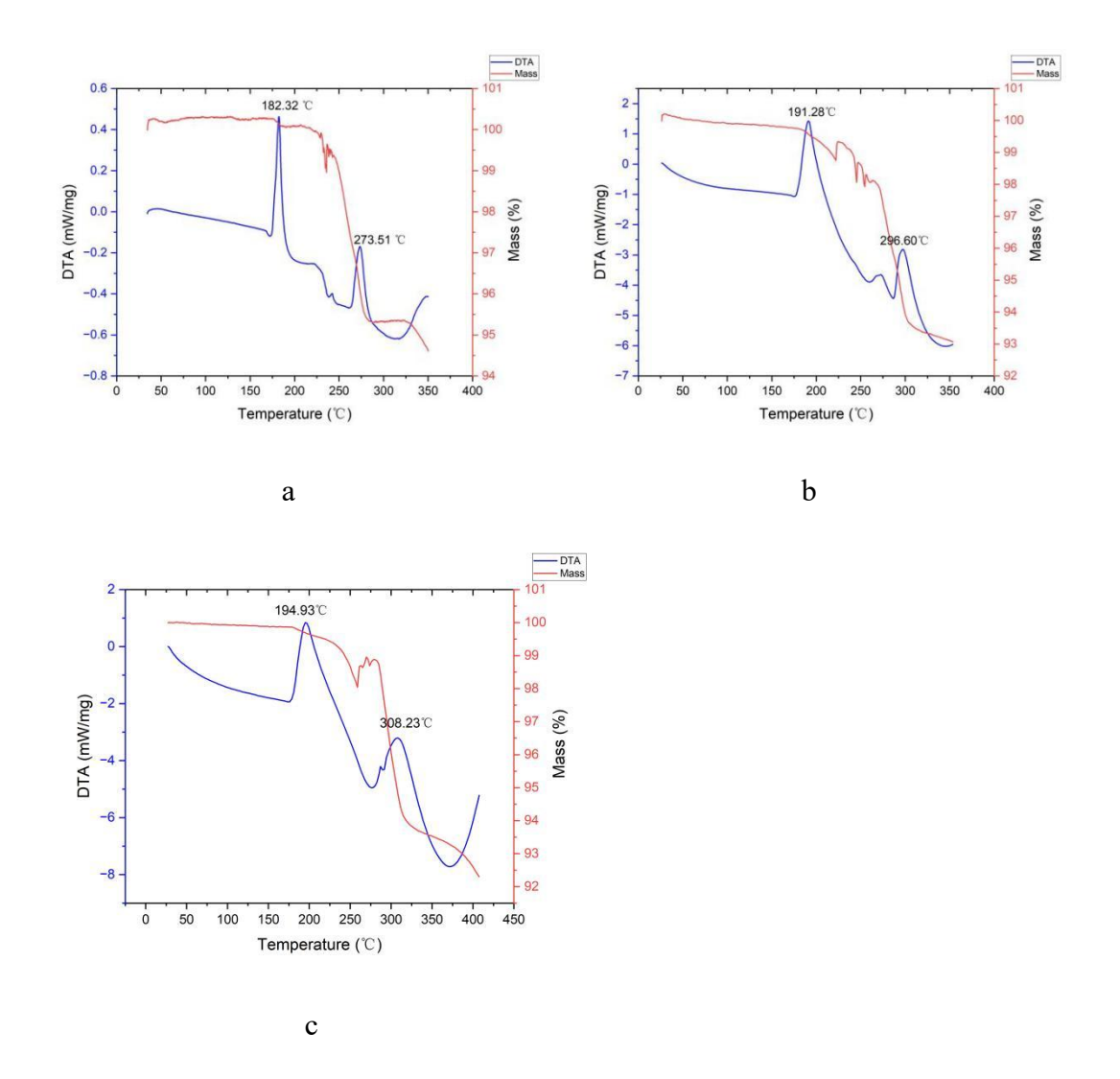
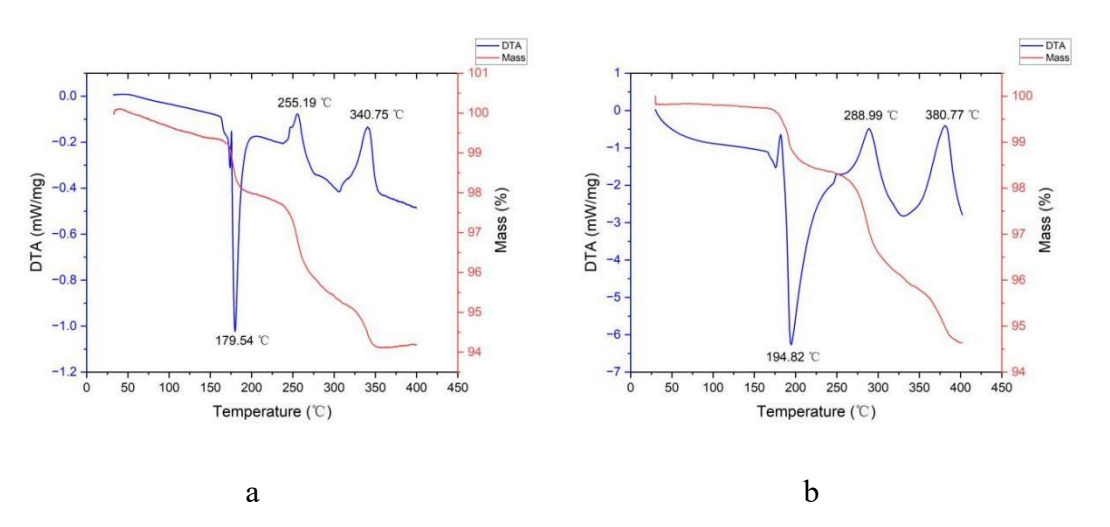


Figure A4-5: TG(red) and DTA(blue) profiles for NaAlH₄ on heating from 35-400 $^{\circ}$ C at different heating rate (a) 2 $^{\circ}$ C min⁻¹(b) 10 $^{\circ}$ C min⁻¹(c) 20 $^{\circ}$ C min⁻¹ under flowing Ar(g).



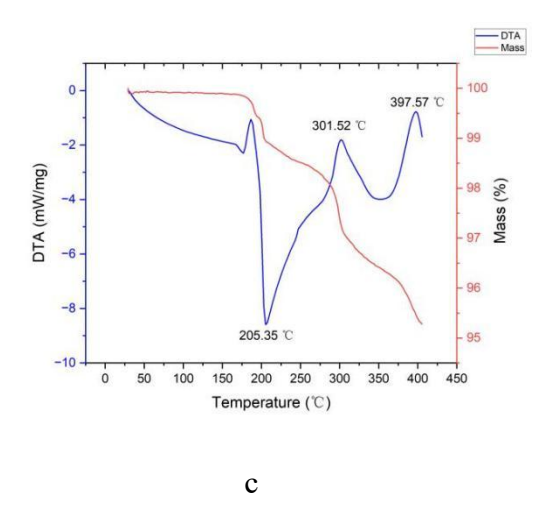


Figure A4-6: TG(red) and DTA(blue) profiles for hand-mixed 1:1 NaAlH₄:NaOH on heating from 35-400 °C at different heating rate (a) 2 °C min⁻¹(b) 10 °C min⁻¹(c) 20 °C min⁻¹ under flowing Ar(g).

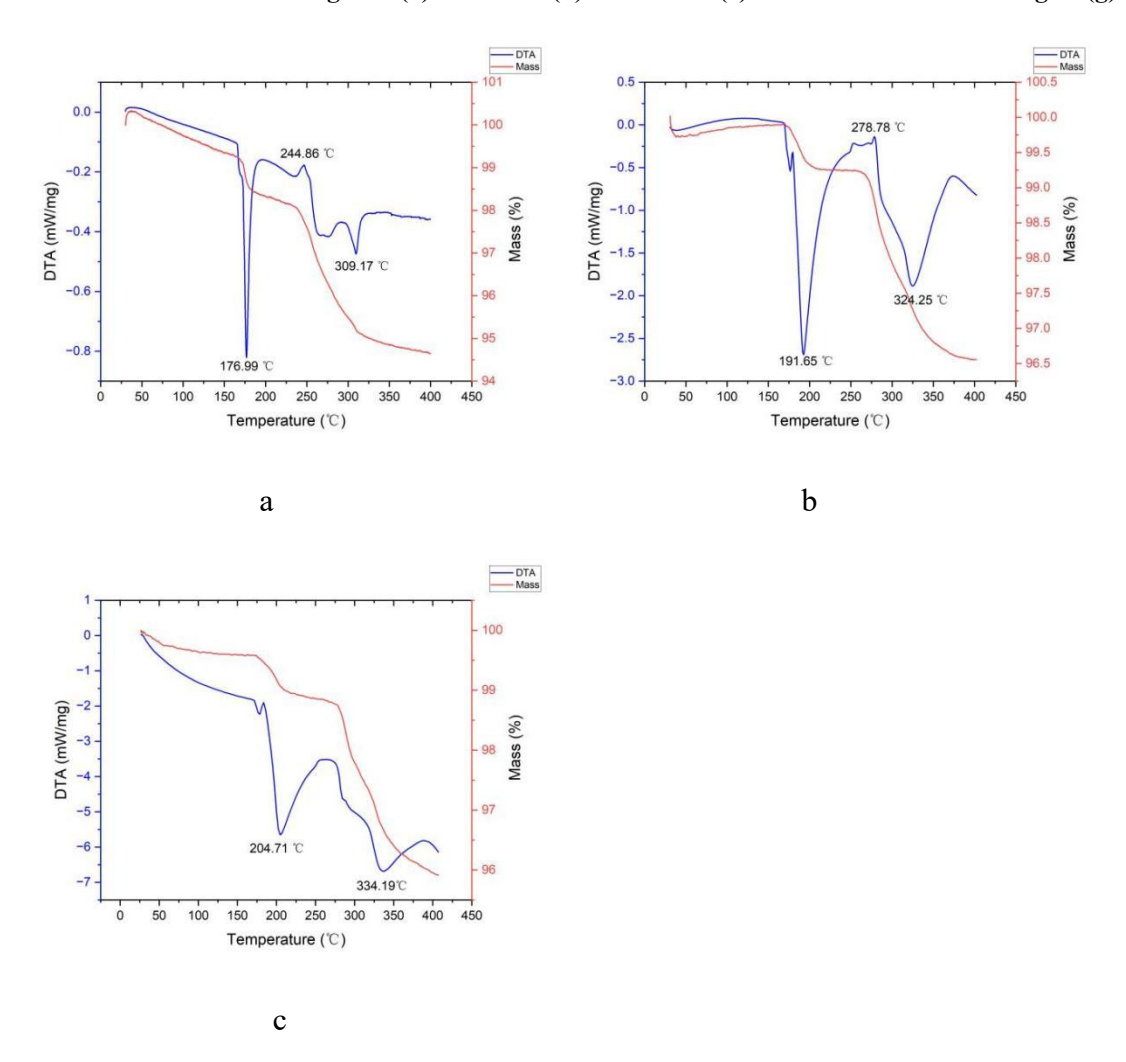


Figure A4-7: TG(red) and DTA(blue) profiles for hand-mixed 1:4 NaAlH₄:NaOH on heating from 35-400 °C at different heating rate (a) 2 °C min⁻¹(b) 10 °C min⁻¹(c) 20 °C min⁻¹ under flowing Ar(g).

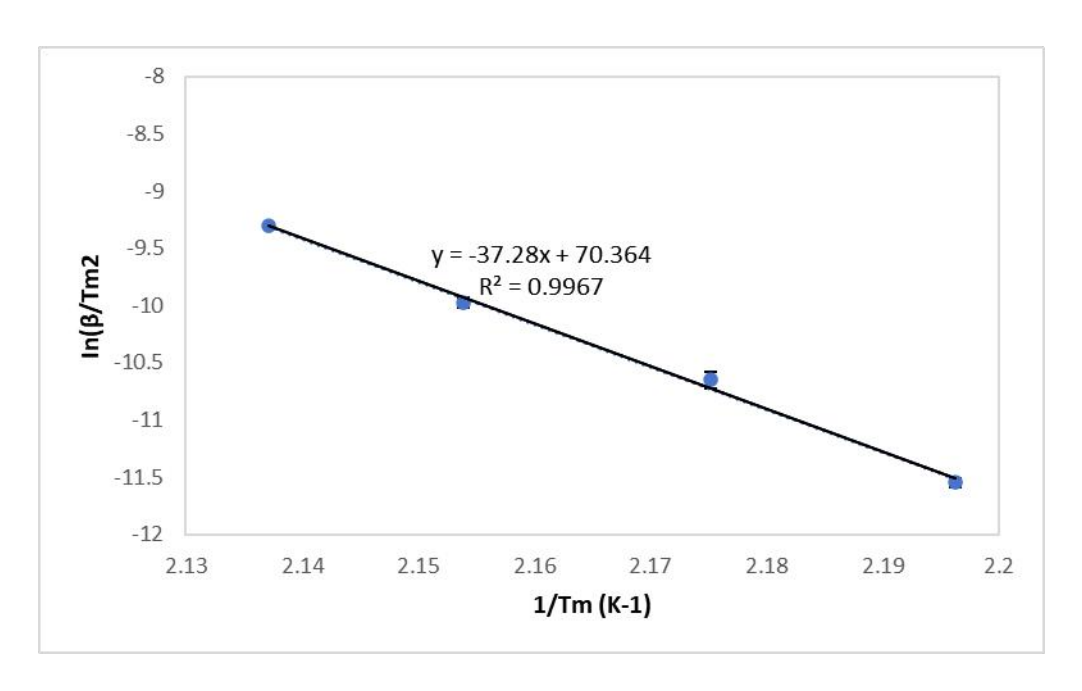


Figure A4-8: Kissinger plots for the first dehydrogenation reaction of NaAlH₄ on heating from 35-400 °C at heating rate 2, 5, 10 and 20 °C min⁻¹ under flowing Ar(g). $E_a = 309.95 \pm 12.61 \text{ kJ mol}^{-1}$

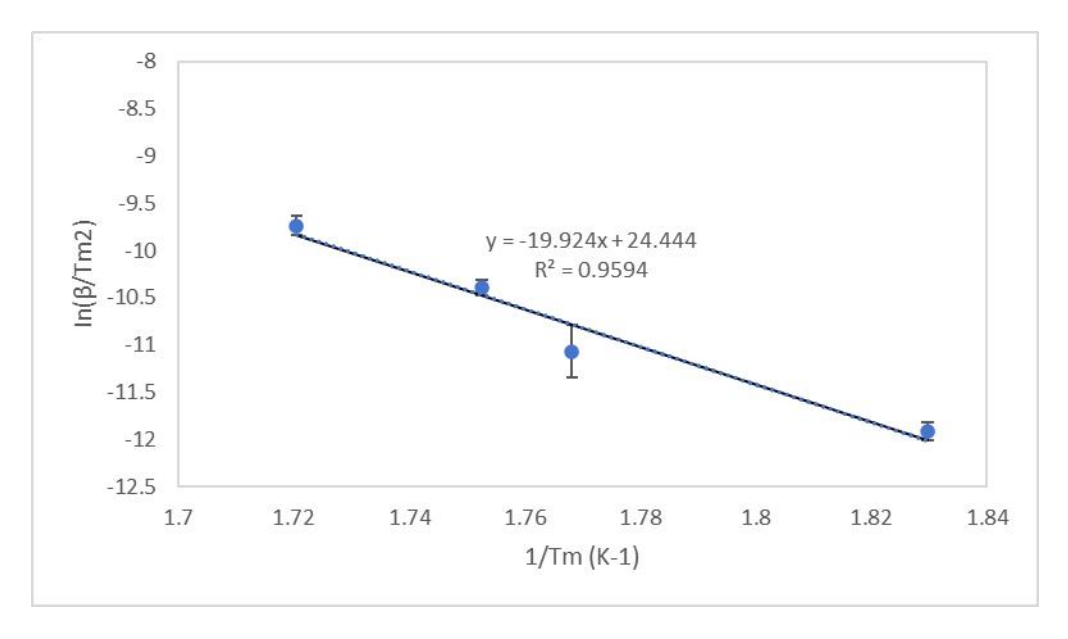


Figure A4-9: Kissinger plots for the second dehydrogenation reaction of NaAlH₄ on heating from 35-400 °C at heating rate 2, 5, 10 and 20 °C min⁻¹ under flowing Ar(g). $E_a = 165.65 \pm 24.03 \text{ kJ mol}^{-1}$

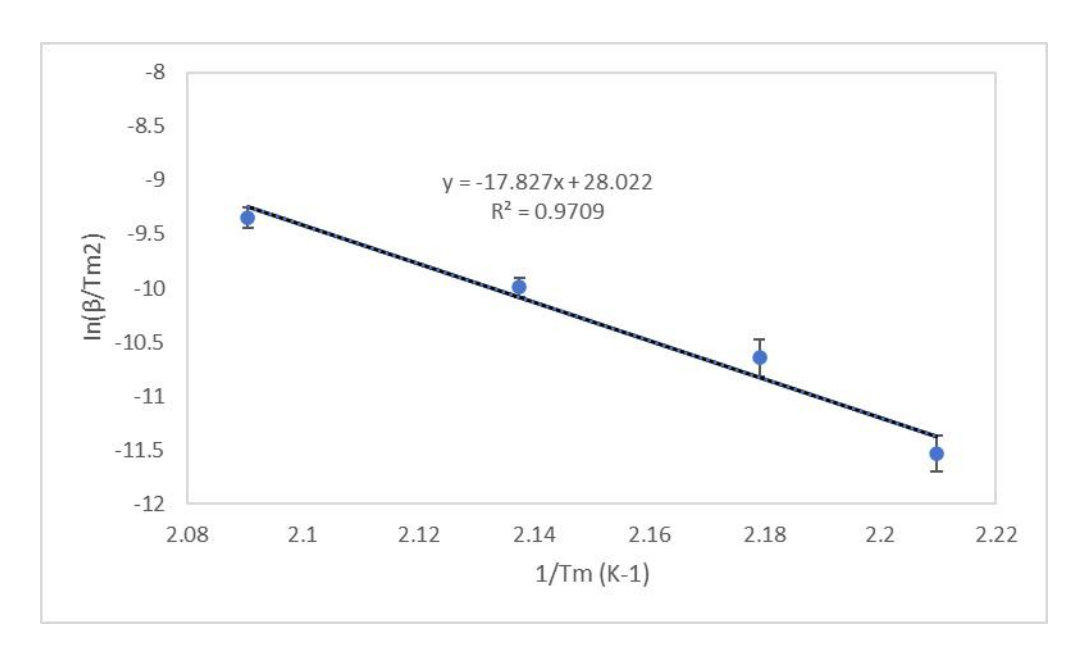


Figure A4-10: Kissinger plots for the first dehydrogenation reaction of hand-mixed 1:1 NaAlH₄:NaOH on heating from 35-400 °C at heating rate 2, 5, 10 and 20 °C min⁻¹ under flowing Ar(g). E_a =148.21 \pm 18.14 kJ mol⁻¹

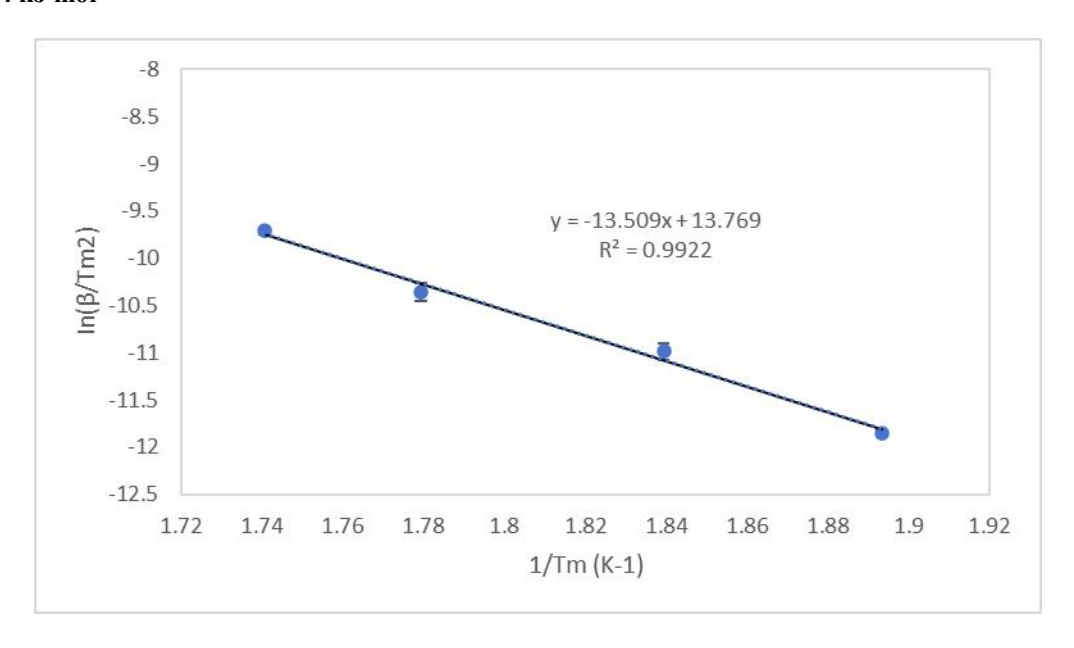


Figure A4-11: Kissinger plots for the second dehydrogenation reaction of hand-mixed 1:1 NaAlH₄:NaOH on heating from 35-400 $^{\circ}$ C at heating rate 2, 5, 10 and 20 $^{\circ}$ C min⁻¹ under flowing Ar(g). E_a =112.31 ± 7.05 kJ mol⁻¹

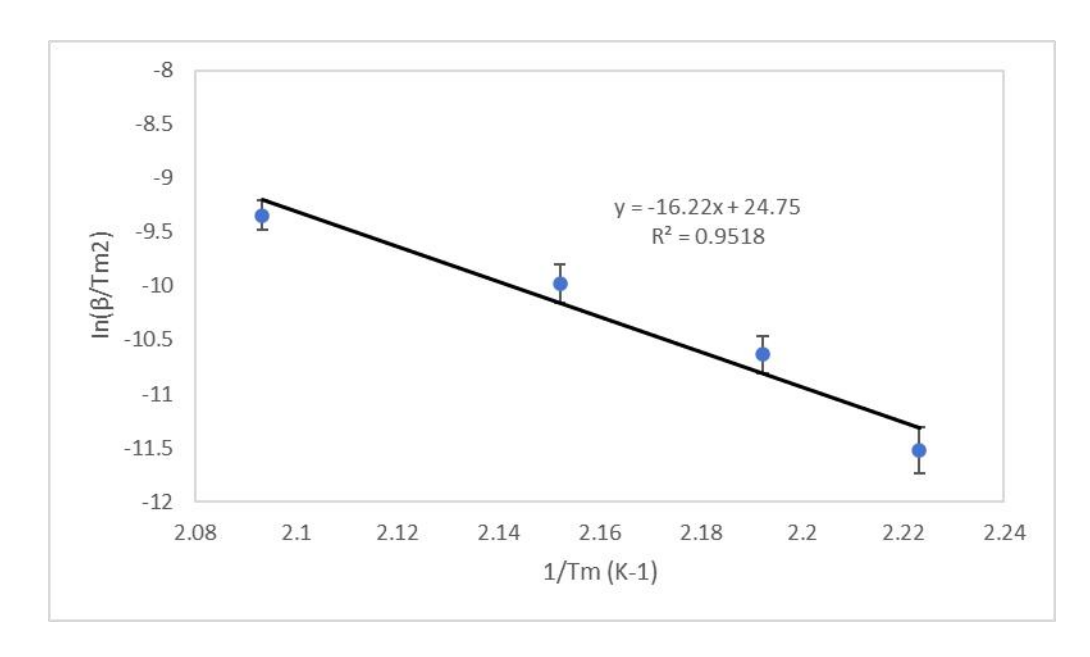


Figure A4-12: Kissinger plots for the first dehydrogenation reaction of hand-mixed 1:4 NaAlH₄:NaOH on heating from 35-400 °C at heating rate 2, 5, 10 and 20 °C min⁻¹ under flowing Ar(g). E_a =134.85 \pm 21.46 kJ mol⁻¹

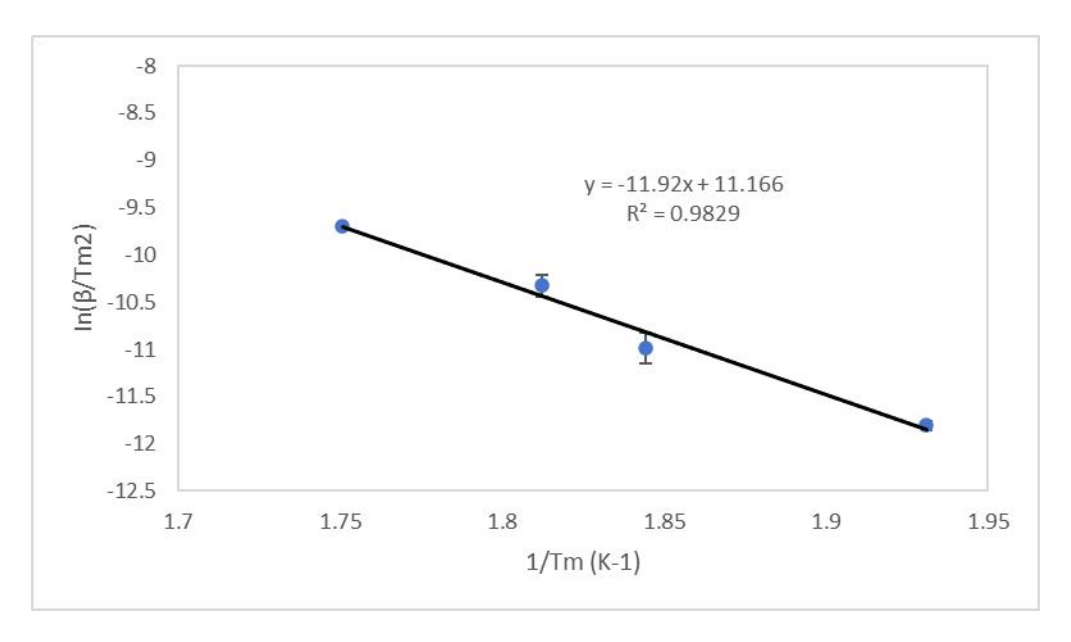
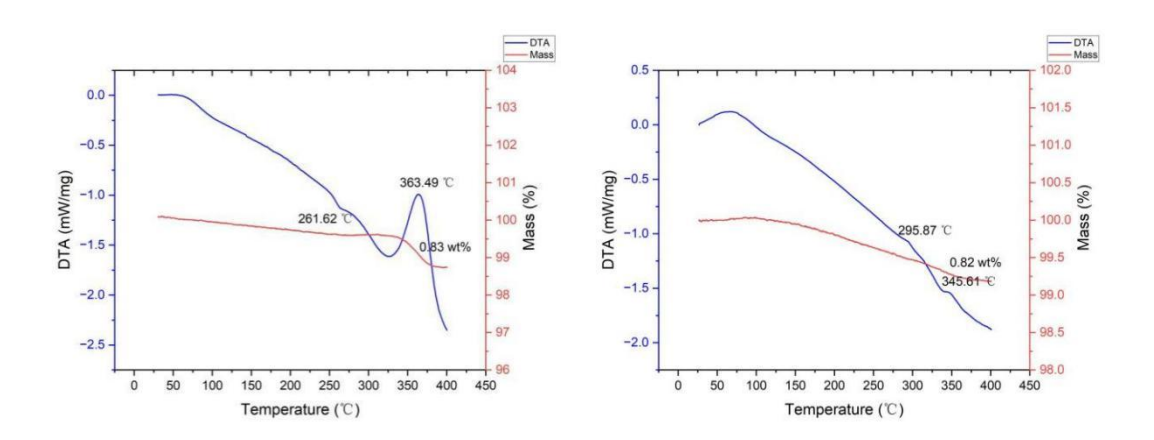


Figure A4-13: Kissinger plots for the second dehydrogenation reaction of hand-mixed 1:4 NaAlH₄:NaOH on heating from 35-400 $^{\circ}$ C at heating rate 2, 5, 10 and 20 $^{\circ}$ C min⁻¹ under flowing Ar(g). E_a =84.195 ± 9.23 kJ mol⁻¹



a b

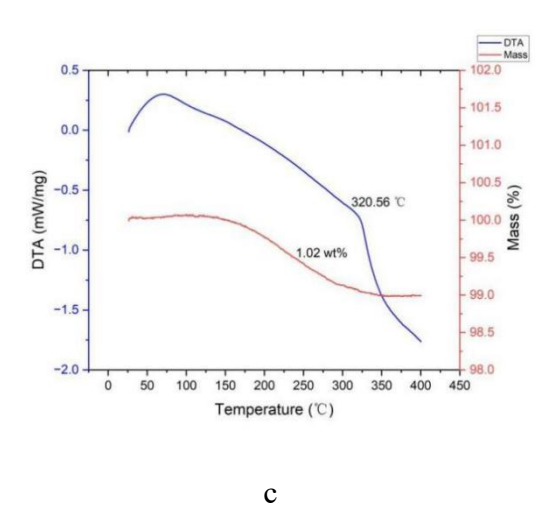


Figure A4-14: TG(red) and DTA(blue) profiles for ball-milled 1:x NaAlH₄:NaOH (a)x=2 (b)x=3 (c)x=4 on heating from 35-400 °C at 5 °C min⁻¹ under flowing Ar(g).

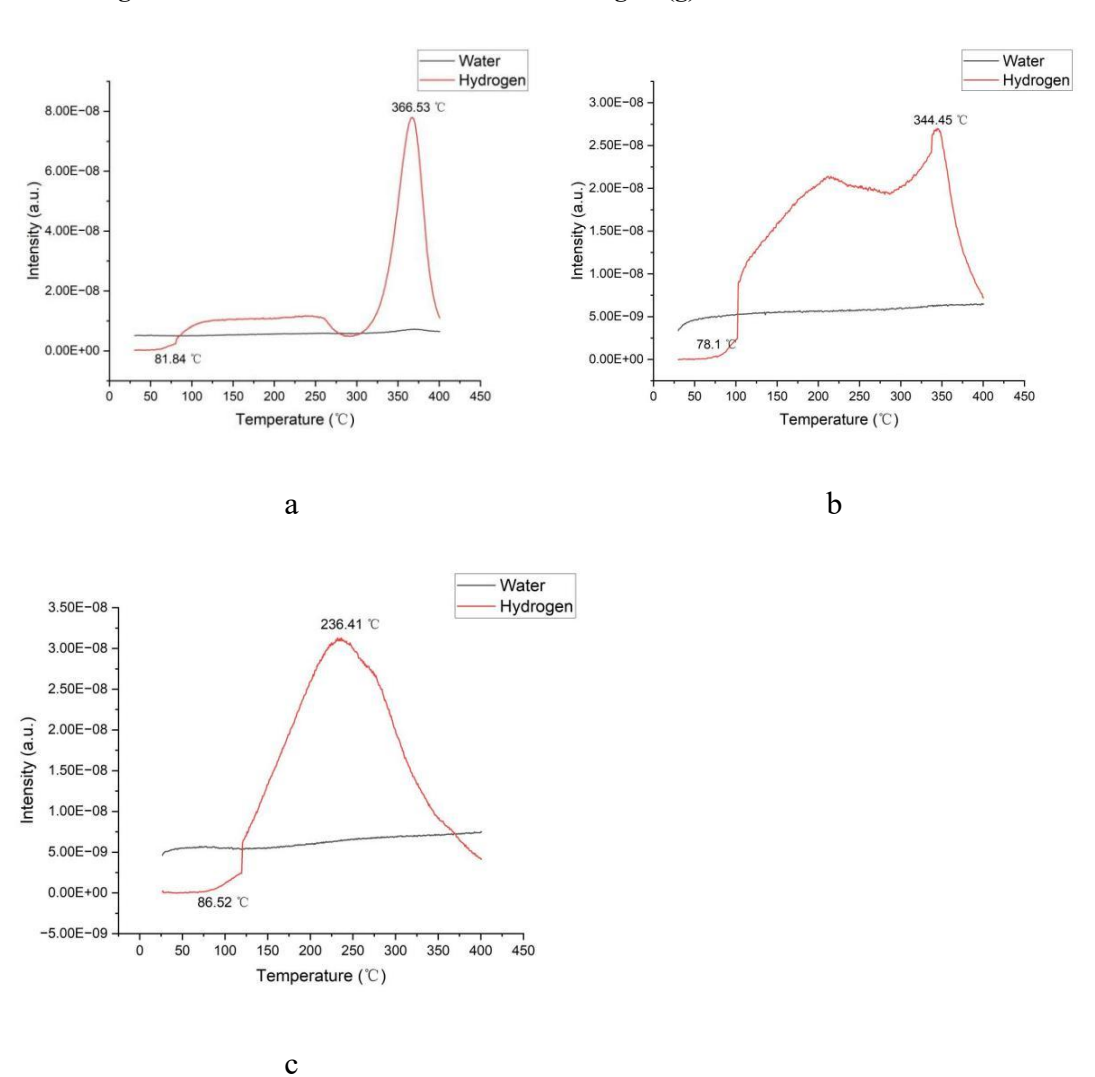


Figure A4-15: Mass spectrometry output for water (m/z = 18; black) and hydrogen (m/z = 2; red) as a function of temperature for ball-milled 1:x NaAlH₄:NaOH (1h, 300rpm) with molar ratio of (a)x=2 (b)x=3 (c))x=4 on heating from 35-400 °C at 5 °C min⁻¹ under flowing Ar(g).

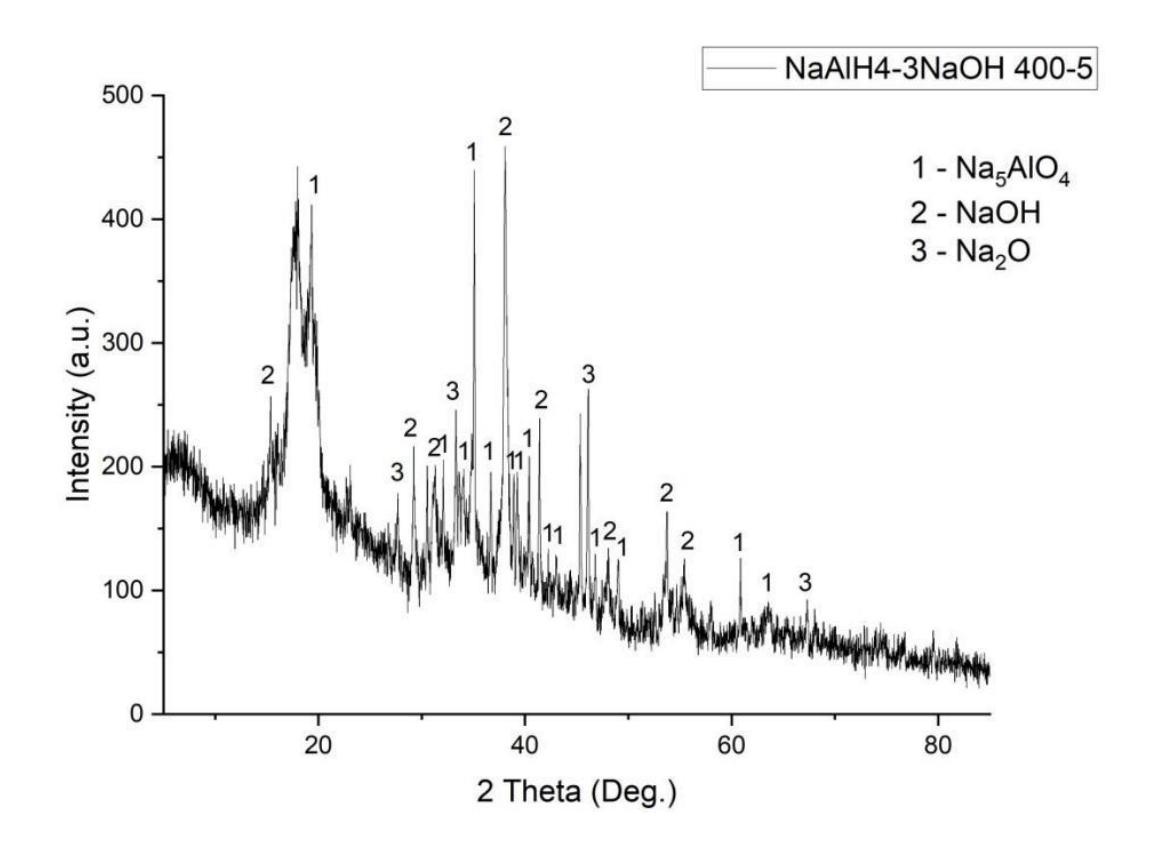


Figure A4-16: PXD pattern of ball-milled 1:3 NaAlH₄:NaOH (4h, 400rpm) after heating to 400 °C under flowing Ar(g). (1 represent Na₅AlO₄; 2 represent NaOH; 3 represent Na₂O)

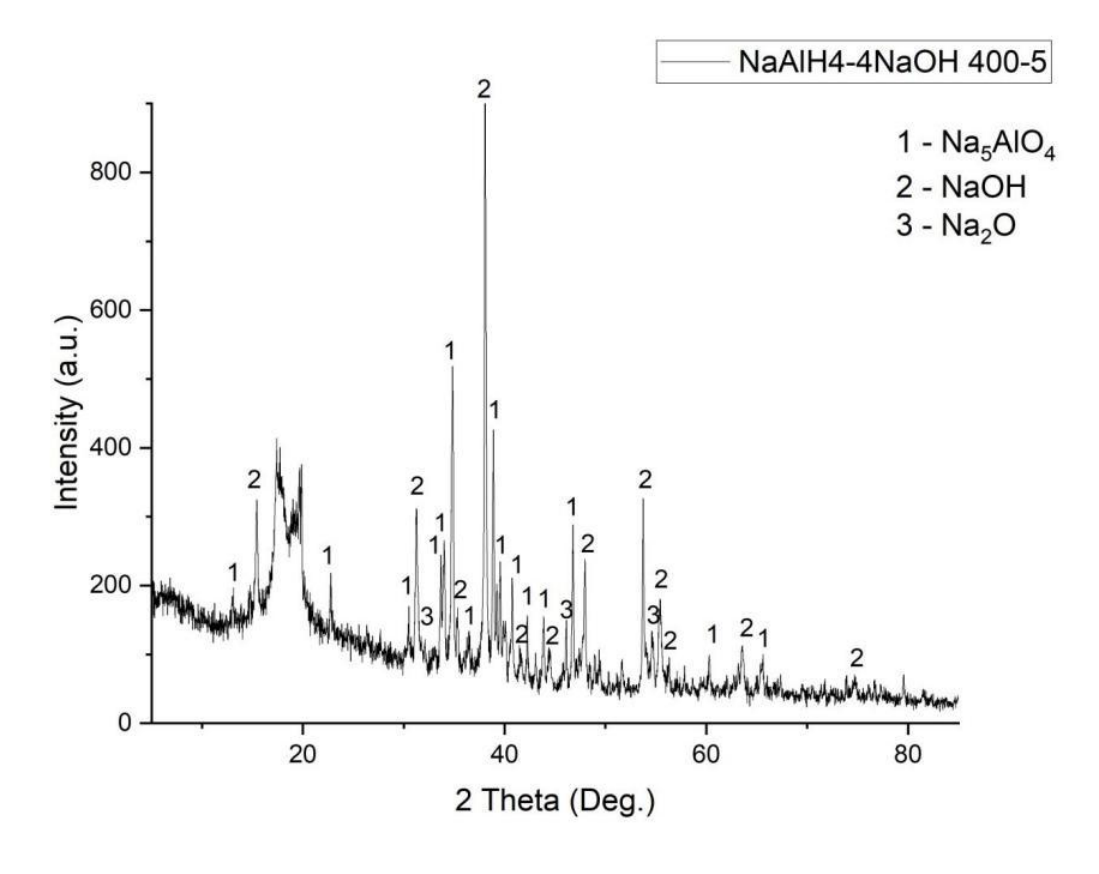


Figure A4-17: PXD pattern of ball-milled 1:4 NaAlH₄:NaOH (2h, 400rpm) after heating to 400 °C under flowing Ar(g). (and cooling to room temperature) (1 represent Na₅AlO₄; 2 represent NaOH; 3 represent Na₂O)

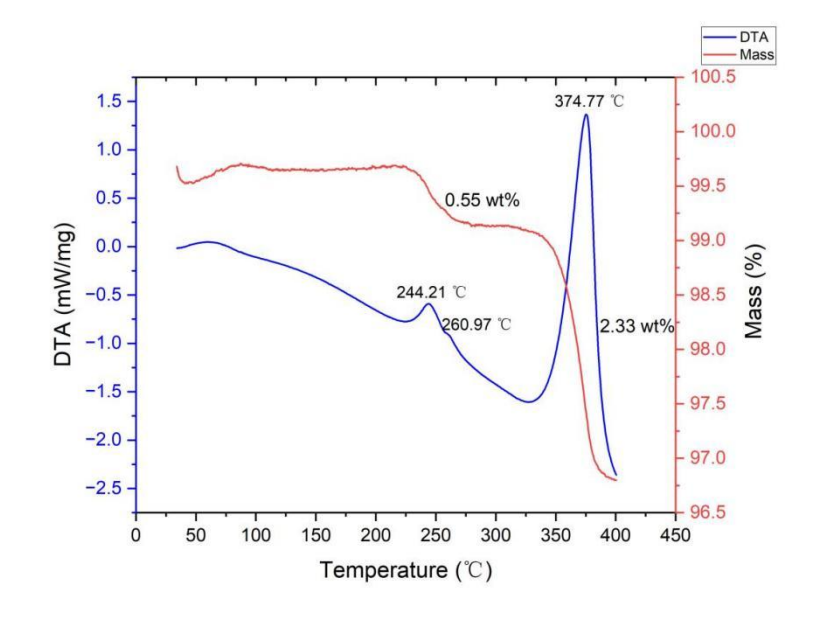


Figure A4-18: TG-DTA pattern of the dehydrogenation of Na_3AlH_6 -1NaOH from room temperature to 400 °C with 5 °C/min.

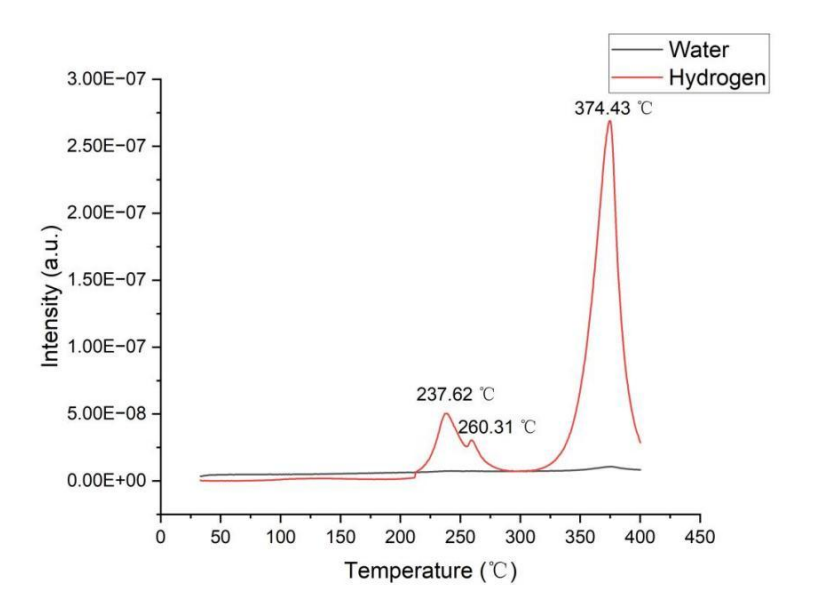


Figure A4-19: Mass spectra for water and hydrogen vs. temperature for Na₃AlH₆– 1NaOH on heating from room temperature to 400 $^{\circ}$ C at 5 $^{\circ}$ C/min.

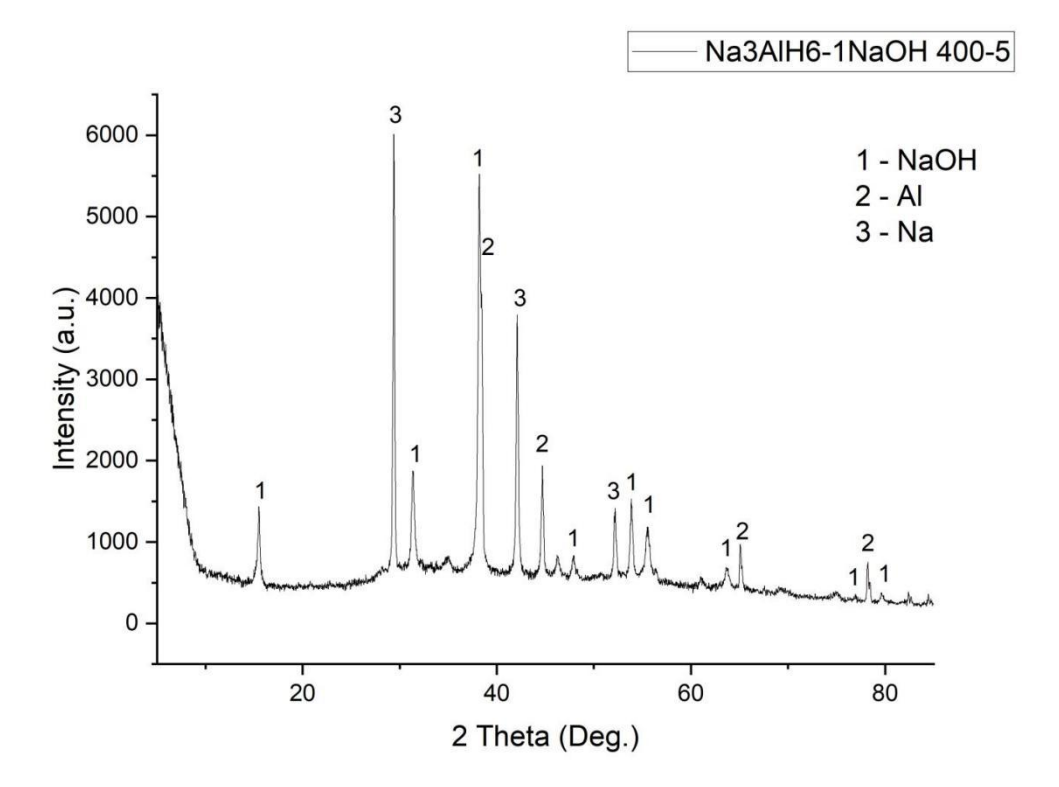


Figure A4-22: PXD pattern of ball-milled (2h) Na₃AlH₆-1NaOH after heating to 400 °C.

6.Ca₄Mg₃H₁₄-NaH dehydrogenation reaction

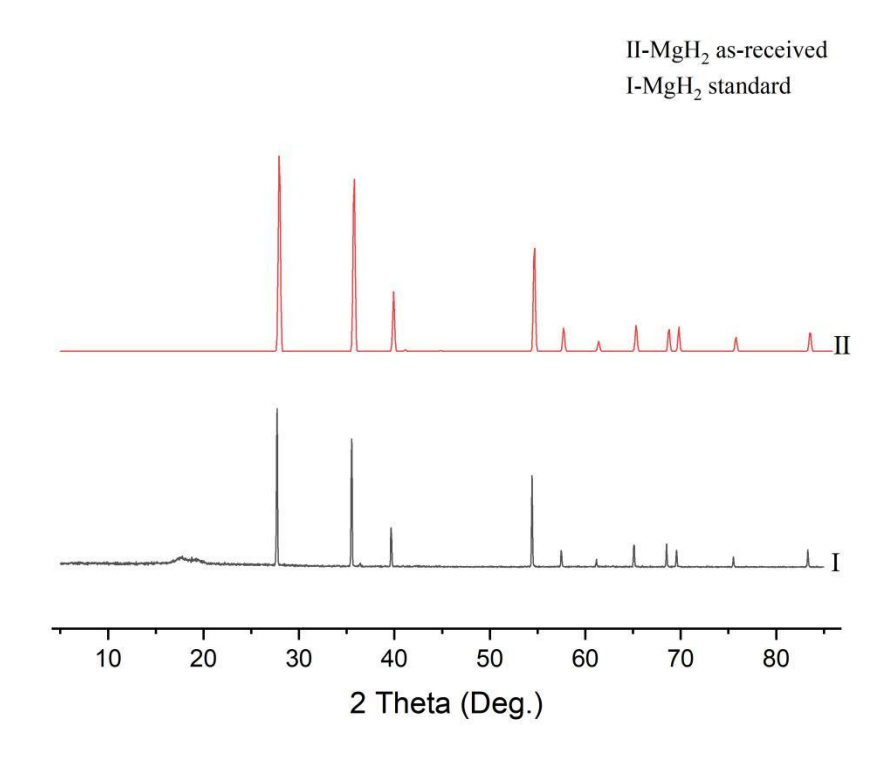


Figure A6-1: PXD pattern of MgH2 as-received(II) and standard MgH2(I)

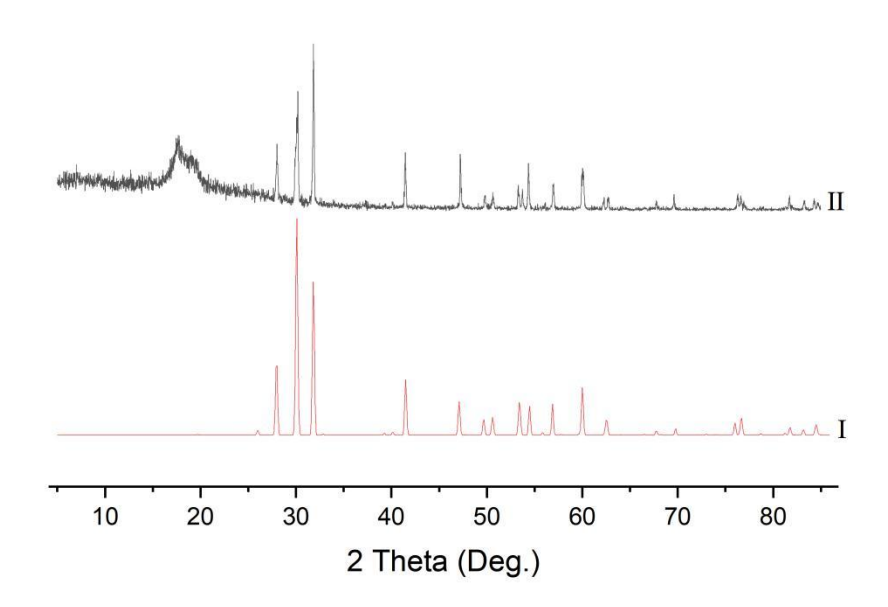


Figure A6-2: PXD pattern of CaH2 as-received(II) and standard CaH2(I)

7. Guanidine-MgH₂

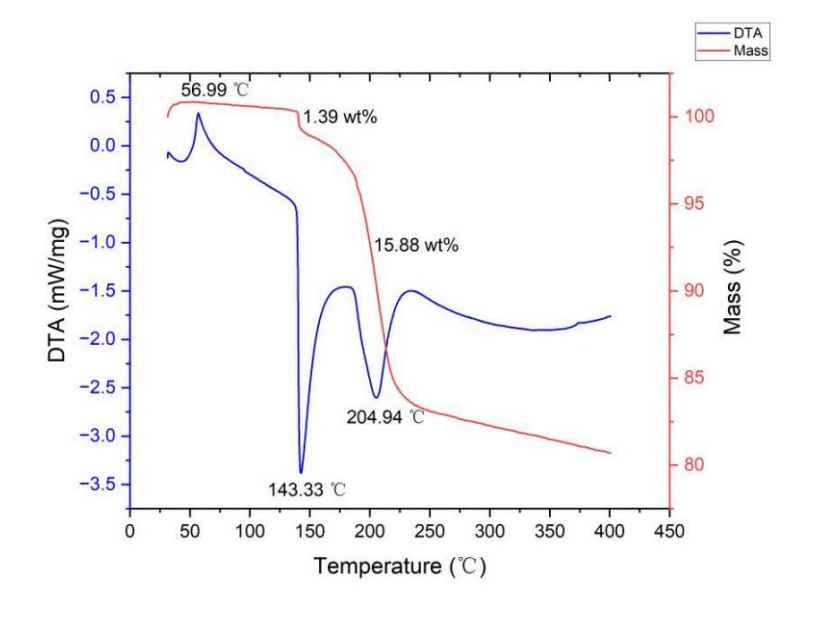


Figure A7-1: TG-DTA pattern of hand-mixed guanidine-MgH $_2$ (1 : 2.5) on heating from room temperature to 400 °C at 2 °C/min.

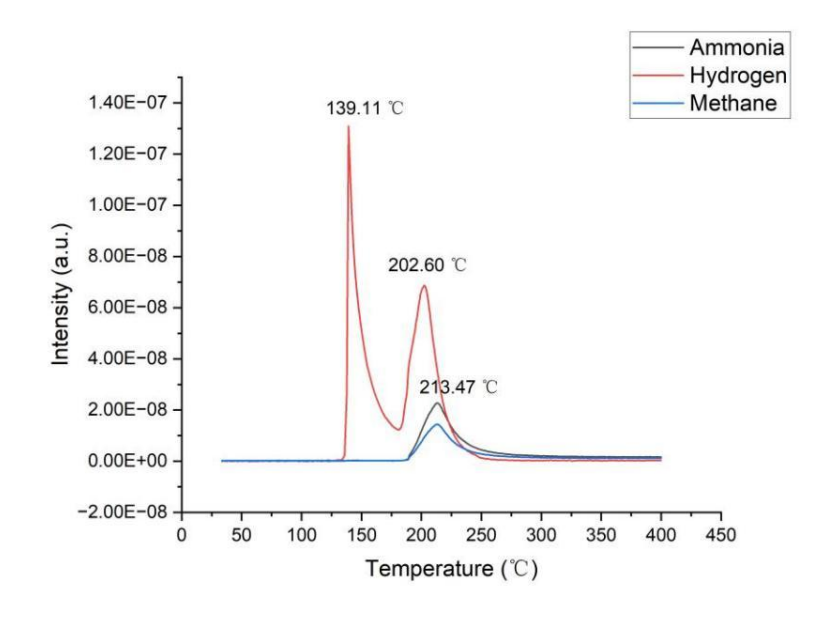


Figure A7-2: Mass spectra for water and hydrogen vs. temperature for hand-mixed guanidine-MgH₂ (1:2.5) on heating from room temperature to 400 $^{\circ}$ C at 2 $^{\circ}$ C/min.

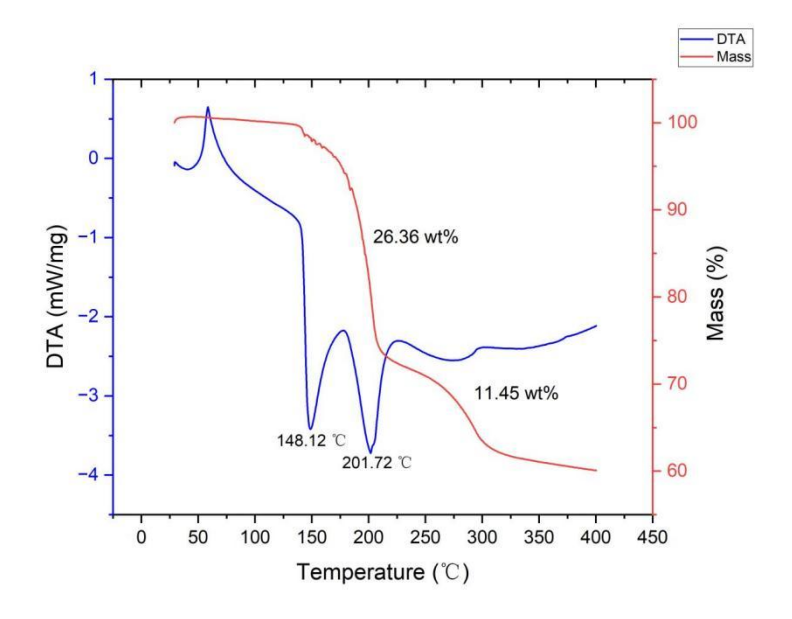


Figure A7-3: TG-DTA pattern of ball-milled (100 rpm, 1h) CH_5N_3 -MgH $_2$ (1 : 1) on heating from room temperature to 400 °C at 5 °C/min.

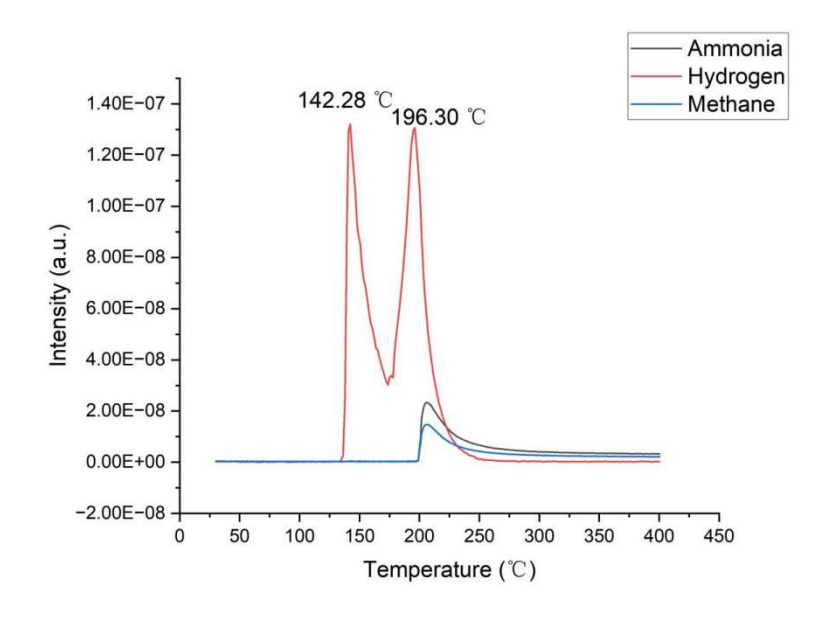


Figure A7-4: Mass spectra for water and hydrogen vs. temperature for ball-milled (100 rpm, 1h) CH_5N_3 -MgH₂ (1:1) on heating from room temperature to 400 °C at 5 °C/min